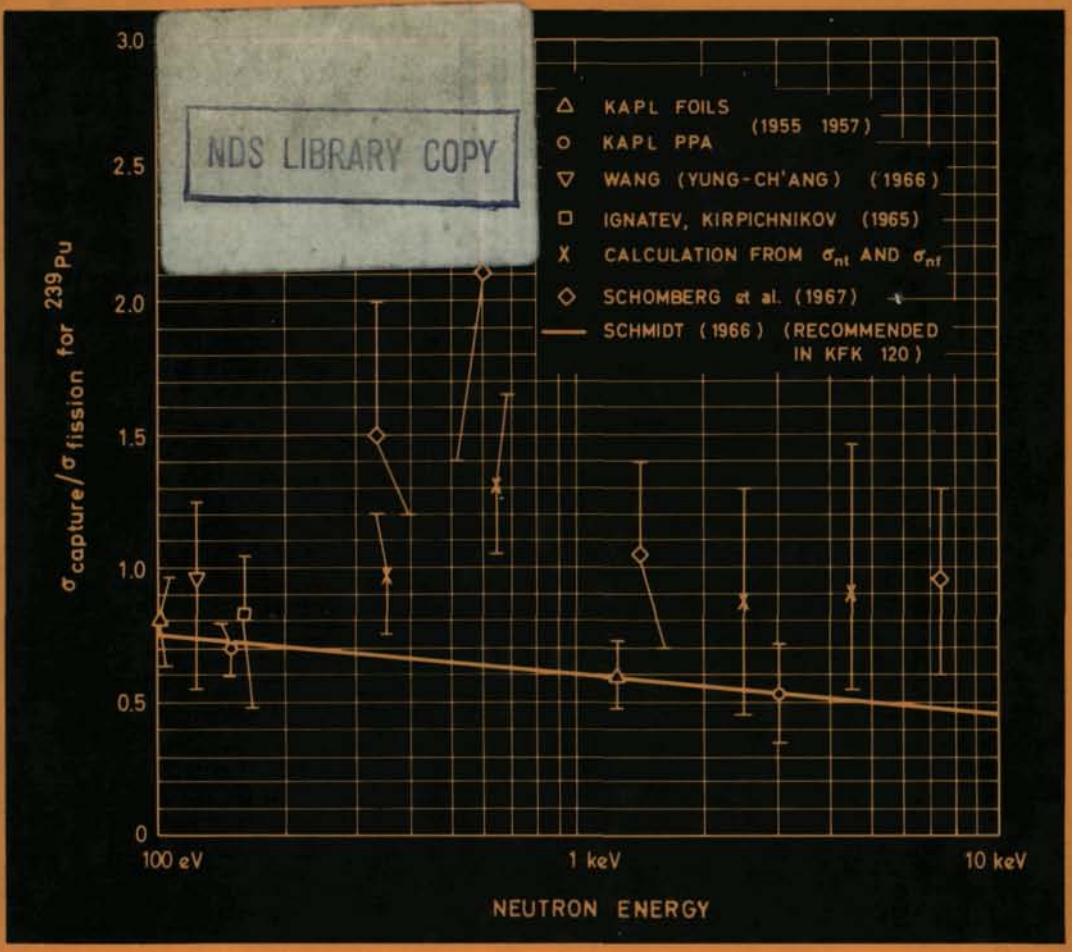

FAST REACTOR PHYSICS

PROCEEDINGS OF A SYMPOSIUM, KARLSRUHE, 30 OCTOBER - 3 NOVEMBER 1967

VOL. II

INTERNATIONAL ATOMIC ENERGY AGENCY, VIENNA, 1968

FAST REACTOR PHYSICS

VOL. II

The following States are Members of the International Atomic Energy Agency:

AFGHANISTAN
ALBANIA
ALGERIA
ARGENTINA
AUSTRALIA
AUSTRIA
BELGIUM
BOLIVIA
BRAZIL
BULGARIA
BURMA
BYELORUSSIAN SOVIET SOCIALIST REPUBLIC
CAMBODIA
CAMEROON
CANADA
CEYLON
CHILE
CHINA
COLOMBIA
CONGO, DEMOCRATIC REPUBLIC OF
COSTA RICA
CUBA
CYPRUS
CZECHOSLOVAK SOCIALIST REPUBLIC
DENMARK
DOMINICAN REPUBLIC
ECUADOR
EL SALVADOR
ETHIOPIA
FINLAND
FRANCE
GABON
GERMANY, FEDERAL REPUBLIC OF
GHANA
GREECE
GUATEMALA
HAITI
HOLY SEE
HUNGARY
ICELAND
INDIA
INDONESIA
IRAN
IRAQ
ISRAEL
ITALY
IVORY COAST
JAMAICA
JAPAN
JORDAN
KENYA
KOREA, REPUBLIC OF
KUWAIT
LEBANON
LIBERIA
LIBYA
LUXEMBOURG
MADAGASCAR
MALI
MEXICO
MONACO
MOROCCO
NETHERLANDS
NEW ZEALAND
NICARAGUA
NIGERIA
NORWAY
PAKISTAN
PANAMA
PARAGUAY
PERU
PHILIPPINES
POLAND
PORTUGAL
ROMANIA
SAUDI ARABIA
SENEGAL
SIERRA LEONE
SINGAPORE
SOUTH AFRICA
SPAIN
SUDAN
SWEDEN
SWITZERLAND
SYRIAN ARAB REPUBLIC
THAILAND
TUNISIA
TURKEY
UGANDA
UKRAINIAN SOVIET SOCIALIST REPUBLIC
UNION OF SOVIET SOCIALIST REPUBLICS
UNITED ARAB REPUBLIC
UNITED KINGDOM OF GREAT BRITAIN AND NORTHERN IRELAND
UNITED STATES OF AMERICA
URUGUAY
VENEZUELA
VIET-NAM
YUGOSLAVIA

The Agency's Statute was approved on 23 October 1956 by the Conference on the Statute of the IAEA held at United Nations Headquarters, New York; it entered into force on 29 July 1957. The Headquarters of the Agency are situated in Vienna. Its principal objective is "to accelerate and enlarge the contribution of atomic energy to peace, health and prosperity throughout the world".

Printed by the IAEA in Austria

May 1968

PROCEEDINGS SERIES

FAST REACTOR PHYSICS

PROCEEDINGS OF A SYMPOSIUM ON
FAST REACTOR PHYSICS AND RELATED
SAFETY PROBLEMS
HELD BY THE
INTERNATIONAL ATOMIC ENERGY AGENCY
IN KARLSRUHE, 30 OCTOBER - 3 NOVEMBER, 1967

In two volumes

VOL. II

INTERNATIONAL ATOMIC ENERGY AGENCY
VIENNA, 1968

FAST REACTOR PHYSICS
(Proceedings Series)

ABSTRACT. Proceedings of a Symposium organized by the IAEA and held in Karlsruhe, 30 October - 3 November 1967. The meeting was attended by 183 scientists from 23 countries and three international organizations.

Contents: (Vol.I) Review of national programmes (5 papers); Nuclear data for fast reactors (12 papers); Experimental methods (3 papers); Zoned systems (7 papers); Kinetics (7 papers). (Vol.II) Fast critical experiments (8 papers); Heterogeneity in fast critical experiments (5 papers); Fast power reactors (13 papers); Fast pulsed reactors (3 papers); Panel discussion.

Each paper is in its original language (50 English, 11 French and 3 Russian) and is preceded by an abstract in English with a second one in the original language if this is not English. Discussions are in English.

(Vol.I: 551 pp., Vol.II: 589 pp., 16 x 24 cm, paper-bound, 434 figures)

Price: Vol.I: US $11.00; £4.11.8
Vol.II: US $12.00; £5. 5.0

FAST REACTOR PHYSICS
IAEA, VIENNA, 1968
STI/PUB/165

FOREWORD

The Symposium on Fast Reactor Physics and Related Safety Problems, arranged by the International Atomic Energy Agency, was held at Karlsruhe from 30 October to 3 November, 1967. One hundred and eighty-three scientists, representing 23 different countries and three international organizations, attended. Sixty-three papers were presented.

It became clear that participants were confident that the fast reactor would become a major source of nuclear power and it was to be expected that the papers would show determined progress towards that goal. Three separate trends can be discerned.

First, much attention is being given to the heterogeneity problem and several different methods of calculation are being developed. Such techniques must be effective before it is possible to validate a cross-section set with the results of critical experiments and then to use it to do calculations, for, say, a power reactor with fuel in an entirely different physical form.

Second, several laboratories are using zone techniques to do effective fast-reactor experiments in thermal reactors. Although this calls for a high level of theoretical and experimental competence, it is well worthwhile, in view of the high cost of all-fast systems.

Third, much work, both theoretical and experimental, has been done in recent years on steam-cooled fast reactors, particularly in Europe. However, despite the apparent advantage of using heavy steam to reduce troublesome coolant void effects, very little attention appears to have been given to this point over the same period.

One of the most significant features of the meeting was the accumulating evidence that the parameter α ($\sigma_{capture}/\sigma_{fission}$) for ^{239}Pu in the 1-keV region was substantially higher than had hitherto been thought. This shift has serious economic implications for many fast-reactor designs at present under consideration, particularly those cooled by steam and those using oxide fuel. In fact, any plutonium-burning reactor might be less effective than previous calculations had led one to believe.

In view of the interest shown in this point, an impromptu panel discussion was organized on the last day of the symposium to discuss the new information. The group of experts considered three aspects of the problem: the best α values to use; implications of the increased α value; and ways of improving the existing knowledge. A record of this panel discussion is printed at the end of this book, which contains the full proceedings of the symposium.

For the success of the meeting thanks are due in large measure to the staff of the Kernforschungszentrum Karlsruhe, whose hospitality and help were greatly appreciated by all participants.

EDITORIAL NOTE

The papers and discussions incorporated in the proceedings published by the International Atomic Energy Agency are edited by the Agency's editorial staff to the extent considered necessary for the reader's assistance. The views expressed and the general style adopted remain, however, the responsibility of the named authors or participants.

For the sake of speed of publication the present Proceedings have been printed by composition typing and photo-offset lithography. Within the limitations imposed by this method, every effort has been made to maintain a high editorial standard; in particular, the units and symbols employed are to the fullest practicable extent those standardized or recommended by the competent international scientific bodies.

The affiliations of authors are those given at the time of nomination.

The use in these Proceedings of particular designations of countries or territories does not imply any judgement by the Agency as to the legal status of such countries or territories, of their authorities and institutions or of the delimitation of their boundaries.

The mention of specific companies or of their products or brand-names does not imply any endorsement or recommendation on the part of the International Atomic Energy Agency.

CONTENTS OF VOL. II

FAST CRITICAL EXPERIMENTS (Session VI)

HETEROGENEITY IN FAST CRITICAL EXPERIMENTS
(Session VII, Part 1)

FAST POWER REACTORS
(Session VII, Part 2, Session VIII, and Session IX, Part 1)

FAST PULSED REACTORS (Session IX, Part 2)

FAST CRITICAL EXPERIMENTS

(Session VI)

Chairman: E. HELLSTRAND

MASURCA 1-A ET 1-B – RESULTATS PRELIMINAIRES

J. KREMSER, M. BARBERGER*, J.G. BRUNA, J.P. BRUNET, J.C. MOUGNIOT, A.P. SCHMITT ET P. VERRIERE
CEA, CENTRE D'ETUDES NUCLEAIRES DE CADARACHE, FRANCE

Abstract — Résumé

MASURCA 1-A AND 1-B-PRELIMINARY RESULTS. The MASURCA fast-neutron critical model at Cadarache went critical in December 1966 with a plutonium configuration, using graphite as diluent so as to obtain a neutron spectrum lying within the spectral range of high-power fast reactors. The authors describe the construction of the first core, composed of the MASURCA 1-A lattice using a U-Pu-Fe alloy with 25% Pu, and also their experimental techniques. Spectral index measurement data and reactivity coefficients for various materials are quoted. The material buckling value of the assembly was determined experimentally using spatial distributions for various reaction rates. Some measurement data are compared with the corresponding theoretical values calculated from transport theory or by a Monte Carlo method. The paper ends with an analysis of the causes of error and indicates improvements which should be made in experimental methods and in interpretation of the measurements.

MASURCA 1-A ET 1-B – RESULTATS PRELIMINAIRES. La maquette critique à neutrons rapides de Cadarache MASURCA a divergé en décembre 1966 sur une configuration au plutonium, utilisant le graphite comme diluant afin d'obtenir un spectre de neutrons se situant dans la gamme des spectres de réacteurs rapides de puissance élevée. La réalisation du premier cœur, constitué par le réseau MASURCA 1-A utilisant l'alliage U-Pu-Fe à 25% de plutonium, est décrite ainsi que les techniques expérimentales utilisées. On présente les résultats des mesures d'indices de spectre et de coefficients de réactivité de différents matériaux. La valeur du laplacien matière de l'assemblage a été déterminée expérimentalement à partir des distributions spatiales de divers taux de réaction. Certains résultats de mesures sont comparés à leur valeur calculée en théorie du transport ou à l'aide d'une méthode de Monte-Carlo. En conclusion, on présente une analyse de causes d'erreurs et des améliorations à apporter aux méthodes expérimentales ainsi qu'à l'interprétation des mesures.

1. MASURCA 1-A: PRESENTATION ET DESCRIPTION (fig. 1 et 2)

L'installation pour maquettes critiques à neutrons rapides MASURCA fait partie de l'ensemble des dispositifs expérimentaux construits par l'Association Euratom-CEA pour l'étude et le développement de la filière des réacteurs à neutrons rapides. Cet ensemble comprend, outre MASURCA, le réacteur source HARMONIE et le réacteur rapide RAPSODIE. Il est implanté au sud-est du Centre d'études nucléaires de Cadarache.

MASURCA est destinée aux études neutroniques expérimentales sur des assemblages critiques rapides, exploités à puissance nulle et utilisant principalement le plutonium comme combustible. On en trouvera une description détaillée dans les références [1] et [2]. Rappelons qu'il s'agit d'une machine monobloc à axe vertical. Les éléments de simulation, qui sont, soit des réglettes de section carrée pour les matériaux inertes, soit

* Détaché par l'EDF auprès du CEA.

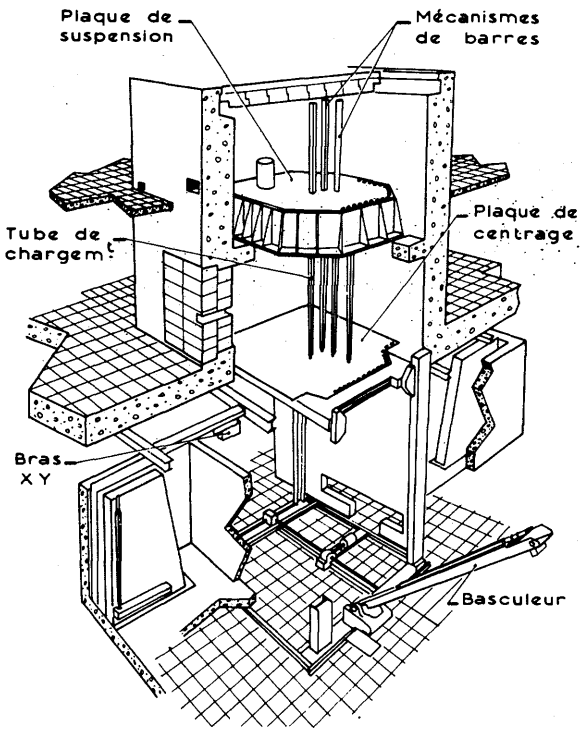

FIG.1. MASURCA, vue d'ensemble.

des billettes de section circulaire pour le combustible, et dont les dimensions sont de 12,7 mm pour le côté ou diamètre (1/2"), et 101,6 ou 203,2 mm pour la longueur (4" ou 8"), remplissent par paquets de 8×8= 64 éléments des tubes d'acier inoxydable de section carrée (a = 105 mm). Ces tubes, ainsi chargés, sont suspendus par la «tête» à une taque très rigide et forment un faisceau vertical de tubes parallèles constituant l'assemblage. En fin de chargement une plaque de centrage des «pieds de tubes» vient assurer un positionnement précis de l'ensemble. Des tubes spéciaux, mobiles, répartis dans le faisceau et jouant le rôle de barre de sécurité ou de pilotage, permettent le contrôle de l'évolution neutronique dans cet assemblage. L'ensemble est refroidi et sa température régulée par circulation d'air dans les tubes autour des colonnes de combustible.

Le réacteur est entouré d'une protection biologique en béton lourd, partiellement amovible, permettant de travailler dans l'enceinte étanche lorsqu'il fonctionne à sa puissance nominale (500 W).

Les critères qui ont été appliqués à la définition du cœur de démarrage sont:

- nombre minimal de types de réglettes pour la simplicité du chargement,
- spectre des neutrons dans la gamme de la filière des réacteurs rapides de puissance,

- volume critique > 200 litres pour permettre l'insertion dans le cœur des quatre barres de sécurité (deux barres lentes et deux barres rapides),
- masse critique voisine de l'inventaire disponible en combustible plutonium, soit 175 kg.

On a donc été conduit à la définition de la cellule type 1-A de quatre réglettes: une d'alliage U-Pu-Fe pour trois de graphite.

Le cœur a une hauteur de $6 \times 10,16 = 60,96$ cm et un rayon critique moyen de 37,2 cm. Il est entouré d'une couverture en uranium appauvri à 0,414% de 18 cm d'épaisseur moyenne, et d'un écran d'acier de 30 cm d'épaisseur moyenne qui renforce la protection biologique.

Le chargement critique initial est celui de la figure 3 comportant 620 colonnes combustibles, dont 40 d'uranium enrichi à 30%. A ce moment, le canal radial situé dans le plan médian du cœur, dont la section hors tout équivaut à celle d'une cellule de quatre réglettes, ainsi que les différents canaux verticaux ayant chacun la section d'une réglette, sont vides.

Parallèlement à l'expérience 1-A on a entrepris l'étude du milieu 1-B, pour lequel le combustible U-Pu-Fe est remplacé par de l'uranium enrichi à 30%, dans une expérience exponentielle utilisant HARMONIE comme source de neutrons. Il est prévu dans MASURCA de passer du milieu 1-A au milieu 1-B par substitutions progressives.

2. MASSE CRITIQUE

2.1. Masse critique expérimentale

Avec les canaux remplis de graphite dans la zone cœur et d'acier partout ailleurs la configuration critique de référence comporte 578 colonnes de combustible Pu et 40 colonnes de combustible ^{235}U.

Un certain nombre de corrections expérimentales sont à effectuer pour déterminer la masse critique du cylindre homogène équivalent, seule comparable directement avec les calculs.

2.1.1. Equivalence uranium-plutonium à la périphérie du cœur

Le remplacement du combustible uranium par du combustible plutonium se traduirait par une perte sensible de réactivité provenant essentiellement du fait que les masses de matière fissile contenues dans une réglette ne sont pas équivalentes: 70 g environ de ^{235}U contre 46 g environ de plutonium fissile pour une réglette cylindrique de 4" de longueur.

Des expériences de substitution ont permis d'évaluer la perte de réactivité globale consécutive au remplacement des 40 colonnes de combustible uranium, soit

$$\rho_1 = (-234 \pm 3)\, 10^{-5}\ \frac{\Delta K}{K}$$

Au cours de ces expériences le rapport $(\Delta K/K)/(\Delta M/M)$ donnant l'équivalence en réactivité de la variation relative de masse critique correspondant à une légère variation du rayon du cœur a été évalué à $0,193 \pm 0,003$.

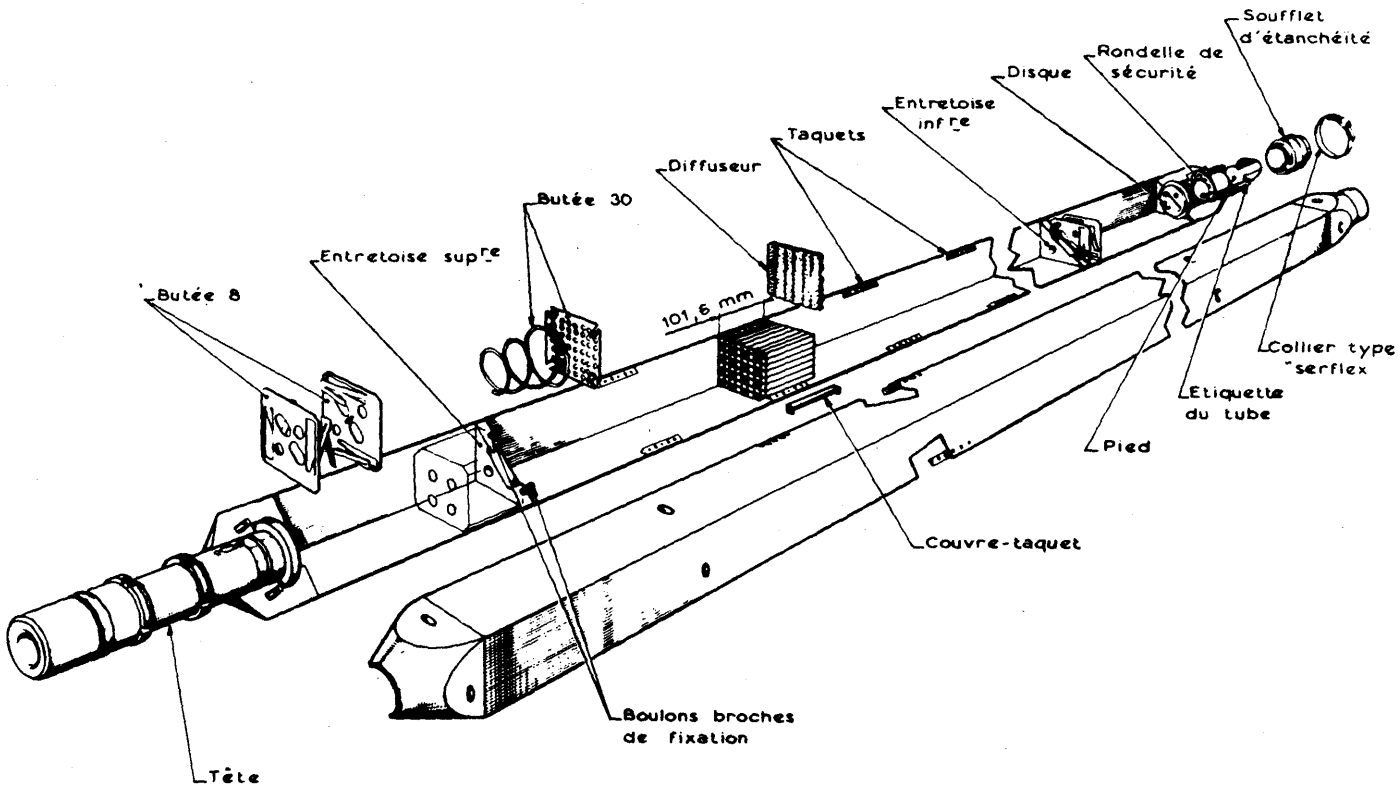

FIG.2. MASURCA, tube de chargement.

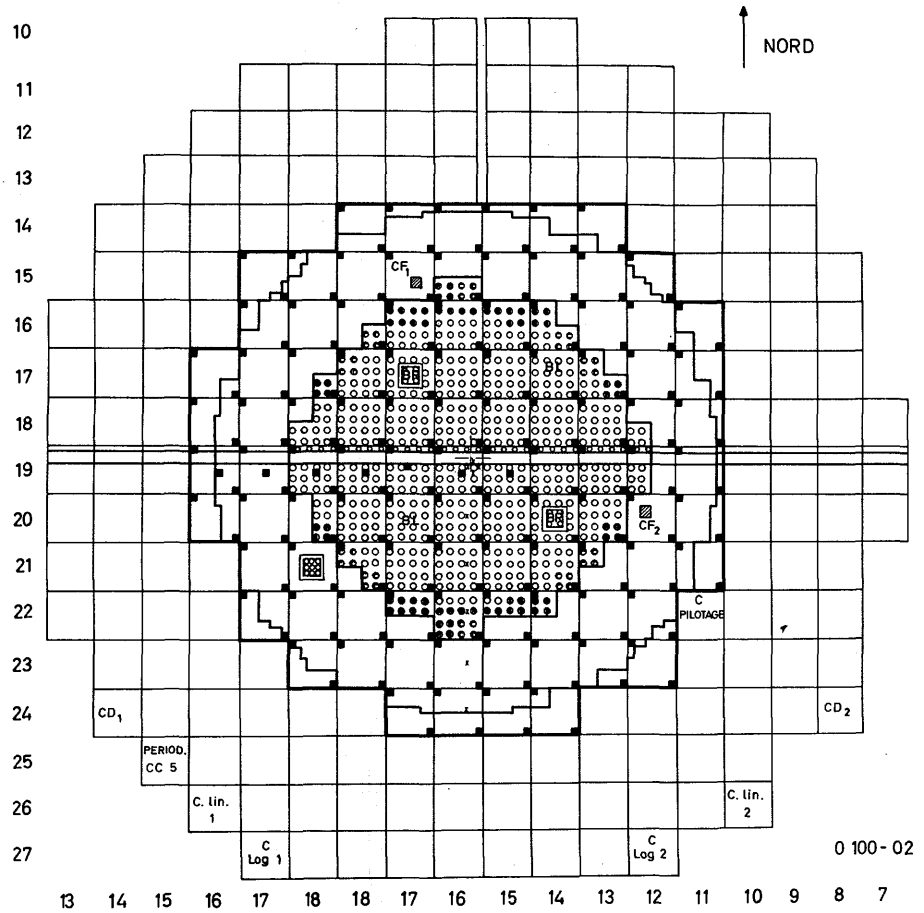

FIG.3. MASURCA, plan de chargement.

2.1.2. Effet de cylindrisation du cœur

Il a été déterminé par application d'une loi linéaire de l'effet en réactivité correspondant au remplacement d'assemblages cœur par des assemblages couverture ou réciproquement au voisinage de l'interface. La détermination expérimentale de cette loi a donné

$$\Delta\rho = [4,44 - 0,58(r - r_0)]\, 10^{-5} \frac{\Delta K}{K} / cm^2$$

$r - r_0$ = distance à l'interface du centre de gravité de l'assemblage ou de la fraction d'assemblage substitué.

Par sommation algébrique sur tout le pourtour du cœur des poids des éléments de surface situés au-delà et en-deçà du périmètre circulaire moyen on a trouvé pour l'effet de cylindrisation

$$\rho_2 = (+252 \pm 30)\, 10^{-5} \frac{\Delta K}{K}$$

Le tableau I récapitule ces données.

TABLEAU I. EFFETS EN REACTIVITE (10^{-5} $\Delta K/K$)

Substitution du combustible uranium par du combustible plutonium	- 234 ± 3
Cylindrisation du cœur	+ 252 ± 30
Correction de barre de pilotage	- 41 ± 0,5
Bilan	- 23 ± 30

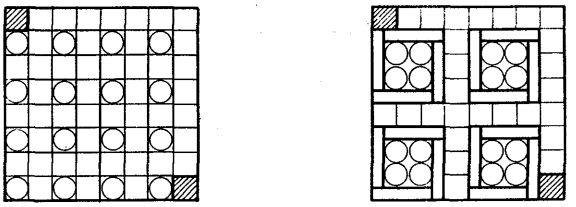

FIG.4. MASURCA, principe du chargement des colonnes de combustible.

Le cylindre hétérogène équivalent compterait donc une colonne combustible supplémentaire et, compte tenu du fait que les perturbations dues aux différents canaux ainsi qu'aux structures des barres rapides se compensent en moyenne à une colonne de combustible près, on prendra le nombre critique de colonnes combustibles au plutonium du cylindre hétérogène équivalent égal à 619 ± 2, soit 170 ± 0,6 kg de plutonium-239 + 241.

$$R_c = 37,2 \text{ cm} \quad V_c = 265 \text{ litres}$$

2.1.3. Effet d'hétérogénéité

C'est de loin la correction la plus importante sur la masse critique mesurée expérimentalement. Elle a été évaluée de la façon suivante: dans un tube de chargement les colonnes de combustible ont été regroupées par quatre conformément à la figure 4. L'effet en réactivité de ce re-

TABLEAU II. COMPOSITIONS
(En 10^{22} atomes/cm^3)

Elément	Cœur	Couverture	Ecran
^{239}Pu	0,16020		
^{240}Pu	0,01495		
^{241}Pu	0,00140		
^{235}U	0,00118	0,01695	
^{238}U	0,52386	4,1668	
Fer	0,54712	0,34864	6,1784
Chrome	0,13855	0,09106	1,6138
Nickel	0,06829	0,15734	0,6356
Carbone	5,6464		

groupement a été mesuré en fonction de la position du tube dans la maquette. On a vérifié ensuite l'additivité de cet effet en opérant le même regroupement de combustible dans quatre tubes adjacents au centre du réacteur. Par extension à l'ensemble du cœur on observerait un gain de réactivité de $(1140 \pm 100)\, 10^{-5}\ \Delta K/K$.

L'extrapolation au milieu homogène fondée sur des études théoriques [3] conduirait à un effet d'hétérogénéité de l'ordre de 2,5% en réactivité, donc à une masse critique homogène de 192 kg environ de plutonium fissile.

On trouvera ci-dessous les principales caractéristiques géométriques et au tableau II les compositions par zone relatives au réacteur homogène utilisées dans les calculs.

Cœur:	hauteur	60,96 cm
	rayon calculé	38,05 cm
Couverture:	épaisseur radiale	20 cm
	épaisseur axiale	20,32 cm
Ecran:	épaisseur radiale	30 cm
	épaisseur axiale	30,48 cm

2.2. Calculs

Compte tenu de la taille de l'assemblage, les calculs ont été effectués à l'aide de la théorie du transport à une ou deux dimensions dans l'approximation S4. Les sections efficaces utilisées sont les sections à 16 groupes d'Hansen et Roach [4] corrigées pour tenir compte de l'autoprotection des

TABLEAU III. MASSES CRITIQUES (kg)

	MASURCA 1-A		ZEBRA 6-A		ZPR 48	
	Exp.	Calculs	Exp.	Calculs	Exp.	Calculs
Cylindre homogène	192	178	186	183	297	296
Sphère homogène	178	165	174	171		

résonances. Afin de tester la validité de la méthode utilisée, les mêmes calculs ont aussi porté sur les assemblages de spectres voisins, ZEBRA 6-A et ZPR 48. Les résultats figurent au tableau III.

3. MESURES DE TAUX DE REACTION

3.1. Etude de la zone d'équilibre du spectre

Afin de reconnaître l'existence et de préciser l'étendue d'une zone centrale du cœur où le spectre des neutrons est en équilibre, c'est-à-dire où le mode fondamental prédomine, entraînant par voie de conséquence que les sections efficaces effectives moyennées sur l'ensemble de ce spectre et les indices que l'on peut former à partir d'elles sont constants dans cette zone, on a relevé des cartes de taux de fission pour un certain nombre d'isotopes présentant ou non un seuil.

Chaque carte se compose d'une distribution radiale et d'une distribution verticale relevées dans les canaux déjà mentionnés. Les détecteurs utilisés sont des chambres à fissions miniatures cylindriques de 4 mm de diamètre extérieur et dont la surface de dépôt est de l'ordre de 1 cm^2 (longueur du dépôt 1 cm). Deux chambres de ce type, dont l'une nécessairement à ^{235}U, sont montées côte à côte sur une canne coaxiale double solidaire d'un dispositif mécanique de positionnement. Pour les distributions radiales, le canal est rempli de briques de graphite percées en leur centre d'un trou de 13,5 mm de diamètre permettant le passage de la canne; pour les distributions verticales les canaux sont vides.

Parmi ces distributions, les plus caractéristiques sont représentées sur les figures 5, 6 et 7. La courbe 1 de la figure 5 et la courbe continue de la figure 6 représentent les distributions normalisées en leur centre des fissions de ^{235}U et de ^{232}Th respectivement, dans le tube le plus central. Elles se caractérisent par de fortes anomalies au voisinage des points de cote ± 100 mm consistant en une remontée du taux de fission de ^{235}U et une dépression du taux de fission de ^{232}Th se traduisant sur l'indice $^{235}U/^{232}Th$ par des «cornes» de 12% d'amplitude environ.

Ces anomalies ont été attribuées à la présence de bouchons d'acier aux extrémités des réglettes d'alliage combustible U-Pu-Fe, bouchons de 2 mm d'épaisseur à chaque extrémité pour les réglettes courtes (4''), et de 4 mm ou 7 mm d'épaisseur suivant l'extrémité pour les réglettes longues (8''). Dans le cas du tube central chargé en modules longs, l'épaisseur d'acier est donc de 11 mm en moyenne. Elle introduit une discontinuité dans la répartition spatiale des sources de fission et une augmentation locale de la densité de ralentissement.

A noter l'étendue de ces anomalies qui se propagent sur plusieurs centimètres comme il ressort de l'examen de la courbe d'indice de la figure 6, la largeur à mi-hauteur des «cornes» valant 4 cm environ. Ainsi est illustrée brutalement l'importance des effets d'hétérogénéité, qu'il ne faut pas sous-estimer, même dans les réacteurs à neutrons rapides.

En ce qui concerne la distribution radiale (fig. 7) on observe aussi des anomalies, mais de moindre amplitude, au voisinage des parois de tube (2 mm d'acier séparés par 1 mm de vide lorsqu'on passe d'un tube à un autre).

On a vérifié la validité des hypothèses ci-dessus en introduisant dans un calcul de flux en théorie du transport des plaques d'acier à l'endroit des zones de bouchon pour la distribution axiale ainsi que les parois des tubes pour la distribution radiale. L'indice calculé $^{235}U/^{232}Th$ présente bien les anomalies relevées expérimentalement, comme il apparaît sur les courbes discontinues des figures 6 et 7.

Les mêmes phénomènes ont été observés avec la même importance relative des anomalies pour les indices $^{235}U/^{238}U$ et $^{239}Pu/^{238}U$ obtenus avec d'autres couples de chambres à fissions ainsi que pour l'indice capture ^{238}U/fission ^{238}U étudié à l'aide de détecteurs d'activation.

3.2. Mesures du laplacien matière

3.2.1. Définition — Possibilités de mesure

Plaçons-nous dans le cas d'un formalisme multigroupe. L'équation de propagation du flux peut en général s'écrire avec une bonne approximation:

$$\Delta\vec{\phi}(\vec{r}) + M\vec{\phi}(\vec{r}) = 0$$

où $\vec{\phi}(\vec{r}) = \{\varphi_i(\vec{r})\}$, $\varphi_i(\vec{r})$ représentant le flux du groupe i au point $\vec{r}$.

M est une matrice qui, dans une région homogène, ne dépend pas de $\vec{r}$. Elle possède un vecteur propre $\vec{\phi}_1$, dont toutes les composantes sont positives et à qui est associée une valeur propre λ_1. Quand λ_1 est positif nous posons $\lambda_1 = B_m^2$, laplacien matière du milieu.

Le flux $\vec{\phi}(\vec{r})$ peut s'écrire

$$\vec{\phi}(\vec{r}) = \sum_i a_i f_i(\vec{r})\,\vec{\phi}_i$$

où les $\vec{\phi}_i$ sont les vecteurs propres de M associés aux valeurs propres λ_i et les $f_i(\vec{r})$ sont les solutions des équations

$$\Delta f_i(\vec{r}) + \lambda_i f_i(\vec{r}) = 0$$

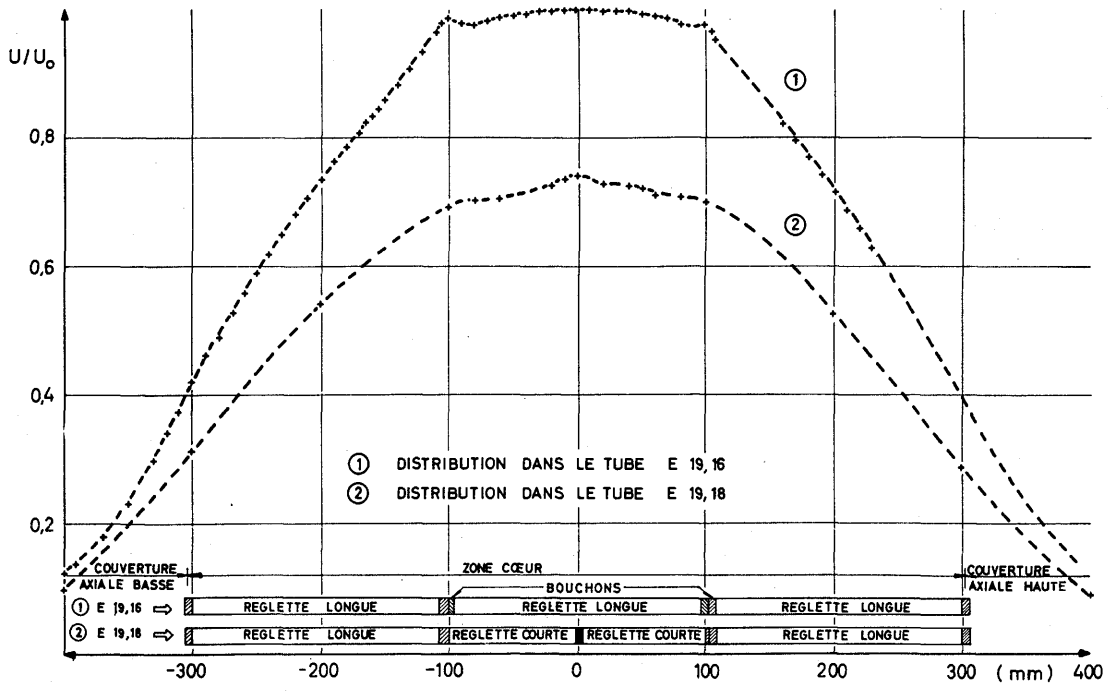

FIG. 5. MASURCA, distribution axiale des fissions de ^{235}U par chambre.

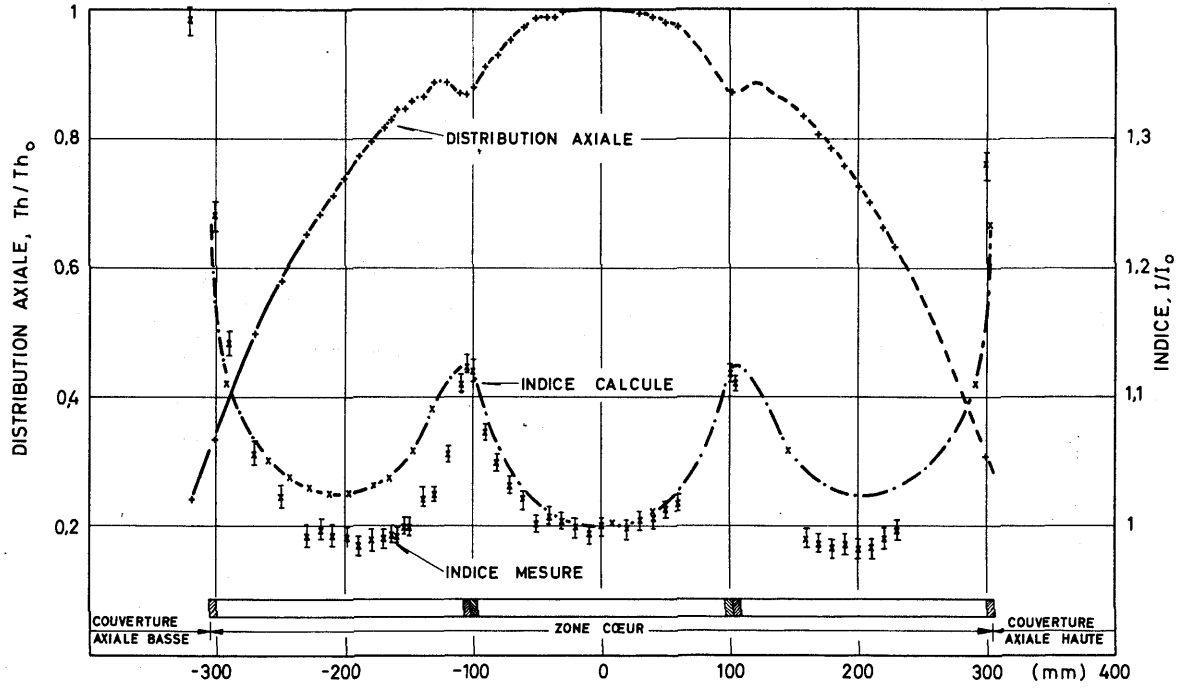

FIG.6. MASURCA, distribution axiale des fissions de ^{232}Th et indice ^{235}U/^{232}Th.

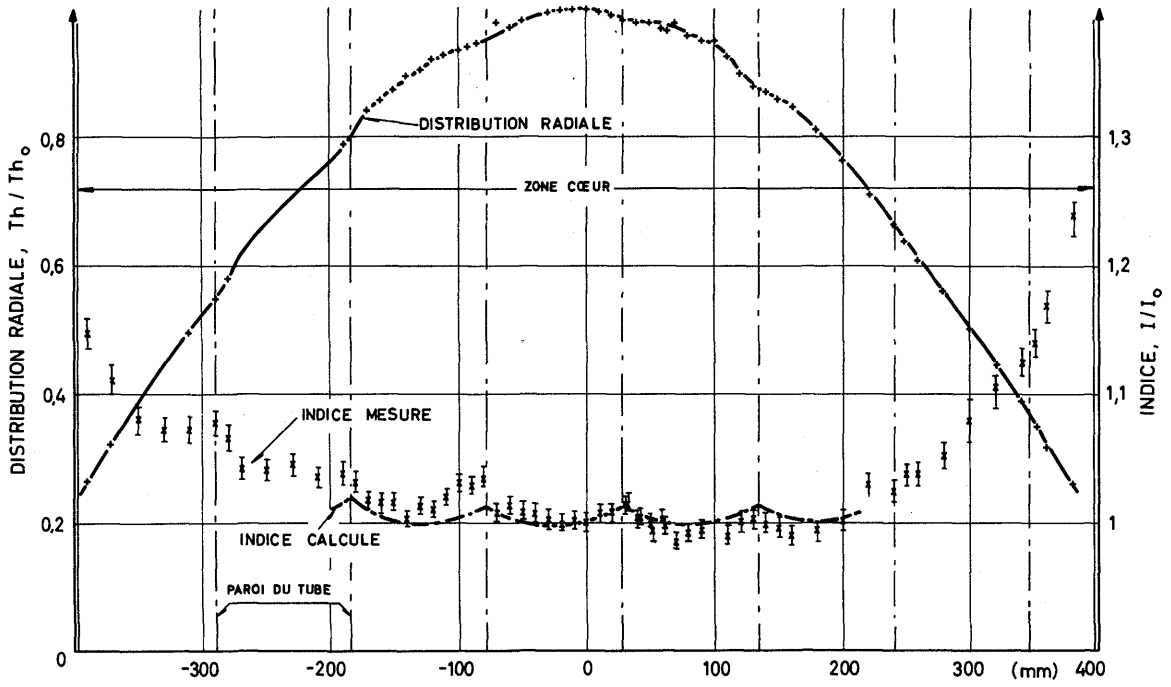

FIG.7. MASURCA, distribution radiale des fissions de ^{232}Th et indice ^{235}U/^{232}Th.

Les constantes a_i dépendent des conditions aux limites imposées à la région considérée.

Dans le cas du cœur de l'assemblage MASURCA 1-A le flux $\vec{\phi}(\vec{r})$ s'écrit

$$\vec{\phi}(r, z) = a_1 f_1(r, z)\,\vec{\phi}_1 + \vec{\epsilon}(r, z)$$

avec

$$\vec{\epsilon}(r, z) = \sum_{i>1} a_i f_i(r, z)\,\vec{\phi}_i$$

Nous avons vérifié par le calcul, en utilisant l'équation de la diffusion et le formalisme multigroupe habituel, que $f_1(r, z)$ se réduisait sur l'axe $r = 0$ et $z = 0$ aux fonctions simples

$$f_1(0, z) = \cos \alpha z$$

$$f_1(r, 0) = J_0(\beta r)$$

malgré la présence d'une couverture.

A cet effet, nous avons utilisé le vecteur $\vec{\phi}_1^*$, vecteur propre de M* et associé à la valeur propre λ_1. Il est orthogonal à $\vec{\epsilon}(r, z)$. La forme analytique de $f_1(r, z)$ s'étudie en formant le produit scalaire

$$\langle \vec{\phi}_1^*, \vec{\phi}(r, z) \rangle = a_1 f_1(r, z) \langle \vec{\phi}_1^*, \vec{\phi}_1 \rangle$$

Le calcul numérique donne pour $\alpha^2 + \beta^2$, calculé grâce à $\vec{\phi}_1^*$, et pour B_m^2, calculé directement comme valeur propre, une différence relative inférieure à $6 \cdot 10^{-4}$, le réacteur étant critique.

$\vec{\phi}_1^*$ serait donc un détecteur insensible, en particulier, aux effets d'interface. Soit $\vec{D} = \{\Sigma_i\}$ la section efficace des détecteurs utilisés en réalité. Leur taux de réaction s'écrit

$$R(r, z) = \langle \vec{D}, \vec{\phi}(r, z) \rangle$$

$$= a_1 f_1(r, z) \langle \vec{D}, \vec{\phi}_1 \rangle + \langle \vec{D}, \vec{\epsilon}(r, z) \rangle$$

L'amplitude de ce dernier terme est variable selon la nature de $\vec{D}$. Il est faible au centre d'un assemblage tel que MASURCA (fig. 8) et ses variations sont lentes dans un assez grand domaine autour du centre.

La mesure de $R(r, z)/R(0, 0)$ permet donc de déterminer α et β, mais avec une erreur systématique variable d'un détecteur à l'autre (tableaux IV et V).

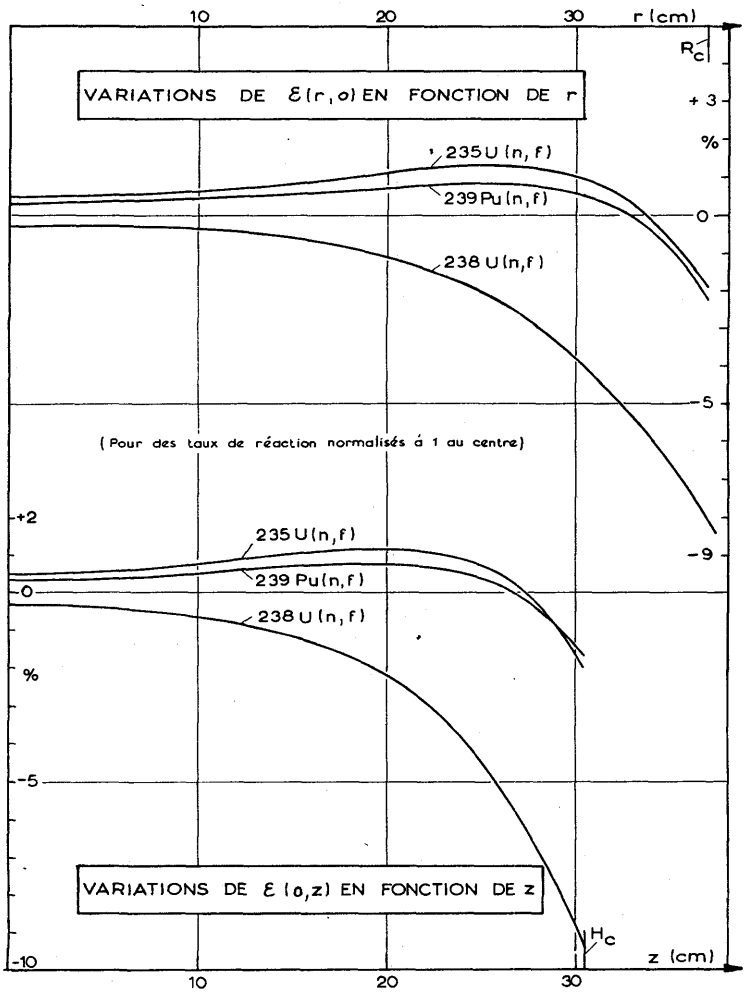

FIG.8. MASURCA, variations de $\epsilon(r,0)$ et de $\epsilon(0,z)$.

3.2.2. Résultats expérimentaux

Laplacien axial α^2

Le laplacien axial α^2 est déterminé en ajustant par une méthode de moindres carrés la fonction cos αz sur les taux de réaction mesurés. Les réactions utilisées sont du type (n, f) avec les isotopes ^{235}U, ^{238}U et ^{232}Th.

Le tableau IV donne les valeurs de α obtenues. La précision $\delta\alpha$ des résultats tient compte des erreurs aléatoires de mesure et correspond à 2σ.

Deux perturbations gênent la détermination de α: l'effet des transitoires dus à l'interface cœur-couverture, et l'effet des bouchons qui ferment les réglettes de combustible.

La première est rendue aussi faible que possible en éliminant les mesures près de l'interface. La perturbation due aux bouchons décroît sensiblement selon une exponentielle avec une constante de relaxation de l'ordre de 3,3 cm. Elle n'atteint donc au milieu des réglettes, aux cotes -20 et 20 cm, que le 1/20 de sa valeur maximale. Pour l'ajustement de cos αz nous n'avons donc retenu que les points de mesure situés près du milieu des réglettes longues. Dans ces conditions, les corrections dues aux bouchons sont faibles ou négligeables.

Le tableau IV montre qu'en dépit de ces précautions la dispersion des résultats est supérieure à leur précision. Les effets de transitoires d'interfaces ne sont donc pas totalement éliminés.

Pour mieux approcher le α qui correspond à la distribution fondamentale du flux nous proposons de former un modèle approché du détecteur idéal en combinant linéairement les taux de réaction de ^{235}U et de ^{238}U (réaction n,f). La courbe d'importance $\vec{\phi}_1^*$ se relève en effet aux énergies supérieures à 1 MeV à cause des fissions de ^{238}U. La combinaison ci-dessus est donc logique. Les coefficients A et B sont calculés en ajustant par moindres carrés $A.\vec{D}(^{235}U)+B.\vec{D}(^{238}U)$ sur $\vec{\phi}^*_1$. On tient compte du flux en pondérant les différentes composantes de groupe par $\vec{\phi}_1$. Cet ajustement dépend du jeu de sections efficaces utilisé, puisque $\vec{\phi}_1$ et $\vec{\phi}_1^*$ sont des vecteurs calculés. Les valeurs par groupe des taux de réaction $\phi_1\phi_1^*$ et $\phi_1\phi_1^*$ approché sont représentées par unité de léthargie à la figure 9.

Les jeux de constantes ABN [5] et Hansen et Roach [4] n'ont pas donné de résultats sensiblement différents pour la nouvelle valeur $\bar{\alpha}$ (voir tableau IV).

Laplacien radial β^2

Le laplacien radial β^2 a été déterminé de manière analogue à α^2 en ajustant $J_0(\beta r)$ sur les taux de fission mesurés à l'aide de ^{235}U, de ^{238}U et de ^{232}Th. Pour tenir compte des perturbations aux interfaces de tubes et à l'interface cœur-couverture, nous avons utilisé les mesures faites au centre des tubes et dans l'intervalle -20, +20 cm.

La dispersion des β obtenus (tableau V) nous conduit à calculer une nouvelle valeur $\bar{\beta}$ en utilisant le vecteur $(\vec{\phi}_1^*)$ approché défini au paragraphe précédent.

Laplacien matière du milieu

Les valeurs du laplacien $B_m^2 = \alpha^2 + \beta^2$ obtenues à l'aide des différents détecteurs sont indiquées au tableau VI.

Nous avons formé deux vecteurs $(\vec{\phi}_1^*)$ approché en calculant les coefficients A et B de la combinaison $A\,\vec{D}(^{235}U)+B\,\vec{D}(^{238}U)$ successivement avec les jeux de sections efficaces Hansen et Roach et ABN. Les valeurs de laplacien qui en résultent sont indiquées avec une précision qui correspond aux erreurs statistiques de mesure. Il faut y ajouter une erreur systématique que le procédé employé ne permet pas de chiffrer, mais qui

TABLEAU IV. VALEURS DE α ET S_z

Détecteur	α (cm^{-1})		Gain réflecteur axial S_z (cm)	
	Expérience	Calcul	Expérience	Calcul
^{235}U (n, f)	0,03749 ± 0,00011	0,03641	11,42 ± 0,15	12,66
^{238}U (n, f)	0,03678 ± 0,00022	0,03748	12,23 ± 0,25	10,88
^{232}Th (n, f)	0,03727 ± 0,00029	0,03797	11,67 ± 0,34	10,89
$\vec{\varphi}_1^*$		0,03717		11,66
$(\vec{\varphi}_1^*)$ appr. par A ^{235}U + B ^{238}U — H. et R.	0,03728 ± 0,00010	0,03689	11,66 ± 0,15	11,98
$(\vec{\varphi}_1^*)$ appr. par A ^{235}U + B ^{238}U — ABN	0,03732 ± 0,00010	0,03679	11,61 ± 0,15	12,09

H_c calculé = H_c expérimental = 60,96 cm.

TABLEAU V. VALEURS DE β ET S_r

Détecteur	β (cm^{-1})		Gain réflecteur radial S_r (cm)	
	Expérience	Calcul	Expérience	Calcul
^{235}U (n, f)	0,04807 ± 0,00036	0,04608	12,83 ± 0,35	13,06
^{238}U (n, f)	0,05026 ± 0,00067	0,04716	10,65 ± 0,60	11,80
^{232}Th (n, f)	0,04855 ± 0,00110	0,04715	12,34 ± 1,00	11,81
$\vec{\varphi}_1^*$		0,04674		12,25
$(\vec{\varphi}_1^*)$ appr. par A ^{235}U + B ^{238}U — H. et R.	0,04881 ± 0,00032	0,04651	12,07 ± 0,30	12,51
$(\vec{\varphi}_1^*)$ appr. par A ^{235}U + B ^{238}U — ABN	0,04868 ± 0,00032	0,04648	12,20 ± 0,30	12,51

R_c calculé (diffusion, jeu H. et R.) = 39,20

R_c expérience = 37,2 ± 0,2 cm.

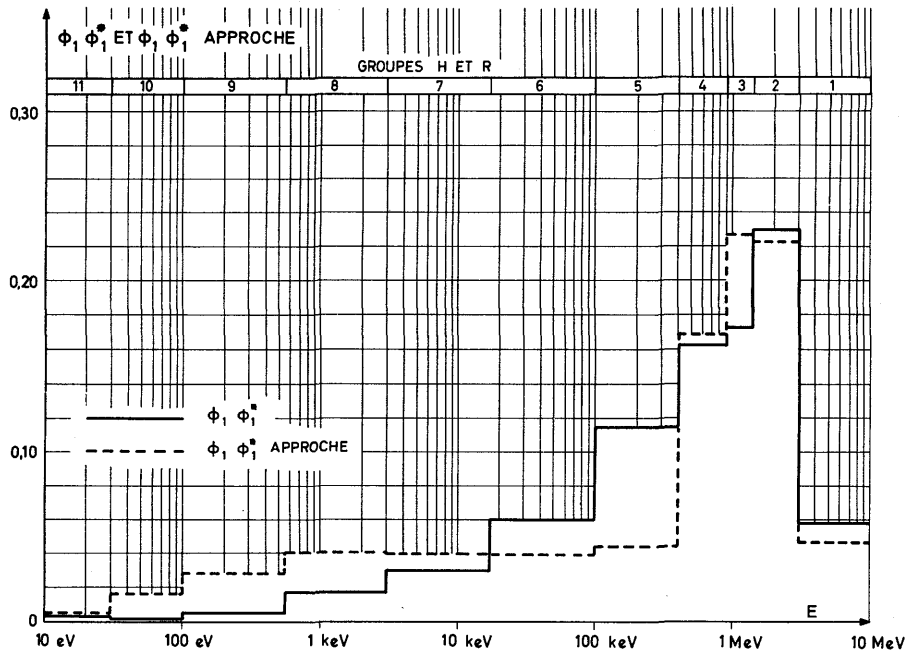

FIG.9. MASURCA, taux de réaction $\varphi_1\varphi_1^*$ et $\varphi_1\varphi_1^*$ approché, par unité de léthargie.

TABLEAU VI. VALEURS DE $B_m^2 = \alpha^2 + \beta^2$

Détecteur	B_m^2 (cm^{-2})	
	Expérience	Calcul
^{235}U (n, f)	0,003716 ± 0,000036 (1%)	0,003449
^{238}U (n, f)	0,003879 ± 0,000069 (1,8%)	0,003667
^{232}Th (n, f)	0,003746 ± 0,000110 (2,9%)	0,003665
$\vec{\varphi}_1^*$		0,003564
$(\vec{\varphi}_1^*)$ appr. par H. et R.	0,003772 ± 0,000033 (1%)	0,003524
A ^{235}U + B ^{238}U ABN	0,003763 ± 0,000033 (1%)	0,003523

devrait être faible compte tenu de l'écart minime (2, 5‰) obtenu avec les deux jeux de constantes.

L'emploi d'une plus grande variété de détecteurs et leur combinaison systématique fournira, dans des expériences ultérieures, une meilleure base pour évaluer cette erreur systématique.

3.2.3. Application des mesures du laplacien

Importance du mode fondamental

A l'aide d'une soixantaine de détecteurs au ^{239}Pu répartis dans tout le cœur nous avons pu évaluer l'intégrale des fissions de cet isotope en calculant

$$I(Pu) = \int_{\text{cœur}} \langle \vec{D}(^{239}Pu), \vec{\phi}(r, z) \rangle \, dV$$

$$= 0,1378 \cdot 10^6$$

Les taux de réaction sont normalisés à 1 au centre.

Nous avons calculé par ailleurs, à l'aide de α et β déterminés expérimentalement grâce à $\vec{\phi}_1^*$ approché, l'intégrale

$$I(B_m^2) = \int_{\text{cœur}} J_0(\beta r) \cos \alpha z \, dV$$

$$= 0,1369 \cdot 10^6$$

Ce résultat diffère de I(Pu) de 7‰ seulement et montre expérimentalement que l'effet des transitoires d'interface est faible. Les calculs le prévoient également; dans le cas du plutonium, les valeurs calculées de $\epsilon(r, z)$ (voir fig. 8) ne dépassent 1% qu'à la limite du cœur.

Gain réflecteur

A partir de α et β, et des dimensions critiques H_c et R_c du cœur, nous définissons un gain réflecteur axial S_z et un gain réflecteur radial S_r à l'aide des relations ci-dessous:

$$\alpha = \frac{\pi}{H_c + 2S_z}$$

$$\beta = \frac{2,405}{R_c + S_r}$$

Les tableaux IV et V donnent les résultats expérimentaux ainsi que les gains réflecteurs calculés en théorie de la diffusion multigroupe et les constantes multigroupes de Hansen et Roach.

On constate que les gains réflecteurs calculés à l'aide de $\vec{\phi}_1^*$ sont en très bon accord avec les mesures obtenues à l'aide de $\vec{\phi}_1^*$ approché.

Correction de la masse critique

Aussi bien le calcul que l'expérience nous ont montré que la connaissance du laplacien permet de déterminer avec une bonne approximation les variations spatiales du flux dans MASURCA 1-A. La connaissance supplémentaire des gains réflecteurs axial et radial permet donc en principe d'évaluer la masse critique.

En réalité, il vaut mieux partir d'une masse critique calculée que l'on corrige globalement en tenant compte des différences calcul-expérience du laplacien et des gains réflecteurs. A cet effet, nous avons différencié les deux relations:

$$M_c = \pi R_c^2 H_c$$

$$B_m^2 = \left(\frac{\pi}{\mu_c + 2S_z}\right)^2 + \left(\frac{2,405}{R_c + S_r}\right)^2$$

entre la masse critique et les dimensions critiques d'une part, le laplacien matière, les dimensions critiques et le gain réflecteur d'autre part. Dans MASURCA 1'ajustement de la masse critique se fait à hauteur constante. Nous obtenons dans ces conditions:

$$\frac{\Delta M_c}{M_c} = - \left(1 + \frac{S_r}{R_c}\right) \left(1 + \frac{\alpha^2}{\beta^2}\right) \left[\frac{\Delta B_m^2}{B_m^2} + a \frac{\Delta S_z}{S_z} + b \frac{\Delta S_r}{S_r}\right]$$

$$a = 2 \frac{\alpha^2}{B_m^2} \cdot \frac{S_z}{H_c/2 + S_z}$$

$$b = 2 \frac{\beta^2}{B_m^2} \cdot \frac{S_r}{R_c + S_r}$$

Le laplacien B_m^2 du milieu hétérogène MASURCA 1-A ainsi que les gains réflecteurs auraient pu être mesurés indépendamment d'une expérience critique, au moyen d'une expérience exponentielle par exemple. Nous avons corrigé, à l'aide de la formule ci-dessus, la masse critique calculée, en utilisant les écarts entre les valeurs mesurées et les valeurs calculées à l'aide de $\vec{\phi}_1^*$ du laplacien (tableau VI) et des gains réflecteurs (tableaux V et VI).

Le tableau VII, qui résume les résultats, met en évidence la prépondérance de la correction due au laplacien. Les gains réflecteurs n'interviennent en général que faiblement et les erreurs que l'on commet en les calculant n'ont pas d'incidence notable sur les corrections de masse critique.

La masse critique expérimentale est de 170 kg de Pu fissile.

La masse critique calculée prise comme référence était de 189,5 kg de Pu fissile: calcul diffusion à deux dimensions, jeu de sections efficaces multigroupe Hansen et Roach.

TABLEAU VII. EFFET DE B_m^2, S_z ET S_r SUR $\Delta M/M$ (%)

Détecteur	B_m^2	S_z	S_r	Effet total $\Delta M/M$	Masse critique corrigée (kg Pu fissile)
^{235}U (n,f)	- 8,82	+ 0,96	- 2,83	-10,69	171,1
^{238}U (n,f)	- 17,38	- 2,12	+ 9,39	-10,11	172,1
^{232}Th (n,f)	- 10,40	- 0,04	- 0,35	-10,79	170,9
$\vec{\varphi}_1^*$ H.et R.	- 11,79	0,00	+ 0,93	-10,86	170,8
approché ABN	- 11,32	+ 0,20	+ 0,26	-10,86	170,8

3.3. Indices de spectre absolus

3.3.1. Mesure

L'indice de spectre absolu $^{238}U/^{235}U$ est mesuré à l'aide de chambres à fission. Deux méthodes d'étalonnage sont utilisées.

Première méthode: deux chambres à fission contenant des dépôts de l'ordre du milligramme de ^{235}U à 99% et d'uranium appauvri sont étalonnées au centre du réacteur rapide HARMONIE où l'indice de spectre $^{238}U/^{235}U$ a été mesuré avec des détecteurs par activation. La valeur obtenue est en bon accord avec le calcul. Les détecteurs par activation sont des disques d'uranium métallique irradiés par couple d'enrichissements différents (93% et 0,4% de ^{235}U). L'activité γ des produits de fission formés dans chaque détecteur est mesurée (γ d'énergie supérieure à 511 keV). Une relation simple relie le rapport de ces activités à l'indice de spectre $^{238}U/^{235}U$ en tenant compte des masses et des enrichissements.

Seconde méthode: deux chambres à fission (diamètre 4 mm) contenant des dépôts de ^{235}U à 90% et d'uranium naturel sont étalonnées dans une colonne thermique où l'on peut obtenir la réponse de ^{235}U dans chaque dépôt. La connaissance des compositions isotopiques permet de calculer les masses d'uranium enrichi et d'uranium naturel.

Résultats

- 1ère méthode: $^{238}U/^{235}U = 0,0228 \pm 0,0002$ (incertitudes dues à la statistique des comptages)
- 2e méthode: $^{238}U/^{235}U = 0,0228 \pm 0,0002$

3.3.2. Calculs

La méthode utilisée pour l'étude de la masse critique (section 2) a permis de calculer les valeurs de différents indices de spectre au

centre des assemblages MASURCA 1-A, ZEBRA 6-A et ZPR 48. Les valeurs présentées au tableau VIII sont ramenées à la fission de ^{235}U.

L'écart très important observé dans le cas de MASURCA 1-A est lié à la nature hétérogène de la cellule et reste conforme à l'étude de structure fine réalisée dans l'assemblage ERMINE [6]. L'utilisation du spectre à l'emplacement de la chambre, donné par un calcul Monte-Carlo utilisant les sections efficaces Hansen et Roach corrigées pour l'auto-protection des résonances dans cette configuration, conduit à

$$^{238}U/^{235}U = 0,0231$$

valeur qui se compare bien à l'expérience.

4. COEFFICIENTS DE REACTIVITE AU CENTRE

4.1. Méthode de mesure

Des coefficients de réactivité ont été mesurés dans le canal radial au centre géométrique du réacteur par une méthode d'oscillation. Les matériaux testés, sous forme de réglettes standard et pour certains d'échantillons de petite taille, sont insérés dans un train de graphite remplissant le canal et rendu solidaire d'un dispositif mécanique de déplacement.

La mesure est faite, soit par lecture de la position moyenne de la barre de pilotage usuelle, soit lorsque l'effet à mesurer n'excède pas quelques 10^{-5} en réactivité, par l'utilisation d'un pilote automatique selon la technique exposée par Bennett et Long [7]. Dans ce cas l'erreur standard est de $2 \cdot 10^{-7}$ en réactivité pour un temps de mesure de l'ordre de 1000 sec. La partie active du pilote est un disque de polyéthylène placé dans le plan médian du réacteur à l'interface cœur-couverture. Le tableau IX résume les caractéristiques des échantillons utilisés.

4.2. Résultats et comparaison avec les calculs

La valeur de ^{235}U, qui ne varie guère avec la dilution comme l'ont montré les calculs [3], étant déduite de celle de l'uranium enrichi à 30%, il reste l'effet de ^{238}U dont la valeur a été conservée pour sa contribution dans l'alliage U-Pu-Fe, les dilutions dans les deux combustibles pour cet isotope étant voisines.

Une correction doit être apportée aux valeurs expérimentales pour tenir compte des différences de spectre dues à l'hétérogénéité du milieu dans lequel elles sont mesurées. Pour cela on a effectué des calculs de cellule par une méthode de Monte-Carlo [8] pour le milieu homogénéisé d'une part, et la cellule hétérogène d'autre part. Les valeurs en milieu homogène ainsi obtenues peuvent alors être comparées aux valeurs calculées par un code de perturbation utilisant les flux direct et adjoint calculés par un code de transport (tableau X).

Remarques. La correction Monte-Carlo réduit les écarts entre la valeur expérimentale brute et la valeur calculée pour ^{238}U, l'acier et le graphite. Dans ce dernier cas, elle rend bien compte du changement de

TABLEAU VIII. INDICES DE SPECTRE

Isotope	MASURCA 1-A			ZEBRA 6-A			ZPR 48		
	Expér.	Calcul	Ecart (%)	Expér.	Calcul	Ecart (%)	Expér.	Calcul	Ecart (%)
^{233}U (n,f)		1,339		1,423	1,410	-0,9	1,480	1,423	- 3,9
^{239}Pu (n,f)		0,901		0,961	0,966	+0,5	0,976	0,970	- 0,6
^{240}Pu (n,f)		0,157		0,252	0,231	-8,3	0,243	0,218	-10
^{237}Np (n,f)		0,181		0,230	0,267	+16,1		0,254	
^{234}U (n,f)		0,163		0,209	0,242	+15,8	0,204	0,211	+ 3,4
^{236}U (n,f)		0,059		0,072	0,085	+18,1	0,067	0,077	+14,9
^{238}U (n,f)	0,0228	0,0275	+20,6	0,0364	0,0395	+8,5	0,0307	0,0342	+11,4

TABLEAU IX. CARACTERISTIQUES DES ECHANTILLONS

Matériau	Echantillon
^{235}U	Cube d' uranium enrichi à 90% (masse 7,6 g)
^{238}U	Billette d'uranium enrichi à 30% (2")
Plutonium	Billette d' alliage U-Pu-Fe (4") Composition en poids: 25% Pu - 1% Fe - 74% uranium appauvri
Acier inoxydable	Réglette 4" Composition en poids: 18% Cr - 10% Ni - 72% Fe
Sodium	Réglette 4" gainée d' acier inoxydable
Carbone	Réglette 4"
Tantale	Plaquette (épaisseur 1 mm, masse 6,8 g)
Bore naturel	Cube de B_4C (arête 12 mm)
Hydrogène	Cube de polyéthylène (arête 20 mm)

signe. En ce qui concerne le plutonium il ne semble pas possible en corrigeant la valeur expérimentale de l'effet de ^{240}Pu d'obtenir une valeur de ^{239}Pu en meilleur accord avec le calcul. Dans le cas de l'hydrogène et du sodium on observe des écarts importants déjà constatés dans l'expérience ERMINE [6].

5. EXPERIENCE EXPONENTIELLE 1-B

Au cours de l'été 1967, on a réalisé une expérience exponentielle sur un milieu à neutrons rapides de composition voisine de celle existant à ERMINE et de celle qui sera utilisée pour le cœur 1-B de MASURCA.

Cette expérience avait essentiellement pour but d'apprécier la précision avec laquelle on peut obtenir la valeur du laplacien matière d'un tel milieu. La comparaison pourra être effectuée quand MASURCA aura été rendue critique avec le cœur 1-B. Cette expérience a permis également de réaliser d'utiles comparaisons sur les valeurs de certains indices de spectres $^{235}U/^{238}U$ par exemple, mesurés également sur ERMINE [6]. Enfin, des mesures préliminaires de spectres de neutrons ont été effectuées dans la zone asymptotique de cette expérience exponentielle à l'aide de compteurs proportionnels à protons de recul.

TABLEAU X. COEFFICIENTS DE REACTIVITE AU CENTRE

Corps	Expérience			Calculs – code de transport 1D
	Valeur 10^{-5} ΔK/K/g	Valeur normalisée à ^{235}U	Valeur corrigée par Monte-Carlo	
^{235}U	+ 0,564 ± 0,013	1,0	1,0	1,0
^{238}U	- 0,043 ± 0,006	- 0,076 ± 0,007	- 0,083	- 0,088
Pu A[a]	+ 0,683 ± 0,020	+ 1,21 ± 0,04	+ 1,32	+ 1,25[b]
Acier inoxydable	- 0,0228 ± 0,0009	- 0,0404 ± 0,0013	- 0,0465	- 0,0445
Sodium	+ 0,019 ± 0,007	+ 0,033 ± 0,012	+ 0,059	+ 0,0029
Carbone	+ 0,057 ± 0,001	+ 0,101 ± 0,001	- 0,032	- 0,047
Tantale	- 0,466 ± 0,011	- 0,826 ± 0,006		
Bore naturel	- 4,69 ± 0,11	- 8,3 ± 0,2		- 7,1
Hydrogène	+21,4 ± 0,6	+37,9 ± 1,2		+14,8

[a] Pu A = 90,7% ^{239}Pu, 8,4% ^{240}Pu, 0,8% ^{241}Pu, 0,1% ^{242}Pu.

[b] ^{239}Pu seul.

5.1. Description de l'expérience

Le milieu utilisé est constitué d'une matrice en graphite ayant la forme d'un prisme droit à base carrée d'environ 45 cm de côté et de 70 cm de hauteur. Cette matrice est percée de 256 canaux de section carrée et de 2,81 cm d'entraxe. Chaque canal reçoit dans un tube en acier inoxydable sept modules de 4" de réglettes d'uranium enrichi à 30% provenant du stock MASURCA (fig. 10).

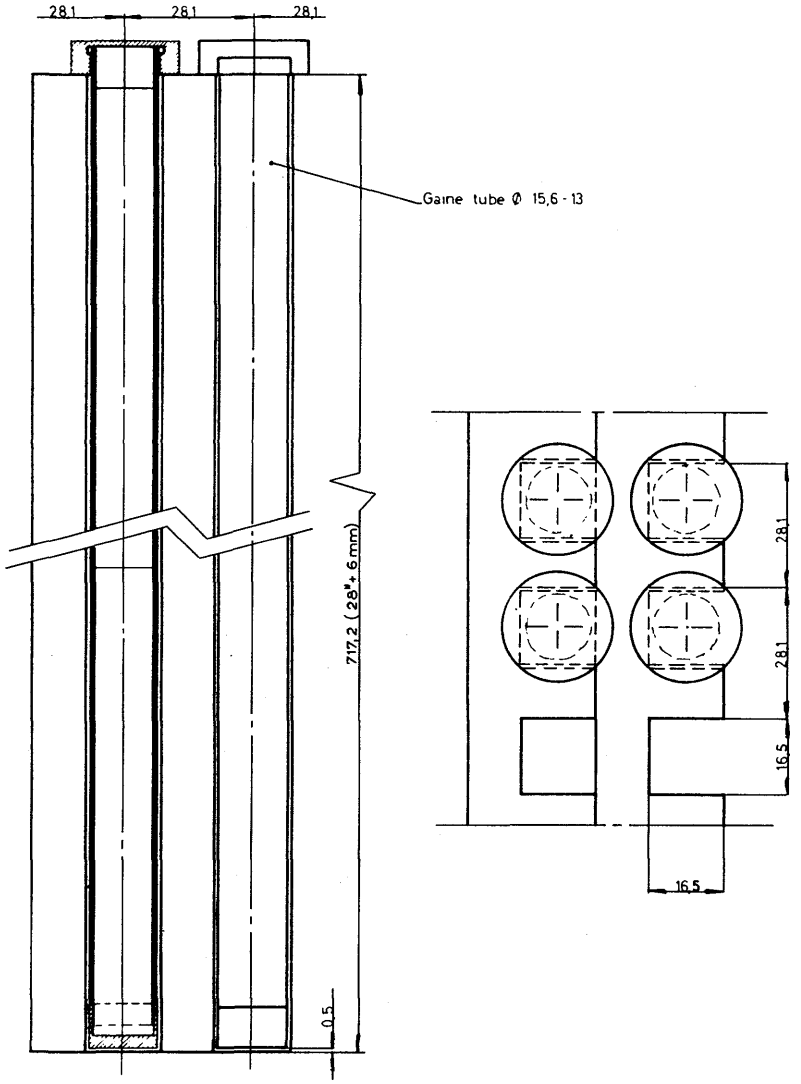

FIG. 10. Massif exponentiel, coupe type de la cellule.

Au centre de la matrice, il a été prévu un canal expérimental de 15 mm de diamètre utile et d'axe parallèle aux canaux recevant les tubes d'uranium enrichi. Un certain nombre de canaux horizontaux de section carrée de 9 mm de côté a également été prévu pour permettre d'effectuer des traverses axiales de taux de réaction avec divers détecteurs.

L'ensemble de cette expérience est placé sur le dessus du réacteur HARMONIE, noyau en position haute. La source alimentant cette expérience exponentielle est constituée par les neutrons de fuite du réacteur en fonctionnement.

5.2. Mesures effectuées

5.2.1. Etude du laplacien matière du milieu

On a étudié les chambres à fission chargées de ^{235}U, ^{238}U et ^{237}Np dont on a déterminé les taux de réaction le long des canaux axial et horizontaux.

La longueur de relaxation et les arches de cosinus qui sont les grandeurs nécessaires à la détermination de laplacien du milieu ne peuvent être évaluées directement que dans la zone de l'expérience où le spectre neutronique est constant. L'étude de la variation de la valeur des indices de spectre relatifs $^{235}U/^{238}U$, $^{235}U/^{237}Np$ le long des canaux de mesures permet de limiter cette zone d'équilibre.

L'application d'un code de moindres carrés aux résultats de mesures des taux de fissions dans cette zone permet de préciser les paramètres géométriques recherchés et leur erreur.

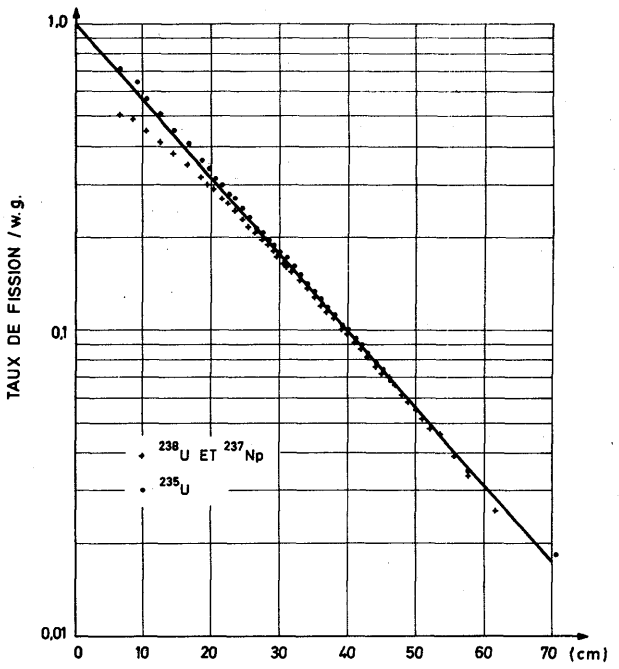

FIG.11. Massif exponentiel, distribution axiale des taux de fission ^{235}U, ^{238}U et ^{237}Np.

Résultats

Longueur de relaxation

Pour chaque matériau fissile utilisé, on peut définir une constante de relaxation apparente:

pour ^{235}U $\gamma_5 = (586,5 \pm 5,5) 10^{-4}$ cm^{-1}
pour ^{238}U $\gamma_8 = (578,6 \pm 3,7) 10^{-4}$ cm^{-1}
pour ^{237}Np $\gamma_7 = (577,8 \pm 3,7) 10^{-4}$ cm^{-1}

On remarque par ailleurs que γ_5 est obtenu par valeur supérieure alors que les deux autres, γ_8 et γ_7, sont atteints par valeur inférieure lorsqu'on s'éloigne de la source (fig. 11).

Dans la mesure où il existe dans cette expérience un γ unique indépendant de la nature du détecteur servant à la déterminer, on peut admettre

$$\gamma = (581 \pm 4)\, 10^{-4} \text{ cm}^{-1}$$

ce qui correspond à une longueur de relaxation de 17,21 cm $\pm$ 0,12.

Arche de cosinus

La même technique de mesure étant utilisée, comme on pouvait s'y attendre, on trouve un écart systématique sur l'arche mesurée avec les chambres à ^{235}U et à ^{238}U.

$$a_5^* = 527,2 \pm 1,7 \text{ mm}$$
$$a_8^* = 535,5 \pm 3,5 \text{ mm}$$

Les longueurs d'extrapolation apparentes mesurées par ces deux matériaux sont donc

$$\ell_5 = 38,6 \pm 0,85 \text{ mm}$$
$$\ell_8 = 42,7 \pm 1,75 \text{ mm}$$

Détermination du laplacien

Deux traitements au moins de ces données expérimentales conduisent à la détermination du laplacien matière du milieu défini par

$$B_m^2 = B_T^2 - \gamma^2$$
$$B_T^2 = 2\left(\frac{\pi}{a^*}\right)^2$$
$$\gamma^2 = \frac{1}{L^2}$$

A) On calcule le laplacien matière à partir des résultats expérimentaux obtenus, d'une part avec les chambres à fissions chargées de ^{235}U, d'autre part avec celles chargées de ^{238}U.

L'erreur sur le laplacien matière s'exprime alors en fonction des erreurs $\sigma(a^*)$ et $\sigma(L)$ obtenues dans la détermination expérimentale de ces deux paramètres a^* et L par la formule

$$\frac{\sigma(B_m^2)}{B_m^2} = \left[\left(2\frac{B_T^2}{B_m^2}\frac{\sigma(a^*)}{a^*}\right)^2 + \left(2\frac{\gamma^2}{B_m^2}\frac{\sigma(L)}{L}\right)^2\right]^{\frac{1}{2}}$$

Il vient:

Laplacien ^{235}U $B^2_{T\,U235} = 0,007102$

$\gamma^2_{U235} = 0,003440$

$B^2_{m\,U235} = 0,003662\ cm^{-2}$ à $\pm 2,2\%$

Laplacien ^{238}U $B^2_{T\,U238} = 0,006884$

$\gamma^2_{U238} = 0,003348$

$B^2_{m\,U238} = 0,003536\ cm^{-2}$ à $\pm 2,8\%$

La moyenne arithmétique de ces deux valeurs conduit à

$$B_m^2 = 0,003600\ cm^{-2} \text{ à} \pm 3,7\%$$

valeur qui contient les deux valeurs précédentes.

B) On peut montrer [9]

- que la constante γ_0 obtenue en supposant que la longueur d'extrapolation ne varie pas avec l'énergie est une bonne approximation de la valeur γ que l'on veut mesurer,
- qu'il est possible, à partir d'une longueur d'extrapolation variable avec l'énergie, de définir une valeur moyenne de ℓ qui ne modifie pas la valeur de γ.

$$\bar{\ell} = \frac{\langle \varphi^*, \ell\varphi \rangle}{\langle \varphi^*, \varphi \rangle}$$

avec $\ell = 2,13\ D$ (D: coefficient de diffusion du milieu homogène), φ et φ^* étant les fonctions propres directe et adjointe du mode fondamental énergétique du milieu.

Le matériau détecteur idéal permettant d'obtenir ℓ vrai serait donc celui dont la section efficace σ_x serait colinéaire au flux adjoint.

$$\bar{\ell} = \frac{\langle \sigma_x, \ell\varphi \rangle}{\langle \sigma_x, \varphi \rangle}$$

Si on effectue le calcul avec φ^*, $\sigma_{f\,U235}$ et $\sigma_{f\,U238}$ on trouve respectivement:

$\bar{\ell} = 35,2$ mm
$\ell_5 = 24,3$ mm
$\ell_8 = 56,1$ mm

On peut alors rechercher en première approximation une combinaison linéaire de ℓ_5 et ℓ_8 permettant de retrouver ℓ:

$$\ell = \alpha \ell_5 + \beta \ell_8$$

avec $\alpha + \beta = 1$. En appliquant aux valeurs ℓ_5 et ℓ_8 déterminées expérimentalement les valeurs de α et β ainsi trouvées, il vient

$$\overline{\ell} = 40 \pm 1,2 \text{ mm}$$

et

$$a^* = 530,0 \pm 2,4 \text{ mm}$$

On trouve alors avec $\gamma = (581 \pm 4) 10^{-4}$ cm^{-1}

$$B_T^2 = 0,007027$$

$$\gamma^2 = 0,003376$$

d'où

$$B_m^2 = 0,003651 \text{ cm}^{-2} \pm 2,4\%$$

Ces deux types de dépouillement conduisent à des valeurs comparatives.

Ces valeurs sont à comparer à 0,003745 cm^{-2} déterminée par le calcul H. et R. à 16 groupes corrigé des effets d'hétérogénéité (autoprotection des résonances et ségrégation des matériaux) évalués à $1,9 \cdot 10^{-4}$ cm^{-2}.

5.2.2. Spectrométrie à protons de recul

La partie centrale de la matrice de graphite est amovible et permet l'introduction à une cote quelconque de compteurs à protons de recul. Des mesures ont été effectuées dans la zone en équilibre définie au cours des mesures du laplacien.

Les compteurs sont du type sphérique fabriqués par la 20th Century Electronics. Leur remplissage est de l'hydrogène pur à 1 et 4 atm, l'anode centrale possédant un dépôt quasi ponctuel de ^{239}Pu pour étalonnage. En fait, un étalonnage complémentaire en neutrons monocinétiques a été effectué à l'aide du Van de Graaff 5 MeV de Cadarache.

La technique de discrimination (n, γ) est identique dans son principe à celle développée par Bennet.

La nature du gaz et les pressions disponibles au moment de ces mesures n'ont pas permis d'obtenir des informations directes sur la partie à haute énergie (au-dessus de 500 keV) du spectre neutronique à mesurer.

Dans les premières mesures effectuées, la limite inférieure d'énergie se situait vers 40 keV. Cette limite a été abaissée pour atteindre 15 keV environ en améliorant la qualité de l'électronique de discrimination malgré la forte intensité γ régnant dans le massif au moment de ces dernières mesures. (Ces mesures suivaient une irradiation importante du massif.)

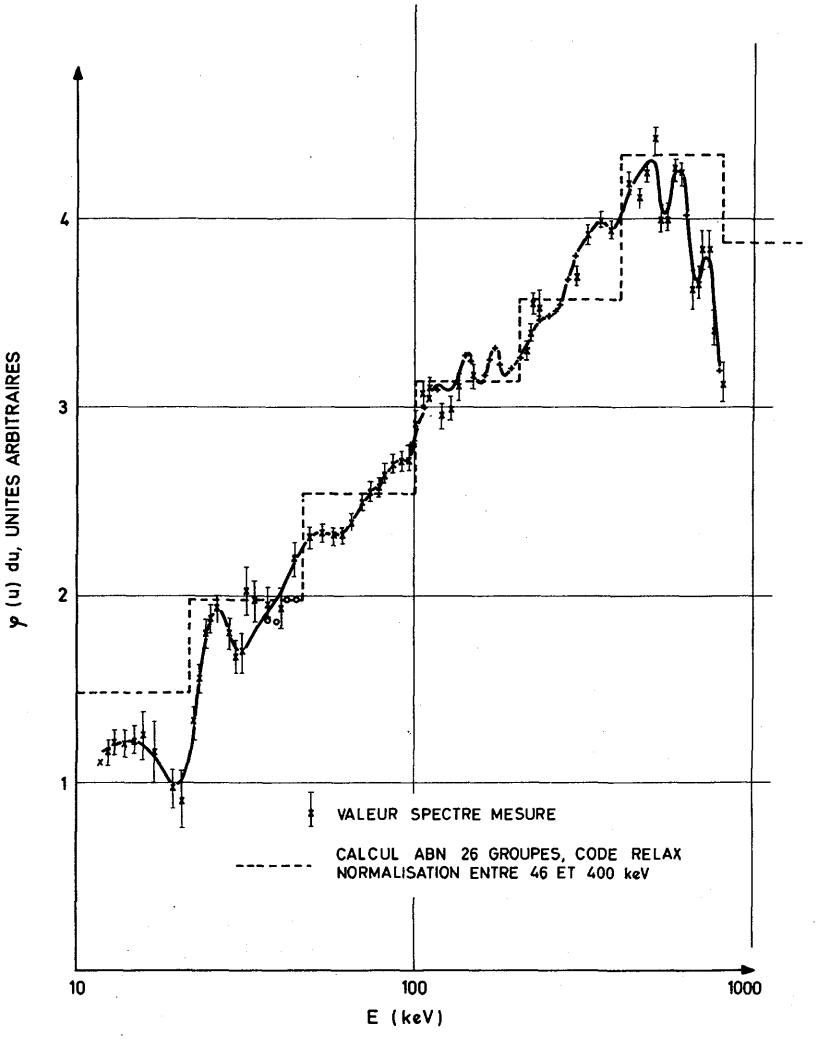

FIG.12. Massif exponentiel, spectre détaillé au centre (protons de recul).

Sur la figure 12 on présente les résultats expérimentaux obtenus ainsi que les résultats d'un calcul à 26 groupes ABN normalisé entre 46 et 400 keV.

CONCLUSION

Au cours des dix premiers mois de fonctionnement du réacteur MASURCA, on s'est avant tout attaché à mettre au point des techniques expérimentales adaptées à la configuration particulière de la machine ainsi que des méthodes d'exploitation des résultats, détermination de

laplaciens par exemple, beaucoup plus qu'à l'obtention de mesures absolues. Cependant, quel que soit le domaine abordé: masse critique, laplaciens, indices de spectre, coefficients de réactivité, toujours se manifeste l'importance des effets d'hétérogénéité rendant l'interprétation des mesures délicate.

Ces effets, primordiaux dans les réacteurs thermiques, ont toujours été considérés dans les réacteurs rapides comme n'introduisant que de faibles corrections appliquées à un dépouillement homogène des résultats, ce qui peut être vrai pour les réacteurs de puissance où le diamètre des aiguilles de combustible ne dépasse pas quelques millimètres. Dans les maquettes critiques en revanche, la structure fine intervient à l'échelle de la mesure. On a alors le choix entre deux possibilités: ou bien utiliser des dispositifs de mesure qui «moyennent» cette structure fine au risque de perturber le réseau (détecteurs de grandes dimensions); ou bien rechercher des conditions de perturbation minimale (petits détecteurs), mais il faut alors faire appel à des méthodes d'interprétation hétérogènes. C'est cette solution qui a été retenue pour MASURCA. Des efforts ont été entrepris dans cette voie avec la mise au point d'un code de perturbation hétérogène et d'une méthode type Monte-Carlo de calcul de la cellule, mais les informations sont encore trop fragmentaires pour permettre un recalage sûr des résultats théoriques sur l'expérience. On peut donc prévoir que ce problème influera notablement tant sur la définition du programme expérimental que sur l'évolution des méthodes d'interprétation.

REFERENCES

[1] SCHMITT, A.P. et al., « MASURCA: maquette critique à neutrons rapides», Exponential and Critical Experiments (C.r. Coll. Amsterdam, 1963) I, AIEA, Vienne (1964) 135.

[2] «Problèmes de sûreté liés à la constitution des maquettes dans MASURCA», Conf. int. sur la sûreté des réacteurs à neutrons rapides, Aix-en-Provence, 1967, communication II A/8.

[3] KHAIRALLAH, A., LACAPELLE, T., STORRER, F., «Hétérogénéité dans l'assemblage 1-A de MASURCA», ces comptes rendus, SM-101/57.

[4] HANSEN, G.E., ROACH, W.H., LAMS-2543.

[5] ABAGYAN, L.P. et al., Sections efficaces à 26 groupes.

[6] BOUCHARD, J., VIDAL, R., MOUGNIOT, J.C., « Etude expérimentale des caractéristiques neutroniques des milieux multiplicateurs rapides dans l'assemblage critique thermique-rapide ERMINE », ces comptes rendus, SM-101/56.

[7] BENNETT, E.F., LONG, R.L., Precision limitations in the measurement of small reactivity changes, Nucl. Sci. Engng 17 (1963) 425-32.

[8] PARISOT, B., communication personnelle.

[9] GOVAERTS, P., communication personnelle.
(Voir aussi: BARRE, J.Y., RAVIER, J., « Imprécisions des paramètres caractéristiques d'un réacteur rapide de puissance dues aux incertitudes actuelles concernant les données neutroniques», ces comptes rendus, SM-101/58.

OPERATIONAL CHARACTERISTICS AND RELATED DESIGN FEATURES OF SNEAK*

P. ENGELMANN, W. BICKEL, H. WALZE AND G. WITTEK
INSTITUT FÜR ANGEWANDTE REAKTORPHYSIK,
KERNFORSCHUNGSZENTRUM KARLSRUHE,
FEDERAL REPUBLIC OF GERMANY

Abstract

OPERATIONAL CHARACTERISTICS AND RELATED DESIGN FEATURES OF SNEAK. SNEAK is a flexible zero-power reactor for investigating the physics of fast reactors with uranium and plutonium fuel. Considerations of safety, operation, and experimental flexibility led to the choice of a fixed vertical assembly with suspended fuel elements loaded into the reactor from below. A short description of the main design features and of the experimental capabilities of SNEAK is given.

In the second part of the paper, the safety and experimental instrumentation is described in some detail. The safety instrumentation consists of 7 channels. The signals from these channels, most of them working in 2-out-of-3 manner, are fed into a self-controlled safety circuit actuating the safety and shim rods and/or the isolation valves of the reactor building. Automatic control of reactor power is possible from 0.1 to 1000 W, i.e. in the range of the logarithmic ionization chamber channel. For very precise regulation a special 'autorod' may be used in connection with one of the experimental linear channels. Linear ionization chamber channels are also used for accurate reactor operation. A deviation meter shows small deviations of reactor power from a set point. With the aid of a small on-line analogue computer continuous reactivity information is obtained. This reactivity meter has proved very useful for many kinds of experiments.

The third part of the paper summarizes the results of measurements on the reproducibility of core geometry, control rod positioning, and reactivity. Temperature variations inside the core and in the reactor building are also reported. It has been found that reactivity reproduces with high precision, and temperature variations are very small.

1. DESCRIPTION OF SNEAK

The fast zero power reactor SNEAK has been in operation at the Karlsruhe Nuclear Research Centre since December 1966. It is a tool for investigating the neutron physics of large fast reactors with uranium and/or plutonium fuel. After a series of physics assemblies, mock-ups are planned for the two 300-MW(e) fast breeder prototypes with sodium and steam cooling.

The SNEAK design was aimed at maximum flexibility and operational safety. From the various types of zero power reactors, such as horizontal split-table, vertical split-table, and vertical fixed machines, the latter was chosen. The fuel elements are suspended from a grid and the loading is performed from below.

There are points in favour of both split table and fixed assemblies. The major reasons for selecting the vertical fixed suspended version were:

(1) There is no large reactivity addition such as that which occurs during the closing of the halves of a split-table machine.

---

* Work performed within the association in the field of fast reactors between the European Atomic Energy Community and Gesellschaft für Kernforschung mbH., Karlsruhe.

(2) The loading from below excludes fuel-rod drop accidents.

(3) Gravity can be used to accelerate the safety rods in case of scram.

(4) The void and steel fractions can be kept very small (6.5% and 7.5% respectively) as no matrix is needed.

(5) The assembly can be easily cooled by blowing air through narrow channels, which are provided by the shape of the fuel element tubes.

(6) The flow pattern of the cooling air is the same with the machine in loading and operating conditions, which is of special importance for plutonium-fuelled assemblies.

(7) It is relatively easy to install loops.

(8) Experimental equipment can be set up immediately around the reactor, which is accessible from all sides.

(9) Automatic machines were available for loading (and unloading) the plate-shaped material pieces into (or out of) the element tubes.

The reactor can accommodate assemblies up to 3.2 m in diameter and 2.7 m in height. It is assembled from square elements that are suspended from a top grid plate and after completion of loading operations are fixed in their positions by eight clamping devices at the bottom part of the circumference. The reproducibility in core geometry, which can be achieved by the clamps, was of major concern before the commissioning of the machine. It turned out, however, to be very good (see section 3).

The design necessitates two loading machines: a lower loading machine, which transports elements between the reactor and the fuel element transit lock, and an upper loading machine, which hoists the elements into the reactor.

The design of SNEAK can be seen from Figs 1, 2, and 3. Figure 4 shows typical core and blanket material pieces. Most core materials have been fabricated into 50.75 × 50.75 mm that are 3.15 mm thick. Also available are plates of other dimensions and 17 × 17-mm rods that are 305 mm long. Plates and rods fit into the core tubes with inner dimensions of 51 × 51 mm, and into the blanket tubes with inner dimensions of 153 × 153 mm.

At present about 830 kg ^{235}U, 175 kg Pu, 50 000 kg natural and depleted uranium, and large amounts of structural materials are available.

As can be seen from Fig. 3, vertical channels for experimental purposes can be generated at any desired location. Figure 5 shows the design of two typical elements with vertical channels. Larger vertical channels penetrating the grid plate can be formed at four locations near the core centre where the top grid has square holes with 55-mm side lengths. These large channels are utilized, e.g. for insertion into a pile-oscillator tube.

Control rods may be placed at any ninth core element position. Up to 20 shim rods, 10 safety rods and 1 regulating rod can be installed.

While the accommodation of vertical channels is very easy, a horizontal channel must penetrate a row of core and blanket elements. To allow this, these elements are provided with windows that give access to a rectangular tube with a cross-section of 31 × 58 mm. The horizontal channel at mid-core level (north-south channel) has been used extensively for detector and material traverses, foil activiation for spectrum measurements, and for the insertion of a pulsed neutron source.

A more detailed description of SNEAK and the planned experiments was given at the Conference on Fast Critical Experiments at Argonne in

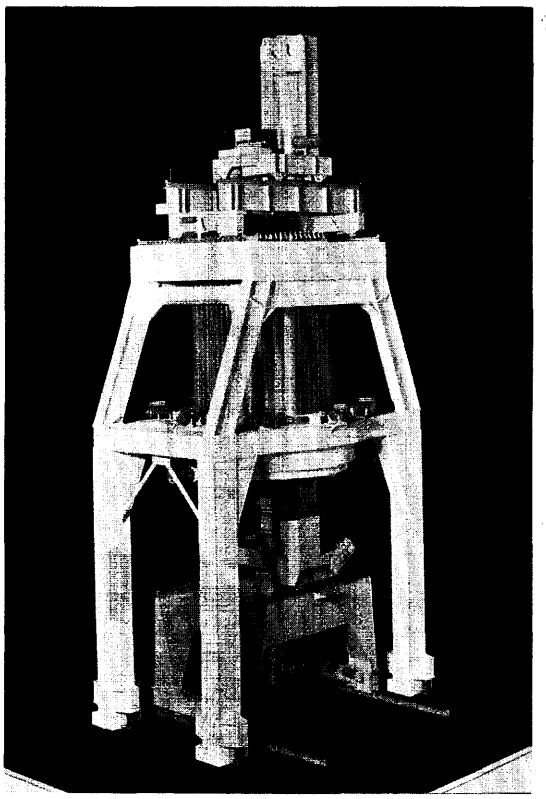

FIG.1. Reactor, support frame, upper and lower loading machines of SNEAK (model picture).

October 1966 [1, 2]. The safety aspects were described at the Conference on Fast Reactor Safety at Aix-en-Provence, September, 1967 [3]. The experiments performed so far are reported in separate papers at this Symposium [4, 5]. In section 2 of this paper, some details are given on the safety instrumentation, controls, and experimental instrumentation. Section 3 deals with the operational characteristics of SNEAK.

2. INSTRUMENTATION AND CONTROL

2.1. Safety instrumentation, safety rods, shut-off valves of the ventilation system

The operating and safety instrumentation consists of seven channels:

(1) Logarithmic counting channel for neutron flux and period measurements in the low-power region (up to 0.5 W);

(2) Logarithmic current channel for neutron flux and period measurements with an ionization chamber in the upper power region (from about 0.05 W up to 1000 W);

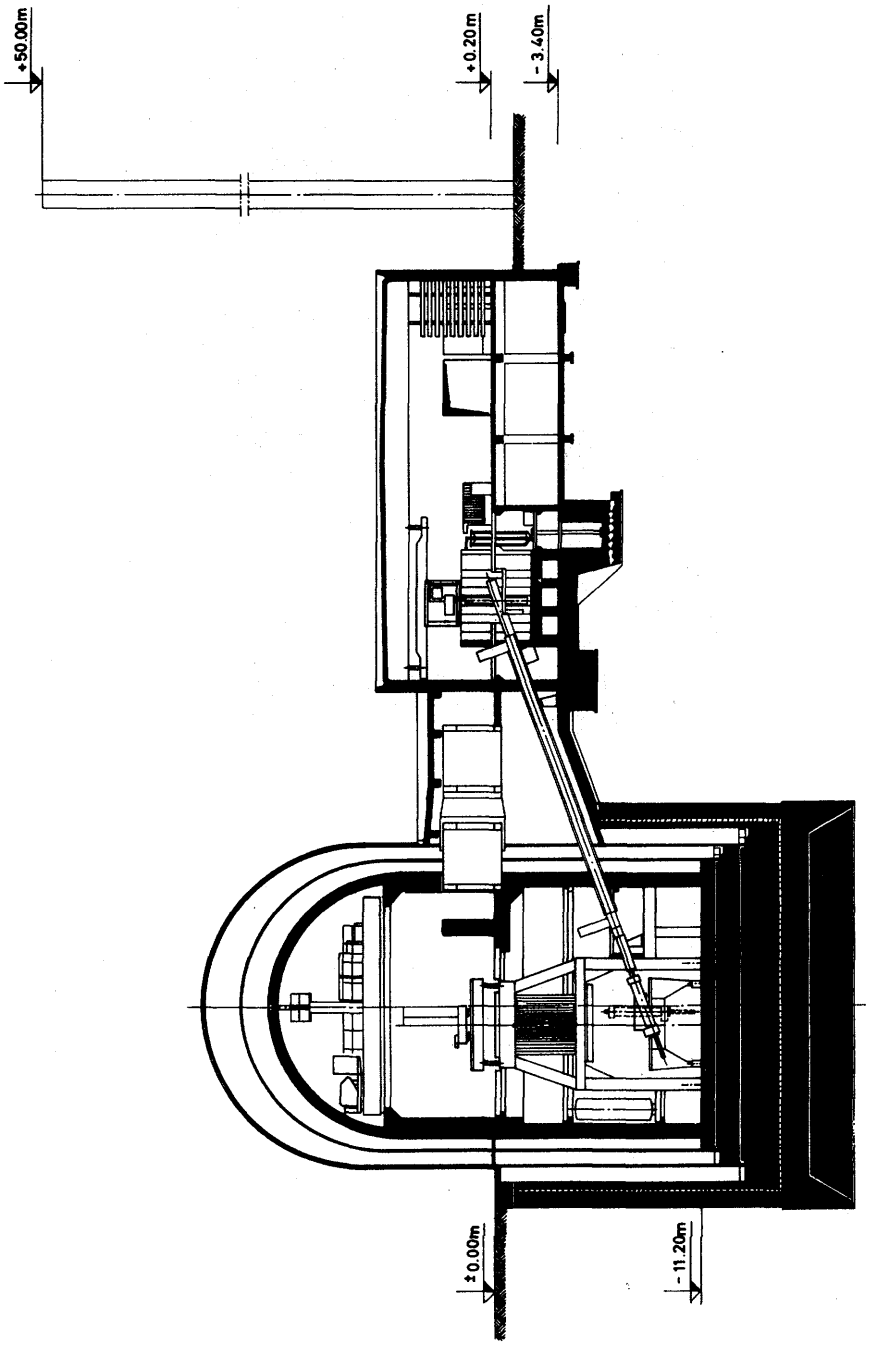

FIG. 2. Section through reactor building and loading area.

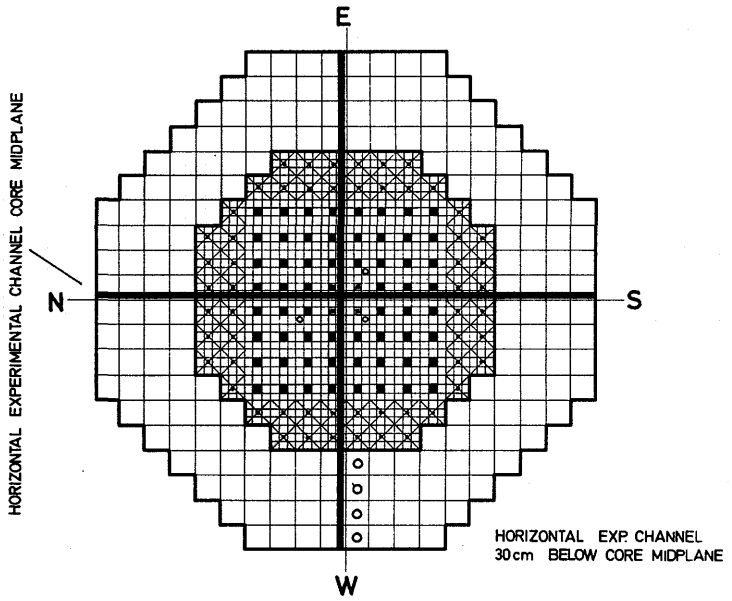

CORE SECTION			
PILE OSCILLATOR	x		
SAFETY RODS		x	
SHIM RODS	x	x	
REGULATING ROD	x	x	
CORE ELEMENTS WITH VERT. EXP. CHANNELS	x	x	x
CORE ELEMENTS	x	x	x

BLANKET SECTION			
BLANKET ELEMENTS WITH VERT. EXP. CHANNELS	x	x	x
BLANKET ELEMENTS	x	x	x
CORE - GROUP - ELEMENTS	x	x	x

FIG.3. SNEAK loading plan.

(3) U/Pu monitoring channel for the exhaust air;

(4) Counting channel for monitoring the concentration of beta emitters in the exhaust air;

(5) Logarithmic counting channel for gamma flux measurement in the reactor building in the upper power region;

(6) Channel for measuring the pressure difference between the space inside each of the two steel shells and atmosphere;

(7) Channel for emergency shut-off by hand or by the opening of certain interlocks.

The air-pressure channel (No. 6) consists of two parallel measuring lines, and the other channels of three parallel lines, which work in a

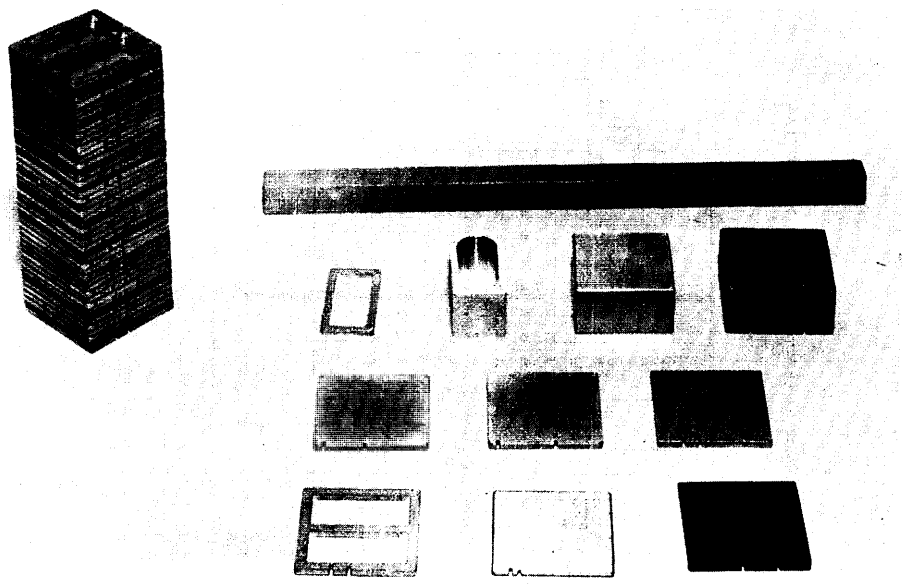

FIG. 4. Core and blanket material pieces.

one-out-of-two or two-out-of-three manner, respectively. These channels may be divided into three parts: analogue part, digital part, and active elements.

(a) Analogue part

In this part the measuring current is generated, indicated, and sometimes recorded. The analogue part is terminated by limiting-value indicators and comparing units which give a signal when a certain value is surpassed or when the difference of the current in two parallel lines is too large. Channel 7 has no analogue part; the limiting-value indicators and comparing units are replaced by switches and contacts.

(b) Digital part (see Fig. 6)

The limiting-value indicators and comparing units also serve as the input units of the digital part. In this part, the one-out-of-two and/or two-out-of-three selection of the signals is made. If two comparing unit signals indicate an excessive deviation in a certain measuring line, this is treated like the signal of the limiting-value indicator in the measuring line in question.

The digital part is terminated by relays, which operate the subsequent safety devices, if a selection unit opens the current path. The digital part of the safety system is continuously automatically inspected for faultless operation. In cyclic progression, short check pulses are fed to the inputs of the individual limiting value indicators and the arrival of these pulses at the output of the limiting-value indicators, the selection units, and the output amplifiers is checked. Thus, within two seconds the whole digital part of the safety system is checked and any defect is indicated and localized. The system distinguishes between "dangerous defects" and "non-dangerous defects".

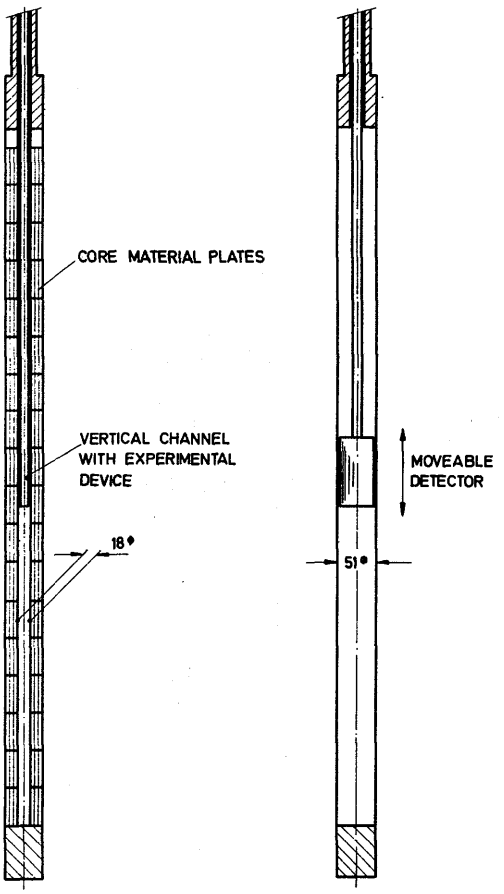

FIG.5. Core elements with vertical channels.

"Non-dangerous defects" are those which without reason trigger a safety operation (e.g. scram), like a limiting-value indicator giving a permanent signal. "Dangerous defects" are those which prevent a necessary safety operation, i.e., for example, a limiting-value indicator giving no signal, although the measured value is above that limit.

When a dangerous defect appears in a measuring line of a two-out-of-three channel this is automatically switched to one-out-of-two selection. In a one-out-of-two channel a dangerous defect will trigger the corresponding safety operation. In this manner a high degree of safety is guaranteed.

(c) Active elements

The terminating relays of the digital part operate various elements. They range from the safety rods to simple indicating relays and are listed below:

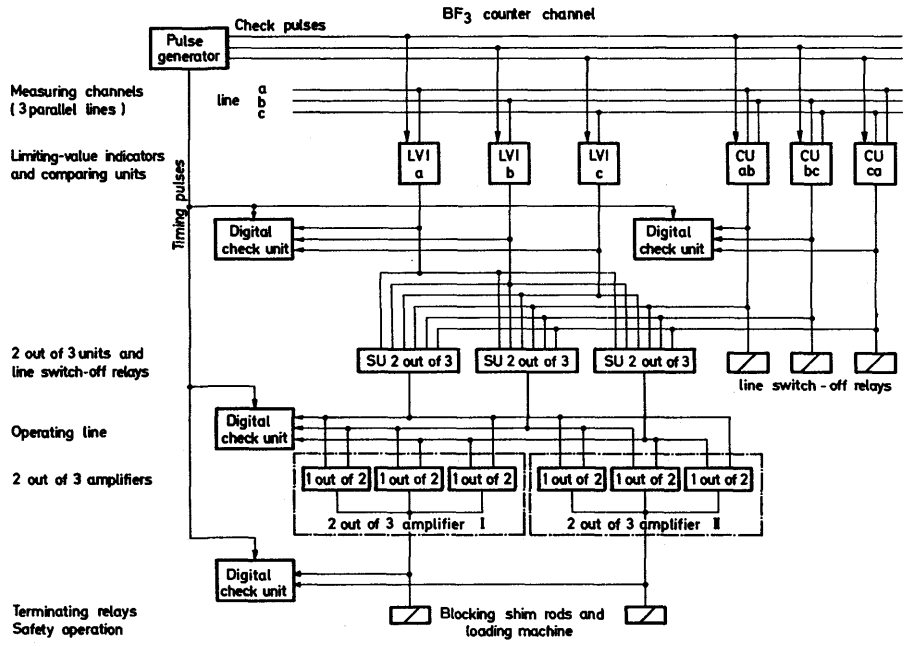

FIG.6. SNEAK safety system, part of channel 1.

(1) Shim and safety rods: In case of scram the safety rods are shot out of the core, while the shim rods are driven out by motors. Scram is initiated by:

Channel 1, if during loading the neutron flux exceeds a certain value, or if the reactor period is less than 3 s, or if the neutron flux exceeds the limit beyond which the pulse counters are no longer working accurately. Normally, however, the high voltage is taken off the counters before that limit is reached.

Channel 2, if the trip level of the neutron flux is reached or if the reactor period is less than 3 s.

Channel 3, if the U/Pu-concentration in the exhaust air is too large (3×10^{-12} Ci/m^3 Pu, or 1.8×10^{-10} Ci/m^3 U).

Channel 4, if the concentration of β-emitters in the exhaust air is too large (about 6×10^{-7} Ci/m^3 in case of ^{41}A).

Channel 5, if the maximum admissible reactor power (1 kW) and the corresponding gamma-flux are exceeded.

Channel 6, if the air pressure inside the reactor building exceeds the atmospheric pressure by more than 10 mm water, or if the pressure inside the reactor building exceeds that in the space between the two shells and the latter exceeds the atmospheric pressure.

Channel 7, if the manual scram button is pushed, or if the mechanical interlock between the doors of the personnel air lock is not functioning, or if the personnel air lock is operated while the reactor is in operation, or in case of a defect in the voltage supply of the reactor instrumentation.

(2) Fast acting pressure valves and ventilation of the reactor building: The pressure valves in the air ducts penetrating the steel shells are closed and the corresponding blowers are switched off by channels 3, 4, and 6 in the same situations as those listed above.

(3) Ventilation of the operation and storage building: This ventilation is switched off and the corresponding valves are closed by channels 3 and 4 in the same events as those listed above.

(4) High voltage of the BF_3-counters in channel 1: The high voltage of these counters is switched off by channel 2, if the neutron flux reaches a value about 2 decades above the minimum measurable flux in channel 2.

(5) Indicating relays for insufficient neutron flux: A visual signal "drive-in neutron source" is given by channel 1, if during reactor operation the neutron flux drops to a value about 2 decades above the minimum measurable flux.

(6) Neutron source drive motor: The neutron source is automatically driven in by channel 1 if during reactor operation the flux drops to a value about 1.50 decades above the minimum measurable flux.

(7) Blocking relays for shim rods and loading machines: Channel 1 prevents the driving in of the shim rods and the operation of the loading machines if the neutron flux drops to a value about 1 decade above the minimum measurable flux.

(8) Indicating relays for short reactor period: The visual signal "reactor period" is given by channels 1 and 2, if the reactor period is less than 10 s.

Of these 8 active elements, the most important ones are the safety rods, the shim rods, and the fast acting pressure valves. The shim rods are described in detail in section 2.2. The safety rods and the pressure valves are described here.

The safety rods (Fig. 7) consist of two tubes, an outer guide tube which has the cross-section of a normal core element, and a somewhat smaller tube which can be moved vertically 1 m inside the guide tube. The inner tube contains platelets of common core material and also in some cases blocks of moderated boron carbide in the upper part of the tube. The inner tube is attached to a holding magnet in the outer tube by means of a steel plate. In addition, a device is provided to accelerate the rod in a downward direction. This consists of a coil and a copper ring connected to a steel tappet. At scram, the current of the holding magnet is switched off and at the same time a capacitor (480 μF), which is loaded to 3 kV, is discharged through the coil giving a current of about 1.6 kA. The copper ring with the tappet is thrust down on to the steel plate by the induced

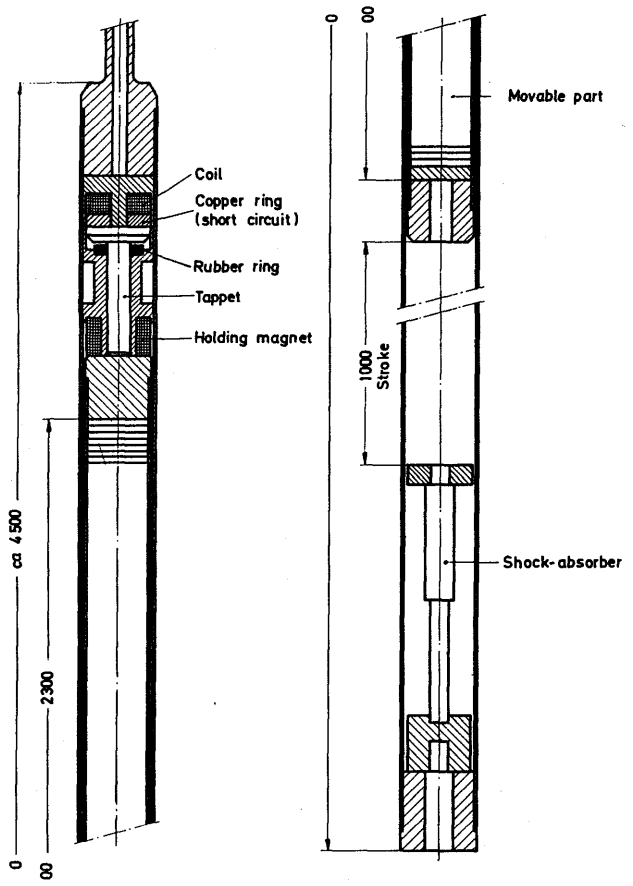

FIG. 7. Safety rod.

short-circuit current. This gives an impulse to the movable part of the rod which is accelerated to 1 m/s within 1 ms [6]. When out of the core, the safety rod is decelerated by a shock absorber mounted in the lower part of the outer tube.

The reactivity reduction due to the removal of one safety rod is shown in Fig. 8 for two cases: (1) free fall, and (2) accelerated with the magnetic gun. It can be seen that the total travel time (380 ms and 470 ms, respectively) differs by only 20%; the reactivity reduction, however, starts much faster in the case with acceleration. Considerably steeper reactivity ramps can, therefore, be controlled by the safety system in this case [3]. With a shut-down reactivity of 2.5% in the safety rods, which is the minimum required, and for an initial power of 0.01 W (1 W), reactivity ramps of up to 2.7 \$/s (5.1 \$/s) can be controlled if the rods are accelerated.

The travel time of all rods is monitored so that deviations from normal caused either by failure of the magnetic gun, sticking of the rod, or failure of the shock absorber, will be discovered immediately. In addition to the travel-time monitors on each safety rod, there is a device

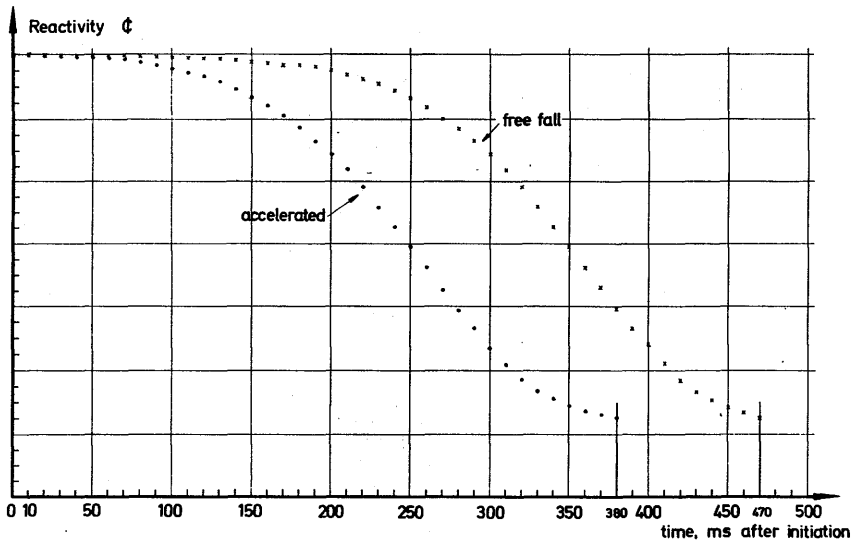

FIG.8. Reactivity reduction versus time at removal of safety rod No.12, SNEAK-3A-1.

by which the travel time of one safety rod can be measured with an accuracy of a few milliseconds.

The fast-acting pressure valves close the ventilation ducts penetrating the steel shells. Ducts penetrating both steel shells have three valves, and those which go to the interspace (penetrating only the outer shell) have two valves. Three different types of valves are used to reduce the probability of a complete failure:

(1) Valves operated by an electric motor, closed within 3 s;
(2) Pneumatic valves operated by a piston, closed within less than 1 s;
(3) Spring-driven valves. These are opened by an electric motor acting against a spring which shuts the valve if the magnetic holding ratchet is released. Closed within less than 1 s.

2.2. Reactor control

All safety rods are cocked during loading and operation of the assembly. The normal operational shut-down is made with the shim rods. Their construction is similar to that of the safety rods. The shim rod (Fig. 9), filled with core material, moves in a guide tube of core element cross-section and has a 1-m stroke. The shim rod is driven by a screw and an electric motor which is placed in the upper part of the guide tube. The space around the screw may be left empty or it may be filled by a steel can filled with B_4C powder. In this case the shim rod acts as a fuel-poison rod.

The rod motor also drives a potentiometer the resistance of which is automatically compensated by a run-after potentiometer in a bridge. The position of the run-after potentiometer is used to indicate the position of the shim rod to an accuracy of ± 0.15 mm.

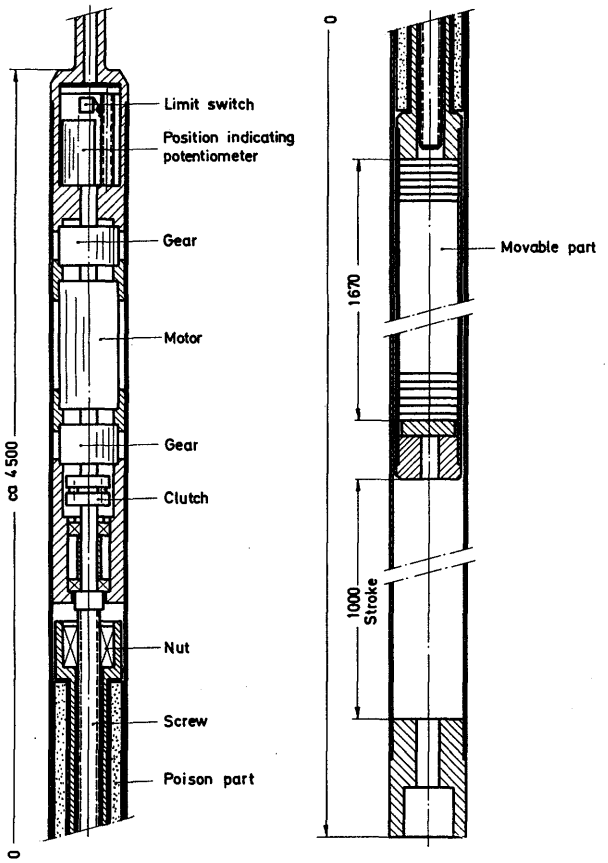

FIG.9. Shim rod.

The shim rods in the SNEAK assemblies have a reactivity worth of at least 4%. Several shim rods can be moved in a bank. The maximum number that may be moved simultaneously is half the number of cocked safety rods. The maximum rate of reactivity insertion is 0.1 \$/s.

The fine control rod has a stroke of 50 cm around the core midplane in order to achieve a characteristic which is almost linear. It consists of a lower fixed part and an upper movable one. The motor and position indicator work as in case of the shim rods.

The fine control rod has a maximum reactivity worth of 0.2%, the reactivity speed is about 0.01 \$/s. It can be used in connection with the log current channel for automatic power control. The power can be kept within ± 1% of the set value.

2.3. Experimental instrumentation

2.3.1. Linear measuring channels

For experimental purposes several linear neutron flux measuring channels are available. BF_3 - and ^3He-filled ionization chambers of high neutron sensitivity can be used with two types of amplifiers.

Type 1 uses an electrometer tube in its input, which only needs 2×10^{-14} A grid current for normal operation. Because of this, the most sensitive range is 1×10^{-13}A full scale. By means of a calibrated internal current suppression, a part of the measured neutron flux can be compensated. This is very useful for oscillating measurements. The installed model has a zero drift of about 1% of full scale in 8 h and an over-all measured linearity of 0.2%. These values are relatively poor, but typical for amplifiers of the electrometer type. Type 2 uses Varactor diodes in its input. By means of these voltage dependent capacitors a high frequency signal is modulated by the input current. The modulated signal drives an a.c. amplifier, which is connected to a phase dependent rectifier. The most sensitive range is 1×10^{-11} A full scale. Zero drift is negligible, and theover-alllinearity was measured to be within 0.03%. If extremely high sensitivity and current suppression are not needed, the type 2 amplifier is preferred.

For easy data acquisition the output voltages of the amplifiers are digitized by voltage-to-frequency converters operating with an integrating capacitor.

Several BF_3 - and ^{3}He-filled proportional counters are available for linear pulse channels. Small ^{235}U, ^{238}U, and ^{239}Pu fission chambers are used for power calibrations of the SNEAK assemblies. The output pulses of the voltage-to-frequency converters and those of the pulse amplifiers are counted during a certain time interval. The count-rates can serve as computer input data.

2.3.2. Deviation-meter and reactivity-meter

The information from the linear ionization chamber channels can be used to operate a deviation-meter and a reactivity-meter. These instruments with display on the control desk have proved to be very useful for stabilizing the reactor power and for measuring small reactivity changes, e.g. in reproducibility experiments.

Figure 10 shows a diagram of the linear channels and the arrangement of the equipment in the reactor building and experiment control room.

The deviation meter uses a chopper stabilized operational amplifier for comparing actual reactor power and the set power. It shows the deviation of reactor power from a set point; the most sensitive range corresponds to a 1% power deviation. The relatively high noise level in the output signal at low reactor power can be reduced by applying a R-C combination.

With the aid of a small on-line analogue computer, programmed for the solution of the inverse reactor kinetic equations, it is possible to obtain continuous reactivity information. Six ranges from 0.5-cent up to 5.0 $ full-scale can be chosen. On the 0.5-cent range the reactivity worth is obtained with an accuracy of ± 0.02-cent, if the reactor power is higher than 30 W. Figure 11 shows the time dependent neutron flux and the calculated reactivity for a part of a horixontal Al-probe traverse in SNEAK assembly 1.

Six chopper stabilized operational amplifiers and one servo-multiplier are the active elements in the fixed wired analogue computer. The delayed neutron terms are taken into account by passive networks.

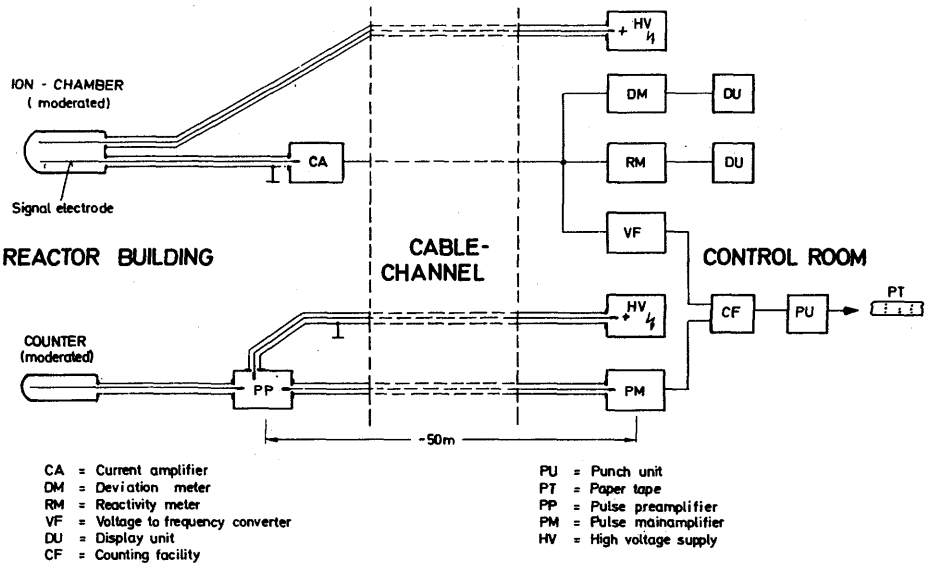

FIG.10. Linear channels.

Automatic switching of the source term simulator occurs simultaneously with range switching of the linear amplifier in the ionization chamber channel. Noise in the reactivity signal is reduced by applying a large time constant between reactivity meter and display unit.

3. OPERATIONAL CHARACTERISTICS

3.1. Temperature behaviour with and without cooling of the core

For a great number of experiments it is important to minimize reactivity changes due to changes in core temperature. Temperature variations result from the fission heat and from the decay heat of plutonium, if this is used as fissile material. While the reactor power normally is in the range of a few watts, the decay heat of 175 kg Pu is about 500W.

The SNEAK core can be cooled by air blown through the gaps between the core element tubes. The air is taken from the building atmosphere and after passing through the core returns to the building atmosphere. The cooling system is also effective during loading changes.

Measurements of core temperature have been made in the U-core SNEAK-1 in order to demonstrate the efficiency of the cooling system. During a run at 650 W reactor power without cooling the temperature rose about linearly from 26°C to 40.1°C with an initial $\Delta T/\Delta t$ of 3.4°C/h and after 5.3 h the temperature was still not levelling off. In a second run at 400 W with cooling the temperature rose from 24.3°C to a constant level at 29.1°C, which was reached within 3 h.

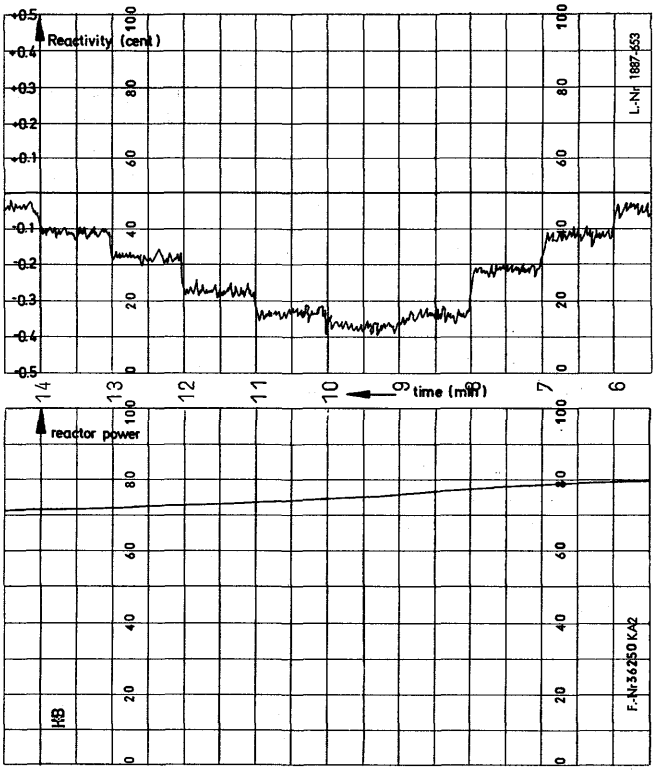

FIG.11. Reactivity traverse of an Al-sample in SNEAK-1 as calculated by the reactivity meter from the time dependent reactor power.

From these results it is expected that in a plutonium assembly a constant temperature will also be reached in a short time after temperature disturbances which occur during loading changes.

3.2. Measurements of reproducibility in reactivity

Many experiments such as void experiments and heterogeneity investigations by plate bunching require that the reactivity after unloading and reloading of fuel elements in the core, after unloading and reloading of plates in a fuel element, after position changes of the control rods and so on, can be well reproduced.

A series of measurements has been made in the assemblies SNEAK-1 and SNEAK-3A-1 to investigate the reproducibility. The results of these measurements are shown in Table I.

It can be seen from Table I that considerable uncertainties arise after a scram or the exchange of two elements of the same kind, but not with identical material plates. This has lead to the following decisions:

(1) Reactivity measurements during which a scram occurred are ruled out;

TABLE I. REPRODUCIBILITY MEASUREMENTS

Operation	Measured reproducibility in the operation, $\Delta k/k\beta$ [a]
1. Core clamping	< ± 0.01 cent
2. Un- and reloading of same element	negligible
3. Rearranging of an array of 6 fuel elements in the core	± 0.014 cent
4. Unloading of an element, un- and reloading of the plates, and reloading into the core	± 0.01 cent
5. Exchange of two elements of same kind	< ± 0.25 cent
6. Control rod positioning	± 0.02 cent
7. Regulating rod positioning	± 0.02 cent
8. Startup after scram	< 0.1 cent

[a] 1 cent $\hat{=} 7 \times 10^{-5}$ $\Delta k/k$

(2) In bunching and void experiments elements are refilled with identical-material plates and the elements are brought back to the same core position.

With these rules applied, the accuracy in reactivity measurements is very satisfactory for all kinds of experiments. It should be mentioned that a special fine regulating rod (auto-rod), with much better reproducibility in rod position than the regulating rod, is also available.

3.3. Dose-rates

To have free access to the reactor for all kinds of experiments, the biological shield is at the building wall. Therefore, during operation, personnel are not allowed in the reactor building. The dose-rate 3 m from the outer edge of the blanket is

5 mrem/h W due to gamma-rays, and

750 mrem/h W due to neutrons.

Outside the biological shield the maximum dose-rates are

4×10^{-3} mrem/h W due to gamma rays and

1×10^{-3} mrem/h W due to neutrons.

As the reactor power is restricted to 1000 W maximum, there is no radiation hazard outside the reactor building.

After shut-down the dose-rate inside the reactor building normally drops rapidly below 2.5 mrem/h, so that the building can be immediately entered. The highest radiation found so far was after an activation experiment in which the reactor was operated for 8.5 h at 600 W. In this case the 3-m dose-rate was 15 mrem/h after shut-down. The dose-rate dropped to 2.5 mrem/h within 9 h.

The radiation exposure in handling an unshielded core element or irradiated fuel plates can be appreciable. A dose-rate of 500 mrem/h was measured 10 cm from the surface of a fuel element, which had been

irradiated for 3.5 h at 10 W reactor power and had been allowed to cool for 20 min.

If possible, to avoid excessive radiation exposure to the operating crew, experiments requiring relatively high reactor power are run at the end of the week, so that the assembly can cool down over the weekend. So far, in only one case has a person received a dose of 50 mrem at one occasion. In this case it was necessary to do a repair job close to the reactor immediately after shut-down. All other exposures could be kept below tolerance.

3.4. Operational experience

3.4.1. Safety system

The reactor was scrammed in only one case because a safety limit had been exceeded. The reactor was on a positive period in order to raise the power. The operator was not careful, so the high power limit was reached and the reactor duly scrammed by the safety system.

In the early operation period a series of faulty scrams occurred, some of them due to failures in the safety circuitry itself, some due to perturbations in the ventilation system leading to pressure deviations. In the meantime, to a great extent, these perturbations could be traced and cured.

3.4.2. Auxiliary equipment

Most of the auxiliary equipment is performing well. Some repairs were necessary on the reactor loading machines and on the fuel-element loading and unloading machines. The reactor was, however, always available for experiments.

3.4.3. Availability of the reactor

Ten per cent of the working time (or about 8 h/week at two-shift operation) is needed for functional tests, maintenance and repairs, the remaining 90% of the time is available for experiments and their preparation.

3.4.4. Time requirements for experiments and loading changes

The time required for set-up and performance of typical zero power experiments in SNEAK is as follows:

(1)	Calibration of 10 control rods and one regulating rod, determination of shut-down reactivity of the safety rods	0.5 d
(2)	Pulsed experiments	2-3 d
(3)	Fission rate ratios (6 materials at core centre)	2 d
(4)	Spectrum measurements over the energy range 1 keV to 1 MeV with a set of proton recoil spectrometers at 1 core position	2 d
(5)	Spectrum measurements with ^{6}Li spectrometer	1-2 d

(6)	Spectrum measurements in the range < 3 keV by foil activation	2 × 0.5 d
(7)	Material worth measurements with high precision, 15 materials at core centre	1 d
(8)	Reaction rate and material worth measurements along a radial traverse, 7 reaction rates and 7 materials	2 d
(9)	Doppler measurements, hot versus cold sample with pile-oscillator	3 d
(10)	Reproducibility in control rod position (1 rod)	1 h
(11)	Unloading and loading of one core element	25 min
(12)	Loading of one core element with vertical experiment channel	1 h

The experimental programme with SNEAK-1 [1] covered a period of four months. In this time new equipment had to be tested and new techniques checked and compared.

The experiments on SNEAK-3A-1, including the loading of the core, the critical experiment, a complete programme of physics measurements and numerous loading changes in the course of heterogeneity studies, required 4.5 months

REFERENCES

[1] ENGELMANN, P., et al., Construction and experimental equipment of the Karlsruhe fast critical facility SNEAK, Proc. Int. Conf. Fast Critical Experiments and Their Analysis, ANL-7320 (1966) 725.

[2] ENGELMANN, P., et al., Initial experiments in the Karlsruhe fast critical facility SNEAK, Proc. Int. Conf. Fast Critical Experiments and Their Analysis, ANL-7320 (1966) 759.

[3] BICKEL, W., et al., Safety considerations for the Karlsruhe fast critical facility SNEAK, Proc. CEA-Conf. Safety of Fast Reactors, Aix-en-Provence, Sept.1967 (to be published).

[4] BÖHME, R., et al., Comparison of measurements in SNEAK-1 and ZPR-3-41, these Proceedings, SM-101/8.

[5] STEGEMANN, D., et al., Physics investigations of a 600 litre steam-cooled fast reactor system in SNEAK Assembly 3A-1, these Proceedings, SM-101/8.

[6] DOSCH, P., KRAUS, H.-J., UHRIG, H., "Design and experimental evaluation of an electromagnetic acceleration system for fast safety rods", Physics and Material Problems of Reactor Control Rods (Proc. Symp. Vienna, 1963) IAEA, Vienna (1963) 571.

DISCUSSION

D. TAIT: Is α_i adjustment of the delayed neutron fractions in the reactivity meter circuit required for different cores, or are the calculated values of α_i for a new core always satisfactory?

P. ENGELMANN: So far we have been able to use the calculated α_i values without major adjustments.

J. SUŠNIK: Regarding Fig. 8, what was the reactivity of the safety rod?

P. ENGELMANN: It was of the order of 90 cents.

W. B. LOEWENSTEIN: In your oral presentation you indicated the time that elapsed between receipt of the signal at the release mechanism and scram. What time is required for the signal to pass from the detector to the release mechanism?

P. ENGELMANN: I should point out that we cannot make the system very fast, otherwise we would get spurious scrams due to neutron statistics at low power. We have therefore inserted a time constant proportional to 1/i (where i is the ionization chamber current) into the circuit in order to smooth out flux signal changes. At very low power the time constant is of the order of one second, going down to 25 ms in the Watt range.

W.K. FOELL: In section 2.3.2. of your paper you state that the reactivity worth is obtained to within ± 0.02 cents at reactor powers higher than 30 W. What determines the upper power limit for these reactivity measurements?

P. ENGELMANN: The radioactivity in the fuel plates.

S. YIFTAH: What are the biggest core volumes that can be studied with SNEAK?

P. ENGELMANN: The maximum overall volume is 28 000 litres. The present core diameter limit of 2.0 m is due to the fuel inventory.

S. YIFTAH: What are your experimental plans for the next two years?

P. ENGELMANN: We intend to continue the SNEAK-3 programme with steam-cooled systems.

N. V. KRASNOYAROV: Has an oscillator been used in the SNEAK reactor?

P. ENGELMANN: Yes, a pile-oscillator with a sensitivity of $\pm 10^{-7}$ in k has been used.

A. ANCARANI: How did you obtain the two curves shown in Fig. 8?

P. ENGELMANN: We used an IBM 7074 computer off line, the recorded flux data being taken as the input data for the inverse kinetics code.

A. ANCARANI: Could they be considered as calibration curves for a typical safety rod?

P. ENGELMANN: No, calibrations are done separately and more slowly. The shape of the curves might be considered typical for SNEAK safety rods.

COMPARISON OF MEASUREMENTS IN SNEAK-1 AND ZPR III-41 *

R. BÖHME, L. BARLEON, K. BÖHNEL, M. EDELMANN,
P. ENGELMANN, G. FIEG, F.W.A. HABERMANN,**
D. KUHN, W. MAYER, ‡ W. SEIFRITZ, D. STEGEMANN,
P.L. van VELZE, ** H. WALZE AND H. WERLE
INSTITUT FÜR ANGEWANDTE REAKTORPHYSIK,
INSTITUT FÜR NEUTRONENPHYSIK UND REAKTORTECHNIK,
KERNFORSCHUNGSZENTRUM, KARLSRUHE,
FEDERAL REPUBLIC OF GERMANY

Abstract

COMPARISON OF MEASUREMENTS IN SNEAK-1 AND ZPR III-41. The experimental programme of the Karlsruhe Fast Zero Power Reactor SNEAK started in the autumn, 1966 with measurements on a 460-litre uranium assembly, a mock-up of ZPR III-41. During a four-month period the experimental installations and techniques of SNEAK were successfully tested. The installations include a movable drawer connected to an automatic sample changer operating in a horizontal experimental channel, a vertical drive unit, a pile oscillator, and a pulsed neutron generator. The techniques used include spectrum measurements with proton recoil counters and foil activation, and several techniques for determining reactor power and β/1, e.g., Rossi- and pulsed neutron source measurements.

In the experimental programme quantities such as critical mass, reaction rate ratios, neutron spectrum, material worths in the centre, radial and axial traverses, β/1, and reactor power were determined. The results were generally in good agreement with those of the ZPR III experiments, and the remaining discrepancies are discussed. These are partly due to small deviations in the material composition of the two assemblies. The experimental data are also compared with calculations using the 16-group YOM, 26-group KFK, and 26-group ABN cross-section sets. While critical mass is best calculated with YOM, the YOM spectrum is too hard, and both KFK and ABN give better agreement with the experimental spectrum.

1. INTRODUCTION

The fast critical facility SNEAK was built to support basic research in fast reactor physics and to investigate mock-ups of designed fast breeder reactors. Its first assembly, called SNEAK-1, became critical on 15 December, 1966. SNEAK-1 was chosen to be similar to a well-known critical assembly. The Argonne-built ZPR III Assembly No. 41 was selected, since it was convenient in size and composition.

1.1. Description of SNEAK

A general description of SNEAK was given in Ref. [1], but a few items should be repeated here. The machine is composed of square stainless-steel elements, each 275 cm long, hanging in an upper grid

* Work performed within the association in the field of fast reactors between the European Atomic Energy Community and Gesellschaft für Kernforschung mbH, Karlsruhe

** Euratom delegate

‡ On leave from Allgemeine Elektricitäts-Gesellschaft (AEG), Grosswelzheim.

plate with a lattice spacing of 5.44 cm. In the outer region aluminium tubes, each with the cross-section of 9 of the central elements, are used. Platelets 5.07 cm × 5.07 cm × 0.31 cm in size are used to build the core, and 1.7 cm × 1.7 cm × 30.5 cm rods compose the blanket. The fuel sections of the control and shim rods contain the same materials as the surrounding core. In the shut-down condition the fuel section is replaced by a poison part containing boron carbide powder and/or B_4C dispersed in a resin.

1.2. Core configuration

To make SNEAK-1 as similar as possible to Assembly 41 of ZPR III it was not possible to construct a simple unit cell within the fuel tubes. The regular element was filled with a stack of the following composition:

36 platelets of natural uranium
52 platelets of 20% enriched uranium
24 platelets of 35% enriched uranium
140 platelets of aluminium with 40% natural density
24 platelets of stainless steel (SS).

The total height of this stack of platelets was 86.9 cm. Above and below this core region a reflector 30.5 cm thick was constructed of depleted uranium rods (0.4% ^{235}U). With this arrangement of the core region, uniformity in composition could be achieved with cells having a volume of approximately 600 cm^3. A typical sequence of platelets in the stack is shown in Fig. 1. A horizontal cross-section through the core and the radial reflector (depleted uranium, reflector thickness about 30 cm) is sketched in Fig. 2.

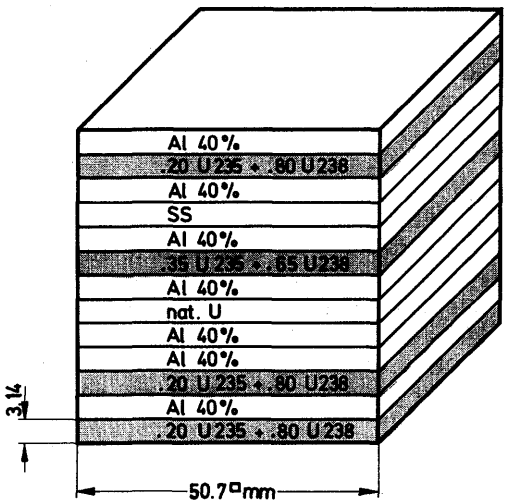

FIG. 1. Typical stack of plates used for loading SNEAK-1 core elements.

The average atom densities of all elements in the core and reflector regions are given in Table I. Also included are the data of ZPR III Assembly No. 41. The average uranium enrichment within the core was 17.2%. The volume fractions in the core were (in YOM-densities):

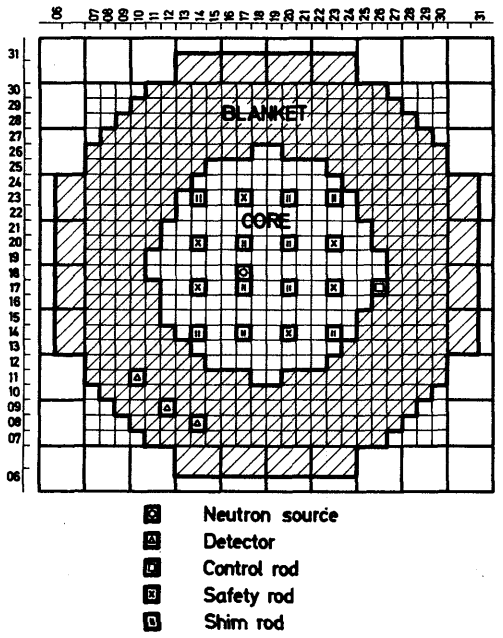

FIG.2. SNEAK-1 horizontal core cross-section.

5.8% ^{235}U; 28.3% ^{238}U; 14.2% stainless steel; 17.0% Al; and 34.6% void. In the blanket were 84.6% depleted uranium (0.4% ^{235}U), 6.8% steel and 8.6% void.

1.3. General remarks

In the following sections most of the experimental data are compared with the calculations. All experimental data were converted to $\Delta k/k$ assuming an effective delayed neutron fraction of $\beta_{eff} = 7.1 \times 10^{-3}$ (see section 3.2.3.3).

The multigroup cross-sections used are abbreviated as follows:

YOM, a 16-group cross-section set published by Yiftah et al. [2].

ABN, a 26-group set with self-shielding corrections published by Abagjan et al. [3]. Within each energy group the flux per unit lethargy used for weighting was assumed constant.

KFK, a 26-group set similar to ABN, but using a typical spectrum of a fast sodium-cooled breeder reactor for weighting. The cross-sections of structural materials differ considerably from ABN [4].

In a few cases ANL-results obtained with ELMOE [5] and ANL 635 [6] are listed. Results of the Argonne Group are taken from Refs [6-10]. The Karlsruhe results were calculated with the multiphase computer code NUSYS. A reproducibility index ρ is defined:

$$\rho = \frac{A_{exp.}^{Ass.41}}{A_{calc.}^{Ass.41}} \times \frac{A_{calc.}^{SNEAK-1}}{A_{exp.}^{SNEAK-1}}$$

TABLE I. ATOM DENSITIES IN SNEAK-1 AND ASSEMBLY No. 41 OF ZPR III

Material	$N_0(10^{20}$ atoms/cm^3)			
	SNEAK-1 core	SNEAK-1 reflector	Ass. 41 core	Ass. 41 reflector
^{235}U	28.09	1.54	28.61	0.91
^{238}U	135.5	399.3	139.7	399.8
Al	99.97	-	107.9	-
SS Fe	84.69	40.12	86.7	45.0
SS Cr	23.36	11.07	22.8	11.8
SS Ni	14.38	10.24	10.9	5.6
Mn	2.08	0.81		
Si	1.64	0.46		
Mg	1.13	-		
Ti	0.42	0.20		
C	0.29	0.14		
Mo	0.10	-		

where A may be any quantity obtained by experiments and calculations using identical methods and cross-section sets. In most cases, this index depends only slightly on the cross-section set used for the calculation. It eliminates the influence of the differences in composition of the assemblies compared. ρ is a measure of the reliability of the quoted results and errors. If ρ is not unity within the error limits, one must assume an inconsistency in the experimental results.

2. CRITICAL MASS

SNEAK-1 was constructed as shown in Figs 1 and 2. The assembly reached criticality with 181 fuel elements in the core region. The critical core volume was then 465.5 litres with one control rod partially inserted. The height of the cylindrical core was 86.9 cm, the diameter approximately 82.6 cm.

Without any correction the critical mass was calculated to be 510.1 ± 0.5 kg ^{235}U, the error arising mainly from the uncertainty in the determination of the isotopic composition of uranium. The critical mass quoted for Assembly 41 of ZPR III was 490.4 kg ^{235}U.

To allow a comparison of the critical masses, a reduction to the critical mass of a homogeneous clean critical sphere was carried out. The corrections applied are given in Table II.

TABLE II. THE CRITICAL DATA OF SNEAK-1 AND ASSEMBLY No. 41

	SNEAK-1	ZPR III Ass. No. 41
Cylinder height (cm)	86.9	81.4
Cylinder diameter (cm)	82.3	82.9
Core volume (litres)	465.5	440.0
Exp. critical mass m_{exp} (kg ^{235}U)	510.1 ± 0.5	490.4
Exp. $\Delta m/m : \Delta k/k$	5.6 ± 0.1	5.0
Correction for irregular shape (kg)	-3.2 ± 0.8	- 0.4
Correction for central gap of ZPR III (kg)	-	- 0.6
Correction for partially inserted control rod (kg)	-2.3 ± 0.1	-
Correction for built-in detectors (kg)	± 0.3	-
m of heterogeneous critical cylinder (kg)	504.9 ± 1.0	483.6
Heterogeneity correction (kg)	+5.9 ± 2.0	+18.6
m of homogeneous critical cylinder (kg)	510.8 ± 2.5	502.6
Shape factor	0.91 ± 0.005	0.92
m of homogeneous critical sphere (kg)	465 ± 4	462
Correction for difference in composition (%)	- 1.65	
m of equivalent spheres (kg ^{235}U)	457 ± 4	462

2.1. Correction for the irregular core outline

Owing to the plate and matrix structure of SNEAK the circumference of the core is not exactly cylindrical. A correction was determined by substituting edge elements of the core by blanket elements. The reactivity value of an edge element at a radius of 41.3 cm was measured to be $(9.9 \pm 0.1) \times 10^{-4}$ $\Delta k/k$, the calculated value was $(9.1 \pm 0.2) \times 10^{-4}$ $\Delta k/k$, independent of the cross-section set used. This value decreased by (9.0 ± 1.5)% per centimetre increase in the average radial position of a core element. From these values could be deducted that an ideal cylindrical core would contain (3.2 ± 0.8) kg ^{235}U less than the real one. This correction is eight times larger than that quoted by the Argonne authors. A similar discrepancy was already found by Ingram et al. [11].

2.2. Correction for the partially inserted control rod

For the fully inserted control rod a supercriticality of 13 cents was determined by period measurement. Using the ratio $\Delta m/m : \Delta k/k = 5.6 \pm 0.1$ for the fuel worth at the core boundary, a correction of (2.3 ± 0.1) kg ^{235}U was found, by which the ideal core is smaller than the real one. In addition to this a correction of 0.3 kg ^{235}U had to be applied because a few elements contained fission chambers and a neutron source canal; these elements were later replaced by regular ones.

So far a corrected critical mass of (504.9 ± 1.0) kg was obtained, where the uncertainties in the measured value and in the individual corrections were added statistically. In this figure heterogeneity corrections are not included.

2.3. Heterogeneity corrections

Heterogeneity experiments were not carried out at SNEAK-1. An estimate was made based on data published for ZPR III Assembly No. 41 [10]. For Assembly No. 41 an increase in reactivity of 330 in-hours $\approx 0.75\%\ \Delta k/k$ going from the homogeneous assembly to 93% enriched uranium metal platelets of 0.32 cm thickness was found by extrapolating measurements with different plate thicknesses. The platelets used in SNEAK have the same thickness but different enrichment: 58.8% of the fissile material is contained in platelets of 20% enrichment and 41.2% in platelets of 35% enrichment. For this reason only a fraction of the heterogeneity effect as determined for ZPR III Assembly 41 was assumed for SNEAK-1.

$$\left(\frac{\Delta k}{k}\right)_{het.} \approx \left(\frac{0.20}{0.93} \times 0.588 + \frac{0.35}{0.93} \times 0.412\right) \times 0.75\%\ \Delta k/k = 0.21\%\ \Delta k/k$$

which corresponds to 5.9 kg ^{235}U added at the circumference of the core. Because this estimate assumes heterogeneity effects to be proportional to the ^{235}U concentration only and neglects the influence of the ^{238}U diluent this figure may be in error by as much as 30%. When it is used, the critical data of the homogeneous cylinder are found to be

$$\begin{aligned} m_{hom.cyl.} &= (510.8 \pm 2.5) \text{ kg } ^{235}U \\ V_{hom.cyl.} &= 466.1 \text{ litres} \\ H &= 86.9 \text{ cm} \\ D &= 82.6 \text{ cm}. \end{aligned}$$

2.4. Shape-factor correction

The shape-factor method was used to obtain from the measured results the critical mass of a homogeneous sphere of SNEAK-composition. With data taken from Ref. [12], the shape factor $SF = 0.91 \pm 0.005$ was found. A 6-group, two-dimensional calculation yielded a shape factor 0.917 ± 0.006 but, to be consistent with ANL, the first value was taken. The final corrected critical mass of a homogeneous spherical core with SNEAK-1 composition was found to be

$$m_{hom.sphere} = 465 \pm 4 \text{ kg } ^{235}U.$$

2.5. Comparison with the ZPR III Ass. 41 critical mass

With each of the cross-section sets used, calculations of the critical mass in spherical geometry gave for Assembly 41 a 1.65% lower value than for SNEAK-1. Therefore, according to the experimental results at SNEAK the critical mass of Assembly 41 should have been 457 ± 4 kg ^{235}U. The comparable figure quoted by ANL is 462 kg ^{235}U, in good agreement with the Karlsruhe experiment, if one assumes an equivalent uncertainty for the Argonne result. The agreement becomes even better, if the correction for irregular core outline of Assembly 41 is increased to the SNEAK-1 value. In Table III experimental and calculated critical masses are compared.

TABLE III. EXPERIMENTAL AND CALCULATED CRITICAL MASS OF A HOMOGENEOUS SPHERE OF SNEAK-1 COMPOSITION

	Laboratory	Cross-section set	Approximation	m(kg ^{235}U)[a]
Experiment	Karlsruhe	-	-	465
	ANL	-	-	470
Calculation	ANL	ANL 635	S_4	464
	ANL	ELMOE	S_4	463
	K	YOM	Diff.	449
	K	ABN	Diff.	418
	K	KFK	Diff.	427
	K	ABN	S_4	399

[a] ANL data increased by 1.65% to allow direct comparison

3. EXPERIMENTAL RESULTS

3.1. Spectral measurements

3.1.1. Proton recoil counter

The neutron spectrum in a central cavity of the SNEAK-1 core was measured with spherical proton recoil counters. To keep the dead-time corrections below 20% the reactor was made subcritical by $\Delta k/k \approx -3.5 \times 10^{-4}$. The dead-time corrections were determined with the life timer of the analyser. For the energy region 10 - 60 keV Bennett's γ-n discrimination method was used [13]. Measurements in the energy range above 60 keV were made without γ-discrimination using four counters containing different gas fillings (1 atm H_2, 2 atm H_2, 4 atm H_2,

2.5 atm CH_4). The spherical counters were made of 0.5-mm stainless steel with a diameter of 3.94 cm.[1]

Measuring time per counter was around 3 h, the counting rate was about 2000 s^{-1}. The statistical error of the measured spectrum was a few percent. The data were corrected for wall effects as described by Benjamin [14]. The energy calibration was made at the Karlsruhe van de Graaf accelerator using the ^{7}Li (p, n) ^{7}Be reaction.

No fitting of adjacent energy regions was required, since the number of scattering atoms per counter was well known. The measured spectrum $\phi(u)$ (neutron flux per lethargy unit) together with a 26-group KFK-set calculation is shown in Fig. 3. In each case $\phi(u)$ was normalized to equal integrals $\int \phi(u)du$ within the energy limits 15 keV and 1400 keV. In Fig. 4 calculated spectra $\phi_i/\Delta u_i$ are compared with the experimental group spectrum $1/\Delta u_i \int_{\Delta u_i} \phi(u)\,du$, where Δu_i is the lethargy width of group i and ϕ_i the neutron flux in group i. The pronounced dips in the measured spectrum can be attributed to resonances of aluminium, iron, and chromium.

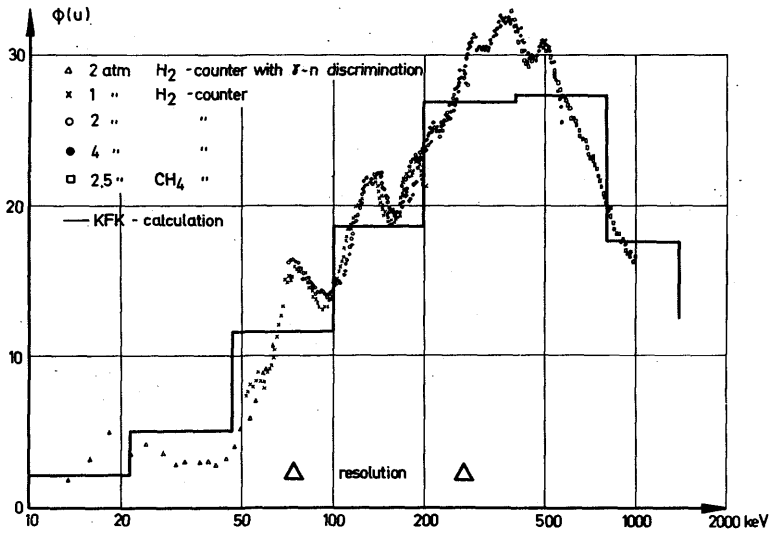

FIG. 3. Flux per unit lethargy measured with proton recoil counters.

3.1.2. Foil irradiations

To obtain information on the neutron spectrum below 10 keV, sandwiches of NaI-crystals and Cd-metal-foils were irradiated in the centre of SNEAK-1. The three-layer sandwiches had a diameter of 18 mm and a thickness of 3 × 0.5 mm. They were placed inside Cd-covers to prevent any thermal irradiation. The evaluation procedure is described in Ref. [15]. The Cd-activity was corrected for higher energy

[1] Manufactured by 20th Century Electronics, United Kingdom

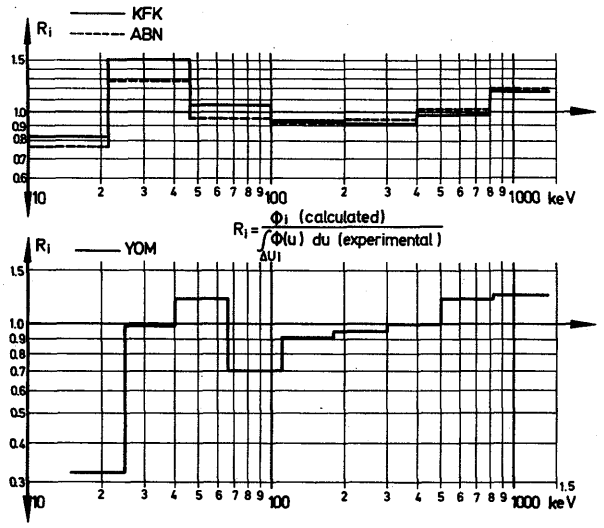

FIG.4. Ratio of calculated to experimental spectrum.

resonance activation assuming a neutron spectrum as obtained from the ABN calculation. The index finally found was

$$\frac{\phi(2.85\ \text{keV})\ \Delta E}{\phi(0.12\ \text{keV})\ \Delta E} = 450 \pm 160, \text{ or } \frac{\phi(u_1)}{\phi(u_2)} = (1.1 \pm 0.4) \times 10^4$$

The calculations gave the following results:

$$\frac{\bar{\phi}(u_1)}{\bar{\phi}(u_2)} = (1.4 \pm 0.4) \times 10^4 \text{ with the ABN cross-section set,}$$

$$\frac{\bar{\phi}(u_1)}{\bar{\phi}(u_2)} = (2.2 \pm 0.6) \times 10^4 \text{ with the KFK cross-section set.}$$

ϕ was obtained from a smoothed-out plot of the step function $\phi(u) = \phi_i / \Delta u_i$.

3.2. Spectral indices

3.2.1. Central fission ratios

Central fission ratios were measured with pairs of parallel plate fission counters of 4-cm diam. placed back to back in a central cavity of SNEAK-1. The counters were constructed as thin-walled flow counters using a 90% Ar, 10% CH_4 mixture. The cathode foils were made of platinum coated with approximately 6×10^{17} or 2×10^{18} atoms/cm^2 ^{233}U, ^{235}U, ^{238}U, or ^{232}Th.[2] The gravimetrically known mass agreed

[2] The foils were fabricated and weighed by the Euratom Central Bureau for Nuclear Measurements, Geel, Belgium

TABLE IV. FISSION RATIOS IN THE CENTRE OF SNEAK-1

	SNEAK-1 experiment	Calculated for SNEAK-1	ZPR III Ass. No. 41 experiment	Calculated for Ass. No. 41	ρ
$\frac{\sigma_f U_{233}}{\sigma_f U_{235}}$	1.52 ± 0.05	YOM 1.58 ABN 1.47 KFK 1.51 [a]	1.52 [b] 1.43 [c]	ANL 635 1.576 ABN 1.512 ELMOE 1.567	0.97 ± 0.03
$10^2 \frac{\sigma_f U_{238}}{\sigma_f U_{235}}$	4.38 ± 0.13	YOM 4.37 ABN 4.18 KFK 4.05	3.99	ANL 635 4.37 ABN 4.19 ELMOE 4.02	0.91 ± 0.03
$10^2 \frac{\sigma_f Th_{232}}{\sigma_f U_{235}}$	1.00 ± 0.09	YOM 0.89 ABN 0.81 KFK 0.80 [a]		ABN 0.84	

[a] fission cross-sections of ^{233}U and ^{232}Th taken from ABN, spectrum calculated with KFK.

[b] quoted in Ref. [9].

[c] Kirn-type counter, quoted in Ref. [10].

within ± 1% for ^{233}U and within ± 3% for ^{238}U with the mass determined by low-geometry α-counting. A correction was applied for fission fragments producing very little ionization energy. This correction applied to thin foils of around 2%, and with thick foils of around 10%. The fission rates for ^{235}U, ^{233}U, ^{238}U were obtained with thin foils, for ^{232}Th with thick foils. With the assumed mass accuracy of ± 1.5% and the background uncertainty the error is ± 3% for the $^{233}U/^{235}U$ and $^{238}U/^{235}U$ fission ratio, and ± 6% for the $^{232}Th/^{235}U$ ratio. The measured fission ratios are listed in Table IV. They are compared with calculated ratios determined from fission rates n^x of the isotopes x

$$n^x = \sum_{i=1}^{26} f_i^x \sigma_i^x \phi_i$$

where f_i is the self-shielding factor and ϕ_i is the neutron flux in energy group i as calculated in the centre of a critical sphere by diffusion calculation. f^{233U} and f^{232Th} are taken equal to 1, since these materials are not contained in the normal core mixture. Also listed are fission ratios measured by Argonne. Calculations indicate that they should not deviate by more than 3% from the Karlsruhe results. The fission ratio $^{233}U/^{235}U$ is in agreement with the calculation and the ANL experiment; the measured threshold indices are higher than the calculated ratios.

This contradicts previous experience, as exemplified by the ANL results, that these threshold indices usually indicate a softer spectrum than is calculated. An intercalibration of fission counters seems appropriate to solve this discrepancy.

3.2.2. Material worth measurements

Several samples of different composition and size were inserted into a central void of the core. This was done using an automatic sample changer and/or a pile oscillator [16]. The drawer of the sample changer was 5.8 cm × 3.1 cm in cross-section and ran horizontally through the core and radial blanket in the height of the core centre. The pile oscillator had a cross-section of 4.7 cm × 4.7 cm; it was located in the element tube at position 17/20, and ran axially through the core and axial reflectors. A central pocket of the sample changing equipment was usually filled with the sample of interest; the remaining volume was filled by structural material only. In the course of the measurement the sample was withdrawn several times to a far outside position and inserted again into the core centre. The automatic sample changer was also used for the measurement of radial material worth traverses, the pile oscillator for axial traverses.

The results of Fourier analyses, as listed in Table V, are not corrected for any possible spectral distortion due to the missing fuel in the sample drawer. Sample sizes varied from approximately 4.7 cm × 4.7 cm × 0.05 cm (^{235}U) to 4.7 cm × 4.7 cm × 2.5 cm (Al). Sample size effects were not investigated in detail.

Reactivity effects were of the order of 2×10^{-5} $\Delta k/k$. The errors shown are derived from the statistical error of 1×10^{-7} $\Delta k/k$. Additional errors may be incurred by sample size effects and possibly by contributions of the transition part of a cycle to the basic harmonic. To facilitate comparisons of measured and calculated values, the absolute value is given only for a 1 g ^{235}U sample and for a Pu sample (Table V),

TABLE V. ABSOLUTE REACTIVITY CHANGE DUE TO THE INSERTION OF FISSILE SAMPLES IN THE CENTRE OF SNEAK-1 (in 10^{-6} $\Delta k/k$)

	SNEAK-1 experiment	Calculated			Sample description
		YOM	ABN	KFK	
1 g ^{235}U-sample	2.28 ± 0.02	2.30	2.32	2.32	93.4% enriched U-metal, 0.05 cm thick, corrected for ^{238}U content
Plutonium sample	104 ± 1	108	105	104	Steel-canned oxide sample of 0.6 cm thickness; contents: 28.9 g ^{239}Pu, 2.6 g ^{240}Pu, 0.6 g ^{235}U, 86.9 g ^{238}U, 17.1 g O, 14.7 g stainless steel

s

TABLE VI. RELATIVE REACTIVITY WORTH PER ATOM IN THE CENTRE OF SNEAK-1

	SNEAK- [a] experiment	Ass. No.41- [b] experiment	YOM	ABN [c]	KFK [c]	ρ [d]
^{235}U	1000.0 ± 10.0	1000.0 ± 17.0	1000.0	1000.0 (999.6)	1000.0 (999.6)	1.00 ± 0.02
^{238}U	-45.3 ± 0.5	-44.3 ± 1.7	-43.2	-43.9 (-43.6)	-42.9 (-42.5)	0.97 ± 0.04
Al	- 4.8 ± 0.1	-4.1 ± 1.3	-2.9	-3.5 (-3.7)	-4.4 (-4.4)	0.80 ± 0.34
C	+ 1.7 ± 0.1	+0.5 ± 1.1	+2.0	+4.5 (+4.6)	+2.8 (+2.9)	0.4 ± 2.2
Ni	-16.2 ± 0.2	-13.0 ± 0.9	-18.8	-18.3 (-16.9)	-21.5 (-19.7)	0.78 ± 0.08
Mo	-39.6 ± 0.4	-33.3 ± 1.3	-42.0	-39.9 (-39.7)	-41.2 (-41.0)	0.84 ± 0.05
^{10}B	-557.0 ± 30.0	-590.0 ± 17.0	-444.0	-497.0 (-496.8)	-524.0 (-523.8)	1.07 ± 0.08
Fe	-8.1 ± 0.5	-8.5 ± 1.0	-9.7	-9.0 (-8.7)	-9.0 (-8.6)	1.02 ± 0.17
Ta	-159.0 ± 1.0	-147.5 ± 3.0				
W	-73.4 ± 0.7	-63.5 ± 1.7				
Ag	-171.0 ± 8.0	-148.0 ± 3.5				

[a] For ^{10}B, Fe, Ag no Fourier analysis was carried out; the values were obtained by the inverse kinetics method.

[b] Quoted in Ref. [10].

[c] The first figure is calculated for a very few sample atoms added to the original core composition, the value in brackets is calculated for a number of atoms per cubic centimetre added, which corresponds to the actual sample density

[d] Set equal to 1 for ^{235}U

in the second part of the table the material worth per sample atom is listed relatively to one atom of ^{235}U, the value of which is set equal to 1000.

As can be seen from the reproducibility index ρ, agreement with Argonne results is obtained within the limits of error for most samples. For Mo and Ni, however, the discrepancy (between ANL and Karlsruhe experiments) is too large. This may be due to a pronounced reduction of reactivity worth for the rather big samples used at Argonne (samples used at Karlsruhe had a thickness of 0.6 cm for Ni and 0.3 cm for Mo, the Argonne samples were about 10 times thicker).

Also listed are reactivity effects as calculated by perturbation theory. The fluxes for these calculations were found using a one-dimensional diffusion code in infinite cylinder geometry. The diffusion code applies a DB^2-correction to the removal cross-section to take into account the separated coordinate. Since the cross-section sets used give too low a critical mass, usually two calculations were carried out:

(a) One with an energy-independent B^2 which renders the reactor critical; and

(b) One with a B^2 estimated from bare calculations and/or fission rate traverses (see Section 3.3), which makes the reactor supercritical by 1 to 2%.

The worth of light scatterers such as carbon is considerably decreased in case (b) (from 3.3 to 2.4 for the KFK set in Table VI). Since neither (a) nor (b) describe the reality correctly, the average of the two cases is quoted in Table VI. The calculated worths of Al and C may therefore be wrong by ± 4% and ± 15%, respectively; the others by ± 1%.

The absolute values given for 1 g ^{235}U and for a Pu platelet of SNEAK are calculated for the exact core radius and an extrapolated core height of 126 cm, which is a reasonable assumption obtained from fission counter traverses. For the calculation of the normalization integral a cosine flux distribution in the axial direction was assumed.

The composition of the perturbed region was taken as the original core mixture plus ΔN^x atoms of the sample atom x per cubic centimetre.

Self-shielding in ABN and KFK is treated by f-factors

$$\sigma^x_{i_{eff}} = f^x_i \cdot \sigma^x_i$$

with

$$f^x_i = f^x_i(\sigma^x_0),$$

where σ^x_0 is the total macroscopic cross-section of all non-x isotopes per x atom: $\sigma^x_0 = \Sigma_t^{non\text{-}x}/N^x$. N is the density of x atoms present in the original core composition plus the ΔN^x atoms added in the perturbation sample: $N^x = N^x + \Delta N^x$. Two calculations were carried out: for $\Delta N^x \ll N^x_0$ (usually 10^{20}), where σ^x_0 does not change very much, and for $\Delta N^x \gg N^x_0$ where σ^x_0 approaches zero.

Table VI shows the perturbations calculated with the first method and in parenthesis the results obtained with the second method. The differences are not grave, since the SNEAK-1 spectrum is so hard that there are only a very few neutrons in the resonance region. The true perturbation should lie somewhere between the two values given in Table VI, tending more towards the value in parenthesis for U, Mo, Ni and Fe.

3.2.3. Measurement of kinetics parameters

Several methods were employed to measure the decay constant of the prompt neutron flux, α. α depends on the multiplication constant k, the effective fraction of delayed neutron β, and the prompt neutron lifetime ℓ:

$$\alpha = \frac{1\ell - k(1-\beta)}{\ell}$$

3.2.3.1. Rossi-α-measurements

A new time-analyser was developed [17] which permits Rossi-α-measurements down to a signal-to-background ratio of 5% and up to trigger rates of 10 α. It consists mainly of a 104-stage fast shift register controlling 32 fast coincidence channels. An incoming pulse starts the analyser, the next pulse is registered in its appropriate time channel and, simultaneously, starts the next cycle. Up to 32 analyser cycles can overlap, the dead time for successive cycles being reduced to one channel width. With this apparatus Rossi-α has been measured in SNEAK-1 up to a reactor power of 10 mW at a subcriticality near 2×10^{-4} $\Delta k/k$. α was determined from the counting rate c(t) of delayed coincidences according to the equation [18, 19]:

$$c(t)\,\Delta t = (a\, e^{-\alpha t} + b)\, b\Delta t$$

with

$$a = \frac{W\chi_2 k^2}{2[1-k(1-\beta)]^2} \cdot \alpha, \qquad b = WF$$

where
- t = delay time
- Δt = channel width
- W = detector sensitivity $\approx 4 \times 10^{-5}$ counts/fission
- F = fission rate
- χ_2 = $\overline{\nu_p(\nu_p - 1)}/\overline{\nu}^2 \approx 0.8$
- ν, ν_p = number of (prompt) neutrons per fission.

Pulses of four ^{3}He-counters, connected in parallel and placed in position 18/20 of the SNEAK-1 core, were used for this autocorrelation experiment. Measuring time was about 1 h at counting rates between 250 s^{-1} (at 1.5 \$ subcriticality) and 12 000 s^{-1} (at 0.03 \$ subcriticality) resulting in signal-to-background ratios a/b between 17.5 and 1.6.

Least-squares fitting of the measured coincidences to an exponential and a constant term yielded the data plotted in Fig. 5 as function of the average time interval between two detected pulses, 1/b, which is a measure of reactivity. In any case only the fundamental exponential mode was observed. Extrapolation of the measured α to delayed critical (i.e. 1/b = 0) yields

$$\alpha_c = \frac{\beta}{\ell} = (5.2 \pm 0.1) \times 10^4\ s^{-1}.$$

3.2.3.2. Pulsed neutron source measurements

The decay constant of the prompt neutron flux was measured at several subcritical states using a pulsed neutron source. The essential

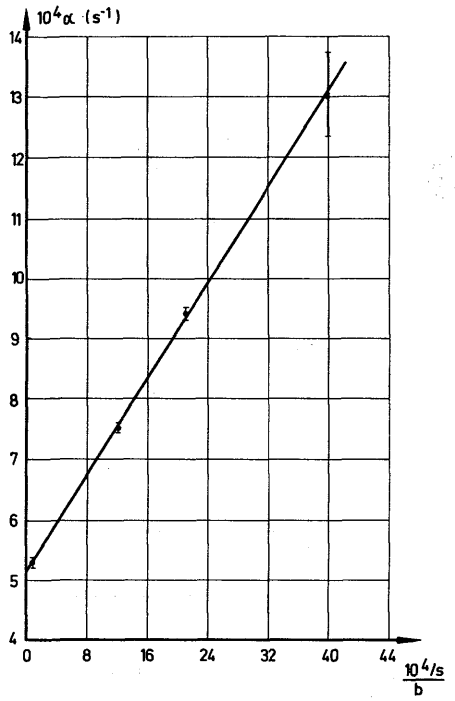

FIG.5. Rossi-α versus average time interval between pulses.

features of the Karlsruhe built[3] neutron generator are a duoplasmatron deuterium ion source [20] on high potential and a tritium target on ground potential at the end of a 2-m-long tube in the centre of the core. The maximum repetition frequency was 2000 s^{-1}, the pulse width was 1 μs, and the maximum source strength used was 5×10^4 neutrons per pulse. A ^{235}U-fission counter in position 17/16 was used as detector. Time analysing was performed with the shift-register mentioned in section 3.2.3.1. The dead time between the 32 channels of the analyser is about 30 ns.

The measured flux decay could be described well by a single exponential. The decay constants are plotted in Fig. 6 versus the reactivity as derived from control rod positions. Extrapolation of the curve to delayed critical yields

$$\alpha_c = (5.3 \pm 0.1) \times 10^4 \ s^{-1}.$$

3.2.3.3. Comparison of measured with calculated α_c

The kinetics parameters of SNEAK-1 were calculated for the delayed critical condition using the data of Keepin [21]. The generation time Λ was obtained by dividing the space-and energy integrated, adjoint weighted neutron density by the adjoint weighted neutron source term.

[3] Built by W. Eyrich, Karlsruhe

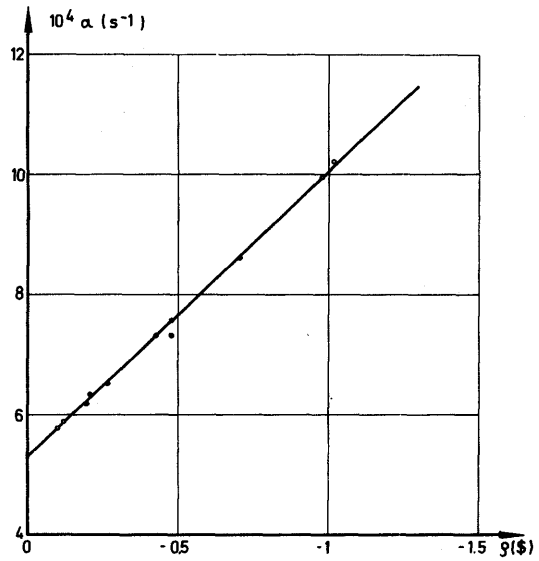

FIG.6. Pulsed measurement: α versus subcriticality.

The effective fraction of delayed neutrons was obtained from a division of the delayed neutron source term by the total adjoint-weighted neutron source term. It is believed that spherical calculations give the most appropriate results, since one-dimensional calculations do not account for the blanket in the separated direction. The results of the calculations are given in Table VII. Calculations for Assembly No. 41 of ZPR III yielded the same β_{eff}, but a 3% shorter lifetime, resulting in a 3% higher value of α_c.

The reproducibility index ρ for Rossi-α-measurements is $\rho = 1.02 \pm 0.05$; this shows good agreement of the ANL and SNEAK-1 results. The pulsed neutron source technique yielded an α_c only 2% higher than Rossi-α at delayed critical.

All calculated α_c are larger than the measured decay constant. But the discrepancy is only 10% for the KFK set, whereas the YOM set and the otherwise excellent ELMOE calculation of Argonne yield α_c about 30% larger than measured.

3.3. Reaction rate traverses

Reaction rates along the central axis of SNEAK-1 were measured with fission chambers placed in a 1.7 cm × 1.7 cm guide tube in element position 19/18. Radial traverses were obtained from fission counters located in a pocket of a horizontal drawer. The axial fission rate traverse of ^{235}U is shown together with a calculated one in Fig. 7; the ^{233}U-fission traverse is plotted in Fig. 8. Within the core the experimental ^{235}U-fission rates are very well fitted by a cosine function with a half-period of 126 cm. Deviations from the calculated traverses occur near the outer boundary of the blanket, possibly owing to streaming in the guide channel. The

TABLE VII. PROMPT NEUTRON DECAY CONSTANT α_c

	Experiment $10^{-4}\ \alpha_c/s^{-1}$	Cross-section set	Calculated β_{eff}	Calculated $10^7\ \Lambda/s$	Calculated $10^{-4}\ \alpha_c/^{-1}$
SNEAK-1					
Rossi-α	5.2 ± 0.1				
Pulsed Measurements	5.3 ± 0.1				
Average	5.25 ± 0.10	YOM	0.00708	1.08	6.6
		ABN	0.00712	1.16	6.2
		KFK	0.00709	1.22	5.8
ZPR III Ass. No. 41					
Rossi-α	5.55 ± 0.16	KFK	0.00709	1.17	6.1
		ANL635	0.0073 [a]	0.95	7.6
		ELMOE	0.0073 [a]	1.03	7.1

[a] estimated.

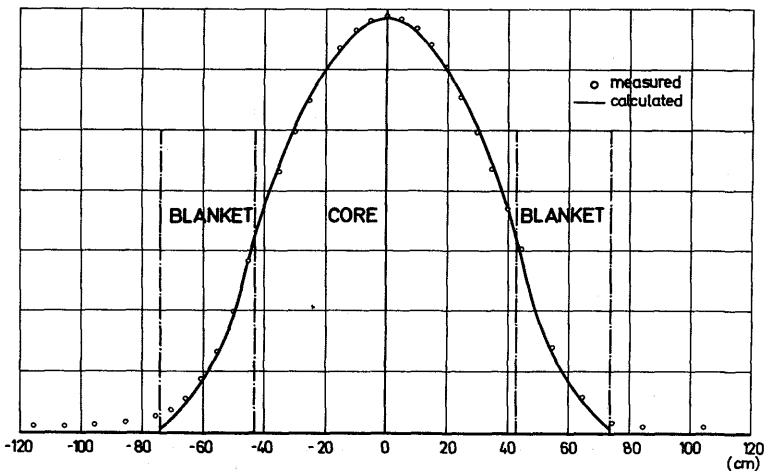

FIG. 7. Axial ^{235}U-fission counter traverse (arbitrary units).

radial dependence of the $^{238}U/^{235}U$ fission ratio is shown in Fig. 9. The deviation from the calculated traverse is mainly due to the ^{238}U fission rate in the blanket, where calculations give only half the experimental value.

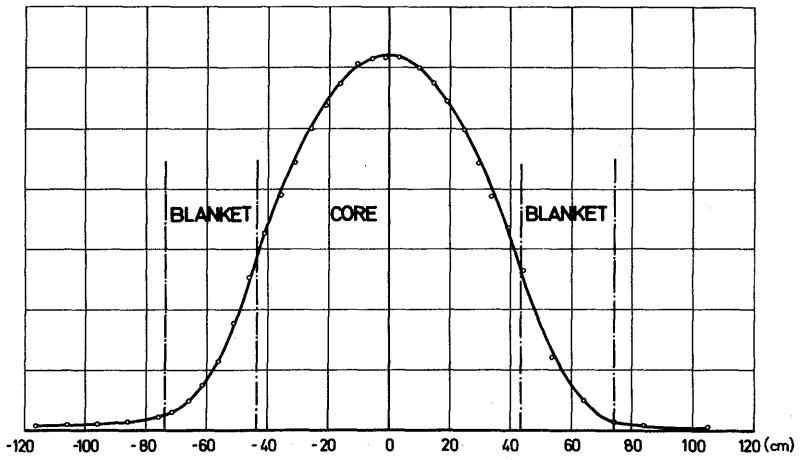

FIG.8. Axial ^{233}U-fission counter traverse (arbitrary units).

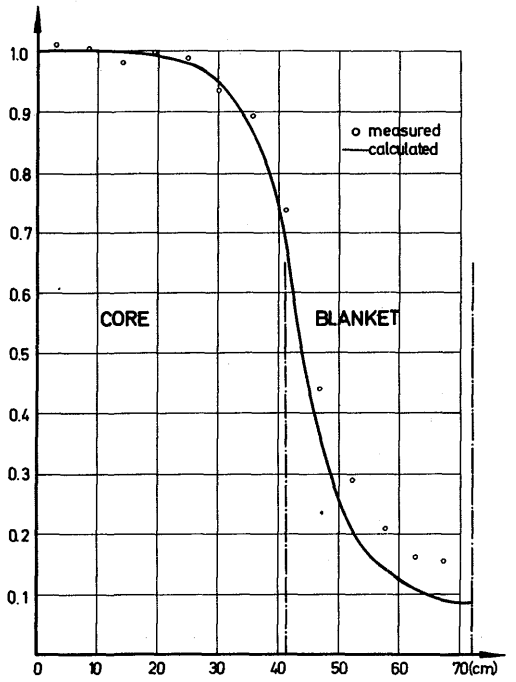

FIG.9. Radial traverse of $\sigma_{f\,U235}/\sigma_{f\,U238}$ (arbitrary units).

3.4. Power calibration

Fission rate measurements with calibrated ^{235}U and ^{238}U counters together with calculated reaction rate traverses were used to estimate the operating power of SNEAK. It was also obtained from a two-detector

cross correlation noise measurement [22] at filter frequencies $\omega \ll \alpha_c$ in the range between 3 and 90 W and in the course of the Rossi-α-measurement from the signal-to-background ratio [19]. The power obtained for a certain detector current was (1.0 ± 0.2) W, (1.5 ± 0.2) W, and (1.2 ± 0.2) W for fission rate, cross-power spectral density, and Rossi-α-measurement, respectively. The error of the first method arises from inaccurate counter calibration and the uncertainty of the calculated traverses; the noise measurements are affected by counting statistics (statistical error less than 10%) and by the uncertainty in a correction factor [23] which accounts for the spatial distribution of the fission processes. The discrepancy between the two noise measurements could not be solved.

4. CONCLUSIONS

The critical mass of a homogeneous sphere as determined by Argonne and Karlsruhe is in satisfactory agreement (ρ = 1.01 ± 0.01). The critical mass calculated by the cross-section sets used at Karlsruhe is up to 15% lower than the experimental one. Best results are still obtained by the application of YOM data or the ELMOE corrected cross-sections. The weighting spectrum used for ABN is much softer than the SNEAK-1 spectrum and the YOM-weighting spectrum, and this may partially account for the discrepancies.

Also, the introduction of improved cross-sections for structural materials and ^{235}U seems to give better agreement, as can be seen from the accurate result obtained with the ANL 635 set. For this reason new multigroup cross-section sets, which will better represent the conditions in SNEAK, are now being developed at Karlsruhe.

The group width of the ABN and KFK sets in the 10 - 1000-keV region ($\Delta u \approx 0.7$) should be reduced to allow better comparison of measured and calculated spectra. So far, ABN and KFK seem to give quite reasonable average values in this energy region. The calculated YOM-spectrum is too hard as can be seen from the slope of the YOM-curve in Fig. 4. In the lower-energy region between 0.1 and 3 keV, where YOM fails completely, the spectra calculated with ABN and KFK give acceptable results.

The fission ratio measurements are not very illuminating, so long as the discrepancy between Karlsruhe and Argonne results is not resolved.

With the exception of Ni and Mo, material worth measurements agree within the limits of error. For Ni and Mo sample size effects seem to produce a large discrepancy. For the thin samples used at Karlsruhe the difference between measured and calculated worth is considerably reduced. Al and C are not useful for a comparison, since their reactivity worth is strongly influenced by slight distortions of the adjoint spectrum which may arise from the sample drawer filling. This leaves fissionable materials and ^{10}B. Good agreement between calculated and experimental results is obtained for the KFK and ABN cross-section set. The measured ratio ^{235}U-worth:Pu-worth is almost 2% lower than the calculated one. Considering the small critical masses calculated with KFK and ABN, it appears possible that the average $(\nu-1)\sigma_{fU_{235}}$ is too high in both sets.

A reduction, perhaps around 2%, would yield a much better estimate of the critical mass and the relative worths of Pu, ^{235}U, ^{238}U, and ^{10}B. The calculated ^{238}U-worth would then be too low by only 2 to 4%, the ^{10}B-worth by 0 to 5%, but the discrepancy in the reactivity worths of the steel components would be slightly enhanced. The changes included in the new SNEAK-set [24] act in this direction.

The decay constant of prompt neutrons at delayed critical, α_c, was obtained by two different methods. The α_c were in good agreement, also with the Argonne measurement. All calculations yield too high an α_c, indicating that the calculated spectrum is too hard. But the KFK-set is only 10% off, which is a considerable improvement as compared to the 25% deviation found with the YOM-set.

5. SUMMARY

It was shown that most experimental results obtained with the SNEAK facility agree with those of Argonne's ZPR III. The application of the KFK cross-section set for calculations reduces the differences between experiments and calculations considerably with the exception of the critical mass, where a discrepancy of 8% was encountered.

ACKNOWLEDGEMENT

We would like to thank the operation staff of SNEAK for continuous support during the experimental work. Thanks are due to Mrs. Braun for helping with the calculations, and to Mr. F.H. Helm for his correction of the manuscript.

REFERENCES

[1] ENGELMANN, P. et al., ANL-7320, (Oct.1966) 725.
[2] YIFTAH, S., OKRENT, D., MOLDAUER, P.A., Fast Reactor Cross Sections, Pergamon Press (1960).
[3] ABAGJAN, L.P. et al., KFK-tr-144 (1964) translation.
[4] KÜSTERS, H., METZENROTH, M., ANL-7120 (1965).
[5] RAGO, A.L., HUMMEL, H.H., ANL-6805 (January 1964).
[6] DAVEY, W.G., ANL-6570 (May 1962).
[7] HESS, ALLEN L., GASIDLO, J.M., Critical Studies with ZPR III of a 440 litre Fast Reactor Core Containing Uranium Enriched to 17%, ANS-Meeting, Salt Lake City (1963).
[8] DAVEY, W.G., Nucl. sci. Engng 19 (1964) 159-273.
[9] THALGOTT, F.W. et al., ANS-Meeting on "Fast Reactor Technology" Detroit (1965).
[10] McVEAN, R.L., DAVEY, W.G., FISCHER, G.J., "The role of the fast critical facility in the power reactor programme", Exponential and Critical Experiments (Proc. Symp. Amsterdam, 1963) 1, IAEA, Vienna (1964) 85.
[11] INGRAM, G. et al., AEEW-R 315 (1963).
[12] ARGONNE NATIONAL LABORATORY, ANL-5800, Second Edition (1963).
[13] BENNET, E.F., Rev. sci. Instr. 35 (1962) 1153.
[14] BENJAMIN, P.W. et al., AWRE No. NR2/64 (1964).
[15] EHRET, G., Atompraxis 1 (Nov.1961) 393-400.
[16] ENGELMANN, P. et al., ANL-7320, (Oct.1966) 730.
[17] EDELMANN, W. et al., KFK-522 (Jan. 1967).
[18] ORNDOFF, J.D., Nucl. sci. Engng. 2 (1957) 450.
[19] BORGWALDT, H., STEGEMANN, D., Nukleonik 7 (1965) 313.

[20] EYRICH, W., SCHMIDT, A., "Two compact, high-intensity pulsed neutron sources", Pulsed Neutron Research (Proc. Symp. Karlsruhe 1965) II, IAEA, Vienna (1965) 589.
[21] KEEPIN, G.R., Physics of Nuclear Kinetics, Addison-Wesley (1965).
[22] SEIFRITZ, W. et al., Proc. Symp. Neutron Noise, Waves and Pulse Propagation, Gainsville, Florida, AEC-Symp. Ser. No. 9 (1966) 195 and
SEIFRITZ, W., STEGEMANN, D., Nukleonik 9 (1967) 169.
[23] OTSUKA, M., JIJIMA, T., Nukleonik 7 (1965) 488.
[24] KÜSTERS, H. et al., These Proceedings SM-101/12.

DISCUSSION

S. YIFTAH: I should like to ask two questions. First, have you compared material worth measurements with calculations for samples not in the centre of the core? Second, how were the calculations made?

R. BÖHME: We have tried to make reactivity worth traverses, but the results were so inaccurate that we could not draw any significant conclusions. The traverses shown in Fig. 11 of paper SM-101/11 are the best obtained so far. The calculations were first-order perturbation calculations in the diffusion approximation. The material in the perturbed region was assumed to consist of the original homogeneous core composition plus N sample atoms per cm^3. Using the f-factor concept of Bondarenko, we varied N between 10^{20} and the actual sample density in order to obtain information about the influence of self-shielding.

E. TÜRKCAN: Have you carried out any experiments with the probability analyser to determine α, apart from the Rossi-α measurements?

D. STEGEMANN: Perhaps I can answer this question, as a co-author of the paper under discussion. We have made measurements with the probability analyser, but there were unforeseen dead-time effects in the linear channel and the results could not be compared with those yielded by other techniques.

E. HELLSTRAND: Is the reactivity worth per atom of ^{10}B the value for an infinitely thin sample?

R. BÖHME: No, the sample consisted of 2.9 g of ^{10}B powder pressed into a tablet with a 15-cm^2 surface and a height of 1 mm.

E. HELLSTRAND: Did you apply shielding corrections?

R. BÖHME: No, we did not.

J.L. ROWLANDS: I should like to ask whether, in view of the fact that you use uranium of a lower enrichment, the SNEAK assembly is less heterogeneous than the ZPR III assembly and whether this would have an effect on the comparison of the $^{238}U/^{235}U$ fission ratios for the two assemblies.

R. BÖHME: It is true that our assembly is less heterogeneous, since we use platelets of 20% and 35% enrichment instead of the 93% used at Argonne. And we do know, from fine-structure measurements of the ^{238}U fission rate, that this could affect the comparison of the average $^{238}U/^{235}U$ fission ratios. However, we do not believe that the 9% discrepancy is due solely to this effect.

I should like to add that we were not aware of the volume averaging of fission ratios measured at Argonne; in our experiment the detectors were placed in a large (about one litre) cavity in the centre of SNEAK-1.

W.K. FOELL: In your oral presentation, you mentioned that there was a considerable discrepancy between the reactivity worth results for aluminium and graphite. You implied that this might be due to the influence of the environment on the adjoint function. Could you please elaborate on this and describe the sample environment in your experiments?

R. BÖHME: Originally, we arranged platelets in the vicinity of the sample in such a way that they corresponded to the average core composition. Since the Fourier analyses were affected by the loss of delayed neutron precursors due to the withdrawal of the fissionable materials contained in the sample drawer, we had to alter the loading of the sample drawer: we removed all fuel and left only the structural materials, thereby decreasing the fuel concentration in the vicinity of the sample. This, we suspect, resulted in slight changes in the adjoint-energy distribution. From calculations we know that minor changes in the adjoint-energy distribution result in completely different material worths for liquid scatterers, making an interpretation very complicated.

G.S. BRUNSON: What counters were used in the Rossi-α and pulsed neutron experiments?

D. STEGEMANN: In the Rossi-α experiment we used four ^{3}He counters, connected in parallel close to the centre of the assembly. In the pulsed source experiments we used a ^{235}U fission chamber located near the centre.

G.S. BRUNSON: Have any runs with the pulsed neutron source been made with the counter located in the reflector?

D. STEGEMANN: No.

H.V. KRASNOYAROV: Was the dependence of α on the location of the detector measured?

R. BÖHME: No, the detector was kept in one place.

H.V. KRASNOYAROV: Working with the BFS assembly we have found for one of the systems that α remains independent of the location of the detector in the Rossi-α experiments. Is there any indication that in systems with reflectors there are different values of α for the core and the reflector (as stated by Mr. Kockum in his oral presentation of paper SM-101/54)?

R. BÖHME: On the basis of our investigations so far, I would say that it depends on the effect the reflector has on the kinetic behaviour of the system. One extreme is a not-too-small fast core surrounded by a normal depleted uranium reflector. We did calculations involving a modal synthesis treatment and could not find any space dependence. With this system, therefore, we placed the detector close to the centre in all cases. The other extreme is the fast coupled system STARK, where we have found space dependence both from theoretical studies and from Rossi-α experiments (see report KFK 522 published by the Gesellschaft für Kernforschung m.b.H, Karlsruhe).

W. ROTTER: With regard to Fig. 6, how did you measure the reactivity?

R. BÖHME: The reactivity scale is that of the shim rods, which had been previously calibrated one at a time in a critical core. Errors arose because the reactivity values are not strictly additive.

W. ROTTER: The α measurements, made with a pulsed source, were not used in determining the reactivity (by, for example, the Gavel-Russell or the Gozani method). What does the comparison of these ρ_{pulse} values with the reactivity values given in Fig. 6 indicate?

R. BÖHME: At a few reactivities the area method yielded values which were within a few per cent of those obtained by control rod calibration.

W. ROTTER: Is the linearity of $\alpha = f(\rho)$ conserved at higher values of $|\rho|$?

R. BÖHME: We have not yet evaluated measurements made at higher reactivities.

PHYSICS INVESTIGATIONS OF A 670-LITRE STEAM-COOLED FAST-REACTOR SYSTEM IN SNEAK, ASSEMBLY 3A-1*

D. STEGEMANN,
L. BARLEON, A. BAYER, R. BÖHME, K. BÖHNEL,
K. BURKART, J. C. CHOU, P. ENGELMANN, G. FIEG,
F. W. A. HABERMANN+, D. KUHN, W. MAYER‡, M. METZENROTH,
A. RABERAIN+, H. SEUFERT,
P. L. VAN VELZE+, H. WALZE, H. WERLE AND D. WINTZER
INSTITUT FÜR ANGEWANDTE REAKTORPHYSIK,
INSTITUT FÜR NEUTRONENPHYSIK UND REAKTORETECHNIK,
KERNFORSCHUNGSZENTRUM KARLSRUHE,
KARLSRUHE, FEDERAL REPUBLIC OF GERMANY

Abstract

PHYSICS INVESTIGATIONS OF A 670-LITRE STEAM-COOLED FAST-REACTOR SYSTEM IN SNEAK, ASSEMBLY 3A-1. A series of experiments is under way at the Karlsruhe fast zero power reactor SNEAK for the investigation of steam-cooled fast reactors in the 100-MW(e) range. This series started in May with the critical experiment of SNEAK 3A-1, a 670-litre uranium system containing 7.41×10^{20} atoms/cm^3 of hydrogen in the form of polyethylene foils. The neutron physics of this assembly has been studied in detail. The neutron energy spectrum has been measured by various methods from the eV-region to more than 1 MeV in the core centre and at the periphery, reaction rates have been measured in the centre and in axial and radial traverses, and the initial breeding ratio and the reactivity worth of selected materials have been determined. Measurements of the Doppler reactivity effect, the steam void effect and of β/ℓ have been performed. Special attention has been given to the experimental investigation of heterogeneity effects. The experimental results are compared with calculations using the 26-group ABN set and a specially prepared 26-group cross-section set KFK-SNEAK using latest cross-section information and the SNEAK-3A spectrum as a weighting spectrum. The heterogeneity results are compared with theoretical models including space-dependent resonance self-shielding.

The series of SNEAK-3 experiments is now being continued with the uranium Assembly 3A-2, which has about twice the hydrogen concentration of 3A-1. After the measurements in this system have been completed the inner part of the core will be replaced by an equivalent plutonium-fuelled zone thus forming the two-zone core SNEAK-3B.

1. INTRODUCTION

For the fast-breeder development programme a number of considerations – discussed more fully in Ref. [1] – led to the decision to construct one sodium and one steam-cooled fast-breeder prototype of about 300 MW(e) in the Federal Republic of Germany. As a result of this the reactor physics investigations carried out with the fast zero power facilities at Karlsruhe have been concentrated on assemblies containing hydrogen,

---

* Work performed within the association in the field of fast reactors between the European Atomic Energy Community and Gesellschaft für Kernforschung m. b. H., Karlsruhe.

+ Euratom delegate.

‡ On leave from Allgemeine Elektrizitäts-Gesellschäft, Frankfurt.

because very little information is available about such systems, in contrast with those containing sodium. The first exploratory experiments on these lines were carried out in STARK [2] and SUAK [3]; a series of systematic experiments is now under way at SNEAK.

Assembly 3A-1 is a 667.2 litre uranium-fuelled system. The average hydrogen concentration of 7.41×10^{20} atoms/cm^3 corresponds to a steam density of 0.0317 g H_2O/cm^3 in the coolant volume (35%) of a steam-cooled fast-breeder reactor. The steam is simulated here by polyethylene foils.

Assembly 3A-2 has about twice the hydrogen concentration of 3A-1 so that the corresponding steam density is close to the design value for normal operating conditions in steam-cooled fast-reactor power plants envisaged at the moment. The experiments have begun in Assembly 3A-2.

The Assembly 3B series will follow after completion of 3A-2. The inner part of the core will be replaced by an equivalent plutonium-fuelled zone, thus forming a two-zone system.

The main results obtained in Assembly 3A-1 are described. For their evaluation a number of different aspects had to be taken into account:

(a) Comparison of experiment and theory regarding the influence of basic nuclear data together with the weighting spectrum on the preparation of group cross-section sets. Comparison has been made with the recently prepared SNEAK set described in Ref. [4] as well as with the Soviet cross-section set [5], referred to as the ABN set. Of primary importance to this aspect are the neutron spectrum, the initial breeding ratio and the steam void effect.

(b) Comparison of experiment and theory concerning theoretical approximations and numerical procedures that may not be appropriate for systems containing hydrogen. For this purpose different types of calculations have been primarily compared with measured reaction rate distributions in core and blanket in view of power density calculations in steam-cooled fast-power breeders.

(c) Comparison of experiment and theory referring to heterogeneity effects due to the plate structure in SNEAK in order to derive correction factors for k_{eff} and other quantities of interest. Integral reactivity effects as well as flux fine structure have been measured and compared with a theoretical model including space-dependent resonance self-shielding, described in Ref. [6].

The experiments on Assembly 3A-1 started in May 1967 and were completed in the middle of September 1967. Taking this into consideration and paying due regard to the novelty of hydrogen-containing fast-reactor systems, it is not surprising that from the results obtained a number of questions remained for further investigation.

2. CALCULATIONAL METHODS AND CROSS-SECTION SETS USED

The codes for the calculations are part of the Karlsruhe nuclear code system NUSYS, and were run on an IBM 7074 computer. For comparison

with the experiments of Assembly 3A-1 the followlwing codes have been used so far: A one-dimensional diffusion code for cylinder and plate geometry, a one-dimensional S_N code, and appropriate evaluation codes. The number of energy groups was 26 in these cases. The group structure is given in Ref. [8]. Furthermore, a two-dimensional diffusion code (DIXY) was applied with 10 energy groups and 1600 space points for the geometry of 3A-1, as shown in Fig. 1. The heterogeneity calculations were performed with the code ZERA, described in Ref. [6].

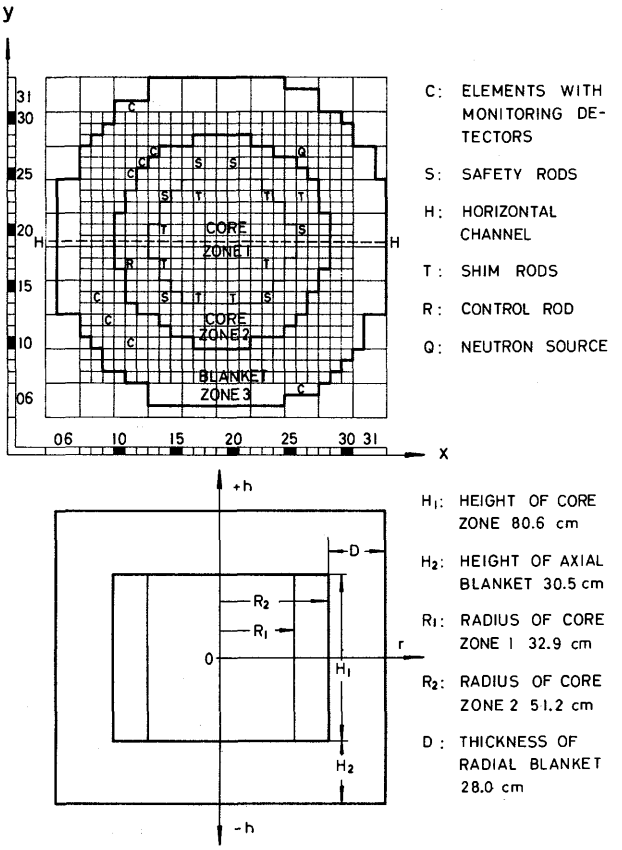

FIG. 1. Configuration and dimensions of SNEAK Assembly 3A-1.

Different cross-section sets were used for comparison with measurements and comparison of calculations. The three sets are:

(a) KFK-SNEAK set, referred to as SNEAK set. The preparation of the set, the microscopic cross-sections used for it and results of calculations are described in detail in Ref. [4]. Special features of the set are the use of the SNEAK Assembly 3A-2 spectrum as a weighting spectrum, and the adoption of recently recommended microscopic cross-section data.

(b) KFK 26-10 set, referred to as KFK set. This set uses a sodium-cooled breeder spectrum as weighting spectrum and was specially prepared for the calculation of such reactors. A description is given in Ref. [7].

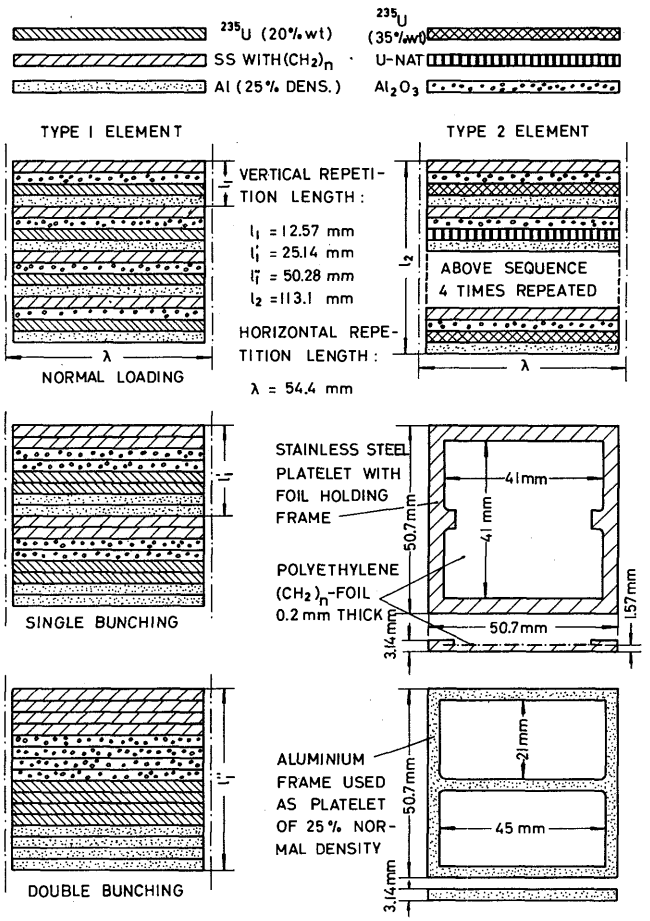

FIG.2. Cell structures and special platelets used in SNEAK Assembly 3A-1.

Although this cross-section set is not particularly well suited for the computation of steam-cooled fast-reactor systems it has, nevertheless, sometimes been included in the comparison so that trends can be studied.

(c) Soviet cross-section set, referred to as ABN set. A description of the set preparation, together with the data, is given in Ref. [8]. A 1/E spectrum is used as weighting spectrum. Using this set for comparison was of special interest because it had been used for a series of design calculations.

3. COMPOSITION, CRITICAL MASS AND EFFECTIVE MULTIPLICATION FACTOR

A description of the SNEAK facility and its special experimental equipment is given in Ref. [9]. The actual configuration of Assembly

3A-1 is shown in the upper part of Fig. 1. In the lower part the idealized dimensions are given, which were the basis for all calculations.

The special platelets and cell structures used in 3A-1 are shown in Fig. 2. The steam was simulated by square polyethylene foils of 0.2-mm thickness fixed to stainless-steel platelets as indicated. Uranium platelets with 20 wt% ^{235}U were filled into elements of type 1. Type 2 was composed of those with 35 wt% ^{235}U together with natural uranium platelets in order to approximate the same average composition in both types. Type 1 dominates in core zone 1 and type 2 in core zone 2. The cell structure for the heterogeneity experiments (see Section 5) is also indicated.

The average atom densities in the different zones are listed in Table I. These densities were used for all homogeneous calculations. For the heterogeneity calculations the atom densities are given in Table II. They were calculated by smearing the atom numbers of the platelet together with those of the adjacent stainless-steel tube over an area of 29.59 cm^2 (54.4 mm × 54.4 mm). The four platelets in Table II form one unit cell for which the atom densities are also given. They are not identical with those used for the homogeneous calculations.

The measured critical mass of the cylindrical reactor with the dimensions shown in Fig. 1 is given by

$$M_{3A-1} = 524.5 \pm 1.0 \text{ kg } ^{235}U$$

This value has been obtained after correcting for the irregular core periphery in the same manner as explained for Assembly 1 in Ref. [10]. The error arises mainly from the uncertainty regarding the uranium isotopic composition.

Results for k_{eff} from homogeneous two-dimensional calculations are given below, together with corrections due to transport and heterogeneity effects:

	SNEAK set				KFK set	ABN set
	Homog.	S_4 correction	Heterogen. correction	Total	Homog.	Homog.
$k_{eff\ 3A-1}$	0.9895	+0.0027	+0.0025	0.995	1.015	1.019

From this comparison it follows that the SNEAK set gives the best agreement with the experiment. Applying equivalent corrections to the KFK and ABN set they underestimate the critical mass appreciably.

4. INVESTIGATION OF THE ASSEMBLY WITH STANDARD CELL STRUCTURE

All experiments described in this section have been performed with a cell structure designated as "normal loading" in Fig. 2.

TABLE I. Atom densities (in 10^{20} cm^{-3}) of SNEAK 3A-1 used for homogeneous calculations

	Al	C	Cr+Mn	Fe	H	Ni	O	Si	Ti	^{235}U	^{238}U	Mg
Core zone 1	128.8	4.12	36.6	123.1	7.40	19.0	144.7	1.84	0.53	20.314	81.023	0.37
Core zone 2	128.9	4.13	36.7	123.3	7.42	19.0	144.8	1.88	0.55	20.221	81.066	0.37
Blanket zone 3	-	0.14	11.9	40.1	-	10.2	-	0.46	0.2	1.54	399.3	-

TABLE II. Atom densities (in 10^{20} cm^{-3}) of SNEAK 3A-1 used for heterogeneity calculations

	Al	C	Cr+Mn	Fe	H	Ni	O	Si	Ti	^{235}U	^{238}U	Mg
SS platelet + CH_2 foil	-	16.01	110.7	373.3	29.48	51.4	-	4.24	1.68	-	-	-
Al platelet (25% Al)	130.1	0.13	12.24	39.54	-	5.86	-	1.30	-	-	-	1.48
U platelet (25% ^{235}U)	-	0.13	11.78	39.54	-	12.9	-	0.44	-	81.282	324.19	-
Al_2O_3 platelet	385.3	0.13	11.78	39.54	-	5.86	578.6	0.44	-	-	-	-
Unit cell	128.9	4.10	36.6	123.0	7.370	19.0	144.6	1.61	0.42	20.320	81.048	0.37

4.1. Neutron spectrum

A comparison of calculated neutron spectra at the centre of the assembly has been made for the three cross-section sets used in order to see their influence on the spectrum. The results are shown in Fig. 3. The spectrum calculated with the SNEAK set has been used as a reference spectrum. Due to the logarithmic scale in the upper part of Fig. 3 differences cannot be clearly recognized, therefore the ratio of calculated fluxes versus energy is shown in the lower part. Compared with the SNEAK set the spectrum calculated by the KFK set has more flux in groups 1 to 7 except group 6. The large discrepancies between both sets in groups 12 to 14 are due to the sodium breeder weighting spectrum. Compared with the spectrum calculated by the ABN set, the SNEAK set produces systematically lower fluxes down to 200 keV, and higher fluxes below this value so that the spectrum is remarkably "softened". The same comparison has been made between the three sets for spectra at the core boundary, where the same results were found. Furthermore, spectra

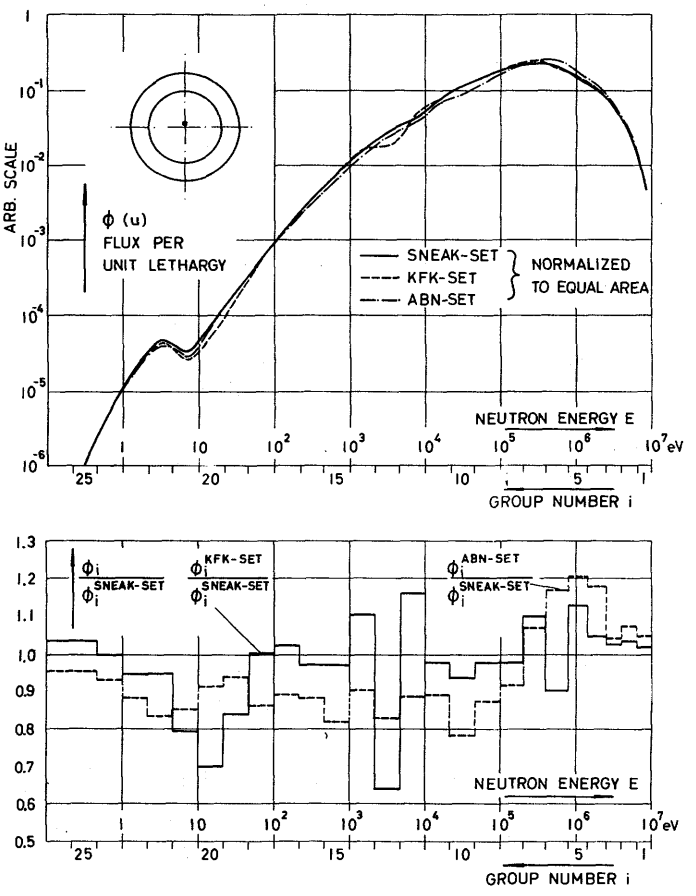

FIG. 3. Comparison of calculated neutron spectra at the centre of 3A-1 using different cross-section sets.

calculated at the centre and boundary by S_4 approximation were identical with those resulting from diffusion theory.

Spectrum measurements have been performed using the proton recoil spectrometry technique and the ^{6}Li sandwich spectrometer. Both methods have been applied for measurements close to the core centre (position x=19, y=20) for which the results are shown in Fig. 4. The proton recoil measurements were made with spherical proportional counters. Gas type (H_2 and CH_4), gas pressure and high voltage were adjusted to the energy range of interest. For the low-energy part a gamma-discrimination technique, described in Refs [11, 12], was applied. The proton recoil data were corrected for wall effects. The ^{6}Li semiconductor sandwich spectrometer was used to measure the high energy part of the spectrum. The ^{6}Li foil between the detectors could be removed for background measurements and had a thickness of 57 $\mu g/cm^2$ ^{6}LiF. The pulse-height distribution was unfolded using measured response functions to

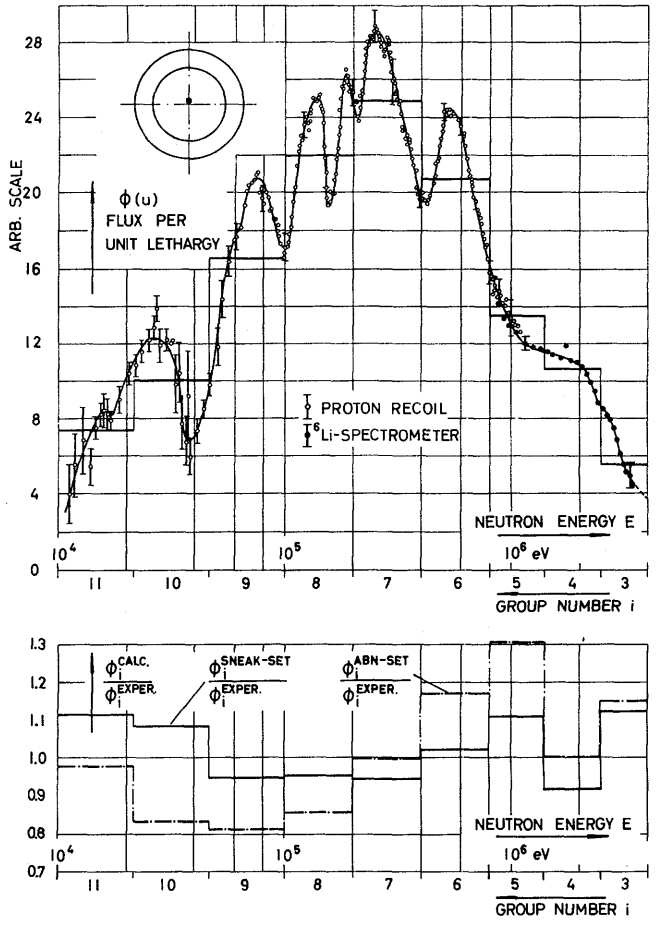

FIG. 4. Comparison between calculated and measured neutron spectrum at the centre of 3A-1.

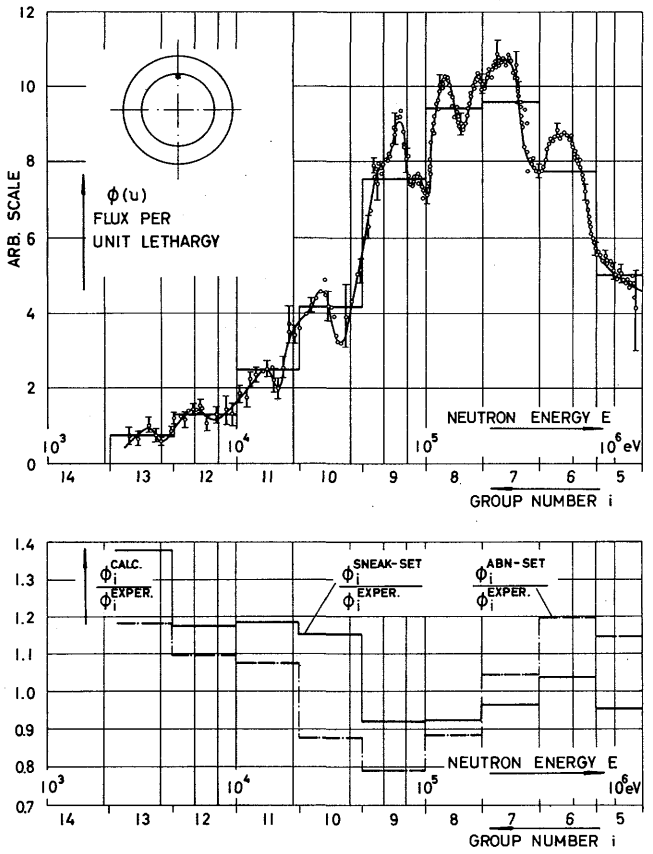

FIG. 5. Comparison between calculated and measured neutron spectrum at the core boundary of 3A-1.

derive the neutron spectrum. The ^{6}Li data were fitted to the proton recoil data around 1 MeV. Full details of both spectrometry techniques, including the performance of analysis, are given in Ref. [13]. Measurements with the proton recoil counters have also been made at the core boundary (position x=19, y=28). The results are shown in Fig. 5.

A comparison of measured and calculated neutron spectra in both positions is shown in the lower part of Figs 4 and 5 respectively. Because the neutron spectrum is strongly space-dependent at the core boundary, a special zone according to the dimensions of the counter was introduced into the calculations so that an average neutron spectrum of this zone was available to compare with the measurements. The measured data were averaged over corresponding energy groups. Those parts of the measured and calculated spectra to be compared were normalized to equal area and the ratio of equivalent ϕ_i was formed. Although we are aware of the fact that the structure of 26 energy groups is much too coarse for a detailed analysis, the comparison allows, nevertheless, certain conclusions. For both positions the calculated spectrum using the SNEAK set gives from groups 5 to 10 (approximately half width of ϕ(u) maximum)

TABLE III. Data of resonance activation foils

Isotope	Material	Thickness of foil mm	Lowest resonance energy eV
^{23}Na	NaI crystal.	0.5	2850
^{114}Cd	metal	0.5	120.2
^{139}La	metal	0.250	72.4
^{186}Wo	metal	0.025	18.8
^{98}Mo	metal	0.2	12 (467)
^{197}Au	metal	0.025	4.906
^{115}In	In-Pb alloy	0.050	1.456

much better agreement with the experiment than the ABN set. Common to both positions and sets is that a broader distribution of $\phi(u)$ seems to be calculated than measured.

To gain knowledge about the neutron spectrum below 5 keV, resonance activation foils in sandwich geometry have been irradiated at the centre of the assembly. A description of this method is given in Ref. [14]. Data from the foils used for this experiment are given in Table III. The foil diameter was 18 mm. They were covered by Cd of 0.5-mm thickness and positioned in a cavity at the core centre. Only foils of the same material were irradiated at the same time. The neutron flux level was monitored for each irradiation.

The results of the sandwich experiments are shown in Fig. 6. They have been plotted together with the other experimental data and the calculated spectrum (SNEAK set). The ^{23}Na results were used to normalize experiment and calculation. Error margins have not been given because no detailed information is available so far concerning how the results are affected by either the contribution of higher resonances or the inaccuracy of resonance data available at present. These systematic errors, however, cannot be solely responsible for the fairly large discrepancies between experiment and calculation. The conclusion is, therefore, that the sandwich experiments indicate higher fluxes in the energy range below 200 eV compared with calculation with the SNEAK set.

4.2. Spectral indices

Measured and calculated spectral indices at the centre of the assembly are given in Table IV. Indices No. 1 to 4 were measured by absolutely calibrated parallel plate fission chambers positioned in a cavity at the centre of the core. Index No. 5 was measured by irradiating uranium foils (0.2 and 19.8% ^{235}U) attached to a parallel plate fission chamber containing ^{235}U. During the irradiation time the pulses from the fission chamber were counted so that the foil was calibrated against the fission chamber. The ^{238}U capture rate was determined absolutely by the technique described in Ref. [15]. Indices 6 to 8 were also measured by foil

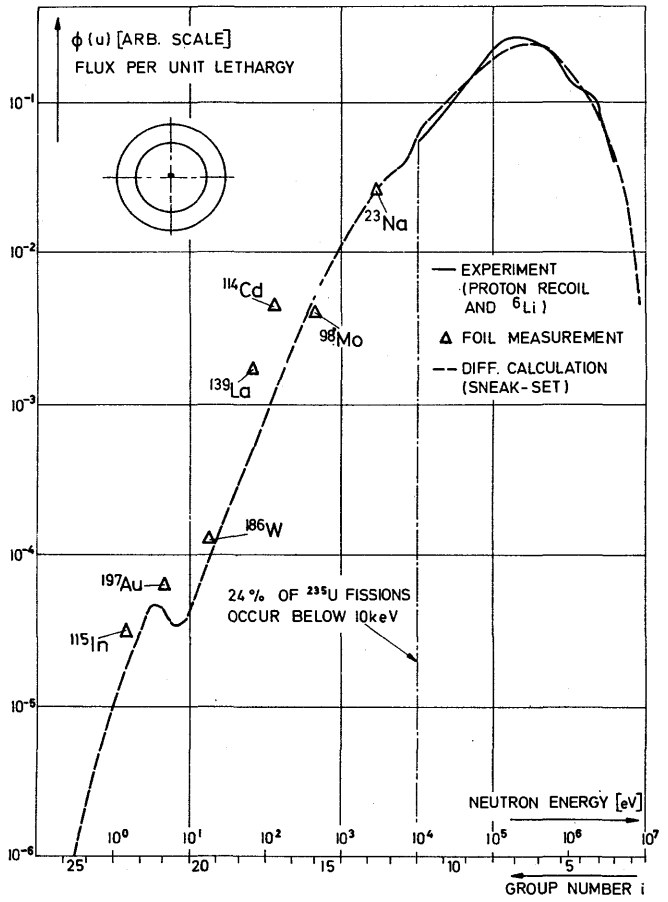

FIG.6. Investigation of the low energy part of neutron spectrum at the centre of 3A-1.

activation. The ^{235}U fissions were determined again via the calibrated ^{235}U fission chamber and the activity of the other foils was determined by absolute counting techniques. All the experiments were monitored by three intercalibrated monitor channels in order to cover the whole power range of interest. They were used as reference points so that the different experimental runs could be compared and cross-checked.

The comparison between experiment and calculation regarding indices 1 to 3 shows the largest deviations from the experiment for the calculations performed with the SNEAK set. This fact is not understood yet and will be further investigated. This includes a recalibration of the parallel plate fission chambers and an improvement of fission foil fabrication, which is under way now. For index 5 the agreement is best for the SNEAK set. This is of special interest in connection with the initial breeding ratio determination further discussed below. Index 6 shows less ^{23}Na captures than calculated by the SNEAK set.

TABLE IV. Spectral indices at the center of assembly 3A-1

No.	Index	Experiment	Calculation			Calcul./Exper.		
			SNEAK set	KFK set	ABN set	SNEAK Exp.	KFK Exp.	ABN Exp.
1	$\frac{^{238}U \text{ fission}}{^{235}U \text{ fission}}$	0.0336 ±5%	0.0301	0.0301	0.0316	0.90	0.90	0.94
2	$\frac{^{233}U \text{ fission}}{^{235}U \text{ fission}}$	1.48 ±3%	1.572	-	1.45	1.06	-	0.98
3	$\frac{^{239}Pu \text{ fission}}{^{235}U \text{ fission}}$	1.03 ±3%	0.958	0.971	1.001	0.93	0.94	0.97
4	$\frac{^{232}Th \text{ fission}}{^{238}U \text{ fission}}$	0.209 ±6%	0.198	-	0.194	0.95	-	0.93
5	$\frac{^{238}U \text{ capture}}{^{235}U \text{ fission}}$	0.142 ±4%	0.143	0.129	0.127	1.01	0.91	0.89
6	$\frac{^{23}Na \text{ capture}}{^{235}U \text{ fission}}$	0.959×10^{-3} ±3%	1.054×10^{-3}	0.846×10^{-3}	0.882×10^{-3}	1.10	0.88	0.92
7	$\frac{^{115}In \text{ capture}}{^{235}U \text{ fission}}$	0.205 ±5%	0.208	-	-	1.01	-	-
8	$\frac{^{103}Rh(n,n')}{^{235}U \text{ fission}}$	0.176 ±10%	0.154	-	-	0.88	-	-

4.3. Fission and capture rate traverses, initial breeding ratio

Radial and axial traverses of ^{235}U and ^{238}U fission rates, and ^{238}U capture rates, have been measured along one radius and along the central axis of the reactor. For the determination of fission rates two different experimental techniques were applied. In the one case a stack of four small cylindrical fission chambers (20th Century Electronics, G.B., Type FC4) were placed in a 17 mm × 17 mm guide tube within an element at position x=19, y=18. The remaining volume of the element was filled with platelets of smaller size in a way that the average core composition was closely approximated. These chambers with different layers served to map the axial fission rate distribution. The same stack was positioned in the horizontal drawer, designated by H in Fig. 1, to measure the radial distribution. In the other case uranium foils were inserted into the standard cell where Al_2O_3 platelets were replaced by aluminium foil holders to measure the axial traverse. For the radial traverse the foils were inserted into the pockets of the horizontal drawer, which has a somewhat different cell pattern. Two uranium foils (0.2% and 20% enriched), separated by an aluminium foil, were placed into one foil holder so that ^{235}U fissions, ^{238}U fissions and ^{238}U captures could be determined from one irradiation.

The results of both types of fission rate measurements agreed within 1 to 2% over the core volume, whereas discrepancies up to 10% were observed for points measured in the outer blanket. The foils gave systematically higher values than the chambers. This may be partly due to streaming effects caused by the guide tube of the chambers and perhaps, partly due to the presence of enriched foils in the depleted blanket material. This discrepancy will be studied in more detail. The experimental results for radial and axial ^{235}U fission rate traverses, obtained with chambers, are shown in the upper part of Fig. 7. The corresponding results for ^{238}U fission rates, also from chambers, are plotted in Fig. 8. ^{238}U capture rate traverses in axial and radial directions measured by foils are shown in Fig. 9.

Reaction rates have been calculated in three different ways:

(a) Calculation by a one-dimensional diffusion code in plate and cylinder geometry for which the radial and axial bucklings were properly chosen to render the reactor critical.

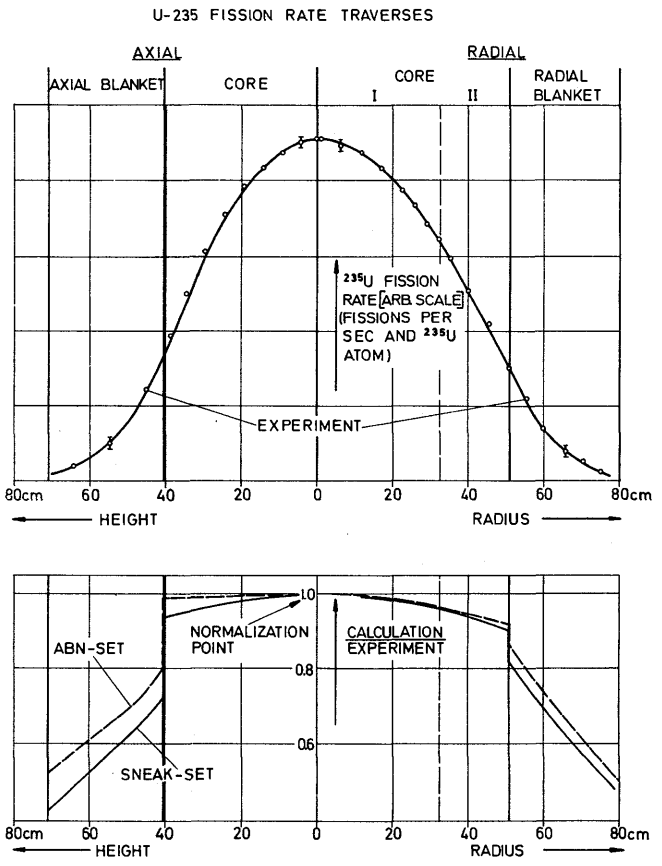

FIG. 7. Comparison of measured and calculated ^{235}U fission rates in SNEAK Assembly 3A-1.

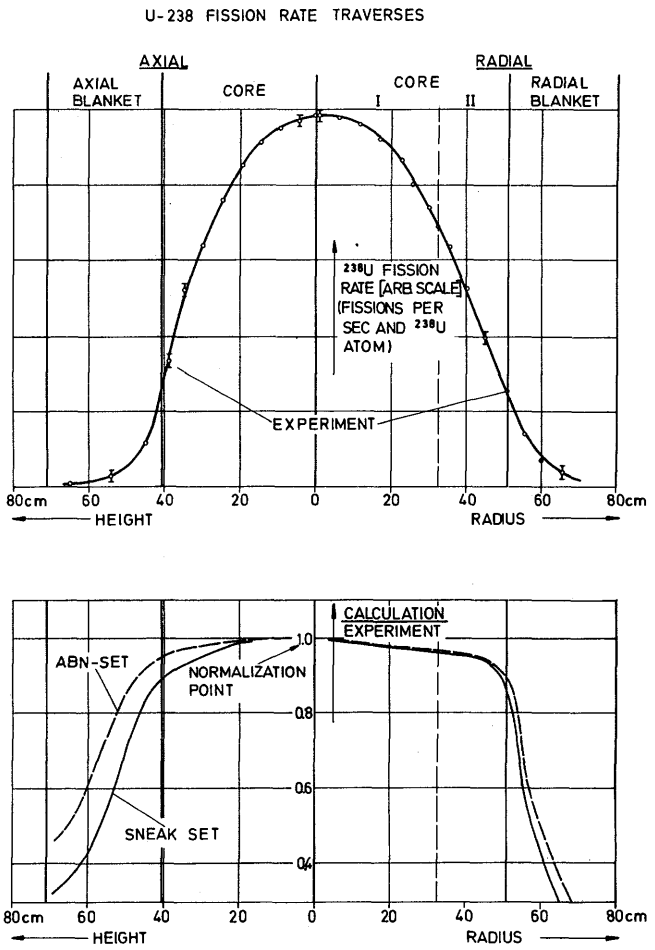

FIG. 8. Comparison of measured and calculated ^{238}U fission rates in SNEAK Assembly 3A-1.

(b) Calculation by a one-dimensional S_4 code in the same manner as in (a).
(c) Calculation by a two-dimensional diffusion code with the reactor dimensions given in Fig. 1 and the composition given in Table I.

The shapes of the reaction rate traverses from these calculations were compared and found to be almost identical.

Comparison of experiment with these calculations has been made by plotting the ratio of calculated-to-measured reaction rates as function of radius and core height in the lower part of the corresponding figure. In general, there is fairly good agreement within the core except towards the boundary, but there is strong disagreement in the blanket regardless of the cross-section set used. The strong discrepancy in the blanket region is believed to be mainly due to the theoretical treatment of resonance self-shielding in the different reactor zones. In the codes used the

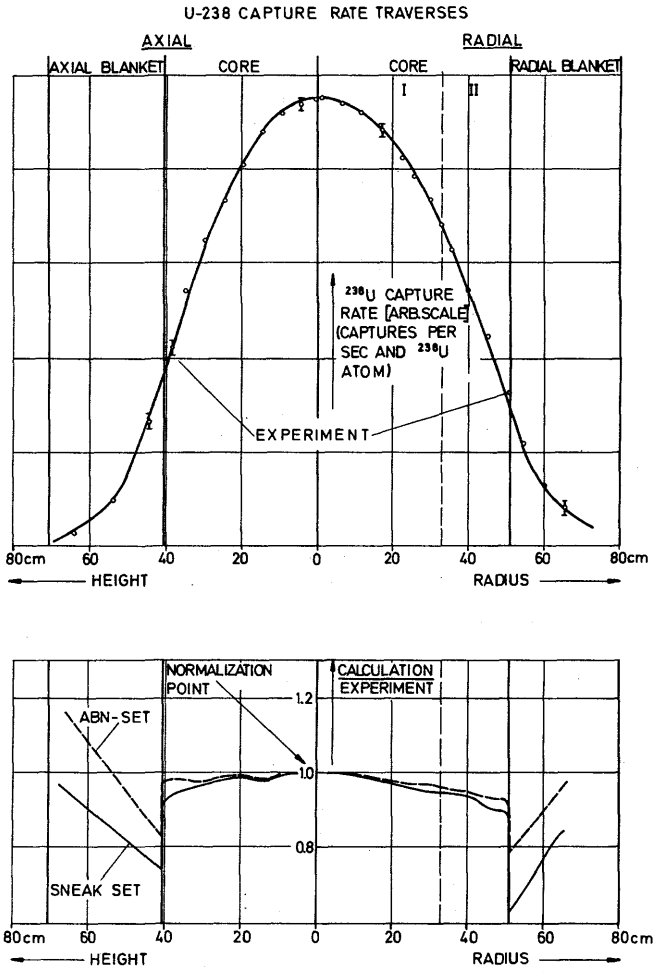

FIG.9. Comparison of measured and calculated ^{238}U capture rates in SNEAK Assembly 3A-1.

self-shielding factors are calculated for one complete zone according to composition. These factors change, therefore, stepwise by crossing the zone boundary. The strong space dependence of resonance self-shielding between zones of different composition is not taken into account. It is apparent that discrepancies between experiment and theory due to this treatment become more visible the more the number of neutrons in the resonance region is increased by softer spectra.

Reaction rate ratios could also be derived from the measurements, because the cylindrical fission chambers were calibrated against the parallel plate fission chambers, and the ^{238}U capture rate was measured absolutely by the procedure described in Ref. [15] and was also corrected for heterogeneity effects. The results are shown in Fig. 10. The ratios plotted are the quotients of the reaction rates per atom. Comparison of

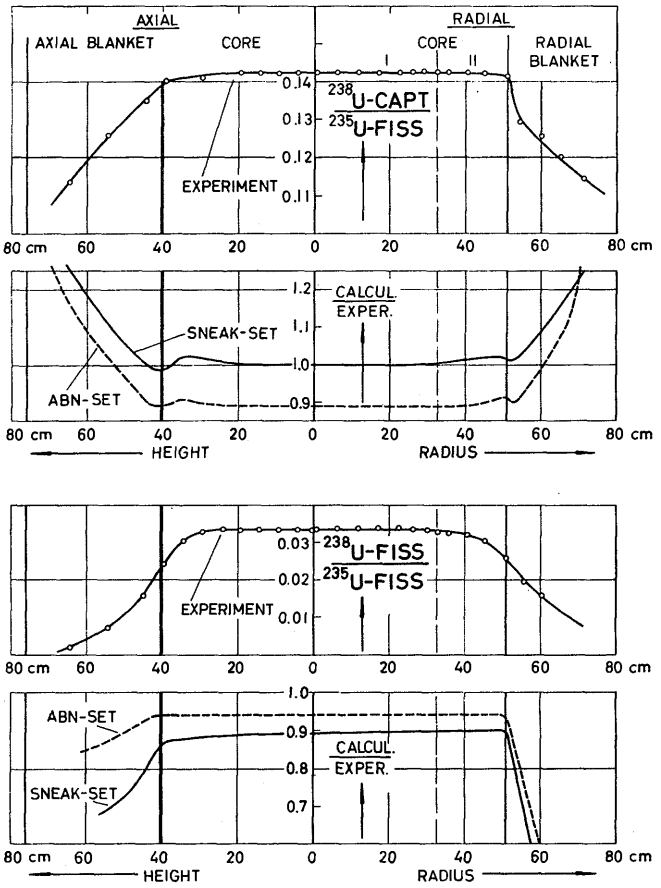

FIG.10. Comparison of measured and calculated reaction rate ratios in SNEAK Assembly 3A-1.

calculation and experiment is made by forming the quotient of calculated-to-measured reaction rate ratios.

The initial breeding ratio (IBR), defined in this case as

$$\text{IBR} = \frac{^{239}\text{Pu produced by capture in } ^{238}\text{U}}{^{235}\text{U consumed by fission and capture}}$$

has also been investigated. For this purpose the integral fission and capture rates INT ^{235}U fission, INT ^{235}U capture and INT ^{238}U capture were determined by integrating over core and blanket. The initial breeding ratio follows as

$$\text{IBR} = \frac{\text{INT } ^{238}\text{U capture}}{\text{INT } ^{235}\text{U fission} + \text{INT } ^{235}\text{U capture}}$$

The theoretical IBR was derived from two-dimensional diffusion calculations with the actual geometry and composition of the assembly. The results are given in Table V. When comparing the theoretical values it has to be kept in mind that the calculated reactors were not exactly

TABLE V. Initial breeding ratio (IBR) for assembly 3A-1

	INT ^{238}U capture / INT ^{235}U fission	INT ^{235}U capture / INT ^{235}U fission	IBR
SNEAK set	1.384	0.279	1.081
KFK set	1.307	0.287	1.016
ABN set	1.298	0.298	1.000
Experiment	1.385 ± 3 %	(0.279)	1.08 ± 0.03

critical as discussed in Section 3. From the experiment, INT ^{235}U fission and INT ^{238}U capture have also been determined by integration, taking into account the actual composition in the different zones. Because the experimental data agreed best with the theoretical results using the SNEAK set, the corresponding reactor-averaged ^{235}U capture-to-fission ratio has been used to derive the "experimental" IBR given in Table V. The error margins indicated result from a fairly rough error estimation due to the fact that only one radial and axial traverse for each reaction rate was used for the evaluation.

4.4. Prompt neutron decay constant

Prompt neutron decay constants have been measured by the pulsed source technique. A 150-kV Cockroft-Walton type accelerator with duoplasmatron ion source, designed by W. Eyrich, was used. Characteristic data of the neutron generator are: pulse width about 1 μs, repetition frequency up to 2000 p/s, maximum source strength about 5×10^4n/p. The target was positioned within the open half of the horizontal channel close to the core centre. A ^{235}U fission chamber was located at position x=22, y=18. As time analyser a fast 32-channel shift register (manufactured by Borer and Co., Solothurn, Switzerland) with scalar memory was used, as described in Ref. [16].

Prompt neutron decay constants were measured at several subcritical states from about 2 dollars to a few cents below delayed critical. The experimental value for the prompt neutron decay constant α_c, obtained by extrapolation to delayed critical, is given in Table VI, together with calculated values using $\beta_{eff} = 7.1 \times 10^{-3}$.

The comparison of the data shows the well-known over-estimation of α_c by calculation. The SNEAK set gives a value closest to the experimental one.

4.5. Material worth measurements

A number of sample reactivity measurements were made using the horizontal drawer and the sample changer (see Ref. [9]). Except for the

TABLE VI. Prompt neutron decay constant α_c of assembly 3A-1

	Experiment	SNEAK set	KFK set	ABN set
$\alpha_c = \beta/l \left[\text{sec}^{-1}\right]$	$2.05 \cdot 10^4 \pm 2\%$	$2.42 \cdot 10^4$	$2.53 \cdot 10^4$	$2.73 \cdot 10^4$
$\frac{\text{Calculation}}{\text{Experiment}}$	-	1.18	1.23	1.33

sample position the drawer was filled with core material to minimize perturbation of the core.

Two series of measurements have been performed. In the first series the samples were contained in otherwise empty stainless-steel boxes of 2 in. × 2 in. × 1 in. Central reactivities of these samples were measured by the asymptotic period technique. A period measurement with a reference box was made before the various samples were measured at the core centre. It was not necessary to interrupt reactor operation since the resulting reactivity variations were made small enough to prevent large power fluctuations. The reactor periods were generally larger than 1000 s; flux data were collected during 10 min for each sample.

In the second series of measurements the remaining space in the box was filled with core material. Those boxes were used for radial reactivity traverses with some of the samples for which the central worths had been measured. The inverse kinetics method was used to determine reactivities during the traverses. The sample was stopped for 5 min at each position to reduce the effect of removal of delayed neutron precursors from the reactor, caused by the movement of core material in the sample drawer. This period was also long enough to collect sufficient flux information for a statistically accurate reactivity calculation.

The material worths were calculated against void by a perturbation calculation in which a very small quantity (generally 10^{20} atoms) of the perturbing sample material was added to 1 cm^3 of core mixture. The dimensions and the transverse buckling correspond to the actual dimensions of the critical reactor.

Measured and calculated central reactivity worths are compared in Table VII. Measured and calculated radial reactivity traverses are shown in Fig. 11. The data are not normalized. Poor agreement between calculation and experiment is found especially for graphite, aluminium and CH_2. The ABN set generally gives values closer to the experiment except for ^{239}Pu and Cr. In order to start investigations to resolve the discrepancies between theory and experiment the influence of the surroundings has been studied. The comparison of the two experimental procedures I and II shows that these effects are small compared with the discrepancies.

4.6. Reactivity worth of control rods

Assembly 3A-1 contains ten shim rods, six safety rods and one fine control rod, as shown in Fig. 1. All rods are filled with core material

in such a way that the reactor has a homogeneous core composition with all rods inserted. The shim rods have poison followers of B_4C powder, and the safety rods have followers of a solid dispersion of this powder in epoxy resin. The followers protrude axially through the largest part of the core with the rods in the shutdown position.

The ten shim rods and two of the safety rods were calibrated by the continuous run method. The fine control rod and two of the shim rods were also calibrated by moving the rod stepwise to obtain better statistics at some rod positions for the reactivity worth as derived with the inverse kinetic equations from the flux history. The neutron flux was detected by two ionization chambers at opposite positions (x=11, y=31) and (x=26, y=06) just outside the blanket, as indicated in Fig. 1.

Measured and calculated reactivity worths of shim rods are given in Table VIII. It can be seen from the values that the measured rod worth depends on the position of the ionization chamber. The differences are larger than could be expected from statistical uncertainties. The ionization chamber that is closest to a rod gives a higher value. This space dependence could not be eliminated by averaging the current of the two chambers. The subcritical measurements also show space-dependent effects. During these measurements an AmBe source was inserted at the core boundary. Its effective strength was determined from the flux history after a reactivity step between two subcritical states. The calibration of the fine control rod was checked with some asymptotic period measurements, the results of which do not depend on the detector location.

The worth of individual shim rods was calculated in the following manner. First the central worth of the poison part of a rod compared with core material was determined by a one-dimensional diffusion calculation (with the KFK set) in cylindrical geometry with an axial buckling corresponding to the extrapolated height of Assembly 3A-1. The poison part of the control rods does not fill the core over the whole axis; the calculated central poison worth was converted to the worth of a rod in its actual geometry by $\cos^2$ weighting. The worths of rods at the various radial locations were finally obtained from the central one by J_0^2 weighting.

Those calculations were cross-checked by a calculation in (r, θ) geometry for shim rod T1, using the SNEAK set and six energy groups. Both values agreed within 5%.

5. INVESTIGATION OF HETEROGENEITY EFFECTS

All experiments and results described in this section have been made by changing the normal cell structures to "bunched" cell structures in parts of the core volume. The two types of bunching, namely single bunching and double bunching, are indicated in Fig. 2.

A series of bunching experiments in different core positions has been performed to measure the influence of heterogeneity on k_{eff} and to get some information about the leakage component of heterogeneity effects.

5.1. Integral heterogeneity effects

5.1.1. Radial dependence of bunching effects in the central test zone

A central zone, consisting of 21 fuel elements, was bunched (single bunching) in six successive steps, as indicated in Fig. 12a. The numbers

TABLE VII. Central material worths of SNEAK assembly 3A-1

Material	Sample weight [g]	Sample dimensions [mm]	Measured central reactivity worth [$\not{e}$/g x 10^3]		Calculation / Experiment		
			I Sample in empty box	II Sample in filled box	SNEAK set / Exper.I	KFK set / Exper.I	ABN set / Exper.I
^{235}U	3.413	46.6x46.6x0.1	+ 33.34 ± 0.6	+ 33.37 ± 0.7	1.15	1.11	1.09
^{238}U	61.56	46.8x46.8x1.6	- 2.41 ± 0.04	- 2.25 ± 0.03	1.20	1.00	0.96
Mo	33.86	46.8x46.8x3.2	- 4.80 ± 0.07	-	1.28	1.23	1.17
C	48.68	46.8x46.8x12.8	+ 5.55 ± 0.1	+ 5.57 ± 0.06	0.25	0.48	0.60
^{10}B	2.90	diam.43x1	-779 ± 1.0	-762 ± 0.7	1.36	1.29	1.16
Al	159.24	50.8x50.8x25.1	- 0.207± 0.02	- 0.232± 0.02	4.68	3.10	2.05
Ta	53.36	46.8x46.8x1.6	- 14.7 ± 0.08	-	-	-	1.33
SS	108.60	46.8x46.8x6	- 0.97 ± 0.03	- 1.225± 0.015	1.37	1.38	1.11
CH_2	2.527	50.8x50.8x1	+234 ± 0.7	+235 ± 0.8	0.66	0.74	0.62
Ni	114.33	46.8x46.8x6	- 1.42 ± 0.06	-	1.73	1.84	1.55
Fe	127.67	46.8x46.8x8	- 0.87 ± 0.05	-	1.47	1.41	1.05
Cr	110.18	46.8x46.8x10	- 0.76 ± 0.03	-	1.39	1.58	1.58
^{239}Pu	28.94	with PuO_2-UO_2	+ 48.1 ± 0.5	+ 50.45 ± 0.5	1.10	1.11	1.12
PuO_2-UO_2	136.45	50x50x5	+ 9.10 ± 0.015	+ 9.71 ± 0.02	1.15	1.15	1.17

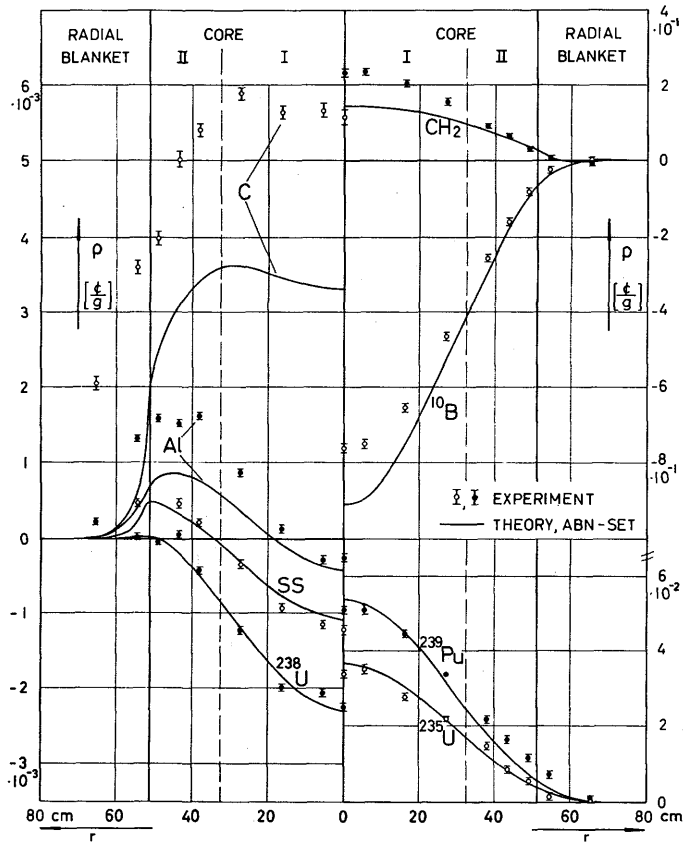

FIG.11. Radial reactivity traverses of different materials in SNEAK Assembly 3A-1.

1 to 6 correspond to the number of the step. The resulting reactivity effects per element in cents, together with calculated values, are also shown in Fig. 12a. They show that the bunching effects are nearly additive, and that the smaller values for the last steps can be explained by a loss of importance with increasing radius. The conclusion is drawn that a zone of 21 bunched elements is large enough to neglect surface effects of the bunched zone.

The calculated values have been obtained by perturbation calculations with "heterogeneity corrected" cross-sections. These cross-sections are an extract of multigroup cell calculations performed with the code ZERA. Details of the calculation methods are explained in Ref. [6].

5.1.2. Variation of the axial extension of the bunched zone

The axial extension of the bunched region of 21 central elements has been varied in four steps: 16, 32, 48, and 64 cells corresponding to quarter, half, three-quarter and full core height. The experiments have been done to look for heterogeneity effects on global diffusion in a direction

TABLE VIII. Reactivity worth of control rods in assembly 3A-1

Rod No.	Position (x/y)	Reactivity worth [¢]				
		Inverse kinetic meth.		Subcrit. measurements		Calculation
		Ion chamber 1	Ion chamber 2	Ion chamber 1	Ion chamber 2	(KFK set)
T 1	17/23	102.5	94.0	104.2	102.2	93.1
T 3	23/17	94.8	100.3	94.1	108.1	93.1
T 6	17/14	79.2	82.9	78.5	88.0	75.4
T 8	20/14	84.1	91.1	82.7	97.4	81.2
T 9	14/20	87.1	83.2	86.2	87.7	81.2
T12	23/23	74.3	73.1	78.6	82.3	68.7
T14	26/23	33.1	32.7	-	-	27.3
T15	14/17	78.9	78.8	77.8	82.3	74.9
T16	26/17	43.9	45.4	-	-	40.9
R	11/17	12.35	12.36	12.37 (period measurements)		

perpendicular to the plate surfaces. In Fig. 12b the measured reactivity effects are compared with theoretical values. The latter have been calculated without modifications of the diffusion properties. From the agreement it follows that heterogeneity effects on diffusion perpendicular to the plates can be neglected, as is discussed more generally in Ref. [6].

5.1.3. Reactivity effect of double bunching in the central zone

The effect of double bunching the 21 central elements over the full core height has also been measured. The resulting reactivity change is shown in Fig. 13a, together with the results of single bunching. Calculated values for single and double bunching as well as for the homogeneous case are also shown. Whereas the calculated result using the SNEAK set agrees fairly well with the experiment, the one using the ABN set shows poor agreement. One reason for this can be found from fine structure measurements, and is discussed in Section 5.2.

5.1.4. Reactivity effects of bunching near the core boundary

It was expected that the heterogeneity effects of elements near the core boundary are strongly influenced by a kind of "streaming" effect caused by platelets with small transport cross-sections. Therefore, the bunching experiments have been continued at the periphery of the core, as indicated in Fig. 13b. The reactivity changes, after bunching of two groups of elements over the full core height with slightly different mean radial positions at the periphery, are shown in Fig. 13b (right side) for two degrees of bunching ($\ell/\ell_1 = 2$ and $\ell/\ell_1 = 4$). The effects become negative near the core edge.

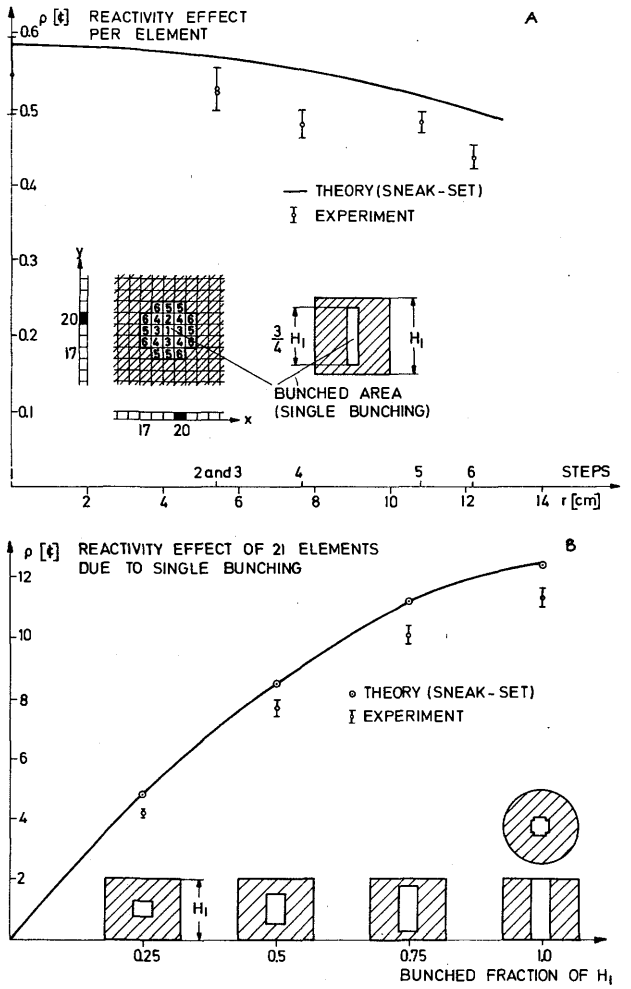

FIG.12. Radial and axial reactivity effects of single bunching in SNEAK Assembly 3A-1.

The relative differences between experimental and calculated values are larger than in the core centre, but the change in sign of the bunching effect is in satisfactory agreement with the calculated curve. The designation theory I means that the calculation has been performed without changing diffusion coefficients, whereas theory II includes heterogeneity corrections to the diffusion coefficients.

To confirm that the negative heterogeneity effects near the core periphery are really caused by changes in radial diffusion properties, the two following experiments have been performed:

(a) Thirteen elements in the boundary core zone were loaded as shown schematically in Fig. 14a. The platelets were vertically positioned over

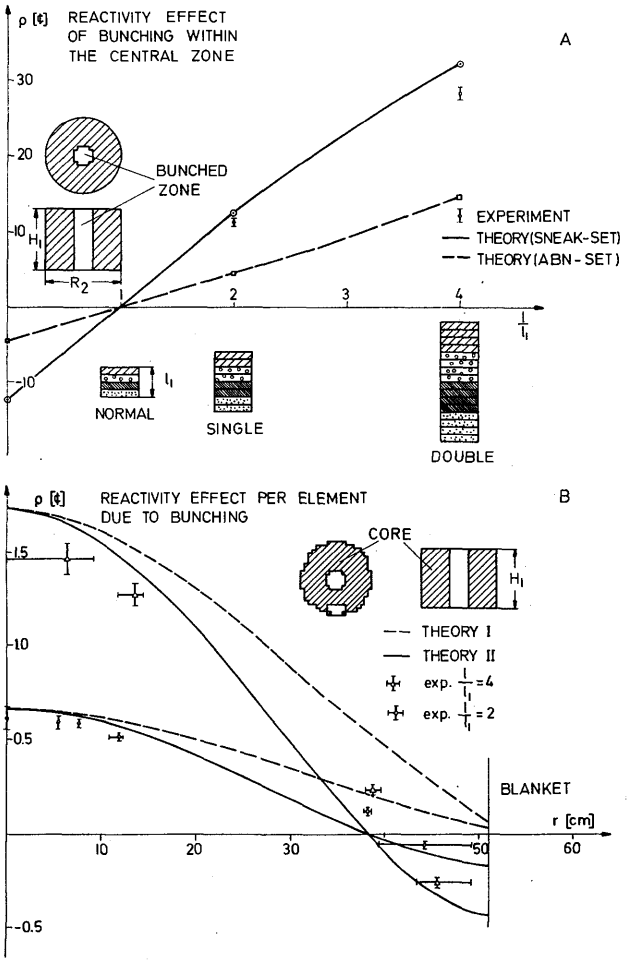

FIG. 13. Reactivity effects of single and double bunching in SNEAK Assembly 3A-1.

7/16 th of the core height so that their surface normals had a direction nearly parallel to the flux gradient. In this direction streaming channels are avoided. The reactivity effects caused by bunching these vertically positioned platelets are also shown in Fig. 14a. They agree rather well with the values calculated without changing the radial diffusion coefficients during bunching.

(b) The 13 elements have been turned round in four steps of 90° for each of the three structures (ℓ/ℓ_1 = 1, 2, and 4) with the platelets vertically positioned. As indicated in Fig. 14b, in two of the four steps the surface normal of the vertically positioned platelets was either parallel or perpendicular to the flux gradient. The mean reactivity value of the two "parallel" steps was compared with the mean value of the two "perpendicular" steps.

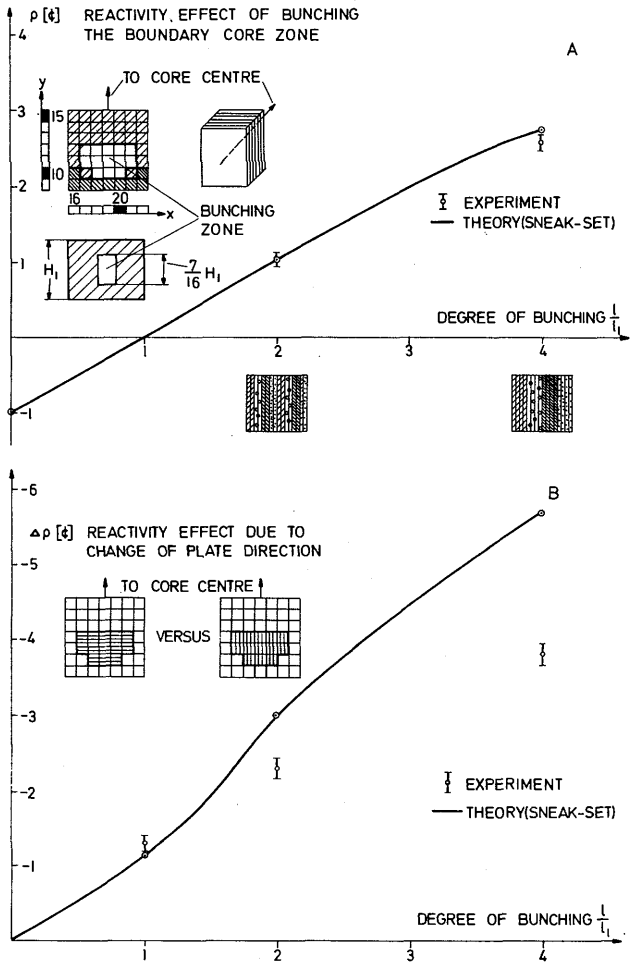

FIG.14. Reactivity effects in the boundary core zone of SNEAK Assembly 3A-1.

The reactivity difference shown in Fig. 14b is obviously caused by the difference between the diffusion coefficients parallel and perpendicular to the platelets. Since the heterogeneity influence on the latter is small, it is essentially the influence of heterogeneity on leakage parallel to the platelets which has been measured. An increased leakage and its negative reactivity contribution is always present for the outer parts of the core if the platelets are horizontally positioned, which is the normal case. This negative contribution, however, is strongly compensated by the positive reactivity contribution due to bunching, found in experiment 1. This is consistent with the results shown in Fig. 13b for the boundary core zone.

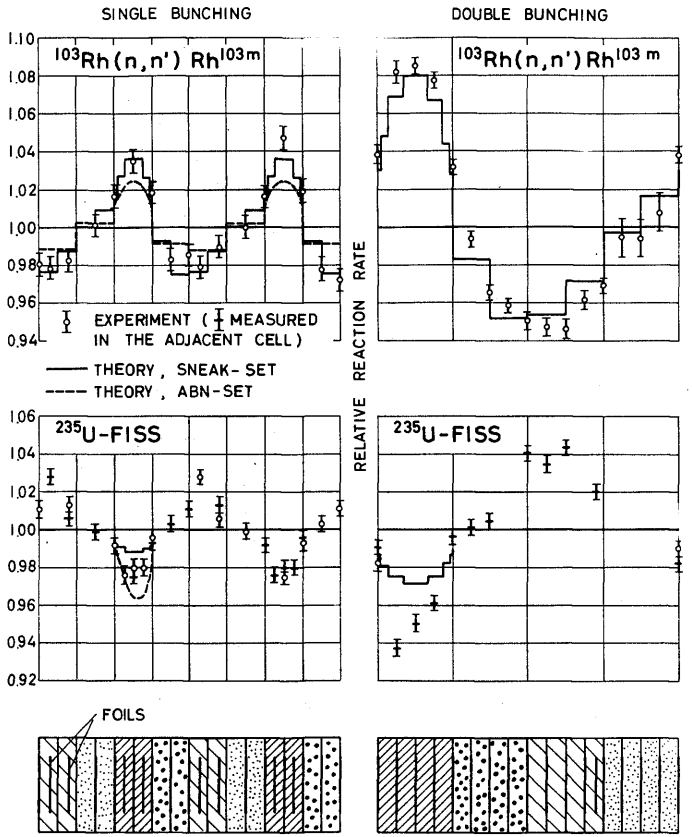

FIG.15. Fine structure at the centre of SNEAK Assembly 3A-1.

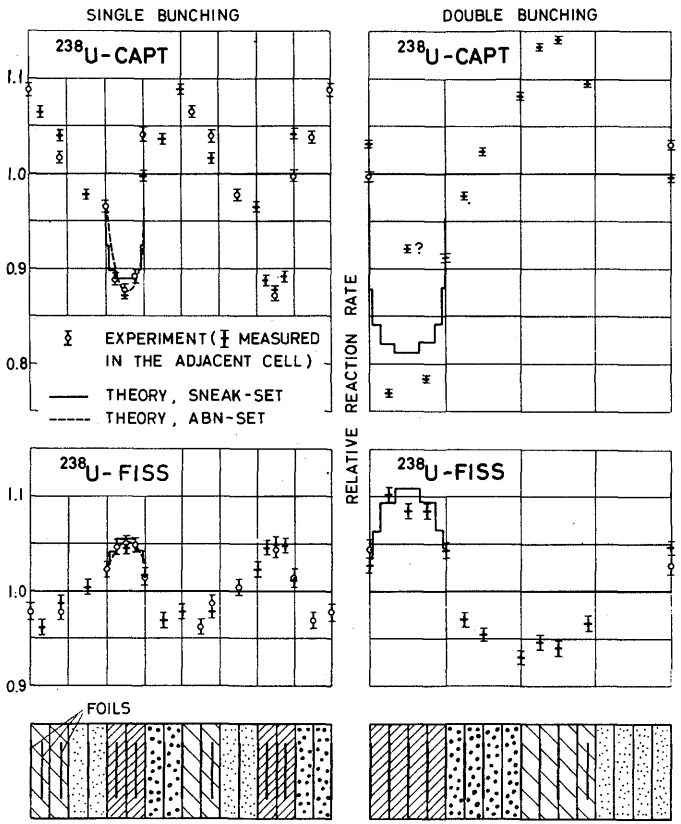

FIG.16. Fine structure at the centre of SNEAK Assembly 3A-1.

5.2. Investigation of flux fine structure

The results of fine structure measurements shown in Figs 15 and 16 give some more differential information about the heterogeneity effects. The main contribution to the $^{103}Rh(n, n')^{103m}Rh$ activation and to ^{238}U fission is caused by neutrons with energies above 200 keV and 1 MeV respectively. A comparison of the measured cell traverses with the results of ZERA calculations show that the flux fine structure for high energy neutrons is in good agreement with the experiment, if the SNEAK set is used. Calculations with the ABN set underestimate the space dependence of the $^{103}Rh(n, n')$ activation strongly. This gives an insight into why the reactivity effects from bunching, which in this case get their main contribution from the high energy part of the spectrum, are underestimated by the ABN set, as shown in Fig. 13a.

The agreement between experiment and calculation (SNEAK set) is not so good for the fine structure of the ^{238}U capture rate shown in Fig. 16. The calculations seem to underestimate the space dependence within the uranium platelets. This is to be expected because the spectrum measurements by foils, shown in Fig. 6, and life-time measurements indicate more neutrons in the 10 to 100 eV range than calculated. It is just this region where self-shielding effects are especially large.

Probably the discrepancy between measured and calculated ^{235}U fission rate distributions with the cell, shown in Fig. 15, is due to the same reasons. The ^{235}U fission curves result from a partial compensation of a flux depression (within the uranium platelets) at low energies and a flux peaking at high energies. Small errors in the rate distribution caused by low energy neutrons will, therefore, lead to large errors in the resulting ^{235}U fission rate distribution.

Generally, it can be stated that such fine structure measurements are sensitive to changes in the over-all neutron spectrum. They can, therefore, be used to test cross-section sets, provided that the calculational methods used for fine structure investigations are sufficiently accurate.

5.3. Additional results obtained during the bunching experiments

Pulsed source measurements were performed when the central zone of 21 elements was doubly bunched. For the prompt neutron decay constant at delayed critical, α_c, no difference could be found within the error limits compared with that given in Section 4.4. for the normal cell structure. This is in agreement with the heterogeneity calculations performed with the SNEAK set, whereas those with the ABN set predicted a 3% lower value for α_c caused by bunching.

Neutron spectrum measurements by the proton recoil technique were also performed in the centre of the doubly bunched zone. The resulting neutron spectrum is shown in Fig. 17, together with the one obtained for normal cell structure. The position of the spherical counter in respect to the platelets is indicated. A qualitative comparison of the measured spectra shows that the resonances, mainly due to oxygen and aluminium, are less pronounced in the case of double bunching than for the normal cell structure. A quantitative comparison of the two experiments has been made by

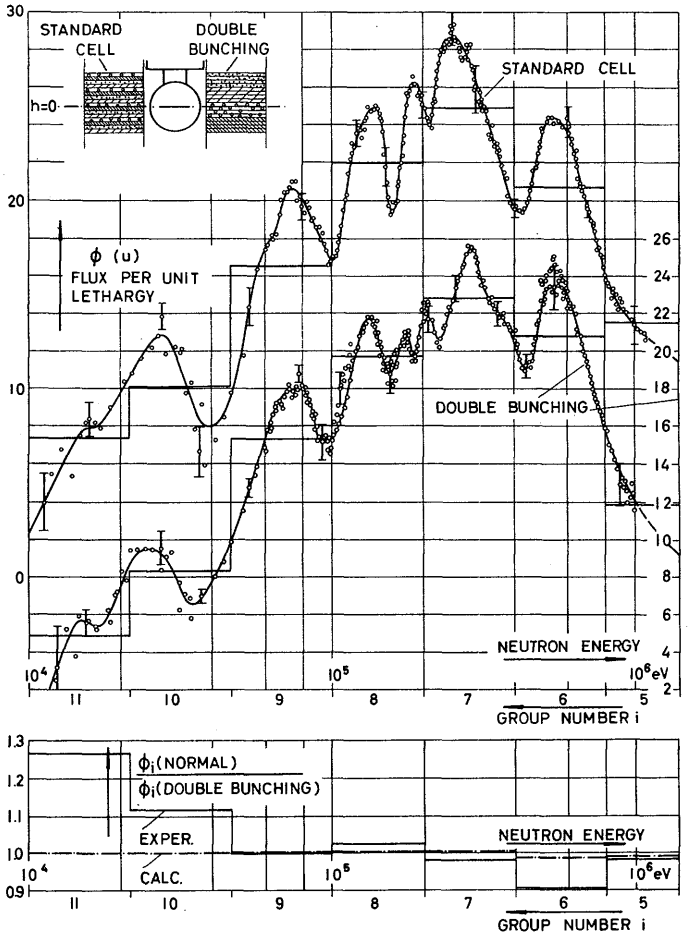

FIG.17. Comparison between neutron spectra obtained with normal and doubly bunched cell structure in SNEAK Assembly 3A-1.

averaging over groups, normalizing to equal area, and forming the ratio of equivalent fluxes per unit lethargy. This is shown in the lower part of Fig. 17, together with the corresponding ratio derived from heterogeneity calculations with the SNEAK set. There are almost no differences for the calculated spectra and only minor differences for the experimental ones, except for the two lowest groups. This, however, should not be over-estimated because of the fairly large statistical errors in this region. It can be concluded from this comparison that the over-all neutron spectrum above 10 keV is not changed remarkably by double bunching. This is consistent with the result found for the prompt neutron decay constant.

During the phase of single bunching within the central zone, temperature-dependent reactivity effects of a metallic natural uranium sample were measured using the pneumatic square wave pile oscillator. The construction and the dimensions of the heated sample can be seen from Fig. 18. The

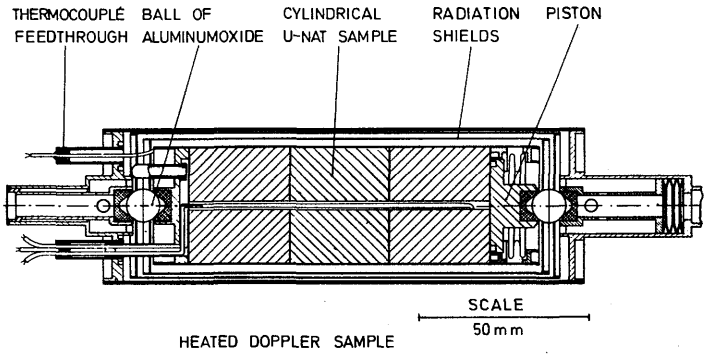

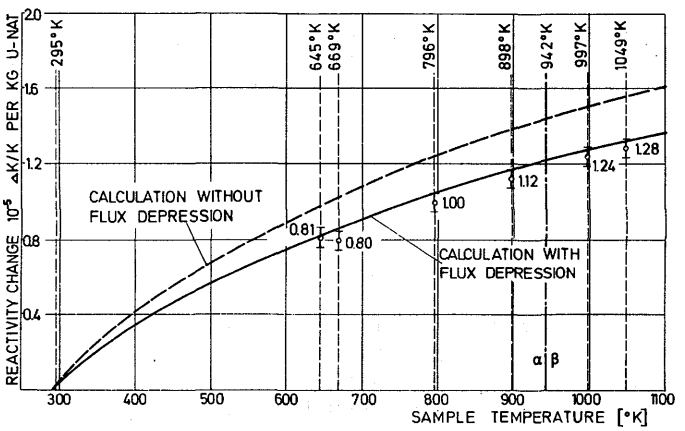

FIG.18. Temperature-dependent reactivity effect of metallic natural uranium Doppler sample in Assembly 3A-1.

sample and an equivalent dummy were inserted into a fuel element loaded with core material. The measured reactivity change for temperatures up to 1049° K is shown in Fig. 18.

Two types of calculations have been made for this experiment using the method described in Ref. [17], which is part of the NUSYS code system. For the one type the flux depression within the sample was taken into account, whereas this was not the case for the other type. Both calculations were made in cylindrical geometry with diffusion theory. The finite size of the sample was taken into consideration by a properly chosen σ_p. The calculated results are also shown in Fig. 18. The calculation without flux depression yields results approximately 20% higher than the measured values. This shows the influence of flux depression very clearly. The good agreement between experiment and theory for the other case should not be over-estimated. In both calculated cases the Doppler coefficient is proportional to $T^{-1.146}$.

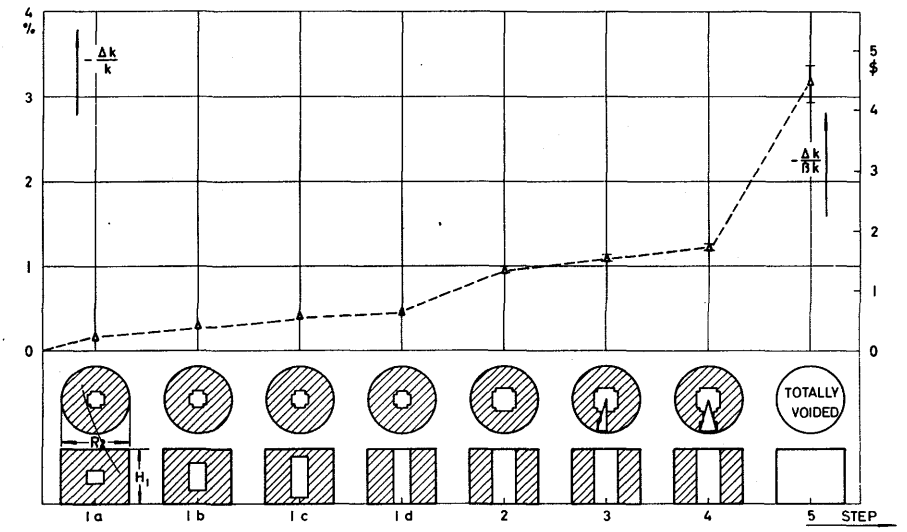

FIG. 19. Measured steam void effect in SNEAK Assembly 3A-1.

6. INVESTIGATION OF THE STEAM VOID EFFECT

The reactivity effect of voiding various core zones in Assembly 3A-1 has been measured and compared with calculations.

In a series of experiments the polyethylene foils were removed in a central cylinder of $\bar{r}$ = 14.07 cm, consisting of 21 core elements, as indicated in Fig. 19. In steps 1a to 1d the polyethylene was removed from the zone in 16, 32, 48, and 64 (full core height) unit cells of each element. This gave the axial dependence of the void effect.

In the following steps 2, 3 and 4 a wider cylinder of 45 elements ($\bar{r}$ = 20.59 cm) and two core sectors have been voided respectively. From these steps the radial dependence could be derived. The reactivity effect of voiding the total core was extrapolated from the sector experiment. It was assumed that

$$\Delta k_{\text{Void, Core}} = \frac{\Delta k_{\text{Void, Sector}}}{V_{\text{Sector}} / V_{\text{Core}}}$$

where $\Delta k_{\text{Void, Sector}}$ is the reactivity effect of voiding the second sector. The experimental results for the different steps including the extrapolation to the totally voided core zone are plotted in Fig. 19.

Experimental results are compared with calculations in Table IX. The experimental error in steps 1 to 4 is mainly due to uncertainties in the worth of control rods used to compensate reactivity. After each step the rods were recalibrated. Deviations in rod worth were about 1% to max. 4% so that the reactivity changes could be determined to about ± 2%. The reactivity change of voiding the 16 outer elements of step 4 was by 6% smaller than the equivalent one of step 3, indicating that voiding

TABLE IX. Comparison of measured and calculated steam void effects in SNEAK assembly 3A-1

Step	Neg. reactivity effect $\frac{\Delta k}{k}$ [%]				Calculation / Experiment		
	Experiment	Calculation					
		SNEAK set	KFK set	ABN set	SNEAK set	KFK set	ABN set
1a	0.164±0.004	0.130	0.113	0.094	0.79	0.69	0.57
1b	0.304±0.006	0.251	0.217	0.181	0.83	0.71	0.60
1c	0.410±0.008	0.345	0.298	0.248	0.84	0.73	0.60
1d	0.459±0.009	0.386	0.333	0.278	0.84	0.73	0.60
2	0.935±0.018	0.782	0.674	0.563	0.84	0.72	0.60
3	1.0 9±0.022	-	-	-	-	-	-
4	1.214±0.028	-	-	-	-	-	-
5	3.18 ±0.22	2.67	2.31	1.90	0.84	0.73	0.60

the first sector decreased the flux in this part of the core. The error in the extrapolated value for total core voiding was estimated to be about ± 7%.

Calculations were made by one-dimensional diffusion codes in cylindrical and plate geometry using transverse bucklings, which rendered the reactor approximately critical in the unvoided case. No two-dimensional calculations have been made so far, nor have final heterogeneity corrections been applied. Preliminary heterogeneity corrections show an increase to the calculated values by a few per cent. The experimental values are on the average 16% higher than those calculated with the SNEAK set. Both KFK and ABN sets give a much too small void effect.

7. CONCLUSIONS

With regard to the integral quantities of interest for the design of steam-cooled fast-reactor systems, the agreement between theory and experiment is improved considerably by applying the recently prepared SNEAK set for calculating Assembly 3A-1.

The effective multiplication constant, k_{eff}, although underestimated by the SNEAK set, is closer to 1 than the fairly strong overestimation by the KFK and ABN set. The underestimation of k_{eff} is decreased to 0.5% by correcting for transport and heterogeneity effects. The heterogeneity correction in particular is very reliable, as can be concluded from the heterogeneity experiments performed in this assembly. Although the accuracy in k_{eff} is reasonable, further two-dimensional calculations with more than ten energy groups seem to be interesting in order to see the effect of group collapsing on k_{eff}.

The initial breeding ratio of 1.08 calculated for this assembly using the SNEAK set gives also the best agreement with that derived from the experiment. As regards the measurements for determining the initial

breeding ratio it can be concluded that more detailed investigations of reaction rates in the blanket and over the whole core volume are necessary to achieve a better experimental accuracy. Measurements within the blanket are particularly important in external breeder systems like this assembly.

The steam void effect experiments also show the best agreement with the results obtained using the SNEAK set. The comparison between experiment and calculation needs to be further extended by the inclusion of two-dimensional calculations and by investigating in more detail the influence of the neutron spectrum below 1 keV on the steam void effect. It is supposed that the underestimation of the calculated void effect is partly due to the underestimation of the calculated neutron flux below about 300 eV as concluded from the sandwich foil experiments.

From the axial and radial fission and capture rate measurements it can be concluded that a special theoretical effort is necessary to eliminate the fairly large discrepancies between calculated and measured reaction rates at the core boundary and within the blanket. The discrepancies are believed to be partly due to the zone-wise treatment of resonance self-shielding, which is apparently not suitable for steam-cooled fast-reactor systems with softened spectra.

The results of the heterogeneity experiments showed on the one side the applicability of the theoretical model used to calculate reliable correction factors, because the integral reactivity effects of the bunching experiments as well as their trends were very well predicted in general. On the other side, the calculated heterogeneity results – in particular the flux fine structure – are rather sensitive to changes in the cross-section sets. In this respect the SNEAK set also gave the best agreement to the experiment.

From the comparison of calculated and measured neutron spectra it can be concluded that the SNEAK set was also closest to the experiment. This is also true for the results found for the prompt neutron decay constant at delayed critical. There is, however, still a remarkable discrepancy left over.

Whereas the application of the SNEAK set improved the agreement between theory and experiment in all cases mentioned before, this is not so for the material worth measurements and for a few spectral indices. So far this result is not understood.

ACKNOWLEDGEMENTS

The authors gratefully acknowledge the continuous support by the operation staff of the SNEAK reactor during the experiment. We are also indebted to Dr. H. Küsters for many helpful discussions, and to E. A. Fischer and W. Schwetje for performing the Doppler effect calculations and special control rod calculations respectively. Furthermore, we thank Dr. W. Eyrich and W. Keller for their help during the pulsed source experiments.

REFERENCES

[1] HÄFELE, W., "The German fast breeder project", these Proceedings, paper SM-101/5.

[2] BARLEON, L., BAYER, A., BRÜCKNER, Chr., BURKART, K., KUHN, D., KUSSMAUL, G., MEISTER, H., STEGEMANN, D., Investigations with Assembly 2 of the Fast-Thermal Argonaut-Reactor STARK, Rep. KFK-592 (1967) (in German).

[3] KÜCHLE, M., MITZEL, F., WATTECAMPS, E., WERLE, H., "Measurements of Neutron Spectra and Decay Constants with the Fast Subcritical Facility SUAK", Proc. of the Int. Conf. on Fast Critical Experiments and Their Analysis, Rep. ANL-7320 (1966) 506.

[4] BACHMANN, H., HUSCHKE, H., KIEFHABER, E., KRIEG, B., KÜSTERS, H., METZENROTH, M., SIEP, I., WAGNER, K., WOLL, D., "The group cross-section set KFK-SNEAK: preparation and results", these Proceedings, paper SM-101/12.

[5] ABAYAN, L.P., BAZAZJANC, N.O., BONDARENKO, J.J., NIKOLAEV, M.N., Group Constants of Fast and Intermediate Neutrons for the Calculation of Nuclear Reactors, State Committee for the Use of Atomic Energy in the USSR (in Russian).

[6] WINTZER, D., "Heterogeneity calculations including space dependent resonance self-shielding", these Proceedings, paper SM-101/13.

[7] ABAYAN, L.P., BAZAZJANC, N.O., BONDARENKO, J.J., NIKOLAEV, M.N., German Translation of Ref. [5], Rep. KFK-tr-144.

[8] KÜSTERS, H., METZENROTH, M., "The influence of some important group constants on integral fast reactor quantities", Proc. of the Conf. on Safety, Fuel, and Core Design in Large Fast Power Reactors, Rep. ANL-7120 (1965) 423.

[9] ENGELMANN, P., BICKEL, W., DÄUNERT, U., HABERMANN, F.W.A., VAN VELZE, P.L., WALZE, H., WITTEK, G., "Construction and experimental equipment of the Karlsruhe fast critical facility, SNEAK", Proc. Int. Conf. on Fast Critical Experiments and Their Analysis, Rep. ANL-7320 (1966) 725.

[10] BARLEON, L., BÖHME, R., BÖHNEL, K., EDELMANN, M., ENGELMANN, P., FIEG, G., HABERMANN, F.W.A., KUHN, D., MAYER, W., SEIFRITZ, W., STEGEMANN, D., VAN VELZE, P.L., WALZE, H., WERLE, H., "Comparison of measurements in SNEAK-1 and ZPR 3-41", these Proceedings, paper SM-101/8.

[11] BENNETT, E.F., Neutron spectrum measurements in a fast critical assembly", Nucl. Sci. Engng 27 (1967) 16.

[12] STRAUSS, M.G., BRENNER, R., General Purpose Analog Pulse Height Computer, Rev. scient. Instrum. 36 (1965) 1857.

[13] BLUHM, H., FIEG, G., LALOVIC, M., STEGEMANN, D., WATTECAMPS, E., WERLE, H., Fast reactor spectrum investigations on the facilities SUAK and SNEAK at Karlsruhe, Trans. Am. nucl. Soc. 10 2 (1967) (Full text to be published).

[14] EHRET, G., The measurement of epithermal neutron spectra by use of resonance detector foils (sandwich method), Atompraxis 1 (1961) 393.

[15] SEUFERT, H., STEGEMANN, D., A method for absolute determination of ^{238}U capture rates in fast zero-power reactors, Nucl. Sci. Engng 28 (1967) 277.

[16] EDELMANN, M., MURLEY, T.E., STEGEMANN, D., Investigation of Prompt Neutron Kinetics in the Fast-Thermal Argonaut-Reactor STARK by Noise Analysis, Rep. KFK-522 (1967).

[17] FROELICH, R., Theorie der Doppler-Koeffizienten schneller Reaktoren unter Berücksichtigung der gegenseitigen Abschirmung der Resonanzen, Rep. KFK-367 (1965).

DISCUSSION

W.B. LOEWENSTEIN: Have you performed a central material replacement experiment with plutonium, and, if so, how does it compare with calculation?

D. STEGEMANN: Yes, we have performed such measurements, with a normal SNEAK platelet containing plutonium (approximately 7% ^{240}Pu). The results are given in Table VII of the paper. The disagreement with theory is about 10%.

W.B. LOEWENSTEIN: Does this mean that the α values presented in paper SM-101/41 are too high?

D. STEGEMANN: No, I would not like to draw such a conclusion from this experiment, since the theoretical model used in comparing theory with experiment needs to be improved before really reliable statements can be made.

P.A. ENGELMANN: Perhaps I can add something to Mr. Stegemann's first reply. We used a normal, 2 in. × 2 in. × $\frac{1}{4}$ in., SNEAK platelet containing a UO_2-PuO_2 mixture (75% depleted UO_2 and 25% PuO_2). This sample was rather large and the results had to be corrected for the contribution of the uranium. We have now ordered new samples made of a plutonium-aluminium alloy containing two kinds of plutonium: one with 8% and the other with 3.5% of the higher isotopes. Better plutonium worth measurements will be possible with these samples.

W.K. FOELL: I was interested to note that you presented the proton recoil, sandwich foil and ^6Li spectrometer results on one graph (Fig. 6). From the fact that the measured foil results at low energy were considerably higher than the calculated results, it has been suggested that the calculated results might be in error. How did you normalize the measured results, and in particular the foil measurements?

D. STEGEMANN: The proton recoil and ^6Li-spectrometer results were normalized to equal the area under the calculated spectrum between 10 keV and 4 MeV. The sandwich foil data were normalized to the experimental and calculated results for ^{23}Na.

W.K. FOELL: Figure 18 shows rather good agreement between measured and calculated low-energy spectra. Does this not contradict your results?

D. STEGEMANN: The good agreement may to some extent be fortuitous. I would therefore hesitate to draw any conclusions.

A.E. KHAIRALLAH: Could you tell us the value of the correction due to movement of the fuel compared with the heterogeneity effect proper in the heterogeneity experiments (grouping of fuel platelets)?

D. STEGEMANN: It was found to be very small compared with the total heterogeneity effect.

H. VOLLMER: One of the decisive design parameters for steam-cooled fast-reactor power plants is the density coefficient $dk/d\rho$. To what extent do your experiments support calculations of this coefficient, and how do the measured and calculated coefficients compare?

D. STEGEMANN: The results of criticality calculations for the voided core, the 3A-1 core and the 3A-2 core indicate that $dk/d\rho$ is reasonably well predicted if the SNEAK set is used. The calculated value of $dk/d\rho$ differs by about 10% from the experimental value.

H.R. KLEIJN: In his presentation of paper SM-101/9, Mr. Beckurts indicated that we need to review a number of cross-sections, for example, the capture cross-section of ^{238}U. On the other hand, Mr. Küsters said in his presentation of paper SM-101/12 that various quantities such as breeding ratios were not strongly dependent on cross-sections. Now, Mr. Stegemann has reported experimental results which, with the exception of those for positions near the core boundary, show good agreement with calculations (and if I understood Mr. Stegemann correctly, the differences near the core boundary are probably due to incorrect self-shielding calculations). My question is – do we or do we not need to review certain cross-sections, and, if so, which ones and in what energy range?

D. STEGEMANN: This is a very interesting question, which should in my opinion be the subject of a special discussion.

NEUTRON SPECTRUM MEASUREMENTS IN THE FAST REACTOR ASSEMBLY VERA 19A AND TESTS OF THE TIME-OF-FLIGHT SPECTROMETRY METHOD IN VERA 5A AND VIPER 1

W.J. PATERSON, P.W. BENJAMIN, D. HATTON*,
W.B. McCORMICK AND J.W. WEALE
UNITED KINGDOM ATOMIC ENERGY AUTHORITY,
ALDERMASTON, BERKS., UNITED KINGDOM

Abstract

NEUTRON SPECTRUM MEASUREMENTS IN THE FAST REACTOR ASSEMBLY VERA 19A AND TESTS OF THE TIME-OF-FLIGHT SPECTROMETRY METHOD IN VERA 5A AND VIPER 1. The neutron energy spectrum has been measured in VERA 19A using time-of-flight methods, proportional counters and photographic plates. Assembly 19A is fuelled with plutonium oxide, uranium oxide and Polythene homogeneously mixed, with a H: Pu ratio of 20. It is designed to provide data for checking the accuracy of calculations of critical parameters of fast reactor fuel elements in slightly moderated assemblies.

VERA 5A is fuelled with ^{235}U and contains a small amount of carbon and hydrogen. It has been used for investigations into the accuracy and validity of time-of-flight spectrometry results. The time-of-flight measurements have been compared with sandwich foil activation measurements, the effect of source and beam-hole geometry has been investigated and the dependence of the results on reactivity has been measured.

1. INTRODUCTION

The methods of neutron spectrometry used on the low power fast reactor assembly, VERA, have been described by Weale et al. [1]. The present paper describes the application of these techniques to determine the neutron energy spectrum in the VERA assembly 19A and some further tests of the time-of-flight technique made on VERA assembly 5A and the AWRE pulsed reactor VIPER [2].

2. SPECTRUM MEASUREMENTS IN VERA 19A

Description of VERA 19A

VERA 19A is an assembly of homogeneous compacts of $PuO_2/U(nat)O_2/CH_2$ designed to test calculations for plutonium systems in which an appreciable fraction of the fissions occurs in the few keV region.

The assembly consists of a 12 × 12 array of vertical mounted square elements surrounded by an outer reflector of natural uranium and steel rods, 2.92 cm diameter, which extends to an overall diameter of 104 cm. The elements are arranged in a square lattice with a pitch of 4.69 cm. Those in the outer region of this array, forming the inner reflector, are unsealed, square steel tubes containing stacks of natural uranium blocks separated by steel spacer rings. Each block is 4.29 cm square × 2.52 cm high and the gap between blocks caused by the steel rings is 0.26 cm. The same arrangement

---

* Reactor Physics Department, University of Birmingham, United Kingdom.

TABLE I

VERA 19A Composition by Nuclei, nuclei/cm^3 x 10^{-20}

	^{239}Pu	^{240}Pu	^{241}Pu	^{238}U	^{235}U	O	C	H	Al	Fe	Cr	Ni
Core	18.77	1.174	0.106	59.71	0.433	160.35	190.42	380.7	0.754	60.84	15.97	6.65
Axial Reflector				344.0	2.5					62.67	16.26	6.84
Inner Radial Reflector				344.0	2.5					64.64	16.82	7.08
Rod Reflector				361.0	2.6					65.82	17.13	7.21

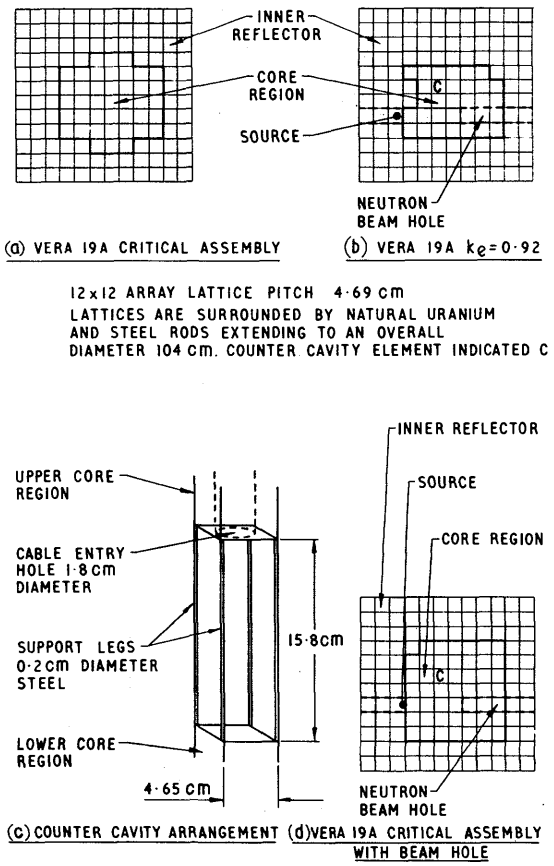

FIG.1. Sketch plans of the 19A assemblies and counter cavity arrangement.

of the inner and outer reflector zones was used for VERA uranium assemblies 1A to 7A and a more detailed description is given by Weale et al. [3].

The elements forming the central core region are sealed square steel tubes and each is fuelled with a stack of 14 $PuO_2/U(nat)O_2/CH_2$ compacts. For convenience in handling the compacts are separated from each other by 0.0025 cm foils of aluminium and each stack is sealed in a polyethylene bag. Each compact is 4.32 cm square by 2.15 cm high and the core height is 30.2 cm. Natural uranium blocks and steel spacer rings above and below the compact stacks form the axial reflectors. A plan view of the core region and inner reflector of a critical assembly is given in Figure 1(a) and the nuclear compositions of the assembly regions are listed in Table I.

Experimental and calculated critical sizes of VERA 19A

The critical size of the assembly shown in Figure 1(a), corrected for excess reactivity is (39.76 ± 0.25) elements or (19.65 ± 0.12) kg ^{239}Pu which represents a core volume of (26.37 ± 0.17) litre. The edge irregularity correction is estimated to be - 0.15 kg ^{239}Pu and a shape factor 0.952 has

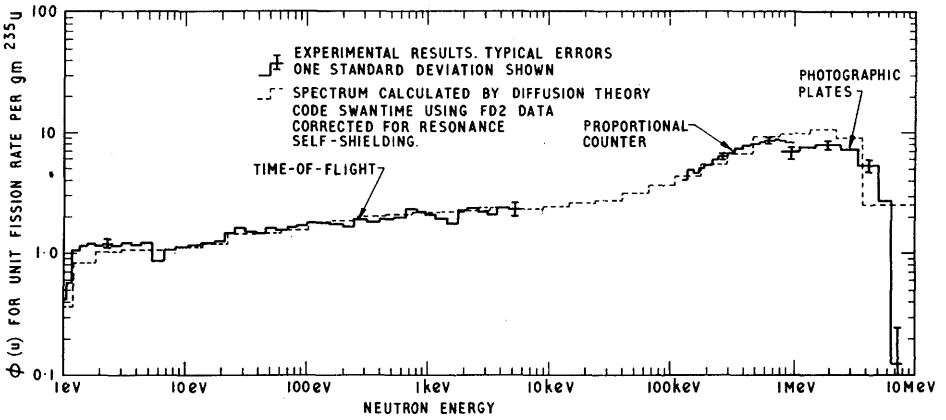

FIG.2. VERA 19A. Neutron energy spectrum at core centre.

been derived from transport calculations in spherical and cylindrical geometry on similar assemblies. These lead to a smooth sphere critical mass of (18.6 ± 0.2) kg ^{239}Pu which corresponds to a sphere radius of (18.3 ± 0.06) cm.

A diffusion theory calculation in spherical geometry using the SWAN code [4] with FD2 data [5] corrected for resonance self-shielding gives a critical mass 26.8 kg ^{239}Pu which is 1.44 times the measured value. A transport theory calculation using the TURTLE code [6] with the same nuclear data gives a smooth cylinder critical mass 24.02 kg ^{239}Pu which is 1.23 times the equivalent measured mass. This difference between transport and diffusion theory results is significantly greater than for other VERA assemblies of similar size but with harder spectra.

Spectrometry in VERA 19A

Measurements of the neutron energy spectrum have been made in a 32 element assembly which has an estimated reproduction factor $k_e \sim 0.92$. A plan of this assembly is given in Figure 1(b) which shows the locations of a neutron beam hole for time-of-flight measurements and a special element to house a hydrogen-filled proportional counter and photographic emulsions. The neutron beam hole which is at the core centre-height is 4.3 cm wide by 6.4 cm high and the steel case of the element at the end of the hole is cut away so that neutrons from the fuel compact stacks emerge directly into the beam. A similar hole through the reflector allows an accelerator target at the core edge to provide a pulsed or steady source of 14 MeV neutrons. A diagram of the special counter element in Figure 1(c) shows the dimensions of the cavity, which has compacts stacked below it and plutonium and diluent plates above it arranged to simulate the average core composition. A minimum amount of the steel of the element remains in the region of the cavity and the steel in adjacent faces of the surrounding fuel elements is cut away so that the compact material is directly viewed in a considerable proportion of the solid angle subtended at the detector. The results of the measurements, using the techniques described by Weale et al. [1] are plotted in Figure 2 together with a spectrum calculated for an equivalent spherical assembly using the diffusion theory code SWANTIME [7]. This code can be used to calculate spectra in spherical subcritical assemblies driven by a neutron source in a spherical shell at some specified radius. It therefore gives central spectra which would be obtained with a point source calculation. The measured and calculated

spectra have been normalised to the same ^{235}U fission rate scale. To achieve this the measurements were all monitored by a ^{235}U fission counter in the counter cavity. To normalise the time-of-flight measurements it was also necessary to measure the ^{235}U fission rate at the end of the 50 m flight path relative to the monitor in the counter cavity. The proportion of the total counts in the ^{235}U fission monitor due to direct source neutrons is very small but in the neutron beam, which is in line with the source, an appreciable fraction of the ^{235}U fission rate is caused by 14 MeV source neutrons. For this reason the fission rate in the beam per monitor count had to be measured with the reactor critical with no source, as in Figure 1(d). The result is believed to be insensitive to the reactivity and geometry change and no correction has been applied.

Discussion of VERA 19A results

Apart from the 6 keV to 120 keV range which was not measured, the neutron spectrum at the core centre agrees well with the calculated spectrum between 6 eV and 400 keV. Below 6 eV the time-of-flight fluxes are greater than those calculated by up to 30%. The photoplate results are 20 - 30% lower than the calculated fluxes in the energy range 800 keV to 4 MeV. It is interesting that in this assembly the central spectra predicted by the diffusion theory and the transport S_4 calculation agree with each other to within ± 2% throughout whereas the calculated critical sizes are respectively 44% and 23% too large. The production to absorption ratio for the core region given by the diffusion theory calculation is 1.36, much smaller than for other VERA assemblies of similar size with harder spectra, but it appears that the core leakage is still being considerably overestimated. Both calculations indicate that 42% of the ^{239}Pu fissions occur below 1 eV, in the region not covered by the time-of-flight measurements. It is possible that the nuclear data in this region are responsible for some of the inaccuracy in the calculated critical masses.

3. EXPERIMENTAL TESTS OF THE ACCURACY OF THE TIME-OF-FLIGHT SPECTROMETRY TECHNIQUE

The time-of-flight method appears to be the only means of measuring in detail the low energy part of the neutron spectrum in fast reactors and because this region is the one where the Doppler effect arises it is important to obtain a high degree of confidence in these measurements. Three experiments have recently been done on VERA assembly 5A to check certain features of the time-of-flight method. First, a comparison has been made of results obtained by time-of-flight and results obtained by activation of metal foils in sandwich arrays which determine the neutron flux at a resonance energy. Second, the effect of making a drastic change in the geometrical lay-out of the pulsed source and the beam extract hole has been measured. Third, the dependence of the time-of-flight result on the degree of sub-criticality of the reactor assembly has been determined over the range $k_e = 0.8$ to $k_e = 0.95$.

VERA 5A is a small ^{235}U-fuelled fast reactor assembly which is part of a series of experiments designed to check data and calculation methods. The core is constructed of square stainless steel fuel elements loaded with square plates of 93% enriched U and of graphite, both 0.317 cm thick, and 0.079 cm plates of polythene. The material is arranged in cells, each containing 1 plate of enriched U, 4 plates of graphite and 2 plates of polythene. The core is reflected on all sides by a thick reflector of natural U and steel. The critical core height is 28.4 cm, its volume is 23.1 litres and the critical mass is 59.7 kg of ^{235}U. A more detailed description of the assembly and the results of other measurements have been published earlier [8],[9].

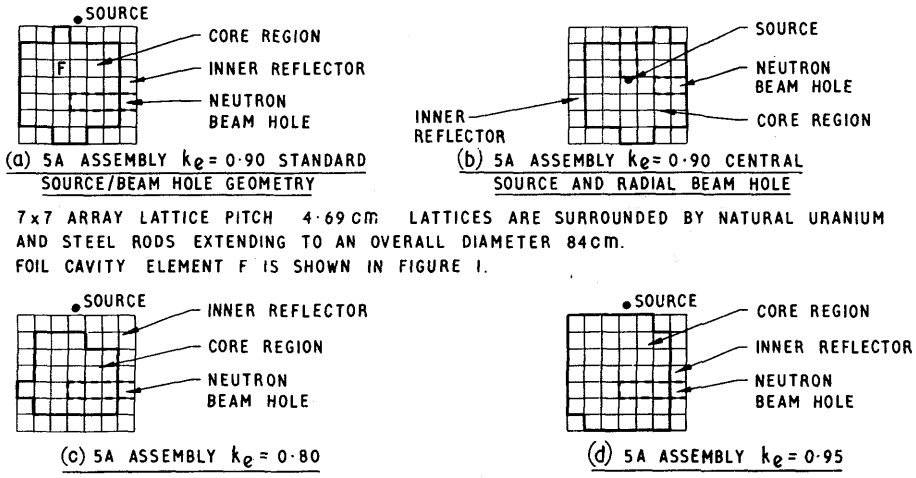

FIG.3. Sketch plans of the VERA 5A assemblies.

Comparison of time-of-flight and foil activation results

Resonance flux measurements by the sandwich foil technique have been compared with time-of-flight spectrum measurements in a 33 element 5A assembly with an estimated reproduction factor $k_e \sim 0.90$. Figure 3(a) shows the arrangement of the elements, the accelerator source and the neutron beam hole which has the same dimensions as that used in VERA 19A. The three-foil sandwiches were mounted in the centre of the cavity in element F which is the same as that shown in Figure 1(c). A ^{235}U fission counter, 0.64 cm diameter, in a corner of the cavity was used to monitor the foil and time-of-flight measurements. As in the VERA 19A measurements the steel is cut away from the adjacent surfaces of elements surrounding the cavity and from the element surface at the inner end of the beam hole.

The sandwich foil method has been described by many workers and a recent review is given by McCracken [10]. The basis of the method is that for foils of suitable thickness the inner foil of a sandwich is effectively screened from neutrons with resonance energies whilst the three foils are uniformly activated by neutrons at energies away from resonances where the cross-section is relatively small. The difference between the inner and outer foil activities is therefore proportional to the fluxes at resonance energies.

The sandwich samples were calibrated in the AERE reactor GLEEP in which the thermal and epithermal fluxes are accurately known [11]. The fluxes in GLEEP at the resonance energies have been calculated on the assumption that the slowing down flux has a 1/E distribution. Details of the sandwich materials and the results are given in Table II. The corrections for the minor resonance effects arise because the VERA 5A spectrum does not vary as 1/E.

A separate measurement of the ratio of the ^{235}U fission rates at the end of the 50 m flight path and in the foil cavity was required to normalise the time-of-flight and the foil measurements to the same fission rate scale.

The sandwich foil results are compared with the time-of-flight spectrum in Figure 4. Also shown is a spectrum calculated, using SWANTIME, for an

TABLE II

Properties of Sandwich Materials and Results, VERA 5A

Material	Main Resonance Energy (eV)	Diameter (cm)	Thickness (cm)	Correction for Effect of Subsidiary Resonances	$\phi(u)$ per Unit Fission Rate in 1 g ^{235}U
W	18.8	1.52	0.005	- 9%	0.34 ± 0.04
Co	130	1.52	0.005	- 1%	0.99 ± 0.12
Mn	337	1.52	0.0125	- 2.4%	2.03 ± 0.24
Cu	580	1.52	0.0125	-15.4%	2.20 ± 0.26
Na	2850	2.22(NaCl)	0.159	0%	6.57 ± 0.80

Errors shown as one standard deviation.

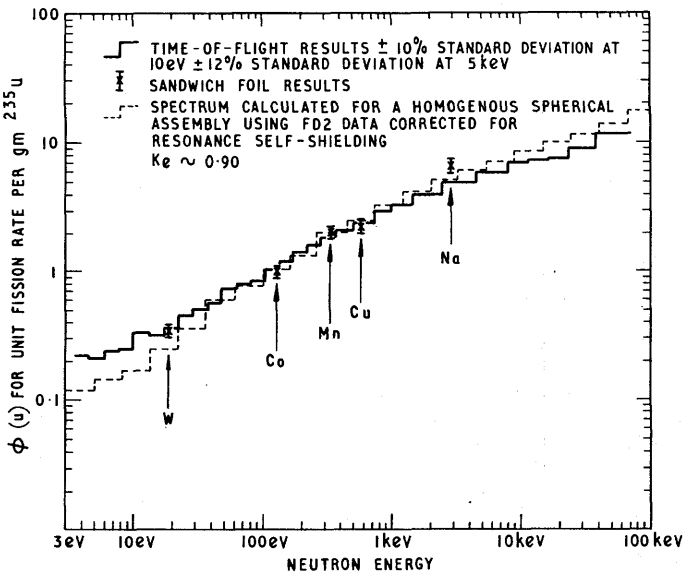

FIG.4. VERA 5A. Spectrum by time-of-flight and sandwich foils.

equivalent spherical assembly with a spherical shell source at the appropriate radius.

Dependence of time of flight results on the geometrical arrangement

The usual geometrical arrangement of source and beam hole for the 5A measurements is shown in Figure 3(a). The neutron beam direction is approximately perpendicular to a core radius passing through the inner end of the beam hole and is also perpendicular to components of the flux gradients produced at the beam origin by the accelerator source. Neglecting perturbations due to the beam hole itself and localised flux gradients arising from heterogeneities in the assembly, the relationship between directional and scalar fluxes given by diffusion theory suggests that this arrangement would provide a beam spectrum proportional to the scalar flux spectrum.

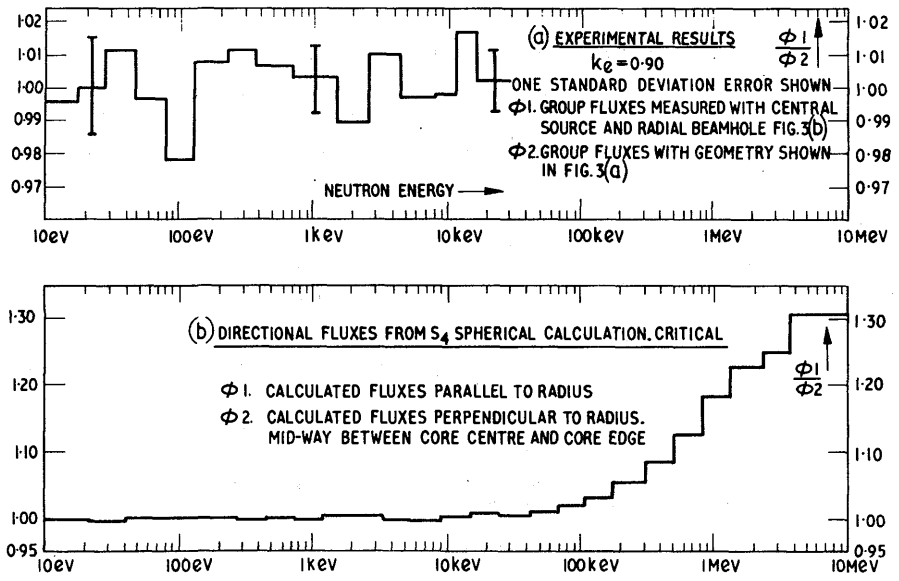

FIG.5. VERA 5A. Source and beam-hole geometry investigations.

A comparison has been made with results obtained using the geometrical arrangement shown in Figure 3(b). Here the beam direction is parallel to the flux gradients at the beam origin. Flux ratios obtained with the two geometrical arrangements are plotted in Figure 5(a) showing that in the energy range below 30 keV there is no discernable difference in the spectrum shapes. This result is supported by a transport S_4 calculation for an equivalent spherical critical assembly. Figure 5(b) shows the ratios of the calculated fluxes parallel and perpendicular to a radius at a position half-way to the core-edge. Only at energies above 30 keV is there any appreciable variation in the flux spectrum shapes.

Variation of spectrum shape with reactivity

Time-of-flight measurements in multiplying systems are made at a degree of subcriticality which depends on the energy resolution required. It is often desirable to relate the measured spectrum to that corresponding to a critical assembly. Confidence in calculated adjustments would be enhanced if it could be shown that the reactivity dependence of the spectrum shape in the time-of-flight range is not large and well predicted by calculation. The time-of-flight measurements at $k_e \sim 0.90$ have been extended to include assemblies at $k_e \sim 0.80$ and $k_e \sim 0.95$ shown in Figures 3(c) and 3(d) respectively. The variations in the spectrum shapes obtained are illustrated by flux ratios plotted against energy in Figures 6(a) and 6(b). Figure 6(c) shows similar flux ratios derived from the core centre spectrum for the critical assembly, calculated using the SWAN code, and the calculated spectrum plotted in Figure 4 for the system with $k_e = 0.90$.

Discussion of time-of-flight experiments

The total experimental error on the sandwich foil results is estimated to be ± 12% standard deviation. The time-of-flight experimental errors are ± 10% standard deviation at 10 eV increasing slightly to ± 12% standard

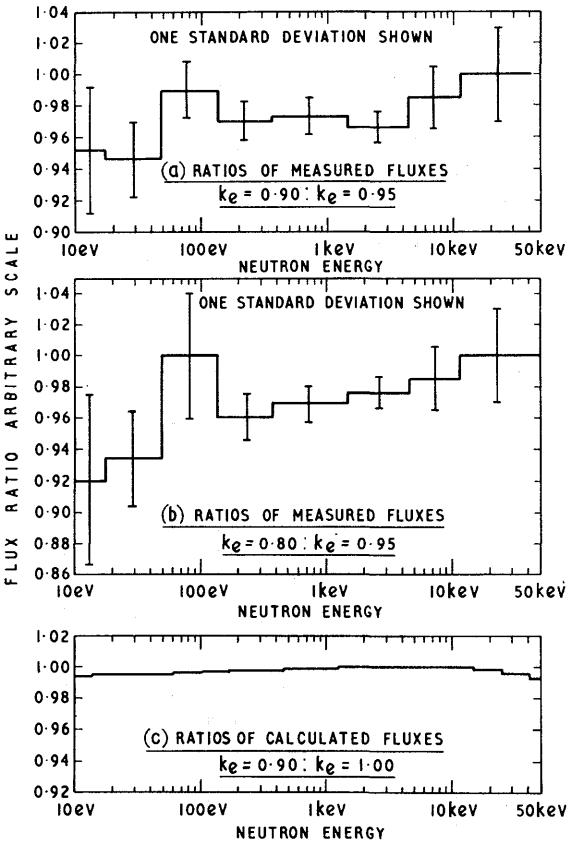

FIG.6. VERA 5A. Spectrum variations with reactivity.

deviation at 50 keV. Four of the five sandwich foil results are in good agreement with the time-of-flight spectrum and differences are smaller than one standard deviation of the combined error. This agreement inspires greater confidence in both measurements. The sodium sample result differs from the time-of-flight and calculated spectra by a little more than two standard deviations. This larger difference may be due to difficulties introduced by a long activity ^{35}S, and a short activity ^{38}Cl from the chlorine present in the detector.

The results of investigations into the effects of source and beam hole geometry on the shape of time-of-flight spectra provide reassuring evidence that the position of the beam hole and source is not very important in the energy range below 50 keV. This is supported by the calculated directional fluxes. This calculation shows, however, that in certain geometrical arrangements the spectrum above 50 keV would be affected appreciably and this could be important when using beam fission rates to normalise the time-of-flight results to in-core measurements. Further investigations are required into the effect of source position alone as this experimental result may be due to two cancelling effects.

The changes in spectrum shape with reactivity variations in the range k_e = 0.8 to 0.95 are not large, but the deviations from the critical

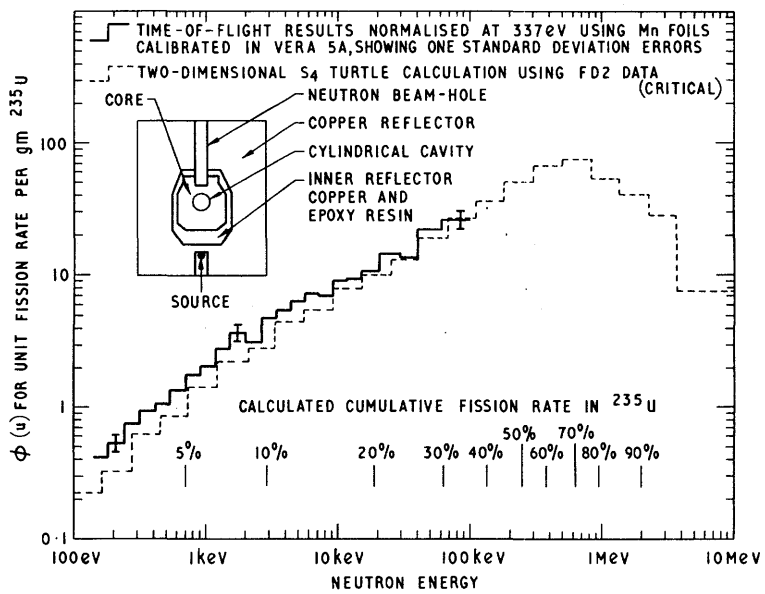

FIG.7. VIPER 1. Spectrum by time-of-flight.

spectrum given by the SWANTIME calculation are not similar. It appears that a better representation of the experimental geometry is necessary to calculate accurate adjustments to the spectrum to allow for reactivity changes.

4. COMPARATIVE NORMALISATION OF TIME-OF-FLIGHT MEASUREMENTS BY THE FOIL SANDWICH TECHNIQUE

When the accelerator neutron source is in line with the extracted neutron beam, the ^{235}U fission rate in the beam, used to normalise time-of-flight measurements to the same flux scale as the in-core methods, must be measured without the source, at critical. This is frequently not convenient and introduces some uncertainty from possible changes in the beam fission rate per core monitor count produced by the reactivity increase. An alternative method is to use the resonance foil sandwich technique to normalise time-of-flight measurements to an absolute in-core flux. In VERA 5A where the source is well away from the neutron beam axis, the spectrum has been normalised using the beam fission rate measurement and the known spectrum has been used to calibrate manganese foil sandwiches. The same foils were then irradiated in the AWRE pulsed reactor VIPER to provide an absolute flux at 337 eV which was used to normalise the VIPER spectrum measured by time-of-flight. The resulting spectrum is plotted in Figure 7 which also shows a sketch of the assembly lay-out. A spectrum calculated for the critical assembly using the TURTLE code is also shown, normalised to the same fission rate scale.

At 337 eV where the VIPER time-of-flight spectrum is normalised to the manganese sandwich foil result the calculated flux is 31% lower than that of the measurements but it agrees with the time-of-flight spectrum at 100 keV. There is therefore an error in the calculated spectrum shape in the region below 100 keV and the normalisation by the manganese foil method is probably correct. This result taken with the other foil measurements suggests

that this method of normalising time-of-flight measurements, using a few different samples, could be as accurate as the beam fission rate method. Unlike the latter it has the advantage that it is not affected by local distortions in the beam spectrum at energies outside the time-of-flight range.

5. ACKNOWLEDGMENTS

We should like to thank Dr. A. Brickstock, Mr. A.R. Davies and Mr. J. Cameron for providing the calculation results quoted, and Mr. J. Redfearn and Mr. D.L.E. Smith for assistance with the experiments. We are also grateful to Mr. A.K. McCracken, AERE Harwell, for advice concerning the foil measurements.

REFERENCES

[1] WEALE J.W., BENJAMIN P.W., KEMSHALL C.D., PATERSON W.J., REDFEARN J., Neutron spectrum measurements in the zero power fast reactor VERA. Conference on radiation measurements in nuclear power, Berkeley, UK (1966).

[2] WEALE J.W., GOODFELLOW H., McTAGGART M.H., WARNKE E.G., A new fast pulsed reactor VIPER. Symposium on fast reactor physics, Karlsruhe (November 1967) SM-101/39.

[3] WEALE J.W., GOODFELLOW H., McTAGGART M.H., The versatile experimental reactor (VERA). AWRE Report No. R2/62 (1962).

[4] BRICKSTOCK A., DAVIES A.R., SWAN A multigroup one-dimensional diffusion code for the IBM 7030, AWRE Report No. O-99/65 (1965).

[5] SMITH R.W., ROWLANDS J.L., WARDLEWORTH D., UKAEA Report No. AEEW-R491 (1966).

[6] SAWARD M.P., WADE R.D., Solution of the two-dimensional axially symmetric multi-group stationary neutron transport equation, AWRE Report No. O-66/63 (1963).

[7] BRICKSTOCK A., DAVIES A.R., SMITH I.C., SWANTIME: A time-dependent multi-group diffusion code for the IBM 7030, AWRE Report No. O-3/66 (1966).

[8] WEALE J.W., McTAGGART M.H., GOODFELLOW H., PATERSON W.J., Operating experience with the zero energy fast reactor VERA. IAEA Conference, Vienna (1964).

[9] McTAGGART M.H., GOODFELLOW H., PATERSON W.J., WEALE J.W., Interim report on uranium-fuelled VERA reactor experiments, AWRE Report No. R5/66 (1966).

[10] McCRACKEN A.K., Techniques with resonance foil sandwich detectors. Conference on radiation measurements in nuclear power, Berkeley, UK (1966).

[11] AXTON E.J., Absolute measurement of the neutron flux density in the AERE reactor GLEEP, J. Nucl Energy A/B 17 125 (1963).

DISCUSSION

P. A. ENGELMANN: Does the uncertainty of ± 10% given for the resonance activation spectrum measurements include the error due to higher resonances?

J. W. WEALE: Yes, it does.

P. A. ENGELMANN: Do you think it is necessary to use the time-of-flight technique, or is resonance foil activation alone sufficient in the energy range below 3 keV?

J. W. WEALE: Firstly, I think it would be unwise to rely on one single experimental check of sandwich detector and time-of-flight methods against each other; the experiment ought to be repeated by other workers. Secondly, there should be a check of the pulse-shape-discrimination proportional counter method against the time-of-flight method, because one of these techniques will be needed to check the detailed structure of the low-energy spectrum.

F. EBERSOLDT: You did not mention the methods used in determining the neutron spectrum on the basis of the measured time distribution. Did you assume that the pulse was a δ-function, or that it decayed in a single exponential mode? Alternatively, did you use the actual measured response, in combination with an interative method?

It seems to me that the iterative method you put forward last year at Berkeley (Ref. [10]) was not explained very clearly. Have you proved the convergence of this method in general, or does it converge only if certain limitations are applied? Do you, in order to facilitate the convergence, smooth out the recorded time distribution before applying the iterative process?

J. W. WEALE: For the analysis of time-of-flight data we use the reactor pulse shape determined experimentally by measuring the count rate of a fission counter located in the reactor core. We combine this result with the time distribution of events recorded by the time-of-flight detector in an iterative procedure to obtain the corresponding reactor spectrum. A smoothing process is first applied to the time distribution data. Full details of this method of analysis, together with the results of some tests of its validity, are given in report AWRE 0-8/67 (1967) by W. J. Paterson and K. Shutler.

M. F. TROYANOV: How can you be so sure that the spectrum in the beam is the same as the spectrum in the centre of the reactor?

J. W. WEALE: Firstly, the time-of-flight results are in good agreement with the in-core proportional counter results in the energy range where the two techniques overlap. Secondly, the time-of-flight results agree with the in-core measurements based on sandwich foil methods. However, it is possible that the latter agreement is due to cancelling of errors. We therefore plan a further check, which will be done by placing a proportional counter in the extracted beam.

D. STEGEMANN: With regard to Fig. 2, why is the energy region between 10 and 100 keV not measured by proton recoil spectrometry? Have there been any major difficulties?

J. W. WEALE: The proportional counter gives its best results if the count rate is kept below a certain limit. This causes difficulties in

plutonium-fuelled systems because of the high level of neutron flux due to spontaneous fission and the gamma-ray background. The count rate can be reduced by working in a sub-critical system, but it seemed preferable in this case to use a near-critical assembly and to accept a limitation on the energy range covered. No pulse shape discrimination measurements were made.

ANALYSIS OF DOPPLER ACTIVATION MEASUREMENTS IN ZEBRA

T. D. BEYNON
DEPARTMENT OF PHYSICS,
UNIVERSITY OF BIRMINGHAM,
BIRMINGHAM, UNITED KINGDOM

Abstract

ANALYSIS OF DOPPLER ACTIVATION MEASUREMENTS IN ZEBRA. An analysis is made of some recent Doppler activation foil measurements in the UKAEA zero-power fast reactor ZEBRA. A model is used to approximate the system of a foil, oven and heterogeneous reactor by a foil and homogenized reactor. The collision probabilities obtained by this reduction are used in the computer programme SDR-GENEX which produces a detailed continuous-energy slowing-down spectrum in the foil for the range 0-15 keV. The spectrum above 15 keV is obtained using the multigroup diffusion code SCRAMBLE. The measured (n, γ) activation ratio for a 12.19 mm × 0.254 mm U_3O_8/Ni foil is 1.024 ± 0.003 in ZEBRA core 6A and 1.020 ± 0.003 in core 6D compared with the calculated values 1.022 and 1.020, respectively.

The model, although approximate in its treatment of homogenizing the reactor core, is a useful tool for understanding the more important physics of the (n, γ) activation experiment. A comparison is made of the calculated energy distributions of the Doppler effect in the foil and in the core. It shows the median energy of each distribution to be at 900 eV and 1550 eV, respectively. This relative displacement is attributed to the differing degree of self-shielding of the ^{238}U resonances in the foil and in the core. In the core the background scattering cross-section is about 50 barns per ^{238}U atom compared with an effective scattering cross-section of 250 000 barns in the thin foil. The effect of this dilution in the foil is to lower the Doppler contribution from the predominantly scattering resonances around 1 or 2 keV and to increase the percentage contribution of the strongly absorbing low-energy resonances. We observe this as a relative shift in energy of the foil and core Doppler distributions. The analysis shows that, by equalizing the scattering cross-section per absorbing atom in the foil and core, the activation ratio and its energy distribution are also approximately equalized in the foil and core. We may therefore optimize the design of the activation experiment. For example, in a typical fast reactor core, a long circular cylinder of natural uranium would require a diameter of 0.53 cm, or a 2.54-cm-diam. disc a thickness of 0.33 cm, to produce an optimum response.

1. INTRODUCTION

In this paper we present an analysis of some Doppler activation experiments on the UKAEA zero-power fast reactor ZEBRA. The object of the activation technique is the measurement of the (n, γ) activity of uranium samples irradiated at different temperatures in a furnace embedded in a cold reactor. The experiment will therefore yield information on the Doppler properties of ^{238}U in the reference spectrum of the cold fast reactor. Recent experiments by Perkin et al. [1], using analytically simple geometries with an antimony-beryllium photoneutron source, inspire some confidence in ^{238}U data by obtaining satisfactory agreement with predictions of the $^{238}U(n,\gamma)$ Doppler coefficient for the energy range 0-25 keV. The analysis of activation experiments would therefore appear to be primarily one of providing an adequate model for the transport and slowing down of neutrons in a sample-core configuration.

The present calculations are based on a simple analytical model which, using a collision probability approximation of the transport, is used with a continuous energy representation up to 15 keV. Above this energy we resort to a multigroup diffusion method.

2. THE EXPERIMENTAL METHOD

Firstly, we briefly describe the activation experiments performed by Smith and Stevenson [2] on core 6 of ZEBRA, a dilute-plutonium-fuelled assembly with natural uranium, graphite and sodium as diluents. Core 6 has been described by Adamson et al. [3].

Two identical electrically heated furnaces, each surrounded with four thermal radiation shields, are placed side by side inside a steel oven, 9.08 × 9.08 × 9.08 cm. The oven, inside a reactor fuel element sheath, is positioned to be level with the core centre-line, having fuel plates above and below it. By forcing air to circulate around and between the furnaces, one furnace is maintained at 900°K whilst the other remains at ambient temperature. The samples are contained in nickel 'pill box'-type holders, thickness 0.076 cm, which fit accurately within each furnace. Table I lists the isotopic content of the samples, 1.22 cm diameter and 0.025 cm thick, made of U_3O_8 in a nickel base with a thin nickel plate overall, giving a resultant ^{238}U density of 2.86 mg/cm^2.

The sample irradiations have been performed near the centre of ZEBRA core 6 for periods of four hours at maximum reactor power. The ^{238}U capture is determined by counting the resultant ^{239}Np gamma ray at 106 keV with a suitable correction for the fission product activity appearing with the ^{239}Np gamma activity.

TABLE I. ISOTOPIC CONTENT OF THE SAMPLE USED IN THE ZEBRA EXPERIMENTS, WITH HOMOGENIZED NUMBER DENSITIES

Isotope	No. density $\times 10^{-20}$ (cm^{-3})
^{238}U	2.8465
O	7.5905
Ni	6.2378×10^2

3. CALCULATION OF THE REACTION RATES

3.1. Homogenization of the system

We have chosen to represent the system of the samples and oven described in section 2 by a single foil surrounded by an oven embedded

in a homogenized core. This simplification is dictated wholly by our desire to obtain a continuous energy representation of the slowing down, whilst keeping the computing effort within reasonable bounds by limiting the number of regions for the collision probability calculations. To calculate the reaction rates in the sample the problem will be further simplified in section 3.6 by a two-region representation of a three-region problem.

Considerations of the effects of the core heterogeneity have been postponed in favour of a simplified approach which nevertheless has the advantage of allowing us some insight, albeit semi-quantitative, into the physics of the heated sample experiment.

3.2. The slowing-down model

The spatially averaged neutron scalar flux per unit energy interval at an energy E in the foil, $\phi_1(E)$, may be written as

$$V_1 \Sigma_{t1} \bar{\phi}_1(E) = \sum_j P_{j1}(E) V_j \bar{S}_j \qquad (1)$$

The summation $\sum_j$ is over the range of indices j = 1, x, 2 denoting the sample, the oven and the core, respectively. Σ_{tj} is the macroscopic total cross-section in a region of volume V_j. The spatially averaged source factor, $\bar{S}_j$, is

$$\bar{S}_j = \sum_{i,\epsilon} \int_E^\infty \Sigma^i_{Sj}(E') P(E' \to E)\, \bar{\phi}_j(E')\, dE' \qquad (2)$$

where Σ^i_{Sj} denotes the macroscopic scattering cross-section of the i^{th} nuclide in the j^{th} region and $P(E' \to E)$ is a normalized transition probability per unit energy interval. $\sum_{i\epsilon}$ doubly sums over all the nuclides in a region and over all scattering events ϵ, both elastic and inelastic. Equation (1) represents the neutron steady-state balance in the sample with a spatially flat scattering source of neutrons in each region including the core. With the usual assumption that the scattering in the laboratory system is isotropic, our collision probabilities P_{j1} satisfy the reciprocity theorem [4]

$$P_{ij} \Sigma_{t1} V_1 = V_j \Sigma_{tj} P_{j1}$$

which enables us to write Eq.(1) more conveniently as

$$\bar{\phi}_1(E) = \sum_j (P_{ij} / \Sigma_{tj}) \bar{S}_j \qquad (3)$$

3.3. The SDR-GENEX programmes

A numerical solution of Eq.(3) can be obtained by the Fortran programmes SDR and GENEX which have been described in detail by Brissenden and Durston [5]. For the range 0-20 keV SDR works with tabulated cross-sections at each of 250 000 energy mesh points. The resonance parameters for the calculation are generated statistically by GENEX for ^{238}U, ^{239}Pu and ^{235}U with the measured ^{238}U parameters of Firk et al.[6] incorporated up to 1.8 keV. These parameters enable the Doppler-broadened capture, fission and scattering cross-sections to be evaluated in a multi-level formalism described by Buckler and Pull [7].

The state of the SDR routine at the time of the present work allowed the reaction rate to be computed in each of only two arbitrarily shaped regions containing resonance material provided the relevant collision probabilities could be described. The measurements of Pflasterer et al. [8] demonstrate the importance of the intermediate oven region in the activation experiment, and we must therefore make the allowance for its presence even with the two-region limitation imposed by SDR. We now present a method, based on the narrow resonance approximation, which reduces the three-region problem (sample, oven and homogenized core) to an approximate representation as a two-region problem (sample and homogenized core) with an implicit dependence on the omitted region, the oven. This technique will enable us to use SDR up to its 20-keV limit, above which we resort to a multigroup diffusion code.

3.4. A narrow resonance approximation

The first-order energy dependence of the flux near to a resonance may be obtained from Eq.(3) by assuming that, for an energy range containing a large number of resonances, the flux is known to behave approximately as $1/E^n$ where n is some constant. This assumption is based solely on detailed calculations of large dilute fast cores and cannot be justified on a simple analytical model. With this knowledge we can evaluate the source term $\bar{S}_j$ in Eq.(3) through a resonance in terms of the flux between such resonances. This is the well-known narrow resonance (NR) approximation which is usually associated with a 1/E (asymptotic) flux for evaluating $\bar{S}_j$. We recall that in this conventional NR model we evaluate $\bar{S}_j$ as

$$\bar{S}_j = \Sigma_{pj} \bar{\phi}_{NR}(E)$$

where $\Sigma_{pj} = \sum_i \Sigma_{pj}^i$ the total macroscopic potential scattering: $\phi_{NR}(E) = k/E$ where k is a normalization constant for the neutron birth rate above a resonance. Equation (3) now becomes

$$\bar{\phi}_1(E) = \bar{\phi}_{NR}(E)\left(\sum_j \frac{P_{ij}\Sigma_{pj}}{\Sigma_{tj}}\right) \qquad (4)$$

The analytical advantages of the form of Eq.(4) are well known in thermal reactor resonance absorption theory (cf. Dresner [9]). Many authors [8, 10, 11] have used the form of Eq.(4) with an implicit $1/E^n$ dependence of $\bar{\phi}_{NR}(E)$. In this case it can be shown [12] that a better NR approximation is

$$\bar{\phi}_1(E) = \bar{\phi}_{NR}(E)\left(\sum_j \frac{P_{ij}\Sigma_{pj}H_j(E,n)}{\Sigma_{tj}}\right) \tag{5}$$

where $H_j(E,n)$ is a function weakly dependent upon energy. Computing the H_j functions we find [12] that Eq.(4) will underestimate $\bar{\phi}_1(E)$ in the range 500 eV to 20 keV by up to 8% and by up to 15% for energies in excess of 20 keV. Table II lists some values of $H_j(E,n)$ for the present case with $1/E^n$ fluxes calculated by Smith et al.[13].

3.5. The collision probabilities

We need to define the collision probabilities P_{ij} in Eq.(5). We write

$$\begin{aligned} P_{11} &= 1 - P_0 \\ P_{1x} &= (1 - \Omega)P_0 \\ P_{12} &= \Omega P_0 \end{aligned} \tag{6}$$

where P_0, the escape probability for the sample, is evaluated by the Wigner rational approximation

$$1 - P_0 = \frac{\Sigma_{t1}\ell}{1 + \Sigma_{t1}\ell} \tag{7}$$

Here $\ell = \tau\left(\frac{4V_1}{S}\right)$ is the effective mean chord length of the sample of surface area S, and τ, an empirical correction factor, is well tabulated [14]. The function Ω is the probability that a neutron leaving the sample will suffer its next collision in the core. Using Eqs (6) and (7) we manipulate Eq.(5) into the form

$$\bar{\phi}_1(E) = \left\{ (1-\Omega)\left[\frac{\sigma_{p1} + \sigma_{eff}\left(\frac{H_x}{H_1}\right)}{\sigma_{eff} + \sigma_{t1}}\right] H_1 + \frac{\sigma_{p2}}{\sigma_{t2}} H_2 \Omega \left[1 + \frac{\sigma_{p1}\sigma_{p2}}{(\sigma_{eff} + \sigma_{t1})\sigma_{p2}}\left(\frac{H_1}{H_2}\right) \right.\right.$$

$$\left.\left. \frac{-\sigma_{t1}}{(\sigma_{eff} + \sigma_{t1})} \right] \right\} \bar{\phi}_{NR}(E) \tag{8}$$

TABLE II. THE WEIGHTING FUNCTIONS $H_j = F_j + G_j$ FOR THE SAMPLE, OVEN AND CORE, $j = 1, x, 2$ RESPECTIVELY, IN FLUXES OF THE FORM $1/E^n$
The functions G_j have been evaluated at energies $\frac{1}{4}, \frac{1}{2}$ and $\frac{3}{4}$ along the indicated energy range

n \ j		F_j		G_j		$\frac{H_1}{H_2}$	$\frac{H_x}{H_1}$	Energy range
	1	x	2	1	2			
-1	1.068	1.074	1.094	0	0	0.976	1.006	0.4 - 500eV
0	1.032	1.036	1.045	0.041	0.042	0.987	0.966	500eV - 20keV
				0.054	0.052	0.988	0.954	
				0.062	0.063	0.987	0.947	
$+\frac{1}{2}$	1.014	1.018	1.019	0.054	0.072	0.995	0.937	20 - 100 keV
				0.061	0.087	0.988	0.931	
				0.075	0.100	0.989	0.920	

The quantities σ_{pj} and σ_{tj} denote, respectively, the microscopic potential and total cross-sections per ^{238}U atom in region j: $\sigma_{eff} = 1/N\ell$ is the effective background scattering where N is the ^{238}U number density. From Table II we see that only 1 or 2% error will be obtained by setting $(H_x/H_1) = (H_1/H_2) = 1$ in Eq.(8) for the range 0-20 keV.

3.6. A two-region approximation

Consider now the fluxes in a two-region cell consisting of the sample (region A) and the homogenized core (region B). A similar analysis to that in section 3.5 produces, with the same notation,

$$\bar{\phi}_A(E) = \left\{ P_{AA} \frac{\sigma_{pA}}{\sigma_{tA}} H_A + P_{AB} \frac{\sigma_{pB}}{\sigma_{tB}} H_B \right\} \bar{\phi}^{+}_{NR}(E) \tag{9}$$

where $\bar{\phi}^{+}_{NR}$ is the NR flux in the absence of the oven which will differ from ϕ_{NR} in Eq.(8) by about 1 part in 10^5 since $V_x/V_2 \sim 10^{-6}$. Consequently, comparing Eqs (8) and (9), we note that if we identify the pseudo-collision probabilities P_{AA} and P_{AB} as

$$P_{AA} = (1 - \Omega)$$

$$P_{AB} = \Omega \left[1 + \left(\frac{\sigma_{p1}}{\sigma_{eff} + \sigma_{t1}} \right) \left(\frac{\sigma_{t2}}{\sigma_{p2}} \right) - \frac{\sigma_{t1}}{\sigma_{t1} + \sigma_{eff}} \right] \tag{10}$$

then

$$\bar{\phi}_1(E) = \bar{\phi}_A(E)$$

since $H_A = H_1$, $H_B = H_2$ and we have put $H_x/H_1 = H_1/H_2 \sim 1$. This procedure, is, of course, only an approximation since it will yield for the core flux

$$\bar{\phi}_B(E) = \left\{ \frac{\sigma_{p2}}{\sigma_{t2}} H_2 - \left(\frac{V_1}{V_2} \right) \frac{\Omega \sigma_{eff}}{(\sigma_{eff} + \sigma_{t1}) \sigma_{t2}} \times \left[1 + \frac{\sigma_{p1} \sigma_{t2}}{\sigma_{p2} \sigma_{eff}} \right] \left[\frac{\sigma_{p2}}{\sigma_{t2}} \sigma_{t1} H_2 - \sigma_{p1} H_1 \right] \right\} \bar{\phi}_{NR}(E) \tag{11}$$

which should be compared with the flux obtained from the three-region analysis which yields

$$\bar{\phi}_2(E) = \left\{ \frac{\sigma_{p2}}{\sigma_{t2}} H_2 - \left(\frac{V_1}{V_2} \right) \frac{\Omega \sigma_{eff}}{(\sigma_{eff} + \sigma_{t1}) \sigma_{t2}} \left[\sigma_{t1} \frac{\sigma_{p2}}{\sigma_{t2}} H_2 - \sigma_{p1} H_1 \right] - \left(\frac{V_x}{V_2} \right) P_{x2} \left[\frac{\sigma_{p2}}{\sigma_{t2}} H_2 - \frac{\sigma_{px}}{\sigma_{t2}} H_x \right] \right\} \bar{\phi}_{NR}(E) \tag{12}$$

In both Eqs (11) and (12) all cross-sections have been normalized to one ^{238}U atom in the sample. However $|\phi_B - \phi_2|$ is made of second-order importance since $V_1/V_2 \gg 1$ and $V_x/V_2 \ll 1$, a necessary condition if the sample-oven system is to measure the Doppler changes in the unperturbed reactor. We see that this two-region approximation still contains an explicit dependence on the oven region through the transmission probability Ω.

3.7. Details of the calculation

Using the collision probabilities P_{AA} and P_{AB} defined in Eq.(10), we have performed a series of two-region SDR calculations for the range 0-20.6 keV. Reaction rates have been computed in the sample at 300 and 900°K with a constant temperature in the homogenzied core of 300°K. All nuclear data, other than that obtained from the GENEX programme, is derived from Schmidt's compilation [15].

The oven region, for the purpose of the calculation, contained all the components in the steel cube (cf. section 2) except for the foil and its thin nickel plate and was represented as a homogenized spherical shell of outer diameter 5.08 cm. To calculate Ω, the transmission probability, point isotropic emission from the centre of the shell was assumed. (This ignores the finite size of the foil which is allowed for separately by the Wigner rational approximation.) This gives

$$\Omega = \exp(-n)$$

where n is the total number of mean free paths along a radius through the wall of the sphere.

3.8. A multigroup treatment for the high energy absorption

Since the GENEX programme does not operate above 20 keV we resort to the multigroup diffusion code SCRAMBLE (cf. Hassit [16]) with the 33-group FD2 data of Rowlands and Wardleworth [17] to compute the high energy absorption. We evaluate the core flux in the absence of the sample and oven in a group g, $(\bar{\phi})_g$, and hence the corresponding sample flux, $(\bar{\phi}_1)_g$, as

$$(\bar{\phi}_1)_g = (\bar{\phi}_2)_g \left[\left(\frac{\sigma_{p2}}{\sigma_{t2}} \right)_g^{-1} (1-\Omega) + \Omega \right] \qquad (13)$$

This follows from Eqs (8) and (12) with $\sigma_{eff} \gg \sigma_{p1}$ since for our present sample we have, from Table I, a σ_{eff} of 250 000 b per ^{238}U atom and a σ_{p1} of 2200 b per ^{238}U atom. The sample absorption and its Doppler change is now obtained as

$$\sum_g (\bar{\phi}_1)_g (\sigma_{c1})_g \qquad \text{and} \qquad \sum_g (\bar{\phi}_1)_g \, \delta(\sigma_{c1})_g$$

respectively, with $(\sigma_{c1})_g$ and $\delta(\sigma_{c1})_g$ obtained from the recipes in Ref. [17]. This approach has been used to calculate the sample absorption

above 15 keV. Normalizing the SDR fluxes below 15 keV and the group fluxes above 15 keV to the same slowing-down density at 15 keV produces the neutron absorption over the complete energy range. Although SDR extends in energy to 20.6 keV we choose the 15-keV division to correspond to the lower limit of the nearest group in the FD2 set, the next occurring at 24.8 keV.

4. NUMERICAL RESULTS AND COMPARISON WITH EXPERIMENT

4.1. Temperature change above 15 keV

Table III lists the absorption in the sample above and below 15 keV, normalized to unit slowing density at this energy. We note that the dilute sample used in this experiment possesses a zero temperature coefficient above 15 keV according to the SCRAMBLE calculations. This is in substantial agreement with the SDR calculations which show that about 2% of the total Doppler change in the sample occurs between 15 and 20 keV. We also note that about one half of the total absorption in the sample occurs at energies greater than 15 keV.

TABLE III. CALCULATED SAMPLE ABSORPTION RATES AT 300 AND 900°K BELOW AND ABOVE 15 keV
With the full oven (a) and with a 50 % reduction in the wall thickness of the 2 in. steel cube (b); case (c) corresponds to the removal of the core sodium; all absorptions are normalized to unit slowing down density at 15 keV

Case	Temperature (°K)	Absorption below 15 keV ($\times 10^4$)	Absorption above 15 keV ($\times 10^4$)	Total absorption ($\times 10^4$)	Activation ratio
(a)	300	3.7245	5.2143	8.9388	1.022
	900	3.9189	5.2143	9.1332	
(b)	300	3.0655	5.0471	8.1126	1.024
	900	3.2602	5.0471	8.3073	
(c)	300	3.3561	5.2143	8.5705	1.020
	900	3.5286	5.2143	8.7429	

4.2. Effect of oven region

As part of an investigation of the effect of the oven region on the temperature coefficient of the sample the computations have been repeated with a 50% reduction of the wall thickness of the steel cube surrounding the sample. This amounts to a 25% reduction in the total amount of scattering material in the homogenized oven region (cf. case (b), Table III). This results in Ω, the oven transmission probability, changing from 0.818 to 0.839 and produces an 8% increase in the 2.17% Doppler change, indicating that the experimental is not oversensitive to the particular oven design.

4.3. Effect of core sodium

Table III, case (c) shows the results of computations made with complete removal of the core sodium. The wide scattering resonance in sodium at 2.85 keV is seen to increase the overall sample absorption below 15 keV by 10%. In terms of sample activation ratios (the ratio of the total ^{238}U capture at the higher temperature to that at the lower temperature) there is a small but measurable difference predicted for the cases (a) and (c) in Table III.

TABLE IV. A COMPARISON OF THE CALCULATED AND MEASURED VALUES OF THE (n, γ) ^{238}U SAMPLE ACTIVATION RATIOS IN CORES 6A AND 6D OF ZEBRA

Zebra core	Activation ratio	
	Calculated (300 - 900°K)	Measured (308 - 875°K)
6A	1.022	1.024 ± 0.003
6D	1.020	1.020 ± 0.003

4.4. Comparison with measurements; discussion

Comparisons between our present calculations and measurements of activation ratios are made in Table IV, the calculations corresponding to a sample temperature change 300 to 900°K and the measurements 308 to 875°K. The measured results quoted in Table IV have been made [2] in ZEBRA cores 6A and 6D, the latter core being similar to 6A except for complete sodium removal.

We see that the overall agreement between theory and measurement is encouraging. At this point however it is worthwhile considering the approximations which have been made to obtain the apparently good

agreement. We list these approximations in their probable order of importance.

(i) Homogenization of the core. Some recent calculations by Nicholson [18] and some measurements by Davy and Amundson [19] indicate that the observed activation ratio for very thin samples may be sensitive to the relative positioning of the fuel plate assembly. It is not apparent in our present calculations, where the core has been uniformly homogenized, whether there has been a cancellation of errors due to the heterogeneities present or whether for this particular core 6 assembly the activation ratio is insensitive to these localized heterogeneities. We therefore regard this effect as the largest uncertainty in the present calculations.

(ii) It is unfortunately necessary, at the present time, to use two different techniques, SDR and SCRAMBLE, to calculate the absorption below and above 15 keV. We have seen from Table III that about one half of the ^{238}U absorption in our sample occurs at energies above 15 keV. A 20% error in this computation would be reflected as a 10% change in the Doppler change for the complete energy range.

(iii) Even if we can satisfactorily homogenize the heterogeneities discussed in (i), we still have the error obtained from representing the core in SDR by a single region with a uniform scattering source of neutrons. By neglecting the flux depressions at the surface of the sample and the core, we overestimate our sample absorption by a flat source approximation. A sub-division of the core into two or more regions in SDR would allow for this effect.

5. AN APPROACH TO THE DESIGN OF ACTIVATION SAMPLES

5.1. The energy distribution of the Doppler change

Figure 1 is drawn to show the percentage fraction, occurring in each FD2 energy group, of the calculated total ^{238}U Doppler change in both the sample and the central region of core 6A in which it was placed. Since no experimental results are available, the Doppler distribution for the core has been obtained from the SCRAMBLE computations as

$$\frac{\delta(\sigma_{c2})_g(\bar{\phi}_2)_g}{\sum_g \delta(\sigma_{c2})_g(\bar{\phi}_2)_g}$$

with the notation of 3.8. We see from Fig. 1 that the sample has, broadly speaking, reproduced the core spectrum. Because of the dilution of its ^{238}U content, the sample possesses a relatively lower shielding of its resonances than the core material. The effect of this dilution is most marked at energies around a few keV where the ^{238}U resonances are predominantly scattering. In our sample, therefore, the low energy strongly absorbing ^{238}U resonances contain a higher proportion of the total Doppler

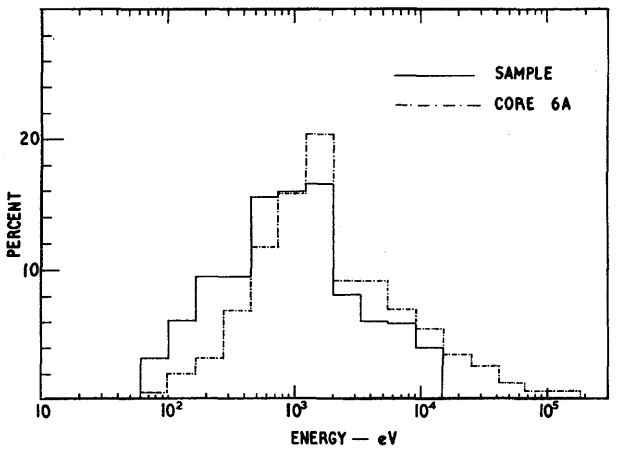

FIG.1. A comparison of the calculated percentage, occurring in each energy group, of the total (n, γ) ^{238}U Doppler change in the sample and the central region of core 6A.

change than they do in the core. We observe this as a softening of the Doppler spectrum in the sample relative to the core spectrum. In Fig. 1 the median energies for the distributions occur at 900 eV for the sample and at 1550 eV for the core. We conclude from this that the thin sample is not providing the best information on the Doppler effect in the cold core.

5.2. The design of heated samples

Pursuing this question further, a series of calculations and analyses have been made to investigate the relationship between the sample size, specified by σ_{eff} , and the measured activation ratio. For brevity's sake only the results of this investigation are presented in the present paper; further details will be published in due course.

It is a reasonable assumption that we can approximately equalize the resonance self-shielding in the sample and the core to produce the same Doppler energy distribution in each and, since the sample is sitting in a spectrum principally determined by the core, to equalize the activation ratios of the sample and the unperturbed core. We can hazard a guess and say that a suitable condition for such an optimum design would be

$$\sigma_{p1} + \sigma_{eff} \sim \sigma_{p2} \qquad (14)$$

where σ_{p2} represents a cross-section for the core suitably averaged to contain the bulk of the ^{238}U Doppler change in the core.

The validity of condition (14) has been demonstrated by a series of multigroup calculations based on Eqs (8) and (12). Figure 2, based on these calculations, shows the activation ratio of the sample divided by the activation ratio of core 6A for the same temperature range as a function of $\sigma_{p1} + \sigma_{eff}$. At $\sigma_{p1} + \sigma_{eff}$ = 50 b the activation ratios are equal

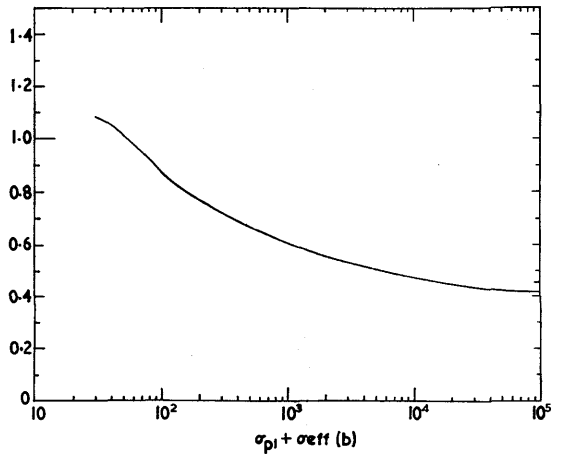

FIG.2. The sample activation ratio divided by the core activation ratio as a function of $\sigma_{p1} + \sigma_{eff}$, for ZEBRA core 6A.

to within ± 5%. If we examine the individual energy group contributions to the Doppler change of the ^{238}U capture in the core we find that 90% is obtained from those groups with a scattering cross-section in the range 40-60 b. An examination of the relative energy distributions of the total Doppler change in the ^{238}U capture in the sample and core shows the peak of the sample distribution moving to lower energies as we increase the Doppler dilution of the sample. Only for $\sigma_{p1} + \sigma_{eff} \sim 50$ b are the sample and core distributions similar.

With the use of the NR model of Eqs (8) and (12), condition (14) can be shown analytically to be valid for a large dilute fast core where the low energy ^{238}U resonances contain a negligible fraction of the total ^{238}U Doppler change. With this model, condition (14) will produce equality of the core and sample activation ratios as well as their energy distributions. The model also predicts the relative shift to lower energies of the sample distribution as $\sigma_{p1} + \sigma_{eff}$ is increased.

6. DISCUSSION

It is of interest to note the size of samples demanded by our design criterion (14). Putting $\sigma_{p2} = 50$ b in the core, a circular disc of natural uranium (density 18.5) with a diameter of 1.0 in. would require a thickness of 0.13 in., compared with a thickness of 0.18 in. for a disc of diameter 0.5 in. On the other hand, a disc of UO_2 (density 10.2) requires a thickness of 0.56 in. for a diameter of 1.0 in. We see that these sample sizes are considerably larger than the foils presently favoured in activation experiments but are still sufficiently small to produce small perturbations of the cold core flux. A surprising alternative is to abandon the idea of using small samples in favour of large samples. For example, a long circular cylinder of natural uranium would require a diameter of 0.21 in. compared with 0.58 in. for a cylinder of UO_2. Such large samples could presumably form the basis of a combined activation-perturbation

experiment with the additional advantage of minimizing the fuel plate heterogeneity effect discussed earlier.

ACKNOWLEDGEMENTS

This study was initiated during a period spent with the Theory Group, Fast Reactor Physics Division, AEE, Winfrith. I should like to extend my gratitude to Mr. J. Codd, Dr. A. R. Baker and Mr. J. L. Rowlands for valuable discussions and constructive criticism of the work contained in this paper.

REFERENCES

[1] PERKIN, J.L., FIELDHOUSE, P., BRICKSTOCK, A., DAVIES, A.R., J. nucl. Energy 20 (1966) 921.
[2] SMITH, M.J., STEVENSON, J.M., unpublished (1967).
[3] ADAMSON, J., ABSALOM, R.M., BAKER, A.R., INGRAM, G., PATTENDEN, S.K.I., STEVENSON, J.M., Proc. Int. Conf. Fast Critical Experiments and their Analysis, Argonne National Lab. Rep. ANL 7320 (1966) 216.
[4] CASE, K., De HOFFMAN, F., PLACZEK, G., Introduction to the Theory of Neutron Diffusion 1, US Government Printing Office, Washington D.C. (1953).
[5] BRISSENDEN, R.J., DURSTON, C., Proc. Conf. Application of Computing Methods to Reactor Problems, Argonne National Lab. ANL 7050 (1965) 51.
[6] FIRK, F.W.K., LYNN, J.E., MOXON, M.C., Nucl. Phys. 41 (1963) 614.
[7] BUCKLER, P.A.C., PULL, I.C., UKAEA Rep. AEEW-R.226 (1962).
[8] PFLASTERER, G.R., SHER, R., MAYER, W.A., WARZEK, F.G., Proc. Conf. Safety, Fuels and Core Design in Large Fast Power reactors, Argonne National Lab. Rep. ANL 7120 (1965) 616.
[9] DRESNER, L., Resonance Absorption in Nuclear Reactors, Pergamon Press, London and New York (1960).
[10] REYNOLDS, A.B., Nucl. Sci. Engng 22 (1965) 487.
[11] FISCHER, E.A., Karlsruhe Rep. KFK 473 (1966).
[12] BEYNON, R.D., to be published.
[13] SMITH, R.W., ROWLANDS, J.L., WARDLEWORTH, D., UKAEA Rep. AEEW-R.491 (1966).
[14] PITCHER, H.H.W., UKAEA Rep. AEEW-M.469 (1964).
[15] SCHMIDT, J.J., Karlsruhe Rep. KFK 1200 Part II (1962).
[16] HASSIT, A., UKAEA Rep. TRG-229(R) (1962).
[17] ROWLANDS, J.L., WARDLEWORTH, D., UKAEA Rep. AEEW-M.472.(1964).
[18] NICHOLSON, R.B., Proc. Int. Conf. on Fast Critical Experiments and their Analysis, Argonne National Lab. Rep. ANL-7320 (1966) 386.
[19] DAVEY, W.G., AMUNDSON, P.I., Trans. Am. nucl. Soc. 9 1 (1966) 226.

DISCUSSION

D.H. WINTZER: Have you used the SDR code in the case where the composition of the sample is the same as that of the surrounding core material and compared the results with those of multigroup calculations? You should get fairly detailed information about the low-energy part of the spectrum.

T.D. BEYNON: No, I have not performed such a calculation, and I am not sure what the comparison with a multigroup spectrum would reveal.

D.H. WINTZER: How much machine time do such SDR calculations require?

T.D. BEYNON: The reported calculations took about forty minutes for each temperature, but programming improvements have now substantially reduced the time needed.

W. ROTHENSTEIN: How sensitive are your results to the transmission probability through the oven, and is it desirable to calculate this quantity more precisely?

T.D. BEYNON: An indication of this is given in section 4.2 of the paper, where it is shown that a 25% reduction in the amount of scattering material in the oven produced an 8% increase in the Doppler change. On general grounds, however, I would say that it is desirable to allow for the oven region as accurately as possible, particularly for very thin samples.

H. SEUFERT: What advantage does your method of calculating the capture rate offer over the more common method of calculating the effective resonance integral?

T.D. BEYNON: By "more common method" I presume you meant the J-function technique. For the heated-sample/cold-core experiment the J-functions must be evaluated at two temperatures. The advantage of the method described in the paper, using SDR, is quite simply that of greater accuracy.

STUDIES OF THE DOPPLER COEFFICIENT AND THE REACTIVITY EFFECT OF POLYTHENE IN SOME FAST REACTOR SPECTRA

L. I. TIRÉN, I. GUSTAFSSON, E. HELLSTRAND AND R. HÅKANSSON
AB ATOMENERGI,
STUDSVIK, NYKÖPING, SWEDEN

Abstract

STUDIES OF THE DOPPLER COEFFICIENT AND THE REACTIVITY EFFECT OF POLYTHENE IN SOME FAST REACTOR SPECTRA. The Doppler broadening of the ^{238}U capture and the ^{235}U fission cross-sections in fast reactor spectra has been studied by irradiating heated foils or plates of the isotopes of interest in a small furnace at the centre of the zero-energy fast reactor FRO. The experiments have been applied to cores fuelled with 20% enriched uranium and diluted with graphite and polythene. Very thin plates of the different core materials have been used in a region surrounding the furnace in order to minimize heterogeneity effects. The measured quantity is the difference in the induced γ-activity of samples irradiated at ambient temperature and at temperatures up to 1500°C. The effects of varying sample thickness and of scattering in the furnace wall have also been studied.

Measurements of the reactivity effect of polythene have been made in two FRO assemblies. The neutron spectra of the cores were broadly similar to those of current steam-cooled fast reactor concepts. The experiments include a study of the spatial distribution of the reactivity coefficient of polythene. The results are in reasonable agreement with calculated values. The latter are sensitive to small changes in the absorption cross-section in the low neutron energy range. Most of the calculations have been made with a one-dimensional diffusion theory programme using 16 energy groups but a two-dimensional code and a transport theory code have also been used.

Additional measurements have been made on vertical polythene rods, 2.2 cm and 4.5 cm thick, inserted in the central fuel element. The measured distributions of the fission rate in ^{235}U and the capture rates in ^{55}Mn, ^{115}In and ^{197}Au inside and around the rods have been compared with results of multigroup calculations.

INTRODUCTION

This paper describes recent experimental work on the fast zero energy reactor FRO. The presentation is divided into two major parts. In Part I Doppler measurements on U^{235} and U^{238} by the foil activation technique are summarized. These measurements are similar to those made by Pflasterer [1] and by Davey [2] but have been extended to higher temperatures and are made in different neutron spectra. In Part II measurements of the reactivity and flux peaking effects of polythene are dealt with. This part contains two sections, the first concerning the reactivity coefficient of thin samples and the second dealing with the effect of a thick polythene rod. The experiments with polythene have been made in connection with current work on steam cooled fast power reactors.

A description of the FRO reactor and previous experimental and theoretical work is given elsewhere [3].

PART 1. DOPPLER MEASUREMENTS BY FOIL ACTIVATION

1. Scope of work

Doppler activation measurements on U^{238} and U^{235} are currently being made on FRO assemblies with different neutron spectra. The activation method

is preferred to the more usual reactivity oscillation technique because of the difficult expansion effects encountered with the latter method in a small core.

The measured quantities are the changes in the U^{238} capture and the U^{235} fission rates with temperature. A thin sample containing either of these materials is heated in a small oven located in a homogenized region at the core centre. A similar sample is located outside the oven for monitoring purposes. The samples are irradiated for about 20 minutes at room temperature or at an elevated temperature (up to 1800 °K). The Doppler effect, D, is expressed in terms of the relative increase in reaction rate R on heating, i.e.

$$D = \frac{R(hot)}{R(cold)} - 1$$

The reaction rates in either material are measured by detecting the induced γ-activity using NaI crystals. As the change in activation rate with temperature may be very slight in some cases a high precision in foil counting is required. In the present measurements of an activation ratio a precision of 0.05-0.10 % is achieved in routine work. The total uncertainty in one measurement of R(hot)/R(cold), which involves activation ratios from two separate irradiations, is 0.3-0.4 %. A large portion of this error is attributed to a lack of reproducibility in the positioning of the oven and the samples.

To date, measurements of the Doppler effect have been made in cores 5 and 8 of FRO, having core centre neutron spectra plotted in Figure 1. The measurements will be complemented by irradiations in a harder spectrum (core 3), also shown in the figure. The softest of these spectra (core 5) is similar to that of a steam cooled fast power reactor, and the hardest one (core 3) is not too different from that of a voided Na-cooled reactor. All three cores are fuelled with uranium metal, enriched to 20 % in U^{235}. They are diluted with graphite to 29.2 vol. %. In addition cores 8 and 5 contain 1.8 and 7.5 % of polythene, respectively. The atomic compositions of FRO cores discussed here are given in Table I.

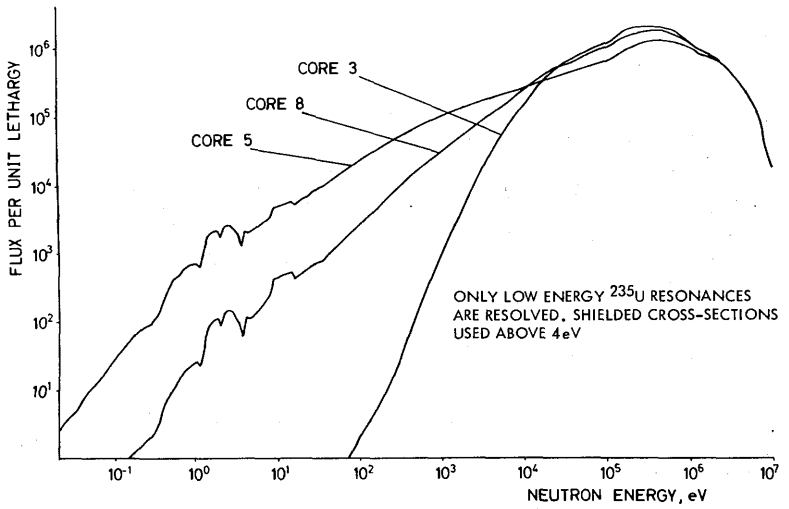

FIG.1. Calculated core centre neutron spectra.

TABLE I: Composition of FRO assemblies

Region	Atomic densities, 10^{22} at/cm^3							
	U^{235}	U^{238} [1]	C	H	Fe	Cr	Ni	
Core 3	0.568	2.234	2.47	-	0.408	0.096	0.048	
Core 5	0.498	1.963	2.77	0.604	0.408	0.096	0.048	
Core 7	0.425	1.678	1.53	0.604	0.408	0.096	2.04	
Core 8	0.498	1.963	2.55	0.150	0.408	0.096	0.048	Al: 0.34
Reflector	-	-	-	-	0.408	0.096	0.048	Cu: 7.48

1) Including 0.16 % U^{234}

Two different ovens have been used, one for the heating of uranium metal foils to 900 °K and one for UO_2 plates up to 1800 °K. In the case of U^{235} the temperature has been limited to 1500 °K, because of the problem of leakage of volatile fission products from the plate surface at higher temperatures. Since gross fission product γ-ray counting is employed, a leakage of fission products during irradiation would introduce a systematic error.

The method has been checked by irradiations in a thermal spectrum, in which there is no Doppler effect. These experiments confirm, within a limit of error of 0.1-0.2 %, that no systematic errors due to the heating of uranium metal to 900 °K or oxide to 1500 °K exist. A metal foil (U^{235}), heated to 1100 °K, however, showed a reduction in fission product activity of (1.3 ± 0.2)% compared with the cold foil, and this reduction is attributed to leakage of fission products.

In the fast spectrum irradiations the effects of several shortcomings in the experimental set-up were investigated. These effects are represented by the following titles, which will be discussed in para. 6:

- Heterogeneity of core composition
- Effect of collisions in the oven wall
- Finite sample thickness.

2. Construction of ovens

Figures 2 and 3 show the ovens used for heating to 900 °K and 1800 °K, respectively. The former is heated by a thermocoax resistance wire, which is embedded in a steel structure. The dissipated heat is transferred by conduction to a foil holder made of aluminium. The foil holder and heating element are surrounded by a thin heat shield. The oven wall is made of aluminium 0.5 mm thick. The hot joints of chromel-alumel thermocouples are located in the foil holder on each side of the foil. This arrangement makes it possible to determine the foil temperature to about ± 5 °K. A power of about 8 W is needed to heat the foil to 900 °K. The enriched (93 % U^{235}) or depleted (0.4 % U^{235})uranium metal foil is 13.5 or 15.0 mm in diameter and 0.050 or 0.062 mm thick. The foil has a central 2 mm diameter hole which facilitates an accurate alignment in the oven and in the sample holder for counting.

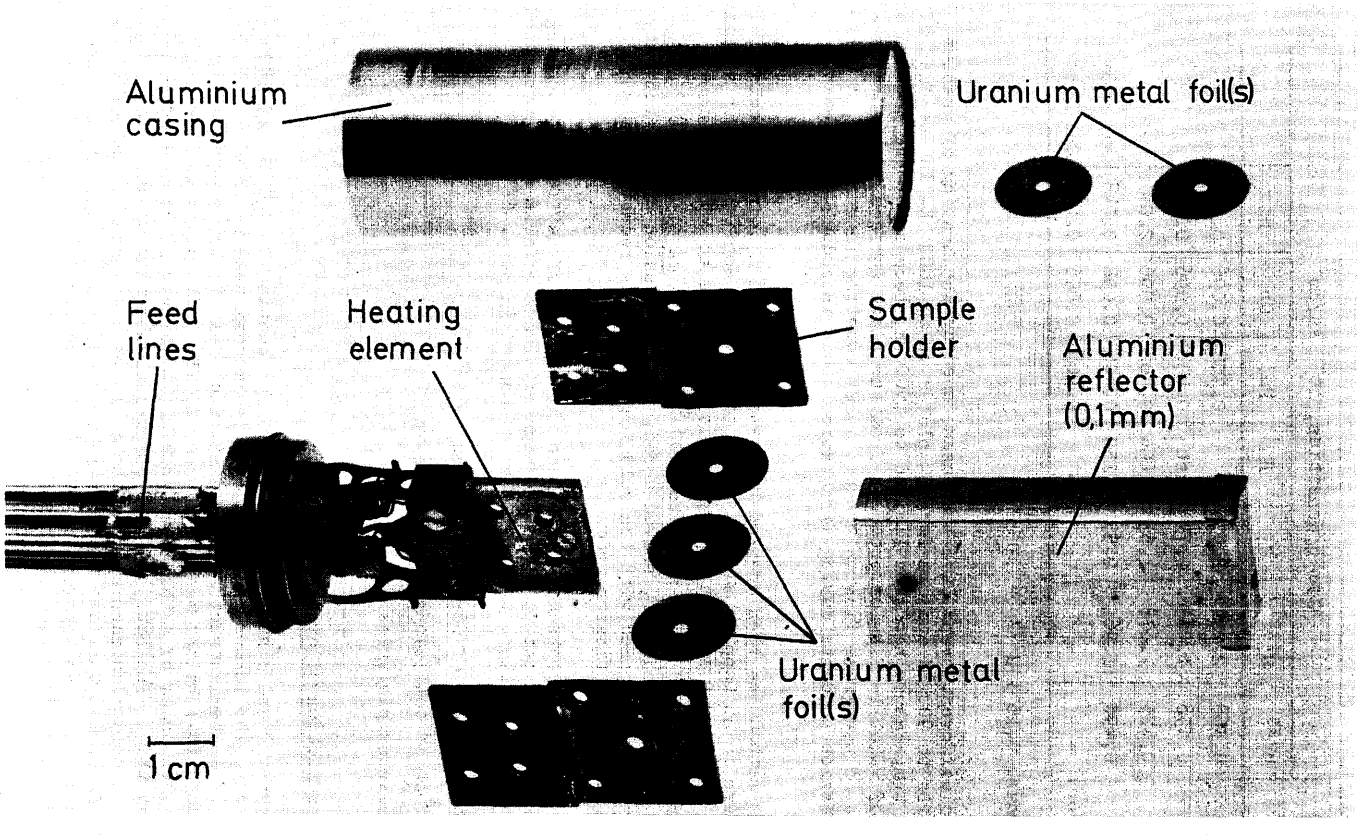

FIG.2. Oven for heating of U metal foils to 900°K.

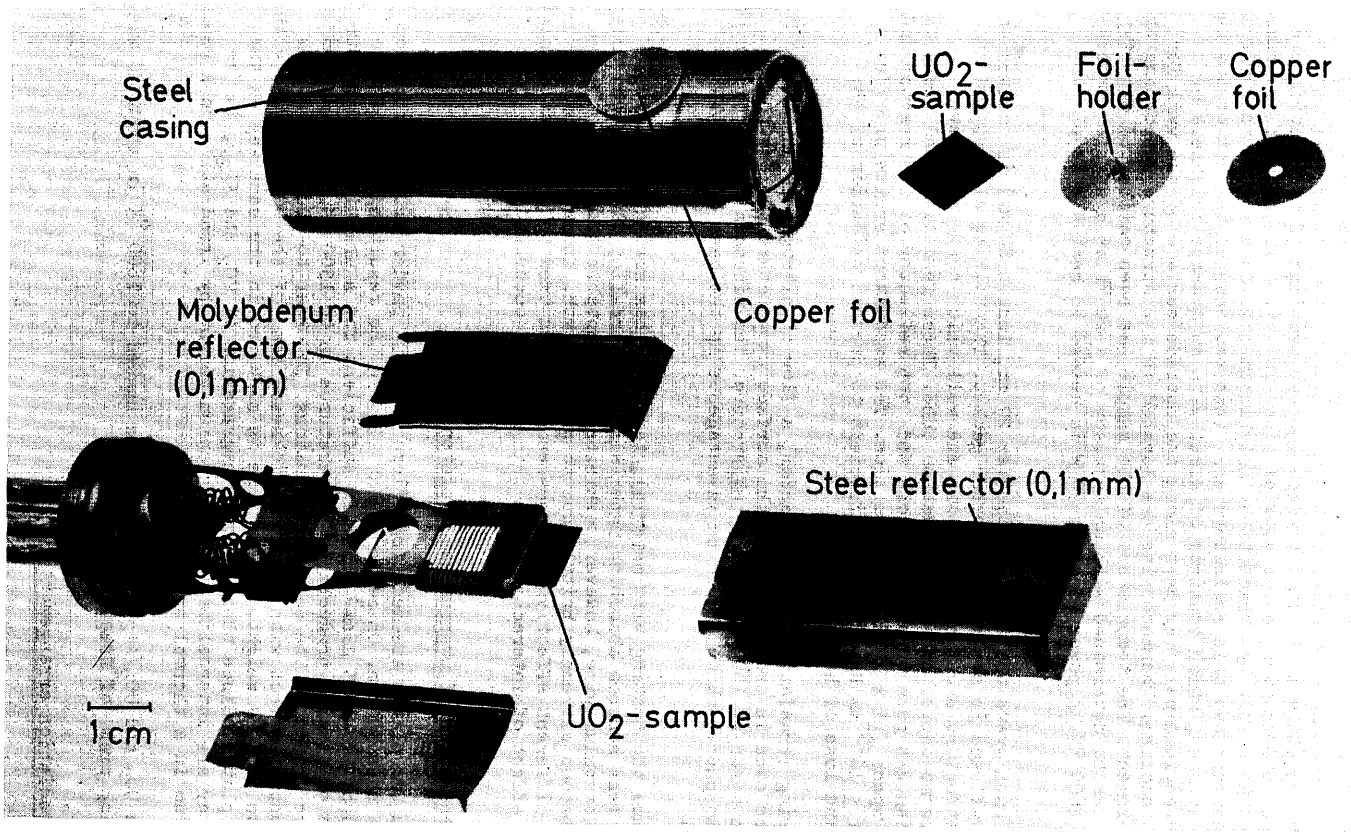

FIG. 3. Oven for heating of UO_2 plates to 1800°K.

The high temperature oven, shown in Figure 3, employs a tantalum wire for heating. The wire is wound around pins of alumina which are supported by molybdenum wires passing through the alumina pins and welded to a thin Mo structure. The samples consist of 0.3 mm thick UO_2 plates, 12 x 12 mm^2 in area. The UO_2 plate is located between the two sections of the heating wire and passes into grooves in the alumina pins. In this oven the heat is transferred to the sample by radiation. Molybdenum shields surround the wire and sample. Another two thin reflectors are inserted between the heater and the wall of the oven, which consists of steel with an average thickness of 0.45 mm. Longitudinal fins pass along the outside surface of the wall for efficient cooling. Thermocouples are located in the structure supporting the heating element. The temperature of the sample has been calibrated out-of-pile and can be determined with an accuracy of $\pm$ 20 °K at a sample temperature of 1800 °K. A power of about 70 W is needed to heat the sample to 1800 °K.

In both ovens the casing (diameter 29 mm, length 80 mm) is screwed onto the end wall and is sealed by a rubber gasket. The heating element and supporting structure are fastened to the end wall which contains inlets for power, thermocouples and the evacuation tube. These feed lines and those used for cooling gas pass through the core and top reflector of the reactor and occupy a space 7.1 x 14.2 mm^2 in section. The evacuation system provides a vacuum of $\leq 10^{-3}$ mm Hg. This is sufficient to prevent oxidation of the samples and loss of heat.

During irradiation in the reactor, a flow of nitrogen is maintained around the oven in order to limit the surface temperature to less than 370 °K in a run at 1800 °K sample temperature. The nitrogen also provides an inert atmosphere, which should be advantageous in the case of a rupture of the oven.

Since the heating wire material, tantalum, has strong resonances, wires of less neutron absorbing materials (Mo, Zircalloy II) have been tried. Only the tantalum wire, however, exhibits an acceptable life. The other materials become extremely brittle due to grain growth. Therefore tantalum wires of different effective thicknesses have been used to show that no significant effect of interaction with this material occurs.

3. Preparation of uranium oxide plates

The UO_2 plates are made from micronized UO_2 powder with a carbon content less than 70 ppm. On sintering at 2100 °K the resulting samples have densities of 9.5-10.5 g/cm^3 which is sufficient for a practically complete retention of fission products at temperatures up to 1500 °K. The sintered plates are ground to the correct dimensions. In order to study variations in the Doppler effect with uranium thickness, some of the UO_2 is mixed with alumina to 50 % by weight. The mixture is sintered in the same way as the pure UO_2 plates. Since there is some segregation of UO_2 and Al_2O_3 in the plates they are intercalibrated for uranium weight by irradiation on a rotating drum in a thermal spectrum.

The UO_2 and UO_2/Al_2O_3 plates can be heated to 1800 °K in about 30 min. without any risk of fracture.

4. Irradiation arrangement

Figure 4 shows the positioning of the oven in the central fuel element. The surrounding uranium, graphite and polythene plates are arranged in a

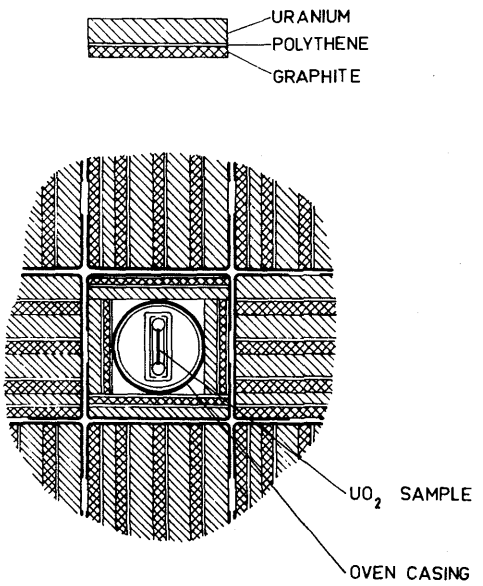

FIG.4. Positioning of oven in a fuel element (heterogeneous core).

heterogeneous pattern. The typical uranium and graphite plate thickness is 3.55 or 7.10 mm. The heterogeneity of composition introduces a source of systematic uncertainty. After initial measurements in core 5 the core region around the oven was therefore homogenized. The uranium and graphite plates in the homogenized zone are 0.6 mm thick and the polythene plates 0.1 mm thick. The irradiation arrangement with the homogenized zone around the oven is shown in Figure 5. The zone has an average thickness of about 2.8 cm, which corresponds to 1.6-1.7 neutron mean free paths in the resonance energy region. Most of the neutrons ($\sim$ 80 %) which are absorbed by the sample have therefore made their last collision in the homogenized zone.

Each experiment involves two irradiations, one hot and one cold. In addition to the flux monitoring uranium sample on the end wall of the oven, copper foils are fastened at various positions on the casing as a check of reproducibility. In initial experiments at 870 ^{o}K copper foils were also placed adjacent to the uranium sample inside the oven for flux monitoring. But the activation rate in copper proved to be temperature-dependent - due to Doppler broadening - and no suitable temperature-independent monitor has been found.

5. Counting of samples

A layout of the γ-counting station is shown in Figure 6. It is assembled from commercial units mainly. The detectors consist of two NaI crystals which are 3 in. in diameter and 1 in. thick. Most of the electronics is transistorized and is very stable. The equipment is installed in a temperature stabilized room. An automatic sample changer is included in the arrangement, and its operation is controlled by the SAMSES unit, which, after each completed counting interval, causes the relevant information to be punched onto the output tape. The data are processed by a code which performs all the necessary corrections and calculates the R(hot)/R(cold) ratio

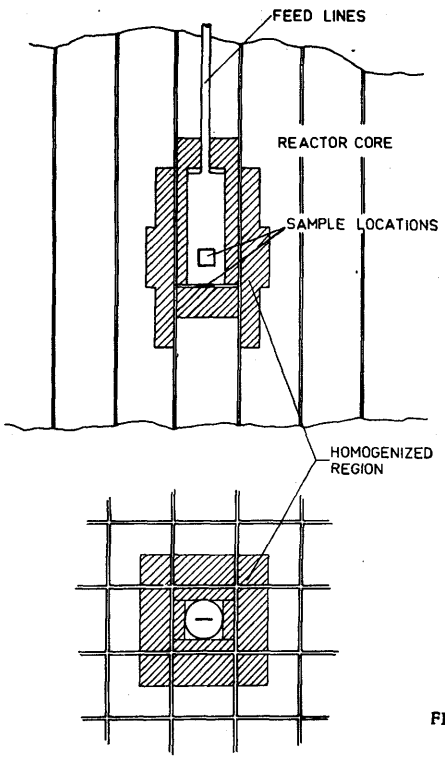

FIG. 5. Irradiation arrangement with homogenized zone.

together with a statistical analysis of the data. The errors in determining the activity ratio of two samples by means of this equipment have been examined. It was found that the lack of reproducibility in the count rate ratio not due to the statistics of radioactive decay is less than 0.03 %. Furthermore, pairs of foils which were believed to be identical, except for an accurately determined small difference in weight, were compared. The corrected count rate ratios of such pairs (U^{235}, U^{238} and Cu samples) deviated in no case by more than 0.10 % from the expected values.

When fission products are being counted the decaying integral count rate $N(t)$ is fitted to a function of the type

$$N(t) = \frac{A}{t+\theta}$$

over evaluation intervals during which $N(t)$ does not change more than, say, a factor of two. A and θ are the parameters to be fitted.

In the case of U^{238} the Np^{239} decay is detected in a $\sim$ 40 keV window around the main 106 keV peak. An activity contribution from fission products of several per cent is present in this energy interval, however. The correction is obtained in complementary measurements by means of a γ-γ coincidence detector station [4] in which the fission product contribution is suppressed to less than 1 %. This manner of counting is used only in a few runs on each core since the low coincidence count rate necessitates a very long counting period (several days) to yield the required accuracy.

6. Results and discussion

The results of Doppler activation measurements in cores 5 and 8 are shown in Figures 7-10. The first of these illustrates the effect of variations in the wall thickness of the casing of the oven. The effect was studied by inserting steel plates between the oven and the surrounding core region. The abscissa is the effective transmission probability of the wall. The uncertainty in transmission probability represented by the horizontal bars in the figure arises from the contribution to the reaction rate by neutrons passing through the end walls and supporting structure inside the oven. Figure 7 shows that the wall effect is fairly small. Extrapolation to zero wall thickness involves a correction of the measured values of 3-7 %.

Figure 8 illustrates the result of measurements with samples of different thicknesses. Since theoretical calculations of the Doppler effect are very complicated for finite sample thickness, the experimental values are extrapolated to zero thickness, which introduces corrections of 4-5 %.

It should be pointed out that the two kinds of correction discussed here are not independent of each other. For example, if the oven wall were very thick the dips in the spectrum at resonance energies would be smoothed out, resulting in zero Doppler effect for an infinitely thin sample. A thicker sample would produce its "own" resonance shielding and consequent Doppler effect. In the present experiments each of the corrections is small, however, and a simple superposition should be adequate.

The effect of heterogeneity has been studied in the softest spectrum - core 5 - by comparing results from the first set of measurements with 3.55-7.10 mm uranium plates with those of the later runs with 0.6 mm plates. In the latter case an additional test has been made by surrounding the oven on all sides with 0.6 mm uranium plates. In the normal arrangement there is a uranium plate on one side of the oven and a graphite or polythene plate on the opposite side (cf. Figure 4). The following results have been obtained for the Doppler effect in U^{238}:

I:	870 °K	0.6 mm U-plates:	$D = 0.118 \pm 0.004$
		3.55/7.10 mm U-plates:	$D = 0.106 \pm 0.005$
II:	1770 °K	U-plates on all sides:	$D = 0.188 \pm 0.004$
		Normal arrangement:	$D = 0.182 \pm 0.004$.

These values indicate that the effect of heterogeneity in the normal "homogeneous" arrangement is insignificant in the softest neutron spectrum. The same conclusion will hold in the harder spectra also, in which the fine structure is less pronounced.

Since the Doppler coefficient is expected to vary approximately as T^{-1} in fast reactor spectra, it is convenient to use the quantity $\log \frac{T_1}{T_0}$ as abscissa in a diagram of the Doppler effect, D, versus temperature. A straight line in the diagram then represents a T^{-1} behaviour of the Doppler coefficient; a positive second derivative indicates a $T^{-\alpha}$ dependence with $\alpha < 1$, and a negative second derivative corresponds to $\alpha > 1$.

The final results are displayed in Figures 9 (U^{238}) and 10 (U^{235}). The temperature dependence of the Doppler effect has been studied only in the case of U^{238} and in the softest spectrum. Figure 9 indicates that the α-value is slightly smaller than 1 in this case; the value estimated by a least squares fit is $\alpha = 0.87 \pm 0.13$.

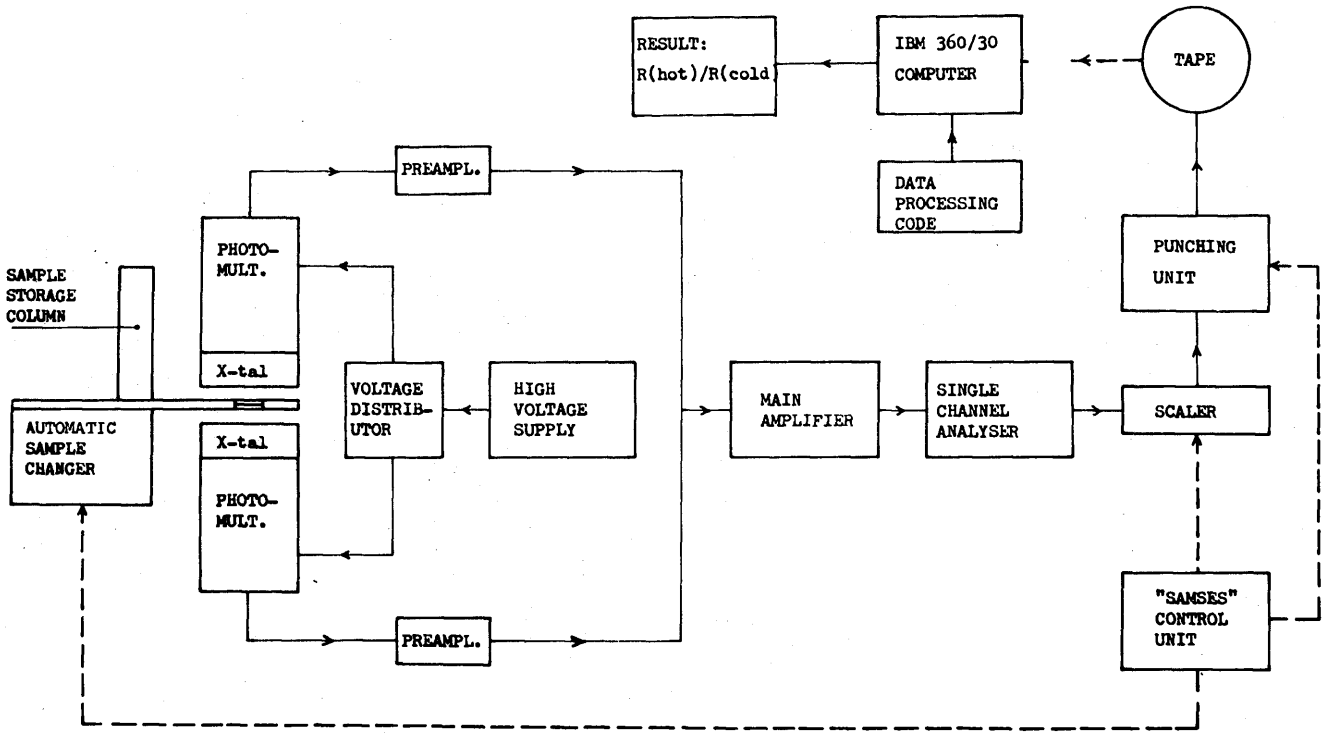

FIG. 6. Gamma counting system.

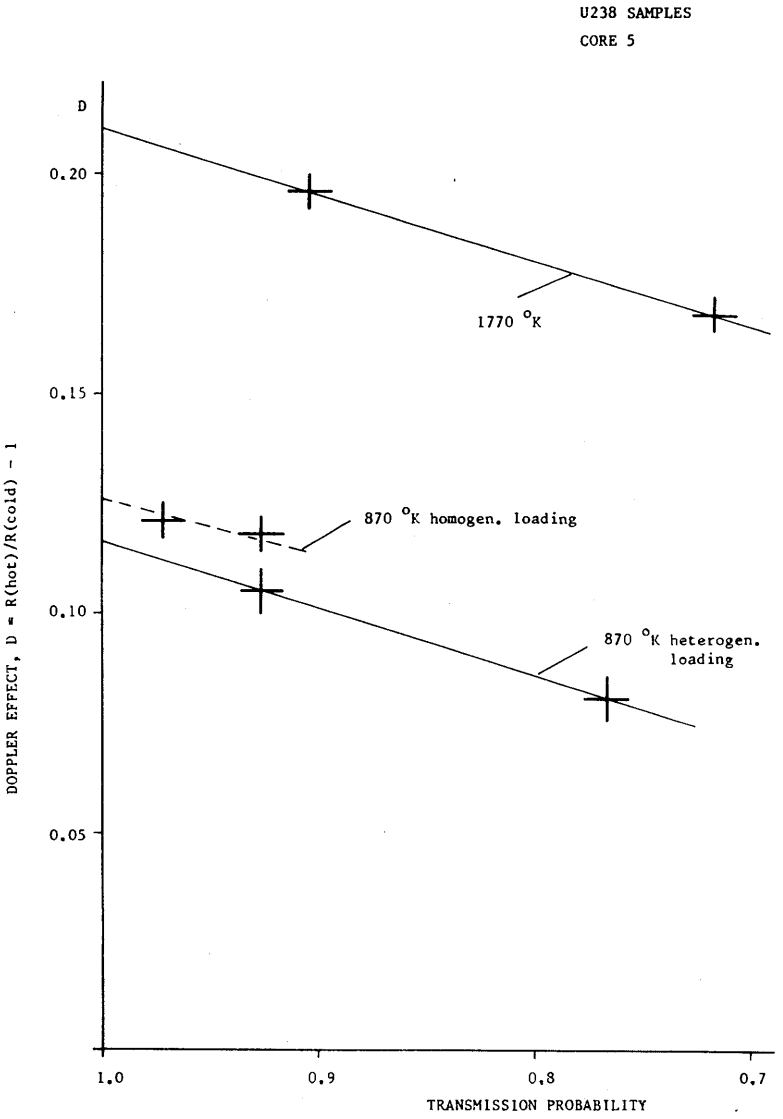

FIG.7. Variations in the Doppler effect with wall thickness of the oven.

Figures 9 and 10 also show the decrease in the Doppler effect with a hardening neutron spectrum (core 5 → core 8). The Doppler effect in U^{235} fission is very small in comparison with that in U^{238} capture. In the harder spectrum of core 8 the U^{235} Doppler effect is equal to zero within the experimental uncertainty of 0.2 %. In the still harder spectrum of core 3 the measurements will therefore be limited to U^{238}.

Preliminary theoretical calculations of these experiments have been reported previously [3]. The theoretical methods will have to be refined, however, and therefore no calculated values are given at this time.

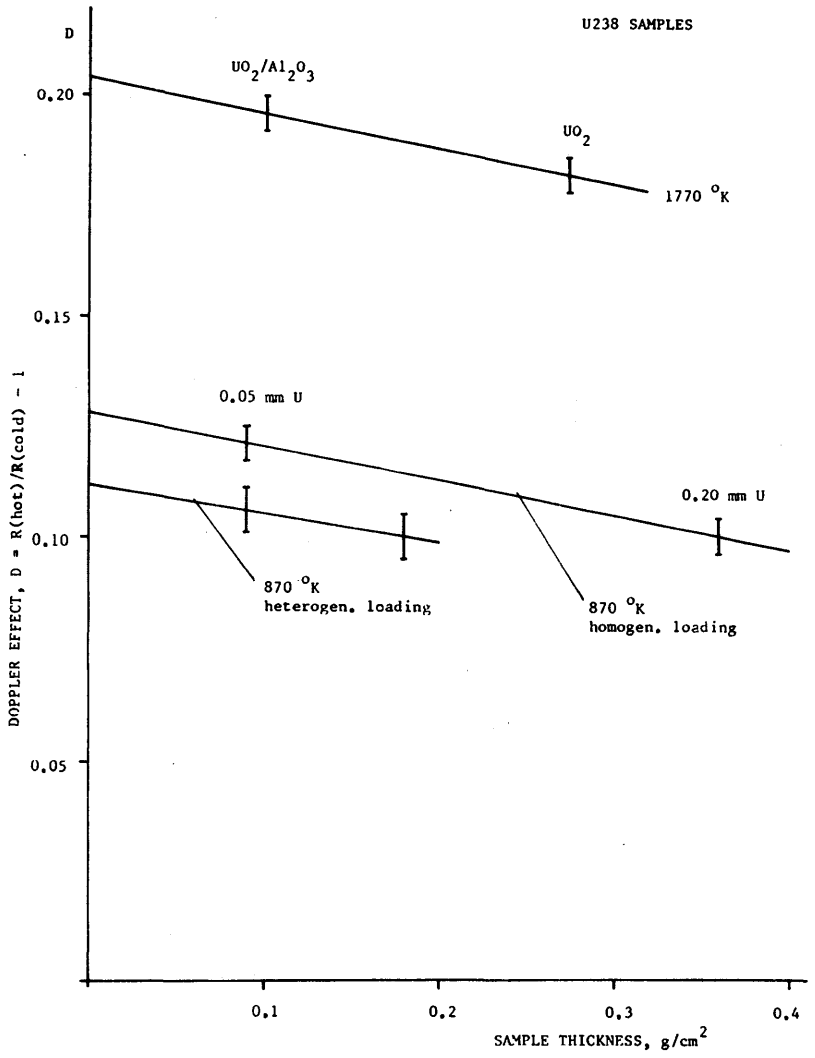

FIG.8. Variations in the Doppler effect with sample thickness.

A study of the Doppler effect in Pu^{239} fission by the activation method would be of considerable interest but cannot be made on FRO as yet, since no Pu fuel is available. The heating of Pu samples to high temperatures also entails extensive safety precautions.

PART II. REACTIVITY AND FLUX PEAKING EFFECTS OF POLYTHENE

1. Reactivity coefficient of polythene

For the safe operation of steam cooled fast reactors the change of reactivity with steam density is a relationship of fundamental significance.

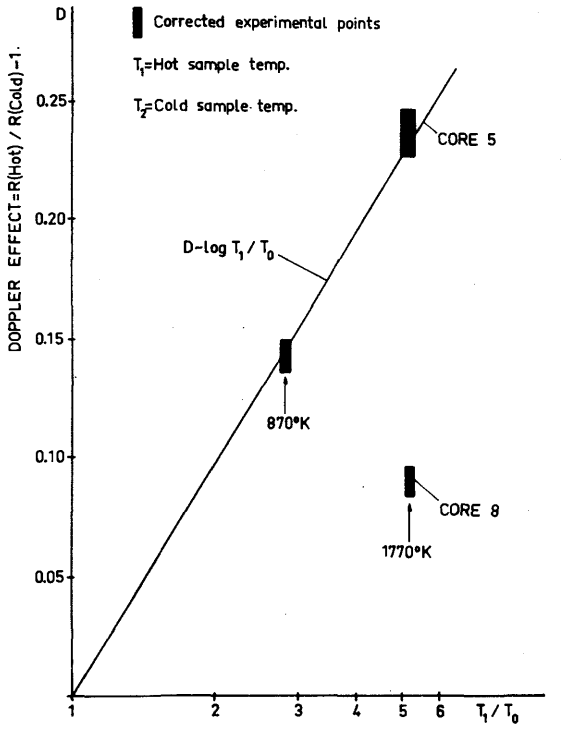

FIG.9. Doppler effect in U^{238} (zero wall thickness and zero sample thickness).

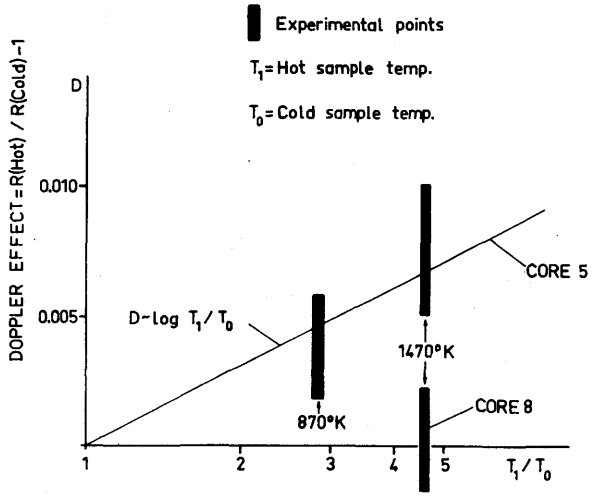

FIG.10. Doppler effect in U^{235}.

In particular the steam reactivity coefficient at the operating point has great effect on the inherent stability of the reactor. The necessity of obtaining experimental information about the coefficient is therefore obvious. Measurements of the reactivity effect of polythene (CH_2) in FRO give information related to steam coefficients and have been carried out for this reason. The two cores considered, Nos. 5 and 7, had neutron spectra broadly similar to those of current steam cooled fast reactor concepts. Their compositions are given in Table I. The fuel is uranium metal (20 % U^{235} enrichment). Both cores were diluted with polythene (7.5 vol. %) and graphite (29.2 and 14.6 vol. %, respectively) and were surrounded by a thick copper reflector. Core 7 also contained nickel to 21.9 vol. %. The different core materials are in the form of 4.3 x 4.3 cm^2 plates with the following thicknesses:

Plate type	Thickness, mm
Fuel	7.1 or 3.55
Graphite	3.55
Nickel	3.55
Polythene	0.9

Since the cores did not contain plutonium or fission products the numerical figures obtained are of little interest as such. But the experiments have been used to test calculational methods, yielding information about the significance of various approximations and the sensitivity to errors in the cross sections.

1.1 Method of measurement

The reactivity worth of polythene plates versus void was measured at various positions in the assemblies. The procedure was to replace one or more polythene plates in a fuel element by polythene or aluminium plates of reduced density. The aluminium-to-void reactivity was found in complementary measurements in which full-density aluminium plates were used. Reactivity was measured by the doubling time technique in a manner described elsewhere [5]. It is the most suitable method in the reactivity range of interest here, 10^{-3} - 10^{-4} in Δk. When converting doubling time to reactivity, an effective β-value of $784 \cdot 10^{-5}$ was used. The uncertainty in this quantity will not be included in the errors attaching to the experimental results. When measurements of a reactivity difference were repeated the reproducibility was 1 x 10^{-5} in Δk or better.

The reactivity coefficient of polythene has previously been determined at the centre of core 5 by Utzinger [6] using a similar technique.

1.2 Experimental results

Three series of measurements were made:

- Reactivity coefficient of polythene at core centre and axial distribution.
- Radial distribution of the reactivity of a thin polythene slab through the core.
- Reactivity change on a uniform reduction of the polythene density in a quadrant of the core (assembly 5 only).

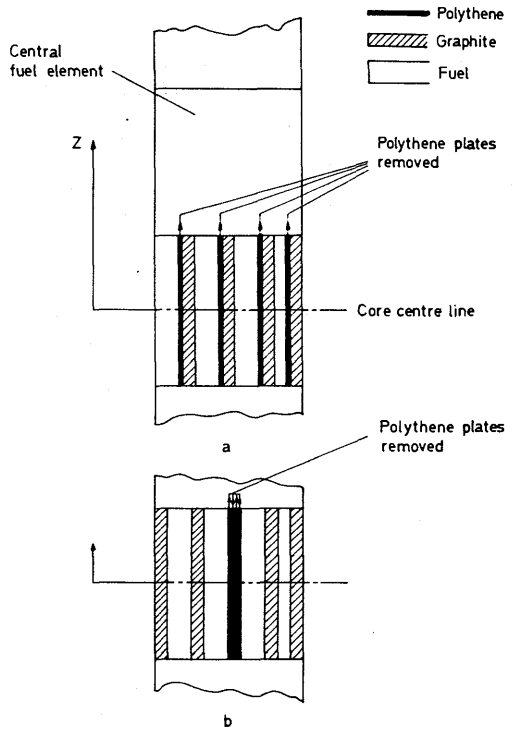

FIG.11. Loading patterns in fuel element in core 5.

1.2.1 Reactivity coefficient of polythene at core centre and axial distribution

The loading pattern of the central fuel element in core 5 is shown in Figure 11a. The normal location of the polythene plates was between a fuel and a graphite plate. As shown in the figure four plates were removed. The "bunched" arrangement shown in Figure 11b was used in a complementary measurement in order to get an idea of the magnitude of heterogeneity effects.

Similar loading arrangements were used in core 7. The core centre reactivity coefficients are shown in Table II.

In core 5 the result for the "bunched" arrangement (Fig. 11b) is in agreement with Utzinger's values which also refer to a heterogeneous pattern of plates. The latter show that the dependence on sample size is negligible. The heterogeneity effect, taken as the difference between the results in the two present arrangements, amounts to 11 % in core 5 and 2 % in core 7.

Since the corresponding thicknesses of polythene plates were 0.9 and 3.6 mm, the error involved when regarding the 0.9 mm plates as infinitely thin should be small. This is important when comparing the results with calculations using a homogeneous model, as discussed in para. 1.4.

The axial distributions are plotted in Figure 12.

TABLE II: Reactivity coefficient of polythene at core centre

Arrangement	Central reactivity coefficient of polythene, 10^{-5}/g		Sample weight, grams
	Core 5	Core 7	
Normal (Fig. 11a)	6.9 ± 0.2	5.3 ± 0.2	6.26
Bunched (Fig. 11b)	7.7 ± 0.2	5.4 ± 0.2	6.26
Utzinger [6]	7.5 ± 0.2		6.3
Utzinger [6]	7.5 ± 0.3		3.1

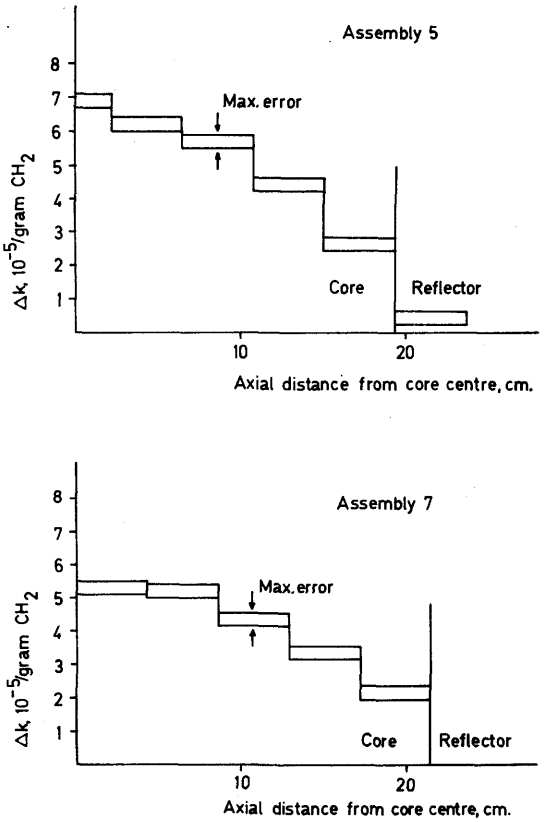

FIG.12. Reactivity coefficient of polythene, axial distributions.

1.2.2 Radial distribution of the reactivity of a polythene slab

Figure 13a illustrates the arrangement of a polythene slab in core 5 extending throughout the reactor, including the top and bottom reflectors. The slab cross section was 0.09x 4.3 cm^2 and the polythene linear density 0.364 g/cm. The polythene was replaced by aluminium.

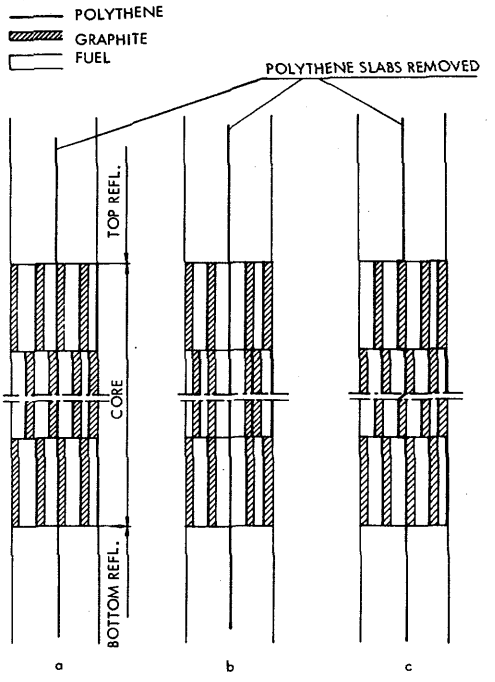

FIG.13. Loading arrangements for polythene slab in core 5.

TABLE III: Reactivity coefficient of polythene slab

Arrangement	Reactivity coefficient of polythene slab, 10^{-5}/g	
	Core 5	Core 7
Normal (Fig. 14a)	5.06 ± 0.04	4.02 ± 0.03
(Fig. 14b)	4.92 ± 0.04	
(Fig. 14c)	5.11 ± 0.04	
From axial distribution (Fig. 12)	5.04 ± 0.14	4.09 ± 0.13

In complementary runs in the central fuel element of assembly 5 the polythene slab was surrounded on both sides by fuel plates (Figure 13b), or polythene plates were staggered in the core region in order to prevent streaming effects to occur in the voided channel (Figure 13c). The results are shown in Table III.

In all values except those in the bottom row there is an additional common uncertainty of about ± 0.1 x 10^{-5} due to the effect of the aluminium. The values in the bottom row were obtained by integrating the step curves in Figure 12. The results show that the effects of heterogeneity and streaming are inconsiderable in these measurements. Since the effects of the polythene

plates in the axial measurements add up to the effect of the slab, interaction effects between closely located plates are negligible.

It was found that the parts of the polythene slab passing through the end reflectors did not contribute appreciably to the reactivity effect. The results are therefore also applicable to slabs passing through the core only.

The measurements on assembly 7 were analogous. The radial distributions are plotted in Figure 14. The curves were drawn to fit the measured points.

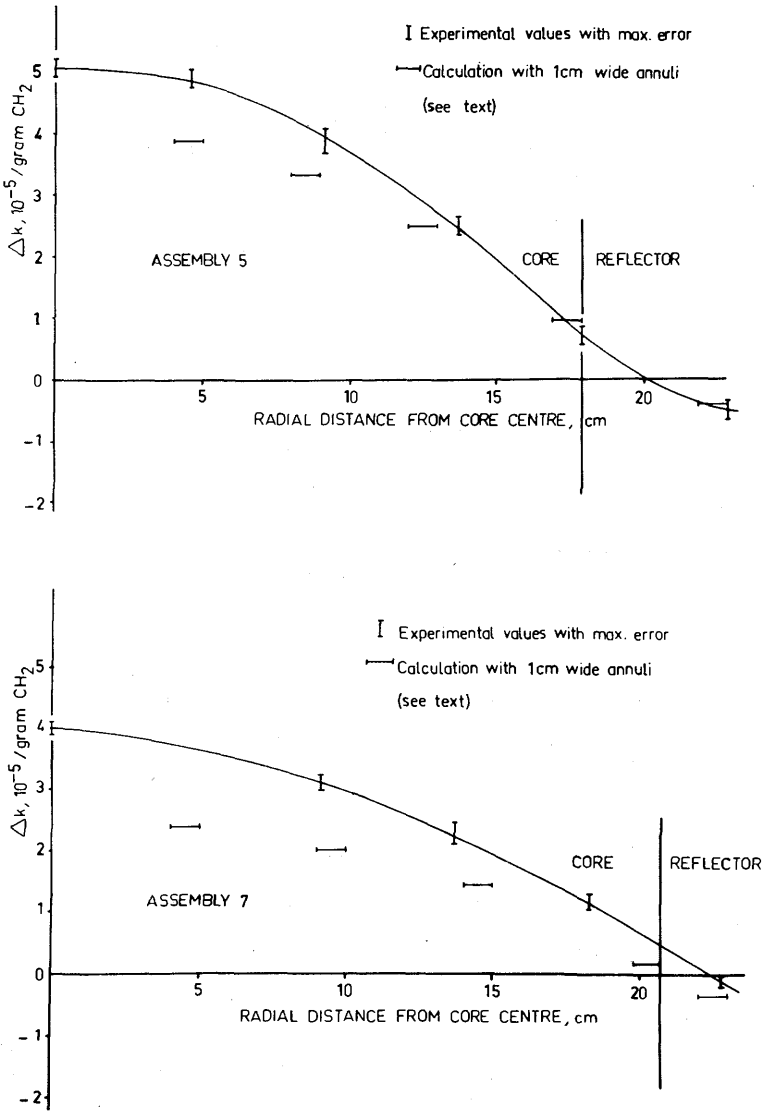

FIG. 14. Reactivity effect of polythene slab, radial distributions.

1.2.3 Reactivity change on a uniform reduction of the polythene density in a quadrant of the core

In one quadrant of core 5 (excluding the central fuel element) every fourth polythene plate was replaced by a similar one having a central hole (2 cm diam.). This arrangement was made as uniformly over the quadrant as possible and effected a 4 % reduction of the average polythene density in the quadrant. The resulting reactivity change was measured in the usual manner. A core average reactivity change was determined, assuming that the contributions from all quadrants and the central element are additive. Expressed in terms of the reactivity change on a 10 % increase in the polythene density the following figures were obtained:

Arrangement	Reactivity change, 10^{-5} Core 5
Density change in quadrant of core	840 ± 10
Volume integration of slab experiment (Fig. 14)	770 ± 40

The latter result was obtained by a numerical integration of the values obtained with polythene slabs at different radii as given in Figure 14a. The difference of 9 % between the two values can be attributed to the very different experimental arrangements. Further comments will be given in para. 1.4.

1.3 Calculations

Since the experiments involved small changes in reactivity, a perturbation method might seem to provide a suitable theoretical approach. But as the spectrum change is of major importance, rather than the cross section change inducing it, the usual first-order perturbation theory, in which the change in neutron flux is ignored, is in general inadequate. Since a general high-order perturbation programme was not available, full criticality calculations were made. The small changes in k to be calculated (about 10^{-3} in Δk) necessitated a fairly stringent requirement on convergence. An inaccuracy in the calculated eigenvalue of 10^{-5} was generally the accepted level, but this was relaxed to 10^{-4} in a few cases for which a higher accuracy would lead to unreasonable computation times.

Most of the calculations were made with the one-dimensional diffusion theory programme MONDAY [7] which computes the eigenvalue with the required high accuracy in about 0.5-0.7 min. (IBM-7044) in a typical case. The two-dimensional programme 20-GRAND [8] and the one-dimensional transport theory programme DSN [9] were also used in complementary calculations.

1.4 Comparison of experiment and theory

When simulating the experimental situations the MONDAY-programme was used in cylinder geometry with 16 energy groups. An axial buckling was derived assuming a reflector saving, δ, of 10 cm. This value has been found consistent with measured axial flux distributions in all FRO assemblies so far studied. Calculating the effect of a uniform change in the polythene density over the core was then straightforward.

The radial distribution of the reactivity effect was calculated by removing the polythene content (7.5 vol. % in the core) in annular zones of

1 cm width located at various distances from the core centre. The mesh in the zone and in adjacent layers was 0.2 cm, which was found to be adequate. The reactivity worths of the removed polythene quantities, reduced to equivalent reactivity coefficients, are plotted together with the experimental values for the polythene slabs in Figure 14. A direct comparison with these experiments, however, is valid only if the effects of small amounts of polythene are additive. If they are, then the reactivity of the experimental polythene slab would be unchanged when forming a part of an annulus, as in the MONDAY calculation. Now the experimental results quoted in para. 1.2 show that the assumption of additivity is valid with good approximation. There were no appreciable sample size effects, the effect of bunching was small, and the reactivities of plates at different axial positions or slabs at different radial positions were approximately additive. A theoretical check on additivity was obtained by comparing the integrated effect of the removal of polythene in annular zones with that of the uniform density change. The results, all referring to a 10 % change in the polythene density in the whole core, are summarized in Table IV.

The experimental values are consistently 15-40 % higher than the calculated ones (cf. also Figure 14). If transport theory had been used, as will be described in the next paragraph, the theoretical values would increase by about 34 % and 15 % for cores 5 and 7, respectively, improving the agreement, particularly for core 5.

The k-values computed with MONDAY were below 1 for both assemblies (Assy 5: k = 0.96 ; Assy 7: k = 0.95). It is therefore probable that the calculated reactivity changes are low because of an overestimate of the absorption probability rather than an underestimate of the leakage probability. Either of these errors would yield low values. A test was made by reducing the absorption cross section in core 7 by 10 % in the energy range below 25 keV. This resulted in an increase of 60 % in the calculated reactivity coefficient of polythene. Consequently quite moderate errors in the low energy cross sections will have a great influence on the result.

The change of sign of the reactivity coefficient in the side reflector is reproduced in the calculations.

1.5 Intercomparison of calculations of the core average reactivity coefficient

In this paragraph the sensitivity of the calculated values to different approximations involved will be discussed. The approximations we have in mind are represented by the following titles:

- Reflector saving to account for end reflectors. Two-dimensional calculation.
- Number of energy groups.
- Comparison of diffusion and transport theory.

The different points were investigated in respect of a 10 % polythene density change in cores 5 or 7.

The reflector saving, δ, was increased from 10 to 15 cm in one case and the axial buckling reduced accordingly. A calculation with spherical geometry was also made. The radius of the spherical core was determined by applying a shape factor for critical mass according to Davey [10]. Finally, a two-dimensional calculation with the 20-GRAND code [op. cit.] was carried

TABLE IV: Comparison of experiment and theory

	Item	Reactivity change, 10^{-5}	
		Core 5	Core 7
Experiments	Density change in quadrant of core	840 ± 10	-
	Slab experiment	770 ± 40	856 ± 50
MONDAY calculations	Uniform density change	642	599
	Annular zones	660	545

out with 6 energy groups. The value quoted below, however, is converted to 16 groups by assuming the same ratio of 16-to-6 group results to be valid in one- and two-dimensional calculations (cf. below):

Calculation		Reactivity change, 10^{-5} Core 5
MONDAY	δ = 10 cm	642
	δ = 15 cm	553
	Spherical	569
20-GRAND, 2 dim.		591

If the result due to 20-GRAND is regarded as "correct", the choice of cylinder geometry and δ = 10 cm (based on experimental information) in the one-dimensional calculation yields a value 9 % too high, and spherical geometry a value 4 % too low. The reactivity change is sensitive to the value of δ. In cases not involving pancake cores a calculation in spherical geometry will therefore probably give the more reliable result as regards the core average reactivity coefficient.

The multigroup cross sections used in the present calculations were obtained from data in the SPENG library [9]. A weighting spectrum was obtained by a calculation with about 500 energy points on a bare core using the SPENG programme. The normal number of groups was 16, but this was reduced to 6 groups in a test case. No effort was made to optimize the group structure. The reduction from 16 to 6 groups increased the reactivity coefficient of polythene by 11 % (Assy 5). No general conclusion can be drawn from this one test case, but the fairly small difference noticed indicates that 16 groups give adequate precision in the cases studied here.

The DSN-programme, which solves the Boltzmann equation in S_4-approximation in spherical geometry, was used with 16 energy groups for one test case on each of the studied assemblies. Unfortunately the convergence process in the DSN code employed is very slow, impeding further calculations. The results, compared with those of the MONDAY code, are as follows:

Method	Reactivity change, 10^{-5} Core 5	Core 7
MONDAY	569	517
DSN	764	592
DSN/MONDAY	1.34	1.15

For larger systems with less leakage the difference between transport theory and diffusion theory results is likely to be smaller.

The neutron spectra obtained with the two methods were practically identical, even at the core-reflector interface.

In summary, the reported calculations indicate that a one-dimensional model is adequate for comparisons with the experiments. A considerable improvement in the agreement with the experiments is obtained if the S_4 (DSN) rather than the diffusion theory code is used.

In all calculations anisotropy in scattering has been taken into account only to the extent that transport cross sections of the form $\Sigma_{tr} = \Sigma_{tot} - \bar{\mu} \Sigma_s$ are used. Since anisotropy in collisions with hydrogen is very pronounced, a theoretical study of this effect by more exact methods would be of great value.

1.6 Conclusions

In the measurements of the polythene reactivity coefficient reported here an internal consistency between results of different experiments has been obtained. The reactivity contributions from small polythene samples have been found to be approximately additive. No large effects of heterogeneity or interaction between samples have been observed. Comparisons with calculations using a homogeneous model are therefore relevant.

The experimental results are largely in reasonable agreement with calculated values. The latter are very sensitive to moderate changes in the cross sections at low neutron energies. The agreement with experiment is improved if transport rather than diffusion theory is used.

2. Effect of substituting polythene for fuel in the central element

The removal of burned fuel from steam cooled fast reactors will most likely be made with the reactor in a flooded state. The removed fuel cluster will leave a hole filled with water, the reactivity effect of which could be of some concern. It is obvious that the effect will be strongly dependent on the size of the hole and the isotopic composition of the plutonium fuel. This latter dependence, especially, cannot be studied in FRO, but experiments can be made that should be well suited for testing calculational methods.

The present study is a first step in this direction. The normal constituents of a central fuel element in core 5 were gradually replaced by polythene, and the resulting reactivity increase was compensated by a decrease in the peripheral core loading. The measurements comprised studies of reactivity effects and of reaction rates with different kinds of foils. A qualitative simulation of Pu^{240} in the fuel layer next to the polythene was made in a special experiment using thin strips of indium.

2.1 Reactivity measurements

The reactor was first made critical with the normal core 5 loading in all fuel elements. A stepwise substitution of polythene for uranium and graphite was then made in the central element starting at the core centre. Each polythene block was of half module size (2.15 x 4.3 x 4.3 cm^3), representing a reactivity increase of not more than 200 x 10^{-5}. The change in reactivity per unit mass of polythene with the distance from the centre

showed the same pattern as that for small samples. The insertion of polythene was extended throughout the whole core and the top and bottom reflectors. The total length of the polythene column was 97 cm, the core part constituting about one third of this. The section area was 4.3 x 4.3 cm^2.

The water hole created by a fuel cluster box in a power reactor will have a larger section area, but holes of such sizes could not readily be accommodated in the reactor. An approximate measure of the size dependence was obtained by repeating the measurements with a column of half the section area (2.15 x 4.3 cm^2).

The adjustment of the core edge along with the fuel-polythene substitution was made in such a way as to keep a reasonably good cylindrical form of the outer surface. The reactivity effect of core-reflector material substitutions was periodically measured along with the reduction of the core radius. The doubling time technique was used. At each step measurements were made at different distances from the core centre so that a value at the actual effective core radius could be obtained by interpolation.

The changes in reactivity on replacing uranium and graphite by polythene in the central element are listed in Table V. The values of critical mass were converted to reactivity by using the measured values of reactivity equivalence of fuel at the core boundary as a function of critical mass. The limits of error are quite large for these first sets of measurements. The major contributions come from the differences in core boundary irregularities and from the uncertainty in the relative worth of fuel and copper for the different core boundaries.

TABLE V: Results from the polythene rod substitution experiment

Configuration		Mass of polythene, g	Critical mass kg U^{235}	Reactivity %
Unperturbed core	0	0	75.8	0
Poly in core part only:	1/2 module*	231	70.5	1.25 ± 0.10
	1/1 "	462	66.4	2.20 ± 0.10
In core + top reflector:	1/2 module			
	1/1 "	924	67.1	2.05 ± 0.10
In the whole central element:	1/2 module	693	71.5	1.00 ± 0.10
	1/1 "	1386	68.0	1.85 ± 0.10

* 1/2 module: Section area = 2.15 x 4.3 cm^2

1/1 module: Section area = 4.3 x 4.3 cm^2

As shown in the table the reactivity effect of the full-thickness polythene rod is only about 1.8 times the effect of the half-thickness rod. Some shielding effect thus occurs in the thicker rod. Furthermore, as in the case of small samples, polythene in the reflector causes a slight decrease in reactivity. Most of that effect comes from a region fairly close to the core-reflector boundary.

The experiments have been compared with theoretical results due to Häggblom [11]. One-dimensional transport theory (DSN, 20 groups) calculations were made for the case with the central element filled with polythene. Cylinder geometry was used, the axial dimension being described by a buckling parameter, and the square section polythene rod was simulated by a cylindrical rod with equal section area. The energy region 0-4 eV was divided into four groups for which cross sections were derived by means of the thermal lattice programme FLEF. The calculated reactivity worth of the polythene rod was 2.68 % to be compared with the measured value of 2.20 ± 0.10 %. A less comprehensive treatment of the very low energy neutrons proved to be entirely inadequate, yielding even a negative reactivity value. It is concluded that the positive effect of the polythene rod is largely due to thermalized neutrons.

The quite primitive experiment made to illustrate the reactivity effect of a strong low energy absorber like Pu^{240} was performed with strips of thin indium foils. The strip thickness was 0.01 cm, the width 4.3 cm and the length equal to the core height. Indium has a strong resonance at 1.45 eV which dominates the indium capture in the neutron spectrum existing in and close to the polythene rod. In this respect it resembles Pu^{240} but quantitative conclusions cannot be drawn from the present experiment.

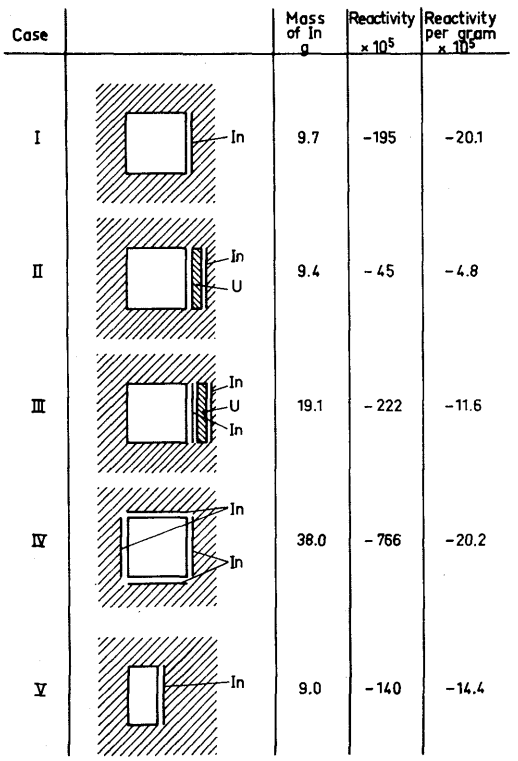

FIG.15. Geometric arrangements and results from the indium strip measurements (the hatched areas represent the normal core region).

Altogether five different geometrical arrangements were used. These are illustrated on Figure 15 together with the results of the reactivity measurements. The effect per unit weight of indium placed close to the polythene rod is quite high, as seen from the last column, case No. I. The effect is reduced by almost a factor of five when the indium strip is moved to a location behind the first uranium fuel plate. This indicates that most of the reactivity effect in the first case is caused by low energy neutrons, i.e. by those with energies around 1.45 eV. As seen from case No. IV only moderate amounts of indium are required to compensate a substantial part of the positive effect of the polythene. Pu^{240} in the fuel surrounding a water hole will have much the same effect, efficiently reducing the positive effect of the water.

2.2 Reaction rate measurements

The large moderating power of polythene enhances the low energy part of the spectrum. It is of importance to know the extent of this spectrum distortion both in energy and in space. Reaction rate measurements were therefore made with resonance detectors such as indium, gold and manganese along a radius at the core midplane. Additional measurements were made with U^{235} foils.

The measurements discussed here were made before thin plates of fuel and dilution materials were available. Despite the fact that homologous foil positions were used whenever possible, the heterogeneity of the arrangement of the core constituents caused some difficulty when comparing the results

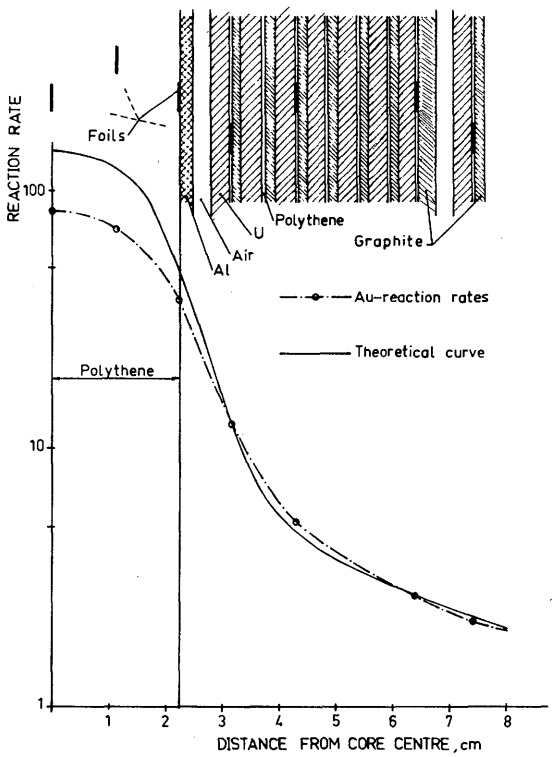

FIG.16. Experimental and calculated reaction rates for gold.

with calculations. This is especially true for the layer closest to the central element.

The results from measurements and calculations of the $Au^{197}(n,\gamma)$ and $U^{235}(n,f)$ rates are summarized in Figures 16 and 17. Group cross sections generated by means of the FLEF and SPENG programme and group fluxes from the DSN runs have been used in the calculations. The experimental and calculated curves have been normalized in the unperturbed region beginning about 5 cm from the polythene rod, where the shapes of the curves are approximately equal. The calculated reaction rates at the centre of the rod are overestimated by about 70 % (Au^{197}) and 40 % (U^{235}). This is not a large discrepancy in view of the fact that the reaction rates in the rod are higher than in the unperturbed core by a factor of 50-100. Analysis shows that the discrepancy can be attributed partly to an overestimate of the flux in the lowest energy group, below 0.25 eV. It may also to some extent be caused by the use of a circular instead of a square rod section in the calculations.

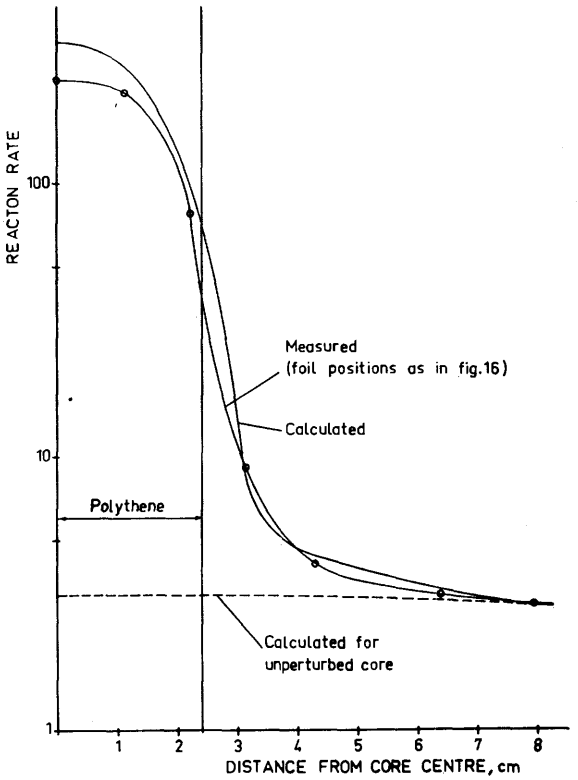

FIG.17. Experimental and calculated reaction rates for U^{235}.

Acknowledgements

Many persons have actively and skilfully assisted in the present work. The authors wish to acknowledge specifically the following contributions: computer programming by Å. Ahlin; theoretical calculations on the polythene

rod by H. Häggblom; manufacture of uranium oxide samples by K.E. Jansson and L. Storm; construction of sample changer and electronics by S. Sjööquist; experimental assistance by B. Karmhag and S.Å. Klingfeldt; reactor operations by the FRO Group under A. Pettersson; and typing of manuscript by Mrs. Paula Granath.

REFERENCES

[1] PFLASTERER, G.R., Jr. et al., ANL-7120 (1965) 616
[2] DAVEY, W.G., AMUNDSON, P.I., Trans Am. nucl. Soc. 9 1 (1966) 226
[3] ANDERSSON, T.L. et al., ANL-7320 (1966) 159
[4] TIRÉN, L.I., Nukleonik 10 (1967) 141
[5] HELLSTRAND, E. et al., AB Atomenergi Rep. AE-207 (1965)
[6] UTZINGER, E., HÅKANSSON, R., AB Atomenergi Rep. AE-FFX-73 (1967)
[7] LINDE, S., AB Atomenergi Rep. TPM-RFN-259 (1967)
[8] TOBIAS, M.L., FOWLER, T.B., ORNL-3200 (1962)
[9] HÄGGBLOM, H., AB Atomenergi Rep. AE-194 (1965)
[10] DAVEY, W.G., Nucl. Sci. Engng. 19 (1964) 259
[11] HÄGGBLOM, H., AB Atomenergi Rep. TPM-RFR-673 (1967)

DISCUSSION

P. A. ENGELMANN: When you inserted the polyethylene rod you got a reactivity increase of over 2%. How did you measure this reactivity change – by compensating with control rods or by changing the radius?

E. HELLSTRAND (Chairman): Perhaps I may be allowed to answer this question as one of the co-authors. We did it by changing the core radius and measuring the reactivity worth of the fuel at the core boundary. We then performed an integration from the original to the final radius.

H. SEUFERT: My question relates to your studies of the effect of heterogeneity on Doppler experiments. Have you an explanation for the discrepancies between your results, on the one hand, and those of Davey and the theoretical predictions of Nicholson, on the other? I think they found that heterogeneity had a very strong effect on such experiments.

L. I. TIRÉN: As far as Nicholson is concerned, the large effect predicted by him in the paper presented last October at the International Conference on Fast Critical Experiments and their Analysis, held at the Argonne National Laboratory, was for a rather extreme case.

J. L. ROWLANDS: I should like to comment on the significance of heterogeneity in your polyethylene reactivity worth measurements. You appear to deduce from your bunching experiments that heterogeneity is not important. In my opinion, a bunching experiment does not necessarily give a measurement of the effect of heterogeneity on resonance shielding in fuel isotopes, because the shielding for your size of fuel plate is already very large. Have I understood you correctly?

L. I. TIRÉN: My conclusions regarding heterogeneity effects were restricted to these particular polyethylene-void measurements. I do not suggest that the normal plate thickness (0.71 cm uranium) yields insignificant heterogeneity in the resonance region.

H. R. KLEIJN: How do you know that your calculated spectra are the actual spectra in which you are measuring?

L. I. TIRÉN: We believe that by extrapolating the results to zero wall thickness and zero sample thickness we obtain quantities which can be compared with the calculations.

H. R. KLEIJN: What was the enrichment of your foils?

L. I. TIRÉN: The depleted uranium foils contained 0.2% ^{235}U, while the enriched uranium foils contained 93% ^{235}U.

H. R. KLEIJN: For similar experiments we are using a Zircaloy oven. Have you ever considered this material rather than stainless steel or aluminium?

L. I. TIRÉN: In view of its small cross-section, I think aluminium is the best material.

MEASUREMENT OF THE EFFECTIVE CAPTURE-TO-FISSION RATIO IN Pu^{239} AND U^{235} IN TWO DIFFERENT FAST REACTOR SPECTRA

T.L. ANDERSSON, E. HELLSTRAND, R. HÅKANSSON AND Z. BAJBOR*
AB ATOMENERGI,
STUDSVIK, NYKÖPING, SWEDEN

Abstract

MEASUREMENT OF THE EFFECTIVE CAPTURE-TO-FISSION RATIO IN Pu^{239} AND U^{235} IN TWO DIFFERENT FAST REACTOR SPECTRA. Integral values of α for U^{235} and Pu^{239} have been deduced from experiments in two different cores (median U^{235} fission energy 50 keV and 180 keV, respectively) in the FRO reactor. The method of measurement is the same as that used for instance at ZEBRA [1]. The experiment includes reactivity measurements of the sample material and of a standard, B^{10}, as well as an absolute determination of the fission rate in Pu^{239} and U^{235} and the capture rate in B^{10}.

The experimental α values agree well with the calculated ones for the hard spectrum core measurements, both for U^{235} and Pu^{239}. The measured value for Pu^{239} in the soft core is slightly higher than the calculated one. The discrepancy for U^{235} is large and hitherto unexplained.

I. INTRODUCTION

Despite the great efforts made to measure the capture and fission cross-sections for Pu^{239} and U^{235} there are still some considerable gaps in the knowledge concerning these cross-sections. This is in particular true for the Pu^{239} capture cross-section in the energy region 1 keV to 15 keV. It seems evident from the analysis, for instance, by Sowerby et al. [2], that most cross-section libraries used in the past have been too optimistic concerning the capture-to-fission ratio, α, in this energy region. It is a question of a quite drastic underestimate - almost a factor of two - and such changes in α will unfavourably affect the calculated breeding ratio for a given system with appreciable amounts. This is especially the case for the steam-cooled systems and it is urgent to obtain more experimental data concerning α.

Recently, integral values of α, $\int \phi \sigma_c \, dE / \int \phi \sigma_f \, dE$, have been determined in fast systems at ZEBRA [1]. The method used involves reactivity measurements on small samples of U^{235} or Pu^{239} and a standard together with an absolute determination of the fission rate in the fissile material and the reaction rate in the standard. The principle of the method was originally designed by F. Feiner and used for determination of the epithermal α for U^{235} and Pu^{239} in well thermalized assemblies [3].

Redman and Bretscher [4] have developed the method further by using a calibrated fission source (Cf^{252}) for establishing the worth of virgin fission neutrons relative to that of the neutrons absorbed in the sample. This improvement of the method cannot yet be commonly used as only very few calibrated californium sources exist.

---

* On leave from the Institute of Nuclear Research, Swierk, Warsaw, Poland

TABLE I: VOLUMETRIC COMPOSITION OF CORES 5 and 8 [a]

Assembly No.	Uranium (20 % U^{235})	Steel	Graphite	Polythene	Aluminium	Air
5	51.1	6.5	29.2	7.5		5.7
8	51.1	6.5	29.2	1.9	5.6	5.7

[a] Atomic densities are given in Table I of Ref. [6]

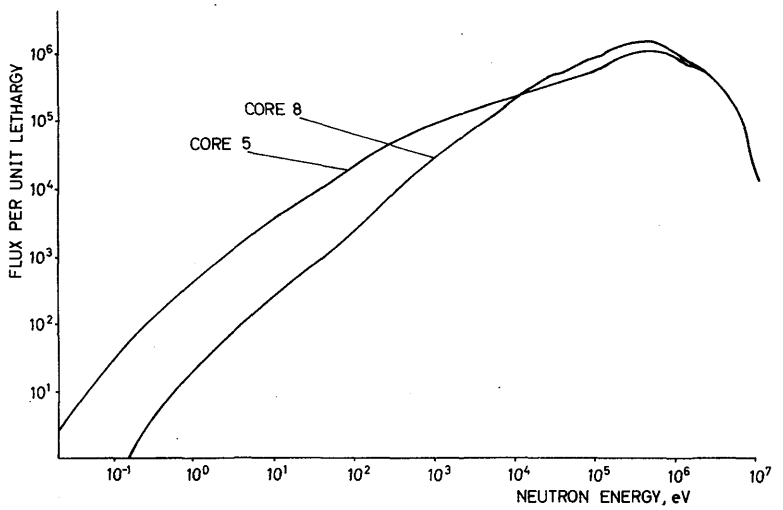

FIG.1. Calculated spectra for cores No.5 and 8. For clarity the dips appearing in the resonance region have been smoothed out.

We have applied the version of Feiner's method that was used at ZEBRA[1]. The cores studied at that reactor had spectra similar to those of sodium-cooled fast power reactors. We have been more interested in steam-cooled systems in Sweden and the quite high α value, obtained in DIMPLE [5] for a neutron spectrum characteristic of a steam-cooled reactor, gave additional incentive to start a series of measurements at the FRO reactor.

Experiments have been performed in two different cores, No. 5 and 8. The volumetric composition of these cores is given in Table I. The neutron spectrum of core 5 resembles broadly that of a steam-cooled fast power reactor while that of core 8 is considerably harder. The calculated spectra for the two cores are given in Figure 1.

The thin plates of fuel and dilution materials available at FRO were used in the same way as described in [6] to mock up a nearly homogeneous central zone in the different cores. The in-core measurements pertaining to the α-experiments were performed at the centre of this homogeneous region. Systematic errors caused by heterogeneity could thereby effectively be avoided.

[1] The specific plutonium and uranium samples used in the measurements were kindly lent to us by the ZEBRA group.

II. METHOD OF MEASUREMENT

II.1 General

The relations between measured quantities and their theoretical counterparts are obtained from first-order perturbation theory and straightforward expressions for the different reaction rates. For simplicity we assume that the fissionable materials and the standard (boron) all are infinitely thin. Furthermore, they are assumed to consist of 100 % pure Pu^{239}, U^{235} and B^{10}, respectively. Denoting the fissionable material with index x and the standard with B the reactivity signals and the reaction rates (fission in x, capture in B^{10}) may then be written (ρ = reactivity, N = reaction rate).

$$\rho^x = k_1 \left[\sum_j \phi_j^* \chi_j^x \sum_i (\nu\sigma_f)_i^x \phi_i - \sum_i \phi_i^* (\sigma_f + \sigma_c)_i^x \phi_i\right]$$

$$\rho^B = - k_1 \sum_i \phi_i^* \sigma_{ci}^B \phi_i$$

$$N^x = \sum_i \sigma_{fi}^x \phi_i$$

$$N^B = \sum_i \sigma_{ci}^B \phi_i$$

Combining the equations we get

$$1 + \alpha' = \frac{\sum_j \phi_j^* \chi_j^x \sum_i (\nu\sigma_f)_i^x \phi_i}{\sum_i \phi_i^* \sigma_{fi}^x \phi_i} - \frac{\rho^x}{|\rho^B|} \frac{N^B}{N^x} \frac{\sum_i \phi_i^* \sigma_{ci}^B \phi_i}{\sum_i \phi_i \sigma_{ci}^B} \frac{\sum_i \phi_i \sigma_{fi}^x}{\sum_i \phi_i^* \sigma_{fi}^x \phi_i} \qquad (1)$$

α' is the importance weighted capture-to-fission ratio for x, i.e. $\sum_i \phi_i^* \sigma_{ci}^x \phi_i / \sum_i \phi_i^* \sigma_{fi}^x \phi_i$. The usual definition of α does not contain the adjoint flux. α' is converted into α by multiplying with the factor $\sum_i \phi_i \sigma_{ci}^x \sum_j \phi_j^* \sigma_{fj}^x \phi_j / (\sum_i \phi_i \sigma_{fi}^x \sum_j \phi_j^* \sigma_{cj}^x \phi_j)$ obtained by calculation. The adjoint flux ϕ^* varies slowly with energy and the factor above can be calculated with good accuracy.

The RHS of Eq. 1 contains a combination of calculated and measured quantities. This will be given further consideration in Section III.1.

II.2. Measuring procedure

As discussed above the quantities to be measured were the reactivity effect and reaction rate per atom of x (Pu^{239} or U^{235}) and of the boron standard. These quantities enter as ratios in Eq. 1 in such way that especially the reaction rate measurements are simplified.

Some details concerning the different types of measurements will be given below.

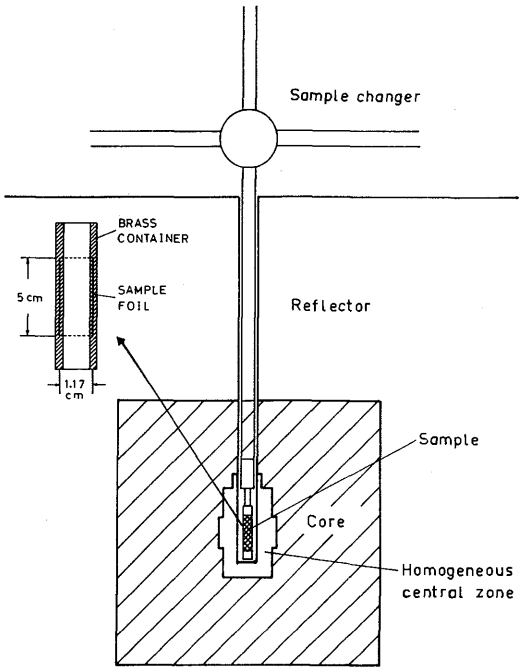

FIG. 2. Sample changer and holder arrangement.

TABLE II: DATA FOR THE SAMPLES

Sample	Total weight g	Thickness cm	Length cm	Sample diameter (o.d.), cm	Weight of brass container, g
Pu^{239}[a]	4.60	0.018	5	1.17	18.50
U^{235}[b]	6.547	0.023	5	1.17	18.33
B_1^{10}[c]	0.219	0.018	5	1.17	18.08
B_2^{10}[c]	0.465	0.037	5	1.17	19.91

[a] Pu content 98.93 %. Isotopic comp.: Pu^{239}: 94.71 %, Pu^{240} 4.94 %, Pu^{241} 0.35 %.

[b] U content 99.8 %. Isotopic comp.: U^{234} 1.11 %, U^{235} 92.88 %, U^{236} 0.27 %, U^{238} 5.74 %.

[c] B content 93.5 %. Isotopic comp.: B^{10} 90.8 %, B^{11} 9.2 %.

II.2.1. Reactivity worth measurements

The FRO reactor is at present not equipped with a pile oscillator and the reactivity worths of the samples were therefore determined with the positive period technique. A sample changer was used allowing successive measurements to be made on the boron standard, the Pu^{239}, the U^{235} samples and a dummy without shutting down the reactor. The sample holder arrangement is illustrated in Figure 2. Measurements had to be made with and without samples in the holders to account for the small reactivity differences between the holder arms.

The samples were tubular in form and encased in brass containers, compare Figure 2. The dimensions and other properties are given in Table II.

The reactivity worth of the samples ranged from 3 to 9 x 10^{-5} in the different spectra. The reactivity measurements had to be made to an accuracy better than one per cent. The margin of errors should consequently not exceed a few times 10^{-7}. This requirement can customarily be met without too great a difficulty either oscillator or positive period technique is used. The temperature coefficient of reactivity for FRO is comparatively large ($\sim$ 3 x 10^{-5} per ^{o}C), however, and very accurate measurements would require high temperature stability. Unfortunately, the temperature drift was not negligible for FRO. The measurements consequently had to be stretched out over long periods of time, with alternating measurements on the different samples and the dummy. Even so, the errors were not smaller than about one per cent for the smallest reactivity signals.

The reactor power was registered with two different channels. In one of these, pulses from a fission chamber were fed to a scaler and printer unit, in the other one an ionization BF_3 chamber was used. The amplified signal from the latter was converted to pulses with the aid of a voltage-to-frequency converter. The pulses went to a similar scaler and printer unit as for the fission detector channel.

The core was loaded in such way that the reactor was supercritical by 15 to 20 x 10^{-5} with all control rods fully in and the most reactive sample in its "in" position. During a set of measurements only a fine control rod (reactivity equivalence about 50 x 10^{-5}) was moved. For a given sample the power was kept constant - at a low level - with the fine control rod. After a suitable time the rod was inserted to its fully "in" position and the power increase was followed with the channels described above. The corresponding doubling time, τ, and reactivity, ρ, were calculated with a simple code in which τ was obtained from a least squares fit to an exponential and ρ subsequently determined from the inhour formula. The values of the delayed neutron fractions, β_i, vary somewhat from one core to another. The same data have been used for both cores, however, as the differences in β_i are small and the measured reactivities only enter as ratios.

Self-screening effects could not be measured for the Pu^{239} and U^{235} samples as only one sample of each material was available. The finite thickness was taken into account by calculations (compare Section III). For boron, measurements were made on two samples and the reactivity worth per unit weight for zero sample sizes was obtained by extrapolation.

II.2.2. Reaction rate measurements

The standard detectors [7] used for fission ratio measurements at FRO were utilized for determining the Pu^{239} and U^{235} fission rates. These

aluminium walled chambers have an outer diameter of 0.6 cm and a coated anode length of either 1 or 2 cm. The layer thickness is less than 250 $\mu g/cm^2$, i.e. thin enough not to cause any problems with self shielding.

The boron reaction rate was determined with a small BF_3 counter, outer diameter 0.6 cm and effective length 5 cm. The gas filling was a mixture of enriched BF_3 (100 mm) and argon (600 mm).

A narrow vertical channel from the top of the reactor to a point just below the core centre was accommodated in the central fuel element. The relative reaction rates in the BF_3 counter and, alternately, the Pu^{239} and the U^{235} chambers were determined. The detectors were mounted side by side in such way that their midpoints closely coincided with the core centre. The axial variation of the flux in this region was small enough that the difference in effective length between the BF_3 counter and the fission chambers was of no concern.

The ratios obtained from the FRO measurements were only proportional to the quantity N^B/N^x entering into Eq. 1. The necessary proportionality constant was obtained from complementary runs in a thermal column. The detectors were mounted as in FRO and inserted in a narrow channel in the thermal column of the R2-0 reactor.

The same electronic equipment - cables, preamplifiers, main amplifiers, discriminators and scalers - was used for each detector in the FRO and the thermal column runs. Furthermore, a precision pulse generator was used before and after each run to check the amplification and discriminator levels ascertaining that drifts in the electronic equipment did not cause any systematic errors.

Denoting the measured reaction rates R_{th} and R_f for the thermal column and the FRO measurements, respectively, the following expression for N^B/N^x can easily be derived.

$$\frac{N^B}{N^x} = \frac{R_f^B}{R_f^x} \times \frac{R_{th}^x}{R_{th}^B} \times \frac{\sigma_o^B}{\sigma_o^x g^x} \qquad (2)$$

The σ_o:s are the 2200 m/s fission (x) and capture (boron) cross-sections and g^x is the Westcott factor taking into account the deviation from 1/v for the fission cross-sections. The neutron temperature in the middle of the large graphite column was assumed to be the same as that of the graphite.

The neutron gradient was not negligible in the thermal column. A careful flux mapping was made to allow a correction for the difference in counter length. The correction turned out to be negligible.

Eq. 2 requires that the pulse spectrum from the detectors is the same in the thermal and fast neutron fluxes. This should be true to a high degree of accuracy for the fission detectors. For BF_3 counters, especially those of a small size, this is not the case. There are several effects that have to be considered. High energy neutrons yield boron and fluorine recoils through elastic collisions. These recoils together with gamma induced pulses give rise to a background that is not present in the thermal column run. This is clearly demonstrated in Figure 3, in which the data from the hard neutron spectrum core 8 are displayed together with a pulse spectrum from the thermal column.

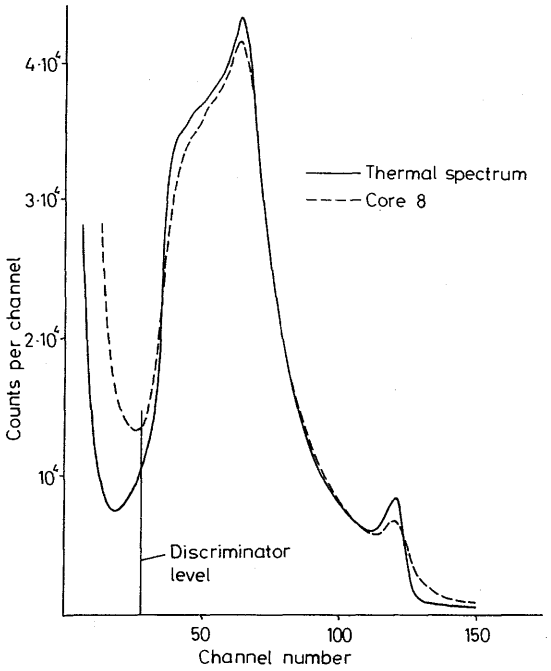

FIG.3. Pulse spectra from a BF_3 counter in a thermal flux and in the hard spectrum core No.8.

There are two other effects that may cause a systematic error in the B^{10} reaction rate determination. The pulse amplitude distribution from (n,α) reactions caused by high energy neutrons differs from that from thermal neutrons in two respects. The neutron kinetic energy adds to the Q value of the (n,α) reaction and the branching ratio for the formation of the excited and ground states in Li^7 is neutron energy dependent. With a low enough discriminator level the latter two effects should be small but the former one must then be corrected for (compare Section III.3).

A small difference is also caused by the threshold reactions B^{10}(n,2α) and fluorine(n,α) in spectra containing high energy neutrons. Using existing cross-section data [8] it has been concluded, however, that these effects are negligibly small.

III. EVALUATION OF $1 + \alpha'$

The measured and calculated quantities on the right-hand side of Eq. 1 will be discussed in turn below.

III.1. Real and adjoint fluxes. Group constants

When considering the degree of sophistication with which the real group fluxes have to be calculated it should be borne in mind that these fluxes enter in very much the same way in both the numerator and denominator of the different expressions. This, together with the fact that the adjoint

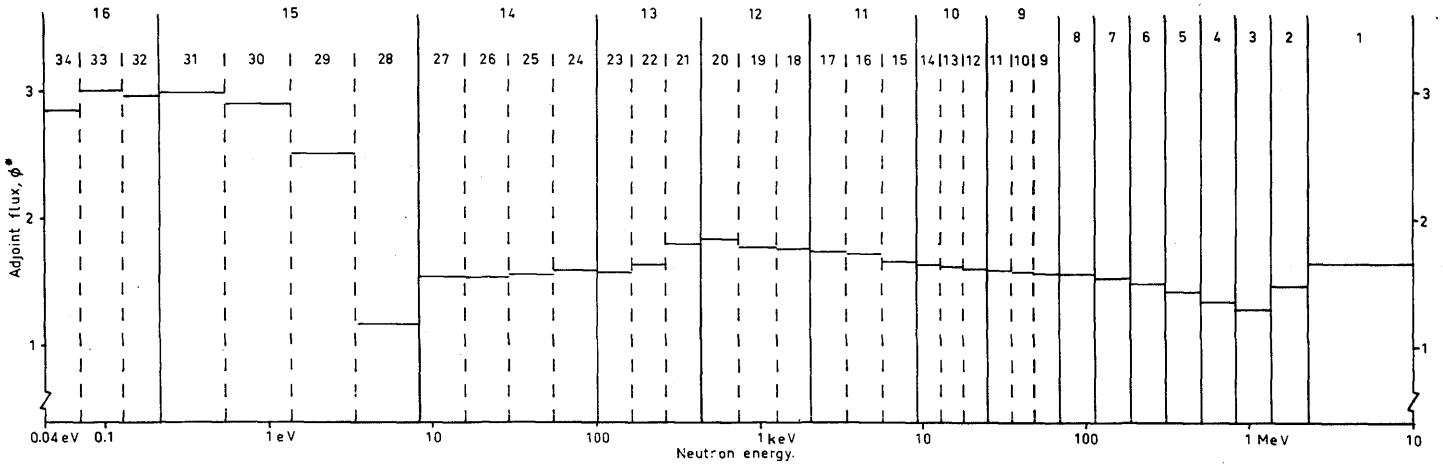

FIG.4. The group structure for the 16- and 34-group calculations together with the 34-group adjoint flux for core 5.

flux generally varies only slowly with energy, makes it possible to use group fluxes calculated for the unperturbed system. The hole in the centre to accommodate the sample can thus be neglected.

16-group transport theory (DSN) and 34-group diffusion theory (MONDAY) calculations have been used for determining ϕ_i and ϕ_i^x. The group structure and ϕ_i^x for core 5 are illustrated in Figure 4. For the hard spectrum core the calculated ratios appearing in Eq. 1 are not very sensitive to the number of groups. In core 5, on the other hand, a large proportion of the total reaction rates in the fissionable materials and in boron occurs below a few hundred electron volts. The adjoint weighted reaction rates thereby become sensitive to the division in energy of the groups as there appear local dips in the adjoint flux in energy regions where U^{238} has strong resonances. The effect is especially important for boron, less so for Pu^{239} and even less for U^{235}. The product of the last two ratios in Eq. 1 differs for instance with x = Pu^{239} by 2.5 % when going from the 16-group calculation to one with 34 groups - the additional 18 groups in the latter case then being used to subdivide the low energy groups in the 16-group treatment.

The sensitivity of the choice of lethargy steps was investigated by some separate calculations. It was found that once the lower groups, especially Nos. 13, 14 and 15, had been divided into 3-4 subgroups, no change in the above-mentioned product was obtained by an increased number of subgroups.

Group constants for capture in boron-10 were obtained from the recent measurements by Diment [9] for energies below 500 keV and from an available UKAEA library tape for higher energies.

Groups values of χ^x, ν^x and the fission and capture cross-sections in U^{235} and Pu^{239} were obtained from the SPENG programme and its library [10, 11]. The ν values used in SPENG are based on the following expressions: $\nu = 2.43 + 0.12\ E\ (U^{235})$ and $\nu = 2.87 + 0.13\ E\ (Pu^{239})$, the units of E being MeV. The energy independent term in both expressions is the dominant one. It is known to an accuracy of 0.5 % [12].

The difference in weight between the virgin fission neutrons and those absorbed in the sample is taken into account in the first term in the RHS of Eq. 1. The correction is not large - at most about 5 % - and the total uncertainty of the effective ν value is put equal to $\pm$ 1 %.

The U^{235} data are the same as those used for some time at FRO. The fission cross-sections between 40 keV and 14 MeV are based on White's measurements [13]. The α value from 10 eV to 1 MeV is taken from [14] and the resonance parameters for U^{235} up to 1 keV from [15] and [16]. The data between 1 keV and 40 keV are obtained from [15] and [17].

The Pu^{239} cross-sections are based on a number of measurements and evaluations. Rather than quoting these references the fission cross-sections and α values used are displayed for some discrete energies in Table III. Above 100 keV the data from Davey's analysis [18] are used and below 1 keV Schmidt's evaluation [19] has been used.

It should be stressed that when deducing a value of α from our measurements the effect of erraneous assumptions concerning the cross-sections for boron and the fissionable materials is strongly reduced by the fact that the cross-sections in question appear in the numerator as well as in the denominator in the terms on the RHS of Eq. 1.

TABLE III: σ_f AND α FOR Pu^{239} FOR THE ENERGY REGION 1.5 TO 100 keV

E (keV)	100	86	75	63	52	42.5	37.5	27.3	25.0	21.0	17.5	12.5	9.0	7.0	5.5	4.5	3.5	2.5	1.5
σ (b)	1.56	1.66	1.53	1.64	1.66	1.55	1.77	1.78	1.82	2.14	2.20	2.22	2.30	2.21	2.71	2.31	2.75	2.64	3.82
α	0.112	0.179	0.166	0.178	0.185	0.246	0.270	0.310	0.365	0.400	0.450	0.55	0.65	0.72	0.76	0.78	0.82	0.87	0.93

III.2. Correction of reactivity signals

In the evaluation of α for Pu^{239} we assume that there is no overlapping between the core fuel resonances and those in the plutonium sample. For an infinitely thin sample unshielded Pu^{239} cross-sections should therefore be used in Eq. 1. However, the sample used was not thin enough to make self-shielding effects negligible. The conversion of the measured Pu reactivity signal per atom in the actual sample to that for an infinitely thin sample was determined by a perturbation calculation. The correction was slightly less than 5 % for core 5 and about 1 % for core 8.

The effect of the Pu^{240} and Pu^{241} content was calculated with the same perturbation code.

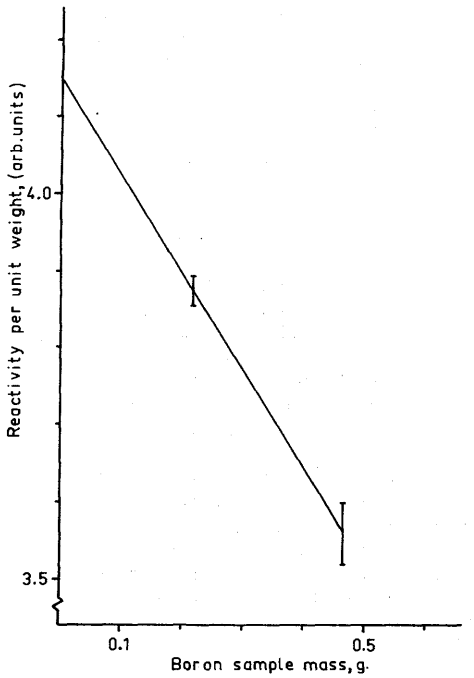

FIG.5. The boron reactivity signal in core 5 as a function of sample mass.

The U^{235} sample was heavily shielded by the surrounding core fuel. The additional shielding in the sample itself should be small and was set equal to one per cent for core 5 and to zero for core 8. The former figure was an estimate based on a determination of the fission rate in the centre of the core with and without the tubular U^{235} sample surrounding the fission chamber. The correction for the U^{238}, U^{236}, and U^{234} content was obtained as for the Pu sample.

The effective background cross-section for U^{235} in core 5 and core 8 was 110 b and 90 b, respectively. The U^{235} cross-sections corresponding to these background values were used in Eq. 1. The experimental values of α should consequently be compared with the values calculated with these shielded cross sections.

The size dependence of the boron signal was measured in core 5. Two samples of different thickness but otherwise identical form were used. The results are displayed in Figure 5. A linear extrapolation to zero thickness has been made. The correction amounted to (7.2 ± 1.0)%.

No such measurement was made for core 8. Instead the ratio of the boron reaction rate at the core centre with and without the surrounding boron samples was measured and compared with the same value for core 5. The reactivity correction for core 8 relative to that for core 5 could with sufficient accuracy be obtained from the difference in the two reaction rate ratios. The correction applied was 1 %.

The small effects of slowing down and of other capture reactions than $B^{10}(n,\alpha)$ have been estimated theoretically. Furthermore, the boron content of the boron samples was only 93.5 %. A chemical analysis revealed no impurities that could affect the reactivity signal of the sample, however.

III.3. Correction of reaction rates

The correction for other isotopes than Pu^{239} and U^{235} in the fission chambers is straight-forward. The self shielding in the two chambers was negligible. The reaction rates thus corresponded to unshielded cross-sections for Pu^{239} and to those for the core composition for U^{235}.

For the boron counter results the effect of boron and fluorine recoils had to be taken into account. The correction could not be estimated by calculations because wall effects, anisotropy in the scattering and uncertainties concerning the ratio of elastic to inelastic events made it a too difficult problem. An approximate estimate was instead obtained in the following way. We assumed that for small pulse amplitudes (close to the discriminator level) the fast spectrum curve (compare Figure 3) was only distorted by the effect of the recoils. The difference, A, between the normalized fast and thermal spectrum curves was then equal to the recoil contribution for these amplitudes. It should decrease rather rapidly with increasing pulse amplitudes and we have crudely put the integrated effect equal to one fourth of what it would have been for a constant recoil contribution A for all channels used. In this way we obtained a correction for core 5 corresponding to a reduction of the measured rate by (1.5 ± 1)% and for core 8 by (3.5 ± 1.5)%.

Each type of reaction rate was measured with two different detectors. The ratios for Eq. 1 derived from different combinations of these detectors agreed within 1 %.

IV. RESULTS

The different terms in Eq. 1 have been listed in Table IV together with the experimental and calculated values of α.

In calculating the experimental errors (standard deviations) the following contributions have been estimated for the different terms and factors in Eq. 1: ± 1 % for the first term, ± 2 % (core 5) and 1.5 % (core 8) for the reactivity ratios (including shielding corrections), ± 1.5 % (core 5) and 2.5 % (core 8) for the reaction rate ratios and ± 1 % each for the following two calculated ratios. The main part of the uncertainties quoted for the reaction rate ratios stems from the boron measurement.

TABLE IV: VALUES OF THE DIFFERENT TERMS IN Eq. (1).
COMPARISON BETWEEN CALCULATED AND EXPERIMENTAL α - VALUES

Core		First term, ν_{eff}, RHS, Eq. 1	Second term, RHS, Eq. 1	$1 + \alpha'$	$\frac{\alpha}{\alpha'}$ (calc.)	α	
						Exp.	Calc.
5	Pu^{239}	2.778	1.328	1.450	0.939	0.42 ± 0.05	0.36
	U^{235}	2.304	0.860	1.444	0.975	0.43 ± 0.04	0.32
8	Pu^{239}	2.997	1.816	1.181	0.928	0.17 ± 0.07	0.20
	U^{235}	2.463	1.221	1.242	0.972	0.24 ± 0.05	0.25

The conversion of α' to α (Section II.1) is a correction of about 8 % for Pu^{239} and 3 % for U^{235}. The uncertainty in this figure should be less than 10 % corresponding to an uncertainty in α of about ± 1 %.

The calculated values are based on the SPENG data discussed in Section III.1. The capture cross-sections for Pu^{239} below 1 keV are unfortunately not up to date and should be increased somewhat to match the data above 1 keV recommended by Sowerby [2]. It is estimated that such a change would increase α^{49} for core 5 to 0.37 - 0.38.

The experimental value of α^{49} in core 5 is slightly higher than the theoretical but with the changes mentioned above the values agree within the experimental error. The old data of σ_c^{49} between 1 and 15 keV would have given a calculated value of 0.33 which is clearly outside the experimental error. Assuming the calculated group fluxes to be correct (compare below) the present measurement thus supports Sowerby's evaluation.

For core 8 the calculated and experimental values agree well but the relative error of the latter is large.

The cross-section data for U^{235} are better established than those for Pu^{239}. Good agreement was therefore expected between experiments and calculations. For core 5, however, the experimental value is much higher than the calculated one. This could be an indication that the calculated group fluxes in the low energy end of the spectrum are too low. Quite drastic changes are required, however, to bring the calculated value for U^{235} up close to the experimental one. Thus an increase of the flux below 500 eV by a factor of two only raises α from 0.32 to 0.37 which is still outside the experimental limits of error. Detailed reaction rate measurements with different detectors will in the near future be performed in the homogeneous central region of core 5 in an effort to check the spectrum calculations.

For core 8 the difference is small, the calculated value being well within the limits of error for the experimental one.

The hard spectrum measurements have larger uncertainties than those for core 5. This is due to the difficulties encountered with the boron reaction rate determination, not expected when the measurements started. We actually also made a set of measurements on a core with a still harder spectrum (core 3, spectrum given in [6]), but the recoil correction for that spectrum was quite dominant and hence, the results became very uncertain. Measurements on a core with a spectrum between that of core 5 and core 8 would have been a better choice.

The result of the present work as well as that of other authors clearly indicates that good relative accuracy in the integral α measurements can only be obtained in soft spectrum cores. Due to the strong increase of α at low energies, however, measurements on such cores entail the requirement that the calculation of the low energy part of the neutron spectrum must be quite accurate to allow a meaningful comparison between calculated and experimental α values.

ACKNOWLEDGEMENT

The authors want to express their sincere thanks to the FRO crew under A. Pettersson who skilfully took part in and with great patience endured the sometimes quite tedious measurements. They also gratefully acknowledge the advice and help concerning theoretical questions and cross-section data given by H. Häggblom.

The authors are furthermore much indebted to the ZEBRA group at Winfrith for the loan of the Pu^{239} and U^{235} samples.

REFERENCES

[1] ADAMSON, J., ABSALOM, R.M., BAKER, A.R., INGRAM, G., PATTENDEN, S.K.I. and STEVENSON, J.M., ANL-7320 (1966) 216

[2] SOWERBY, M.G. and PATRICK, B.H., "An Evaluation of $\alpha(E)$ for Pu^{239} in the Energy Range 100 eV to 15 MeV" (private communication)

[3] FEINER, F. and ESCH, L.J., "Reactor Physics in the Resonance and Thermal Regions", Vol. II, 1966, The MIT Press, Cambridge, USA

[4] REDMAN, W.C. and BRETSCHER, M.M., Nucl. Sci. and Eng. 27 (1967) 34 Compare also ANL-7210 (1966)

[5] FOX, W.N., RICHMOND, R., SKILLINGS, D.J. and WHEELER, R.C., Journal of BNES 6 No. 1 (1967) 63

[6] TIRÉN, I., GUSTAFSSON, I., HELLSTRAND, E. and HÅKANSSON, R., "Studies of the Doppler Coefficient and the Reactivity Effect of Polythene in Some Fast Reactor Spectra", SM-101/3, this conference

[7] ANDERSSON, T.L., "Reaction Rate Distributions and Ratios in FRO Assemblies 1, 2 and 3", AE-229 (1966)

[8] BNL-325, Second Edition, Suppl. No. 2, Vol. I (1964)

[9] DIMENT, K.M., "The Average Neutron Total Cross Section of B^{10} from 100 eV to 10 MeV and Absorption Cross Section up to 500 keV", (private communication)

[10] NYMAN, K. and HÄGGBLOM, H., AB Atomenergi, Sweden, Internal Report RFR-540 (1966)

[11] NYMAN, K., AB Atomenergi, Sweden, Internal Report RFN-279 (1967)

[12] WESTCOTT, C.H., EKBERG, K., HANNA, G.C., PATTENDEN, N.J. SANATANI, S. and ATTREE, P.M., Atomic Energy Review, Vol. 3, No. 2 (1965)

[13] WHITE, P.H., J. Nucl. Energy 19 (1965) 325

[14] de SAUSSURE, G., WESTON, L.W., GWIN, R. and RUSSELL, J.E., WASH-1053 (1964)

[15] BNL-325, Second Edition, Supplement 2, Vol. III (1965)

[16] SCHMIDT, J.J., "Evaluation of Neutron Resonance Data of U^{235} for KFK 120, Parts II and III", AEC-ENEA Seminar on the Evaluation of Neutron Cross Sections, BNL (1965)

[17] MICHAUDON, A., GENIN, R., JOLY, R. and VENDRYÈS, G., CEA-1093 (1958)

[18] DAVEY, W.G., Nucl. Sci. Eng. 26 (1966) 149

[19] SCHMIDT, J.J., "Evaluation of Neutron Resonance Data of Pu^{239} in the Energy Regions of Resolved and Unresolved Resonances, AEC-ENEA Seminar on the Evaluation of Neutron Cross Sections, BNL (1965)

DISCUSSION

R.D. SMITH: Have you calculated the breeding gains of plutonium-fuelled reactors with spectra similar to those for which you have measured α? If so, how much lower are the calculated breeding gains of these reactors than the values calculated with the α-values commonly used before the recent data from Harwell became available?

K.M. JIRLOW: Perhaps I may be allowed to answer this question. We have not made any direct comparison between the breeding ratio obtained with the FD2 set and that obtained from the plutonium cross-sections referred to by Mr. Hellstrand. However, we have compared results obtained using these cross-sections with those derived from the plutonium data recommended in KFK 120, Parts II and III (published by the Gesellschaft fur Kernforschung m.b.H., Karslruhe, in 1962). We found that for steam-cooled reactors of the D1 type the decrease in breeding ratio is only about 0.03, whereas the doubling time penalty is about 20% larger, owing to the increased enrichment.

HETEROGENEITY IN FAST CRITICAL EXPERIMENTS

(Session VII, Part 1)

Chairman: W.B. LOEWENSTEIN

HETEROGENEITE DANS L'ASSEMBLAGE 1-A DE MASURCA

A. KHAIRALLAH, T. LACAPELLE ET F. STORRER
ASSOCIATION EURATOM-CEA,
CENTRE D'ETUDES NUCLEAIRES DE CADARACHE,
FRANCE

Abstract — Résumé

HETEROGENEITY IN THE MASURCA 1-A ASSEMBLY. This paper describes a study of the heterogeneity problem in the 1-A core of MASURCA. Attention is given mainly to the effects of heterogeneity on the critical mass, which are studied under two headings: (1) effects of heterogeneity in an infinite medium, including the effect of the metal plugs of the fuel rods – the calculations were carried out with both a Monte Carlo code and the PERHET code; (2) effects of heterogeneity on leakages, including the effect of the cooling spaces round the rods and the interstices between tubes – the calculations were carried out with a Monte Carlo code and by the Benoist methods for calculating leaks. The results are presented and discussed.

HETEROGENEITE DANS L'ASSEMBLAGE 1-A DE MASURCA. Le mémoire décrit l'étude du problème de l'hétérogénéité dans le cœur 1-A de MASURCA. L'intérêt porte surtout sur les effets de l'hétérogénéité sur la masse critique. L'étude de ces effets a été divisée en deux parties: 1) effets d'hétérogénéité en milieu infini, incluant l'effet des bouchons d'acier des réglettes de combustible – les calculs ont été effectués parallèlement avec un code Monte-Carlo et avec le code PERHET; 2) effets de l'hétérogénéité sur les fuites, incluant l'effet des vides de refroidissement autour des réglettes et des vides inter-tubes – les calculs ont été effectués, d'une part avec un code Monte-Carlo, d'autre part par les méthodes de Benoist pour le calcul des fuites. Les résultats obtenus sont présentés et discutés.

1. INTRODUCTION

En plus de sa haute teneur en carbone, l'assemblage 1-A de MASURCA, décrit dans un autre mémoire [1], se distingue des assemblages réalisés dans d'autres maquettes critiques par son type d'hétérogénéité. Les éléments de combustible sont en effet composés d'un alliage métallique U-Pu-Fe enrichi à 25% sous forme de barreaux cylindriques (diamètre 12,7 mm, longueur 101,6 ou 203,2 mm) gainés d'acier inoxydable. Chaque barreau comporte à chaque bout un bouchon d'acier dont l'épaisseur est d'environ 2% de la longueur du barreau. Comme ces barreaux sont insérés dans un réseau de réglettes carrées, chaque barreau est entouré de quatre petits canaux vides qui servent au passage de l'air de refroidissement (fig. 1a). D'autre part, un intervalle vide de 1 mm existe entre deux tubes voisins (tubes carrés de 10 cm de côté). La forme cylindrique des éléments de combustible rend difficile l'emploi des méthodes de transport habituelles du type SN à une dimension, couramment utilisées pour le calcul des effets d'hétérogénéité dans les réseaux à plaquettes.

Les calculs effectués et décrits ici ont pour principal objet l'évaluation des effets de l'hétérogénéité sur le coefficient de multiplication, c'est-à-dire sur la masse critique de l'assemblage 1-A. Ces calculs sont de deux types:

a) Calculs analytiques plus ou moins approchés

L'effet d'hétérogénéité en milieu infini est calculé en utilisant le code de perturbations PERHET [2] sur un réseau simplifié et rendu critique par l'introduction de captures fictives équivalentes aux fuites.

L'effet sur les fuites des vides inter-tubes et de la structure hétérogène du réseau (en particulier vides de refroidissement) est calculé en utilisant la théorie de Friedman [3] pour une fente centrale, et la théorie de Benoist [4] pour le coefficient de diffusion dans un réseau comportant des cavités.

b) Calculs Monte-Carlo

Le code Monte-Carlo utilisé n'est pas adapté au calcul précis de faibles variations de réactivité (inférieures à 100×10^{-5} ΔK), à moins d'y consacrer des temps de calcul prohibitifs. Il a surtout servi à obtenir avec une bonne précision une valeur globale des effets d'hétérogénéité dans la géométrie réelle du cœur, et à vérifier l'ordre de grandeur de certains effets calculés par les méthodes analytiques.

Les résultats de ces calculs sont comparés à ceux que l'on peut déduire des expériences d'hétérogénéité effectuées dans l'assemblage 1-A (groupement de barreaux quatre par quatre [1]), en utilisant pour l'extrapolation une courbe calculée.

Dans l'ensemble, les différents résultats de calcul et d'expérience sont assez cohérents. L'effet global de l'hétérogénéité dans l'assemblage 1-A serait de l'ordre de $(2,5 \pm 0,5)\%$ sur K_{eff}, ce qui correspondrait à un gain de près de $(13 \pm 2,5)\%$ sur la masse critique homogène.

2. DESCRIPTION ET RESULTATS DES CALCULS ANALYTIQUES

Le jeu de sections efficaces multigroupes utilisé est celui à 16 groupes de Hansen et Roach [5]. Des corrections de «dilution» (auto-protection des résonances) ont été effectuées séparément pour le milieu homogène et pour chacun des milieux hétérogènes étudiés. Pour les corrections de dilution en milieu hétérogène, la section efficace effective de diffusion de potentiel a été définie selon la relation d'équivalence bien connue entre un milieu hétérogène et le milieu homogène correspondant. La relation utilisée pour le calcul de $\bar{\sigma}_{p_x}$ pour l'isotope x du combustible est:

$$N_x \bar{\sigma}_{p_x} = \sum_{j \in comb.} N_j \sigma_{p_j} + \frac{a\,(1-c)}{\bar{\ell}}$$

où

N_x = nombre d'atomes de l'isotope x par cm^3 du combustible
N_j = nombre d'atomes de l'isotope j par cm^3 du combustible
$\bar{\ell}$ = corde moyenne de l'élément combustible
(1-c) = facteur de Dancoff calculé dans l'approximation de Sauer [6]
a = facteur de Bell, calculé suivant la méthode de Leslie et al. [7]

2.1. Calculs de l'effet en milieu infini, à l'aide du code PERHET

Le code PERHET [2] est un code de perturbation employant le formalisme des probabilités de collision, qui permet de calculer l'effet d'hétérogénéité sur le coefficient de multiplication dans le milieu

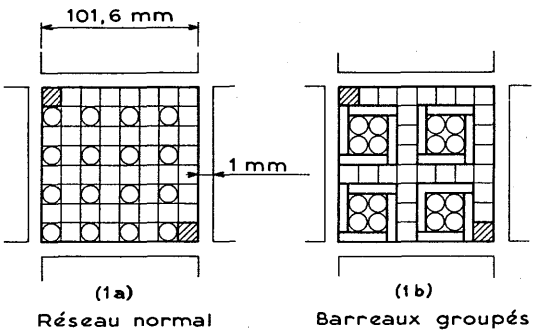

FIG.1. Coupe d'un tube cœur.

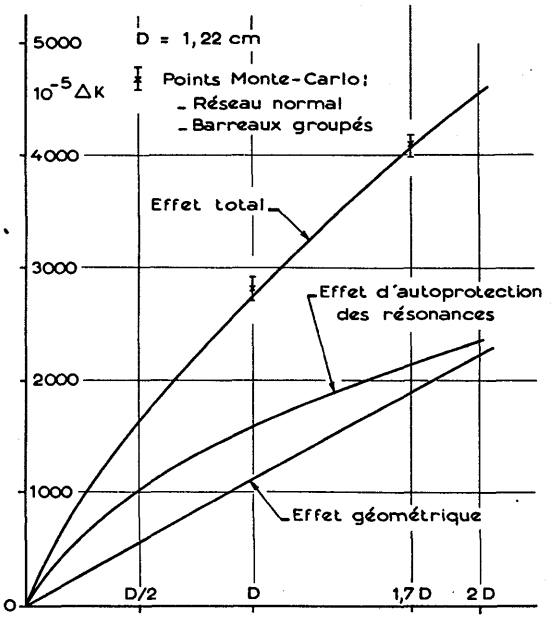

FIG.2. Effet d'hétérogénéité en milieu infini en fonction du diamètre du barreau (PERHET).

infini équivalent au milieu fini étudié. Ce milieu infini est rendu critique par l'introduction de sections efficaces de capture fictive équivalentes aux fuites nettes du cœur. Ces dernières sont tirées du bilan de neutrons d'un calcul de transport à deux dimensions du réacteur homogène critique. Pour l'utilisation de PERHET, on a supposé le milieu hétérogène composé de deux régions: le combustible, supposé en colonnes continues (c'est-à-dire sans bouchons) mais de densité réduite pour garder constante la masse de combustible; le diluant, comprenant tous les autres matériaux homogénéisés (graphite, parois de tubes, taquets d'acier, vides de refroidissement et vides inter-tubes, gaines et bouchons des barreaux de combustible); le rapport des volumes de ces deux régions est pris égal au rapport réel $V_{combust.}/(V_{total} - V_{combust.})$.

En plus de la cellule de base du réseau actuel (diamètre des barreaux D = 12,2 mm), des calculs ont été effectués pour les cas D/2, 1,7 D et 2 D, en vue d'obtenir la courbe de l'effet d'hétérogénéité en fonction du diamètre du barreau. Ces calculs ont donné les résultats suivants:

Diamètre du barreau	D/2	D	1,7 D	2 D
Effet d'hétérogénéité sur K_{eff} (10^{-5} ΔK)	+ 1610	+ 2735	+ 4035	+ 4535

Les résultats se trouvent également sur la figure 2, où sont aussi tracées les deux courbes correspondant aux deux composantes de l'effet global: l'effet de géométrie et l'effet de variation des sections efficaces effectives.

On peut remarquer que l'effet d'hétérogénéité en fonction du diamètre du barreau n'est pas linéaire. On reviendra sur ce point à la section 4.

2.2. Effets des hétérogénéités sur les fuites

On évalue de façon indépendante les effets
- de la structure de réseau comportant: barreaux de combustible (u), canal de refroidissement (c) et modérateur (m) (réseau normal: cf. fig. 3a; barreaux groupés quatre par quatre: cf. fig. 3c);
- des intervalles de 1 mm entre les tubes (cf. fig. 1a).

2.2.1. Structure en barreaux

L'effet de la structure en barreaux sur les coefficients de diffusion est évalué suivant la méthode classique de Benoist [4], dont nous utilisons les notations.

On fait les approximations suivantes: diffusion isotrope, flux plat, corrections de couplage entre groupes d'énergies négligées, milieux cylindrisés à volumes constants pour passer aux géométries de calcul (fig. 3b et 3d).

Le calcul du coefficient de diffusion D_k dans la direction k (k = r ou z) nécessite alors simplement l'évaluation des probabilités de collision directionnelles P_{ij}^{k} * tenant compte des interactions entre barreaux.

Ces probabilités sont évaluées à l'aide:
- du sous-programme ALCOLK (une dimension, 50 milieux pouvant comporter des vides [8]),
- du code PROCOPE [9, 10] (deux dimensions, deux milieux, pas de vides).

Ce dernier code, assez coûteux en temps de calcul, a servi à étudier l'interaction entre barreaux. On a vérifié pour quelques groupes d'énergie qu'il suffisait d'utiliser ALCOLK, en cylindrisant la cellule élémentaire du réseau à volumes constants.

Ayant ainsi calculé les écarts (D_k - D_{hom}), on a évalué leurs effets en réactivité par calculs de perturbations. L'effet total obtenu est de

- 93×10^{-5} ΔK pour le réseau normal
- 142×10^{-5} ΔK quand les barreaux d'U-Pu-Fe sont groupés quatre par quatre.

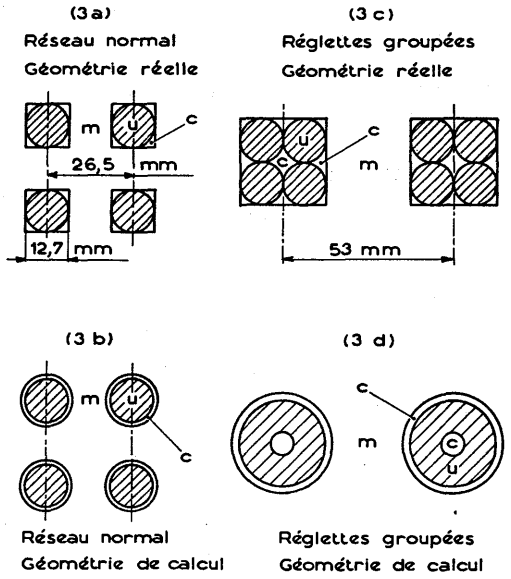

FIG.3. Effet de la structure en réglettes sur le coefficient de diffusion.

L'incertitude sur ces valeurs est probablement relativement faible.

Au tableau I on a porté le détail, suivant les groupes d'énergie, des anisotropies calculées et de leurs effets en réactivité.

2.2.2. Intervalles entre tubes

Supposant les tubes homogénéisés avec leur contenu, on cherche à évaluer l'effet en réactivité du passage du réacteur homogène au réacteur réel avec son réseau de fentes et de mêmes dimensions extérieures.

On a utilisé la théorie de perturbations pour les piles à fente centrale, élaborée indépendamment par Friedman [3] et par Benoist et Horowitz [11].

Les approximations faites sont les suivantes: théorie à un groupe, pile nue cubique. Pour un réseau de fentes, nous négligeons de plus les interactions entre fentes.

Considérons d'abord une fente centrale; cherchons la variation de réactivité quand on passe du réacteur à fente ① au réacteur homogénéisé de même taille extérieure ③ (fig. 4).

Soient:

B_2^2 le laplacien géométrique ($\simeq 0,00375\ cm^{-2}$)
B_r le laplacien radial ($\simeq 2/3\ B^2 = 0,00250\ cm^{-2}$)
M^2 l'aire de migration des neutrons ($\simeq 168\ cm^2$)
L la hauteur totale extrapolée de la pile ($\simeq 88,8$ cm)
λ le libre parcours moyen des neutrons ($\simeq 3,5$ cm)
δ la largeur de la fente (= 0,1 cm)

La théorie de la pile à fente centrale [3] donne pour l'effet en réactivité du rapprochement des deux moitiés du cœur (passage de ①

TABLEAU I. MASURCA 1-A - EFFET DE LA STRUCTURE EN BARREAUX SUR LES COEFFICIENTS DE DIFFUSION

Groupe Hansen & Roach	Réseau normal			Barreaux groupés quatre par quatre		
	$\left(\frac{D_z}{D_{hom}} - 1\right)$ (%)	$\left(\frac{D_r}{D_{hom}} - 1\right)$ (%)	ΔK_{total} ($\times 10^{-5}$)	$\left(\frac{D_z}{D_{hom}} - 1\right)$ (%)	$\left(\frac{D_r}{D_{hom}} - 1\right)$ (%)	ΔK_{total} ($\times 10^{-5}$)
1	0,51	0,27	- 5,4	0,77	0,42	- 8,3
2	0,46	0,24	-12,7	0,69	0,38	-19,4
3	0,15	0,075	- 1,9	0,28	0,13	- 3,4
4	0,20	0,098	- 3,8	0,41	0,20	- 7,9
5	0,31	0,16	- 4,6	0,52	0,24	- 8,9
6	0,86	0,48	-16,8	1,2	0,70	-24,5
7	1,3	0,76	-18,0	1,9	1,1	-26,0
8	1,7	0,99	-14,8	2,4	1,5	-21,4
9	3,1	1,9	-10,4	4,3	2,9	-15,1
10	3,5	2,2	- 3,0	4,9	3,3	- 4,3
11	5,5	3,5	- 1,4	7,5	5,4	- 2,0
12	3,1	1,9	- 0,2	4,3	2,9	- 0,32
13	17,3	12,0	- 0,16	22,7	17,9	- 0,22
14	27,2	19,7	- 0,05	35,1	28,5	- 0,06
15	288	241	- 0,003	336	301	- 0,004
16	219	182	- 0,00007	256	229	- 0,00009
Total			-93,2			-141,9

à ②, fig. 4):

$$\left.\frac{\Delta K}{K}\right|_{① \to ②} = \frac{M^2B^2}{1 + M^2B^2}\left[4\frac{B_r^2}{B^2}\frac{\delta}{L} - \frac{3}{2}\frac{B_r^2}{B^2}\frac{\delta^2}{L\lambda}\ln\left(\frac{B_r\,\delta}{2}\right)\right]$$

Pour une fente étroite le premier terme est prédominant. L'effet du passage du réacteur «compacté» ② au réacteur homogénéisé ③, qui comporte une augmentation de hauteur et une diminution corrélative de densité, peut s'évaluer par la théorie élémentaire des perturbations.

On obtient finalement

$$\left.\frac{\Delta K}{K}\right|_{① \to ③} = \frac{M^2B^2}{1 + M^2B^2}\left[2\frac{B_r^2}{B^2}\frac{\delta}{L} - \frac{3}{2}\frac{B_r^2}{B^2}\frac{\delta^2}{L\lambda}\ln\left(\frac{B_r\,\delta}{2}\right)\right]$$

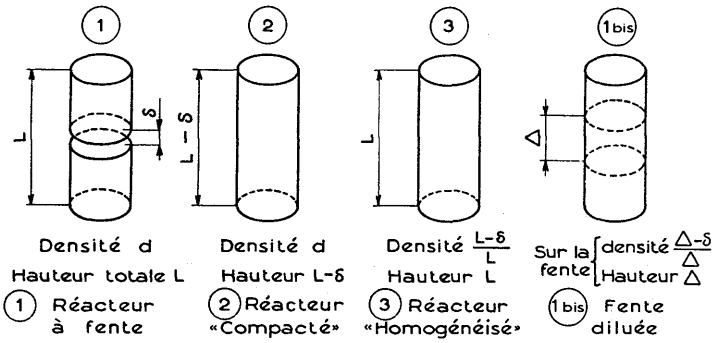

FIG.4. Effet des intervalles entre tubes.

Considérons maintenant un réacteur (1bis) où la fente centrale serait diluée sur une largeur Δ : $\delta \ll \Delta \ll L$.

On montre aisément que l'effet du passage du réacteur à «fente diluée» (1bis) au réacteur homogène (3), évalué par théorie de perturbations élémentaire, n'est autre que le terme du premier ordre en δ dans le passage de (1) à (3) :

$$\left.\frac{\Delta K}{K}\right|_{1bis \to 3} = \frac{M^2 B^2}{1 + M^2 B^2} \frac{B_r^2}{B^2} \frac{2\delta}{L}$$

Pour un réseau serré de fentes couvrant tout le réacteur, ces termes du premier ordre ont une contribution globale nulle, par compensation entre fentes centrales et fentes placées en périphérie, dont les effets du premier ordre en δ sont de signes contraires. Seul subsiste le terme du deuxième ordre; celui-ci a été considéré comme une capture localisée supplémentaire, et pondéré sur le carré du flux.

Pour une pile nue équivalente à MASURCA 1-A, le terme du deuxième ordre vaut

pour une fente centrale: $7,5 \times 10^{-5}\ \Delta K$

pour un double réseau de fentes: environ $60 \times 10^{-5}\ \Delta K$.

On en conclut qu'avec une très forte incertitude (non chiffrable) due aux larges approximations, l'effet en réactivité des intervalles entre tubes dans MASURCA 1-A est voisin de $-60 \times 10^{-5} \Delta K$.

2.2.3. Effet total

Finalement l'effet total des hétérogénéités sur les fuites représenterait environ $-150 \times 10^{-5}\ \Delta K$ pour le réseau normal

environ $-200 \times 10^{-5}\ \Delta K$ pour le réseau à barreaux groupés quatre par quatre.

L'incertitude est importante, mais cet effet ne constitue qu'une correction dans l'effet d'hétérogénéité global.

2.3. Conclusion

Des résultats qui précèdent on peut conclure que les effets d'hétérogénéité sur les fuites sont faibles par rapport à l'effet d'hétérogénéité

sur K_{eff} en milieu infini. De ces résultats on déduit une première évaluation de l'effet global d'hétérogénéité pour le réseau normal de l'assemblage 1-A:

$$[2735 - (90 + 60)] \times 10^{-5} = 2585 \times 10^{-5}\ \Delta K$$

3. CALCULS MONTE-CARLO

Le code utilisé pour ces calculs est un code Monte-Carlo multigroupe [12], écrit spécialement pour le calcul de réacteurs dont la géométrie (hétérogénéité, contour irrégulier) peut être d'une assez grande complexité. Le code peut traiter des milieux finis ou infinis. Diverses particularités dans la poursuite des neutrons et dans la programmation [13] permettent d'atteindre des précisions statistiques correctes en des temps de calcul raisonnables. Pour donner un ordre de grandeur des temps de calcul nécessaires, on peut dire qu'en 10 minutes d'IBM 360/75, les écarts-types (σ) obtenus sur K_{eff} sont de l'ordre de:

$30 \times 10^{-5}\ \Delta K$ pour un milieu infini homogène

100 à $150 \times 10^{-5}\ \Delta K$ pour un milieu infini hétérogène

400 à $500 \times 10^{-5}\ \Delta K$ pour un milieu fini, homogène ou hétérogène,

suivant la complexité de la géométrie. Il faut évidemment beaucoup plus de temps de calcul pour atteindre de plus grandes précisions statistiques, ce dernier étant, grosso modo, inversement proportionnel à la variance σ^2. Quoique ce code semble être nettement plus rapide que d'autres codes Monte-Carlo du même type, il est clair qu'il n'est pas adapté au calcul précis de faibles variations de réactivité de l'ordre de 100 à $200 \times 10^{-5}\ \Delta K$.

Il a servi principalement à obtenir un effet global d'hétérogénéité dans des conditions de complexité géométrique très proches de la réalité et à tester la validité des approximations utilisées dans les calculs analytiques précédents.

Deux types de calculs ont été effectués:

3.1. Calcul des effets d'hétérogénéité en milieu infini

Le but de ces calculs est de vérifier que les approximations utilisées par le code PERHET, en particulier l'homogénéisation du diluant et l'homogénéisation des bouchons d'acier des barreaux dans le diluant, n'introduisent pas d'erreur appréciable.

De la même façon que pour PERHET, les fuites nettes du cœur sont représentées par des sections efficaces de capture fictive constantes sur tous les milieux du réseau. Les résultats des différents calculs effectués sont les suivants:

	$\Delta K \pm \sigma$
$1 \longrightarrow 2$	$+ (2830 \pm 115) \times 10^{-5}$
$1 \longrightarrow 3$	$+ (2825 \pm 115) \times 10^{-5}$
$1 \longrightarrow 4$	$+ (2690 \pm 115) \times 10^{-5}$

Le cas 1 est celui d'une cellule où tous les matériaux sont mélangés de façon homogène; le calcul est effectué avec les sections efficaces effectives homogènes. Dans le cas 2, la cellule est hétérogène et est

constituée par un tube du cœur de MASURCA 1-A, incluant tous les détails de géométrie; les sections efficaces effectives sont celles du milieu hétérogène. La différence entre les cas 1 et 2 donne l'effet de toutes les hétérogénéités en milieu infini. Le cas 3 sert à vérifier l'approximation qui consiste à homogénéiser le diluant (sauf les bouchons des barreaux). La comparaison du gain de réactivité obtenu entre 1 et 3 à celui obtenu entre 1 et 2 montre que cette hypothèse est justifiée.

Enfin le cas 4 est celui de la cellule utilisée dans PERHET. Le gain de réactivité obtenu entre 1 et 4 est en bon accord avec le résultat du calcul PERHET. Sa comparaison avec le gain obtenu entre 1 et 2 semble indiquer que la représentation schématisée de la cellule dans PERHET tendrait à sous-estimer légèrement l'effet d'hétérogénéité, encore que la précision des calculs Monte-Carlo ne permette pas de trancher.

Conclusion

De ces résultats Monte-Carlo en milieu infini et des résultats analytiques concernant les fuites, on tire une deuxième évaluation des effets d'hétérogénéité dans l'assemblage 1-A, légèrement supérieure à celle déduite du calcul PERHET, soit $(2830 \pm 115) \times 10^{-5} - 150 = (2680 \pm 115) \times 10^{-5}\ \Delta K$. L'écart-type de $115 \times 10^{-5}\ \Delta K$ ne tient pas compte de l'incertitude sur les effets d'hétérogénéité sur les fuites.

3.2. Calculs Monte-Carlo en milieu fini

Malgré les temps de calcul importants, quelques calculs Monte-Carlo ont été effectués en milieu fini pour obtenir un effet global d'hétérogénéité dans la géométrie réelle de MASURCA 1-A.

L'assemblage 1-A comporte une couverture et un écran d'acier dont les épaisseurs sont respectivement: environ 18 et 30 cm dans la direction radiale, 20 et 30 cm dans la direction axiale.

Dans tous les calculs Monte-Carlo en milieu fini, la couverture et l'écran ont été remplacés par une couverture de 30 cm d'épaisseur dans toutes les directions. On a vérifié que cette simplification n'a pratiquement pas d'influence sur la réactivité.

Les résultats des calculs en milieu fini sont résumés dans le tableau II.

Le cas 1 est le calcul homogène de référence: c'est celui d'un cylindre homogène de rayon 37,23 cm, rayon du cylindre de volume égal à celui du cœur actuel.

Le cas 2 correspond au réacteur homogène ayant le contour réel de l'assemblage 1-A, sans vides inter-tubes. La perte de réactivité de $-(300 \pm 200) \times 10^{-5}\ \Delta K$ due à l'effet de contour est à comparer à la valeur de $-360 \times 10^{-5}\ \Delta K$ obtenue en théorie de diffusion à deux dimensions [14].

Dans le cas 3, les vides inter-tubes ont été mis en place dans le cœur et dans les couvertures axiale et radiale. Les tubes de cœur et de couverture sont toujours supposés homogènes, mais leur densité est augmentée dans le rapport $(V_{tube} + V_{vide\ inter\text{-}tube}) / V_{tube}$, pour garder constante la quantité de matériaux dans le cœur et dans la couverture. La perte de réactivité de $-(200 \pm 160) \times 10^{-5} \Delta K$ est la résultante de trois

TABLEAU II. CALCULS MONTE-CARLO EN MILIEU FINI

Cas	Type de milieu	$K \pm \sigma$	$\Delta K \pm \sigma$
1	Cylindre homogène R = 37,23 cm	$0,99437 \pm 188 \times 10^{-5}$	
2	Contour réel, homogène sans vides	$0,99136 \pm 112 \times 10^{-5}$	$-(300 \pm 220) \times 10^{-5}$
3	Contour réel, homogène avec vides inter-tubes	$0,98936 \pm 111 \times 10^{-5}$	$-(200 \pm 160) \times 10^{-5}$
4	Contour réel, hétérogène avec vides inter-tubes	$1,01235 \pm 143 \times 10^{-5}$	$+(2300 \pm 180) \times 10^{-5}$
			$+(2100 \pm 180) \times 10^{-5}$

effets qui se compensent partiellement: augmentation des fuites à travers les vides inter-tubes, diminution des fuites à cause de l'augmentation de la densité des tubes et déplacement des matériaux depuis les vides inter-tubes vers l'intérieur des tubes. Cette valeur est à comparer à la valeur de $-60 \times 10^{-5} \Delta K$ obtenue au paragraphe 2.2.2.

Enfin le cas 4 correspond à la géométrie réelle du cœur dans tous ses détails: barreaux de combustible avec leurs bouchons et leurs gaines, vides de refroidissement, parois de tubes, vides inter-tubes, taquets d'acier. Ce calcul est effectué avec des corrections de dilution correspondant au milieu hétérogène. Le gain de réactivité de $+(2100 \pm 180) \times 10^{-5} \Delta K$ par rapport au cas 2 représente l'effet total d'hétérogénéité.

Discussion

Il apparaît un écart significatif entre cette troisième évaluation et celles déduites aux paragraphes 2.3 et 3.1 à partir des calculs en milieu infini et des corrections de fuites.

Il ne semble pas que cet écart doive être attribué à une mauvaise évaluation de l'effet des vides inter-tubes: en effet, on retrouve cet écart si l'on compare les gains de réactivité dans des situations où l'effet des vides inter-tubes n'intervient pas, c'est-à-dire:

$+(2300 \pm 180) \times 10^{-5} \Delta K$, entre les cas 3 et 4 des calculs Monte-Carlo en milieu fini;

$+ 2645 \times 10^{-5} \Delta K$ et $+ (2740 \pm 115) \times 10^{-5} \Delta K$ obtenus en retranchant l'effet sur les fuites de l'hétérogénéité de réseau ($90 \times 10^{-5} \Delta K$), respectivement des résultats PERHET et Monte-Carlo en milieu infini.

L'écart ne peut pas être non plus imputé à l'effet sur les fuites de l'hétérogénéité de réseau ($90 \times 10^{-5} \Delta K$), qu'on pense être assez bien évalué, ni aux effets de déplacement de combustible qu'on estime être de l'ordre de $20 \times 10^{-5} \Delta K$ pour le cœur entier.

On peut songer à mettre en cause l'artifice de calcul qui a été utilisé pour transformer le milieu fini en un milieu infini équivalent.

Cet artifice consistait à introduire une capture fictive représentant les fuites de l'ensemble du cœur. Or, si un tel procédé conserve le spectre moyen dans le cœur, on ne peut dire à quelle erreur il conduit sur le spectre moyen du flux adjoint. De plus, il est clair que pour une pile réfléchie un calcul de l'hétérogénéité à partir des spectres moyens des flux et flux adjoints et des sections efficaces de fuite moyennes ne donne pas l'effet d'hétérogénéité moyen. On envisage d'améliorer la précision des résultats obtenus au moyen de PERHET, en ne traitant pas le cœur dans son ensemble mais en le subdivisant en un certain nombre de zones concentriques. De la sorte on obtiendra l'effet d'hétérogénéité en fonction de la position, et par sommation on obtiendra une meilleure approximation de l'effet global. On pourra alors vérifier si ce résultat est, comme on l'espère, plus proche de celui obtenu par un calcul Monte-Carlo pour le cœur fini. Il faut noter que, même en subdivisant le cœur en plusieurs zones, le calcul PERHET reste beaucoup plus rapide que le calcul Monte-Carlo.

4. COMPARAISON AVEC LES RESULTATS EXPERIMENTAUX

4.1. Résultats expérimentaux

Le principe des expériences d'hétérogénéité effectuées dans l'assemblage 1-A est de grouper les barreaux de combustible quatre par quatre dans un ou plusieurs tubes (fig. 1b). Dans ce groupement, les barreaux sont déplacés vers leur centre de gravité, afin de rendre aussi faibles que possible les effets de déplacement de combustible tout en gardant un réseau régulier dans la zone où le groupement est effectué. Les corrections de déplacement, calculées à partir des mesures de la valeur en réactivité d'un barreau de combustible en fonction de sa distance à l'axe du réacteur, sont inférieures à 6% des effets mesurés. Deux types d'expérience ont été effectués:

- un tube avec barreaux groupés a été déplacé suivant un «diamètre» du cœur, afin d'obtenir la variation de l'effet d'hétérogénéité en fonction de la distance à l'axe du réacteur;
- l'additivité de l'effet a été vérifiée au centre de l'assemblage, en mesurant l'effet du groupement dans quatre tubes adjacents, d'abord pour chaque tube séparément, puis pour l'ensemble des quatre tubes.

Tous les renseignements que l'on peut tirer de ces expériences ne sont pas encore exploités. On a pu cependant, à partir des résultats des mesures et des corrections de déplacement, déduire la valeur de la variation de réactivité due à la seule hétérogénéité entre le réseau normal et celui où tous les barreaux de combustible seraient groupés quatre par quatre. Cette valeur est de:

$$+ (1140 \pm 100) \times 10^{-5} \Delta K$$

4.2. Calcul de la variation de réactivité due au groupement des barreaux

Cette variation de réactivité a été calculée à la fois par PERHET (cf. fig. 1) et par Monte-Carlo en milieu infini, et corrigée par la méthode de Benoist de la variation de l'effet de l'hétérogénéité de réseau sur les fuites (cf. paragraphe 2.2). Il a été admis que les fuites dans les vides inter-tubes ne changent pas entre le réseau normal et le réseau à barreaux groupés.

Le code PERHET ne permettant pas, dans sa version actuelle, de calculer directement un réseau de barreaux groupés, il est nécessaire de définir un barreau cylindrique équivalent à la grappe de quatre barreaux. On admet que le barreau équivalent est celui dont la probabilité d'auto-collision est la même que celle de la grappe. On trouve que pour D = 1,22 cm le rapport $D_{équiv.}/D$ se situe entre 1,65 et 1,75, suivant les groupes d'énergie. Une valeur moyenne $D_{équiv.} \simeq 1,7\ D$ a été adoptée, et les corrections de dilution pour les grappes de quatre barreaux ont été effectuées comme pour un réseau dont les barreaux auraient ce diamètre équivalent.

Dans le calcul Monte-Carlo, la géométrie exacte du réseau à barreaux groupés est respectée, et les corrections de dilution sont les mêmes que ci-dessus. L'avantage de ce calcul par rapport au

calcul PERHET correspondant est qu'on ne fait d'autre approximation que celle sur les corrections de dilution.

Les résultats obtenus à partir de ces deux calculs et par l'expérience sont résumés dans le tableau III.

L'accord satisfaisant entre les variations de réactivité calculées par PERHET et par Monte-Carlo montre que la schématisation de la grappe par un barreau de diamètre $D_{équiv.}$ n'introduit pas d'erreur appréciable.

On retrouve un écart entre les valeurs déduites des calculs en milieu infini et la valeur expérimentale. Cet écart est de même signe, quoique beaucoup moins net que celui constaté plus haut entre calculs en milieu infini et calculs en milieu fini.

4.3. Extrapolation du résultat expérimental

Ne disposant pas encore d'une autre valeur expérimentale (par exemple pour un réseau à barreaux de diamètre D/2), on a obtenu l'effet d'hétérogénéité entre le réacteur homogène et le réseau normal en utilisant l'effet de groupement mesuré et une extrapolation fondée sur les valeurs calculées.

De la valeur expérimentale en milieu fini de l'effet de groupement on a déduit une valeur «expérimentale» en milieu infini en retranchant la correction due à la variation des fuites, soit $(1140 \pm 100) - (-50) = (1190 \pm 100) \times 10^{-5} \Delta K$.

On en déduit une valeur «expérimentale» de l'effet d'hétérogénéité du réseau normal en milieu infini en se fondant sur le rapport calculé entre l'effet d'hétérogénéité du réseau normal et celui du groupement:

$$\Delta K\Big|_{0\rightarrow D}^{\ll \text{exp.} \gg} = \Delta K\Big|_{\text{group.}}^{\text{exp.}} \times \frac{\Delta K\Big|_{0\rightarrow D}^{\text{calcul}}}{\Delta K\Big|_{\text{group.}}^{\text{calcul}}}$$

Cela suppose que l'écart relatif entre expérience et calculs en milieu infini est indépendant du diamètre des barreaux. On a ainsi obtenu deux valeurs «expérimentales» en milieu infini:

$$+ (2500 \pm 260) \times 10^{-5} \Delta K \text{ (extrapolé PERHET)}$$
$$+ (2750 \pm 500) \times 10^{-5} \Delta K \text{ (extrapolé Monte-Carlo).}$$

En ajoutant à ces valeurs les effets calculés des variations de fuites ($-150 \times 10^{-5} \Delta K$), on obtient deux valeurs «expérimentales» des effets d'hétérogénéité en milieu fini, soit:

$$+ (2350 \pm 260^{a}) \times 10^{-5} \Delta K \text{ (extrapolé PERHET)}$$
$$+ (2600 \pm 500^{a}) \times 10^{-5} \Delta K \text{ (extrapolé Monte-Carlo)}$$

([a] Ces écarts-types ne comprennent pas d'incertitude sur les variations des fuites ni sur la méthode d'extrapolation.)

La valeur «expérimentale» finalement adoptée est la moyenne entre les deux valeurs extrapolées, soit:

$$+ (2475 \pm 280) \times 10^{-5} \Delta K \text{ (un seul écart-type)}$$

TABLEAU III. EFFET DE GROUPEMENT DES BARREAUX
VARIATION DE L'EFFET D'HETEROGENEITE ENTRE LE RESEAU NORMAL ET LE RESEAU A BARREAUX GROUPES

1 ΔK en milieu infini, par PERHET ($\times 10^{-5}$)	$+1300 \pm 75$ [a]	-
2 ΔK en milieu infini, par Monte-Carlo ($\times 10^{-5}$)	-	$+1230 \pm 160$
3 ΔK dû aux variations des fuites ($\times 10^{-5}$)	-50 [b]	-50
Effet global ($\times 10^{-5}$)	$+1250 \pm 75$	$+1180 \pm 160$
Expérience (corrigée des effets de déplacement) ($\times 10^{-5}$)	$+1140 \pm 100$	

[a] L'incertitude de $\pm 75 \times 10^{-5} \Delta K$ correspond à l'incertitude de $\pm 0,05$ sur le rapport $D_{équiv.}/D$.
[b] Variation de l'effet de l'hétérogénéité sur les fuites entre le réseau normal et le réseau à barreaux groupés: $(140 - 90) \times 10^{-5} \Delta K$.

soit pratiquement:

$+ (2,5 \pm 0,56)\% \Delta K$ (avec deux écarts-types).

5. CONCLUSIONS

Les résultats des différentes évaluations des effets d'hétérogénéité dans le réseau actuel de MASURCA 1-A sont rassemblés dans le tableau IV.

TABLEAU IV. DIFFERENTES EVALUATIONS DES EFFETS D'HETEROGENEITE DANS MASURCA 1-A

Calcul	Extrapolation de l'expérience
PERHET + corrections de fuites $+2585 \times 10^{-5} \Delta K$	Extrapolation PERHET $+(2350 \pm 260) \times 10^{-5} \Delta K$
M.C. infini + corrections de fuites $+(2680 \pm 115) \times 10^{-5} \Delta K$	Extrapolation M.C. infini $+(2600 \pm 500) \times 10^{-5} \Delta K$
M.C. fini $+(2100 \pm 180) \times 10^{-5} \Delta K$	-
-	Meilleure valeur (moyenne des deux précédentes) $+(2475 \pm 280) \times 10^{-5} \Delta K$

De l'ensemble des études résumées dans ce mémoire on peut tirer les conclusions suivantes:

Avec les mêmes approximations, Monte-Carlo en milieu infini et PERHET sont en bon accord, ce qui démontre la validité, au moins pour ce type de milieu, du formalisme et des hypothèses de PERHET (flux plat, homogénéisation du diluant). Il est à noter que PERHET est 20 fois plus rapide que Monte-Carlo en milieu infini.

Les calculs Monte-Carlo en milieu fini et en milieu infini présentent un écart significatif qu'on tentera de tirer au clair.

La meilleure estimation qu'il soit possible d'avancer actuellement pour l'effet global sur la réactivité de l'hétérogénéité du cœur 1-A de MASURCA est de $2,5\% \Delta K$. Les valeurs calculées sont en relativement bon accord avec cette valeur «expérimentale».

La meilleure valeur calculée est de 2,1%. La meilleure valeur expérimentale est de 2,5%; il est à noter que les barres d'erreur sont telles que ces deux valeurs ne sont pas incompatibles.

La meilleure valeur calculée peut être en défaut à cause des données de base ou à cause de toutes les limitations de la méthode de calcul (diffusion isotrope, théorie multigroupe, corrections de dilution, etc.).

La valeur «expérimentale» de 2,5% peut être en défaut à cause de la méthode d'extrapolation. Ce point pourrait être éclairci en complétant les expériences de groupement par des expériences de subdivision.

REFERENCES

[1] KREMSER, J., BARBERGER, M., BRUNA, J.G., BRUNET, J.P., MOUGNIOT, J.C., VERRIERE, P., « Masurca 1-A et 1-B – Résultats préliminaires», ces comptes rendus, SM-101/59.

[2] STORRER, F., KHAIRALLAH, A., CADILHAC, M., BENOIST, P., Heterogeneity calculation for fast reactors by a perturbation method, Nucl. Sci. Engng 24 (1966) 153.
KHAIRALLAH, A., STORRER, F., Calculation of the Sodium Void and Doppler Reactivity Coefficients in Fast Reactors and Critical Assemblies, with Heterogeneity Taken into Account, ANL-7320 (1966).

[3] CHERNICK, J., KAPLAN, I., The nuclear reactor with a transverse air gap, J. nucl. Energy 2 (1955) 41-51.

[4] BENOIST, P., Théorie du coefficient du diffusion des neutrons dans un réseau comportant des cavités, CEA-R-2278 (1964).

[5] HANSEN, G.E., ROACH, W.H., Six and Sixteen-Group Cross Sections for Fast and Intermediate Critical Assemblies, LAMS-2543 (1961).

[6] SAUER, A., "Escape probability from fuel rods in lattices", EAES Symp. Advances Reactor Theory, Karlsruhe, 23-24 April 1963.

[7] LESLIE, D.C., HILL, J.G., JONSSON, A., Improvements to the Theory of Resonance Escape in Heterogeneous Fuel: I. Regular Arrays of Fuel Rods, AEEW-R-353 (Feb. 1964); voir aussi Nucl. Sci. Engng 22 (1965) 78.

[8] KAVENOKY, A., Communication personnelle.

[9] AMYOT, L., BENOIST, P., First flight collison probabilities in pin clusters and rod lattices, Nucl Sci. Engng 28 (1967) 215-55.

[10] DAOLIO, C., PROCOPE – A Code to Evaluate Collision Probabilities in Pin Clusters and Infinite Rod Lattices, EUR-3296e (1967).

[11] BENOIST, P., HOROWITZ, J., Rapport interne CEA.

[12] PARISOT, B., Communication personnelle.

[13] MOREAU, J., PARISOT, B., Rapport CEA (à paraître).

[14] MARTIN, J., Communication personnelle.

DISCUSSION

W. HART: I did not understand how you performed your Monte Carlo calculations. Did you use a perturbation technique, or were your heterogeneity effects obtained from the subtraction of independent runs? Also, what were the computer times necessary to obtain the statistical errors quoted in your paper?

A. KHAIRALLAH: We did not use a perturbation technique; the effects obtained are the difference between direct independent calculations. The computer times vary according to the complexity of the medium under consideration. In a finite medium they are of the order of 1 - 1½ h on an IBM 360/75. In an infinite medium they are of the order of 15-20 min.

H.W. KÜSTERS: How did you treat the effect of resonance self-shielding in the heterogeneous array?

A. KHAIRALLAH: The corrections for resonance self-shielding in the heterogeneous array are based on the definition of a potential diffusion cross-section according to the conventional equivalence relation. In this relation, the Dancoff correction is calculated according to the Sauer approximation and the Bell factor according to the work of Leslie, Hill and Jonsson.

L. I. TIRÉN: Do you also use equivalence theory to account for resonance shielding in the heterogeneous lattice in the case of Monte Carlo calculations?

A. KHAIRALLAH: Yes, since Monte Carlo calculations are multigroup calculations. We used the same effective cross-sections both for the Monte Carlo calculations and for PERHET.

РАСЧЕТ ГЕТЕРОГЕННЫХ ЭФФЕКТОВ В КРИТИЧЕСКИХ СБОРКАХ НА БЫСТРЫХ НЕЙТРОНАХ

А.М.СИРОТКИН, И.С.СЛЕСАРЕВ, В.В.ХРОМОВ, Л.Н.ЮРОВА
МОСКОВСКИЙ ИНЖЕНЕРНО-ФИЗИЧЕСКИЙ ИНСТИТУТ, МОСКВА,
и
М.Ф.ТРОЯНОВ
ФИЗИКО-ЭНЕРГЕТИЧЕСКИЙ ИНСТИТУТ, ОБНИНСК, СССР

Abstract — Аннотация

CALCULATION OF HETEROGENEOUS EFFECTS IN FAST-NEUTRON CRITICAL ASSEMBLIES. The paper describes a method developed for analysing heterogeneous effects in fast-neutron critical assemblies consisting of zones with alternate flat layers of various materials (BFS-type assemblies).

With the method of calculation adopted the effect of heterogeneous phenomena in assemblies with zones having different properties can be accurately estimated by reducing two-dimensional calculations to equivalent one-dimensional calculations; this involves the use of group bucklings which take into account the flow of neutrons between the assembly zones. The magnitude of the group bucklings in zones of different average composition was determined by two-dimensional multi-group diffusion calculations for assemblies with homogenized zones based on the generalized method for conventional separation of spatial variables.

The heterogeneous structure of the zones was studied using 18-group one-dimensional non-diffusion calculations and simultaneously considering up to 60 layers with different nuclear properties. This theoretical study resulted in a new method of solving the kinetic equation for neutron transport in multi-layer media.

The studies also dealt with the effect of heterogeneous structure on the spatio-energetic distribution of neutrons, the effective multiplication factor and other characteristics in the BFS-8 and BFS-16 critical assemblies. The first of these is a reactor of simple composition, and the second is a BN-350 reactor mock-up of complicated heterogeneous structure. With the method used it was possible to take into account the irregular arrangement of the layers simulating the composition of active zones of varying degrees of enrichment in the BFS-16 assembly. It is shown that, with a zone of heterogeneous structure, taking account of the arrangement of the layers in the entire zone results in a big correction to the change in the multiplication factor obtained by the lattice method of calculation.

With the BFS-8 assembly a study was made of the effect of changing the structure of the elementary cells of the active zone for the same average homogeneous cell composition.

The paper gives details of the spatial distributions of the neutron flux in different energy groups and the density of various reactions, indicating the character of the flux oscillations and the spectrum changes by the heterogeneous structure of the zone. The calculated data are compared with experimental data and shown to be in good agreement.

РАСЧЕТ ГЕТЕРОГЕННЫХ ЭФФЕКТОВ В КРИТИЧЕСКИХ СБОРКАХ НА БЫСТРЫХ НЕЙТРОНАХ. В докладе описана разработанная методика анализа гетерогенных эффектов в критических сборках на быстрых нейтронах, состоящих из зон с чередующимися плоскими слоями различных материалов (типа сборок БФС).

Принятый расчетный метод позволяет произвести корректный учет влияния гетерогенных эффектов в сборках с различными по свойствам зонами путем сведения двумерных расчетов к эквивалентным одномерным с помощью групповых лапласианов, учитывающих перетечку нейтронов между зонами сборки. Значения групповых лапласианов в зонах с различным средним составом определялись диффузионными многогрупповыми двумерными расчетами сборок с гомогенизированными зонами на базе обобщенного метода условного разделения пространственных переменных.

Гетерогенная структура зон изучалась при проведении недиффузионных 18-ти групповых одномерных расчетов с одновременным рассмотрением до 60 слоев с различными ядерно-физическими свойствами. В основу этого расчетного исследования положен новый метод решения кинетического уравнения переноса нейтронов в многослойных средах.

В процессе исследований изучалось влияние гетерогенной структуры на пространственно-энергетическое распределение нейтронов, эффективный коэффициент размножения и другие характеристики в критических сборках БФС-3 и БФС-16. Первая является простым по составу реактором, вторая – моделью реактора БН-350 со сложной гетерогенной структурой. Использованная методика позволила учесть нерегулярное размещение слоев, имитирующих состав активных зон различного обогащения в сборке БФС-16. Показано, что при переходе к гетерогенной структуре зоны учет расположения слоев по всей зоне дает существенную поправку в изменение коэффициента размножения по сравнению с расчетами по методу ячейки.

Для сброски БФС-8 изучался эффект изменения структуры элементарной ячейки активной зоны при сохранении среднего гомогенного состава ячейки.

В докладе приводятся детальные пространственные распределения потока нейтронов в различных энергетических группах и плотности различных реакций, показывающие характер осцилляций потока и изменения спектра, вызываемые гетерогенной структурой зон. Проведены сравнения расчетных данных с экспериментальными и показано их хорошее согласие.

I. ВВЕДЕНИЕ

При изучении быстрых критических сборок неизбежно возникает вопрос о роли и величине эффекта гетерогенного размещения материалов, входящих в состав сборки. Существование этого эффекта затрудняет экстраполяцию результатов измерений, полученных на критсборке-модели, к условиям энергетического реактора. Кроме того, влияние гетерогенных эффектов может, в принципе, затруднить использование результатов физических экспериментов для проверки сечений, либо помешать анализу точности расчетных методов. В критических экспериментах на стенде БФС используются цилиндрические таблетки различных материалов толщиной 5 – 10 мм. Они помещаются в круглые вертикальные трубы, и таким образом, все материалы располагаются слоями, перпендикулярными оси сборки. При такой конструкции естественно ожидать влияния гетерогенного размещения материалов на распределение нейтронного поля и различные интегральные физические характеристики. Экспериментальное изучение структуры нейтронного поля производилось на критических сборках БФС-16 – моделях реактора БН-350, где с хорошим "разрешением" были получены детальные распределения скоростей различных реакций, с помощью активирующих фольг, а также малогабаритными камерами деления [1,2]. Ранее на сборке БФС-8 был экспериментально определен эффект увеличения гетерогенности [3]. Результаты расчетного анализа, выполненного В.И.Матвеевым и В.Н.Морозовым, приведенные в работе [1], получены S_B-методом для отдельной ячейки активной зоны сборки БФС-16. Однако необходимо иметь в виду, что выделение типичной ячейки оказывается возможным далеко не всегда. Сборка может состоять из большого числа ячеек различной композиции и размеров, периодичность размещения ячеек может быть нарушена. Кроме того, сведение расчета реактора к расчету ячейки требует дополнительных предположений относительно утечки нейтронов из его зон в радиальном и аксиальном направлении и характера условий на границе ячейки. Это обусловливает внесение погрешностей в расчетные исследования. Все указанные моменты явились побуждением к тому, чтобы разработать новую методику

расчета гетерогенных эффектов критических сборок типа БФС, свободную от недостатков расчетов с помощью ячеек, предъявив к ней следующие основные требования:

корректный учет двумерности сборки,
многогрупповой подход к решению задачи,
учет многозонности системы,
использование достаточно высоких приближений при решении кинетического уравнения.

Точное решение задачи в указанном объеме практически невозможно, но результаты высокой точности для рассматриваемой проблемы можно получить, используя идеи синтеза решения сложной задачи из решений более простых задач.

2. РАСЧЕТНЫЙ МЕТОД

Расчетный алгоритм при решении поставленной задачи включал в себя два синтетических метода:

1) Обобщенный метод разделения пространственных переменных r и z [4], который использовался для учета двумерности системы;
2) Метод условного разделения пространственной и угловой переменных [5] – "R_n-метод", позволяющий с высокой точностью решать кинетическое уравнение в плоскопараллельных системах.

Первый из этих методов позволяет выделить в рассматриваемой сборке любой коаксиальный слой и описать его нейтронные поля вдоль оси z одномерными групповыми уравнениями. Перетечка нейтронов в радиальном направлении учитывается добавлением к сечению поглощения в каждой группе j поправки:

$$\alpha_j^2 \frac{1}{3\Sigma_{tr}^j}$$

где α_j^2 – групповой лапласиан рассматриваемой зоны, зависящий от формы группового потока в радиальном направлении,
Σ_{tr}^j – транспортное сечение в группе j для гомогенизированного состава зоны. Значения лапласианов α_j^2 определялись на гомогенных составах зон по программе 18-RZ-36 для расчета двумерного реактора с 36 зонами в 18-групповом диффузионном приближении.

Гетерогенная структура зон учитывалась на второй стадии расчета, когда выделенные описанным выше способом слои рассчитывались R_n-методом как многозонные плоскопараллельные системы по программе 26-хм-1200 [1]. Эта программа обладает следующими основными характеристиками:

количество зон – до 60,
количество пространственных узлов – до 360,
количество энергетических групп – до 26,
максимальный порядок приближения n = 20, что соответствует, примерно, точности S_{40}-метода.

Возможности R_n-метода можно продемонстрировать на примере расчета нейтронного поля в двухзонной ячейке [6], где толщина зоны с постоян-

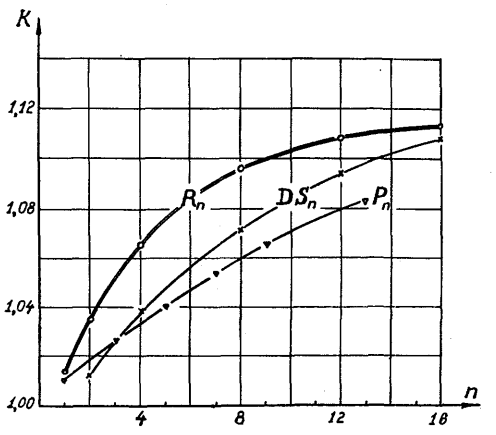

Рис.1. Зависимость отношения $K = \widetilde{\Phi}_s / \widetilde{\Phi}_{ns}$ от номера n в различных приближениях:
R_n – метод условного разделения переменных,
DS_n – дискретный метод Карлсона,
P_n – метод сферических гармоник.

ным распределением источников много меньше длины свободного пробега нейтронов в ней. На рис.1 показана зависимость отношения $\widetilde{\Phi}_s / \widetilde{\Phi}_{ns}$, где $\widetilde{\Phi}_s$ – средний поток в зоне с источником, а $\widetilde{\Phi}_{ns}$ – средний поток в зоне без источников, от номера приближения "n" различных методов, в том числе и R_n-метода.

R_n-метод, имеет хорошую скорость сходимости, и позволяет снизить по сравнению с S_n-методом объем вычислительной работы. Для детального описания спектра нейтронов в сборках использовалась 18-групповая система констант [1], полученная путем укрупнения энергетических интервалов 26-групповой системы констант [7] в области ниже 10 кэв.

3. КРИТИЧЕСКИЕ СБОРКИ И ИХ РАСЧЕТНЫЕ МОДЕЛИ

Подробный расчетный анализ был проведен для двух критических сборок БФС-8 и БФС-16, описанных ранее в работах [1, 3] с указанием размеров и гомогенных составов всех зон. Поэтому здесь отметим лишь основные моменты, существенные для последующего изложения. В сборках БФС-8 и БФС-16 использовался набор таблеток различных материалов. Таблетки образуют слои, состав которых приведен в табл.1, где концентрации определены с учетом стальных стенок труб, в которые помещены таблетки, алюминиевого покрытия урановых таблеток и пористости межтрубного пространства. Активная зона сборки БФС-8 по высоте состояла из 14 ячеек одинакового состава. В каждой ячейке было следующее чередование таблеток: 33133. В центре активной зоны находилась таблетка обогащенного урана. Для экспериментального изучения влияния гетерогенности на критические параметры собирался другой вариант сборки БФС-8а, в котором на высоте активной зоны размещалось 7 укрупненных ячеек, каждая из которых имела состав: 3333113333. Гомогенные концентрации в обоих вариантах были одинаковыми. В расчетах форма активной зоны сброски БФС-8 прини-

ТАБЛИЦА 1. СОСТАВ СЛОЕВ СБОРОК БФС.

Материал	Условный номер	Концентрации $(1/см^3)\cdot 10^{-22}$						Средняя толщина слоя (мм)
		^{235}U	^{238}U	O	Al	Нержав. сталь[а]	Fe	
Обогащ. уран 36% / 90%	1	1,005 / 2,71	1,750 / 0,288	—	0,650	0,535	—	5,6[б]
$^{238}UO_2$	2	—	1,374	2,80	0,280	0,535	—	9,8
Fe	3	—	—	—	—	0,535	6,350	10,0
Al	4	—	—	—	4,00	0,535	—	9,9
Al_2O_3	5	—	—	5,17	3,45	0,535	—	10,1
Кольцо из нержав. стали[а]	6	—	—	—	—	1,785	—	5,0

[а] Нержавеющая сталь IXI8H9T, $\rho_0 = 8{,}47\cdot 10^{22}\frac{1}{см^3}$.

[б] С учетом алюминиевой оболочки, толщиной 0,3 мм.

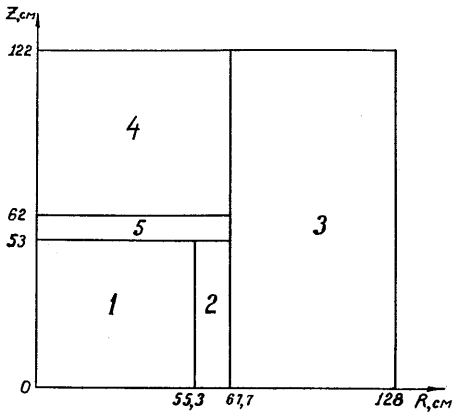

Рис.2. Расчетная схема сборки БФС-16:
1 – Зона меньшего обогащения – ЗМО,
2 – Зона большего обогащения – ЗБО,
3 – Боковой экран,
4 – Торцевой экран,
5 – Конструкционная прослойка.

малась цилиндрической, с диаметром равном 72,8 см, и высотой – 63,6 см, активная зона была окружена экраном толщиной 60 см; состав экрана приведен в работе [3]. Расчет нейтронных полей в аксиальном направлении в сборках БФС-8 и БФС-8 а приводился с учетом указанной слоистой структуры активных зон при гомогенизированных торцевых экранах. Лапласианы, учитывающие утечку нейтронов из активной зоны в радиальном направлении находились из двумерного расчета гомогенизированной модели. Сборка БФС-16 имеет гораздо более сложную гетерогенную структуру по высоте активной зоны, к тому же различную в двух частях активной зоны. Размещение таблеток по высоте сборок для зон меньшего и большего обогащения приводится на рис.7–9. В гомогенизированной расчетной модели реактор может представляться схемой, приведенной на рис.2. По этой схеме проводился двумерный расчет и определялись радиальные лапласианы в различных частях активной зоны. Одновременные расчеты с учетом гетерогенности проводились отдельно для зон большого и малого обогащения, с использованием полученных лапласианов. При этом из-за ограничений по

числу зон часть таблеток, примыкающих к торцевому экрану гомогенизировалась, а экраны рассматривались как гомогенные. Полувысота активных зон в этих расчетах была равной 53 см.

4. ИССЛЕДОВАНИЕ ГЕТЕРОГЕННЫХ ЭФФЕКТОВ В СБОРКЕ БФС-8

4.1. Определение порядка R_n-приближения

Исследование зависимости расчетной формы потока $K_{эфф}$ системы от номера "n" R_n-приближения при расчетах сборки БФС-8 проводилось на отдельной ячейке и представлено на рис.3 и в табл.2. Анализ ячеек показал, что для выявления влияния гетерогенности на различные интегральные характеристики системы (включая $K_{эфф}$) в большинстве случаев достаточно использования R_4-приближения. При необходимости определения разностных эффектов с большой точностью проводились расчеты в более высоких приближениях.

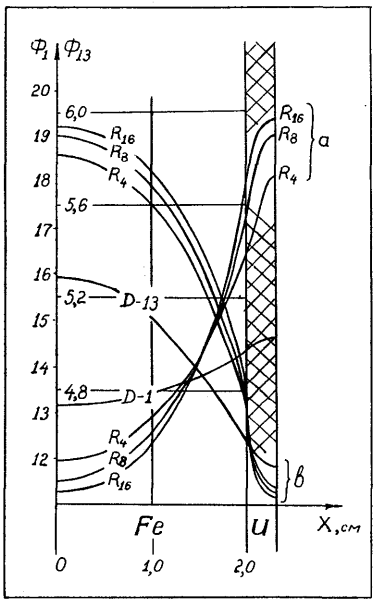

Рис.3. Расчетная форма потока нейтронов 1 и 13 групп в различных приближениях R_n – метода для ячейки сборки БФС-8:
a. 1 группа (6,5 – 10,5 Мэв),
b. 13 группа (0,465 – 2,15 кэв),
D-1 и D-13 диффузионное приближение.

4.2. Пространственно-энергетическое распределение нейтронов

Пространственное распределение нейтронов в различных энергетических группах по высоте сборки БФС-8 представлено на рис.4. Характерными по своему пространственному распределению являются потоки нейтронов в двух энергетических диапазонах. В жесткой части

ТАБЛИЦА 2. ЗАВИСИМОСТЬ ОТНОШЕНИЯ $K_{эфф}^{(n)}/K_{эфф}^{(n-1)}$ ОТ НОМЕРА ПРИБЛИЖЕНИЯ R_n-МЕТОДА

	Номер приближения			
	2	4	8	16
БФС-8	1,0031	1,0015	1,0005	1,0000
БФС-8а	1,0074	1,0030	1,0010	1,0001

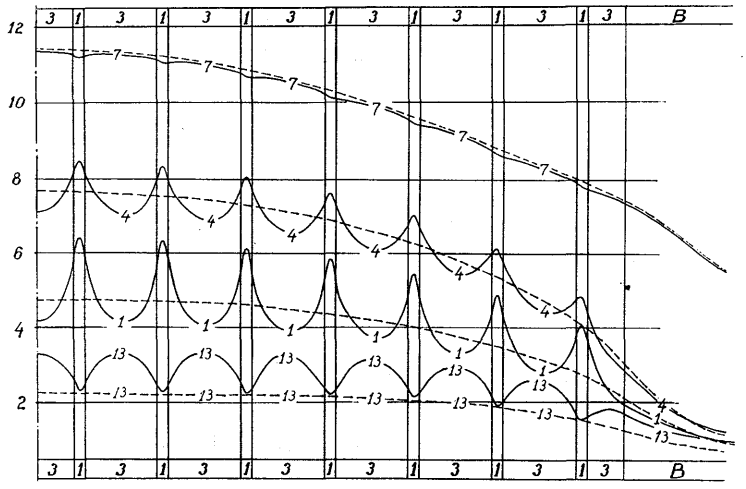

Рис.4. Пространственное распределение нейтронов 1, 4, 7 и 13 групп по высоте сборки БФС-8. Пунктиром отмечено распределение соответствующих групп в гомогенизированной модели.

Масштаб: 1 группа 1:1
4 " 1:25
7 " 1:60
13 " 4:1

спектра (область выше 0,2 Мэв, $j<7$) поток нейтронов имеет всплески в урановых таблетках, обусловленные наличием источников быстрых нейтронов в них. Нейтроны второго энергетического диапазона (область энергий ниже 0,2 Мэв) образуются в основном за счет замедления более быстрых нейтронов между урановыми таблетками и претерпевают сильное поглощение в уране. Поэтому для нейтронов этого диапазона характерны всплески потоков в пространстве между таблетками урана. Амплитуды колебаний групповых потоков значительно увеличиваются при переходе к крупной гетерогенности, имевшей место в сборке БФС-8 а.

4.3. Спектр нейтронов

Спектр нейтронов в таблетках, содержащих железо, мягче чем спектр в урановых таблетках. Этим объясняется поведение распределений ско-

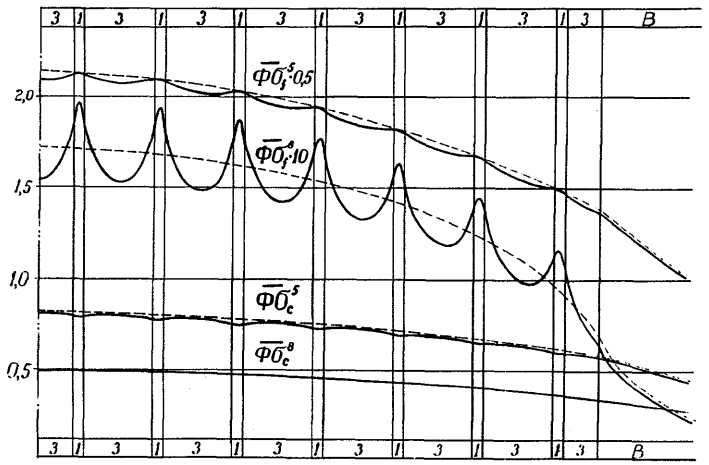

Рис.5. Распределение скоростей процессов деления ($\bar{\Phi}\sigma_f$) и захвата ($\bar{\Phi}\sigma_c$) по высоте сборки БФС-8 для ^{238}U и ^{235}U. Пунктиром обозначено распределение процессов в гомогенной модели.

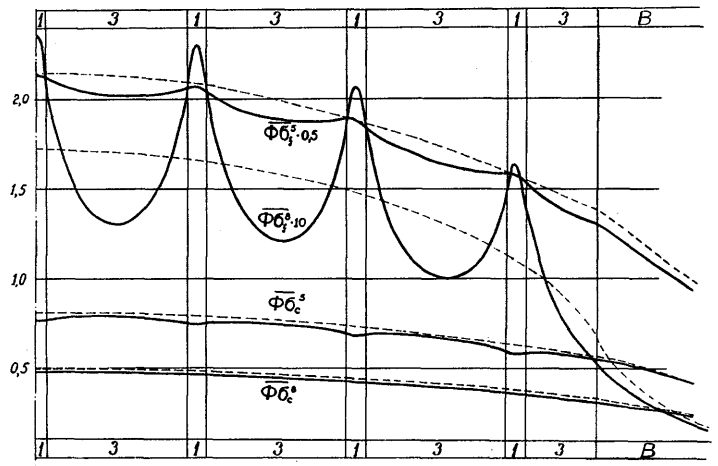

Рис.6. Распределение скоростей процессов деления ($\bar{\Phi}\sigma_f$) и захвата ($\bar{\Phi}\sigma_c$) по высоте сборки БФС-8 а для ^{238}U и ^{235}U. Пунктиром обозначено распределение процессов в гомогенной модели.

ростей процессов радиационного захвата и деления ^{238}U и ^{235}U, рассчитанных в различных точках систем и представленных на рис.5 и 6. По мере укрупнения гетерогенности, тенденция к дифференциации спектров усиливается. В табл.3 показано изменение интегральных по объему активной зоны спектров нейтронов в укрупненных энергетических интервалах при переходе от гомогенной структуры сборки (БФС-8Г) к сборкам с мелкой (БФС-8) и крупной (БФС-8 а) гетерогенностью. Переход к гетерогенной структуре сопровождается некоторым размытием спектра. В верхней части он становится немного жестче за счет уменьшения роли железа как рассеивателя. В мягкой части спектр

ТАБЛИЦА 3. ИНТЕГРАЛЬНЫЕ СПЕКТРЫ СБОРКИ БФС-8.

Энергетический интервал	Интегральные потоки			Изменение групповых потоков по отношению к БФС-8Г(%)	
	БФС-8Г	БФС-8	БФС-8а	БФС-8	БФС-8а
2,5 – 10,5 Мэв	3,92	3,93	3,95	+ 0,24	+ 0,76
0,8 – 2,5 Мэв	17,87	17,75	17,54	- 0,67	- 1,84
0,2 – 0,8 Мэв	48,79	48,72	48,58	- 0,14	- 0,43
21,5 – 200 кэв	28,62	28,76	29,00	+ 0,49	+ 1,33
2,15 – 21,5 кэв	0,78	0,81	0,88	+ 3,85	+ 12,8
Ниже 2,15 кэв	0,02	0,03	0,05	+50,0	+150

нейтронов смягчается за счет возникновения блокировки поглощения нейтронов в уране. Укрупнение гетерогенной структуры усиливает деформацию спектра.

4.4. Влияние гетерогенности на коэффициент размножения

Коэффициент размножения в гетерогенной модели сборки больше, чем в гомогенной. Расчеты показали, что для сборки БФС-8 этот эффект составляет 1,02%, а для БФС-8 а – 2,86%. Расчетный эффект укрупнения гетерогенности равен, таким образом, 1,84%. Экспериментальный эффект получен по разности критических масс этих сборок и известному вкладу в реактивность периферийных топливных стержней и равен 1,9%. Роль различных энергетических областей в формировании суммарного эффекта изменения коэффициента размножения можно проследить по вкладу разных групп в суммарный источник нейтронов деления

$$k_j = \int_H dz\, \Phi_j(z) \nu_f^j \Sigma_f^j(z)$$

Причем, если потоки Φ_j нормировать так, чтобы число нейтронов, поглощаемых в активной зоне и вытекающих из нее в единицу времени, в сумме было равным единице, то

$$\sum_j k_j = k_{эфф}$$

В табл.4 представлены рассчитанные значения k_j для гомогенной и гетерогенных моделей сборок БФС-8. Из нее отчетливо видно, что при увеличении гетерогенности нейтронов наиболее высоких энергий дают определяющий положительный эффект.

5. ИССЛЕДОВАНИЕ ГЕТЕРОГЕННЫХ ЭФФЕКТОВ В СБОРКЕ БФС-16

При исследовании гетерогенных эффектов в сборке БФС-16 было использовано R_4-приближение, которое, как показали расчеты, в этом случае является достаточным.

ТАБЛИЦА 4. ВКЛАД РАЗЛИЧНЫХ ЭНЕРГЕТИЧЕСКИХ ИНТЕРВАЛОВ В ИСТОЧНИКИ НЕЙТРОНОВ ДЕЛЕНИЯ

(сборки БФС-8)

Энергетический интервал	K_j			K_j гетерог. – K_j гомоген.	
	БФС-8Г	БФС-8	БФС-8а	БФС-8	БФС-8а
2,5 – 10,5 Мэв	0,0394	0,0488	0,0628	+ 0,0094	+ 0,0234
0,8 – 2,5 Мэв	0,1550	0,1635	0,1790	+ 0,0085	+ 0,0240
0,2 – 0,8 Мэв	0,4189	0,4156	0,4115	- 0,0033	- 0,0074
21,5 – 200 кэв	0,3607	0,3567	0,3500	- 0,0040	- 0,0107
2,15 – 21,5 кэв	0,0188	0,0183	0,0178	- 0,0005	- 0,0010
Ниже 2,15 кэв	0,0014	0,0015	0,0017	+ 0,0001	+ 0,0003
Σ	0,9942	1,0044	1,0228	+ 0,0102	+ 0,0286

5.1. Пространственно-энергетическое распределение нейтронов

Так же как и в сборке БФС-8, нейтронное поле в зонах большего (ЗБО) и меньшего (ЗМО) обогащения сборки БФС-16 имеет осцилляции, вызванные гетерогенной структурой этих зон (рис.7 и 8). Однако, осциллирующие кривые распределения нейтронов в различных группах зоны меньшего обогащения плохо согласуются в среднем с соответствующими кривыми, полученными на гомогенизированном составе зоны. Это объясняется заметным отличием гомогенизированных составов различных ячеек от гомогенизированного состава всей зоны, что обусловлено неидентичностью размеров и композиции ячеек гетерогенной структуры зоны. Аналогичная, но менее выраженная картина наблюдается и во второй зоне.

5.2. Спектр нейтронов

Спектр нейтронов в обеих зонах сборки БФС-16 значительно мягче спектра БФС-8.

Изменение интегрального спектра в зонах сборки БФС-16 по сравнению с их гомогенными моделями иллюстрируется таблицей 5. Отметим, что при переходе к гетерогенной структуре существенное влияние на деформацию спектра оказывает неидентичность ячеек этой структуры. Поэтому гетерогенный расчет ЗМО даже в диффузионном приближении предсказывает большую часть деформации спектра. В меньшей мере это относится к ЗБО, где гетерогенная структура имеет более регулярный характер. Для зоны большого обогащения расчет распределений отношений скоростей некоторых реакций был сопоставлен с экспериментом, в котором детальная структура распределений была определена с помощью активируемых фольг [1, 2, 8]. На рис.9 приведены результаты экспериментов и расчетов, хорошо согласующиеся друг с другом. Эти результаты показывают, что при сравнении расчетных отношений

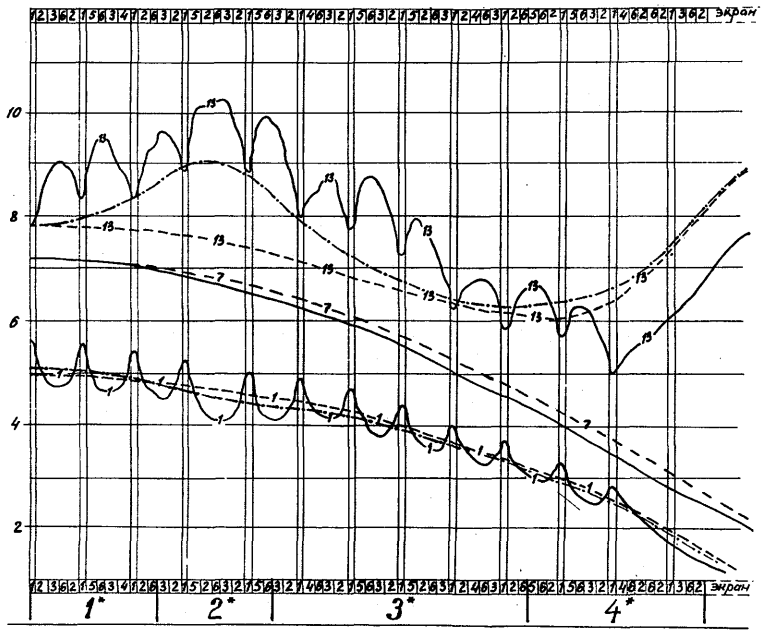

Рис.7. Распределение нейтронов 1, 7 и 13 групп по высоте ЗМО сборки БФС-16. Пунктиром отмечено распределение нейтронов при гомогенизации всей активной зоны. Штрих-пунктир обозначает распределение нейтронов при гомогенизации областей 1, 2, 3 и 4.
Масштаб: 1 группа 1:1
7 " 1:80
13 " 1:2

сечений с экспериментальными, полученными с помощью камер, следует интегрировать детальное расчетное распределение по высоте камеры.

5.3. Пространственно-угловое распределение нейтронов

Для иллюстрации значительной угловой анизотропии нейтронов на рис.10 приводится угловое распределение нейтронов в центральной ячейке ЗБО, полученное интегрированием по лучам при известном интеграле столкновений.

5.4. Влияние гетерогенности на коэффициент размножения

Наиболее подробный анализ роли гетерогенной структуры сборки БФС-16 был выполнен для ее верхней половины в предположении о симметричности сборки относительно центральной плоскости. В таком предположении общее изменение коэффициента размножения при переходе от гомогенной модели к гетерогенной равно +2,81%, причем вклад ЗМО равен 2,2%, а ЗБО – 0,61%. Роль различных групп нейтронов в формировании этих эффектов иллюстрируется таблицей 6. Увеличение

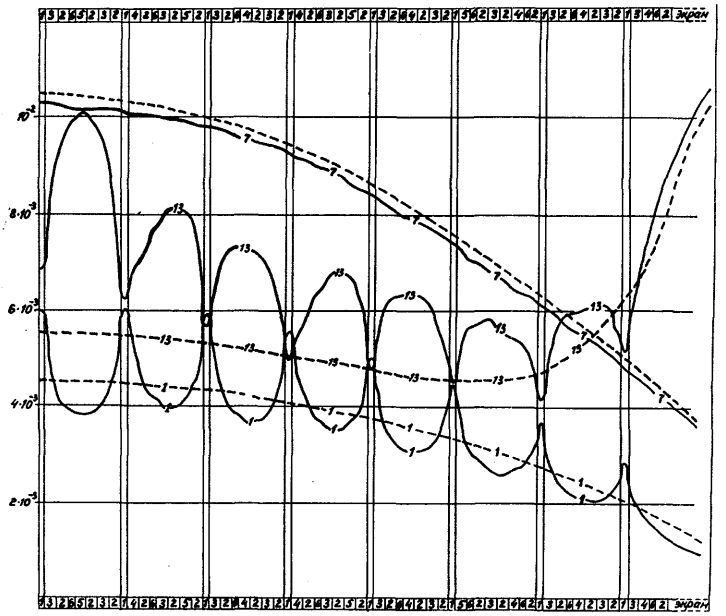

Рис.8. Распределение нейтронов 1, 7 и 13 групп по высоте ЗБО сборки БФС-16. Пунктиром обозначено распределение нейтронов при гомогенизации всей активной зоны.

Масштаб: 1 группа 1:1
7 " 1:40
13 " 1:1

ТАБЛИЦА 5. ИНТЕГРАЛЬНЫЕ СПЕКТРЫ СБОРКИ БФС-16.

Энергетический интервал	Интегральные потоки				Изменение по отношению к гомогенным потокам (%)	
	ЗМО		ЗБО			
	Гомогенная	Гетерогенная	Гомогенная	Гетерогенная	ЗМО	ЗБО
2,5 – 10,5 Мэв	3,33	3,27	4,42	4,37	- 1,80	- 1,13
0,8 – 2,5 Мэв	12,24	12,08	15,35	15,12	- 1,31	- 1,50
0,2 – 0,8 Мэв	32,61	32,23	35,57	34,99	- 1,16	- 1,63
21,5 – 200 кэв	42,06	41,82	37,35	37,55	- 0,57	- 0,54
2,15 – 21,5 кэв	9,14	9,87	6,99	7,53	+ 7,98	+ 7,73
Ниже 2,15 кэв	0,62	0,73	0,32	0,44	+17,7	+37,5

$K_{эфф}$ в рассмотренном случае определяется, в основном, следующими двумя факторами:

Во-первых, нерегулярностью расположения отдельных ячеек и различием их состава, что приводит к некоторому эффективному смещению урана-235 к центральной плоскости по сравнению с гомогенной моделью;

Во-вторых, гетерогенностью самих ячеек.

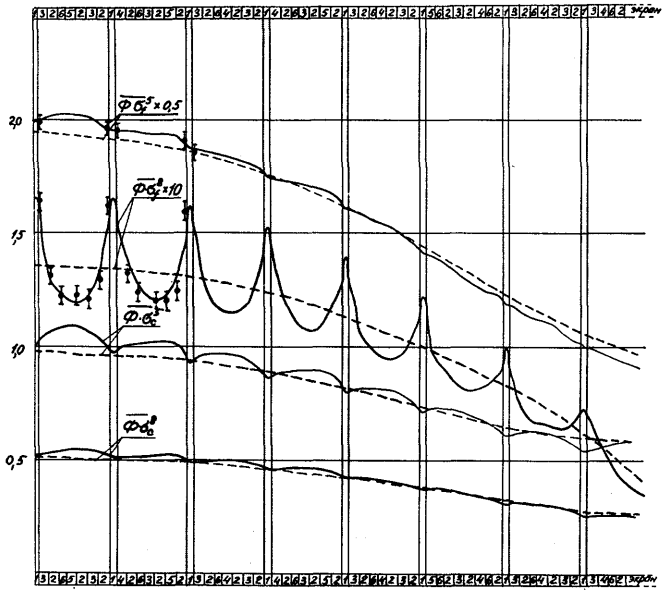

Рис.9. Распределение скоростей процессов деления ($\bar{\Phi}\sigma_f$) и захвата ($\bar{\Phi}\sigma_c$) по высоте ЗБО сборки БФС-16. Точки – эксперимент. Пунктиром отмечено распределение процессов в гомогенной модели.

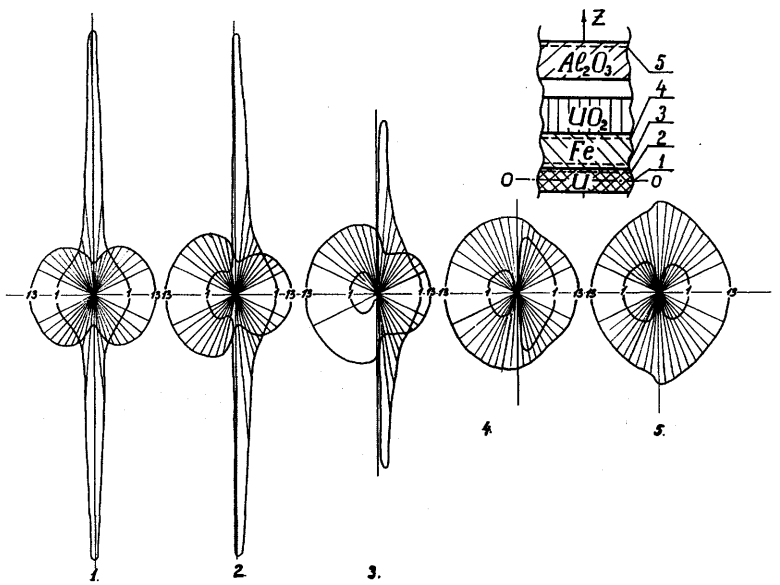

Рис.10. Угловое распределение нейтронов 1 и 13 групп в местах, указанных на верхней части рисунка для центральной ячейки ЗБО сборки БФС-16.

ТАБЛИЦА 6. РОЛЬ РАЗЛИЧНЫХ ЭНЕРГЕТИЧЕСКИХ ИНТЕРВАЛОВ В ИЗМЕНЕНИИ ИСТОЧНИКОВ НЕЙТРОНОВ ДЕЛЕНИЯ ПРИ ПЕРЕХОДЕ ОТ ГОМОГЕННОЙ МОДЕЛИ К ГЕТЕРОГЕННОЙ ВЕРХНЕЙ ПОЛОВИНЫ СБОРКИ БФС-16.

Энергетический интервал	K_jгетерог. − K_jгомоген.		
	ЗМО	ЗБО	По обеим зонам
2,5 − 10,5 Мэв	+0,0028	+0,0081	+0,0109
0,8 − 2,5 Мэв	+0,0037	+0,0118	+0,0155
0,2 − 0,8 Мэв	+0,0023	−0,0004	+0,0019
21,5 − 200 кэв	+0,0006	−0,0106	−0,0100
2,15 − 21,5 кэв	+0,0102	−0,0033	+0,0069
Ниже 2,15 кэв	+0,0024	+0,0005	+0,0029
Σ	+0,0220	+0,0061	+0,0281

Эффект обусловленный первым фактором является преобладающим в ЗМО (~2%). Этот же эффект обуславливает большую роль в увеличении числа делений при учете гетерогенности области энергий 2 − 20 кэв (табл.6) для ЗМО. Роль нерегулярности ячеек для ЗБО меньше и дает около одной трети полного эффекта в этой зоне. Расчетный анализ, выполненный на отдельных ячейках, показал, что перестановка неурановых таблеток в пределах ячейки почти не сказывается на $K_{эфф}$ − эффект составляет 0,01 − 0,04%. Полное изменение $K_{эфф}$ сборки БФС-16 при переходе от гомогенной модели к гетерогенной с учетом нижней половины составило

$$\frac{\Delta K_{эфф}}{K_{эфф}} = +1{,}1\%$$

На результирующем эффекте сказалось то обстоятельство, что в нижней части сборки таблетки расположены так, что уран-235 несколько смещен к нижнему торцевому экрану.

6. УЧЕТ ГЕТЕРОГЕННОЙ СТРУКТУРЫ СБОРОК В РАСЧЕТАХ ИХ ГОМОГЕННЫХ МОДЕЛЕЙ

Гетерогенность зон и вызываемые ею изменения спектра нейтронов могут быть учтены в гомогенных моделях, если предварительно усреднить групповые константы в зонах по потокам с учетом их детального хода по высоте:

$$\bar{\Sigma}^j = \frac{\int_{V_k} \Phi_j(z)\, \Sigma^j(z) dz}{\int_{V_k} \Phi_j(z) dz}$$

С такими усредненными константами был выполнен расчет в диффузионном приближении верхней половины сборки БФС-16 и определен эффект

гетерогенности путем сравнения с результатом расчета гомогенной модели. Эффект оказался равным 0,5% для ЗБО и 1,85% – для ЗМО, т.е. определен довольно хорошо. Расчеты гомогенных моделей сборок с усредненными константами, учитывающими изменения спектра за счет гетерогенной структуры, позволили оценить роль гетерогенности в величине времени жизни мгновенных нейтронов и эффективной доли запаздывающих нейтронов. Изменение этих величин при учете гетерогенности оказались невелики и составляли для времени жизни и для эффективной доли запаздывающих нейтронов 1 – 2%. Это означает, что имеющиеся расхождения между экспериментальными и расчетными временами жизни мгновенных нейтронов не могут быть объяснены эффектами гетерогенности.

7. ВЫВОДЫ

Разработанный и реализованный расчетный метод исследования гетерогенных эффектов позволяет производить их оценку в критических сборках с учетом двумерности, различий в составах зон, непериодичности расположения отдельных ячеек. Метод использует многогрупповой подход и высокие приближения при решении кинетического уравнения переноса нейтронов. Проверка метода путем сравнения расчетных эффектов гетерогенности с экспериментальными данными показала его хорошую точность. Проведение с помощью предложенного метода исследования критических сборок БФС-8 и БФС-16 позволили выявить роль гетерогенных эффектов в этих сборках.

ЛИТЕРАТУРА

[1] ЛЕЙПУНСКИЙ, А.И. и др., Экспериментальные и теоретические исследования по физике быстрых реакторов. Доклад № 4А/3 на Лондонской конференции по реакторам, 1966.
[2] ЮРОВА, Л.Н. и др., В сб. "Физика ядерных реакторов". Атомиздат, 1967 (в печати).
[3] ЛЕЙПУНСКИЙ, А.И. и др., 3rd Int. Conf. peaceful Uses atom. Energy (Proc. Conf. Geneva, 1964) Paper 28/P/368.
[4] ХРОМОВ, В.В. и др., В сб. "Некоторые вопросы физики и техники ядерных реакторов". Атомиздат, 1965, стр.51 – 69.
[5] ХРОМОВ, В.В., СЛЕСАРЕВ, И.С., Атомная энергия 19 6 (1965) 540.
[6] MENEGHETTI, D., Physics of Fast and Intermediate Reactors, (Proc. Seminar, Vienna, 1961) 1 IAEA, Vienna (1962) 457.
[7] АБАГЯН, Л.П. и др., Групповые константы для расчета ядерных реакторов, Атомиздат, 1964.
[8] ЮРОВА, Л.Н., БУШУЕВ, А.В., Атомная энергия 18 5 (1965) 518, 20 1 (1966) 60.

DISCUSSION

J. L. ROWLANDS: How did you treat resonance shielding in the heterogeneous reactor? Did you use equivalence methods?

M. F. TROYANOV: No, each layer was considered as a separate zone and the cross-sections of the individual zones were determined in accordance with their composition.

D. H. WINTZER: Have you tried to measure the fine structure of ^{238}U capture rates?

M. F. TROYANOV: No, but we intend to study the flux fine structure by considering a variety of reactions and using resonance detectors.

HETEROGENEITY STUDY FOR AN INTERMEDIATE-ENERGY CORE PROGRAMME

H. KUROI, H.Y. TOMIOKA, H. MITANI AND J. HIROTA
JAPAN ATOMIC ENERGY RESEARCH INSTITUTE,
TOKAI-MURA, IBARAKI-KEN, JAPAN

Abstract

HETEROGENEITY STUDY FOR AN INTERMEDIATE-ENERGY CORE PROGRAMME. An intermediate-energy spectrum core programme has been proposed and will be carried out very soon in the JAERI fast critical facility, especially for obtaining information on the group constants in the resonance-energy region. Various analytical results, obtained for the programme by use of the ABN cross-section set, are discussed.

The intermediate-energy core will be composed of 20%-enriched uranium metal plates and a suitable amount of hydrocarbon compound or beryllium. To obtain information on the cross-sections from the so-called integral experiments, it is necessary to carry out the experiments in the varied series of an appropriate system. One such series can be achieved by changing the moderator atomic density N^{Be}/N^{235} in the range 0 to 100.

It is shown that valuable information on the cross-sections in the resonance-energy region may be obtained from various experimental results, including those on the criticality, the heterogeneity effect on the criticality induced from the configuration of fuel plates, and the Doppler effect, because the contribution from the resonance-energy region to the experimental results is large.

The heterogeneity effect on the criticality in the intermediate-energy core is shown to be interesting and different from that in the fast reactor system. This is caused by the difference in the fission-capture ratios of the heterogeneous and homogenous system due to the different self-shielding factors of fission and capture cross-sections.

Doppler measurement by heating a sample is discussed with emphasis on the heterogeneity effect of the sample. Highly sensitive Doppler reactivity change of the sample and considerable amount of the moderator used in the system are useful for measuring the heterogeneity effect of the sample. The importance of the contribution of gross neutron spectrum variation to the Doppler effect of the system are also discussed in a sample calculation.

INTRODUCTION

Considering the limited amount of fuel (135 kg of ^{235}U) available for the first stage of the JAERI fast critical facility [1], an intermediate-energy spectrum core programme has been proposed and will be carried out very soon especially for obtaining information on the group constants in the resonance energy region. The intermediate core will be composed of 20%-enriched uranium metal plates and a suitable amount of hydrocarbon compound or beryllium.

In so far as the resonance energy region is concerned, the intermediate core is expected to give the most sensitive experimental results. The experimental results obtained in such a system are not directly the same as those obtained in a fast reactor system. However, useful information may well be obtained on the cross-section set in the resonance region from the measured results of criticality, neutron spectrum, Doppler effect and other reactivity measurements.

To obtain information on the cross-sections from the so-called integral experiments, it is necessary to carry out the experiments in the varied series of appropriate systems. One such series can be achieved by changing the moderator atomic density N^{Be}/N^{235} in the range 0 to 100.

Some analytical results, with emphasis on the heterogeneity effect, obtained for the programme by using the ABN cross-section set are discussed in this paper. The study of heterogeneity effect is not only important for the interpretation of experimental results but also useful for obtaining information on the cross-section set in the resonance region from various results measured in the intermediate-energy core.

Heterogeneity effect on criticality

Although the fast reactor critical assembly is, in general, composed of a periodic lattice of fuel and diluent plates, the homogeneous model is used for most reactor computations. In the intermediate-energy core, however, this model is less valid than for ordinary fast reactors. The heterogeneity due to the plate structure will cause a spatial fine structure of neutron flux distribution and this fine structure will affect the criticality of the system.

The heterogeneity effect on the criticality is usually evaluated through a modification of the group constants which are used for the calculation in an equivalent homogeneous system. The computer code "HUMPTHUMP" has been prepared for this purpose. This code is composed of linked codes which enable the calculation of fine structure of neutron flux distribution, of modified group constants and of criticality up to 25 energy groups.

(1) Computing method

The modification of the group constants for the heterogeneity is achieved by equating the reaction rate in a heterogeneous system and that in the equivalent homogeneous system. Thus, the corrected cross-section is given by

$$\langle \sigma_j^k \rangle = \frac{\sigma_j^k \sum_i N_{ij} V_i \bar{\phi}_i^k}{\langle \phi^k \rangle \sum_i N_{ij} V_i} \qquad (1)$$

where $\langle \sigma_j^k \rangle$: corrected cross-section of the j-th element in the k-th energy group,
σ_j^k : uncorrected cross-section,
N_{ij} : atomic density of the j-th element in the i-th region,
V_i : volume of the i-th region,
$\bar{\phi}_i^k$: average neutron flux in the k-th energy group in the i-th region, and
$\langle \phi^k \rangle$: neutron flux in the equivalent homogeneous system.

In this study, the homogeneous flux is assumed to be represented by

$$\langle \phi^k \rangle = \sum_i \bar{\phi}_i^k V_i \Big/ \sum_i V_i \qquad (2)$$

In the relatively high-energy region where all cross-sections are smooth with respect to the energy, the average neutron flux in the i-th region is obtained by solving the multi-group integral transport equation in the infinite slab geometry by means of the collision probability method. Precise discussions on the numerical solution of the collision probability method used in this study are described in Ref. [2].

In the energy region where the cross-section is strongly dependent upon the energy, it is, in actual cases, difficult to apply the above method for obtaining the spatial fine structure of neutron flux. Therefore, the Wigner approximation [3] was used to obtain the modified group constant for evaluating the heterogeneity effect on the criticality.

The modified group constant in the resonance energy region is practically equal to the effective resonance integral. By using the approximation, the modified cross-section in a lump is expressed as

$$RI=\left(1+\frac{1}{\Sigma_p \ell}\right)\int_0^\infty \frac{\Sigma_p \Sigma_a}{\Sigma_t+\ell^{-1}}\,du \qquad (3)$$

Here $\Sigma_t = N(\sigma_s+\sigma_a)+\Sigma_p$

$$\ell = \frac{\gamma 4V}{S}$$

where σ_a and σ_s : absorption and scattering cross-section, respectively,
N : atom density of the resonance material,
Σ_p : potential scattering cross-section,
S and V : surface area and volume of a lump of fuel,
γ : Dancoff factor.

The integral in Eq. (3) is evaluated by using the F-table given in the ABN cross-section set [4]. By using the modified group constant obtained, the criticality calculation in a heterogeneous system is reduced to that in an equivalent homogeneous system. Thus, the criticality was obtained by means of the conventional multi-group diffusion equation, up to 25 energy groups for one dimensional geometry.

(2) Analytical results and discussion

The intermediate core is composed of 20%-enriched uranium metal plates and a suitable amount of beryllium, polyethylene or graphite plates. The geometry used for criticality calculations is a spherical core with a 30-cm-thick natural uranium blanket.

To give a general idea of this system, the neutron spectrum, fission rate and mean fission energy in a typical intermediate system are shown in Figs 1 and 2. The peak position of the spectrum in the present system is shown to be higher than in a typical large fast core, and is not changed appreciably by the moderator concentration; however, it raises the neutron spectrum in the region lower than its peak energy.

The following has been shown by the survey calculations of criticality. The neutron spectrum in the graphite system is very close to that in the beryllium system, but the critical mass is extremely large. The neutron spectrum in the hydrogenous system is not so widely variable as in the beryllium system because of neutron pile-up near the thermal-energy region due to the high moderating power of hydrogen. For this reason, beryllium or a carbon-rich hydrogenous material is recommended as a moderator for the intermediate system.

The critical masses of various intermediate systems, evaluated by using the code HUMPTHUMP, are given in Tables I and II; and the geo-

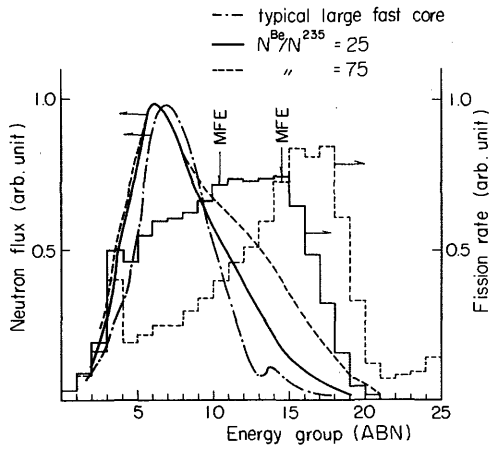

FIG.1. Neutron spectrum and fission rate at centre of a 20%-enriched uranium/Be system.

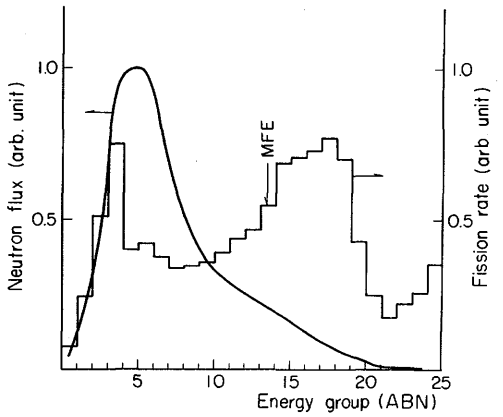

FIG.2. Neutron spectrum and fission rate at centre of a 20%-enriched uranium/graphite/polyethylene system.

metry of the heterogeneity are also shown in Fig. 3. In these talbes, "NO-WIGNER" means that the corrected group cross-sections used for criticality calculation were obtained by means of Eq. (2) and the collision probability, and that group cross-sections appearing in the procedure were assumed to be those in the infinite media. Therefore, the corrected group constants obtained in the case of "NO-WIGNER" are evidently underestimated.

In the case of "WIGNER", the corrected group constants in the resonance-energy region (that is to say, in the energy groups where the F-table is given in the ABN cross-section set) were evaluated by means of the Wigner approximation given in Eq. (3); and the corrected group constants in the other energy regions, were obtained by the same manner as for "NO-WIGNER". In this case, the corrected group constants are

TABLE I. HETEROGENEITY EFFECT ON CRITICAL MASS
(20%-enriched uranium-polyethylene-graphite system with a 30-cm-thick natural uranium blanket)

Method \ Case	A	B	C	D	B-1	B-2	C-1	C-2
Homog.	56.9	75.1	94.0	127.3	75.1	75.1	94.0	94.0
WIGNER	53.2	66.6	74.6	87.9	66.0	67.7	74.1	76.3
BELL	-	61.3	72.0	-	-	-	-	-
NO-WIG.	-	50.1	55.2	-	-	-	-	-

(the critical mass is given in kg ^{235}U)

probably overestimated. In the case of "BELL", the Dancoff correction was applied for the resonance-energy region.

As shown in the tables, the heterogeneity effect on the criticality is considerably large and positive in all cases; and the rearrangement of fuel and moderator plates does not affect strongly the criticality. The difference in critical mass among the cases of WIGNER, NO-WIGNER and BELL (shown in the tables) is induced only by the different group constants in the resonance-energy region used for the criticality calculation because the same process was used, except for the resonance-energy region in each case.

From the discussion given below, the conclusion may be drawn that the main reason for this positive heterogeneity effect is due to the difference in self-shielding characters of the fission and capture cross-sections of 20%-enriched uranium fuel between the homogeneous and the heterogeneous systems. This causes a difference in the fission-absorption ratio in the resonance-energy region between the homogeneous and the heterogeneous systems. A typical example of this difference in the fission-absorption ratio is shown in Fig. 4. In the beryllium-moderated system, the difference is seen in the resonance-energy region and in a very high energy region. The latter may be due to the (n, 2n) reaction of the beryllium. In the polyethylene-graphite moderated system, it is not observed because of the small absorption cross-section of the moderator in the high-energy region.

The spatial distribution of the neutron flux in the beryllium-moderated system is shown in Fig. 5. This space-dependence does not seem to be so strong as to be able to explain the positive effect mentioned above.

The Doppler effect of the whole system is also influenced by the heterogeneity arrangement of fuel and diluent material, and a typical example is given in Table II.

The heterogeneity effects described in this section also appear in a large, dilute fast-reactor system. However, these effects on criticality are small so that it is difficult to obtain information on the cross-sections in the resonance-energy region from the study of criticality in the large, dilute fast-reactor system. In the intermediate system, however, these effects are emphasized so that it is expected to obtain useful information

TABLE II. HETEROGENEITY EFFECT ON CRITICAL MASS AND DOPPLER EFFECT
(20%-enriched uranium-beryllium system with a 30-cm-thick natural uranium blanket)

Critical mass (kg ^{235}U)
N_{Be}/N^{235} = 75, T = 300°K

Method \ Case	E	F	Homog.
NO-WIG.	69.8	69.0	113.0
WIGNER	85.2	78.7	-
N_{Be}/N^{235} = 75, T = 2100°K			
NO-WIG.	72.5	-	(-4.00%)
WIGNER	90.6	-	-
N_{Be}/N^{235} = 25, T = 300°K			
NO-WIG.	107.3 (2.07%)	152.5 (2.27%)	170.9 -
WIGNER	117.8 (0.19%)	112.8 (1.07%)	- -

The value given in the brackets gives the excess reactivity compared with homogeneous system at 300°K.

Doppler effect

Doppler effect induced by heating the whole core of the N_{Be}/N^{235} = 75 system.

HOMOG. -4.0% $\Delta k/k$/ (2100-300)°K
WIGNER -1.3% $\Delta k/k$/ (2100-300)°K
NO-WIG. -0.76% $\Delta k/k$/ (2100-300)°K

for the cross-section in the resonance-energy region from the study of the heterogeneity effect on criticality in the system.

Heterogeneity effect in sample reactivity measurement

The reactivity change, induced by the insertion of a small sample into the reactor system, is widely measured to obtain useful information on reactor physics. However, the correction due to the heterogeneity of

U | P | G	U	G	P	G	U	
case A	3.18	1.60	3.18	1.6		mm
case B	3.18	3.18	3.18	3.18		
case C	3.18	6.36	3.18	6.36		
case D	3.18	9.54	3.18	9.54		
P | U | P	G	P	U	P	G	
case B-1	6.32	1.6	3.18	1.6		mm
case C-1	12.64	1.6	3.18	1.6		
P | U | G	P	U	G	P	U	
case B-2	3.18	3.18	6.32			mm
case C-2	3.18	3.18	12.64			
B | U | B	U	B	U	B	U	
case E	3.18	18.0				mm
case D	6.36	36.0				
case F	3.18	6.9				
case G	6.36	13.8				

Abbreviation: U : uranium, P : polyethylene,
G : graphite, B : beryllium.

10.6v/o of iron and 4.8v/o of void are homogeneously distributed in each region.

FIG.3. Configuration of fuel and diluent plates.

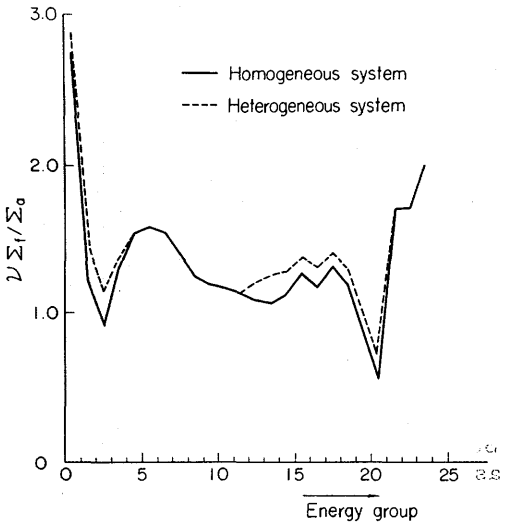

FIG.4. Heterogeneity effect on $\nu\Sigma_f/\Sigma_a$ in a 20%-enriched uranium/Be system. Fuel thickness = 0.32 cm. $N^{Be}/N^{235} = 75$.

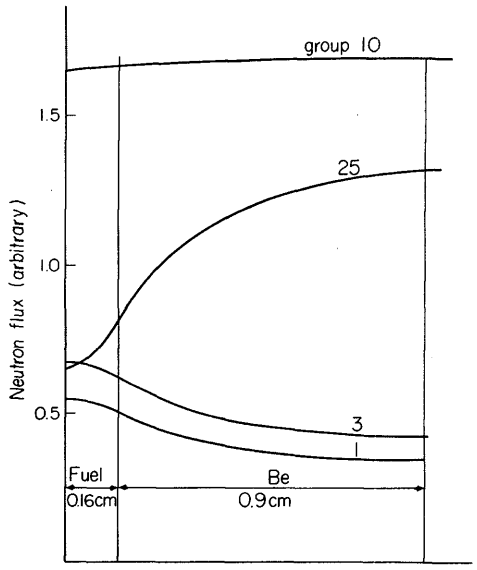

FIG.5. Spatial distribution of neutron flux in the unit cell (N^{Be}/N^{235} = 75).

the sample and surrounding medium is probably important for the interpretation of the measured reactivity change. For example, the Doppler experiment is, in general, performed by measuring a reactivity change induced by heating a small sample in a reactor system. In actual fact, however, the composition of the sample is usually different from that of the surrounding media. The concentration of the material of interest in the sample is very high, e.g. ^{235}U, ^{239}Pu, and it is diluted by the fertile, coolant and structural materials in the surrounding media.

This different concentration introduces the heterogeneity effect, which may have an influence on the interpretation of the measured Doppler effect. This kind of heterogeneity effect was first studied by Storrer [5] by means of non-leakage probability; but he assumed the same composition in the sample and the surrounding media and the heterogeneity effect was induced only by the temperature difference between the sample and the surrounding media. This paper discusses the heterogeneity effect which is induced by both the difference in the concentration and the temperature between the sample and the surrounding media.

(1) Method of analysis

The perturbation theory was used for the analysis of induced reactivity change. Suppose that the reactor equation can be written in the general form, as

$$[O_1 - \nu O_2]\phi(r,u) = 0 \qquad (4a)$$

Here, $\phi(r,u)$ denotes the neutron flux as a function of the space and lethargy, and $[O_1 - \nu O_2]$ symbolizes an operator chosen appropriately for the system at hand, and ν is the hypothetical average number of neutrons per fission.

If we allow an alteration in the reactor system, the perturbed system is expressed as

$$\left[O_1' - \nu' O_2' \right] \phi' (r, u) = 0 \tag{4b}$$

Suppose that each of the primed quantities in Eq. (4b) takes the form

$$\begin{aligned} O_1' &= O_1 + \delta O_1 \quad , \quad O_2' = O_2 + \delta O_2 \\ \nu' &= \nu + \delta \nu \quad , \quad \phi' = \phi + \delta \phi \end{aligned} \tag{5}$$

By using the adjoint function

$$\delta \nu = \frac{\langle \Phi^* (\delta O_1 - \nu \delta O_2) \phi \rangle + \langle \Phi^* (\delta O_1 - \nu \delta O_2) \delta \phi \rangle}{\langle \Phi^* O_2 \phi \rangle + \langle \Phi^* \delta O_2 \phi \rangle + \langle \Phi^* O_2 \delta \phi \rangle + \langle \Phi^* \delta O_2 \delta \phi \rangle} \tag{6}$$

If we consider the reactivity change induced by inserting a small sample into a reactor system, the operator will not change in the media surrounding the sample. Let us discuss the effect of the second-order small quantities in the perturbation theory, as given by Eq. (6). In general, the $\delta \phi$ takes a maximum value in the sample and the integration in the numerator of Eq. (6) is carried out over the small volume of the sample; therefore, the second term in the numerator may sometime exhibit a considerable effect on the reactivity change. The first and third terms in the denominator of Eq. (6) are evaluated by integrating over the whole reactor volume but the value of $\delta \phi$ in the surrounding media is small. Therefore, the ratio of the third to the first term in the denominator is much smaller than that of the second to the first term in the numerator, so that the third term in the denominator may be neglected. The second and fourth term in the demoninator are evaluated by integrating only over the small volume, while the first term is obtained by integrating over the whole reactor system. Therefore, these terms may be negligible, compared with the first term.

Consequently, the second-order small quantities in perturbation will affect the reactivity change mainly through the second term in the numerator. As a result, Eq. (6) is approximately expressed by

$$-\frac{\delta k}{k} \simeq \frac{\langle \Phi^* (\delta O_1 - \nu \delta O_2) (\phi + \delta \phi) \rangle}{\nu \langle \Phi^* O_2 \phi \rangle} \tag{7}$$

The most predominant contribution to the reactivity change is, in many cases, induced by the changes in fission and capture cross-sections. By analogy with the one-velocity model, it can be shown from Eq. (7) that a correction should be first made for the change of fission and capture reaction rates due to the perturbed flux.

The reaction rate of the sample in a reactor system will be discussed by using the concept of non-leakage probability. By using the uniform collision density in each region, the reaction rate J in the sample is obtained,

$$J = q_0 V_s \left\{ \frac{\Sigma_p^s}{\Sigma_p^r} \int_u^{u'} \frac{\sigma_a^s}{\ell^{-1}+\sigma^s}\, du + \frac{1}{\ell} \int_u^{u'} \frac{\sigma_a^s}{\ell^{-1}+\sigma^s} \frac{1}{\sigma^r}\, du \right\} \tag{8}$$

where q_0 : slowing down density in the surrounding region,
V_s : volume of the sample,
Σ_p^s, Σ_p^r : potential scattering cross-section in the sample and surrounding region respectively,
σ^s, σ_a^s : total and absorption cross-section in the sample,
σ_r : total cross-section in the surrounding region,
ℓ : mean chord length,
u', u : upper and lower lethargy of the energy group of interest.

For simplicity, the resonance interference effect is ignored and the same resonance material is considered both in the sample and the surrounding media. The reaction rate in the energy group of interest is thus approximately obtained by

$$J = q_0 V_s \sum_k \frac{\Gamma_{kx}}{E_k} \left\{ \frac{\Sigma_p^s}{\Sigma_p^r} \int_0^\infty \frac{\psi_k(\theta)}{\alpha_k+\psi_k(\theta)}\, dx + \frac{1}{\ell N^r \sigma_{k0}} \int_0^\infty \frac{\psi_k(\theta)}{\alpha_k+\psi_k(\theta)} \cdot \frac{dx}{\beta_k+\psi_k(\theta')} \right\} \tag{9}$$

where $\alpha_k = \dfrac{\ell^{-1}+\Sigma_p^s}{N^s} \cdot \dfrac{1}{\sigma_{k0}}$, $\beta_k = \dfrac{\Sigma_p^r}{N^r} \cdot \dfrac{1}{\sigma_{k0}}$

$$\psi_k(\theta) = \frac{\theta}{2\sqrt{\pi}} \int_{-\infty}^{\infty} \frac{\exp\left[-\frac{1}{4}\theta^2 (x-y)^2\right]}{1+y^2}\, dy$$

$$\sigma_{k0} = \frac{2.6 \times 10^6}{E_k} g_k \frac{\Gamma_{kn}}{\Gamma_k}, \quad \theta = \frac{\Gamma_k}{\Delta}, \quad \theta' = \frac{\Gamma_k}{\Delta'}$$

and Δ and Δ' : Doppler width,
N^s and N^r : atomic density of resonance material in the sample and the surrounding media respectively,
Γ_k : total width of the k-th resonance,
Γ_{kx} : partial width of the reaction of interest of the k-th resonance.

In the energy region where no experimental knowledge of individual resonance is available, the expected value of reaction rate J is evaluated by using the average quantities of resonance parameters and their distribution functions. After segregating Eq. (9) with respect to neutron angular momentum and compound nucleus spin, the value of J can be obtained by integrating Eq. (9), which has been multiplied by a suitable weight function of the Chi-squared distribution function. In general, the second term in Eq. (9) has to be specially evaluated by numerical integration.

The reaction rate J is introduced in the perturbation equation to obtain the reactivity change by modifying the cross-section $\langle \sigma_x \rangle$ as follows,

$$\sigma_x = \kappa_x f_x \left(\frac{\ell^{-1} + \Sigma_p^e}{N_r^e}, \; T \right) \langle \sigma_x \rangle \qquad (10)$$

Here κ_x is defined as $\kappa_x = J / J_{WIG.}$

where $J_{WIG.}$ is the reaction rate in the sample when the N^r is equal to zero; f_x and $\langle \sigma_x \rangle$ are the self-shielding factor and group cross-section given in the ABN set [4].

(2) Results and discussion

The reactivity change induced by inserting a sample into the core centre was obtained both by the Wigner approximation and the corrected method given in Eq. (10). The heterogeneity effect, as a function of $\ell = 4v/S$, was defined as the ratio of the reactivity change in the case of a finite size of sample to that for $\ell = \infty$. This heterogeneity effect is given in Table III. In the table, (W) means the effect obtained by using the Wigner approximation and (C) means the value by the corrected method including the influence of the resonance material in the surrounding region.

TABLE III. HETEROGENEITY EFFECT ON THE REACTIVITY CHANGE OF THE SAMPLE

^{238}U oxide sample T=300°K

		$\ell=\infty$	$\ell=8$	$\ell=4$	$\ell=2$	$\ell=1$
Large	(W)	1.00	1.01	1.02	1.04	1.08
	(C)	-	1.00	1.00	1.00	1.01
Be-25	(W)	1.00	1.02	1.04	1.07	1.12
	(C)	-	1.01	1.01	1.02	1.04
Be-75	(W)	1.00	1.04	1.08	1.15	1.27
	(C)	-	1.03	1.05	1.10	1.16
Be-150	(W)	1.00	1.05	1.10	1.18	1.35
	(C)	-	-	1.07	1.14	1.25

^{235}U oxide sample T=300°K

Large	(W)	1.00	1.003	1.005	1.009	1.012
	(C)	-	-	1.004	1.006	1.01
Be-25	(W)	1.00	1.004	1.008	1.013	1.021
	(C)	-	-	1.005	1.008	1.014
Be-75	(W)	1.00	1.01	1.016	1.028	1.045
		-	-	-	-	-

From the results given in the table, the following conclusions are obtained for the heterogeneity effect on the reactivity change induced by a sample insertion. In the ^{235}U sample, the heterogeneity effect is very small for the samples larger than $\ell = 1$ and no correction is necessary for the heterogeneity effect. In the ^{238}U sample the effect is larger than that for ^{235}U and the correction due to heterogeneity effect seems to be necessary for the samples smaller than $\ell = 4$. In this case, the influence of ^{238}U in the surrounding region clearly appears in the results and the Wigner approximation overestimates the effect.

The heterogeneity effect on the Doppler reactivity induced by a finite size of heated sample was obtained as a function of sample size, in the same manner as for the effect on the reactivity change. This effect on the Doppler reactivity is shown in Table IV.

TABLE IV. HETEROGENEITY EFFECT ON THE DOPPLER REACTIVITY CHANGE $\Delta k_{Dopp.}$(HETERO.)/$\Delta k_{Dopp.}$ (HOMO.)

		l=∞	l=8	l=4	l=2	l=1
^{238}U oxide sample, T=(1200-300)°K						
Large	(W)	1.00	1.01	1.01	1.02	1.04
	(C)	-	1.015	1.03	1.04	1.08
Be-25	(W)	1.00	1.02	1.03	1.05	1.07
	(C)	-	1.03	1.04	1.07	1.10
Be-75	(W)	1.00	1.05	1.08	1.14	1.24
	(C)	-	1.05	1.08	1.15	1.25
Be-150	(W)	1.00	1.06	1.10	1.18	1.34
	(C)	-	-	1.10	1.18	1.34
T=(2100-300)°K						
Large	(W)	1.00	1.00	1.00	1.00	1.02
	(C)	-	1.02	1.03	1.05	1.08
Be-25	(W)	1.00	1.01	1.01	1.03	1.04
	(C)	-	1.02	1.03	1.06	1.10
Be-75	(W)	1.00	1.02	1.06	1.10	1.20
	(C)	-	1.04	1.06	1.12	1.22
Be-150	(W)	1.00	1.04	1.08	1.15	1.31
	(C)	-	-	1.08	1.14	1.32
^{238}U metal sample T=(2100-300)°K						
Be-25	(W)	1.00	1.00	1.00	1.01	1.02
	(C)	-	1.00	1.01	1.02	1.05
Be-75	(W)	1.00	1.03	1.06	1.10	1.17
	(C)	-	1.05	1.09	1.15	1.22
^{235}U oxide sample, T=(1200-300)°K						
Large	(W)	1.00	0.92	0.87	0.74	0.58
	(C)	-	-	0.87	0.76	0.59
Be-25	(W)	1.00	0.93	0.88	0.77	0.62
	(C)	-	-	0.89	0.80	0.67
Be-75	(W)	1.00	0.94	0.91	0.82	0.69
	(C)	-	-	-	-	-

The following conclusions are obtained from the results in Table IV. The heterogeneity effect acts to increase the magnitude of the Doppler reactivity of the sample of ^{238}U, while it decreases the magnitude for ^{235}U. The heterogeneity effect on the ^{235}U sample is larger than that on the ^{238}U sample, while the effect on the total reactivity change given in Table III shows the opposite tendency.

The influence of the resonance material in the surrounding region tends to increase the magnitude of the Doppler reactivity of the sample both for ^{235}U and ^{238}U; however, this influence is not so large especially for the ^{235}U sample. Therefore the Wigner approximation may give a good correction for the heterogeneity effect on the Doppler reactivity change. There is no significant difference between the oxide and metal

sample and also no important difference between the temperature ranges T = 2100-300°K and 1200-300°K.

In Figs. 6 and 7, the heterogeneity effect on the Doppler reactivity is given energy-groupwise. For the ^{235}U sample, the effect acts to decrease the Doppler reactivity in all the energy groups in the resonance-energy region. On the other hand, for the ^{238}U sample, the effect acts to decrease the Doppler reactivity in the higher-energy groups in the region, but the effect acts to increase it in the lower-energy groups. Therefore the total Doppler reactivity is not so strongly affected by the heterogeneity as with the ^{235}U sample, as shown in Table IV. In the case of ^{235}U sample, the heterogeneity effect appears to be larger in the higher-energy groups than in the lower.

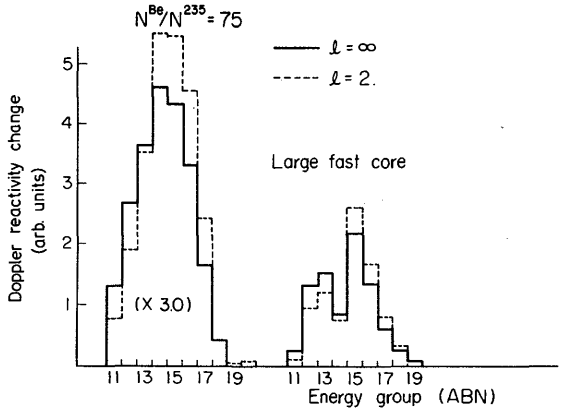

FIG.6. Groupwise Doppler reactivity change of uranium-238 oxide sample ($\Delta T = 1200 - 300°K$).

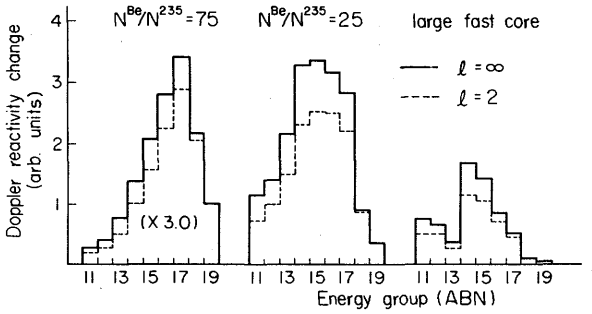

FIG.7. Groupwise Doppler reactivity change of uranium-235 oxide sample ($\Delta T = 1200 - 300°K$).

In the intermediate-energy core, the total Doppler reactivity induced by the inserted sample is significantly larger compared with that in the large, dilute fast core (about ten times as large in the system of $N^{Be}/N^{235} = 75$). Therefore, one can expect to obtain useful information on the cross-section sets in the resonance-energy region from the experimental results of the Doppler reactivity and its heterogeneity effect measured in the intermediate system.

ACKNOWLEDGEMENTS

Thanks are due to Mr. T. Suzuki and Mr. N. Mizoo for their helpful comments on computer codes and methodical computational work; and also to Mrs. Y. Shingai for her preparation of the manuscript.

REFERENCES

[1] HIROTA, J. et al., The JAERI fast critical facility, ANL-7320 (1966) 776.
[2] SUZUKI, T., ISHIGURO, Y., FASTOS code, JAERI-memo-1941 (1965).
[3] DRESNER, L., "Heterogeneous resonance integral-narrow resonances", Ch. 5, Resonance Absorption in Nuclear Reactors, Pergamon Press (1960).
[4] ABAGYAN, L.P. et al., Group Constants for Nuclear Reactor Calculations, Consultants Bureau (1964).
[5] STORRER, F. et al., Theoretical aspects of the measurement of Doppler coefficient in a critical facility, ANL-6792 (1963) 823.

DISCUSSION

W. K. FOELL: Is the Doppler contribution listed in Table II due both to ^{238}U and to ^{235}U, and, if so, does it mean that there is a factor-of-three difference between the homogeneous and the heterogeneous system?

H. KUROI: Yes, it means that the homogeneous assumption is inaccurate when one is evaluating the Doppler effect in the intermediate-energy core system under consideration. Of course, it depends on the fuel thickness used for the system.

HETEROGENEITY CALCULATIONS INCLUDING SPACE-DEPENDENT RESONANCE SELF-SHIELDING*

D. WINTZER
INSTITUT FÜR ANGEWANDTE REAKTORPHYSIK,
KERNFORSCHUNGSZENTRUM KARLSRUHE,
FEDERAL REPUBLIC OF GERMANY

Abstract

HETEROGENEITY CALCULATIONS INCLUDING SPACE-DEPENDENT RESONANCE SELF-SHIELDING. For fast reactors with relatively soft spectra, the influence of heterogeneity on resonance self-shielding becomes important. The widely used Bell-approximation is not applicable if the lattice cell contains an important resonance material in more than one region. The problem of different weighting spectra in different regions of the cell arises.

For this problem a method is proposed in which the weighting spectrum for the evaluation of group parameters is built up by a set of spectra of fictive homogeneous media, characterized by an appropriately chosen set of dilution parameters. The weighting factors for the fictive spectra can be determined, and the group parameters can be calculated using tabulated self-shielding factors for cross-sections.

The method is formulated in terms of collision probabilities. It is restricted to the NR-approximation, but is not restricted to special cell geometries. Furthermore, it is not restricted to rational approximations for the collision probabilities. The method is used in a multigroup cell code with DB^2-corrections to calculate: (a) reaction rates and fluxes for each energy group and for each cell region; (b) k_{eff}-values for the unreflected lattice; (c) cross-sections "corrected" for heterogeneity to be used in global multigroup diffusion calculations.

The group diffusion constants are calculated using Benoist's formula and by neglecting anisotropy of the group diffusion constants. The heterogeneity effect on diffusion constants causes a tendency for the total heterogeneity effect on reactivity to become negative in the outer core region.

For a series of reactor lattices, numerical results are shown and compared with experimental results.

1. INTRODUCTION

Heterogeneity effects must be taken into account in the interpretation of nearly all experiments performed in the lattices of fast assemblies. Several methods have been developed to calculate the influence of heterogeneity on reactivity, and they work rather well for assemblies with hard spectra.

In fast assemblies with rather soft spectra as in steam-cooled fast reactors, the heterogeneity effects in the keV and 100-eV region make an important contribution to the heterogeneity effect. In multigroup calculations the modifications of resonance self-shielding compared with the homogeneous case must be taken into account. This is done frequently by applying equivalence theorems for effective cross-sections, which are based on rational approximations for collision probabilities in the lattice cell. In most applications for fast reactors, Bell's approximation for tight lattices is used [1].

* Work performed within the association in the field of fast reactors between the European Atomic Energy Community and Gesellschaft für Kernforschung mbH., Karlsruhe.

However, this procedure is not useful if the lattice cell contains a material with large resonance cross-sections (for example ^{238}U) in more than one region of the cell or if one wants to subdivide a cell region with resonance cross-sections in order to investigate the spatial fine structure of reaction rates.

In section 4 of this paper an approximation is proposed, which takes into account space dependent self-shielding in a multi-region lattice cell. The method is based on a multigroup collision probability formalism of reaction rates and neutron emission densities in the cell regions (described briefly in sections 2 and 3) and is applied in a computer programme called ZERA. The method is not restricted to small heterogeneity effects and can be applied to thermal reactor problems.

The heterogeneity effect on reactivity is often considerably influenced by a modification of leakage parameters due to heterogeneity. In the mentioned programme such modifications are roughly taken into account as described in section 6.

Several results of ZERA calculations for rod lattices and for plane lattices are shown in the last section. Some of them are compared with experimental results.

2. BASIC EQUATIONS

We start with the integral form of Boltzmann's equation for the critical reactor. Assuming the reactor to consist of N homogeneous regions, and the fission and scattering processes to be isotropic, we get for the mean flux in region n

$$\phi_n(u) = \sum_{m=1}^{N} q_m(u)\, V_m \frac{P_{mn}(u)}{\Sigma_n(u)\, V_n} \tag{1}$$

Here Σ and V are symbols for total cross-section and volume. The collision probabilities P_{mn} have their usual meaning - the probabilities for neutrons, which are isotropically emitted in region m with spatially constant density to suffer their next collision in region n. Thus Eq. (1) involves the assumption that the space dependence of the emission density $q(u,\vec{r})$ within a region can be neglected. If necessary, a subdivision of regions must be performed.

$q_m(u)$ is the average value of $q(u,\vec{r})$ within region m and consists of a fission term (multiplied with an eigenvalue λ) and a down-scattering term:

$$q_m(u) = \int_0^{\infty} du' \phi_m(u') \left[\lambda \nu(u' \to u)\, \Sigma_{f,m}(u') + \Sigma_{s,m}(u' \to u)\right] \tag{2}$$

$\Sigma_{f,m}$ is the macroscopic fission cross-section in region m, $\Sigma_{s,m}(u' \to u)$ is the scattering cross-section for lethargy transitions from u' to u.

Combining (1) and (2), one gets

$$q_n(u) = \sum_{m=1}^{N} \frac{V_m}{V_n} \int_0^{\infty} du' q_m(u') \frac{\lambda \nu(u' \to u)\, \Sigma_{f,n}(u') + \Sigma_{s,n}(u' \to u)}{\Sigma_n(u')} P_{mn}(u') \tag{3}$$

The reaction rate for any collision type α (for example capture) in region n is given by

$$F_{\alpha,n}(u) = \Sigma_{\alpha,n}(u)\,\phi_n(u)V_n = \sum_{m=1}^{N} V_m\, q_m \frac{\Sigma_{\alpha,n}(u)}{\Sigma_n(u)}\, P_{mn}(u) \tag{4}$$

If the reactor or a part of it consists of a periodic lattice, and if the cell concept can be used[1] to calculate the distribution of reaction rates within a unit cell, Eqs (3) and (4) are applicable without formal changes. Only the meaning of two symbols must be modified: N becomes the number of regions or zones within the unit cell, and the collision probabilities P_{mn} must now include contributions of homological zones in neighbouring cells.

3. MULTIGROUP PRESENTATION

For practical calculations it is appropriate to use the multigroup approximation and to express the balance equations in terms of group and zone-averaged emission densities $q_{g,n}$, fluxes $\phi_{g,n}$, and reaction rates $F_{g,\alpha,n}$. The corresponding steps in treating Eqs (1) to (4) are integrations which lead to

$$\phi_{g,n} = \sum_{m=1}^{N} \frac{V_m}{V_n} \left\langle q_m \frac{P_{mn}}{\Sigma_n} \right\rangle_g \Delta u_g \tag{5}$$

$$F_{g,\alpha,n} = \sum_{m=1}^{N} V_m \left\langle q_m \frac{\Sigma_{\alpha,n}}{\Sigma_n} P_{mn} \right\rangle_g \Delta u_g \tag{6}$$

and

$$q_{g,n} = \langle q_n(u) \rangle_g \, \Delta u_g = \sum_{m=1}^{N} \frac{V_m}{V_n} \sum_{k=1}^{G} \left\langle q_m \frac{\lambda \chi_g \nu \Sigma_{f,n} + \Sigma_{k\to g,n}}{\Sigma_n} P_{mn} \right\rangle_k \Delta u_k \tag{7}$$

In these equations, the brackets indicate that the average over the energy group g with a lethargy width Δu_g should be taken:

$$\langle f(u) \rangle_g = \frac{1}{\Delta u_g} \int_{\Delta u_g} f(u)\, du$$

χ_g is the fraction of fission neutrons born into energy group g, so that

$$\chi_g \cdot \nu(u) = \int_{\Delta u_g} \nu(u \to u')\, du'$$

---

[1] The cell concept is applicable if the dimensions of the reactor or the lattice zone in question are large compared with the characteristic cell dimension and with the mean free paths of the neutrons.

The transfer cross-section $\Sigma_{k\to g,n}$ is defined as

$$\Sigma_{k\to g,n}(u) = \int_{\Delta u_g} \Sigma_{s,n}(u\to u')\,du'$$

G is the number of energy groups.

After separation of the emission density in its average group value $\langle q_m(u)\rangle_g$ and an only weakly[2] lethargy-dependent function $w_g(u)$ which is normalized to $\langle w(u)\rangle = 1$, Eqs (5) to (7) can be read as

$$\phi_{g,n} = \sum_{m=1}^{N} \frac{V_m}{V_n}\, q_{g,m} \langle w(u)\, \psi_{mn}(u)\rangle_g \tag{8}$$

$$F_{g,\alpha,n} = \sum_{m=1}^{N} V_m\, q_{g,m} \langle w(u)\Sigma_{\alpha,n}(u)\psi_{mn}(u)\rangle \tag{9}$$

$$q_{g,n} = \sum_{m=1}^{N} \frac{V_m}{V_n} \sum_{k=1}^{G} q_{k,m} \langle w(u)\,[\lambda\chi_g \nu(u)\,\Sigma_{f,n}(u) + \Sigma_{k\to g,n}(u)]\,\psi_{mn}(u)\rangle_k \tag{10}$$

In these equations the abbreviation

$$\psi_{mn}(u) = P_{mn}(u)/\Sigma_n(u) \tag{11}$$

has been introduced. $\psi_{mn}(u)$ is proportional to the flux at lethargy u in region n, caused per unit emission rate in region m.

If the values of the brackets are known, the system of linear equations (10) can be solved to obtain λ, the matrix $q_{g,n}$, group fluxes $\phi_{g,n}$, and reaction rates $F_{g,\alpha,n}$.

The problem is the calculation of the brackets, if the cross-sections are strongly energy dependent within the energy group. They appear in the general form

$$A_{g,\alpha,m,n} = \langle w(u)\,\Sigma_{\alpha,n}(u)\,\psi_{mn}(u)\rangle_g \tag{12}$$

and have the physical meaning of a reaction rate in group g and region n caused per unit emission rate in group g and region m. We will call them "reaction coefficients". The bracket in Eq. (8) can be regarded as a special case of (12), with $\Sigma_{\alpha,n}(u) = 1$ and will be denoted as $A_{g,\phi,m,n}$.

In principle it is possible to calculate the collision probabilities $P_{mn}(u)$ for a series of lethargy points within each energy group and to evaluate the reaction coefficients by numerical integrations. However, if large reso-

---

[2] In the sense of the narrow resonance approximation.

nance cross-sections must be taken into account this procedure is extremely time consuming and causes difficult computer storage problems.

To cope with similar difficulties for homogeneous problems, the Obninsk [2] group has proposed using tabulated self-shielding factors for microscopic cross-sections. These are defined as

$$f_{\alpha,\nu}(\sigma_{\nu 0}) = \frac{\bar{\sigma}_{\alpha,\nu}}{\langle \sigma_{\alpha,\nu}(u) \rangle} = \frac{1}{\langle \sigma_{\alpha,\nu}(u) \rangle} \cdot \frac{\left\langle w(u) \frac{\sigma_{\alpha,\nu}(u)}{\sigma_\nu(u)+\sigma_{\nu 0}} \right\rangle}{\left\langle w(u) \frac{1}{\sigma_\nu(u)+\sigma_{\nu 0}} \right\rangle} \qquad (13)$$

and will be used in the next section.

$\sigma_{\nu 0}$, the background cross-section, is the sum of the cross-section contributions of other nuclides per atom of nuclide ν; it is assumed to be constant within the energy group under consideration.

4. CALCULATION OF THE REACTION COEFFICIENTS

Splitting $A_{g,\alpha,m,n}$ into contributions of individual nuclides

$$A_{g,\alpha,m,n} = \sum_\nu A_{g,\nu,\alpha,m,n} \qquad (14)$$

leads to

$$A_{g,\nu,\alpha,m,n} = N_{\nu n} \langle w(u) \sigma_{\alpha,\nu}(u)\, \psi_{mn}(u) \rangle_g \qquad (15)$$

If $\sigma_{\alpha,\nu}(u)$ contains large resonances in group g, the main contributions to $A_{g,\nu,\alpha,m,n}$ will be due to reactions near resonance energies. For this reason, $\psi_{mn}(u)$ must be carefully calculated near the resonances of nuclide ν. If an overlapping of large resonances of different nuclides does not occur in the cell regions, the energy dependence of ψ_{mn} at resonance values of σ_ν is predominantly determined by the energy dependence of $\sigma_\nu(u)$.

If the resonance character of the cross-sections must be taken into account in one region n of the cell only, the dependence of ψ_{mn} on σ_ν can be approximated by a rational function (see, for example, Refs [1, 3].)

$$\psi_{mn}(\sigma_\nu(u)) = \frac{a_{\nu,m,n}}{\sigma_\nu(u) + b_\nu} \qquad (16)$$

which is proportional to the fine structure of the spectrum near resonances of σ_ν in a fictitious homogeneous medium, as characterized by a background cross-section b_ν per atom of nuclide ν. The fictitious cross-section b_ν involves geometrical parameters of the resonance region. The formal agreement of Eq. (16) with the resonance behaviour of the flux in a homo-

geneous medium[3] is the substance of the well-known equivalence theorem [3] and makes the use of self-shielding factors or resonance integrals possible in many heterogeneous cases.

However, the known equivalence theorems cannot be used in more general cases, where resonance cross-sections of the same nuclide (for example ^{238}U) are present in more than one region of the cell. For this reason, using equivalence theorems it is not possible to subdivide a region with resonance cross-sections, which sometimes would be valuable for studying the spatial fine structure of resonance reactions or to describe more accurately the emission density distribution.

Furthermore, the derivation of Eq. (16) is based on a rational approximation for collision probabilities, which is rather inaccurate for plane cells.

Actually, exact functions or good approximations for the dependence of the collision probabilities on cross-sections and geometrical parameters are known for most cases of practical interest, but in general they lead to a more complicated function for $\psi_{mn}(\sigma_\nu)$ than Eq. (16).

The main advantages of the equivalence theorems (the separation of reaction coefficients or effective cross-sections into nuclide contributions and the use of tabulated self-shielding factors or resonance integrals) can be saved if it is possible to approximate $\psi_{mn}(\sigma_\nu)$ by series of rational functions, i.e., if

$$\psi_{mn}(\sigma_\nu) = \sum_{j=1}^{J} \frac{a_{\nu,j,m,n}}{\sigma_\nu + b_{\nu j}} \tag{17}$$

Introducing (17) into (15), one gets

$$A_{\nu,\alpha,m,n} = N_{\nu n} \sum_{j=1}^{J} a_{\nu,j,m,n} \left\langle w(u) \frac{\sigma_{\alpha,\nu}(u)}{\sigma_\nu(u) + b_{\nu j}} \right\rangle \tag{18}$$

(We have dropped now the group index g.)

The brackets in the last equation can be calculated from self-shielding factors using the relation

$$\left\langle w(u) \frac{\sigma_{\alpha,\nu}(u)}{\sigma(u) + \sigma_{\nu 0}} \right\rangle = \frac{\bar{\sigma}_{\alpha,\nu}}{\bar{\sigma}_\nu + \sigma_{\nu 0}} \tag{19}$$

---

[3] The formal agreement can be seen by specializing Eq. (11) to a one-region cell, which describes a part of a large homogeneous medium with a total cross-section $\Sigma(u)$. The collision probability matrix reduces to one number $P_{11} = 1$, and ψ_{11} becomes

$$\psi_{11} = \frac{1}{\Sigma(u)} = \frac{1/N_\nu}{\sigma_\nu(u) + \sigma_{\nu 0}}$$

N_ν is the number of atoms of nuclide ν in the medium, $\sigma_{\nu 0}$ the background cross-section due to other nuclides.

which follows from

$$\frac{1}{\left\langle \frac{w(u)}{\sigma_\nu(u) + \sigma_{\nu 0}} \right\rangle} = \overline{\sigma}_\nu + \sigma_{\nu 0}$$

(see Eq.(13)).

As in Eq.(16) the parameters $b_{\nu j}$ can be interpreted as background cross-sections, which characterize the dilutions of nuclide ν in a set of J fictitious media. Equation (17) describes a superposition of the corresponding spectra.

In some cases it is possible to derive reasonable values for $b_{\nu j}$ from physical considerations, in which the special neutron optical parameters of the cell are taken into account. However, it is difficult to do this generally.

For this reason, we do not try to derive the $b_{\nu j}$ from cell parameters, but choose them to make the expression (17) flexible in the cross-section interval of interest (that is approximately the interval between $\sigma_{p\nu}$ and the largest resonance cross-section $\sigma_{\nu,\max}$ in the energy group).

It was found that the expression (17) yields a good approximation for the function in the interval $\sigma_{p\nu} < \sigma_\nu < \sigma_{\nu,\max}$, if the parameters $b_{\nu j}$ cover about the same interval uniformly on a log-scale. The achievable accuracy grows with the number J of terms in (17) (see below).

The coefficients $a_{\nu,j,m,n}$ can be obtained by calculating some values of the function $\psi_{mn}(\sigma_\nu) = P_{mn}(\sigma_\nu)/\Sigma_n$ and by fitting the expression (17) to these values.

The advantage of the described approximation is that it is not restricted to a rational approximation for $P_{mn}(\sigma_\nu)$. One is free to use exact formulas or the best known approximations for the calculation of collision probabilities and is not limited to a certain type of cell geometry. The methods for P_{mn}-calculations used in the code ZERA for rod lattices and for plane lattices are described in a paper to be published in the near future.

For the investigation of relatively small heterogeneity effects as they occur in fast reactors, the accuracy of the described method can be improved by a slight modification. The approximation (17) is not used for $\psi_{mn}(\sigma_\nu)$ but for

$$\psi^*_{mn}(\sigma_\nu) = \psi_{mn}(\sigma_\nu) - \psi_{mn,\,hom}$$

where $\psi_{mn,\,hom} = P_{mn,\,hom}/\Sigma_n$ is the limit of ψ_{mn} for cells with extremely small dimensions, but with the same compositions and relative region dimensions as the heterogeneous cell. For this limit, the collision probabilities clearly become:

$$P_{mn,\,hom} = \frac{\Sigma_n V_n}{\sum_{m=1}^{N} \Sigma_m V_m} \qquad (20)$$

At energies near resonances of nuclide ν, $\psi_{mn,\,hom}(\sigma_\nu)$ is then

$$\psi_{mn,\,hom} = \frac{\dfrac{1}{\sum_{m=1}^{N} N_{\nu m} V_m / V_n}}{\sigma_\nu + \sum_{\nu' \neq \nu} \sigma_{\nu'} \dfrac{\sum_{m=1}^{N} N_{\nu' m} V_m}{\sum_{m=1}^{N} N_{\nu m} V_m}} \qquad (21)$$

Again, the energy dependence of the second term in the denominator of (21) at resonance values of σ_ν is neglected.

The advantage of approximating $\psi^*_{mn}(\sigma_\nu)$ instead of $\psi_{mn}(\sigma_\nu)$ is obvious: for cell dimensions which are small compared with the mean free paths of neutrons a small difference of similar functions is approximated; it is this difference which actually represents the heterogeneity effect.

This modification has been applied in a series of test calculations, and it was found that a number of approximately 5 terms in (17) is sufficient to get a good approximation for $\psi_{mn}(\sigma_\nu)$ and to obtain (from Eq. (18)) rather accurate reaction coefficients.

Some typical results are shown in Fig. 1 for a two-region plate cell which is specified in Table I.

The calculations were performed with cross-sections of group 19 of the ABN-set [2]. In this energy group the resonance self-shielding effects, especially for ^{238}U, are rather strong. (Self-shielding factors vary between 0.023 and 1.) Two of the calculated reaction coefficients, the coefficients for absorption ($A_{a,1,2}$) and elastic scattering ($A_{e,1,2}$) are plotted in Fig. 1a as a function of J for constant values $b_{\nu J} = 400\ \sigma_{p\nu}$. The other values $b_{\nu j}$ were placed equidistantly on a logarithmic σ-scale, with the smallest value $b_{\nu 1} = \sigma_{p\nu}$. The same numbers were used for the σ_ν-values for which the fitting values of ψ^*_{mn} were calculated from Eq. (11).

For five or more fictive homogeneous mixtures the results for $A_{a,1,2}$ do not differ by more than 0.5%; for $A_{e,1,2}$ the agreement is even better.

Figure 1b shows the dependence of the reaction coefficients on the highest dilution parameter $b_{\nu J}$ (which is also the highest scanning point for $\psi^*_{mn}(\sigma_\nu)$). All the results shown in Fig. 1b were obtained with 10 fictitious dilutions, so that a good approximation of $\psi^*_{mn}(\sigma_\nu)$ in the interval $\sigma_{p\nu} < \sigma_\nu < \sigma_{\nu J}$ can be assumed. Perhaps it is surprising[4] that even for $\sigma_{\nu J} = 400\ \sigma_{p\nu}$ rather good results are achieved. However, this may be explained by the fact that in large resonances most of the reactions occur in the wings.

[4] For ^{238}U, $\sigma_{\nu J} = 400\ \sigma_{p\nu} \approx 4000$ b is much smaller than the maximum cross-section in group 19 ($\approx 40\,000$ b).

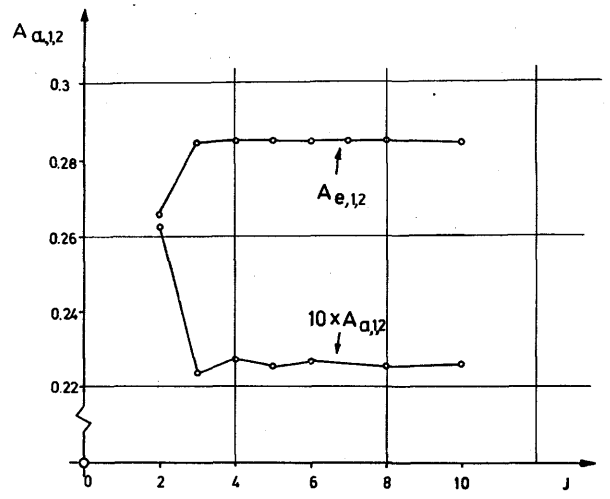

FIG.1(a). Dependence of reaction coefficients on the number J of terms in Eq.(17).

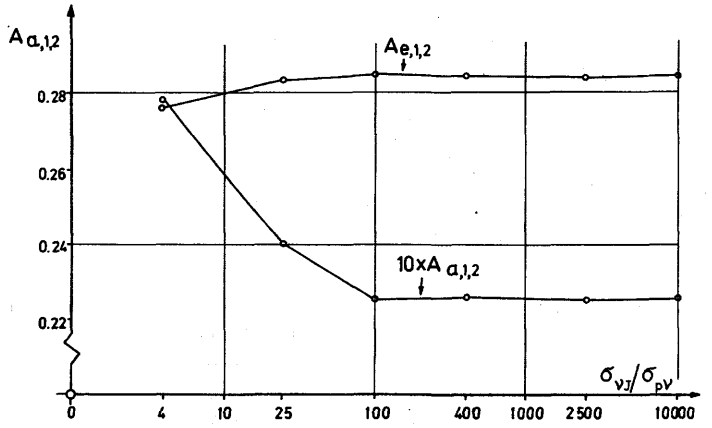

FIG.1(b). Dependence of reaction coefficients on $\sigma_{\nu J}$ (J = 10).

TABLE I. DETAILS OF TWO-REGION PLATE CELL

Plate number	^{235}U-density	^{238}U-density	H-density	Thickness (cm)
1	1×10^{22}	2×10^{22}	-	1
2	-	4×10^{22}	1×10^{22}	1

5. LEAKAGE CORRECTIONS

To find a realistic equilibrium spectrum which takes into account the finite size of the lattice, DB^2-corrections are applied in the cell code ZERA: all reaction rates within an energy group are reduced by a factor

$$f_B = \frac{\text{Removal rate}}{\text{Removal rate} + \overline{D}B^2 \sum_{n=1}^{N} \phi_n V_n} \tag{22}$$

The application of this factor for all cell regions implies the assumption that the spatial distribution of reaction rates is not influenced by the global diffusion of neutrons.

The group diffusion coefficients $\overline{D}$ are calculated from Benoist's formula [4]:

$$3\overline{D} \sum_{n=1}^{N} \phi_n V_n = \sum_{n=1}^{N} \phi_n V_n \sum_{m=1}^{N} P_{n,m} / \Sigma_{tr,m} \tag{23}$$

This formula can be applied if the buckling components in the fundamental directions are equal, i.e. if

$$B_x^2 = B_y^2 = B_z^2 = B^2/3 \tag{24}$$

or, for a cylindrical reactor, if

$$B_r^2 = 2B_z^2 = \frac{2}{3} B^2 \tag{24a}$$

If Eqs (24) or (24a) do not hold, the anisotropy of diffusion, which is due to streaming effects, must be taken into account. We have not done this because it demands the complicated calculation of modified collision probabilities (see Ref. [4]).

However, we think that Eq. (23) at least leads to a reasonable estimate of heterogeneity effects on leakage.

6. DERIVATION AND APPLICATION OF HETEROGENEITY-CORRECTED CROSS-SECTIONS

As already mentioned, the solution of Eq. (10) leads to the eigenvalue λ and to group- and region-dependent fluxes and reaction rates. $1/\lambda$ is the multiplication factor k_∞ for the infinite lattice, if no buckling corrections are applied. If DB^2-corrections are performed as described in the preceding section, $1/\lambda$ becomes the (static) effective multiplication factor k_{eff} for an unreflected finite lattice with a geometrical buckling B^2. (For a homogeneous one-region cell, λ agrees with the result of zero-dimensional calculations using the same cross-section set and the same buckling.)

However, differences in k_{eff}-values of homogeneous and heterogeneous cells do not contain enough information for calculating heterogeneity effects on reactivity for reactors with different lattices in different zones.

For this reason, the code ZERA was extended to calculate "heterogeneity-corrected" cross-sections Σ^*_α in order to use them in multigroup diffusion codes.

They are derived from

$$\Sigma^*_\alpha \cdot \sum_{n=1}^{N} \phi_n V_n = \sum_{n=1}^{N} F_{\alpha,n} \tag{25}$$

The transport cross-sections are calculated from

$$\Sigma^*_{tr} = \frac{1}{3\overline{D}} \tag{26}$$

where $\overline{D}$ is given by Eq.(23). It should be mentioned that these cross-sections are nearly independent of the buckling used.

They also can be applied in perturbation codes, if one is interested in the space dependence of heterogeneity effects. In this case the reactor which is being perturbed is calculated with cross-sections corresponding to homogeneous cells.

In fast reactors with rod lattices, the heterogeneity effect on the diffusion coefficients and the anisotropy of diffusion are usually rather small. Both become more important for reactors with plate lattices, because of the large free paths of neutrons, which impinge under a small angle to the plate surface into plates with small cross-sections. The fraction of neutrons, which have large paths in a cell region with small cross-sections is, for geometrical reasons, appreciably larger than in an equivalent rod lattice cell with the same volume fractions of the cell regions.

If the cell thickness of a plate lattice is small compared with the mean free path of neutrons perpendicular to the plate surfaces, it can be expected that the diffusion coefficient D_Z, corresponding to a flux gradient perpendicular to the plates, is hardly influenced by heterogeneity.

Equation (23) gives the mean of the diffusion ooefficients for the three fundamental directions:

$$\overline{D} = (\overline{D}_x + \overline{D}_y + \overline{D}_z)/3 \tag{27}$$

Since in the homogeneous case it is

$$D_{hom} = D_x = D_y = D_z \tag{28}$$

the difference between $\overline{D}$ and D_{hom} is

$$\overline{D} - D_{hom} = \frac{1}{3}\left[(\overline{D}_x - D_{hom}) + (\overline{D}_y - D_{hom}) + (\overline{D}_z - D_{hom})\right] \tag{29}$$

If the thickness of a plate cell is small enough to neglect $\bar{D}_z - D_{hom}$, and if we consider a cylindrical reactor, Eq.(29) reduces to:

$$\bar{D} - D_{hom} = \frac{2}{3}(\bar{D}_r - D_{hom}) \tag{30}$$

or

$$\bar{D}_r - D_{hom} = \frac{3}{2}(\bar{D} - D_{hom}) \tag{30a}$$

$$\bar{D}_z - D_{hom} = 0 \tag{30b}$$

7. APPLICATIONS

The heterogeneity experiments performed in SNEAK, Assembly 3A-1, were analysed using the methods described above. The radial dependence of reactivity changes owing to bunching, together with calculated curves, is plotted in Fig.2b. A short description of the experiments is presented in Ref. [5]. Figure 2a contains the structure of the normal and bunched cells.

The calculated curves (solid lines in Fig.2b) were gained with a perturbation code by using heterogeneity corrected group cross-sections as described in section 6. The heterogeneity corrections for the diffusion coefficients were calculated from Eqs (30a) and (30b). The agreement between experiment and calculation is satisfactory near the core centre. Only a qualitative agreement is achieved near the core boundary.

The dashed lines in Fig.2b do not contain any heterogeneity corrections for the diffusion coefficients. They cannot explain the change in sign of the bunching effect in the boundary region of the core.

Figures 3 and 4 give some insight into the energy distribution of the heterogeneity effects in a central core zone, in which the spectrum can be assumed to be the equilibrium spectrum corresponding to an energy independent buckling. The curves shown are based on ZERA calculations, in which the buckling has been iterated to give $k_{eff} = 1$. Figure 3 shows the relative difference between the heterogeneous and homogeneous spectrum, calculated as $\Delta\phi_{g,n}/\phi_g\,(hom) = (\phi_{g,n}(het) - \phi_g(hom))/\phi_g(hom)$. The spectra are normalized to the same number of fission neutrons per unit time and volume. The solid lines correspond to the uranium plates, the circles to the steel CH_2 plates. The values of the two other remaining plates in the cell generally lie between the uranium and the steel CH_2 points. The flux concentration in the uranium plates in the MeV-region is the reason for the main contribution to the bunching effect on reactivity (compare Fig.4). The spatial flux distribution in this energy region seems to be rather well calculated, as can be concluded from a comparison of Rh-activation distributions with calculated values (see Ref. [5]). Enlarged diffusion and diminished CH_2 down-scattering upon bunching in the MeV-region lead to a lower flux in all cell regions in the 100-keV region. This is the reason for the negative reactivity contributions in Fig.4. Below 10 keV, the emission density peaks in the polyethylene, and the flux depression in the uranium lead to a remarkable softening of the spectrum (in all plates) in the low energy region, which causes reactivity gains.

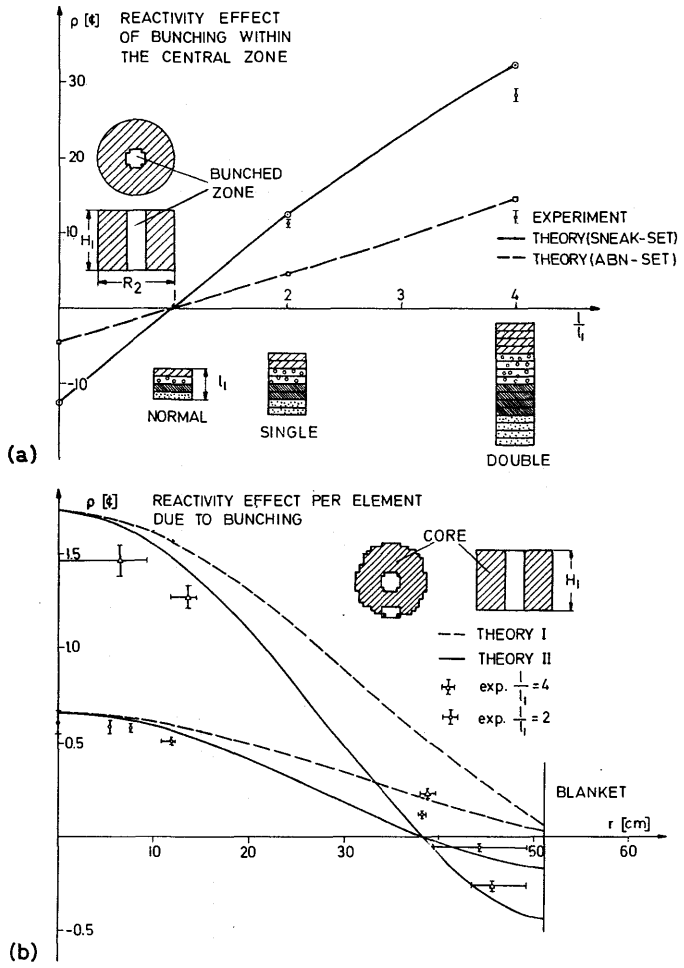

FIG.2(a) and (b). Reactivity effects of single and double bunching in SNEAK Assembly 3A-1.

It can be seen from Fig. 4 that the heterogeneity effects are a result of partially compensating positive and negative effects. The compensating character and the complicated energy distribution tend to make the total reactivity effect rather sensitive to changes in the cross-sections used. This is an explanation for the appreciable difference between the results gained with the ABN- and the SNEAK-set (see Fig. 2a).

It should be noted that the mean hydrogen concentration (7.37×10^{20} atoms/cm^3) is much lower than in a high-pressure steam-cooled reactor, which will be simulated in SNEAK-3A-2. The contributions from the energy region below 10 keV to the total reactivity effect will be considerably larger in SNEAK-3A-2.

Heterogeneity effects in the low energy region are of major importance for the reactivity behaviour during flooding of a steam-cooled fast reactor.

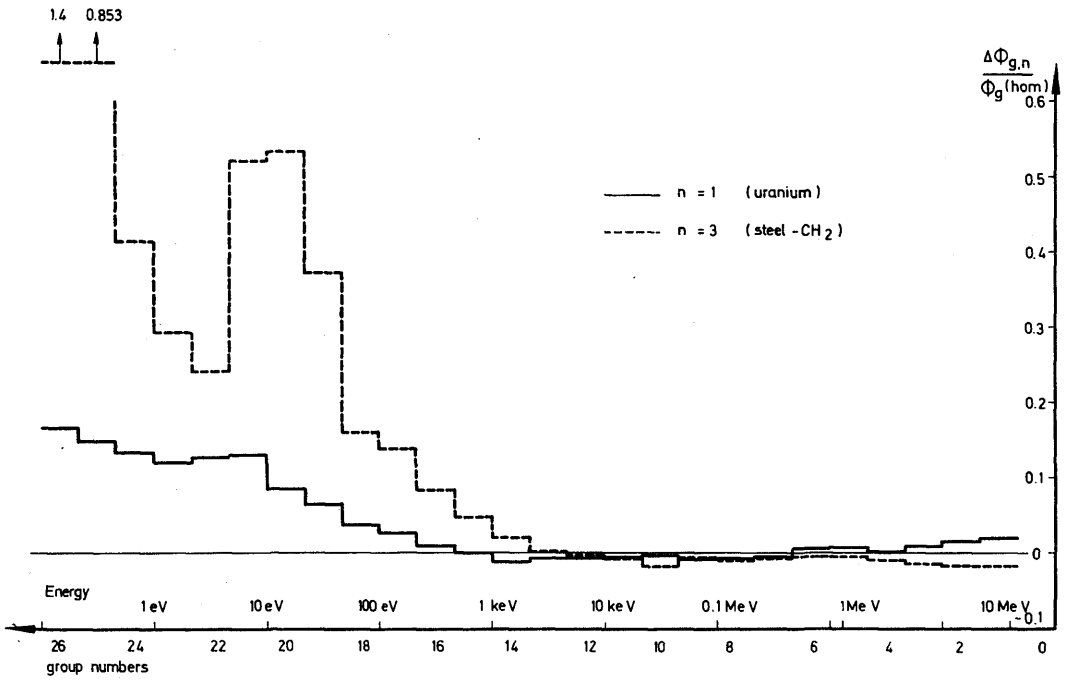

FIG.3. Relative flux changes caused by the heterogeneous cell structure in SNEAK 3A-1.

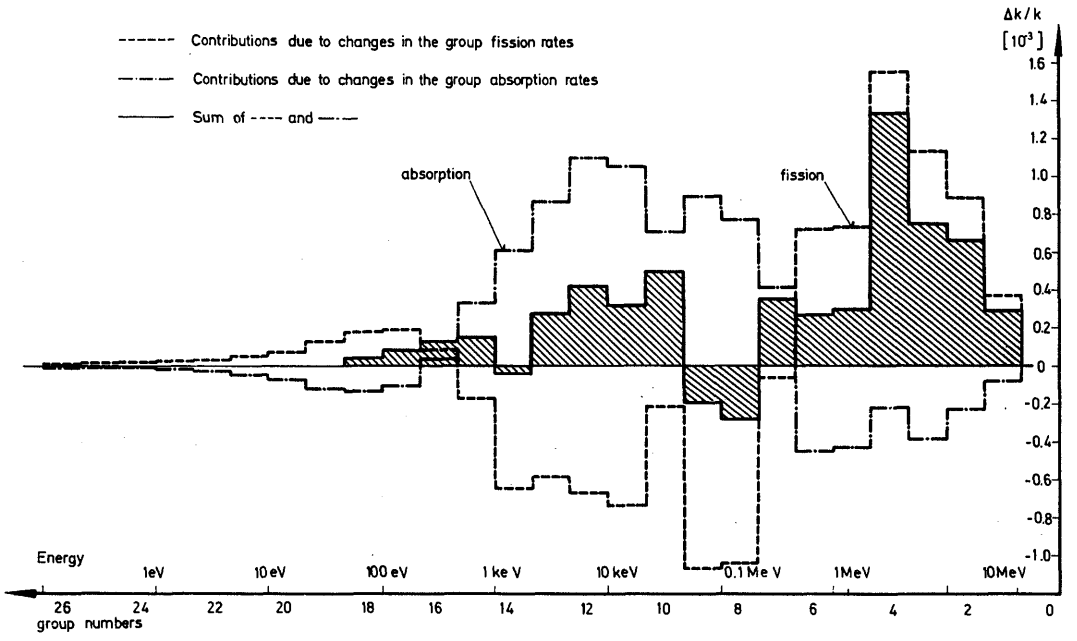

FIG.4. Energy distribution of the bunching effect on reactivity in SNEAK 3A-1.

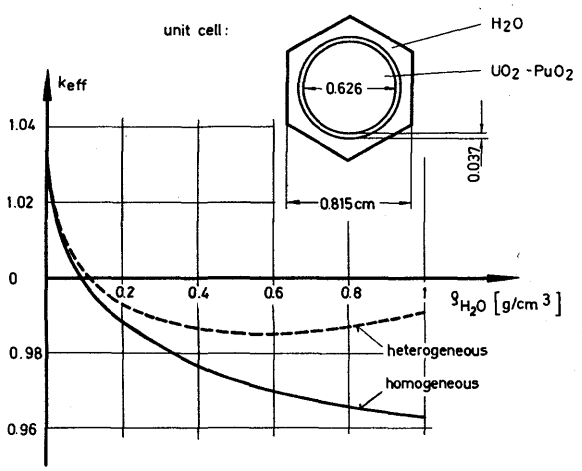

FIG. 5. k_{eff} vs. steam density for D1.

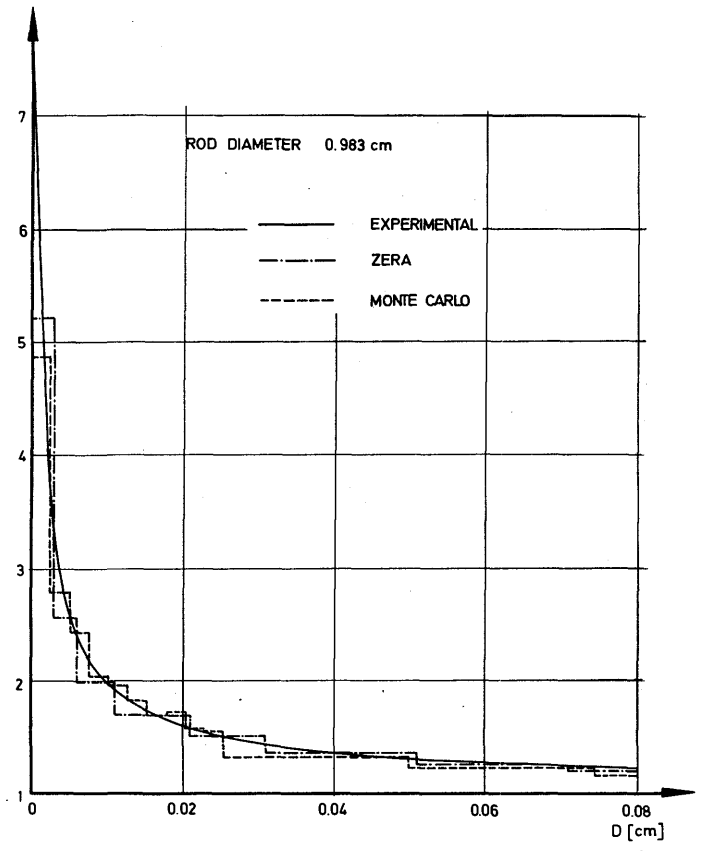

FIG. 6. Captures per ^{238}U atom vs. depth D from rod surface.

Figure 5 gives an impression of the magnitude of the effects for the reference reactor D1, which is described in Ref. [6]. In this figure, the results of cell calculations for the effective multiplication factor k_{eff} for both the homogeneous and the heterogeneous case are plotted versus steam density. The curve for the homogenized core was gained by reducing all cell dimensions by a factor 10^3. The buckling was chosen to give $k_{eff} \approx 1$ at the normal steam density (0.07 g/cm^3). The results show that the calculations for the homogenized core lead to errors of several per cent in k_{eff} at high steam densities.

An application of the described method to a cell of a hexagonal light-water-moderated lattice of a thermal reactor is shown in Fig. 6, which shows the calculated distribution of ^{238}U-captures within a natural uranium rod in the energy region from 3 eV to 10 keV. The rod diameter is 0.983 cm, the rod centre-to-centre spacing 1.44 cm. The measured curve and the results of Monte Carlo calculations are taken from Ref. [7]. The calculated capture densities and the measured curve are normalized to 1 in the centre of the rod. The ZERA-calculations have been performed with ABN cross-section. To find the space dependence of the reaction rates within the rod, the rod was subdivided into 12 concentric regions.

This application is a rather sensitive test for the reaction coefficients, which account for the spatial dependence of resonance self-shielding. The agreement with the experimental curve and with the results of Monte Carlo calculations is surprisingly good. This also holds for the total number of neutrons absorbed in the energy region under consideration in ^{238}U per neutron entering at 10 keV: ZERA gives a number of 0.3140, while the Monte Carlo result is 0.3075.

8. SUMMARY AND CONCLUSIONS

The described method to deal with resonance self shielding in multi-region lattice cells in principle reduces the calculation of resonance reactions to the calculation of collision probabilities for some values of the resonance cross-sections. It is applicable to a wide range of cell problems because it is not restricted to the use of rational approximations for the collision probabilities.

The method is used in a FORTRAN-programme ZERA, which calculates group and region dependent reaction rates, k_{eff}-values for unreflected lattices, and heterogeneity corrected cross-sections, which can be used to calculate heterogeneity effects in different regions of a reactor.

The ZERA results are in good or satisfactory agreement with the bunching effects on reactivity, which were measured in SNEAK-3A-1. The results show the importance of the leakage component of heterogeneity effects in the outer regions of a reactor. The heterogeneity corrections to the diffusion coefficients allow an estimate of this component. The agreement between predicted and experimental results in a core boundary region in SNEAK-3A-1 is not yet satisfactory. Further investigations are planned in this direction.

In fast reactors containing hydrogen, the energy dependence of heterogeneity effects on reaction rates is rather complicated and has a surprisingly strong dependence on the cross-sections used. For this reason, the investigation of heterogeneity effects also can be helpful for testing cross-section sets.

ACKNOWLEDGEMENTS

I wish to thank Prof. W. Häfele and Dr. P. Engelmann for their encouragement of this work and for very valuable discussions. Thanks are also due to Mr. G. Bruhn for his help with the difficult programming work.

REFERENCES

[1] BELL, G.I., A simple treatment for effective resonance cross-sections in dense lattices, Nucl. sci. Engng 5 (1959) 138.
[2] ABAGJAN, L.P. et al., Gruppenkonstanten schneller und intermediärer Neutronen für die Berechnung von Kernreaktoren, KFK-tr-144 (Translation).
[3] DRESNER, L., Resonance Absorption in Nuclear Reactors, Pergamon Press (1960).
[4] BENOIST, P., Théorie du coefficient de diffusion des neutrons dans un réseau comportant des cavités, CEA-R-2278 (1964).
[5] STEGEMANN, D. et al., Physics investigations of a 670-litre steam-cooled fast-reactor system in SNEAK, Assembly 3A-1, these Proceedings, SM-101/11.
[6] MÜLLER, A. et al., Referenzstudie für den 1000 MW(e) dampfgekühlten schnellen Brutreaktor (D1), KFK-392 (1966).
[7] SMITH, G., HARDY, J. Jr., KLEIN, D., Comparison of measurements with a Monte Carlo calculated spatial distribution of resonance neutron capture in a uranium rod, Nucl. sci. Engng 8 (1960) 449.

DISCUSSION

J. ROWLANDS: Could you please give an illustration of the method you use to compute the parameters $b_{\nu j}$ for, say, a multi-region cell?

D. WINTZER: Let us assume that we are interested in a cross-section range that is limited by the potential scattering cross-section and by the highest resonance value of the cross-section in the energy group concerned. We choose the $b_{\nu j}$ values from this range in such a way that they fall equidistantly on a logarithmic σ scale. I would add, however, that the results scarcely depend on the parameter set chosen.

H. KÜSTERS: I should like to draw attention to the fact that the heterogeneity effect for large, steam-cooled fast power breeders gives some 2% in k_{eff} only in the flooded case. Under normal operating conditions the effect is negligible.

M. TROYANOV: In comparing the effect of heterogeneity in a cell with smaller and larger pieces (double, etc.) the effect of displacing the uranium platelets towards or away from the centre of the reactor may be observed. Did this effect not occur in your experiments?

D. WINTZER: There is a linear displacement effect which is positive in one part of the core height and negative in the other. The compensation is fairly good in our case, so that the linear displacement effect can be neglected. More important is a second-order displacement effect proportional to the buckling. We have calculated the corresponding corrections and found them to be about 3% of the total heterogeneity effect in in the worst case.

J. ČERMÁK: Are the collision probabilities P_{mn} in your calculations used to describe spatial dependence for an infinite lattice, or do they take into account the finite dimensions of the lattice?

D. WINTZER: They are for an infinite lattice.

K. JOEST: With regard to the calculation of heterogeneity effects using a small number of groups (for instance, 26), I suppose that heterogeneity of flux distribution is strongly dependent on the removal cross-sections, and these depend to a great extent on the flux fine structure above the energy range under consideration. Could you elaborate on the quantitative influence of fine structure in energy on the spatial flux distribution?

D. WINTZER: I cannot give a quantitative answer. However, if we look at the energy distribution of heterogeneity effects on reactivity in our SNEAK-3A assemblies, we find an energy region at about 100 keV in which the heterogeneity effects are negative. Indeed, I would think that the effects in this region and the net effects, which include a partial compensation of positive and negative effects, would be sensitive to changes in the removal cross-sections.

W. FOELL: Do you use collision probabilities calculated for isotropic or anisotropic sources? If the former, how great is the difference?

D. WINTZER: It was found in earlier calculations of the fast fission factor in H_2O- and D_2O-moderated lattices with collision probabilities for anisotropic sources that the effects of anisotropic scattering did not substantially influence the reaction rates within the cell. We therefore decided to take the simple course and calculate the collision probabilities for isotropic sources.

CALCULATION OF HETEROGENEITY EFFECTS IN FAST CRITICAL ASSEMBLIES

J. ČERMÁK
NUCLEAR RESEARCH INSTITUTE OF THE
CZECHOSLOVAK ACADEMY OF SCIENCES,
ŘEŽ NEAR PRAGUE,
CZECHOSLOVAKIA

Abstract

CALCULATION OF HETEROGENEITY EFFECTS IN FAST CRITICAL ASSEMBLIES. The physical properties of the fast power reactor cores with respect to the neutron transport are usually not essentially influenced by the heterogeneity of the core structure. Nevertheless, when modelling the cores of these reactors by experimental critical assemblies the heterogeneity of the structure becomes essentially greater and cannot be neglected in the analysis of experiments.

In connection with this fact a further development of the previously presented method of homogenization of slab lattices with respect to the chain reaction with fast neutrons is contributed.

Attention is restricted to bare assemblies made up of a periodic lattice of parallel slabs of two different materials, a so-called "sandwich" reactor of materials 1 and 2. The geometry considered is (a) the plane geometry with boundaries parallel to the slabs, (b) the plane geometry with boundaries perpendicular to the slabs, and (c) the cylindrical geometry with boundaries perpendicular to the slabs with infinite or finite height. The restriction to two different media is made because of a simplification only and is not substantial.

The starting point is the integral transport theory based on the solution of the kinetic Boltzmann equation. The solution is sought in the form of a product of asymptotic transport theory solution characterized by the buckling B^2 and representing the general trend of the neutron emission density with the "fine structure", taking account of the heterogeneous structure of alternative layers of media 1 and 2.

As a result the value of the buckling B^2 of the heterogeneous assembly together with energy spectra in each medium is obtained.

As an illustration of the method the chain reaction with fast neutrons in a heterogeneous medium consisting of ^{235}U and ^{238}U plates placed in turn is investigated. For 16 energy groups the buckling B^2 and the energy spectrum in ^{235}U and ^{238}U have been calculated for a 10%, 20% and 30% enrichment with ^{235}U for different cell dimensions of the lattice. In each case when going from the most homogeneous to the most heterogeneous arrangement (for the same enrichment) an increase in the value of the buckling was observed. Finally the possible errors of the method are estimated.

INTRODUCTION

Let us denote the neutron emission density $\psi(\vec{r}, E)$. Then under the supposition of isotropy of elementary phenomena (or if we confine ourselves to the zero moment with respect to density angular distribution), the function ψ will satisfy the following integral equation

$$\psi(\vec{r}, E) = \iint d\vec{r}' \, dE' \, \Delta(E, E') \frac{\exp[-\ell(\vec{r}, \vec{r}')]}{4\pi |\vec{r} - \vec{r}'|^2} \psi(\vec{r}', E') \qquad (1)$$

Here, ℓ is the optical length for neutrons with energy E', and

$$\Delta(E, E') = \nu(E')\Sigma_f(E')S(E) + \Sigma_e(E')U(E, E') + \Sigma_i(E')W(E, E')$$

This quantity, besides having the explicitly formulated dependence on energy, is also a function of the position in general. Here Σ_f, Σ_e and Σ_i denote the macroscopic cross-sections, and S, U and W are spectra for fission and for elastic and inelastic scattering, respectively. The mean neutron number emitted per fission is denoted by ν and in what follows the total macroscopic cross-section is denoted by Σ.

Then, for an infinite homogeneous medium, let us suppose that the neutron emission density can be written in the form

$$\bar{\psi}(E) \exp[iBz]$$

Here, B^2 is the buckling that can be related to the critical thickness of an infinite plane slab reactor with extrapolated boundaries perpendicular to the z axis (parallel to the planes z = const.).

Substituting this expression into Eq. (1), we obtain for $\bar{\psi}$ the following integral equation

$$\bar{\psi}(E) = \int dE' \bar{\Delta}(E, E') \bar{\psi}(E') \qquad (2)$$

$$\bar{\Delta} = \Delta(E, E') B^{-1} \arctan \frac{B}{\Sigma(E')}$$

which gives the condition for the determination of the buckling in the sense that B has to attain such a value that the first eigenvalue of Eq. (2) would be equal to one. In Ref. [1] such a method has been used for numerical calculations of values of B^2 in homogeneous ^{235}U–^{238}U mixtures.

The aim of this paper is to present a method which would allow one to evaluate the influence of the heterogeneous configuration of the assembly on the buckling. The paper is restricted to bare assemblies made up of a periodic lattice of parallel slabs, a so-called "sandwich" reactor. Moreover, we shall consider a lattice consisting of alternating slabs of two media, 1 and 2, but this restriction is not essential for the method and is made for simplification only.

LATTICE ARRANGEMENT AND DESCRIPTION OF METHOD

The geometrical arrangement will be assumed as follows. The z axis of a Cartesian co-ordinate system is perpendicular to the slab faces, and the x and y axes are parallel to them. From the neutron transport aspect, the lattice consists of alternating infinite slabs of two media, 1 and 2, of thickness α_1 and α_2 respectively (with $\alpha = \alpha_1 + \alpha_2$). Different values of the same quantity for each medium will be labelled with the relevant suffix 1 or 2.

It is now convenient to write Eq. (1) as follows:

$$\psi(\vec{r}, E) = \frac{1}{4\pi} \iiint \Delta(E, E') \exp\left[- \frac{\ell(z, z')}{\vartheta} \right] \psi(\vec{r}', E') ds \, d\varphi \, d\vartheta \qquad (3)$$

Here the segment $s = |\vec{r} - \vec{r}'|$. The variables φ and ϑ determine the direction of the vector $\vec{r} - \vec{r}'$ at the point $\vec{r}$; ϑ is the cosine of the colatitude angle ($s\vartheta = z - z'$); and φ is the azimuth angle of $\vec{r} - \vec{r}'$.

When the emission density is a function of the z coordinates only, we can further write Eq. (3) in the cell of thickness α labelled by the integer k as follows:

For $0 \leq z \leq \alpha_1$ (in medium 1)

$$\psi(z+k\alpha, E) = \frac{1}{2}\int dE' \Delta_1(E, E') \sum_{k'=-\infty}^{\infty} \int_0^{\alpha_1} dz' E_1(|\Sigma_1(z'-z) + \Sigma\alpha(k'-k)|)\psi(z'+k'\alpha, E')$$

$$+\frac{1}{2}\int dE'\Delta_2(E, E') \sum_{k'=-\infty}^{\infty} \int_0^{\alpha_2} dz' E_1(|\Sigma_2 z' - \Sigma_1 z + \Sigma\alpha(k'-k)$$

$$+\Sigma_1\alpha_1|)\psi(z'+k'\alpha+\alpha_1, E') \quad (4a)$$

For $0 \leq z \leq \alpha_2$ (in medium 2)

$$\psi(z+k\alpha+\alpha_1, E) = \frac{1}{2}\int dE' \Delta_1(E, E') \sum_{k'=-\infty}^{\infty} \int_0^{\alpha_1} dz' E_1(|\Sigma_1 z' - \Sigma_2 z + \Sigma\alpha(k'-k) - \Sigma_1\alpha_1|)$$

$$\times\psi(z'+k'\alpha, E') + \frac{1}{2}\int dE'\Delta_2(E, E') \sum_{k'=-\infty}^{\infty} \int_0^{\alpha_2} dz' E_1(|\Sigma_2(z'-z)$$

$$+\Sigma\alpha(k'-k)|)\psi(z'+k'\alpha+\alpha_1, E') \quad (4b)$$

where

$$\Sigma\alpha = \Sigma_1\alpha_1 + \Sigma_2\alpha_2 \quad \text{and} \quad E_n(z) = \int_1^{\infty} dt\, t^{-n} e^{-zt}$$

The idea of our method for determining the buckling lies in the fact that we assume ψ in the following form:

$$\psi(z+k\alpha, E) = g^{(1)}(z, E) e^{ikB_\perp\alpha}, \qquad 0 \leq z \leq \alpha_1, \quad (5a)$$

$$\psi(z+k\alpha+\alpha_1, E) = g^{(2)}(z, E) e^{ikB_\perp\alpha}, \qquad 0 \leq z \leq \alpha_2 \quad (5b)$$

$$g^{(\mu)}(z, E) = \sum_{\ell=0}^{\infty} \frac{2\ell+1}{2} \frac{2}{\alpha_\mu} g_\ell^{(\mu)}(E) P_\ell\left(\frac{2z-\alpha_\mu}{\alpha_\mu}\right), \qquad \mu = 1, 2$$

where P_ℓ are Legendre polynomials.

Eqs (5a) and (5b) express the separation of the density distribution into two parts. The first one, $\exp[ikB_\perp \alpha]$, describes the general trend of the density ψ and is of the form of the asymptotic density distribution in the homogeneous assembly. Superimposed on this dependence is the "fine structure" taking into account the heterogeneity of the medium.

Indeed, to clear completely the question under what conditions the density distribution can be expressed in the form (5a), (5b), is not easy. We come to this question later when estimating the possible error of the method. Nevertheless, we can say that one of such conditions is $B_\perp \alpha \ll 1$ in the sense that the better this condition is fulfilled the better the results can be expected.

Let us now insert (5a-b) into (4a-b) and integrate with respect to z in both media. If we confine ourselves to the zero moments $g_0^{(1)}$, $g_0^{(2)}$ only, the following set of homogeneous linear integral equations for these moments may be obtained:

$$g_0^{(1)}(E) = \int D_{11}(E, E', B_\perp) g_0^{(1)}(E')dE' + \int D_{12}(E, E', B_\perp) g_0^{(2)}(E')dE'$$

$$g_0^{(2)}(E) = \int D_{21}(E, E', B_\perp) g_0^{(1)}(E')dE' + \int D_{22}(E, E', B_\perp) g_0^{(2)}(E')dE' \qquad (6)$$

where for instance

$$D_{11} = \frac{1}{2\alpha_1} \Delta_1(E, E') \left\{ \int_0^{\alpha_1} dz \int_0^{\alpha_1} dz' E_1(\Sigma_1 |z' - z|) \right.$$

$$\left. + 2 \sum_{n=1}^{\infty} \cos B_\perp \alpha n \int_0^{\alpha_1} dz \int_0^{\alpha_1} dz' E_1(\Sigma_1 (z' - z) + \Sigma \alpha n) \right\},$$

$$D_{12} = \frac{1}{\alpha_2} \Delta_2(E, E') \sum_{n=1}^{\infty} \cos B_\perp \alpha n \int_0^{\alpha_1} dz \int_0^{\alpha_2} dz' E_1(|\Sigma_2 z' + \Sigma_1 z - \Sigma \alpha n|)$$

and the remaining coefficients are given by similar expressions. When transforming the coefficients D_{12} and D_{21}, the assumption $B_\perp \alpha \ll 1$ has been used.

From the condition that the simultaneous equations (6) should have a non-trivial positive solution one can determine the buckling B_1^2 in the same way as it was done in the homogeneous case. We have used the symbol $B_\perp$ for the buckling since it refers to the direction perpendicular to the layer faces. It can be related to the critical thickness of an infinite heterogeneous slab reactor made up of a periodic lattice of parallel layers with extrapolated boundaries parallel to them.

The solution corresponding to such a determined value of the buckling represents the neutron energy spectrum in media 1 and 2.

The second case of interest connected with slab geometry is that of an infinite plane reactor made up to parallel layers again but with boundaries perpendicular to the layers.

Here the neutron emission density $\psi(\vec{r}, E)$ can be represented in the form of a product as $\exp[iB_{\parallel} x]\,\psi(z, E)$. If we use the relations

$$\int_0^{2\pi} e^{iB_{\parallel}(x-x')}\,d\varphi = \int_0^{2\pi} e^{iB_{\parallel}s\sqrt{1-\vartheta^2}\cos\varphi}\,d\varphi = 2\pi J_0(B_{\parallel}s\sqrt{1-\vartheta^2})$$

Eq. (3) takes on for this geometrical arrangement the form:

For $0 \leq z \leq \alpha_1$

$$\psi(z+k\alpha, E) = \frac{1}{2}\int dE'\Delta_1(E, E')\sum_{k'=-\infty}^{\infty}\int_0^{\alpha_1} dz'\int_1^{\infty}\frac{dt}{t}\exp\left[-|\Sigma_1(z'-z)+(k'-k)\Sigma\alpha|t\right]$$

$$\times J_0\{B_{\parallel}|z'-z+(k'-k)\alpha|\sqrt{t^2-1}\}\,\psi(z'+k'\alpha, E')$$

$$+\frac{1}{2}\int dE'\Delta_2(E, E')\sum_{k'=-\infty}^{\infty}\int_0^{\alpha_2} dz'\int_1^{\infty}\frac{dt}{t}\exp[-|\Sigma_2 z'-\Sigma_1 z+\Sigma\alpha(k'-k)+\Sigma_1\alpha_1|t]$$

$$\times J_0\{B_{\parallel}|z'-z+(k'-k)\alpha+\alpha_1|\sqrt{t^2-1}\}\,\psi(z'+k'\alpha+\alpha_1, E') \qquad (7)$$

For $0 \leq z \leq \alpha_2$

$$\psi(z+k\alpha+\alpha_1, E) = \frac{1}{2}\int dE'\Delta_1(E, E')\sum_{k'=-\infty}^{\infty}\int_0^{\alpha_1} dz'\int_1^{\infty}\frac{dt}{t}\exp\left[-|\Sigma_1 z'-\Sigma_2 z+\Sigma\alpha(k'-k)\right.$$

$$\left.-\Sigma_1\alpha_1|t\right]J_0\{B_{\parallel}|z'-z+(k'-k)\alpha-\alpha_1|\sqrt{t^2-1}\}\psi(z'+k'\alpha, E')$$

$$+\frac{1}{2}\int dE'\Delta_2(E, E')\sum_{k'=-\infty}^{\infty}\int_0^{\alpha_2} dz'\int_1^{\infty}\frac{dt}{t}\exp\left[-|\Sigma_2(z'-z)+\Sigma\alpha(k'-k)|t\right]$$

$$\times J_0\{B_{\parallel}|z'-z+(k'-k)\alpha|t\}\,\psi(z'+k'\alpha+\alpha_1, E')$$

Here $J_0(t)$ is the zero-order Bessel function of the first kind.

Proceeding in the same manner as before and taking into account the fact that the assembly is infinite in the z-direction, we assume ψ in the form:

$$\begin{aligned}\psi(z+k\alpha, E) &= g^{(1)}(z, E), \qquad 0 \leq z \leq \alpha_1,\\ \psi(z+k\alpha+\alpha_1, E) &= g^{(2)}(z, E), \qquad 0 \leq z \leq \alpha_2\end{aligned} \qquad (8)$$

for all k.

Neglecting all terms beyond $g_0^{(\mu)}$, $\mu = 1, 2$, equations (7) reduce to the system (6) again. Of course, the coefficients are now for instance

$$D_{11} = \frac{1}{2}\Delta_1(E, E') \left[\int_0^{\alpha_1} dz \int_0^{\alpha_1} dz' \int_1^{\infty} \frac{dt}{t} \exp[-\Sigma_1 |z' - z| t] J_0\{B_{\parallel} |z' - z| \sqrt{t^2 - 1}\} \right.$$

$$\left. + 2 \sum_{n=1}^{\infty} \int_0^{\alpha_1} dz \int_0^{\alpha_1} dz' \int_1^{\infty} \frac{dt}{t} \exp[-|\Sigma_1(z' - z) + n\Sigma\alpha| t] J_0\{B_{\parallel} |z' - z + n\alpha| \sqrt{t^2 - 1}\} \right]$$

etc.

On the basis of the facts explained up to now, a whole number of properties may be ascertained of assemblies made up of periodic slab lattices. In Ref. [2], besides the determination of the bucklings, the time behaviour of such assemblies is also investigated, together with the anisotropy of diffusion [3] and the behaviour of the bucklings $B_{\perp}^2$ and $B_{\parallel}^2$ in the limit case $\alpha_1 \to 0$, $\alpha_2 \to 0$, $\alpha_1/\alpha_2 = \text{const}$.

Instead of these problems, we shall draw attention to the last and in practice the most interesting case of cylindrical geometry. The investigated assembly is of the form of a cylinder whose vertical axis coincides with the z axis. The arrangement of alternating slabs of two media is the same as before, i.e. the co-ordinate system is chosen with its z axis perpendicular to the slab faces. We denote for the moment the distance of the point $\vec{r}$ from the z axis by ρ. To determine the radial buckling B_r^2 of the assembly we shall look for solutions of Eq. (3) in the form of a product

$$\psi(\vec{r}, E) = J_0(B_r \rho)\psi(z, E)$$

Inserting this expression into Eq. (3) and making use of the relation

$$J_0(B_r \rho') = J_0(B_r \rho) J_0(B_r s\sqrt{1 - \vartheta^2}) + 2 \sum_{k=1}^{\infty} J_k(B_r \rho) J_k(B_r s\sqrt{1 - \vartheta^2}) \cos k\varphi$$

Eq. (3) becomes

$$\psi(z, E) = \frac{1}{2} \int dE' \Delta(E, E') \int_{-1}^{1} d\vartheta \int_0^{\infty} ds \exp\left[- \frac{\ell(z, z')}{|\vartheta|} \right] J_0(B_r s\sqrt{1 - \vartheta^2}) \psi(z', E') \quad (9)$$

Here we have already performed the integration over φ. Then transforming the double integral, using the relation $s\vartheta = z - z'$, Eq. (9) takes on again the form of Eq. (7) where, of course, B_r stands in place of $B_{\parallel}$.

It is unnecessary to treat the case when the assembly is infinite in the z direction, since it does not differ from that of an infinite plane reactor with boundaries perpendicular to the layers; in the following let us draw attention to the general case of finite height.

Assuming the radial buckling or what is the same, the extrapolated radius of the assembly, as constant, we put

$$\begin{aligned} \psi(z+k\alpha, E) &= \exp[ikB_z\alpha]\, g^{(1)}(z, E), \qquad 0 \leqq z \leqq \alpha_1 \\ \psi(z+k\alpha+\alpha_1, E) &= \exp[ikB_z\alpha]\, g^{(2)}(z, E), \qquad 0 \leqq z \leqq \alpha_2 \end{aligned} \tag{10}$$

Here B_z^2 is the asymptotic axial buckling.

Inserting Eq. (10) into Eq. (7) (with B_r instead of $B_{\parallel}$), integrating with respect to z in each medium and neglecting all terms except of $g_0^{(1)}$ and $g_0^{(2)}$, we arrive at the system of equations (6) again.

The coefficients are now

$$D_{11} = \frac{1}{2}\Delta_1(E, E')\left[\int_0^{\alpha_1} dz \int_0^{\alpha_1} dz' \int_1^{\infty} \frac{dt}{t} \exp[-\Sigma_1 |z'-z|\, t]\, J_0\{B_r |z'-z| \sqrt{t^2-1}\}\right.$$

$$+ 2 \sum_{n=1}^{\infty} \cos B_z \alpha n \int_0^{\alpha_1} dz \int_0^{\alpha_1} dz' \int_1^{\infty} \frac{dt}{t} \exp[-|\Sigma_1(z'-z) + n\Sigma\alpha|\, t]$$

$$\left. \times J_0\{B_r |z'-z+n\alpha| \sqrt{t^2-1}\}\right]$$

$$D_{12} = \Delta_2(E, E') \sum_{n=1}^{\infty} \cos B_z \alpha n \int_0^{\alpha_1} dz \int_0^{\alpha_2} dz' \int_1^{\infty} \frac{dt}{t} \exp[-|\Sigma_1 z + \Sigma_2 z' - \Sigma\alpha n|\, t]$$

$$\times J_0\{B_r |z+z'-\Sigma\alpha n| \sqrt{t^2-1}\}$$

and the remaining coefficients are given by similar expressions. Here the condition $B_z\alpha \ll 1$ was used again when transforming the off-diagonal coefficients D_{12} and D_{21}.

To determine B_z we proceed in the same manner as in the other cases.

In practice we can proceed in such a manner that we divide the neutron energy into N groups. If the energy E_κ is ascribed to the neutrons in the κ-th group and if we denote

$$\int_{\kappa} g_0^{(\mu)}(E)dE = g_{0\kappa}^{(\mu)}$$

where the integration is performed over the energy interval of group κ, we substitute the system (6) by the system of 2N homogeneous linear equations. The condition for the existence of a non-trivial positive solution of these equations gives then the condition for the determination of the buckling. The solution itself is then the energy spectrum in two media, 1 and 2, of the heterogeneous assembly.

NUMERICAL EXAMPLE

To illustrate the method we shall calculate the asymptotic buckling B_1^2 in a slab lattice consisting of ^{235}U and ^{238}U plates placed in turn for various ^{235}U enrichments (i.e. for various values of quotient α_1/α_2, e.g. by 10% enrichment we understand the following case: for $\alpha = 1$ cm; $\alpha_1 = 0.1$ cm and $\alpha_2 = 0.9$ cm) and for different dimensions of the lattice (i.e. for different values of α). The subscript 1 corresponds to ^{235}U, subscript 2 to ^{238}U.

This case is the most accessible one to treat since we can express the coefficients in (6) in the form

$$D_{11} = \Delta_1(E, E')\left[\frac{1}{\Sigma_1} - \frac{1}{\Sigma_1^2\alpha_1} A_1\right]$$

$$D_{22} = \Delta_2(E, E')\left[\frac{1}{\Sigma_2} - \frac{1}{\Sigma_2^2\alpha_2} A_2\right]$$

$$D_{12} = \Delta_2(E, E')\frac{A}{\Sigma_1\Sigma_2\alpha_2}, \qquad D_{21} = \Delta_1(E, E')\frac{A}{\Sigma_1\Sigma_2\alpha_1}$$

where

$$A = \int_0^1 dz \, \frac{z\left(1 - e^{-\frac{\Sigma_1\alpha_1}{z}}\right)\left(1 - e^{-\frac{\Sigma_2\alpha_2}{z}}\right)\left(1 - e^{-\frac{\Sigma\alpha}{z}}\right)\cos B_\perp\alpha}{1 - 2e^{-\frac{\Sigma\alpha}{z}}\cos B_\perp\alpha + e^{-\frac{2\Sigma\alpha}{z}}}$$

$$A_1 = \int_0^1 dz \, \frac{z\left(1 - e^{-\frac{\Sigma_1\alpha_1}{z}}\right)\left[1 - \left(e^{-\frac{\Sigma_2\alpha_2}{z}} + e^{-\frac{\Sigma\alpha}{z}}\right)\cos B_\perp\alpha + e^{-\frac{\Sigma\alpha + \Sigma_2\alpha_2}{z}}\right]}{1 - 2e^{-\frac{\Sigma\alpha}{z}}\cos B_\perp\alpha + e^{-\frac{2\Sigma\alpha}{z}}}$$

$$A_2 = \int_0^1 dz \, \frac{z\left(1 - e^{-\frac{\Sigma_2\alpha_2}{z}}\right)\left[1 - \left(e^{-\frac{\Sigma_1\alpha_1}{z}} + e^{-\frac{\Sigma\alpha}{z}}\right)\cos B_\perp\alpha + e^{-\frac{\Sigma\alpha + \Sigma_1\alpha_1}{z}}\right]}{1 - 2e^{-\frac{\Sigma\alpha}{z}}\cos B_\perp\alpha + e^{-\frac{2\Sigma\alpha}{z}}}$$

Assuming that the neutron energy is not changed by elastic scattering on the heavy U nuclei we can write

$$\Delta_\mu(E, E') = \theta_\mu(E, E') + \Sigma_{e\mu}(E')\,\delta(E - E')$$

Then, making use of the notations

$$\int_\kappa g_0^{(\mu)}(E)\,dE = g_{0\kappa}^{(\mu)}, \qquad \int_\kappa \theta_\mu(E, E_\beta)\,dE = \theta_\mu^{\kappa\beta}$$

$$\mu = 1, 2; \quad \kappa, \beta = 1, 2, \ldots, N;$$

in the previously introduced multigroup picture, we replace the system (6) by the set of 2N linear equations that may be written as

$$T(B_\perp)\vec{X} = \vec{X}, \qquad \vec{X} = \begin{pmatrix} \frac{g_{0\kappa}^{(1)}}{\alpha_1} \\ \\ \frac{g_{0\kappa}^{(2)}}{\alpha_2} \end{pmatrix}$$

$$T(B_\perp) = \begin{pmatrix} \theta_1^{\kappa\beta} a^\beta + \Sigma_{e1}^\kappa a^\kappa \delta_{\kappa\beta}\,, & \theta_2^{\kappa\beta} b^\beta + \Sigma_{e2}^\kappa b^\kappa \delta_{\kappa\beta} \\ \theta_1^{\kappa\beta} c^\beta + \Sigma_{e1}^\kappa c^\kappa \delta_{\kappa\beta}\,, & \theta_2^{\kappa\beta} d^\beta + \Sigma_{e2}^\kappa d^\kappa \delta_{\kappa\beta} \end{pmatrix}$$

$$a^\kappa(B_\perp) = \frac{1}{\Sigma_1^\kappa} - \frac{1}{\alpha_1 (\Sigma_1^\kappa)^2} A_1(E_\kappa, B_\perp), \qquad b^\kappa(B_\perp) = \frac{A(E_\kappa, B_\perp)}{\Sigma_1^\kappa \Sigma_2^\kappa \alpha_1}$$

$$d^\kappa(B_\perp) = \frac{1}{\Sigma_2^\kappa} - \frac{1}{\alpha_2 (\Sigma_2^\kappa)^2} A_2(E_\kappa, B_\perp), \qquad c^\kappa(B_\perp) = \frac{\alpha_1}{\alpha_2} b^\kappa(B_\perp)$$

Here, for instance,

$$\Sigma_1^\kappa = \Sigma_1(E_\kappa), \qquad \Sigma_{e1}^\kappa = \Sigma_{e1}(E_\kappa)$$

and

$$\delta_{\kappa\beta} = \begin{cases} 1 & \text{for } \kappa = \beta \\ 0 & \text{for } \kappa \neq \beta \end{cases}$$

As mentioned already the detailed calculations of the buckling in homogeneous mixtures of ^{235}U and ^{238}U have been made in Ref. [1]. The Here we shall use the same procedure for determining the multigroup constants as in Ref. [1]. The neutron energy is divided into 16 groups, the upper limits of whichare 0.02; 0.05; 0.09; 0.14; 0.20; 0.28; 0.40; 0.70; 0.90; 1.20; 1.60; 2.20; 3.00; 4.20; ∞ (MeV). The representative neutron energy for each group is the average energy for these groups, with the exception of the last one, where the average value was taken as 4.60 MeV.

Further,

$$S(E) = \sqrt{\frac{2}{\pi e}} \exp[-E] \sinh\sqrt{2E}$$

ν is dependent on energy as

$$\nu = \begin{cases} 2.47 + 0.125\,E & \text{for } ^{235}U \\ 2.41 + 0.125\,E & \text{for } ^{238}U \end{cases}$$

and

$$W(E, E') = K\sigma_\mu(E) E \exp[2\sqrt{a(E' - E)}]$$

where σ_μ is the effective cross-section of formation of a compound nucleus, K is the normalizing coefficient, and a = 13.2 MeV.

The calculation procedure can be roughly described as follows. First, an approximate value of $B_\perp$, say $B_{\perp 1}$, is chosen. Then with the help of an iterational method with arbitrary initial vector the first eigenvalue $\lambda(B_{\perp 1})$ and the corresponding eigenvector of the matrix $T(B_{\perp 1})$ are computed. It has been found that for $B_{\perp 1} < B_{\perp 2}$ one has $\lambda(B_{\perp 1}) < \lambda(B_{\perp 2})$. Using this inequality and the method "regula falsi", such a value of $B_\perp$ has been found as to make $\lambda(B_\perp) = 1$. The required accuracy was three and in a few cases four valid decimal places. The integrals A, A_1, A_2 have been computed numerically. The calculations were performed on the GIER computer.

The results are given in the following table:

Enrichment	α cm	$10^2 B_\perp^2$ cm^{-2}
10%	0.01	0.321
	0.1	0.389
	0.5	0.660
	1.0	0.821
	1.5	0.895
	2.0	0.893
	2.5	0.858
20%	0.01	1.932
	0.1	1.967
	1.0	2.183
	2.0	1.970
30%	0.01	3.323
	0.1	3.375
	0.5	3.421
	1.0	3.323

For the corresponding homogeneous mixture (with $\Delta = \frac{\alpha_1}{\alpha}\Delta_1 + \frac{\alpha_2}{\alpha}\Delta_2$, etc.) we obtained the following results

Enrichment	10%	20%	30%
$10^2 B_\perp^2$ cm^{-2}	0.317	1.924	3.323

These values do not coincide exactly with the values obtained in Ref. [1]. This is explained by the fact that our multigroup constants may differ from those in Ref. [1] owing to the difficulties in reproducing, for example, the microscopic cross-sections from [1].

From the results obtained it can be seen that the values of $B_\perp^2$ tend in the limit $\alpha \to 0$, $\alpha_1/\alpha_2 = \text{const.}$, i.e. when going to the corresponding homogeneous mixture, to the buckling of the homogeneous case, which confirms the theoretical conclusions in Ref. [2]. Further, when going from the most homogeneous to the more heterogeneous arrangement (for the same enrichment) we observe an increase in the value of the buckling. As for the values of the buckling of the most heterogeneous arrangements in the table, which show a slightly decreasing tendency,

we cannot so far decide whether they reflect a physical reality or if they are due to the inaccuracy of the method.

Here we would like to mention that the results given in our preliminary paper [4], which refers to the same topic, are incorrect owing to a systematic error in the numerical computations. This circumstance also explains some incorrect conclusions in Ref. [4].

We have concentrated our attention on the values of the buckling although together with the calculation of $B_\perp^2$ we get as the eigenvector of the problem the average energy spectra $\frac{1}{\alpha_1} g_0^{(1)}(E)$ and $\frac{1}{\alpha_2} g_0^{(2)}(E)$ in both media.

Without introducing numerical results we shall mention only that in the limit $\alpha \to 0$, $\frac{\alpha_1}{\alpha_2} = \text{const.}$, $\frac{1}{\alpha_1} g_0^{(1)}(E) \cong \frac{1}{\alpha_2} g_0^{(2)}(E) \cong \bar{\psi}(E)$, where $\bar{\psi}(E)$ is the energy spectrum in the corresponding homogeneous mixture. This confirms again the correctness of the conclusions in Ref. [2].

ERROR ESTIMATE AND CONCLUDING REMARKS

The following paragraphs are devoted to the discussion of the estimation of possible errors involved in the method. Naturally we do not want to go into general questions - e.g. to what extent we are allowed to use the concept of the asymptotic buckling for the description of physical properties of a fast critical assembly - since the possibility of using this concept is essential for the method. Nevertheless, when accepting this assumption a number of questions still remain unsolved. The most serious one is: under what conditions can the general spatial trend of the neutron emission density in the form $\exp[ikB_\perp \alpha]$ be expressed, where $B_\perp^2$ is the asymptotic buckling in the direction perpendicular to the layers of the lattice? To answer this question we shall choose the following procedure even if we are aware that it is based more on the physical considerations than on rigorous mathematical techniques.

We again consider an infinite homogeneous medium which, as we know, can be characterized by the asymptotic buckling B^2 determined by the integral equation (2). Now, let us suppose that the neutron emission density can be written, instead of $\bar{\psi}(E)\exp[iBz]$, in the form $\bar{\psi}(E)\exp[ik\bar{B}\alpha]$. Inserting the latter expression into (1) we obtain for $\bar{\psi}$ again the integral equation (2), however, with a different nucleus

$$\bar{\Delta}_{\text{hetero}} = \Delta(E, E')\left\{\frac{1}{\Sigma} - \frac{1}{\alpha\Sigma^2}\int_0^1 dz\, z \left[1 - e^{-\frac{\Sigma\alpha}{z}} + \frac{\left(1 - e^{-\frac{\Sigma\alpha}{z}}\right)\left(1 - e^{\frac{\Sigma\alpha}{z}}\right)\left(e^{-\frac{\Sigma\alpha}{z}}\cos\bar{B}\alpha - e^{-\frac{2\Sigma\alpha}{z}}\right)}{1 - 2e^{-\frac{\Sigma\alpha}{z}}\cos\bar{B}\alpha + e^{-\frac{2\Sigma\alpha}{z}}}\right]\right\}$$

The value $\bar{B}$ calculated with this nucleus depends now on α, the artificially introduced cell thickness. Let us take, for example, the

case of 10% enrichment. In the following table the calculated values of $\bar{B}^2$ with varying α are shown:

α cm	$10^2 \bar{B}^2$ cm^{-2}
0.1	0.315
0.5	0.312
1.0	0.303
1.5	0.294
2.0	0.279
2.5	0.263

The correct value of the buckling in this case was $B^2 = 0.317 \times 10^{-2}$ cm^{-2}.

These results show how the value of the buckling is changed according to the cell thickness. This is due to the fact that we imposed, instead of the correct solution exp[iBz], the approximate solution exp[ik$\bar{B}\alpha$]. In the present case, the values of $\bar{B}^2$ decrease with increasing α. Hence we may conclude that the inaccuracy of the method caused by assuming the emission density in the approximate form (5) tends to decrease the values of the asymptotic buckling of the periodic slab lattice. Though this conclusion is valid so far for the 10% enrichment mentioned above we have found a similar picture also in other cases. For the 20% and 30% enrichment we have

α cm	(20%) $10^2 \bar{B}^2$ cm^{-2}	(30%) $10^2 \bar{B}^2$ cm^{-2}
0.1	1.925	3.329
0.5	1.906	3.295
1.0	1.847	3.193
1.5	1.763	3.047
2.0	1.657	2.873

the correct value of B^2 being 1.924×10^{-2} cm^{-2} for 20% and 3.323×10^{-2} cm^{-2} for 30% enrichment, respectively.

Of course, this procedure gives us the possibility of estimating the error involved in our method of determining the buckling, not only qualitatively but also quantitatively. At the same time it offers the possibility of estimating for which values of the cell thickness α we can still expect the method to give reliable results, B^2 being fixed. So we get a new and better insight into the previously introduced condition $B\alpha \ll 1$.

As for other sources of the inaccuracy of the method we have further to mention the following circumstance, namely that in the development (5) we have restricted our attention to zero moments only. This inaccuracy can be avoided by taking into account a greater number of moments, this being more important with regard to the computing possibilities, whereas for the method itself it is of less importance. Notice that in this respect we also have other possibilities. When studying the expressions for the coefficients D_{ij} in our numerical example, we may see at once that our procedure of solving (4) is in direct connection to the so-called collision probability method. Following this method we may conclude that instead of increasing the number of moments in Eq. (5) it could be more convenient

to divide individual regions of the cell of the lattice into a greater number of sub-regions and to employ for these sub-regions the same procedure.

The method suggests still further points worth considering. In particular there are questions interesting from the mathematical point of view concerned with the existence and uniqueness of the critical value of B^2 and the positivity of the corresponding solution of (6). Without going into details we would like to draw attention to the excellent paper [5] where these questions are solved for B_1^2.

ACKNOWLEDGEMENTS

The author would like to express his gratitude to Mr. M. Hron for his help in numerical calculations on the GIER computer and to Dr. L. Trlifaj for valuable discussions.

REFERENCES

[1] FEIX, M., NICOURD, P., VALENTIN, S., C.r. hebd. Séanc. Acad. Sci., Paris 244 20 (1957) 2502.
[2] TRLIFAJ, L., ČERMÁK, J., Int. Conf. Peaceful Uses atom. Energy (Proc. Conf. Geneva, 1958) 16 (1958) 550.
[3] WEINBERG, A.M., WIGNER, E.P., The Physical Theory of Neutron Chain Reactors, University of Chicago Press (1958) 735.
[4] ČERMÁK, J., MAREK, I., GRMELA, M., J.I.N.R. DUBNA Rep.2415 (1965).
[5] MAREK, I., Aplikace matematiky 11 2 (1966) 89.

GENERAL DISCUSSION

H. W. KÜSTERS: Considerable improvements appear to have been made during recent years in the calculation of heterogeneity effects in fast critical assemblies. For example, Mr. Troyanov and Mr. Wintzer have reported fairly good agreement with experiment. I should like to ask other participants about their views on what ought to be done now in this field.

F. STORRER: I would suggest three areas in which more work might be done.

First, most of the work done so far has been concerned with the heterogeneity in an infinite medium or in the asymptotic mode. Since, in reactors and critical experiments, the flux and adjoint flux spectra differ considerably from the asymptotic spectrum over a large fraction of the core, one should take a closer look at the spatial dependence of heterogeneity.

Second, nobody is investigating the heterogeneity of the blanket, which, while probably not important from the point of view of the reactivity, may be important with regard to other reactor characteristics.

Third, the effect of anisotropic scattering on heterogeneity should be investigated further.

W. H. KÖHLER: The papers presented at this Symposium describe a wide variety of methods of calculating heterogeneity effects: in paper SM-101/57 two direct Monte Carlo calculations are mentioned; in paper SM-101/61 a synthesis method is used; in paper SM-101/29 a modified perturbation theory is employed; and paper SM-101/13 is based on collision probabilities. I wonder whether, in view of these different methods, it might not be possible to arrange a comparative study using a fixed heterogeneous geometry and identical basic nuclear data.

W. B. LOEWENSTEIN (Chairman): Such a study might well be possible. A major problem is probably the accurate description of transverse leakage, which may be the reason for the many approximations and methods used.

J. L. ROWLANDS: I should like to mention a method of treating leakage in heterogeneous cells which has been developed by Brissenden at Winfrith as an extension to the S_N code WDSN. I am not too familiar with the method, but I understand that it is similar to methods developed by Rumyantsev and by Behrens and Oldekop within the framework of diffusion theory. The reactor flux is found as a linear combination of two flux solutions calculated within the cell, the coefficients of the two solutions being periodic in the reactor dimension.

D. H. WINTZER: Almost all groups working on problems of heterogeneity seem to arrive at the problem of interfaces between different zones of a reactor (for example, between core and blanket). As in the study of heterogeneity, one is faced with the problems of a good transport approximation, of treating leakage near the interfaces, and of space-dependent resonance self-shielding. I feel that the groups working in the

field of heterogeneity have a good starting-point from which to study these problems and that they should try to do so by extending their methods.

H. W. KÜSTERS: We have for some time been studying the heterogeneity effect across the core-blanket interface on the basis of transport theory. I should therefore be interested to hear of any other groups working on this problem.

W. B. LOEWENSTEIN: Work is being done in the United States on this effect (for example, by Meneghetti). One approach has been based on spatial averaging of multigroup constants by performing space-dependent S_N calculations with several hundred groups. In another approach space-dependent bucklings are employed.

FAST POWER REACTORS

(Session VII, Part 2; Session VIII;
and Session IX, Part 1)

Chairmen: W.B. LOEWENSTEIN, R.D. SMITH and M.F. TROYANOV

RECENT DEVELOPMENTS IN THE PHYSICS OF DOUNREAY FAST REACTOR OPERATION

D. TAIT AND A.G. EDWARDS
UNITED KINGDOM ATOMIC ENERGY AUTHORITY,
DOUNREAY EXPERIMENTAL REACTOR ESTABLISHMENT,
CAITHNESS, SCOTLAND, UNITED KINGDOM

Abstract

RECENT DEVELOPMENTS IN THE PHYSICS OF DOUNREAY FAST REACTOR OPERATION. The physics work on DFR is largely concerned with the operation of a fast power reactor as an irradiation facility. The experimental rig loading has been increased by minimizing the reactivity margin required to run the reactor. This has been achieved by conducting a preliminary approach to critical before each run to verify that enough reactivity is available and by making careful measurements of the reactivity in hand on the reactor during a run to obtain a better estimate of the reactivity loss with burn-up. Our present knowledge of neutron and gamma fluxes on the reactor is described. A method of checking rapidly the reactivity feedback is now being used. Random noise in flux and temperature signals have been recorded and analysed to produce auto- and cross-correlograms which can be interpreted to some extent in terms of reactor properties. Reactor operation has been simplified by replacing the artificial source by one of metallic beryllium which provides an adequate flux of photoneutrons due to fission-product gamma activity. Finally, some deductions from the performance of the delayed neutron detectors monitoring the liquid metal coolant are reported.

1. INTRODUCTION

The Dounreay Fast Reactor (DFR) operates at a nominal centre flux of $2.5 \times 10^{15} n/cm^2 sec$. about half of which is above 500 keV. The corresponding heat generation is 60 MW and its coolant is a 70:30 alloy of sodium and potassium. It has now fulfilled its function as a fast power reactor experiment, and although there is up to 15 MW by-product electricity, its prime function is to act as a fast flux irradiation facility.

Its design and flux characteristics are very different from those of high power fast reactors at present being studied and built for electricity generation, but it is nevertheless one of a small number of fast power systems which have yielded operational experience. As such, interest attaches to its properties and the technique of its operation, and in a limited way it has acted as a test-bed for reactor instrumentation.

Operation experience in general was reported by Henry and Edwards[1] and information about the flux profiles by Edwards and Atkinson[2]. The present paper overlaps this work in time but not in subject matter, and is in a sense complementary to it.

D.F.R. is an operating power reactor, and physics experiments which reduce the load factor are not justified unless they have a direct bearing on its operational use as a test facility. For the same reason there is an incentive to do many experiments as rapidly as possible, and this affects both the experiments done, and the way in which they are tackled.

2. EFFICIENT USE OF REACTIVITY

2.1 The initial critical approach

Since the reactivity worth of irradiation experiments in a fast reactor is generally a lot less than that of the fuel elements they replace, reactivity

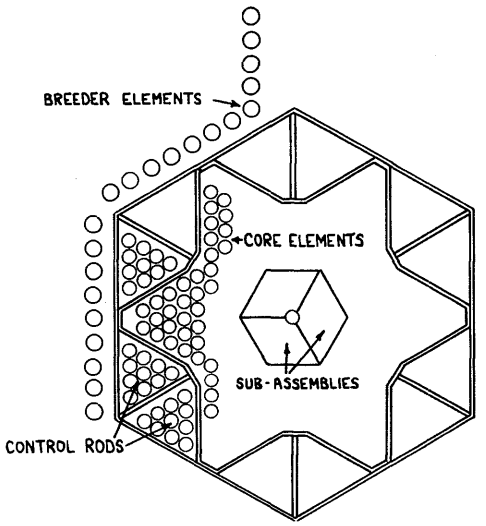

FIG.1. Plan of the Dounreay Fast Reactor core and inner breeder.

considerations limit the number of experiments that can be loaded, and there is considerable incentive to load as closely as possible to the reactivity margin required to run the reactor. However about half of the 300 core fuel elements, at varying degrees of burn-up, are replaced at each shut-down and though the reactivity lost by depletion of the ^{235}U in the elements can be calculated satisfactorily, the reactivity lost by axial swelling of the 75% enriched metal fuel in the elements cannot. It has to be estimated from the average rate of reactivity loss with burn-up, which is about three times that due to depletion of the ^{235}U. For this reason there is appreciable error in the predicted reactivity gain at shutdown on replacing burned-up fuel elements (typically 200 cents with 30 cents error).

The experimental elements which are changed are also worth about 200 cents and there is a similar error in this case because they contain a high proportion of scattering materials for which the reactivity worths are not so well known as for the fissile material. As a result of the total probable error of >40 cents, a conservative number of experiments would have to be loaded to avoid the possibility of being short of reactivity and several might be excluded unnecessarily.

Recently, however, the reactor has been loaded with experiments to the calculated limit and a critical approach made before the reactor top build-up which precedes normal power operation. The loading can be easily adjusted at this stage but suitable operational procedures for the preliminary approach had to be devised since control-rod position indicators are not functional before the build-up. Moreover the radium-beryllium artificial source has been replaced by a simple beryllium one actuated by fission product decay gammas whose strength is variable, and for this exercise it was assumed that only the small natural source strength of the core was present.

An analogue computer[3] was used to obtain the power transient following control rod runaway from a state in which the reactor was just critical at the power corresponding to the natural source strength. The power entered the reactivity feedback range 150 seconds after the ramp began with a doubling time of just under two seconds. High power flux and temperature trips would operate at that point and would have ample time to terminate the excursion

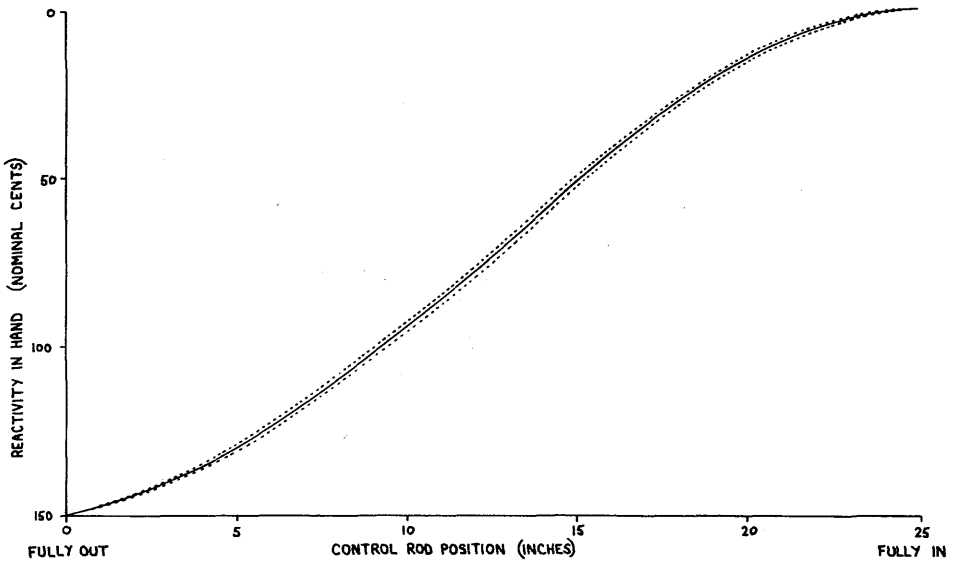

FIG.2. Normalized control-rod worth curve showing maximum range of variation.

before any damage occurred to the reactor or irradiation hazard to personnel on the reactor top. This transient was considered acceptable and preliminary critical approaches have been made at subsequent start-ups without incident.

The reactivity is added at the usual speed, 0.4 cents/second, and counts taken on low-power fission chambers every half rod ($\sim$ 1 dollar) inserted. Because of the low source strength, the chambers give only about 10 c.p.s. when all the moveable fuel rods are withdrawn and the reactivity is -7 dollars. Yet it has been found that a safe approach to within about 30 cents from critical can be made in less than three hours, which is enough to measure the reactivity of the loading to within a few cents.

2.2 Measurement of reactivity in hand

The difficulty in measuring the reactivity in hand accurately on DFR is that the worth of a control rod depends to some extent on the positions of the neighbouring rods, which are very close (Fig. 1). The existence of this interaction effect between rods was suspected for some time but it could not be examined quantitatively because of the time required. A programme of investigation became practicable however when a technique using a reactivity meter was evolved which calibrated two control rods over their full 25 inches of travel in less than an hour.(4)

It was found that the shape of the control-rod worth curve normalised to the same total value did not vary much whatever the position of the adjacent rods when the calibration was done. The range is shown in Fig. 2. Slightly greater variation in the normalised worth curve was found if the adjacent rod was moved during the calibration or if the rods being calibrated contained expts. Neither of these situations arises when the reactor is running normally, however, so the simplification of adopting the mean curve of Fig. 2 as the standard worth curve can be taken without incurring a greater error than two cents for each partly inserted rod.

The second result of the investigation was that the total worth of a control rod decreased when adjacent rods were out of the core, and that the

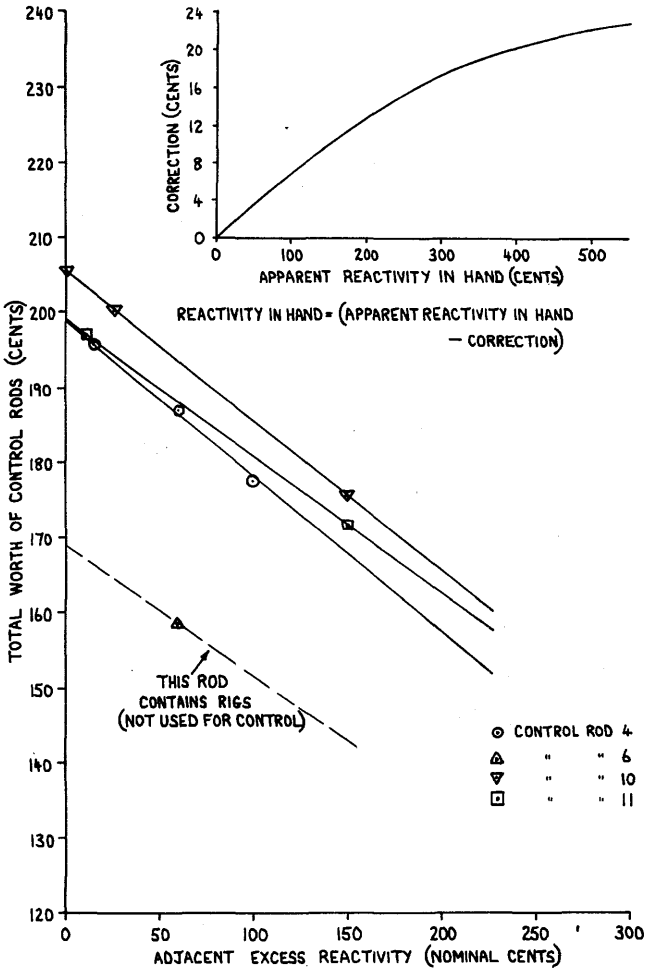

FIG.3. Variation of control-rod worths.

magnitude of the decrease was a simple function of the positions of the adjacent rods. An empirical expression for the decrease is given by the formula:

$$A\left[S(Z_1) + 0.6\ S(Z_2) + 0.4\ S(Z_3) + 0.4\ S(Z_4) + 0.1\ S(Z_5)\right]$$

where A is a constant, S(Z) is the value of the normalised worth curve of Fig. 2 for a control rod at position Z, and Z_1 to Z_5 are the positions of the five closest rods in order. The expression in brackets multiplying A is called the "adjacent excess reactivity" (AER) of the rod, since it is a measure of the amount of reactivity that could be inserted alongside the rod. The AER is measured in nominal cents, the units of S(Z) in Fig. 2. It can be shown that for the decrease in rod worth to be described by the simple linear formula above, the constant A should be the same for all rods. This is shown to be nearly enough the case by the curves of Fig. 3 which show the variation of control rod worth with AER for the rods to be used for control during a run.

When evaluating the control rod worths and the reactivity in hand in the reactor the constant A is not in practice extracted from the curves of Fig.3. Instead the AER for each rod not fully in is calculated, then the corresponding total worth is read off Fig. 3. If any rod is at an intermediate position a correction factor for the total worth is obtained from the worth curve S(Z) of Fig. 2 to give the reactivity in hand on that rod.

For some purposes the total reactivity in hand in the reactor is required. This is not necessarily obtained by taking the sum of all the reactivities available in the control rods, as can be seen by considering a simple example in which two adjacent rods are fully out. If the worth of either rod is measured with the other one down a value of about 170 cents would be obtained, but the total reactivity in hand in the reactor is not 340 cents. This is because, after one rod is motored in giving a reactivity gain of 170 cents the remaining rod would now be worth about 200 cents so that when it is also motored in the total reactivity gain is 170 + 200, i.e. 370 cents. Hence, once the reactivity in hand on a rod has been obtained, it must be considered as fully in when evaluating the AER's of the remaining rods. It is this fact that requires the constant A to have the same value for all rods, since otherwise the value of the reactivity in hand in the reactor could be different if the rods were considered in a different order.

Now that control rod interaction can be allowed for, the reactivity in hand in the reactor can be evaluated to an accuracy of 1%, i.e. 5 cents in 5 dollars whatever the control rod configuration, provided the rods have been well calibrated. Normally this accuracy is not essential and a shorter series of calibrations taking about 4 hours is adequate at each start-up. This provides the data for a graph like Fig. 3, from which the reactivity in hand in the reactor can be obtained correct to 2%, i.e. 10 cents in 5 dollars.

When the reactor reactivity was monitored during a run with the increased accuracy now possible, it was found that the worth of the control rods decreased with burn-up. The decrease is not due to burn-up of the fuel in the rods themselves because it occurs even in rods that are out of the core during the whole run. The change in worth can amount to 10 cents in a rod worth 2 dollars during a run of 40 days at full power, and is probably caused by the increase in the reactor perturbation constant as control rods are motored in to counteract the reactivity lost by burn-up. Now that this effect has been discovered a correction (the insert in Fig. 3) is applied to reduce the estimated reactivity in hand from the "apparent" to the "true" value throughout the run. At the end of each run the control rods are calibrated to provide more information on the decrease in rod worth with burn-up and so improve the correction allowing for it.

As a result of the corrections for the interaction effect and for the decrease in worth of the rods, the graph of reactivity in hand as a function of burn-up during a run is much smoother and more nearly linear than before. In preparation for a run lasting 55 days, it is now reasonable to allocate 300 cents to compensate for burn-up, whereas 350 to 400 cents would have had to be allocated previously because of inaccurate knowledge of the reactivity in hand and the burn-up rate.

3. SPECIFICATION OF REACTOR FLUXES

3.1 Establishing the absolute centre flux value at full power

The elements and rigs are designed to run with a centre neutron flux of 2.5×10^{15} n/cm^2 sec. There are twelve thermocouple positions below the core monitoring the outlet coolant temperature below the three sub-assemblies at the core centre and six of the driver fuel elements. The coolant flow rates through the sub-assemblies and elements are known from water rig measurements and the expected outlet temperature on each thermocouple at the correct centre flux can be calculated from the fission distribution provided by CRAM.[5]

In setting up the reactor power to produce the predicted outlet temperatures more weight is given to the driver element temperatures, since the sub-assemblies are themselves experimental rigs and liable to extra errors on that account. Even so, there are still discrepancies amongst the driver element exit temperatures that are larger than can be attributed to known sources of error such as flow rate uncertainty and incomplete mixing of inlet coolant streams.

Two possible explanations for the discrepancies can be suggested. The first is that instead of the partial mixing of coolant in the inlet header shown by early flow tests using models, there is negligible mixing and the coolant is entering the core in streams from the 24 heat exchangers with a spread of temperatures which is then superimposed on the outlet temperatures. The second explanation is that the flux distribution is being affected significantly by the positions of the control rods, each of which contains about 3% of the core fuel inventory. In fact changes in outlet temperature do occur when control rods are moved, but it is possible that the control rod movements are altering the outlet temperatures through changing the flow patterns rather than by altering the flux.

To resolve experimentally whether significant flux asymetries are occurring due to control rod movement, special monitoring elements with a well metered and insulated coolant flow and their own inlet and outlet thermocouples would have to be installed in several positions in the core. The engineering difficulty of such a scheme is formidable, however, and an attempt is being made to evaluate the effect of control rod movements on the flux by calculation.

3.2 Energy and spatial dependence of neutron flux

Having once established the centre value for say the fission rate in ^{235}U, one must predict sundry reaction rates elsewhere in the core and inner blanket regions. The diffusion theory code CRAM has been used for this purpose. There are several difficulties in deciding the adequacy of this calculation method for DFR geometry. A combination of survey calculations and experiments on the reactor and studies on a zero-energy system similar to it,[6] have led to the belief that the important reactions can be predicted to an accuracy of better than 3% in the core and 5% in the inner blanket.

The core is basically a hexagonal prism in which fuel element positions are defined by "pitch". All fuel elements at the same distance from the central axis are said to be at the same pitch, and because of the system's symmetry they may number up to twelve. The CRAM output has been arranged to apply to an (r,z) calculation an empirical correction derived from an (r,θ) calculation, according to the pitch (and hence the azimuthal angle) specified. An interpolation routine is provided so that data can be predicted for any position. The library file has been extended to include "damage cross-sections" showing the energy dependence of neutron effectiveness in causing atomic displacements in the crystalline lattice.

3.3 Gamma fluxes

The general position on gamma fluxes reported by Edwards and Atkinson[2] has been extended by data from instrumented rigs operating in the first row of the breeder. One such rig was a fixed-position gamma calorimeter used by Dehn in an extension of his earlier work.[7] At reactor mid-plane he obtained a heating rate in mild steel of 1.84 watts/gm at nominal full power (60 MW), a value reduced by 17% if one of the nearest control rods were completely withdrawn.

Because of rig manufacturing tolerances and uncertainties in emissivity, inferred gamma heating rates from other instrumented rigs are not very accurate. This objection does not apply to the same extent to showing the dependence of gamma heating rate on rod configuration. During the gamma calorimeter experi-

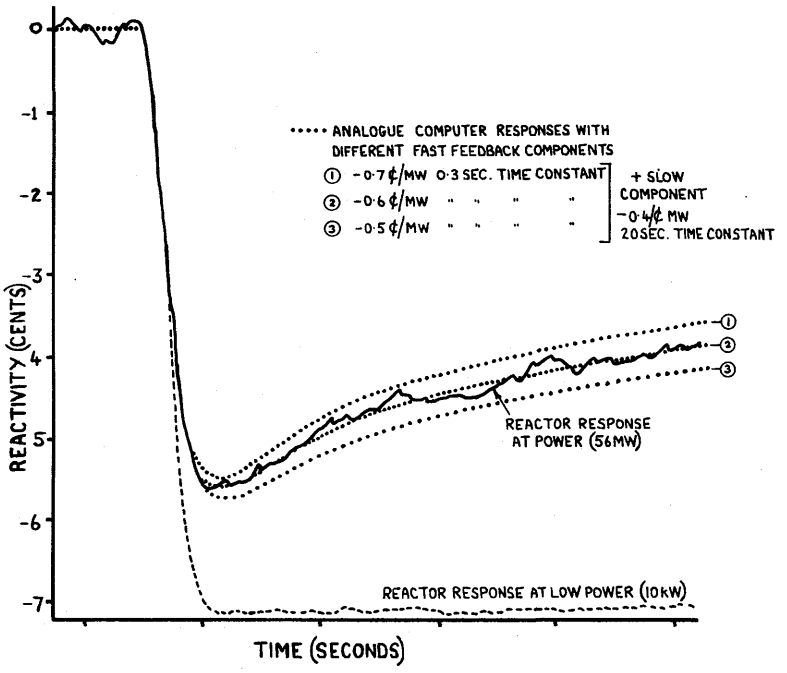

FIG.4. Reactivity meter traces following natural boron rod drops.

ments, for example, an instrumented rig was operating at another inner breeder position at the same distance from the core centre. In this case, however, the lowering of one of the nearest rods reduced the heating rate by only 12%.

4. MEASUREMENT OF REACTOR PARAMETERS

4.1 Monitoring reactivity feedback

The DFR has a fast acting negative reactivity feedback from the expansion of the core fuel and coolant, and a slow negative contribution from expansion in the blanket. As a result the reactor is very stable at power and would remain so even if there was a fairly large change in one of the coefficients. However, the safety clearance for the reactor assumes that the fast negative component will be large enough to mitigate the effect of certain accident conditions, and the feedback must be monitored to ensure that this is the case.

Originally an oscillator was employed[8] but with the simple type of feedback exhibited by the DFR it has been found adequate to use the more rapid technique of analysing the power change after a negative step of reactivity. The step is obtained by dropping a rod containing 200 gm of natural boron into the first row of the breeder. The reactivity worth of the step varies from run to run, but it can be calibrated rapidly at each start-up using the reactivity meter.

The rod is calibrated by dropping it when the reactor is at 10 kW. where there is no reactivity feedback. The power signal is fed to an on-line analogue reactivity meter[4] and a trace similar to that on Fig. 4. is obtained. The reactivity change shows the rod worth to be -7 cents in this case.

Once the reactor has been taken to power, the rod is dropped again, and this time the reactivity change is modified as shown in the figure by the reactivity feedback. The analysis of the rod drop at power is done by matching the reactivity curve from the reactor with curves obtained from the reactivity meter fed by an off-line analogue computer programmed to simulate the reactor. The traces produced by the computer with several values of negative fast feedback are also shown in the figure and illustrate the accuracy obtainable. The worth of the rod can be measured to 2% at low power and assuming the worth does not change with power the magnitude of the fast feedback can be determined to an accuracy of 20%, i.e. it is -0.6 ± 0.1 cents per MW.

The drop-time of the rod is 0.5 seconds, which is just about fast enough to resolve the 0.5 second time constant of the fast feedback. The slow feedback has probably several time constants, but it has been found that a single negative component of 0.4 ± 0.1 cents per MW, with a 20 second time constant provides an adequate fit to the power and reactivity responses for the first minute after the drop.

The use of this rapid method of checking the reactor feedback is only justified because the feedback characteristics of DFR are known and have been shown to be due to mechanisms which have a similar response to positive and negative changes in power. It is not suggested that this system could be used on its own to commission a new design of reactor.

4.2 Analysis of flux noise

A number of DFR studies has been made of the random fluctuations in temperature and flux using the CANDI[9] equipment. The signals of interest are recorded on tape and auto-and cross-correlograms extracted using off-line analogue multiplication with variable delays. The equipment has been used in particular for studying flux noise, and coolant temperature noise as shown by certain thermocouples.

Earlier results were reported by Menzies and Backhouse[10]. They found a characteristic feature of flux correlograms was a damped oscillation with a frequency proportional to coolant flow rate. Since this earlier work, the reactor has been modified by the permanent removal of a number of breeder elements. Subsequent to this the damping of the flux auto-correlogram has been much reduced, i.e. a 'pure' sinusoidal fluctuation has become a more pronounced feature of the reactor noise. Its mean square amplitude is about $10^{-6}\ (\Delta P/P)^2$. The frequency, maximum value 7 c/s, has been observed to vary proportionally with the flow, at least over the range 25% - full flow, but the decay time is much increased having values from one to several seconds. The amplitude, as a fraction of operating power is approximately independent of that power.

A possible cause of this fluctuation is vibration of control rod carriers as a result of vortex shedding, and an attempt is being made to reproduce the effect in an out-of-pile water rig. It is not, in itself, any operational inconvenience in DFR. If its origin is not understood, however, there is a slight possibility that in another reactor design it might be more pronounced, and tight margins on power and doubling time would then be difficult to obtain.

4.3 Thermocouple noise measurements

Below the experimental sub-assemblies installed at the centre of DFR are six thermocouples, two below each. The upper thermocouple of each pair is in the sub-assembly outlet nozzle, the other 12 cm below it. This layout exposes the thermocouples to exit coolant from the sub-assemblies mixed to various extents (coolant flow is downwards).

The auto-correlograms of the temperature noise shown on various thermocouples have been extracted, and described analytically. A majority of the small amount of data available is consistent with a white noise source of an intensity to be expected from sub-assembly properties filtered through the time constant of the thermocouple.

For example, an auto-correlogram for a thermocouple near the sub-assembly outlet was of form:

$$\left[6.6 \exp\left(-t/3.5\right) - 2.2 \exp\left(-t/1.2\right)\right] + 2.06 \exp\left(-t/1.2\right)$$

This is interpreted as arising from a noise source filtered by 3.5 and 1.2 second time constants, with another source filtered by the 1.2 second time constant only. Presumably the shorter time constant is that of the thermocouple and the longer that of the sub-assembly. There are cross and bypass flows in the coolant system, which must be presumed to vary whenever sub-assemblies are moved. This may account for the sudden change in noise characteristics which have been observed following sub-assembly disturbance and even from run to run.

4.4 The use of a beryllium source

The neutron source originally used in the reactor was a radium-beryllium one with a nominal strength of 10^8 neutrons per second. Measurement gave an effective source strength of about 1 milliwatt in the inserted position and about 10μ watts in the withdrawn position. The measured 10μ watt was the sum of the source effectiveness in its withdrawn position and any natural neutron production due, for example, to any plutonium 240 present. Calculation suggested that the former term predominated.

There was some incentive to dispense with the radium-beryllium source on the grounds of expense. The case for doing so became very strong, however, when a leak developed in it, radon escaped through the coolant into the blanket gas and interfered with work on experimental techniques for detecting bursts in radon-loaded fuel pins. It was therefore decided to dispense with the radium-beryllium source, at least temporarily, and use one based on the photo-neutron effect.

Beryllium is the most suitable material, and a calculation study was made of an antimony beryllium source. Homogeneous and heterogeneous arrangements of the antimony beryllium were found to give approximately the same source strength, and it seemed likely that an adequate source could be built into one replacement breeder element. The contribution to the source strength from fission-product gammas is dominated by that from antimony gammas except immediately following a reactor trip.

However, as a temporary expedient a source containing beryllium alone was made, reliance being placed on fission-product gammas to stimulate the neutron emmission. It consisted of about 230 gms of beryllium granules loosely packed inside a stainless-steel helium-filled container mounted at the centre of one of the inner breeder elements.

Apart from some mechanical difficulties this type of source has proved itself quite satisfactory operationally, and the dependence of source strength on time has not been an embarrassment in practice. It seems unlikely that an antimony-beryllium source will now be used.

5. THE PERFORMANCE OF REACTOR INSTRUMENTS

5.1 Delayed neutron monitors

The activity of delayed neutrons in the DFR primary coolant is monitored by BF_3 counters alongside by-pass loops on 4 of the 24 circuits (2 core and

2 breeder). Since the core driver elements are vented to the coolant, the background signal on the core circuit monitors at full power and 100% flow is 15 000 counts per second which is about an order of magnitude less than the calculated estimate. The breeder does not introduce any delayed neutron precursors into its coolant but because the core and breeder have a common inlet header, the breeder receives precursors from the coolant which has left the core and passed through the heat exchangers. Consequently the breeder circuit monitors show a signal of about 800 counts per second which arises from the core precursors after a further two minutes delay corresponding to the extra journey round the heat exchangers done by these precursors.

It is surprising that with these large background signals any extra signal can be detected from failure of cladding on sealed experimental pins, but this has been found to be the case. Twice in the current year a prompt reactivity drop of 1 cent when the reactor was at full power was followed by unmistakeable temporary increases in the delayed neutron monitor signals. In the first incident the signals in one core then one breeder circuit monitors increased by 50% for a minute, reverted to 10% high for 20 minutes then returned to normal. The other two circuits showed no change. In the second incident the two breeder circuits only showed simultaneous increases of 15% for about one minute. In each case examination of experimental elements after the run showed a pin which had burst its containment and allowed fuel to fall to the bottom of the element, thus causing a reactivity change comparable with that observed.

The fact that particular core or breeder monitors may not show any change in such an incident suggests that the coolant passing it has received a negligible proportion of the extra precursors, and hence the mixing in the inlet and outlet headers cannot be as good as was thought from early work using scale models. This streaming of coolant would also partly explain why a single pin bursting can produce a significant change in the monitors at all, since each core monitor is effectively not sampling all 300 core elements but only about 15 of them. The extra signal from exposure of the fuel in a single pin would therefore be more significant if it happened to occur in thestream feeding one of the core circuits with a delayed neutron monitor, and completely lost if it did not. This cannot be the complete explanation for the large signals, however, for two reasons. Firstly, on one occasion both breeder circuits showed an increase, and it is inconceivable that only one core circuit feeds both the breeder circuits that have monitors, since these circuits are on opposite sides of the breeder. Secondly, the fact that the signal is high for only a limited period suggests that the increased precursors have been stored in the pin and that after they have all erupted to the fuel surface or otherwise escaped from the pin, the equilibrium production rate of precursors by recoil from the freshly exposed surface is negligible compared to the background from the vented fuel. For this second reason, delayed neutron monitors may be more effective detectors of sealed pin failure than has been thought possible where there was a background from vented elements.

REFERENCES

(1) HENRY, K., EDWARDS, A. G., A Review of the Operation of the D.F.R., Paper 2/2 BNES Conf., London (1966).

(2) EDWARDS, A. G., ATKINSON, H., U.K.A.E.A. Report TRG 1429 (D) (1966).

(3) JAMES, P. R., TAIT, D., D.F.R. Kinetic computer analogue, Nucl. Engng. 11 123 (1966) 611.

(4) ATKINSON, H., JAMES, P. R., TAIT, D., Design and use of simple reactivity meters for fast reactors, U.K.A.E.A. Report TRG 1526(D) (1967).

(5) HASSITT, A., U.K.A.E.A. Report TRG 229 (R) (1962).

(6) SMITH, J. C., ATKINSON, H., McTAGGART, M. H., U.K.A.E.A. Report TRG 1384 (D) (1966).

(7) DEHN, R., U.K.A.E.A. Report TRG 844 (D) (1964).

(8) WHEELER, R. C., TAIT, D., U.K.A.E.A. Report TRG 864 (D) (1965).

(9) BOARDMAN, F. D. et al. A correlator for investigating random fluctuations in nuclear power reactors, Radio and Elec. Engng. 30 3 (1965) 161.

(10) MENZIES, D. C., BACKHOUSE, A. M., U.K.A.E.A. Report TRG 921 (D) (1965).

DISCUSSION

W.B. LOEWENSTEIN (Chairman): In the second paragraph of section 5.1 you refer to failures in the cladding of sealed experimental pins. Can you be sure that the increases in signal are due to the pins subsequently found to have failed?

D. TAIT: No – although in some cases confirmatory evidence is provided by reactivity changes, which are detailed in the paper.

W.B. LOEWENSTEIN: Do your safety arrangements include a chemical gas sampling system?

D. TAIT: Yes. However, the gas travels to the sampling point by a path taking several hours, with consequent variations in the fission product concentration. Accordingly, no significant changes would be expected to result from a sealed pin failure.

F.W.A. HABERMANN: With regard to the calibration procedures described in section 2.2, did you investigate the effect of detector location on the calibration?

D. TAIT: We use ion chamber detectors located well outside the pressure vessel, and we have found no spatial effect resulting from the control rod movements. This is confirmed by the fact that the changes in control rod worth can be described by the same function for all the rods in the reactor.

THE LONG-TIME BEHAVIOUR OF FAST POWER REACTORS WITH Pu-RECYCLING*

A. JANSEN
INSTITUT FÜR NEUTRONENPHYSIK UND REAKTORTECHNIK,
KERNFORSCHUNGSZENTRUM KARLSRUHE,
KARLSRUHE, FEDERAL REPUBLIC OF GERMANY

Abstract

THE LONG-TIME BEHAVIOUR OF FAST POWER REACTORS WITH Pu-RECYCLING. A study is made of the long-time behaviour of fast power reactors with Pu-recycling, taking into account the internal core and blanket management and the external management of the fuel concerning the reprocessing and refabricating plants. The investigations are based on a suitable reactor model which includes a cylindrical reactor core, an axial and radial blanket, and the external plants for reprocessing the irradiated fuel and refabricating the fuel elements. Charging and discharging of the core and blanket elements are treated as discontinuous processes.

The calculation of the U and Pu output of the core and blankets at a given time is performed in two steps: first the well-known burn-up equations for the fuel with space-dependent coefficients are solved, yielding the space-dependent U and Pu concentrations in the irradiated and discharged elements. Then the total U and Pu content of the discharged elements follow by volume integration. The coefficients of the burn-up equations are determined by the one-group neutron flux $\varphi(r, z)$ and the microscopic one-group cross-sections $\sigma(r, z)$ for absorption and capture at the points of neutron irradiation. To limit the numerical efforts by calculating the long-time behaviour, the one-group constants are regarded as time independent. The feedback of the burn-up of the fuel on the neutron flux and spectrum can be taken into account for a first-order approximation by calculating the one-group constants for an average burn-up state of the reactor. By this procedure it is possible to calculate the U and Pu content of the discharged elements with sufficient accuracy. The one-group neutron flux of the average state of the reactor is normalized to the given total power of the reactor. From these conditions, the U and Pu output of the core, axial and radial blanket are calculated as functions of time, thereby taking the time-dependent initial composition of the core elements into account completely. The initial composition of the fuel elements is re-calculated for every fuel cycle by satisfying two algebraic conditions for each core zone. The first condition maintains criticality of the reactor by keeping the difference of neutron production and consumption per cm^3 and sec constant in respect to time. The second condition keeps the total number of the heavy nuclei per cm^3 constant. The breeding gain is also determined by these conditions.

The numerical results for a 1000-MW(e) sodium-cooled reactor show a strong coupling between the operation of the radial blanket by joint reprocessing of the core and radial blanket elements. This is shown by the time dependence of the Pu-isotopic composition in the fresh and irradiated fuel elements. Furthermore, it is shown that this time behaviour leads to time variations of the amount of Pu which must be charged into the core for criticality, and the breeding gain of the system.

1. INTRODUCTION

The long-time behaviour of fast power reactors with plutonium recycling generally includes the overall time behaviour caused by the fuel burn-up in the reactor and the internal and external fuel management. It is useful to distinguish between two types of problems:

(a) The behaviour of the reactor between two loading events, which refers to the time dependence of neutron flux, reactivity, power distri-

* Work performed within the association in the field of fast reactors between the European Atomic Energy Community and Gesellschaft für Kernforschung m.b.H., Karlsruhe.

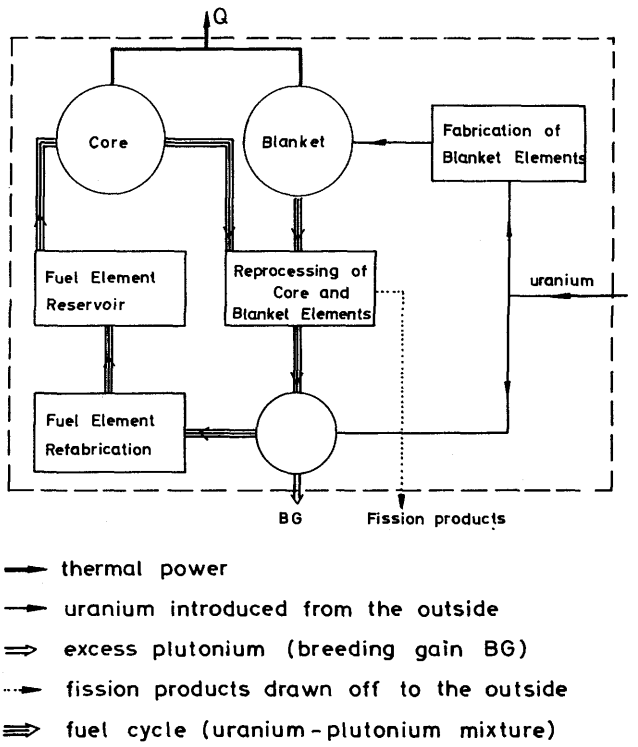

FIG.1. Fuel cycle of a fast power reactor with plutonium recycling.

bution, fuel composition etc.; usually this is the object of the conventional fuel burn-up studies

(b) The behaviour of the reactor over many reloading cycles, which refers to the time dependence of the isotopic composition of plutonium, the uranium and plutonium content of the fuel, the breeding gain etc.

In this paper we will confine ourselves to the second class of problems only. We shall consider a fast power reactor in which the only fissionable material consumed is that bred in the same reactor, except for the plutonium needed to start up the reactor and for a certain period afterwards. Thus, we have a closed fuel cycle including the core and the external plants for reprocessing the irradiated fuel and refabricating the fuel elements. The blanket plutonium is introduced into the closed fuel cycle and the breeding gain is drawn off this cycle. The fuel cycle for joint reprocessing of the core and blanket elements is shown in Fig.1.

The time variations of the isotopic composition of the plutonium in the fuel-cycle system are caused by the neutron irradiation in the reactor and by the internal and external fuel management.[1] The composition of

[1] Internal fuel management is always done to improve the burn-up behaviour of the reactor; external fuel management refers to reprocessing and refabrication.

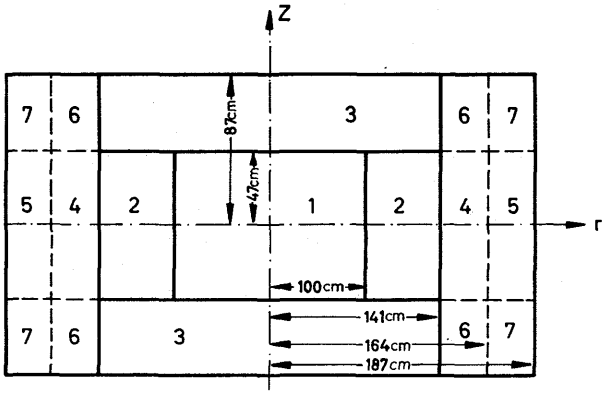

FIG.2. Cross-sectional view of reactor Na 1. Numbers 1 - 7 designate the fuel compositions of the average burn-up state of the reactor given in Table II; 1. core zone 1; 2. core zone 2; 3. axial blanket; 4 - 7 radial blanket.

the refabricated fuel elements is determined by that uranium-to-plutonium ratio which maintains the reactor critical, assuming the total number of heavy isotopes in the fuel elements to be constant.

The problems to be investigated were studied first in Ref.[1] on the basis of an idealized zero-dimensional model without taking into account the internal and external fuel management. Loading and unloading the core and blanket elements were regarded as continuous processes. In this paper we will investigate the long-time behaviour of the plutonium composition in the fuel and the physical aspects of the fuel-cycle economy under more realistic conditions. In particular, loading and unloading the core and blanket elements will be treated as discontinuous processes; the external fuel management and the times for reprocessing and refabrication will be taken into account.

As we shall not be considering the first type of long-time behaviour problems, we can make some simplifications which refer essentially to the secondary time variations of neutron flux and spectrum caused by the fuel burn-up. These simplifications enable us to solve the long-time problems with sufficient accuracy by tolerable numerical efforts. The formalism developed below is applied to a sodium-cooled 1000-MW(e) power reactor [2]. The main numerical results are given in the last section.

2. THE MATHEMATICAL FORMALISM FOR CALCULATING THE LONG-TIME BEHAVIOUR

2.1. Conditions for reactor operation

We consider a cylindrical reactor with a multizoned core, an axial and a radial blanket (Fig. 2). Exchanging the core and blanket elements takes place at each of the discrete time values

$$t_s = s\ \Delta t_C, \quad s = 1, 2, 3, \ldots \tag{1}$$

Δt_C is a given constant correlated to the thermal reactor power Q and the given maximum burn-up of the fuel elements as shown in Eq.(6).

The core elements are loaded and unloaded according to the cyclic burn-up scheme described in Ref.[3]. The core is subdivided into radial regions; the elements of the same radial region are combined into groups of n elements (e.g. n = 3). At each point of time t_s only one element of each group is exchanged for a fresh fuel element. During a period of time $n\Delta t_C$ each element of a group is exchanged once and once only. The life-time of the core elements is $\delta = n\Delta t_C$, i.e. the total irradiation time of a fuel element in the core. At each time t_s only the n^{th} part of the core elements is exchanged for fresh elements. If V_C is the total fuel element volume of the core, the exchanged fuel element volume at t_s is

$$\Delta V_C = \frac{1}{n} V_C \tag{2}$$

The operation of the axial and radial blankets must be in agreement with the rhythm given by Eq.(1); i.e. loading and unloading the blanket elements must proceed at intervals $m\Delta t_C$, where m is a positive integer. The elements of the axial blanket are coupled with the core elements, therefore both are managed jointly. Contrary to this, the management of the radial blanket is largely independent of the core management. We assume the radial blanket to be divided into N_B radial zones which are exchanged as a whole. The life-time of the j^{th} zone of the radial blanket may be

$$\delta_{Bj} = m_j \Delta t_C, \qquad j = 1, 2, \ldots, N_B$$

the integer m_j is related to the maximum burn-up in the j^{th} zone.

The amount of uranium and plutonium discharged out of the core and the axial and radial blankets is calculated in two steps: (a) calculation of the space-dependent uranium and plutonium concentrations of the discharged elements by solving the fuel burn-up equations; (b) calculation of the uranium and plutonium content of these elements by volume integration. The fuel burn-up calculations and the volume integration for the core and blanket elements are discussed in the following sections.

2.2. The fuel burn-up equations

The time behaviour of the fuel composition during neutron irradiation in the reactor is determined by the well-known fuel burn-up equations. As the main components of the fuel we regard the two uranium isotopes ^{235}U and ^{238}U and the four plutonium isotopes ^{239}Pu, ^{240}Pu, ^{241}Pu, and ^{242}Pu. Therefore, we have to solve a system of 6 first-order differential equations in time or flux time, respectively. The coefficients of these equations are the one-group space-dependent neutron flux and microscopic cross-sections for neutron absorption and capture, which are defined in the

multigroup picture as

$$\phi(r, z) = \sum_i \phi_i(r, z)$$

$$\sigma(r, z) = \frac{\sum_i \sigma_i \phi_i(r, z)}{\phi(r, z)} \qquad (4)$$

$\phi_i(r, z)$ is the neutron flux in the i^{th} neutron energy group at r, z; the $\phi_i(r, z)$ are determined by multigroup calculations. The σ_i are the microscopic cross-sections of the heavy nuclei in the fuel for neutron absorption and capture in the i^{th} energy group.

In general, both ϕ and σ are time dependent as a consequence of the variation of the fuel composition in the reactor during neutron irradiation, but it will be possible to calculate the uranium and plutonium concentrations in the irradiated elements at the end of their life-time by solving the fuel burn-up equations with sufficient accuracy, if we take into account time-averaged ϕ and σ instead of the exact time-dependent quantities. The latter, in general, would require the simultaneous solution of the burn-up equations and the criticality equation of the reactor, e.g. multigroup-diffusion equations. In our case the time-averaged one-group quantities are calculated by Eq.(4) with time-averaged neutron spectra determined by multigroup calculations for an average burn-up state of the reactor, assuming a homogeneous distribution of the fuel. The one-group neutron flux for the average burn-up state is normalized to the given reactor power Q which is regarded as constant.

2.3. The uranium and plutonium output of the core and the axial blanket

We suppose that the core is divided into N radial zones of different fuel compositions. The $N_{j,k}(s, 0)$ may be the time-dependent initial concentrations of the nuclei $k = 1, 2, .., 6$[2] in the fuel elements which are loaded into the core zone $j = 1, 2, \ldots, N$ at the time t_s. We presume

$$N_{j,k}(s, 0) \equiv N_{j,k}(0, 0) \quad \text{for all } s < s_0; \quad j = 1, 2, \ldots, N; \quad k = 1, 2, \ldots, 6$$

s_0 designates the time $t(s_0)$ at which refabricated fuel elements are loaded into the core for the first time, i.e. for closing the fuel cycle, and is determined by the external fuel management as shown below. The $N_{j,k}(0,0)$ denote the j^{th} initial composition of the fuel elements at $t_0 = 0$. For all $s \geq s_0$ the $N_{j,k}(s, 0)$ are to be calculated as functions of s, as shown below.

Now we have to calculate the fuel output of the core at time t_s. The $N^*_{j,k}(s, \tau_{maxj})$ may be the concentrations of the heavy nuclei in the fuel elements unloaded from the j^{th} zone at t_s. The corresponding initial concentrations may be given by $N^*_{j,k}(s, 0)$. The $N^*_{j,k}(s, \tau_{maxi})$ are the

---

[2] The indices $k = 1, 2, \ldots, 6$ refer to the isotopes ^{235}U, ^{238}U, $^{239}Pu, \ldots,$ ^{242}Pu respectively, which are the components of the fuel mixture.

solutions of the fuel burn-up equations with these initial values and the space-dependent flux times

$$\tau_{maxj} = n\ \Delta t_C\ \phi(r, z), \qquad j = 1, 2, \ldots, N \tag{5}$$

r, z is any point of the core zone j. τ_{maxj} is related to the maximum fuel burn-up for the elements of the core zone j in MWd/t. From Eq.(5) follows the relation between Δt_C, the maximum burn-up for the inner core zone j = 1 expressed by the corresponding maximum flux time, and the neutron flux at the core centre $\phi(0, 0)$:

$$\Delta t_C = \frac{1}{n} \frac{\tau_{max1}}{\phi(0, 0)} \tag{6}$$

$\phi(0, 0)$ is proportional to the reactor power Q. Obviously, the following relation holds:

$$N^*_{j,k}(s, 0) = \begin{cases} N_{j,k}(0, 0) & \text{for } s-n < s_0, \\ & \qquad j = 1, 2, \ldots, N;\ k = 1, 2, \ldots, 6 \\ N_{j,k}(s-n, 0) & \text{for } s-n \geq s_0, \end{cases} \tag{7}$$

The total number $\Delta N^*_{j,k}(s)$ of the nucleus k which is unloaded from the core zone j at t_s follows by integrating $N^*_{j,k}(s, \tau_{maxj})$ over the volume of the unloaded fuel elements. We obtain

$$\Delta N^*_{j,k}(s) = \frac{2\pi}{n} \int_{-\frac{H+D}{2}}^{\frac{H+D}{2}} \int_{R_j}^{R_{j+1}} N^*_{j,k}(s, \tau_{maxj})\ r\ dr\ dz, \qquad k = 1, 2, \ldots 6 \tag{8}$$

where the discharged nuclei of the axial blanket are included. H denotes the height of the core, D the total thickness of the axial blanket, R_j the inner and R_{j+1} the outer radial boundary of the j^{th} zone. The division by n is necessary, for only the n^{th} part of the elements of the zone j is discharged. In the core range we have to take into account the time dependence of the initial composition of the fuel; in the axial blanket region we take the initial composition of the elements as constant.

The total output of the core and the axial blanket expressed as the total number of the discharged nuclei at the time t_s, denoted as $\Delta N^*_{Ck}(s)$, is

$$\Delta N^*_{Ck}(s) = \sum_{j=1}^{N} \Delta N^*_{j,k}(s), \qquad k = 1, 2, \ldots, 6 \tag{9}$$

2.4. The uranium and plutonium output of the radial blanket

The uranium and plutonium content of the radial blanket zone j at the time of discharging, which may be denoted as $\Delta N^{*}_{Bj,k}$, $j = 1, 2, \ldots, N_B$, $k = 1, 2, \ldots, 6$, is also calculated by a volume integral by analogy to Eq.(8). But in the case of the radial blanket n is equal to 1 and the initial values of the elements are time independent. The flux time distribution in the j^{th} zone for solving the burn-up equation is

$$\tau_{maxj} = m_j \, \Delta t_C \, \phi(r, z), \qquad j = 1, 2, \ldots, N_B$$

r, z is any point in the radial blanket zone j.

For a given value of s only that zone j of the radial blanket is unloaded for which

$$\frac{t_s}{m_j \, \Delta t_C} = \frac{s}{m_j} = \text{an integer} \tag{10}$$

If no value of j exists for a given s, the total output $\Delta N^{*}_{Bk}(s)$, $k = 1, 2, \ldots, 6$ of the radial blanket is zero:

$$\Delta N^{*}_{Bk}(s) = 0 \quad \text{for all k} \tag{11a}$$

If there are ℓ special values of j for a given s, denoted as $j(\ell')$, $\ell' = 1, 2, \ldots, \ell$, for which Eq.(10) is valid, all the designated zones are unloaded at t_s. Thus, the uranium and plutonium output of the radial blanket at t_s is

$$\Delta N^{*}_{Bk}(s) = \sum_{\ell'=1}^{\ell} \Delta N^{*}_{Bj(\ell'),k} \tag{11b}$$

2.5. The composition of the refabricated fuel elements and the breeding gain

In the case of joint reprocessing of core and blanket elements, the total number of nuclei, which are unloaded from the reactor at t_s and which are to be reprocessed, is

$$\Delta N^{*}_{k}(s) = \Delta N^{*}_{Ck}(s) + \Delta N^{*}_{Bk}(s), \quad k = 1, 2, \ldots, 6, \quad s = 1, 2, \ldots$$

the $\Delta N^{*}_{Bk}(s)$ may vanish for certain values of s as shown before. The total numbers of uranium and plutonium nuclei are

$$\Delta N^{*}_{U}(s) = \Delta N^{*}_{1}(s) + \Delta N^{*}_{2}(s), \qquad \Delta N^{*}_{Pu}(s) = \sum_{k=3}^{6} \Delta N^{*}_{k}(s) \tag{12}$$

Losses during reprocessing reduce the number of nuclei by a factor of p_U and p_{Pu}, respectively, Thus, after reprocessing we have

$$\Delta N_U^*(s) \Longleftarrow p_U \, \Delta N_U^*(s)$$

$$\Delta N_{Pu}^*(s) \Longleftarrow p_{Pu} \, \Delta N_{Pu}^*(s)$$

using the same symbols for the reduced numbers. The enrichment of the uranium available after reprocessing is

$$\Gamma(s) = \frac{\Delta N_1^*(s)}{\Delta N_U^*(s)} \tag{13}$$

and the relative composition of the plutonium mixture available for the refabrication of the fuel elements is given by

$$Q_k(s) = \frac{\Delta N_k^*(s)}{\Delta N_{Pu}^*(s)}, \qquad k = 3, 4, 5, 6 \tag{14}$$

The initial uranium and plutonium concentrations of the fuel elements for the j^{th} core zone, which are refabricated from plutonium of the s^{th} discharge, i.e. from $\Delta N_{Pu}^*(s)$, may be denoted as $n_{j,U}(s)$ and $n_{j,Pu}(s)$, respectively. The $n_{j,k}(s)$, $k = 1, 2, \ldots, 6$ may be the initial concentrations of the uranium and plutonium isotopes in the refabricated fuel elements. Thus, the following relations hold:

$$\begin{aligned} n_{j,U}(s) &= n_{j,1}(s) + n_{j,2}(s) \\ n_{j,Pu}(s) &= \sum_{k=3}^{6} n_{j,k}(s) \end{aligned} \qquad j = 1, 2, \ldots, N \tag{15}$$

The $n_{j,U}$, $n_{j,Pu}$ and $n_{j,k}$ are space independent.

The basis for calculating the initial compositions of the refabricated fuel elements are the 2N linear algebraic equations

$$\begin{aligned} \sum_{k=1}^{6} C_{j,k} \, n_{j,k}(s) &= K_j(0) \\ \sum_{k=1}^{6} n_{j,k}(s) &= Z_j(0) \end{aligned} \qquad j = 1, 2, \ldots, N \tag{16}$$

with the abbreviations

$$C_{j,k} = (\nu\sigma^f)_{j,k} - \sigma^a_{j,k}, \qquad k = 1, 2, \ldots, 6$$

$$K_j(0) = \sum_{k=1}^{6} C_{j,k}\, n_{j,k}(0), \quad n_{j,k}(0) \equiv N_{j,k}(0, 0) \tag{16a}$$

$$Z_j(0) = \sum_{k=1}^{6} n_{j,k}(0)$$

The one-group quantities $\sigma^a_{j,k}$ and $(\nu\sigma^f)_{j,k}$ refer to any reference point in the j^{th} zone (e.g. $r = R_j$, $z = 0$). As mentioned above, they are calculated for the average fuel burn-up state of the reactor assuming a homogeneous fuel distribution. The $\nu\sigma^f$ are defined by analogy to Eq.(4).

The equations (16) are used to calculate the 2N unknown initial concentrations $n_{j,U}$ and $n_{j,Pu}$ with a presupposed uranium enrichment and the isotopic composition of the plutonium given by Eq.(14). The first equations (16) are given to maintain criticality. By these equations the reactivity worth of the refabricated fuel elements is fixed approximately at a constant value for each zone by adjusting the fuel composition to a constant difference between neutrons produced and absorbed in the fresh fuel at a given point of each zone. The constant differences are defined by the fresh fuel of the initial reactor at $t_0 = 0$.

The second equations (16) take the total number of heavy nuclei in the fresh fuel elements for each zone to be constant. The constants are given again by the initial conditions at $t_0 = 0$. For simplification we assume that the enrichment of the uranium used for fuel element refabrication is constant and equal to the initial enrichment γ at $t_0 = 0$. Thus, we have the relations

$$\begin{aligned} n_{j,1}(s) &= \gamma n_{j,U}(s) \\ n_{j,2}(s) &= (1-\gamma) n_{j,U}(s) \end{aligned} \tag{17}$$

If only the plutonium mixture from the s^{th} discharge of the reactor is used for refabricating, i.e. in the case of positive breeding gain, the concentrations of the plutonium isotopes are

$$n_{j,k}(s) = Q_k(s) n_{j,Pu}(s), \qquad k = 3, 4, 5, 6 \tag{18}$$

With relations (17) and (18) the equations (16) are rearranged to

$$\begin{aligned} n_{j,U}(s)\, C_{j,U} + n_{j,Pu}(s)\, C_{j,Pu}(s) &= K_j(0) \\ n_{j,U}(s) \qquad + n_{j,Pu}(s) \qquad\quad &= Z_j(0) \end{aligned} \tag{19}$$

with

$$C_{j,U} = C_{j,1}\,\gamma + C_{j,2}(1-\gamma) \tag{19a}$$

$$C_{j,Pu}(s) = \sum_{k=3}^{6} C_{j,k}\, Q_k(s)$$

If $C_{j,Pu}(s) \neq C_{j,U}$ the equations are solved by

$$n_{j,U}(s) = \frac{Z_j(0)C_{j,Pu}(s) - K_j(0)}{C_{j,Pu}(s) - C_{j,U}}$$

$$j = 1, 2, \ldots, N \tag{20}$$

$$n_{j,Pu}(s) = \frac{-Z_j(0)C_{j,U} + K_j(0)}{C_{j,Pu}(s) - C_{j,U}}$$

For physical reasons $n_{j,U}(s)$ and $n_{j,Pu}(s)$ must be positive. If

$$C_{j,U} \leq 0 \tag{21}$$

i.e. $\gamma \leq 1/(1-C_{j,1}/C_{j,2})$, $n_{j,Pu}(s)$ is positive. If relation (21) is true, the numerator of the first equation (20) must be positive, i.e.

$$C_{j,Pu}(s) \geq \frac{K_j(0)}{Z_j(0)}, \quad j = 1, 2, \ldots, N \tag{22}$$

In the most interesting cases of fast power breeders with natural or depleted uranium as the fertile material the two conditions (21) and (22) are always true and the solutions (20) are positive.[3] We shall restrict ourselves to these cases in the following. But the initial compositions for the refabricated fuel elements are only determined by Eq. (20), if the number $\Delta N^{*}_{Pu}(s)$ of the available plutonium nuclei is enough for manufacturing the fuel element volume ΔV_C, i.e. in the case of positive breeding gain. The total number of plutonium nuclei from the s^{th} unloading of the reactor which is required for refabricating the fuel element volume ΔV_C is given by

$$N_{Pu}(s) = \frac{1}{n} \sum_{j=1}^{N} \Delta v_j\, n_{j,Pu}(s)$$

[3] In the cases of higher enrichments of the uranium in the fuel equations (16) continue to be true. The time dependence of the uranium enrichment, which is caused by the fuel burn-up and perhaps by the fuel management is, however, to be taken into account. Especially in the case of starting up the reactor as a converter with ^{235}U as the fissionable material we have to distinguish the time-dependent enrichment of the uranium in the closed fuel cycle according to Eq. (13) and the presupposed enrichment of the uranium which is introduced into the fuel cycle from the outside to compensate for the consumed fertile material. Equations (17) and (19) are modified by these facts. We will not discuss these more general equations and the conditions by which the solutions are positive here.

Δv_j is the total volume of the fuel elements of the core zone j; thus, $\Delta v_j/n$ is the exchanged fuel element volume. Losses during the fuel element fabrication reduce the number of plutonium nuclei by a factor q_{Pu}, therefore, the number of the required plutonium nuclei is $N_{Pu}(s)/q_{Pu}$, instead of $N_{Pu}(s)$. If

$$N_{Pu}(s)\frac{1}{q_{Pu}} \leq \Delta N^*_{Pu}(s) \tag{23}$$

the initial compositions of the refabricated fuel elements are determined by equations (20).

The breeding gain of the s^{th} fuel cycle is defined by

$$N_{BG}(s) = \Delta N^*_{Pu}(s) - \frac{1}{q_{Pu}} N_{Pu}(s) \tag{24}$$

which is positive in accordance with relation (23).

2.6. The parameter s_0

The time required for the external fuel management is $(s_0-1)\,\Delta t_C$ with the definition of s_0 given previously. Thus, the plutonium unloaded from the reactor at t_s is reloaded into the core at $t_{s+s_0-1} = (s+s_0-1)\Delta t_C$. Therefore, we have the relation

$$N_{j,k}(s+s_0-1, 0) = n_{j,k}(s) \quad \text{for all values of k and j} \tag{25}$$

s_0 is determined by the characteristics of the reprocessing and refabricating plants. The external fuel cycle is characterized essentially by the parameters δ_c, δ_r, and δ_f, which are the minimum cooling time and the times for reprocessing and refabricating, respectively. These quantities define a new parameter

$$\delta_{ex} = \delta_c + \delta_r + \delta_f$$

Furthermore, we define

$$p = \left[\frac{\delta_{ex}}{\Delta t_C}\right]$$

[x] is the maximum integer below x.

For simplification we shall assume in the following that the refabricated fuel element volume ΔV_C of any fuel cycle is loaded into the core as a whole, i.e. it should not be distributed over different loading events. We shall express the time for loading the fuel element volume ΔV_C of the s^{th} fuel cycle into the core in terms of p.

The time at which the first elements of the s^{th} fuel cycle are refabricated lies between $t_s+p\Delta t_C$ and $t_s+(p+1)\Delta t_C$ as the case may be, whether or not $\delta_{ex}/\Delta t_C$ is an integer. For economic reasons we assume that the

TABLE I. INITIAL COMPOSITION OF THE CORE AND BLANKET ELEMENTS AT $t_0 = 0$

(in 10^{21} nuclei per cm^3 reactor volume [5])

	Core zone 1	Core zone 2	Axial blanket	Radial blanket
^{235}U	0	0	0	0
^{238}U	5.642	5.299	7.07	10.5
^{239}Pu	0.842	1.107	0	0
^{240}Pu	0.247	0.325	0	0
^{241}Pu	0.028	0.037	0	0
^{242}Pu	0.006	0.007	0	0

time after which the complete volume ΔV_C is refabricated will not exceed Δt_C, i.e. the last elements of the s^{th} cycle may be refabricated not later than $t_s+(p+2)\Delta t_C$. This condition avoids unnecessary accumulations of plutonium in the external fuel cycle. In general, three values of s_0 are possible:

$$s_0 = p+\epsilon, \quad \epsilon = 1, 2, \text{ or } 3, \text{ respectively}$$

$\epsilon = 1$: if $\delta_{ex}/\Delta t_C = p$ and if the fuel element volume ΔV_C is managed as only one batch.

$\epsilon = 2$: (1) if $\delta_{ex}/\Delta t_C \geq p$ and if the fuel element volume ΔV_C is divided into partial batches and the last batch is refabricated not later than $t_s+(p+1)\Delta t_C$; (2) if $\delta_{ex}/\Delta t_C > p$ and if ΔV_C is managed as a whole.

$\epsilon = 3$: only if $\delta_{ex}/\Delta t_C > p$ and if ΔV_C is divided into partial batches and the last batch is refabricated later than $t_s+(p+1)\Delta t_C$.

3. NUMERICAL RESULTS

The numerical results refer to the sodium-cooled reactor Na1 [2]. The load factor is taken as 80%; thus, the thermal power is assumed to be Q = 2000 MW on the average. Furthermore, we suppose n = 3, Δt_C = 200 d for the fuel burn-up cycles in the core. The corresponding maximum burn-up in r = 0 is 86 000 MWd/t averaged in the z-direction. The geometrical data are given in Fig. 2. The initial composition of the core and blanket elements at $t_0 = 0$ is given in Table I. The relative isotopic composition of the initial plutonium mixture is: ^{239}Pu: 75%, ^{240}Pu: 22%, ^{241}Pu: 2.5%, ^{242}Pu: 0.5%, i.e. the so-called Pu^{∞} calculated for the

TABLE II. FUEL COMPOSITIONS FOR THE AVERAGE BURN-UP STATE OF THE REACTOR, USED FOR CALCULATING THE ONE GROUP NEUTRON FLUX AND CROSS-SECTIONS

(in 10^{21} nuclei per cm^3 reactor volume)

Reactor zone	Core zone 1	Core zone 2	Axial blanket	Radial blanket			
Fuel mixture	1	2	3	4	5	6	7
Average burn-up MWd/t	50 000	40 000	2000	5000	300	2000	200
^{235}U	0	0	0	0	0	0	0
^{238}U	5.287	5.078	6.928	10.179	10.421	10.314	10.449
^{239}Pu	0.796	0.997	0.125	0.263	0.075	0.159	0.049
^{240}Pu	0.273	0.342	0.003	0.006	0.001	0.003	0
^{241}Pu	0.040	0.047	0	0	0	0	0
^{242}Pu	0.008	0.009	0	0	0	0	0
Fission product pairs	0.358	0.299	0.015	0.051	0.003	0.024	0.002

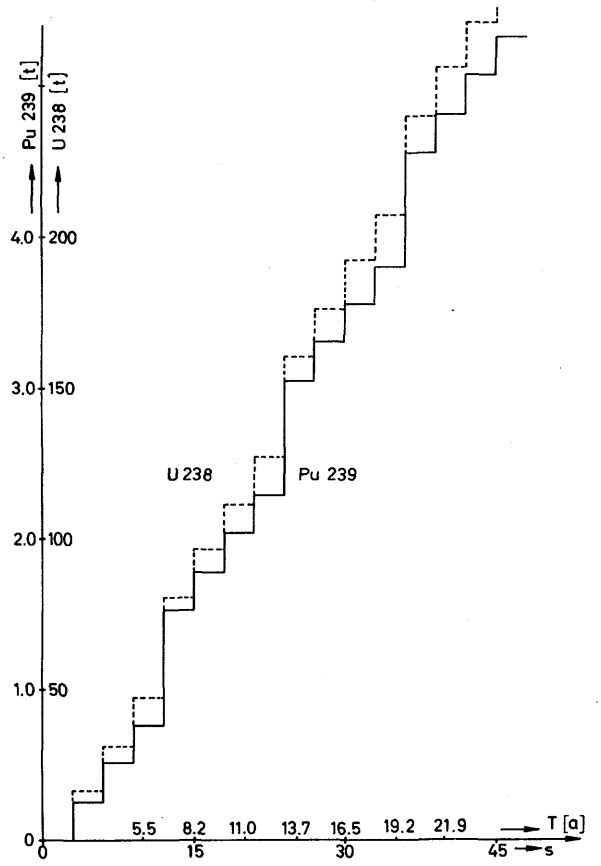

FIG. 3. Total ^{238}U and ^{239}Pu output of the radial blanket up to time $t_s = s\Delta t_c$.

reactor Na1 by the method given in Ref. [1]. The composition of plutonium bred in a thermal power reactor may be similar to this.

The multigroup calculations are carried out for the average burn-up state of the reactor specified in Table II. The fuel compositions given in this table are taken to be constant in the sub-zones of the reactor described in Fig. 2. The Karlsruhe 26-group set [4] is the basis for the multigroup calculations.

The radial blanket is divided into two radial zones, i.e. $N_B = 2$. The radial boundary between the two zones (Fig. 2) is $R = 164$ cm. The inner zone is always exchanged after the irradiation time $3\Delta t_c$, the outer zone always after $12\Delta t_c$, i.e. $m_1 = 3$, $m_2 = 12$. The maximum burn-up of the radial blanket in the plane $z = 0$ is 10 000 MWd/t in the inner and 9500 MWd/t in the outer zone. The ^{238}U and ^{239}Pu output of the radial blanket as functions of time are given in Fig. 3. The unloaded plutonium consists of about 97% ^{239}Pu and 3% ^{240}Pu.

The parameters for the external fuel management are $\delta_c = 100$ days for cooling, $\delta_r = 30$ days for reprocessing, $\delta_f = 70$ days for refabricating. Dividing the discharged fuel element volume ΔV_C into partial batches, we

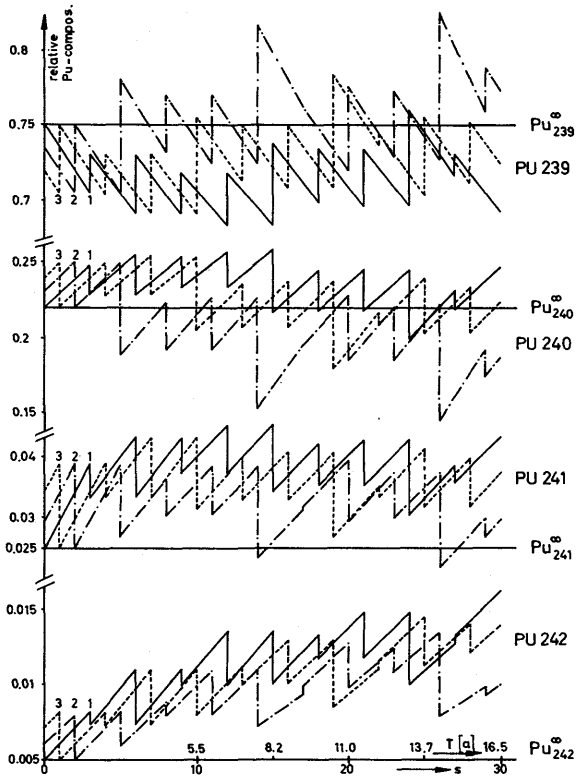

FIG.4. Relative Pu composition of the fuel elements in the core of reactor Na 1 ($n = 3$, $s_0 = 3$).

get $s_0 = 3$. Thus, the external fuel inventory, which corresponds to the fuel element volume of $(s_0 - 1)\Delta V_C = 2\Delta V_C$, amounts to 2020 kg plutonium of the initial composition and 8460 kg uranium.

Figure 4 shows the time behaviour of the relative plutonium composition of the fuel elements in the core. As a consequence of the group structure of the fuel elements in the core with $n = 3$, there are three lines for each plutonium isotope. Each of these refers to those fuel elements which have the same irradiation time and thus are loaded and unloaded jointly. The diagram shows the continuous behaviour of the plutonium mixture in the fuel during neutron irradiation (idealized as linear to simplify plotting) and the discontinuous behaviour at the time t_s caused by exchanging the fuel elements. The initial composition of the plutonium is plotted as Pu^{∞}.

Table III shows the most important quantities of the reactor Na1 which are changed by the time variations of the plutonium composition in the fuel mixture.

The numerical results reveal the dependence of the time behaviour of the plutonium composition in the fuel elements on the fuel burn-up and the internal and external fuel management. In particular, there is strong coupling between the radial blanket operation and the closed fuel

TABLE III. THE MOST IMPORTANT QUANTITIES OF THE REACTOR SYSTEM WHICH ARE CHANGED BY PLUTONIUM RECYCLING AS FUNCTIONS OF THE TIME PARAMETER s

Plutonium loaded into the core at time t_s : $\Delta M_{Pu}(s)$
Plutonium unloaded from the core at time t_s : $\Delta M^{*}_{Pu}(s)$
Uranium loaded into the core at time t_s : $\Delta M_U(s)$
Net uranium introduced into the system from the outside: $M_U(s)$
Breeding gain of the $(s-s_0+1)^{th}$ fuel cycle: $\Delta M_{BG}(s-s_0+1)$, $s_0 = 3$

s	$\Delta M_{Pu}(s)$ (kg)	$\Delta M^{*}_{Pu}(s)$ (kg)	$\Delta M_U(s)$ (kg)	$M_U(s)$ (kg)	$\Delta M_{BG}(s-s_0+1)$ (kg)	Relative Pu composition of $\Delta M_{BG}(s-s_0+1)$ and $\Delta M_{Pu}(s)$			
						^{239}Pu	^{240}Pu	^{241}Pu	^{242}Pu
1	1010	954	4228	456	0	-	-	-	-
2	1010	954	4228	456	0	-	-	-	-
3	1016	954	4222	747	33	0.730	0.229	0.034	0.007
4	1016	954	4222	451	33	0.730	0.229	0.034	0.007
5	971	954	4267	495	333	0.779	0.188	0.027	0.006
6	1016	959	4222	752	33	0.730	0.229	0.034	0.007
7	1016	959	4222	456	33	0.730	0.229	0.034	0.007
8	975	921	4262	455	332	0.770	0.192	0.030	0.008
9	1022	959	4216	746	31	0.718	0.234	0.037	0.010
10	990	959	4248	482	26	0.755	0.205	0.031	0.008
11	975	925	4262	459	332	0.770	0.192	0.030	0.008
12	1022	964	4216	1336	31	0.718	0.234	0.037	0.010
13	994	937	4244	454	26	0.749	0.208	0.033	0.010
14	935	925	4302	444	878	0.817	0.152	0.023	0.007
15	1004	964	4234	769	27	0.738	0.217	0.034	0.010
16	994	940	4244	457	26	0.749	0.208	0.033	0.010
17	979	892	4258	418	333	0.763	0.145	0.032	0.010
18	1007	949	4231	749	27	0.734	0.219	0.035	0.012
19	965	940	4273	486	22	0.784	0.180	0.027	0.009
20	970	928	4268	468	328	0.776	0.185	0.030	0.010
21	1007	951	4231	753	27	0.734	0.219	0.035	0.012
22	997	916	4240	428	25	0.745	0.210	0.034	0.012
23	972	920	4266	457	329	0.773	0.186	0.030	0.011
24	986	951	4252	1358	25	0.760	0.200	0.031	0.010
25	990	943	4248	464	25	0.754	0.203	0.032	0.011
26	930	922	4307	501	871	0.825	0.145	0.022	0.008
27	1010	934	4228	730	27	0.731	0.220	0.036	0.013
28	992	937	4246	456	25	0.752	0.204	0.032	0.012
29	959	887	4278	433	324	0.789	0.175	0.027	0.009
30	1005	954	4233	758	27	0.737	0.215	0.035	0.013
31	961	939	4276	488	21	0.790	0.176	0.026	0.009
32	973	912	4264	446	329	0.771	0.187	0.030	0.011
33	1006	949	4232	751	27	0.736	0.216	0.035	0.014
34	983	913	4255	439	24	0.763	0.196	0.030	0.011
35	970	923	4267	462	328	0.775	0.184	0.030	0.012

cycle in the case of joint reprocessing of the core and blanket elements, which increases the variations of the plutonium composition by exchanging the fuel elements as well as during burn-up (Fig. 4). Furthermore, it follows from the numerical results that the fuel cycle economy of the reactor system depends on the time variations of the plutonium composition in the fuel (Table III).

Finally, the results of this paper show what importance must be attached to the long-time behaviour of the plutonium composition in fast power reactors with plutonium recycling. Further investigation of these problems should determine conditions of the internal and external fuel management for which the variations of the plutonium composition are caused essentially only by the fuel burn-up in the reactor. Thus, the time variations of the plutonium composition may be constant during the long-time operation of the reactor as far as possible, i.e. a so-called quasi-stationary behaviour of the plutonium composition. Finding out such conditions would require additional numerical investigations carried out by the method given in this paper, varying the parameters of the problem. In addition, the method may be extended to cases of partial plutonium recycling where plutonium is fed into the system from the outside in a given composition.

REFERENCES

[1] OTT, K., JANSEN, A., Long-time behaviour of fast breeders, Physics of Fast and Intermediate Reactors (Proc. Seminar Vienna, 1961) 2, IAEA, Vienna (1962) 213-228.

[2] SMIDT, D., MÜLLER, A. et al., Referenzstudie für den Na-gekühlten schnellen Brutreaktor (Na1), Karlsruhe Rep. KFK-299 (1964).

[3] JANSEN, A., OTT, K., SCHROETER, K.E., Zum Abbrandverhalten schneller Reaktoren, PSB Rep. 121/64.

[4] Karlsruhe Rep. KFK 26-10 (1965): for preliminary information: KÜSTERS, K., METZENROTH, M., The influence of some important group constants on integral fast reactor quantities, ANL-7120 (1965) 423-433.

[5] SCHROETER, K. E., Zweidimensionale 26-Gruppen-Diffusions-Rechnungen für den natriumgekühlten 1000 MW(e)-Reaktor Na1 (to be published).

DISCUSSION

K.H. JOEST: Why does the ^{242}Pu concentration in Fig. 4 diverge from the stationary $^{242}Pu^{\infty}$ value instead of oscillating about it?

A. JANSEN: The Pu^{∞} values are steady-state concentrations calculated with an idealized reactor model in which the finite lifetimes of the fuel elements are not taken into consideration. With the realistic model, the fuel elements are exchanged discontinuously, i.e. the lifetimes of the fuel elements are taken into account as burn-up parameters. The proportions of the higher plutonium isotopes therefore increase relative to the given Pu^{∞} value as a result of repeated fuel burn-up.

K.M. JIRLOW: Could you comment on the spatial distribution of plutonium in the blanket under equilibrium conditions?

A. JANSEN: Equilibrium is not established in the radial blanket during reactor operation. The spatial distribution of the plutonium in the blanket corresponds essentially to the space dependence of the neutron

flux. For the given irradiation times, the averaged plutonium composition after discharging is 97% ^{239}Pu and 3% ^{240}Pu.

In the case of the axial blanket, we do achieve equilibrium conditions by cyclic core management. During reactor operation the axial blanket contains 98-99% ^{239}Pu.

ИССЛЕДОВАНИЕ ПОЛЕЙ ТЕПЛОВЫДЕЛЕНИЯ В БЫСТРЫХ РЕАКТОРАХ С ПОГЛОЩАЮЩИМИ СТЕРЖНЯМИ

В.В.БОНДАРЕНКО, А.И.ВОРОПАЕВ,
В.П.ЗИНОВЬЕВ, Б.В.КОЛОСКОВ,
В.П.ПОЛИВАНСКИЙ, М.Ф.ТРОЯНОВ,
Е.М.ХАЛОВ, Н.М.ШАГАЛИН
ФИЗИКО-ЭНЕРГЕТИЧЕСКИЙ ИНСТИТУТ, ОБНИНСК,
СССР

Abstract — Аннотация

A STUDY OF THE HEAT-RELEASE DISTRIBUTION IN FAST REACTORS WITH ABSORBER RODS. Using absorber materials in the burn-up compensation elements of fast power reactors makes it possible to achieve a considerable increase in the period for which the reactor can be operated without interruption, as compared with the case of burn-up compensation by fuel material. However, the use of absorber rods, especially of boron, may cause strong fluctuations in heat release when the rod position is changed during reactor operation, giving rise to undesirable shifts in the heat release and overheating of the fuel elements.

It is a complicated and cumbersome operation to work out the heat-release distribution in a large multi-zone fast reactor with a system of absorber rods in the core. With a view to studying such reactors, experiments and theoretical studies were carried out in the Physics and Energetics Institute to check and confirm the relatively simple methods adopted for calculating the heat-release distributions in a reactor with rods.

The paper gives the results of experimental and theoretical studies of the heat-release distributions of various BFS critical assemblies simulating the BN-350-type reactor.

The case of centrally arranged single absorber rods containing different amounts of boron was considered and the corresponding calculations made.

The calculational design of a reactor with eccentrically arranged single rods or with a group of distributed rods necessitates the use of two-dimensional methods. The paper explains the method of few-group calculations for a reactor with cylindrical geometry using the diffusion approximation.

Experiments are described on the distribution of the heat-release field in a critical assembly with a single eccentric boron rod.

For analysing the effect of inserting a system of shim rods a special critical assembly was selected with six boron compensators. The heat-release distribution was measured on this assembly in different directions with the rod system inserted and extracted. A short description of this assembly is given together with the design model used.

The theoretical and experimental results are compared and it is found that the method used can be adopted for optimizing the arrangement of the absorber rods for burn-up compensation in fast power reactors.

ИССЛЕДОВАНИЕ ПОЛЕЙ ТЕПЛОВЫДЕЛЕНИЯ В БЫСТРЫХ РЕАКТОРАХ С ПОГЛОЩАЮЩИМИ СТЕРЖНЯМИ. Применение поглощающих материалов в органах компенсации выгорания для быстрых энергетических реакторов позволяет значительно увеличить длительность непрерывной работы реактора по сравнению со случаем компенсации выгорания топливным материалом. Однако, использование поглощающих, в частности борных, стержней может приводить к значительным колебаниям тепловыделения при изменении положения стержней во время работы и создавать нежелательные перекосы тепловыделения, приводящие к перегреву топливных элементов.

Расчет поля тепловыделения в большом многозонном быстром реакторе с системой поглощающих стержней в активной зоне является сложной и громоздкой задачей. Для изучения таких реакторов в Физико-энергетическом институте были проведены экспериментальные и расчетные исследования, позволившие проверить и обосновать принятые, сравнительно простые, методы расчетов полей тепловыделения в реакторе со стержнями.

В докладе приводятся результаты экспериментального и расчетного исследования полей тепловыделения нескольких сборок БФС, имитирующих реактор типа БН-350.

Рассмотрен случай центрального расположения одиночных поглощающих стержней с разным количеством бора и проведены соответствующие расчеты.

Расчет реактора с эксцентрично расположенным одиночным стержнем или с группой распределенных стержней требует использования двумерных методов. В докладе излагается методика малогруппового расчета реактора в r_φ-геометрии в диффузионном приближении. Приводится описание экспериментов по распределению поля тепловыделения в критической сборке с одиночным эксцентричным борным стержнем.

Для анализа эффекта введения системы компенсирующих стержней была собрана специальная критическая сборка с шестью борными компенсаторами. На этой сборке были проведены измерения распределений тепловыделения по различным направлениям при введенной и выведенной системе стержней. В докладе дается краткое описание этой сборки и ее расчетная модель.

Приведенные сравнения расчетных и экспериментальных результатов показывают, что использованная методика может применяться для оптимизации распределения поглощающих стержней компенсации выгорания в энергетических быстрых реакторах.

1. ВВЕДЕНИЕ

Одним из требований, предъявляемых к энергетическим быстрым реакторам, является обеспечение достаточно продолжительной непрерывной работы без перегрузки топлива. Выполнение этой задачи возможно при использовании эффективной системы компенсации потери реактивности при выгорании топлива. Для первого советского быстрого энергетического реактора БН-350 это требование в полной мере не ставилось, и система компенсации выгорания в БН-350 сделана из расчета непрерывной работы в течение двух месяцев. Необходимый запас реактивности на этот срок работы обеспечивается шестью топливными компенсаторами, вводимыми в активную зону по мере выгорания топлива [1]. Система топливных компенсаторов БН-350 вносит незначительные искажения в распределение поля тепловыделения. Для увеличения длительности работы, например, до полугода, потребовалось бы значительно увеличить количество топливных компенсаторов, что не представляется рациональным. Более эффективным решением вопроса является использование для компенсации выгорания поглощающих материалов, в первую очередь – карбида бора.

Применение поглощающих материалов в органах компенсации выгорания позволяет значительно увеличить длительность непрерывной работы с помощью сравнительно небольшого числа подвижных органов. Однако, при изменении положения поглощающих стержней в активной зоне могут возникать значительные колебания тепловыделения, приводящие к перегреву топливных элементов. Поэтому расположение и число поглощающих органов компенсации должны выбираться так, чтобы обеспечить надежную работу топливных элементов на всех этапах работы реактора.

Расчет реактора с системой поглощающих стержней – достаточно сложная задача, требующая экспериментальной проверки. С этой целью на стенде БФС были проведены эксперименты по изучению распределений тепловыделения в сборках с различными поглощающими стержнями, а также проведен расчетный анализ тех же распределений.

Эксперименты выполнялись на трех сборках – различных модификациях модели БН-350 – БФС-15, БФС-16 и БФС-17. В каждой сборке активная зона содержала две области с разной концентрацией урана-235 в топливных стержнях – зону меньшего обогащения и зону большего обогащения. Сборки БФС-15 и БФС-16 были описаны ранее [2], там же

приведены их геометрические характеристики и композиция всех зон и имитаторов органов управления. На каждой из этих сборок исследовалось много различных вариантов. Для целей настоящей работы были использованы следующие варианты:

БФС-16-10, БФС-16-12 и БФС-16-13 – сборки с однородными зонами и центрально расположенными борными стержнями;

БФС-15-3 – сборка-модель реактора БН-350 с имитаторами органов управления в положении "выведены" и одним введенным борным стержнем-имитатором регулятора;

БФС-15-4 – та же сборка с дополнительно введенным более мощным борным стержнем-имитатором температурного компенсатора.

Схема сборки БФС-15 показана на рис.1. В сборке БФС-17 в активную зону было введено большое число поглощающих стержней-имитаторов борных компенсаторов. Для уменьшения критразмера граница зоны малого обогащения была сдвинута ближе к центру. Однако состав тепловых стержней был оставлен тем же, что и в предыдущих сборках. Состав стержней с естественным карбидом бора совпадает с составом одиночных борных стержней сборок БФС-16 ($\rho_B = 5{,}81 \cdot 10^{22}$ 1/см^3, $\rho_c = 1{,}317 \cdot 10^{22}$ 1/см^3, $\rho_{ст} = 0{,}581 \cdot 10^{22}$ 1/см^3). Схема этой сборки с введенными борными стержнями приведена на рис.2.

2. ЦЕНТРАЛЬНОЕ РАСПОЛОЖЕНИЕ ПОГЛОЩАЮЩИХ СТЕРЖНЕЙ

Случай центрального расположения поглощающего стержня является наиболее простым для сравнения расчета с экспериментом и позволяет получить сведения о точности избранной расчетной методики. Наиболее простым расчетным приемом является представление стержня в виде отдельной зоны и последующее решение уравнений диффузии во всех зонах реактора, в том числе вблизи стержней и даже внутри них. Основанием для такого подхода может служить значительная "прозрачность" борных стержней в спектре быстрого реактора и отсутствие очень резких градиентов нейтронного потока вблизи стержней. Для проверки справедливости такого подхода на стенде БФС были предприняты эксперименты по изучению распределений делений урана-235 по радиусу сборки при различном количестве бора в центральной области сборки БФС-16. В центр сборки устанавливались один, четыре или семь стержней с естественным карбидом бора. Четыре стержня по площади примерно эквивалентны пакету реактора БН-350. Высота борных стержней равна высоте активной зоны. Эффективные диаметры областей, занятых бором, составляли соответственно 5,4; 10,7 и 14,16 см. Расчет распределений делений урана-235 проводился в 18-групповом диффузионном и P_3-приближениях, причем центральная область, занятая бором, рассматривалась как отдельная зона. 18-групповая система констант описана в докладе [2]. Расчетные и экспериментальные данные приводятся на рис.3 – 5. Сравнение показывает, что P_3-приближение является совершенно достаточным для описания нейтронного поля не только вблизи стержней, но и непосредственно внутри области, занятой бором. Вне борных стержней диффузионное и P_3-приближение прекрасно согласуются друг с другом и с экспериментом. Некоторые расхождения, видные для случая с четырьмя стержнями (рис.4), объясняются только тем, что четверка стержней стоит не точно по оси сборки.

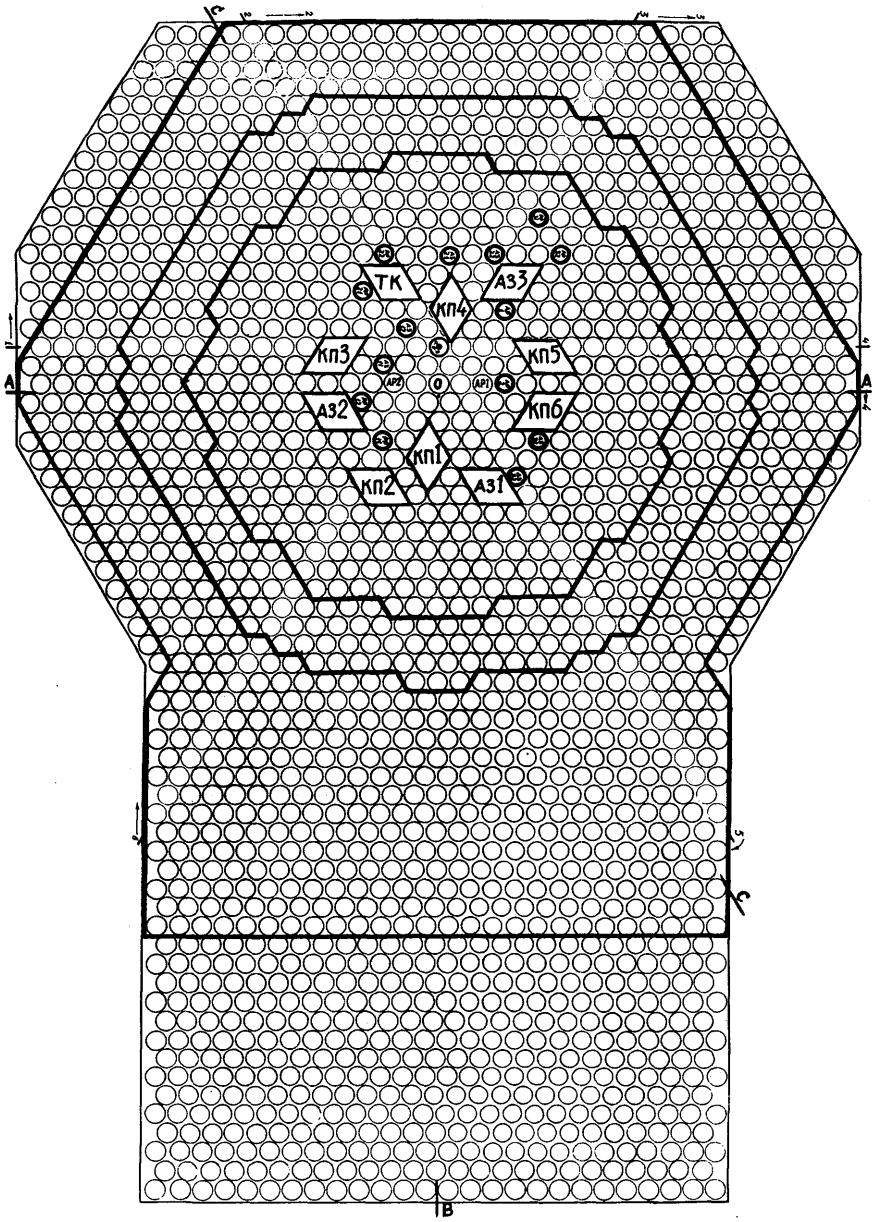

Рис.1. Схема сборки БФС-15-3.

Внутри области, занятой бором, расхождение диффузионного приближения с экспериментальными данными оказывается меньше 10% даже в случае семи стержней. В результате можно сделать вывод, что для анализа искажений полей тепловыделения борными стержнями можно

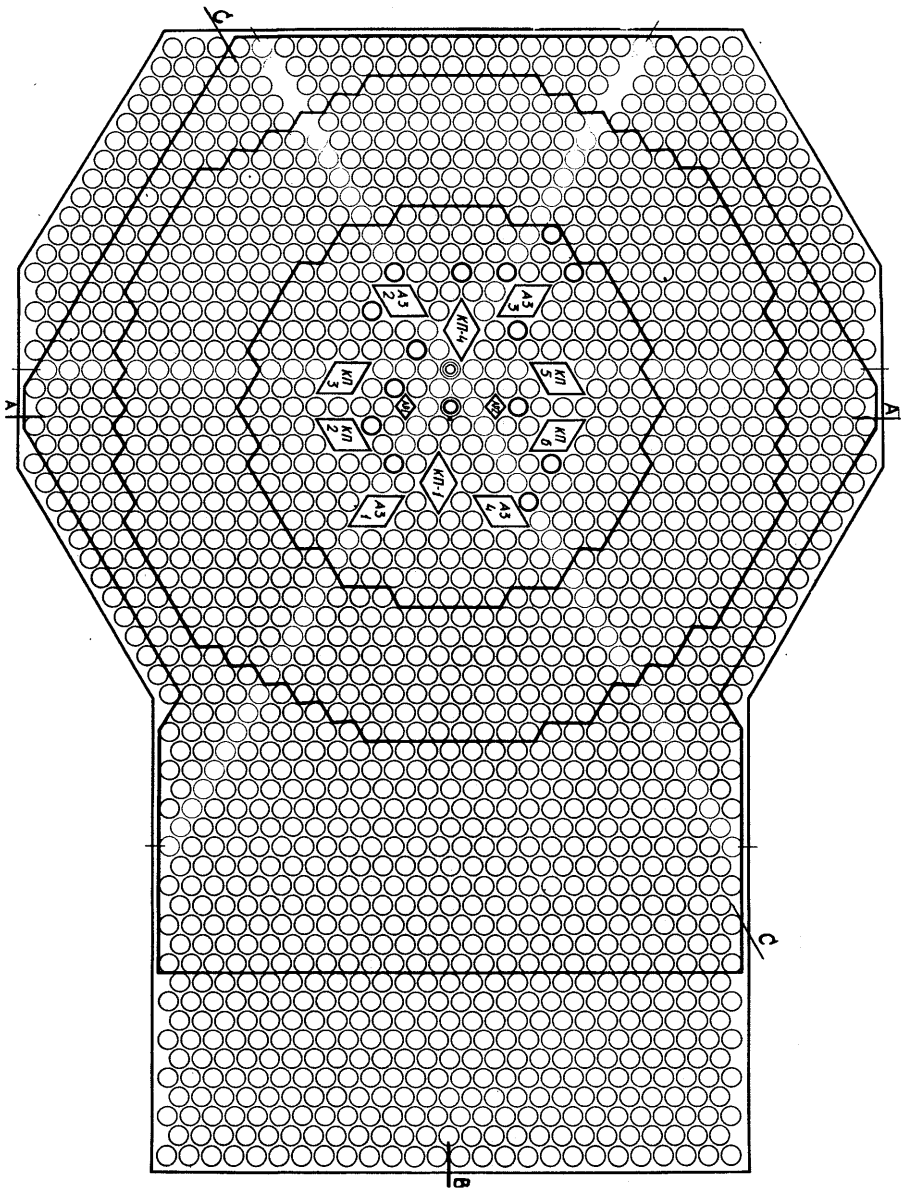

Рис.2. Схема сборки БФС-17-10.

воспользоваться диффузионным приближением и рассматривать каждый стержень как самостоятельную зону реактора. На поверхности такой зоны можно задать граничные условия диффузионного приближения.

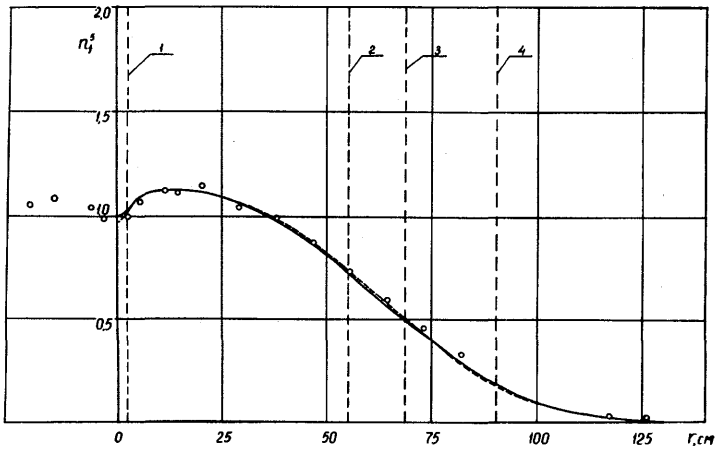

Рис.3. Распределение делений ^{235}U по радиусу сборки БФС-16-10.
——— диффузионное приближение;
- - - P_3 – приближение;
O – эксперимент.
1 – расчетная граница зоны, занятой стержнем;
2 – граница зоны малого обогащения;
3 – граница зоны большого обогащения;
4 – граница тонкого экрана.

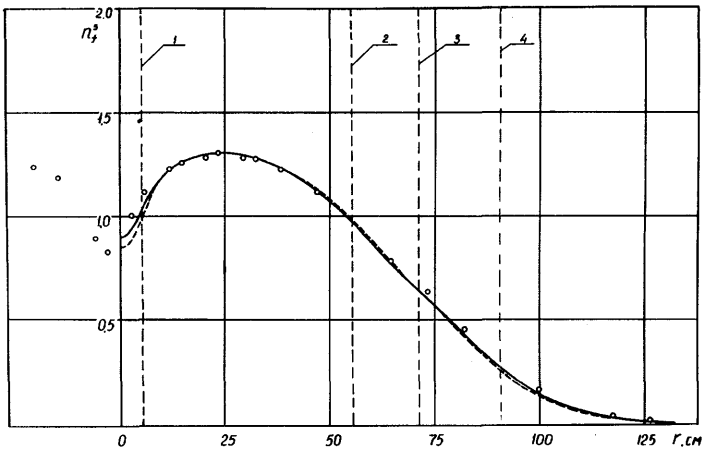

Рис.4. Распределение делений ^{235}U по радиусу сборки БФС-16-12.
——— диффузионное приближение;
- - - P_3 – приближение;
O – эксперимент.
1 – расчетная граница зоны, занятой стержнем;
2 – граница зоны малого обогащения;
3 – граница зоны большого обогащения;
4 – граница тонкого экрана.

3. РАСЧЕТ ПОЛЕЙ ТЕПЛОВЫДЕЛЕНИЯ В (r, φ)-ГЕОМЕТРИИ

Проектирование энергетического быстрого реактора выдвигает задачу расчета полей тепловыделения в активной зоне с азимутальными неоднородностями, вызываемыми, в частности, поглощающими стержнями.

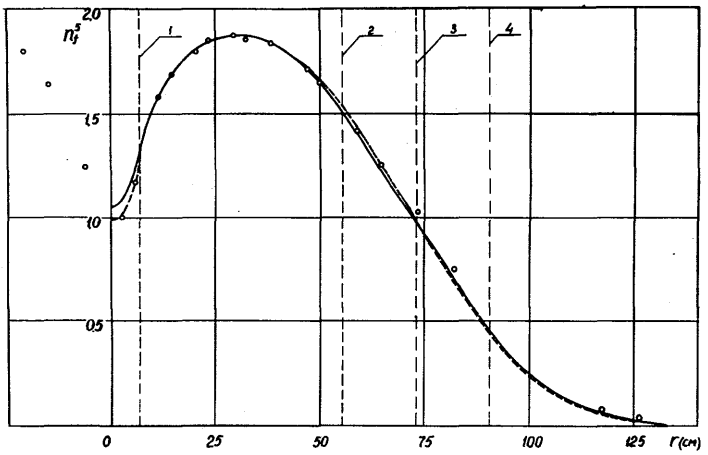

Рис.5. Распределение делений ^{235}U по радиусу сборки БФС-16-13.

——— диффузионное приближение;
- - - P_3 – приближение;
О – эксперимент.

1 – расчетная граница зоны, занятой стержнем;
2 – граница зоны малого обогащения;
3 – граница зоны большого обогащения;
4 – граница тонкого экрана.

Такая задача может быть решена численным интегрированием уравнений диффузии в (r, φ)-геометрии с рассмотрением каждого стержня как самостоятельной зоны реактора. Очевидно, что (r, φ)-геометрии поглощающие стержни будут иметь в сечении форму криволинейных трапеций. В таком представлении для каждого стержня сохраняется координата центра тяжести и площадь сечения. Преимуществом расчета в (r, φ)-геометрии по сравнению с расчетами в координатах (x, y) является более удобное описание границ, более точное соблюдение конфигурации реактора, обычно мало отличающейся от круговой. Недостатком расчета в (r, φ)-геометрии является более медленная сходимость метода и меньшая устойчивость счета, связанная с большой разницей расчетных шагов по радиусу и по углу. Медленная сходимость итерационного процесса приводит к необходимости использования малогрупповых методов.

Решение уравнения диффузии в полярных координатах реализовано в вычислительной программе со следующими основными данными:

количество энергетических групп до 3;
число зон по радиусу до 16;
число угловых диапазонов до 16;
общее количество расчетных узлов до 900.

Решение конечно-разносных уравнений диффузии в каждом цикле итераций источников выполняется по схеме Янга [3]. Утечка в торцы учитывается, как обычно, поправкой к сечениям поглощения. Использование указанной программы требует предварительной подготовки малогрупповых констант. Эта процедура может быть выполнена с помощью специальной программы свертки многогрупповой системы констант к малогрупповой [2, 4] с учетом спектра нейтронов в каждой области реактора. В целях максимальной экономии машинного времени, а также для наибольшей простоты, в расчетах по критсборкам с азимуталь-

ными неоднородностями было использовано одногрупповое представление. Однако, одногрупповые сечения были усреднены по 18-групповым спектрам, полученным из расчетов различных одномерных моделей реактора с детальной разбивкой на большое число зон. В результате методика использует комбинацию одномерных многогрупповых и двумерных одногрупповых расчетов.

Использование такой сравнительно простой методики позволит значительно облегчить расчет полей тепловыделения в реакторах со сложной системой компенсирующих стержней, если только точность метода окажется приемлемой. Критерием точности может быть согласие с экспериментальными данными.

4. ВОЗДЕЙСТВИЕ ОДИНОЧНЫХ ЭКСЦЕНТРИЧНЫХ ПОГЛОЩАЮЩИХ СТЕРЖНЕЙ НА ПОЛЕ ТЕПЛОВЫДЕЛЕНИЯ

Для проверки методики расчета полей тепловыделения в (r, φ)-геометрии были использованы проводившиеся ранее эксперименты на сборках БФС-15-3 и БФС-15-4 [2]. В сборке БФС-15-3 (рис.1) в области введенного борного стержня АР-2, расположенного эксцентрично, создавалась некоторая депрессия поля тепловыделения. Эта сборка была рассчитана в (r, φ)-геометрии, и сравнение расчетных и экспериментальных распределений делений урана-235 показаны на рис.6 для направления А-А, проходящего через стержень АР-2. Расчет хорошо согласуется с экспериментом. В этой же сборке в направлении 0-В были измерены распределения делений плутония-239 и урана-238 (рис.7). Для плутония, как и для урана-235, получено хорошее согласие с экспериментом. При сравнении расчетных и экспериментальных распределений делений урана-238 видно расхождение до ~10%, связанное с неточностью одногрупповых сечений деления урана-238. Эти одногрупповые сечения получены из одномерных расчетов, в которых приводится гомогенизация зон. Опыт расчетов показывает, что способ гомогенизации сказывается на величине средних сечений пороговых реакций. В то же время получить более точные локальные значения одногрупповых сечений деления урана-238 в рамках одномерных моделей не удается.

В сборке БФС-15-4 был создан сильный перекос нейтронного поля за счет введения имитатора температурного борного компенсатора ТК. Расчет этого случая в (r, φ)-геометрии показал также хорошие возможности использованного метода. Экспериментальное и расчетное распределения делений урана-235 по направлению С-С, проходящему через стержень, согласуются с большой точностью во всем диапазоне сравнения (рис.8).

5. СИСТЕМА ПОГЛОЩАЮЩИХ СТЕРЖНЕЙ

Эксперименты по изучению полей тепловыделения в реакторе с системой борных стержней проводились на сборках БФС-17. Из-за недостаточного размера бака, в котором собираются критсборки, в сборке БФС-17 не удалось сделать достаточно толстый боковой экран по всему периметру. С одной стороны экран был тонким и на распределениях делений урана-235 сказывалось влияние графитовой тепловой ко-

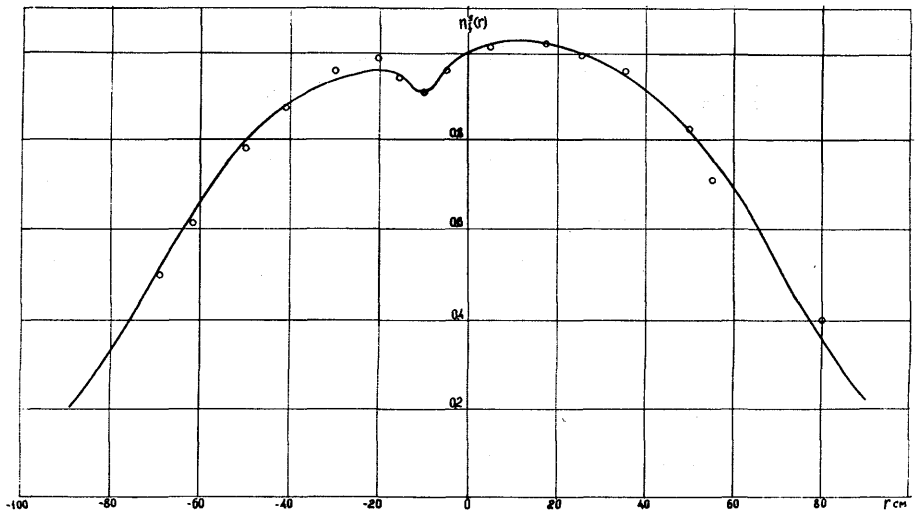

Рис.6. Распределение делений ^{235}U по радиусу сборки БФС-15-3 в направлении А-А, проходящем через регулятор.
О – эксперимент; —— – расчет.

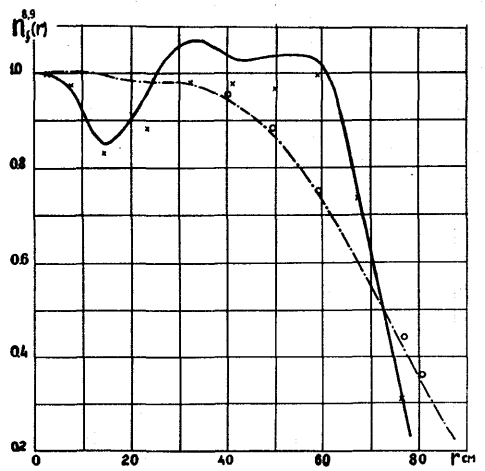

Рис.7. Распределение делений ^{238}U и ^{239}Pu по радиусу сборки БФС-15-3 в направлении 0-В.
$\left.\begin{matrix} x - n_f^8 \\ O - n_f^9 \end{matrix}\right\}$ эксперимент; $\left.\begin{matrix} \text{———}\ n_f^8 \\ - - -\ n_f^9 \end{matrix}\right\}$ расчет.

лонны, расположенной за тонким экраном. Для того, чтобы не принимать во внимание эти эффекты, для сравнений расчетных и экспериментальных данных использовались направления 0-С и 0-В, в которых экран был достаточно толстым.

В сборке БФС-17-2 все стержни находились в положении "выведен" и расположения делений урана-235 в направлениях 0-С и 0-В совпадают

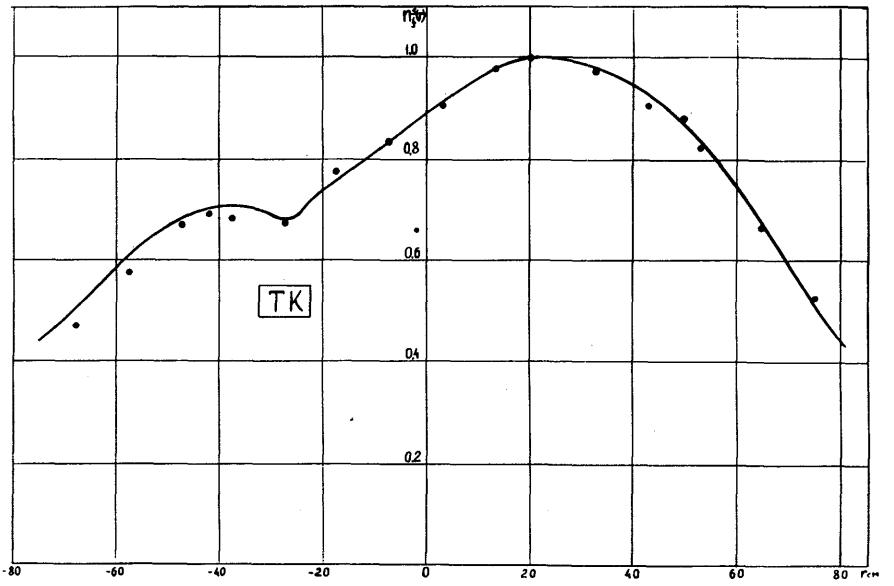

Рис.8. Распределение делений ^{235}U по радиусу сборки БФС-15-4 в направлении С-С, проходящем через борный компенсатор.
● – эксперимент; —— – расчет

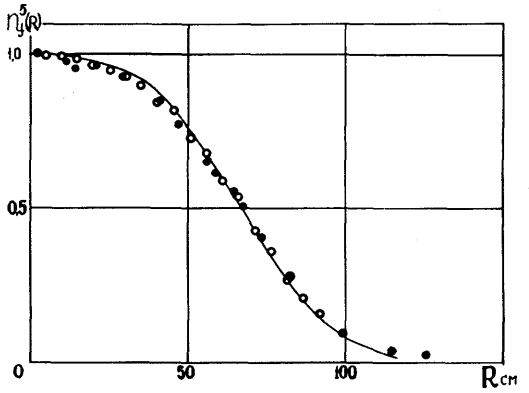

Рис.9. Распределение делений ^{235}U по радиусу сборки БФС-17-2.
● направление 0-В } эксперимент;
○ направление 0-С }
—— расчет

между собой и с расчетом в 18-групповом одномерном диффузионном приближении (рис.9).

В таком случае, когда в активной зоне нет неоднородностей, приводящих к искажениям нейтронного потока, одномерная модель является вполне удовлетворительной. Введение борных стержней приводит к существенной деформации нейтронного поля, различной в разных направлениях из-за неравномерного по углу расположения борных стержней.

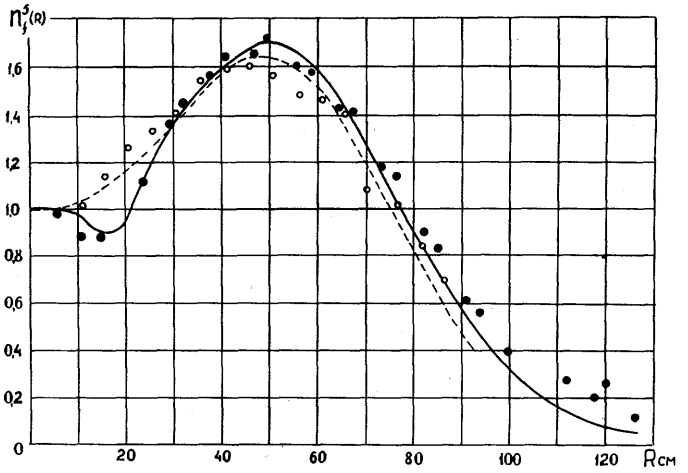

Рис.10. Распределение делений ^{235}U по радиусу сборки БФС-17-10.
Эксперимент { ○ – направление 0-С
● – направление 0-В
Расчет { - - - – направление 0-С
—— – направление 0-В

Гомогенизация такой области с введенными стержнями уже становится необоснованной, и одномерные расчеты использоваться не могут.

Однако расчет сборки БФС-17-10 с введенными стержнями в (r, φ)-геометрии по описанной выше методике показал, что и этот случай может быть рассчитан вполне хорошо. На рис.10 приведены экспериментальные и расчетные распределения делений урана-235 в направлениях 0-С и 0-В. Согласие этих результатов является еще одним подтверждением удовлетворительной точности методики одногруппового диффузионного расчета поля тепловыделения в двумерной (r, φ)-геометрии.

Таким образом, приведенные экспериментальные и расчетно-методические работы показали, что для анализа влияния поглощающих стержней компенсации выгорания на поле тепловыделения в быстром энергетическом реакторе могут быть эффективно использованы много- и малогрупповые методы, основанные на решении уравнения диффузии. Сравнения с экспериментами показали, что точность расчетных методов является вполне достаточной для анализа распределения полей тепловыделения даже в реакторах со сложной системой поглощающих стержней. В результате количество и расположение поглощающих стержней в активной зоне энергетического реактора могут быть оптимизированы достаточно простыми средствами так, чтобы в процессе эксплуатации реактора обеспечить необходимые условия для надежной и безопасной работы топливных элементов.

ЛИТЕРАТУРА

[1] ЛЕЙПУНСКИЙ, А.И. и др., Атомная станция БН-350. Supplement to ANS-100, Detroit, 1965.

[2] ЛЕЙПУНСКИЙ, А.И. и др., Экспериментальные и теоретические исследования по физике быстрых реакторов. Доклад № 4А/3 на Лондонской конференции по быстрым реакторам, 1966.

[3] ВАРГА, Р., Численные методы решения многомерных многогрупповых диффузионных уравнений. В сб. "Теория ядерных реакторов" под ред. Г.Биркхофа и Э.Вигнера. Госатомиздат, М., 1963.
[4] КУЗЬМИН, А.М., ХРОМОВ, В.В., Малогрупповой метод расчета многозонных реакторов. В сб. "Инженерно-физические вопросы ядерных реакторов" под ред. Л.Н.Юровой. Госатомиздат, М., 1966, стр.33.

DISCUSSION

H. SPENKE: In section 1 of the paper it is stated that you used dummy boron control rods. In what form was the boron?

M.F. TROYANOV: In the form of natural boron carbide, the ^{10}B content corresponding approximately to that in actual rods.

H. SPENKE: Did you consider other absorber materials – for example, tantalum – which might give better long-term behaviour than boron?

M.F. TROYANOV: These investigations did not relate to an actual project – we were simply interested in devising suitable experimental methods. Accordingly, the type of absorber was immaterial.

H.W. KÜSTERS: Have you performed any experiments or calculations for partially inserted boron rods?

M.F. TROYANOV: No, only for fully inserted or withdrawn rods. The mathematical analysis of experiments with partially inserted rods would be extremely difficult at present.

W.B. LOEWENSTEIN: You showed good agreement between theory and experiment with regard to reaction rates. Could you comment on the comparison between theory and experiment in relation to the reactivity worth of boron rods inserted into a critical assembly of the type described in your paper?

M.F. TROYANOV: We were interested mainly in the distribution of heat evolution. The k_{eff} values were derived from multigroup one-dimensional and two-dimensional (ρ, z) calculations. In the results of the few-group calculations, k_{eff} differed only slightly from unity. However, these values are unimportant from the point of view of the distribution of heat evolution.

ИССЛЕДОВАНИЕ ДОППЛЕР-ЭФФЕКТА НА УРАНЕ-238 В ЭКРАНЕ ИЗ ОКИСИ УРАНА РЕАКТОРА БР-I

Л.П.АБАГЯН, В.И.ГОЛУБЕВ, Н.Д.ГОЛЯЕВ,
А.В.ЗВОНАРЕВ, Ю.Ф.КОЛЕГАНОВ, М.Н.НИКОЛАЕВ,
М.Ю.ОРЛОВ
ФИЗИКО-ЭНЕРГЕТИЧЕСКИЙ ИНСТИТУТ,
ОБНИНСК,
СССР

(Доклад представил Н.В.Краснояров)

Abstract — Аннотация

INVESTIGATION OF THE DOPPLER EFFECT IN URANIUM-238 IN THE OXIDE BLANKET OF THE BR-1 REACTOR. Studies have been carried out on the Doppler increase in capture rate in thin samples of uranium-238 irradiated in a large block of depleted UO_2 at room temperature. The core of the BR-1 reactor was used as neutron source. The neutron spectrum at the point where the Doppler effect measurements were carried out was close to the asymptotic spectrum of the medium being studied. Measurements taken on this spectrum in the energy range below 10 keV using a set of resonance detectors showed satisfactory agreement with calculated data obtained from the system of constants evolved by V. V. Bondarenko, M. N. Nikolaev, L. P. Abagyan and N. O. Bazazyants. The reaction rate in a heated sample was measured in relation to that in a cold sample irradiated at the same position in the reactor. Gamma rays of energy 74 keV accompanied by beta decay of ^{239}U were recorded. Measurements were carried out in the temperature range 300-2000°K. The effect of the sample dimensions on the measurement results was established, as also was the effect of surrounding the sample by a layer of scattering material (heater material, container material, etc.). The accuracy of the results obtained was 5-6%.

It is shown that in the temperature range studied, the temperature dependence of the proportional increase in the ^{238}U (n,γ) reaction rate in a small heated sample can be written in the form:

$$\frac{\Delta A}{A}(T_2) = b(\sqrt{T_g} - \sqrt{T_x})$$

where T_x = 300°K and b = 0.0132 ± 0.0004 $(°K)^{-\frac{1}{2}}$. The experimental value for the Doppler increase in the ^{238}U (n,γ) reaction rate in a small sample at T_g = 800°K agrees well with the calculated results. The error in calculating the Doppler effect due to the inadequate knowledge of the neutron spectrum was not much greater than the error in the experimental data.

ИССЛЕДОВАНИЕ ДОППЛЕР-ЭФФЕКТА НА УРАНЕ-238 В ЭКРАНЕ ИЗ ОКИСИ УРАНА РЕАКТОРА БР-I. Проведены исследования допплеровского приращения скорости захватов в тонких образцах урана-238, облучаемых в большом блоке двуокиси обедненного урана, находящемся при комнатной температуре. Источником нейтронов служила активная зона реактора БР-I. Спектр нейтронов в том месте, где производились измерения Допплер-эффекта, был близок к асимптотическому спектру изучаемой среды. Результаты измерения этого спектра в области энергий ниже 10 кэв с помощью набора резонансных индикаторов оказались в удовлетворительном согласии с данными расчетов по системе констант, составленной Бондаренко, Николаевым, Абагян и Базазянц. Скорость реакции в нагретом образце измерялась по отношению к скорости реакции в холодном образце, полученном в том же положении в реакторе. Зарегистрировались γ-лучи с энергией 74 кэв, сопровождающие β-распад ^{239}U. Измерения проведены в диапазоне температур 300°K + 2000°K. Оценено влияние на результаты измерений размеров образца и окружения его слоем рассеивающего вещества (материал нагревателя, контейнера и т.п.). Точность полученных результатов 5 + 6%.

Показано, что в исследованном диапазоне температур температурная зависимость относительного приращения скорости реакции ^{238}U (n, γ) в малом нагретом образце может быть представлена в виде:

$$\frac{\Delta A(T_2)}{A} = в(\sqrt{T_г} - \sqrt{T_х})$$

при $T_х = 300°K$ и $в = 0{,}0132 \pm 0{,}0004$ $(°K)^{-1/2}$. Экспериментальная величина допплеровского приращения скорости реакции ^{238}U(n, γ) в малом образце при $T_г = 800°K$ хорошо согласуется с результатом расчета. Погрешность расчета Допплер-эффекта, связанная с неточным знанием спектра нейтронов, оказалась лишь ненамного больше погрешностей экспериментальных данных.

1. ВВЕДЕНИЕ

Определяющий вклад в допплеровский температурный коэффициент реактивности больших разбавленных энергетических реакторов на быстрых нейтронах дает допплеровское уширение резонансов поглощения урана-238. Интересно поэтому оценить точность описания Допплер-эффекта на уране-238 с помощью использующихся в настоящее время систем констант. Такая оценка и являлась основной задачей настоящей работы. С этой целью были выполнены точные измерения температурных приращений эффективного резонансного интеграла поглощения точного образца из окиси урана-238, помещенного в большой блок двуокиси обедненного урана, находящийся при комнатной температуре. Сравнение результатов этих измерений с расчетными данными позволяет судить о точности принятых при расчете констант. Выбор двуокиси обедненного урана в качестве среды, формирующей нейтронный спектр был сделан исходя, в основном, из двух соображений. Во-первых, доля нейтронов, ответственных за Допплер-эффект на уране-238 (т.е. лежащих в интервале 0,2 – 10 кэв) для нейтронных спектров, устанавливающихся в большом блоке двуокиси урана, достаточно велика, что значительно облегчает выполнение измерений (по сравнению с измерением Допплер-эффекта на спектре активной зоны большого реактора, например). Во-вторых, изучение точности описания распространения нейтронов в двуокиси урана, в большой концентрации присутствующей не только в экране, но и в активной зоне больших энергетических реакторов представляло интерес.

Эксперименты проводились в окисном экране быстрого реактора БР-I [1], активная зона которого служила в данном случае просто источником нейтронов. Измерения чисел захватов в исследуемых образцах производились с помощью активационной методики.

2. СХЕМА ЭКСПЕРИМЕНТА

Размеры и геометрия реакторов БР-I с экраном из двуокиси урана изображены на рис. 1. Экран был собран из цилиндрических блочков двуокиси обедненного урана диаметром 47 мм в алюминиевой очехловке толщиной 0,3 мм, установленных в плотную гексагональную решетку. Высота экрана составляла 700 мм. Состав материала экрана приводится в табл. 1.

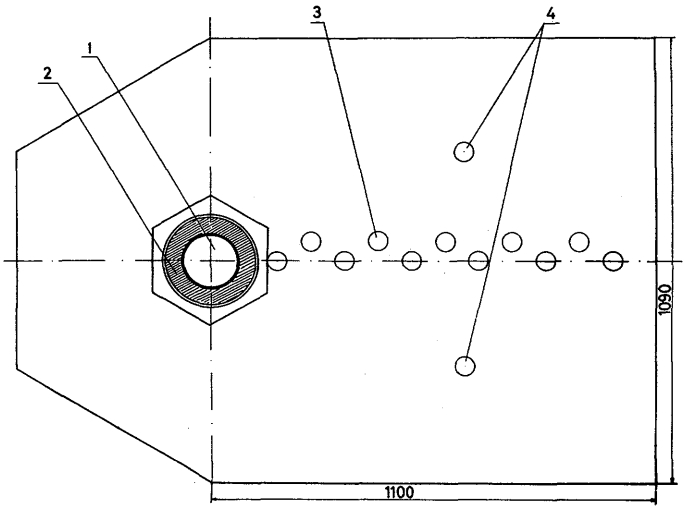

Рис.1. Реактор БР-1 с экраном из окиси урана;
1. Активная зона;
2. Органы регулирования;
3. Экспериментальные каналы;
4. Каналы для измерения Допплер-эффекта.

ТАБЛИЦА 1. СОСТАВ МАТЕРИАЛА ОКИСНОГО ЭКРАНА РЕАКТОРА БР-I

Элемент	Среднее число ядер в $см^3 \times 10^{24}$
Уран	0,0158
Кислород	0,0329
Алюминий	0,00215

Экспериментальные каналы, расположенные вдоль оси симметрии системы, использовались для измерения распределений скоростей различных реакций. Для измерения Допплер-эффекта использовались две полости, симметрично расположенные относительно продольной оси симметрии экрана и отстоящие от центра активной зоны на 68 см. Полости имели шестигранную форму, размером "под ключ" и высотой – по 120 мм. Разность нейтронных потоков в этих полостях, измерявшихся с помощью камеры деления со слоем плутония-239, составляла 0,4%. Выбранная методика обработки данных позволяла практически полностью устранить влияние этой разности на результаты измерений.

3. ИЗМЕРЕНИЕ ДОППЛЕР-ЭФФЕКТА

Измерения допплеровского приращения скорости захватов в уране-238 производились с помощью двух одинаковых малых образцов из окиси

обедненного урана, одновременно облучаемых в описанных выше симметрично расположенных полостях экрана реактора. Облучение проводили в специальных контейнерах-нагревателях. Один из образцов во время облучения разогревался до нужной температуры. Из облученных образцов в специальные чашечки отвешивалось по две одинаковые навески. Окись урана в чашечках уплотнялась до стандартного объема, после чего с помощью однокристального гамма-спектрометра с кристаллом NaI(Tℓ) размером 30 × 20 мм измерялась ее активность. Ширина канала анализатора выбиралась таким образом, чтобы свести к минимуму ошибку в измеренной активности гамма-линии нептуния-239 с энергией 74 кэв, обусловленную статистикой отсчетов, фоном от осколков деления и продуктов естественного распада урана (вклад последних подавлялся путем предварительной химической очистки облучаемых образцов). Поскольку фон был невелик (он составлял около 5% начальной активности), в пределах окна анализатора лежало более 80% площади гамма-пика. При каждой температуре производилась серия измерений из тридцати-сорока облучений. При этом места облучения горячего и холодного образцов поочередно менялись, что позволяло исключить влияние возможного небольшого различия в потоках нейтронов внутри полостей: результат получался как среднее геометрическое из полученных в двух измерениях отношений активностей горячего и холодного образцов. При измерениях до 1200°К нагрев образцов производился в открытых тонкостенных контейнерах из нержавеющей стали с помощью намотанной на эти контейнеры нихромовой спирали. (Электрическая изоляция между спиралью и контейнером осуществлялась с помощью листа слюды). Диаметр контейнера составлял 8 мм, высота засыпки 20 мм. Температура образца контролировалась с помощью двух хромель-алюмелевых термопар, одна из которых помещалась в центре контейнера, а другая – вблизи его стенки. Заметных различий в показаниях этих термопар после установления теплового равновесия не наблюдалось. С помощью еще одной термопары, расположенной у стенки полости, регистрировалась температура окружающей среды, которая при нагреве контейнера не изменялась.

Была произведена специальная проверка того, что используемые образцы достаточно тонки. Для этого при температуре 900°К сравнивались активности навесок, взятых из центра и с периферии облученного образца. Эти активности оказались равными с точностью до ошибки измерения (0,2%). Этот результат не явился неожиданным, поскольку отношение средней толщины образца к длине свободного пробега нейтронов, усредненной с весом вероятности поглощения в уране, – для обоих образцов не превышало 0,2. Для этой же цели были произведены опыты с нагреванием образцов различных диаметров (12 – 3 мм). Удельные активности этих образцов сравнивались с активностью холодного образца постоянного диаметра. Отношения активностей для образцов различных диаметров были одинаковы в пределах ошибок.

При температурах от 1500°К до максимально достигнутой в этих экспериментах температуры 2000°К облучение производилось в молибденовых контейнерах диаметром 5 мм при высоте засыпки порошка 20 мм. Нагрев осуществляли с помощью вольфрамо-рениевой спирали. В качестве изоляции использовалась алундовая обмазка. Контроль температуры осуществлялся с помощью одной вольфрамо-рениевой термопары,

помещенной внутрь контейнера. Все устройство заключалось в откачиваемый баллон из нержавеющей стали с толщиной стенок 1 мм.

Наличие конструкционных материалов контейнеров-нагревателей само по себе заметно увеличивало активность облучаемых образцов за счет деблокировки нейтронного спектра при рассеянии в стенках конейнера. Этот эффект был тщательно измерен при комнатной температуре; он оказался равным ~7% и ~12% соответственно для контейнеров-нагревателей первого и второго типов. Поправка на влияние контейнеров вводилась при предположении, что вероятность поглощения в уране нейтронов, претерпевших рассеяние в стенках контейнеров описывается неблокированными сечениями захвата. Поэтому при высокой температуре увеличение числа захватов в образце за счет этого эффекта уменьшается на столько же, насколько (в процентном отношении) уменьшается разность между эффективным и обычным резонансным интегралом захвата для исследуемого спектра нейтронов. Учет температурной зависимости поправки на влияние контейнера производился расчетным путем. Точность результатов измерений была проконтролирована в серии экспериментов, в которых определялись отношения двух одинаковых в пределах ошибок взвешивания проб, отобранных из одного облученного образца. Результаты этих проверочных измерений указывают на отсутствие систематических ошибок в измерениях, в пределах достигнутой точности. Среднеквадратичный разброс результатов отдельных измерений от среднего по всей серии превышал статистическую ошибку примерно на 20%.

4. СПЕКТР НЕЙТРОНОВ В ОКИСНОМ ЭКРАНЕ РЕАКТОРА БР-I

При сравнении результатов измерений Допплер-эффекта с расчетными данными очень важно знать насколько правильно рассчитан спектр нейтронов: расхождения могут быть обусловлены не столько неточностью принятых температурных изменений групповых констант, сколько неточностью расчета спектра. Экспериментальная оценка спектра производилась двумя путями. Во-первых, вдоль оси экрана были измерены распределения скоростей различных реакций с относительно хорошо известным ходом сечений. Результаты этих измерений оказались в хорошем согласии (см. рис. 2) с данными расчета, выполненного в P_3-приближении по системе констант [2]. (Групповые сечения использованных реакций были взяты из работы [3]). Исключение составляет распределение скорости реакции $^{197}Au(n, \gamma)$, экспериментальные значения которой систематически несколько выше расчетных. Расчетный анализ этих расхождений, опирающийся на результаты измерения спектра нейтронов внутри блока из окиси урана, выполненные методом времени пролета на реакторе ИБР [4], показал, что указанное расхождение, по-видимому, объясняется неточностью расчета спектра в области ниже 100 эв. На результаты расчета скоростей использованных реакций, включая радиационный захват в уране-238, эта неточность сказывается весьма слабо.

Более детальная информация о спектре нейтронов в том месте экрана, где измерялся Допплер-эффект, была получена с помощью метода резонансных фильтров [5 – 7]. Потоки нейтронов были определены при энергиях первых резонансов следующих изотопов: ^{186}W (18,8 эв), ^{59}Co (132 эв), ^{55}Mn (337 эв), ^{63}Cu (580 эв), ^{23}Na (2950 эв) и ^{37}Cl (8700 эв).

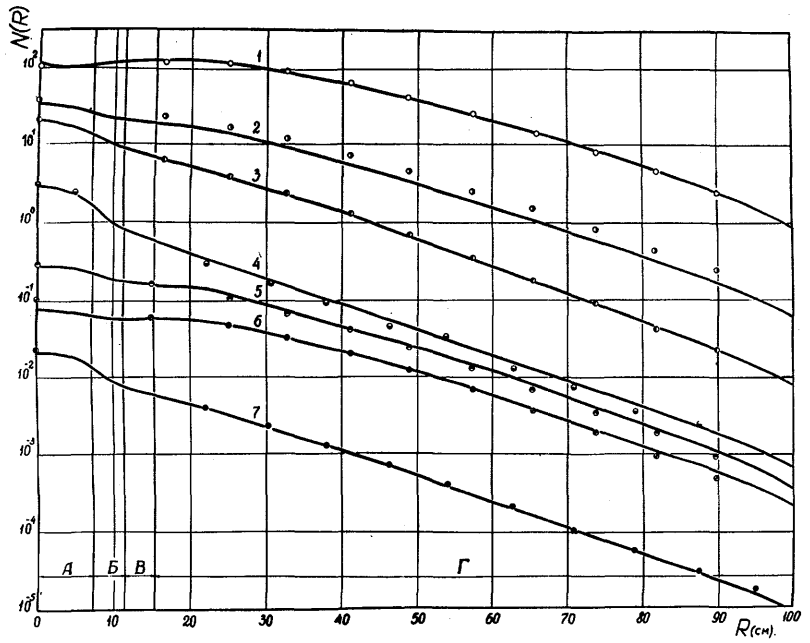

Рис.2. Распределение скоростей реакций в экране из окиси урана реактора БР-1. Сплошные линии – результат расчета на ЭВМ; точки – эксперимент. 1 – $^{55}Mn(n,\gamma)$, 2 – $^{197}Au(n,\gamma)$, 3 – $^{238}U(n,\gamma)$, 4 – $^{239}Pu(n,f)\cdot10^{-2}$, 5 – $^{63}Cu(n,\gamma)\cdot10^{-1}$, 6 – $^{23}Na(n,\gamma)$, 7 – $^{235}U(n,f)\cdot10^{-3}$.

Результаты этих измерений сравниваются с расчетными данными на рис. 3. Оба спектра нормированы на одинаковый интеграл делений в активной зоне реактора. Видно, что в исследованной области энергий (в которой как раз и имеет место Допплер-эффект) расчетный спектр совпадает с экспериментальным в пределах ошибок.

5. РАСЧЕТ СЕЧЕНИЙ ЗАХВАТА НЕЙТРОНОВ В ^{238}U ДЛЯ МАЛОГО ГОРЯЧЕГО ОБРАЗЦА, ПОМЕЩЕННОГО В ХОЛОДНУЮ СРЕДУ

При составлении блокированных групповых сечений (например захвата – $\bar{\sigma}_c$) в работе [2] предполагалось, что спектр нейтронов обратно пропорционален полному сечению среды, т.е.

$$\bar{\sigma}_c(\tilde{\sigma}, T) = \frac{\left\langle \frac{\sigma_c(T)}{\sigma_r(T)+\tilde{\sigma}+\sigma_p} \right\rangle}{\left\langle \frac{1}{\sigma_r(T)+\tilde{\sigma}+\sigma_p} \right\rangle}$$

угловые скобки означают усреднение по энергетическому интервалу группы; T – температура среды, σ_p – сечение потенциального рассеяния, $\sigma_r - \sigma_{tot} = \sigma_c$ – "сечение реакций", $\tilde{\sigma}$ – полное сечение всех осталь-

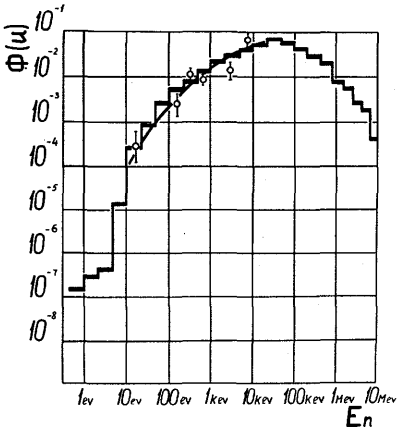

Рис.3. Спектр нейтронов (на единичный интервал летаргии) в экране из окиси урана реактора БР-1 на расстоянии 68 см от центра активной зоны.
Гистограмма – расчетный спектр в P_3 – приближении (по константам [2]);
Точки – результаты измерений методом резонансных фильтров; кривая проведена через экспериментальные точки.

ных элементов, входящих в состав среды, приходящихся на одно ядро рассматриваемого резонансного поглотителя. Однако, в данном случае спектр нейтронов, падающих на образец, формируется холодной средой и, следовательно, блокированные сечения будут зависеть как от температуры образца (T_1), так и от температуры среды (T_2)

$$\overline{\sigma}_c(\widetilde{\sigma}, T_1, T_1 - T_2) = \frac{\left\langle \frac{\sigma_c(T_1)}{\sigma_r(T_2) + \widetilde{\sigma} + \sigma_p} \right\rangle}{\left\langle \frac{1}{\sigma_r(T_2) + \widetilde{\sigma} + \sigma_p} \right\rangle}$$

Для расчета сечений по этой формуле в области изолированных резонансов необходимо знать функции:

$$\kappa'_a(\alpha, \xi_1, \varphi, T_1 - T_2) = \frac{1}{\pi} \int_{-\infty}^{\infty} \frac{\psi(x, \xi_1)dx}{1 + \alpha[\psi(x, \xi_2)\cos 2\varphi + \chi(x, \xi_2)\sin 2\varphi]}$$

$$\xi_2 = \xi_1 \sqrt{\frac{T_1}{T_2}}$$

ψ, χ – функции допплеровского уширения резонансов.

Таблицы функций κ'_a были рассчитаны на ЭВМ по программе Ф.Ф.Михайлуса для случая $\sqrt{T_1/T_2} = 1{,}63$, что соответствует $T_1 = 800°K$ при $T_2 = 300°K$.

С помощью этих функций были вычислены сечения тонкого горячего образца, находящегося в среде, для области, где резонансы урана-238 можно хотя бы приближенно считать изолированными. Результаты расчетов приведены в табл. 2.

ТАБЛИЦА 2. ТЕМПЕРАТУРНЫЕ ПРИРАЩЕНИЯ СЕЧЕНИЙ ТОНКОГО ОБРАЗЦА ИЗ УРАНА-238, НАХОДЯЩЕГОСЯ ПРИ ТЕМПЕРАТУРЕ 800°К, В УРАН-СОДЕРЖАЩЕЙ СРЕДЕ ЭКРАНА РЕАКТОРА БР-I (см. ТАБЛ. 1) С ТЕМПЕРАТУРОЙ 300°К

Номер группы [2]	ΔE_n	$\bar{\sigma}$ (барн)	$\Delta\sigma_c$ (барн)
9	46,5 – 100 кэв	8	0,0035
10	21,5 – 46,5 кэв	8,6	0,0097
11	10,0 – 21,5 кэв	7,9	0,027
12	4,65 – 10,0 кэв	8,2	0,055
13	2,15 – 4,65 кэв	8,2	0,12
14	1,00 – 2,15 кэв	8,2	0,24
15	465 – 1000 эв	8,2	0,38
16	215 – 465 эв	8,3	0,35
17	100 – 215 эв	8,3	0,38
18	46,5 – 100 эв	8,4	0,34
19	21,5 – 46,5 эв	8,5	0,30
20	10,0 – 21,5 эв	8,6	0,75
21	4,65 – 10,0 эв	8,5	1,49

6. РЕЗУЛЬТАТЫ РАСЧЕТА И ЭКСПЕРИМЕНТА

На рис. 4 изображены результаты измерений допплеровского приращения скорости реакции $^{238}U(n,\gamma)$ в диапазоне температур 300°К ÷ 2000°К. Как видно из рисунка, зависимость относительного увеличения скорости реакции довольно хорошо описывается функцией

$$f(\sqrt{T_г} - \sqrt{T_х}) = b(\sqrt{T_г} - \sqrt{T_х})$$

где $T_г$ – температура горячего образца,
$T_х$ – температура холодного образца в °К; наклон прямой линии, определенной методом наименьших квадратов, равен

$$b = (1{,}32 \pm 0{,}04) \cdot 10^{-2} (°К)^{-1/2}$$

Расчетное относительное приращение скорости реакции ^{238}U (n, γ) при нагреве такого образца до 800°К равно 13,6%; экспериментальное значение этой величины 14,8 ± 0,4%. Следует отметить, что сечения захвата в тонком горячем образце, находящемся в холодной среде, существенно отличаются от сечений захвата горячей среды (которые легко вычислить по данным [2]). Использование последних приводит не только к

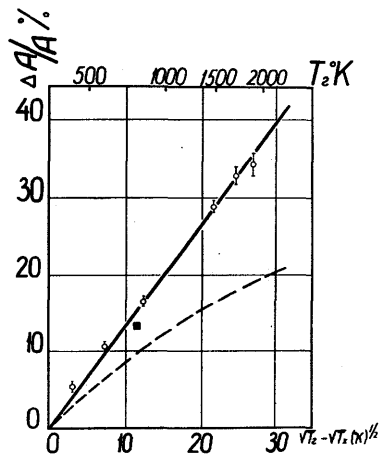

Рис.4. Результаты измерения допплеровского приращения скорости реакции $^{238}U(n,\gamma)$ в экране из окиси урана реактора БР-1:

$T_г$ – температура горячего образца;
$T_х$ – температура холодного образца и среды экрана;
O – эксперимент;
■ – расчет допплеровского приращения при $T_г = 800\,°K$;
—— прямая, проведенная через экспериментальные точки методом наименьших квадратов;
--- расчет температурной зависимости допплеровского приращения скорости реакции по константам [2].

существенному занижению эффекта, но и к иной температурной зависимости этого эффекта (см. пунктирную кривую на рис. 4).

Представляет интерес рассмотреть вопрос о вкладе различных энергетических областей спектра нейтронов, существующего в двуокиси урана, в допплеровское увеличение скорости реакции $^{238}U(n,\gamma)$. На рис. 5 изображен расчетный спектр нейтронов, претерпевающих захват в $^{238}U - \Phi(u)\cdot\bar{\sigma}_c(^{238}U)$, где $\Phi(u)$ – среднегрупповой поток нейтронов на единицу летаргии, и "спектр" увеличения скорости реакции захвата за счет Допплер-эффекта – $\Phi(u)\cdot\Delta\bar{\sigma}_c(^{238}U)$. Из рисунка видно, что 90% всего допплеровского увеличения скорости реакции обусловлено нейтронами с энергиями от 46,5 эв до 10 кэв ($\Delta u = 5{,}4$), 70% этого увеличения сосредоточено в еще более узком диапазоне энергий от 215 эв до 4,65 кэв ($\Delta u \cong 3$).

Интересна также оценка влияния неопределенности нейтронного спектра на точность расчета допплеровского увеличения скорости реакции $^{238}U(n,\gamma)$. Оказывается, вариации спектра в пределах ошибок экспериментальных точек (см. рис. 2) ведут к изменениям расчетной величины температурных увеличений скорости захвата не более чем на 1%, что сравнимо с ошибкой экспериментального определения этой величины. Можно поэтому считать, что точность измерения спектра в данном случае адэкватна точности измерений Допплер-эффекта.

Таким образом, результат расчета допплеровского приращения скорости захвата в образце оказался совпадающим с экспериментальной величиной с точностью до ошибок ее определения и неопределенностей, связанных с возможными неточностями в расчете спектра нейтронов.

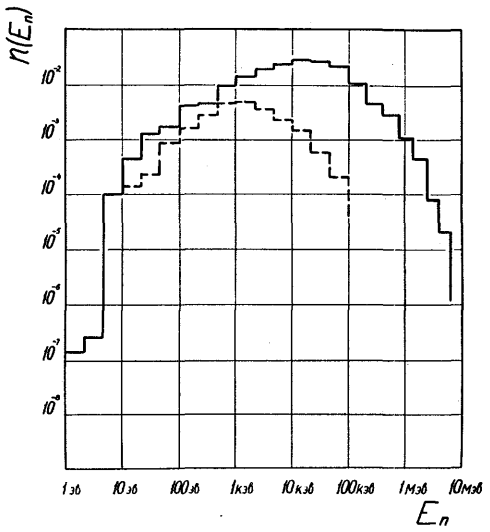

Рис.5. "Спектр" увеличения скорости захвата нейтронов в уране-238 за счет Допплер-эффекта в экране из окиси урана реактора БР-1:
Сплошная гистограмма – "спектр" скорости захвата нейтронов в уране-238 – $\varphi_i \Delta\bar{\sigma}_c^i / \Delta U_i$;
пунктирная гистограмма – "спектр" допплеровского приращения реакции захвата в ^{238}U – $\varphi_i \Delta\bar{\sigma}_c^i / \Delta U_i$;
φ_i – поток нейтронов в i-той группе; ΔU_i – групповой интервал летаргии.

Столь хорошее согласие экспериментальных и расчетных данных намного превышает оценку точности расчета этой величины, исходя из погрешностей ядерных данных, использованных при расчете сечений (~20% в $\Delta\bar{\sigma}_c$). В связи с этим представляет значительный интерес сравнение полученных данных с расчетом при более высоких температурах. Такое сравнение будет проведено в ближайшем будущем. В дальнейшем предполагается также проведение измерений Допплер-эффекта в горячей среде из окиси урана.

В заключение авторы выражают благодарность А.И.Лейпунскому и В.В.Орлову за интерес к работе и ценные замечания.

Авторы благодарят М.Н.Зизина за содействие в проведении расчетов на ЭВМ, а также Ю.К.Комарова, Е.А.Осипова, П.В.Киндинова, А.И.Ашуркина и К.И.Нестерову за помощь в проведении измерений и оформлении результатов.

ЛИТЕРАТУРА

[1] ЛЕЙПУНСКИЙ, А.И. и др., Исследования по физике реакторов на быстрых нейтронах. Доклад №2038, II Международная конференция по мирному использованию атомной энергии, Женева, 1958.

[2] АБАГЯН, Л.П. и др., Групповые константы для расчета ядерных реакторов, Атомиздат, М, 1964.

[3] ГОЛУБЕВ, В.И., НИКОЛАЕВ, М.Н., ОРЛОВ, М.Ю., "Групповые сечения некоторых ядерных реакций, используемых для регистрации нейтронов", Бюллетень ИЦЯД, вып. I, 1964.

[4] ЛЕЙПУНСКИЙ, А.И. и др., Экспериментальные и теоретические исследования по физике быстрых реакторов. Доклад на конференции по быстрым реакторам. Лондон, май 1966.

[5] ГОЛУБЕВ, В.И., ИВАНОВ, В.И., НИКОЛАЕВ, М.Н., СМИРЕНКИН, Г.Н. Атомная энергия II (1961) 522.
[6] АВАЕВ, В.Н., ЕГОРОВ, Ю.А., Сб. Вопросы дозиметрии и защиты от излучения, Атомиздат, М, 1965, стр. 15.
[7] ЗВОНАРЕВ, А.В. и др., Атомная энергия 20 (1966) 518.

DISCUSSION

L. I. TIRÉN: How large were the corrections to the hot/cold activation ratio due to neutron scattering in the oven walls?

N. V. KRASNOYAROV: About 7% and 12% respectively of the increase in sample activation through heating in the two ovens.

MONTE CARLO CODE FOR CALCULATING THE DOPPLER EFFECT IN FAST REACTORS*

W. ROTHENSTEIN AND D. NAOT
DEPARTMENT OF NUCLEAR SCIENCE,
TECHNION – ISRAEL INSTITUTE OF TECHNOLOGY,
HAIFA, ISRAEL

Abstract

MONTE CARLO CODE FOR CALCULATING THE DOPPLER EFFECT IN FAST REACTORS. A Monte Carlo code for calculating the Doppler effect between specified energy limits in fast reactors is described. Neutron histories are followed through the energy interval in which temperature changes in the reactor affect the multiplication rate. The normalization of the results requires additional information which may be obtained from suitable multigroup calculations.

The reaction rates and their changes with temperature are obtained from Monte Carlo estimates of the unperturbed flux, and adjoint weighted with group adjoint fluxes specified in the input. Allowance is made for the resonance fine structure of the importance functions within the narrow resonance approximation.

Geometry routines have been prepared for multiregion spherical geometry, each region containing a homogeneous mixture, and for a multilayer cylindrical geometry with a number of regions in each layer. There is also an option for infinite lattice calculations with top and bottom blankets and reflectors. The resonance cross-sections are based on the Doppler broadened Breit-Wigner single level formula and contain $\ell = 0$ and $\ell = 1$ contributions, the resonance parameters being chosen from their average values and distribution functions.

The code is of value in studying the influence of different temperature excursions on the Doppler effect, since different temperature changes can be specified in each region of the assembly. Interference effects between different resonance sequences are automatically included. The $\ell = 1$ wave contribution to the Doppler effect can be investigated and core heterogeneity effects studied.

Results will be presented showing the type of accuracy of the estimates obtained. In a typical run for a 2500-litre oxide-fuelled spherical assembly the contribution to the Doppler effect in the 16th group of the YOM set was obtained with confidence limits of ± 8% on the 50% level in about 5 min computation time on the Philco 2000 computer, when only the $\ell = 0$ contributions of the nearest resonances of uranium and plutonium to the neutron energy were included in the cross-section calculations.

INTRODUCTION

The direct application of the Monte Carlo method to the calculation of the Doppler effect in fast reactors provides a natural means of including a number of factors in such investigations which may require special techniques in other types of calculations and which have been studied by a number of investigators. These factors include the influence of the large sodium resonance [1] and of resonances of the structural materials on the Doppler effect, the mutual overlap [2, 3, 4] of the resonances of the fertile and fissile nuclei, the effect of the high plutonium isotopes [1], the extent of the influence of the resonance wings, the contribution of p-wave in addition to s-wave resonances [5], the influence of different types of temperature excursions in the assembly and the effect of the space

* Joint research by the Department of Nuclear Science of Technion and the Israel Atomic Energy Commission and partly supported by the KBB (Karlsruhe)-Euratom Association on Fast Reactors, Kernforschungszentrum Karlsruhe.

dependence of the flux in the fuel elements [6]. In the Monte Carlo procedure the cross-sections and their changes with temperature are calculated directly at each neutron energy and it is also possible to trace neutron paths in relatively complex geometries.

The advantages inherent in Monte Carlo calculations with regard to the lack of the need for simplifying assumptions is, however, offset by the need for lengthy computer runs and the statistical inaccuracies of the results obtained. The aim of the present investigation is to study the scope and the limitations of the Monte Carlo technique in Doppler effect calculations.

The change in the multiplication constant, δk, between two different temperature distributions in the reactor assembly could be obtained as the difference between Monte Carlo estimates of the criticality of the system in the two cases. Since this difference is, however, small, it is preferable to make direct Monte Carlo estimates of the changes in the reaction rates in the assembly. In particular δk may be related to the change in the neutron production by fission when the temperature is altered. This procedure will be termed the 'difference Monte Carlo method'. An alternative approach is to estimate the changes of all reaction rates, absorption, production and leakage, and to obtain δk by weighting these with suitable adjoint functions. This will be called the 'perturbation approach'. In addition it is desirable to concentrate the computational effort of the Monte Carlo programme on those energy intervals in which temperature changes affect the resonance cross-sections. Neutron histories are followed only through a small part of the entire energy span between their production and absorption. This limitation necessitates normalization of the results with the aid of information obtained by other calculations such as multigroup diffusion or transport codes. The Monte Carlo estimates of the changes in reaction rates are, however, obtained directly from changes in the cross-sections at each neutron energy without the use of effective cross-sections. In this way the effects mentioned previously, such as overlap between different resonances, are automatically included in the calculations.

In the following, a description will be given of the Monte Carlo code which has been prepared including its geometrical features, the manner in which the resonance cross-sections are calculated, and the procedure of tracing the neutron path through the assembly. An account will then be given of the experience gained with the code based on the 'difference Monte Carlo method' which is an extension of the approach suggested by Matthes [7]. Finally, the 'perturbation approach' will be described and its advantages discussed.

GEOMETRY, CROSS-SECTIONS AND NEUTRON HISTORIES

The code refers to three geometrical configurations of the reactor assembly. In the first option the system consists of a number of concentric spheres, a homogeneous mixture being contained in each region. In the case of cylindrical geometry the assembly is made up of a set of layers each having an outer boundary of the same radius. Each layer is made up of a number of homogeneous regions whose faces form a set of coaxial cylinders. It is assumed that the assembly is symmetrical

with respect to the mid-plane of its central layer. The cylindrical geometry option enables systems with axial and radial blankets and reflectors to be studied. Finally, a lattice geometry may be investigated. It is based on an extension of the code of Richtmeyer et al. [8] for following neutron paths in reactor lattices and is included for the study of core heterogeneity effects allowing for axial blankets and reflectors. In the transverse direction the lattice is of infinite extent and may include a rectangular or hexagonal arrangement of the fuel pins, each of which may be divided into cylindrical sub-regions.

The homogeneous mixtures contained in the different regions are assumed to be made up of materials of three main types. The first consist of nuclides with constant cross-sections except for 1/v absorption. The second type are those nuclides which have large scattering resonances, such as sodium, in which Doppler broadening can be omitted. The third are heavy resonance materials in which the Doppler change of resonance cross-sections is calculated at each neutron energy.

In the case of the heavy resonance nuclides a number of resonance sequences must be included in the cross-section calculations. In general, statistical methods are used to determine their parameters. The contributions to the resonance cross-sections which correspond to the $\ell = 0$ and $\ell = 1$ parts of the incident neutron waves are taken into account. These form resonance sequences distinguished by their parities. For each value of ℓ the sequences with different spin J of the compound nucleus must be considered separately using resonance parameters chosen from their average values and distribution functions. In some cases there may be contributions from two different channel spins to a sequence specified by a particular combination of J and parity. When this happens the neutron width is doubled [9]. An example is ^{239}Pu in which the channel spins 0 and 1 contribute to the resonance sequence $\ell = 1$, $J = 1$.

The Breit-Wigner single-level formula is used for the calculation of the resonance cross-sections. The peak resonance scattering, capture and fission cross-sections and the amplitude of the interference cross-section between resonance and potential scattering are given by

$$\sigma_s^0 = 4\pi\lambda\!\!\!^{-2}\, g_J \left(\frac{\Gamma_n}{\Gamma}\right)^2 \qquad \sigma_a^0 = 4\pi\lambda\!\!\!^{-2}\, g_J \sqrt{\frac{E_0}{E}}\ \frac{\Gamma_n\ \Gamma_\gamma}{\Gamma^2}$$

$$\sigma_f^0 = 4\pi\lambda\!\!\!^{-2}\, g_J \sqrt{\frac{E_0}{E}}\ \frac{\Gamma_n\ \Gamma_f}{\Gamma^2} \qquad \sigma_{int}^0 = 2\sqrt{\sigma_s^0\, \sigma_p\, g_J}$$

where

$$\lambda\!\!\!^{-2}_0 = \frac{\hbar^2}{2mE_0}\left(\frac{A+1}{A}\right)^2 \qquad g_J = \frac{2J+1}{2(2I+1)} \qquad \sigma_p = 4\pi R^2$$

and E_0 is the energy at the resonance peak.

The neutron and gamma widths are input data for the resolved resonances of ^{238}U. For other heavy resonance nuclides and the unresolved ^{238}U resonances, the input data are the strength functions, average level

spacings (energy dependent), and the constant gamma and average energy dependent fission widths. From these:

$$\Gamma_n = \langle \Gamma_n^0 \rangle \sqrt{E}\, x_1 \qquad \langle \Gamma_n^0 \rangle = \xi_\ell \langle D_J \rangle$$

$$D_J = \langle D_J \rangle\, x_w \qquad \Gamma_f = \langle \Gamma_f \rangle x_2$$

where x_1, x_2 and x_w are random variables chosen from χ^2 distributions with one and two degrees of freedom and from the Wigner distribution. (The distributions are all defined so that the random variables x have unit average.)

For a particular neutron energy E the nearest resonances above and below E are located from the tabulated peak energies (for ^{238}U) and, in the case of unresolved resonances, by selecting their spacing D_J^* and locating them so that E lies at a random position between these peaks. $D_J^* = \langle D_J \rangle\, x_w^*$ is taken to be subject to a Wigner distribution modified by the fact that the probability of E being situated between two peaks separated by D_J^* is proportional to D_J^* itself [9]. More distant resonances can be included in the cross-section calculations as required, their locations being selected with reference to the nearest resonance pair by using spacings D_J distributed according to the Wigner distribution; for ^{238}U the tabulated resonances are used whenever possible. All the resonance data for a particular neutron energy E are stored until the neutron is slowed down to ensure that reference is made to the same resonance cross-sections if a neutron encounters the same nuclide in different regions.

The line shape functions by which the peak cross-sections and the interference scattering cross-sections have to be multiplied are given by

$$\psi(x,\theta) = \frac{1}{\sqrt{4\pi\theta}} \int_{-\infty}^{\infty} \frac{e^{-(x-y)^2/4\theta}}{1+y^2}\, dy$$

$$\chi(x,\theta) = \frac{1}{\sqrt{4\pi\theta}} \int_{-\infty}^{\infty} \frac{y\, e^{-(x-y)^2/4\theta}}{1+y^2}\, dy$$

where

$$x = \frac{2}{\Gamma}(E - E_0) \qquad \theta = \frac{4EkT}{A\Gamma^2}$$

They are calculated from the complex probability integral by the method described by O'Shea and Thacher [10].

The neutron histories are followed between specified energy limits E_{max} and E_{min}. At the higher energy the neutrons are injected into the assembly with a spatial distribution which is in accordance with the slowing-down density specified in the form of a histogram in the input. From the initial location and direction, chosen from an isotropic distribution, the number of free paths μ traversed by the neutrons is selected so that its frequency function is $e^{-\mu}$. Translating this into a distance $d = \mu/\Sigma$, where Σ is the total cross-section, the next collision

point may be located. Alternatively if the distance to the region boundary is less than d, a boundary crossing takes place, μ is correspondingly reduced and the collision point located in a subsequent region. When the neutron collides, the nuclide with which the collision occurs is selected in accordance with its scattering cross-section and the new direction of motion is chosen from an isotropic distribution in the centre-of-mass co-ordinate system, transforming this direction appropriately to laboratory co-ordinates. At the relatively low energies to which the code applies the new energy is determined, assuming the scattering to be elastic.

The neutrons are injected into the assembly with unit weight. The calculation of the Monte Carlo estimates of the difference in reaction rates at the two temperature distributions in the reactor assembly depends on the variance reduction techniques adopted and whether or not a perturbation approach is used.

THE 'DIFFERENCE MONTE CARLO' METHOD

In the difference Monte Carlo method, reference is made to the N_0 neutrons slowed down past E_{max} from N neutrons produced by fission in the reactor. In an energy group i between E_{max} and E_{min}, N_i new neutrons are produced by fission and this number changes by ΔN_i with change of temperature. The change in the multiplication constant is then

$$\delta k = \frac{N_0}{N} \sum_i \frac{\Delta N_i}{N_0}$$

The factor N_0/N must be obtained from a separate calculation, using a suitable multigroup code. The Monte Carlo code refers to the evaluation of the change in production rate per neutron history followed between E_{max} and E_{min}, $(\sum_i \Delta N_i/N_0)$. This is the principle of the method outlined by Matthes in his paper cited previously [7].

At two different temperatures, the neutron will follow different paths and be slowed down in a different manner. At the neutron energy corresponding to each event, the resonance parameters have to be selected as indicated above. In the difference method the same paths and slowing-down patterns are used at both temperatures, so that the difference in reaction rates follows from the difference in cross-sections with temperature of the same resonances and for the same neutron energy.

The change in cross-sections with temperature does not only affect the reaction rates but alters also the probabilities which determine the successive neutron events. To use, artificially, the same neutron random walk at the modified as well as at the original temperature, adjustments of the neutron weight must be made. As an example of such an adjustment of the weight at the new temperature we consider the selection of the distance x travelled by neutrons between successive collisions in a particular region. x should be chosen from distributions with frequency functions $\Sigma e^{-\Sigma x}$ and $\Sigma' e^{-\Sigma' x}$ at the two temperatures. If one wishes to ensure in the difference method that the neutron follows the same random walk, the distance x may be chosen from the first distri-

TABLE I. PRODUCTION RATE AND ITS CHANGE WITH TEMPERATURE BETWEEN 1.5 AND 0.5 KeV

Number of histories	N_i/N_0 (Arbitrary units)		$\Delta N_i/N_0$ (Arbitrary units)	
	A	B	A	B
50	0.423	0.487	-0.0029	-0.0140
100	0.463	0.476	+0.0102	-0.0118
150	0.468	0.490	+0.0188	-0.0041
200	0.482	0.486	+0.0334	+0.0004
250	0.480	0.488	+0.0304	+0.0026
300	0.480	0.488	+0.0258	+0.0021
350	0.483	0.486	+0.0187	+0.0031
400	0.469	0.475	+0.0151	+0.0016
450	0.468	0.480	+0.0123	+0.0004
500	0.480	0.478	+0.0113	+0.0014
	±0.018	±0.008	±0.0040	±0.0020

bution and the weight corrected by the factor $\Sigma' e^{-\Sigma' x} / \Sigma e^{-\Sigma x}$ at the modified temperature. The correction ensures that the proper number of collisions will occur per unit distance at x, since the weight is a measure of the collision density at the initial collision point.

In Table I an example is given of the statistics which were obtained for a particular test run in which a 2500-litre PuO_2-fuelled spherical assembly was studied [11]. The change in production rate between 1.5 and 0.5 keV was estimated for a 100°K temperature change in the fuel and 50 and 20 degree temperature increases in the blanket and reflector of 45 and 30 cm thickness respectively. In the cross-section calculations only the nearest resonances were taken into account and contributions due to $\ell > 0$ were ignored. Referring to column A, it can be seen that the production N_i/N_0 converges quite well after 500 histories, but its change $\Delta N_i/N_0$ fluctuates widely when the temperature is increased. (Group i refers to the above energy interval.)

Column B refers to a different sampling technique. Whereas in method A the nuclide n responsible for the collision at each collision point was chosen with reference to the total collision probability Σ_{tn}/Σ_t, where Σ_t refers to the entire mixture, in method B the choice was made according to the scattering probability Σ_{sn}/Σ_s. In the former procedure the history followed the actual neutron events closely and the production rate was calculated after it had been ascertained that a collision with plutonium had taken place. In method B, however, the production and capture rates were calculated at each collision using the appropriate probabilities Σ_f/Σ_t and Σ_c/Σ_t for the entire mixture. The remainder of

the neutron weight, $W\Sigma_s/\Sigma_t$, is left after slowing down. Since collisions with the fissionable isotope are relatively rare, the production rate is obtained from relatively few such events in method A, whereas in method B small contributions to it are recorded at each collision. This is the explanation for the decrease in the 50% confidence interval in the second procedure. The error is, however, still so large that even the sign of the change in production rate with temperature is still in doubt. It should be pointed out that improved accuracy is obtained only slowly (proportional to the reciprocal square root of the number of histories run) at the expense of increased machine time. The time required for each of the above test runs was about 4 minutes on the Philco-2000 computer. Further calculations showed that the statistics became even worse when more distant resonances were included in the cross-section calculations.

The large fluctuations in the change of the production rate are due to the fact that the line shape function ψ decreases with temperature at the resonance peak and increases in the wings. The Doppler effect to be expected may be deduced qualitatively by considering the change of the function $J = \int(\psi/\beta+\psi)dx$ with temperature. Near a very large resonance peak there is no Doppler effect owing to the smallness of β. Far in the wings, where ψ is small and approaches the natural line shape, the effect again vanishes. For the type of resonances encountered in Doppler effect calculations, the change of the integrand $\psi(\beta+\psi)$ due to an increase in temperature is, however, negative for an energy interval of the order of the Doppler width surrounding the resonance peak, while positive values are encountered until quite far out in the wings. The net ΔJ is positive, but is the difference between contributions of opposite sign which are sometimes quite large.

A variance reduction technique which was found to be quite successful aimed at reducing the effects of the resonance wings for the fissile isotope, whose resonance cross-section is relatively a small part of Σ_t. The value of β in the integrand of J is then quite appreciable so that the integrand follows the line shape function over a wide energy range. For this isotope the change in fission probability with temperature $\Delta(\Sigma_f/\Sigma_t)$, from which the change in fission rate is derived, was reduced by $(\Delta\Sigma_f)/\Sigma_b$, where Σ_b is the constant background cross-section. This correction has zero average and its effect is to concentrate the range of integration which defines ΔJ to an interval nearer the resonance peak. In a test run the confidence interval for the change in production was reduced by a further factor of about three when compared with case B of Table I.

The statistical fluctuations were only apparent to a smaller extent in the original calculations made by Matthes [12] with a Monte Carlo code for Doppler effect calculations. In this programme the cross-section calculations were based only on the nearest resonance to the neutron energy, so that the effect of the resonance wings was greatly suppressed.

There is a further reason for the large statistical fluctuations in the difference Monte Carlo method. As the neutron is slowed down, the weight is modified by the scattering fraction at each collision. This fraction may be larger or smaller at the modified temperature according to the location of the neutron energy relative to the neighbouring resonances. Each scattering event introduces therefore fluctuations in

the difference in neutron weight at the different temperature distributions. The final statistical accuracy which may be attained depends then not only on the fluctuations of the difference of the fission probability with temperature at each collision but also on the fluctuations due to the scattering events at previous collisions.

A first-order perturbation approach suppresses the effect of the changes of scattering probabilities with temperature. The neutron history is followed entirely at the initial temperature distribution in the reactor assembly. At each collision Monte Carlo estimates are made of the differences in the reaction rates and the change in multiplication factor follows from appropriate adjoint weighting.

THE PERTURBATION APPROACH

In the perturbation approach the Monte Carlo estimates are weighted with adjoint fluxes to obtain the change in the multiplication factor:

$$\delta k = \frac{1}{C} \int d\bar{x} \int dE \int d\bar{\Omega}\, \phi^*(\bar{x}, E, \bar{\Omega}) \left[-\delta\Sigma(\bar{x}, E)\, \phi'(\bar{x}, E, \bar{\Omega}) + \int dE' \int d\bar{\Omega}' \right.$$

$$\left. \times \left\{ \delta\Sigma_s(\bar{x}, E' \to E, \bar{\Omega}' \to \bar{\Omega}) + \frac{\chi(\bar{x}, E)}{4\pi} \nu\, \delta\Sigma_f(\bar{x}, E') \right\} \phi'(\bar{x}, E', \bar{\Omega}') \right]$$

where

$$C = \int d\bar{x} \int dE \int d\bar{\Omega}\, \phi^*(\bar{x}, E, \bar{\Omega}) \frac{\chi(\bar{x}, E)}{4\pi} \int dE' \int d\bar{\Omega}' \nu\Sigma_f'(\bar{x}, E')\, \phi'(\bar{x}, E', \bar{\Omega}')$$

Here ϕ' is the perturbed flux and Σ_f' the perturbed fission cross-section.

The adjoint fluxes used as weighting functions must be provided as input to the problem. If they are specified as group averages independent of direction it is useful to use the following definitions:

$$\phi^*(\bar{x}, E, \bar{\Omega}) = \phi^*(\bar{x}, E)$$

$$\psi_g^*(\bar{x}) = \langle \phi^*(\bar{x}, E) \rangle_g \text{ for energy group } g$$

$$\psi_f^*(\bar{x}) = \int dE\, \chi(\bar{x}, E)\, \phi^*(\bar{x}, E) \text{ for neutrons produced by fission}$$

If the scattering cross-section $\Sigma_s(\bar{x}, E' \to E, \bar{\Omega}' \to \bar{\Omega})$ is replaced by the zero-order term of its expansion in Legendre polynomials and isotropic elastic scattering in the centre of mass system is assumed, the expression for δk becomes:

$$\delta k = \frac{1}{C} \int d\bar{x} \int dE \left[-\phi^*(\bar{x}, E)\, \delta\Sigma(\bar{x}, E)\, \phi'(\bar{x}, E) + \psi_g^*(\bar{x})\, \delta\Sigma_s(\bar{x}, E)\, \phi'(\bar{x}, E) \right.$$

$$\left. + \psi_f^*(\bar{x})\, \nu\, \delta\Sigma_f(\bar{x}, E)\, \phi'(\bar{x}, E) \right]$$

$$C = \int d\bar{x} \int dE\, \psi_f^*(\bar{x}, E)\, \nu\Sigma_f'(\bar{x}, E)\, \phi'(\bar{x}, E)$$

In the first term the adjoint flux at energy E still appears. To take its resonance fine structure into account, it may be expressed in terms of ψ_g^* and ψ_f^* within the narrow resonance approximation [13]. The adjoint flux is the solution of

$$\phi^*(\bar{x}, E, \bar{\Omega}) = \int_0^\infty ds\ e^{-\int_0^s \Sigma(\bar{x}+s'\bar{\Omega}, E)ds'} \int dE' \int d\bar{\Omega}'\, \phi^*(\bar{x}+s\bar{\Omega}, E', \bar{\Omega}')$$

$$\times \left[\Sigma_s(\bar{x}+s\bar{\Omega},\ E \to E',\ \bar{\Omega} \to \bar{\Omega}') + \frac{\chi(\bar{x}+s\bar{\Omega}, E')}{4\pi} \nu\Sigma_f(\bar{x}+s\bar{\Omega}, E) \right]$$

Making the simplifications described above:

$$\phi^*(\bar{x}, E) = \int_0^\infty \left[\frac{\Sigma_s(\bar{x}', E)\, \psi_g^*(\bar{x}') + \nu\Sigma_f(\bar{x}'E)\, \psi_f^*(\bar{x}')}{\Sigma(\bar{x}', E)} \right] e^{-\int_0^s \Sigma(\bar{x}+s'\bar{\Omega}, E)ds'}\ \Sigma(\bar{x}', E)ds$$

where $\bar{x}' = \bar{x} + s\bar{\Omega}$. Thus $\phi^*(\bar{x}, E)$ is obtained from the values of ψ_g^* and ψ_f^* at the next collision point along the neutron direction $\bar{\Omega}$, which can be selected in the manner described previously in which the number of mean free paths is selected from an exponential distribution. Consequently $\phi^*(\bar{x}, E)$ is replaced by

$$\psi_{g,E}^*(\bar{x}') = \frac{\Sigma_s(\bar{x}'E)\, \psi_g^*(\bar{x}') + \nu\Sigma_f(\bar{x}', E)\, \psi_f^*(\bar{x}')}{\Sigma(\bar{x}', E)}$$

In a first-order approach the perturbed flux ϕ' is replaced by the unperturbed flux ϕ and the neutron weight W samples the collision density. Finally

$$\delta k = \frac{1}{C} \sum_{\bar{x}} \sum_{E} W(\bar{x}, E) \left[\psi_g^*(\bar{x})\ \delta \left\{ \frac{\Sigma_s(\bar{x}, E)}{\Sigma(\bar{x}, E)} \right\} + \psi_f^*(\bar{x})\ \delta \left\{ \frac{\nu\Sigma_f(\bar{x}, E)}{\Sigma(\bar{x}, E)} \right\} \right.$$

$$\left. - \left\{ \psi_{g,E}^*(\bar{x}') - \psi_{g,E}^*(\bar{x}) \right\} \frac{\delta\Sigma(\bar{x}, E)}{\Sigma(\bar{x}, E)} \right]$$

where the summations cover the locations and energies at all collision points.

If the summations are divided by the number of histories run in which unit weight is assigned to each neutron crossing E_{max}, the denominator C must be normalized similarly to one neutron crossing E_{max} in the assembly.

Calculations with the Monte Carlo perturbation code have been made for the 2500-litre PuO-fuelled spherical assembly specified by Shaviv and Yiftah [1] for temperature increases from 300 - 900 and 300 - 1500°K in the core. The adjoint fluxes and normalization factors were obtained from 16-group multigroup diffusion calculations using the YOM [14] group cross-section set.

In the first instance calculations were made for the 16th energy group only – using E_{max} = 2035 eV and E_{min} = 454 eV. In the cross-

section calculations one resonance on each side of the neutron energy was taken into account for the resonance sequences of both ^{239}Pu and ^{238}U and only the $\ell = 0$ part of the neutron wave was included. In the expression for the δk the absorption contribution, dependent on $\delta(\Sigma_a/\Sigma_t) = -\delta(\Sigma_s/\Sigma_t)$, and the production contribution, which depends on $\delta(\nu\Sigma_f/\Sigma_t)$, are shown separately. The third contribution is the transfer term which arises from the change in collision density and is weighted with the difference in group adjoint fluxes at two locations $\bar{x}$ and $\bar{x}'$ in the assembly. The results for the temperature increase from 300 to 900° K in the core are shown in Table II, and the confidence limits on the 50% level are shown after the final neutron history run.

TABLE II. ADJOINT WEIGHTED CONTRIBUTIONS TO δk DUE TO ABSORPTION, PRODUCTION AND TRANSFER IN A 2500-litre PuO-FUELLED SPHERICAL ASSEMBLY FOR A TEMPERATURE INCREASE FROM 300 - 900°K IN THE CORE
E_{max} = 2035 eV, E_{min} = 454 eV (nearest resonances included only). The calculation required 6 minutes of computing time on the Philco-2000 computer.

History	Absorption ($\times 10^6$)	Production ($\times 10^6$)	Transfer ($\times 10^6$)	δk ($\times 10^6$)
50	- 1963	644	277	- 1092
100	- 1989	587	64	- 1337
150	- 2002	520	4	- 1477
200	- 1918	561	22	- 1334
250	- 1899 ± 88	568 ± 52	20 ± 34	- 1311 ± 102

In a subsequent calculation three resonances on either side of the neutron energy were included in the cross-section calculation for each resonance sequence of Pu and two for U, taking again only the $\ell = 0$ neutron wave into account (Table III).

In both the above runs about equal parts of the contributions to δk were recorded in the intervals 2035 - 1000 eV and 1000 - 454 eV. It is seen that the inclusion of more distant resonances in the cross-section calculations changes the relative contributions to δk arising from absorption and production somewhat, but the overall effect on δk itself is small.

In Tables IV and V the calculations were extended to the two lowest energy groups, i.e. E_{max} = 9121 eV and E_{min} = 454 eV. Only the nearest resonances for the $\ell = 0$ part of the neutron wave were included.

Output in finer energy intervals showed that 70% of the value of δk was contributed between 2035 and 454 eV. This shows a rather greater Doppler effect for this energy interval than in the case when E_{max} was chosen as 2035 eV, and shows that in the methods described E_{max} should be high enough to avoid sizeable contributions of the Doppler effect above

TABLE III. ADJOINT WEIGHTED CONTRIBUTIONS TO δk DUE TO ABSORPTION, PRODUCTION AND TRANSFER IN A 2500-litre PuO-FUELLED SPHERICAL ASSEMBLY FOR A TEMPERATURE INCREASE FROM 300 - 900°K IN THE CORE
E_{max} = 2035 eV, E_{min} = 454 eV (more distant resonances included in the cross-section calculations). Computation time 9.6 min.

History	Absorption ($\times 10^6$)	Production ($\times 10^6$)	Transfer ($\times 10^6$)	δk ($\times 10^6$)
50	-1257	417	-41	-881
100	-1396	323	16	-1057
150	-1472	290	47	-1135
200	-1592	245	83	-1264
250	-1629 ± 91	260 ± 43	48 ± 45	-1321 ± 110

TABLE IV. ADJOINT WEIGHTED CONTRIBUTIONS TO δk DUE TO ABSORPTION, PRODUCTION AND TRANSFER IN A 2500-litre PuO-FUELLED SPHERICAL ASSEMBLY FOR A TEMPERATURE INCREASE FROM 300 - 900°K IN THE CORE
E_{max} = 9121 eV, E_{min} = 454 eV (nearest resonances only). Computation time 7.9 min.

History	Absorption ($\times 10^6$)	Production ($\times 10^6$)	Transfer ($\times 10^6$)	δk ($\times 10^6$)
30	-3082	490	541	-2052
60	-3703	471	133	-3099
90	-3248	514	99	-2636
120	-3097	451	157	-2489
150	-3112 ± 188	458 ± 68	172 ± 96	-2481 ± 221

this energy. Some of the discrepancy may also be attributed to slight inconsistencies between the nuclear parameters used in the multigroup adjoint flux and in the Monte Carlo calculations.

Finally the calculation for the temperature increase from 300 to 900°K in the core was repeated for cross-sections which included the effects of the nearest resonances for all the resonance sequences appropriate to the $\ell = 0$ and $\ell = 1$ parts of the neutron waves. The results are shown in Table VI. About 70% of the δk was contributed by the lowest energy group (2035 - 454 eV).

TABLE V. ADJOINT WEIGHTED CONTRIBUTIONS TO δk DUE TO ABSORPTION, PRODUCTION AND TRANSFER IN A 2500-litre PuO-FUELLED SPHERICAL ASSEMBLY FOR A TEMPERATURE INCREASE FROM 300 - 1500°K IN THE CORE
E_{max} = 9121 eV, E_{min} = 454 eV (nearest resonances only).
Computation time 7.9 min.

History	Absorption ($\times 10^6$)	Production ($\times 10^6$)	Transfer ($\times 10^6$)	δk ($\times 10^6$)
30	-4304	651	922	-2732
60	-5160	650	378	-4131
90	-4565	732	269	-3564
120	-4402	654	364	-3384
150	-4434 ± 244	665 ± 91	378 ± 143	-3391 ± 301

TABLE VI. ADJOINT WEIGHTED CONTRIBUTIONS TO δk DUE TO ABSORPTION, PRODUCTION AND TRANSFER IN A 2500-litre PuO-FUELLED SPHERICAL ASSEMBLY FOR A TEMPERATURE INCREASE FROM 300 - 1500°K IN THE CORE
E_{max} = 9121 eV, E_{min} = 454 eV (Nearest resonances for $\ell = 0$ and $\ell = 1$ parts of neutron waves).

History	Absorption ($\times 10^6$)	Production ($\times 10^6$)	Transfer ($\times 10^6$)	δk ($\times 10^6$)
30	-1848	175	402	-1271
60	-1983	279	255	-1449
90	-2178	382	172	-1624
120	-2220	432	27	-1761
150	-2083 ± 154	449 ± 57	-7 ± 77	-1641 ± 189

CONCLUSIONS

The present investigation has shown that the direct Monte Carlo calculation of the Doppler effect in fast reactor assemblies does not lead to reliable estimates in reasonable amounts of computer time. The large statistical fluctuations are due to the fact that the Doppler effect is a fine balance between contributions of opposite sign. In addition, considerable fluctuations are introduced during the random walk and energy degradation of the neutron in the assembly, on account of the changes in collision and scattering probabilities with temperature.

In the perturbation approach using a first-order theory the latter fluctuations are avoided since the results are based on Monte Carlo estimates of the unperturbed flux. Additional input is, however, required since adjoint weighting has to be used. The calculations made for a spherical assembly have shown that reasonable accuracy can be attained in computation times, the lengths of which depend mainly on the energy interval studied and the degree of accuracy demanded in the cross-section calculations.

The procedure outlined makes the direct study of special effects such as resonance overlap, higher angular momenta and more complicated geometries possible, since no simplifying assumptions have to be made.

REFERENCES

[1] SHAVIV, G., The Doppler Effect in Fast Reactors, D. Sc. Thesis, Technion, Israel Institute of Technology (1964); see also SHAVIV, G., YIFTAH, S., The effect of plutonium isotopic composition on the Doppler coefficient in fast reactors, Nucl. Applic. 3 (1967) 213.

[2] CODD, J., COLLINS, O.J., Some Calculations Concerning the Influence of Resonance Overlapping on the Doppler Effect in a Dilute Fast Reactor, ANL-6792 (1963).

[3] HUTCHINS, B.A., The Effect of Resonance Overlap on the Doppler Coefficient in a Fast Ceramic Reactor, GEAP 4630 (1964).

[4] FROELICH, R., OTT, K., About the influence of resonance overlapping on calculated Doppler-coefficients of fast reactors, Nucl. Sci. Engng 22 (1965) 490.

[5] MÖLLER, U., Unterprogramme zur Losung neutronenphysikalischer Probleme mit Hilfe der Monte-Carlo-Methode, Part B, KFK 298 (1965).

[6] SHAVIV, G., YIFTAH, S., Monte Carlo investigation of the heterogeneity of fast reactor cores, Nucl. Sci. Engng 24 (1966) 302.

[7] MATTHES, W., Monte Carlo Calculation of the Nuclear Temperature in Fast Reactors, EUR.309.e (1963).

[8] RICHTMEYER, R.D., van NORTON, R., WOLFE, A., "The Monte Carlo calculation of resonance capture in reactor lattices, 2nd Int. Conf. peaceful Uses atom. Energy (Proc. Conf. Geneva, 1958) 16, UN, New York (1958) 180.

[9] MÖLLER, U., Karlsruhe, private communication (1965); see also Ref. [5].

[10] O'SHEA, D.M., THACHER, H.C., Jr., Computation of the resonance line shape functions, Trans. am. nucl. Soc. 6 (1963) 36.

[11] SHAVIV, G., YIFTAH, S., Calculation of the Doppler Effect in Fast Reactors, IA-1039 (R.E.) (1965).

[12] BLÄSSER, G., MATTHES, W., Recent Investigations Concerning the Influence of Non-Uniform Temperature Distribution in Doppler Effect Calculations, EUR 401.e (1963).

[13] BORGWALDT, H., Karlsruhe, private communication (1967).

[14] YIFTAH, S., OKRENT, D., MOLDAUER, P.A., Fast Reactor Cross Sections, Pergamon Press (1960).

DISCUSSION

W.K. FOELL: From your written report I understand that you use the narrow-resonance approximation in this work, but from your oral presentation it appears that you actually calculate the energy dependence of the adjoint function as a function of energy. Could you please explain which method you use?

W. ROTHENSTEIN: The assumptions made in the derivation of the energy-dependent adjoint function are stated in the paper. The final form is reminiscent of a narrow-resonance description.

W.K. FOELL: Can you estimate the magnitude of the effect of including this fine structure?

W. ROTHENSTEIN: From our calculations so far the fine-structure effect does not appear to be large.

METHODS FOR ESTIMATING THE SODIUM TEMPERATURE COEFFICIENT OF A FAST REACTOR

D. WARDLEWORTH AND G. INGRAM
UKAEA REACTOR GROUP,
ATOMIC ENERGY ESTABLISHMENT,
WINFRITH, DORCHESTER, DORSET,
UNITED KINGDOM

Presented by J. L. Rowlands

Abstract

METHODS FOR ESTIMATING THE SODIUM TEMPERATURE COEFFICIENT OF A FAST REACTOR. Calculations of the sodium temperature coefficient of the United Kingdom Prototype Fast Reactor use multigroup diffusion theory and first-order perturbation theory. These approximate methods have been tested firstly, by comparison with transport theory and exact perturbation theory and secondly, by comparison with experiments in Zebra Assembly 7, which was designed to simulate the Prototype Fast Reactor. Additional calculations are required to treat the heterogeneity effects produced by the plate structure of Zebra and these have also been tested, primarily by comparison with measurements in ZPR-VI. This work shows that, with present techniques, there is an uncertainty (confidence limit) of $\pm 2.6 \times 10^{-6}$ δk/°C in the calculated sodium temperature coefficient of the Prototype Fast Reactor.

1. INTRODUCTION

The variation of reactivity with sodium density is most conveniently calculated using first order perturbation theory and multigroup diffusion theory. This method has been used for calculating sodium coefficients for the United Kingdom Prototype Fast Reactor (P.F.R.). The accuracy of the P.F.R. calculation methods has been assessed by comparing calculation with the sodium removal measurements made in Zebra assembly 7, the assembly designed to simulate the P.F.R.

The use of first order perturbation theory and diffusion theory introduces errors into the calculation of temperature coefficients and sodium removal experiments. These errors are assessed in Section 3, by comparing with more precise calculations.

The heterogeneity of the pin cell structure of the P.F.R. has been calculated to have a negligible effect but the heterogeneity of the plate structure of Zebra is, in general, not negligible. The two aspects of heterogeneity are the effect of the fine structure of the broad group flux within the plate cell, and the effect of resonance self-shielding, primarily of ^{238}U. The former effect is treated using the code CELPERT, the latter using an approximate equivalence theorem. The results of these methods are compared in Section 4 with experiments made with different cell structures in ZPR-VI assembly 3.

On the basis of this assessment of the theoretical methods employed, a comparison is made between the Zebra 7 measurements and calculation in Section 5. This indicates that the sodium temperature coefficient of

the P.F.R. as calculated requires to be adjusted and allows an evaluation of the uncertainty in the adjusted coefficient.

2. THE COMPONENTS OF THE SODIUM COEFFICIENT

When sodium is removed from a reactor there are four main effects:

(a) an increase in leakage, producing a negative reactivity change, named the leakage term;

(b) a decrease in absorption in sodium, producing a positive reactivity change, named the absorption term;

(c) an increase in heavy nuclide resonance self-shielding, primarily in ^{238}U, giving an overall positive reactivity change, named the self-shielding term;

(d) a decrease in moderation which may produce reactivity changes of either sign, depending on the core composition, named the moderation term.

The energy dependences of these terms are illustrated in Table I, which contains values calculated for the central region of ZPR-VI assembly 2. Each effect shows a different energy dependence. The effects also show different spatial variations. The absorption, moderation and self-shielding terms all vary approximately with the product of the flux and adjoint flux and so predominate at the centre of the core. The sum of these terms is named the central term. At the edge of the core the leakage term, which varies as the product of the gradients of the flux and adjoint flux, predominates.

It is desirable to test the ability of calculation to predict each of these terms separately. Experimental results are, however, inevitably a combination of these effects. A separation of the leakage term is possible by measuring the sodium coefficient for different regions in the core. A separation of the absorption term is possible by sodium activation measurements. A partial separation of the self-shielding term is possible in a heterogeneous reactor by changing the cell structure.

The sodium coefficient is the sum of terms of different sign and, as will be seen, may itself be much smaller than the terms of which it is composed. It is misleading, therefore, to consider uncertainties in the coefficient in percentage terms. In this paper uncertainties are considered in the leakage term and central term separately.

Adjustments to the calculations made for Zebra 7 to allow for approximate methods will be derived from calculations made for ZPR-VI assembly 2. These two systems have roughly the same critical mass, sodium fraction and flux spectrum. However, the adjoint spectra are very different, and, as a result, the central terms are very different. Percentage adjustments to the central term of ZPR-VI assembly 2 cannot, therefore, be applied directly to Zebra 7. In this paper adjustments to the central term are considered in terms of absolute reactivity per gram of sodium removed from the centre of the systems.

Much of this paper is devoted to considering uncertainties in calculation methods. In this context it will be useful to bear in mind

TABLE I

Energy dependence of the components of the sodium coefficient at the centre of ZPR VI assembly 2, 10^{-7} δk/g

Group	Lower energy bound	Leakage	Absorption	Moderation	Self-shielding
1	3.68 MeV	- 0.008	0.021	+ 0.154	
2	2.23 "	- 0.012	0.0	+ 0.303	
3	1.35 "	- 0.016	0.001	+ 0.439	
4	0.821 "	- 0.026	0.001	- 0.089	
5	0.498 "	- 0.050	0.004	- 0.379	
6	0.302 "	- 0.038	0.008	- 0.126	
7	0.183 "	- 0.030	0.010	- 0.062	0.001
8	0.111 "	- 0.020	0.010	- 0.059	0.003
9	67.4 keV	- 0.015	0.012	- 0.060	0.007
10	40.9 "	- 0.012	0.012	- 0.145	0.018
11	24.8 "	- 0.006	0.011	- 0.131	0.023
12	15.0 "	- 0.004	0.010	- 0.141	0.013
13	9.12 "	- 0.003	0.008	- 0.131	0.012
14	5.53 "	- 0.001	0.006	- 0.075	0.015
15	3.36 "	- 0.001	0.007	- 0.040	0.028
16	2.04 "	- 0.001	0.029	- 0.011	0.040
17	1.23 "	- 0.001	0.010	- 0.011	0.028
18	0.748 "		0.002	- 0.012	0.008
19	0.454 "		0.001	+ 0.001	0.004
20	0.275 "				0.001
21	0.167 "				0.001

that measurements of the sodium coefficient have, at this time, an uncertainty of about 0.04 x 10^{-7} δk/g and that this is equivalent to 6% in the leakage term at the edge of the core in Zebra 7.

3. ACCURACY OF THEORETICAL METHODS

3.1 Theoretical Techniques

The critical enrichment of the Prototype Fast Reactor is calculated using two-dimensional diffusion theory. The change in reactivity on removal of sodium is calculated using multigroup perturbation theory. Data are taken from the FD2 set [1] in which the cross sections for sodium and certain other light elements were obtained using the code ELMOE [2]. When making calculations for Zebra or ZPR-VI, the code CELPERT [3] is used to take account of the fine structure in the plate cells of these reactors. The dependence of ^{238}U resonance self-shielding on the cell structure is allowed for by an approximate equivalence theorem, described in Appendix 1. However, before these methods can be compared with experiment it is necessary to examine the chief uncertainties arising from the use of the approximations entailed.

3.2 Perturbation Theory

In Table II, first order and exact perturbation theory are compared for two regions in a spherical model of ZPR-VI assembly 2. The regions comprise a central sphere with a radius of about 10 cm

TABLE II

Comparison between 1st order and exact perturbation theory, ZPR VI assembly 2 ($10^{-7}\ \delta k/g$)

Region	Method	Leakage	Moderation	Absorption and Self-shielding	Total
Centre	1st order δD	- 0.121	- 0.677	+ 0.396	- 0.402
	1st order $\delta \Sigma_{tr}$	- 0.108	- 0.677	+ 0.396	- 0.388
	Exact	- 0.111	- 0.656	+ 0.391	- 0.376
	Perturbed flux	- 0.116	- 0.647	+ 0.387	- 0.376
	Perturbed adjoint	- 0.106	- 0.665	+ 0.395	- 0.376
Edge	1st order δD	- 1.521	+ 0.087	+ 0.060	- 1.374
	1st order $\delta \Sigma_{tr}$	- 1.329	+ 0.086	+ 0.060	- 1.182
	Exact	- 1.380	+ 0.095	+ 0.058	- 1.227
	Perturbed flux	- 1.385	+ 0.101	+ 0.057	- 1.227
	Perturbed adjoint	- 1.376	+ 0.089	+ 0.060	- 1.227

and a spherical shell about 10 cm thick at the core edge; these are typical of the region sizes used in the experiments in Zebra and ZPR-VI. Exact perturbation theory values can be obtained either using the unperturbed flux and the perturbed adjoint flux or by using the perturbed flux and the unperturbed adjoint. Both methods give the same total sodium coefficient, but differ in the magnitude of the contributions. In Table II, both values are included, as well as the average of the two - labelled "exact".

First order perturbation theory may also be defined in different ways. The leakage term may be made proportional to δD, the change in the diffusion coefficient, or to $\delta\Sigma_{tr}$, the change in the transport cross sections. In Table II both values are included, labelled "δD" and "$\delta\Sigma_{tr}$" respectively.

In this size of zone in ZPR-VI assembly 2 the δD first order theory overestimates the leakage term by 10%, whereas the $\delta\Sigma_{tr}$ theory underestimates by 5%, the two theories differing by 15%. In Zebra 7 the difference between the two theories is 20%, and so the $\delta\Sigma_{tr}$ theory should underestimate the leakage term by $7 \pm 3\%$. In ZPR-VI assembly 2 which was ^{235}U fuelled the first order moderation term is too negative by 0.02×10^{-7} $\delta k/g$. Zebra 7 was ^{239}Pu fuelled, and since the moderation term depends on the energy shape of the adjoint flux and therefore on the fuel, it is necessary to examine this error in more detail.

Table III gives a group breakdown of the moderation term for first order and exact perturbation theory.

The moderation term is proportional to $\phi \frac{\partial \phi^*}{\partial u}$, where ϕ is the flux and $\frac{\partial \phi^*}{\partial u}$ is the lethargy gradient of the adjoint. It can be seen from Table II that when the perturbed adjoint is used the change in the moderation term is small. The perturbed adjoint is an adjoint where sodium, a scattering material, has been removed from the system. The adjoint is steeper, an effect which can clearly be seen in Table III around the turning point in the adjoint at the ^{238}U fission threshold, near group 4. There is also a change in the adjoint shape near the 3 keV resonance of sodium. The perturbed flux is a flux where sodium has been removed and is therefore, harder, there being more neutrons in groups 1-5, fewer neutrons below group 7.

The difference between first order and exact theory for the moderation term is very complex in form and it is, therefore, difficult to predict the precise error in Zebra 7. The differences in the group contributions are, however, small, one or two per cent in most cases, and the overall difference is smaller than the experimental error. An adjustment of the same size as that necessary for ZPR-VI assembly 2, $+ 0.02 \times 10^{-7}$ $\delta k/g$, with a standard deviation of 0.02×10^{-7} $\delta k/g$ should be adequate.

3.3 Diffusion Theory

Table IV compares diffusion theory with transport theory (S_4 approximation) for ZPR-VI assembly 2. The S_4 calculations used the code, STRAINT [4], together with the perturbation theory code, SPERT [5].

TABLE III

Group breakdown of the moderation term (10^{-7} $\delta k/g$) comparing first order and exact perturbation theory

GP	First order	Perturbed flux		Perturbed adjoint	
1	+ 0.166	+ 0.169	+ 3	+ 0.168	+ 2
2	+ 0.326	+ 0.331	+ 5	+ 0.331	+ 5
3	+ 0.474	+ 0.475	+ 1	+ 0.492	+ 18
4	- 0.102	- 0.104	- 2	- 0.092	+ 10
5	- 0.432	- 0.446	- 14	- 0.461	- 29
6	- 0.151	- 0.151	0	- 0.154	- 3
7	- 0.075	- 0.074	+ 1	- 0.075	0
8	- 0.067	- 0.066	+ 1	- 0.065	+ 2
9	- 0.066	- 0.064	+ 2	- 0.059	+ 7
10	- 0.156	- 0.154	+ 2	- 0.154	+ 2
11	- 0.141	- 0.135	+ 6	- 0.138	+ 3
12	- 0.152	- 0.143	+ 9	- 0.151	+ 1
13	- 0.141	- 0.134	+ 7	- 0.146	+ 5
14	- 0.081	- 0.076	+ 5	- 0.090	- 9
15	- 0.043	- 0.045	- 2	- 0.072	- 29
16	- 0.011	- 0.013	- 2	+ 0.024	+ 34
17	- 0.012	- 0.008	+ 4	- 0.011	+ 1
18	- 0.013	- 0.009	+ 4	- 0.013	0

The S_4 and diffusion approximations are compared using both exact perturbation theory and first order perturbation theory, for a central sphere of radius 23 cms, and using first order perturbation theory for the two regions considered in Section 3.2, (a central sphere of radius 10 cm and an edge shell of 10 cm thickness). The first order theory is here defined with the leakage term proportional to $\delta\Sigma_{tr}$.

Both exact and first order calculations show a difference of about 5% in the leakage term and about 0.045 x 10^{-7} δ k/g in the moderation term.

TABLE IV

Comparison of S_4 and Diffusion Theory
ZPR VI assembly 2, sodium coefficients 10^{-7} δk/g

Region	Method	Leakage	Moderation	Absorption and Self-shielding	Total
Sphere radius 23 cms	Exact				
	Diffusion theory	- 0.491	- 0.505	+ 0.309	0.686
	S_4	- 0.468	- 0.459	+ 0.310	0.618
	1st Order				
	Diffusion theory	- 0.469	- 0.555	+ 0.332	0.693
	S_4	- 0.449	- 0.512	+ 0.333	0.628
Sphere radius 10 cms	Diffusion theory	- 0.108	- 0.677	+ 0.396	0.388
	S_4	- 0.093	- 0.629	+ 0.399	0.323
Core edge 10 cms thick	Diffusion theory	- 1.329	+ 0.086	+ 0.060	1.182
	S_4	- 1.290	+ 0.098	+ 0.059	1.133

A group breakdown of the moderation term is shown in Table V. The difference between S_4 and diffusion theory arises out of the different estimates of the leakage fraction. This produces a slightly steeper adjoint spectrum in the S_4 approximation. This difference will be a function of the leakage fraction, not of the fuel type, and should therefore be of the same magnitude in Zebra 7, about $0.05 \pm 0.02 \times 10^{-7}$ δk/g.

The spatial variation of the leakage term is shown in Table VI. The error in diffusion theory is very large at the centre of the system, where the leakage term is small, falling to less than 5% where the leakage term is important. The error in diffusion theory should be of the same magnitude in the Zebra 7 experiments, about $3 \pm 1\%$.

TABLE V

Group breakdown of the moderation term comparing diffusion theory and the S_4 approximation (10^{-7} $\delta k/g$)

GP	Diffusion theory	S_4	
1	+ 0.166	+ 0.173	+ 7
2	+ 0.326	+ 0.333	+ 7
3	+ 0.474	+ 0.481	+ 7
4	- 0.102	- 0.091	+ 11
5	- 0.432	- 0.421	+ 11
6	- 0.151	- 0.145	+ 6
7	- 0.075	- 0.072	+ 3
8	- 0.067	- 0.066	+ 1
9	- 0.066	- 0.066	0
10	- 0.156	- 0.157	- 1
11	- 0.141	- 0.142	- 1
12	- 0.152	- 0.153	- 1
13	- 0.141	- 0.142	- 1
14	- 0.081	- 0.082	- 1
15	- 0.043	- 0.043	0
16	- 0.011	- 0.011	0
17	- 0.012	- 0.012	0
18	- 0.013	- 0.013	0

4. COMPARISON WITH EXPERIMENTS IN ZPR-VI

4.1 ZPR-VI Assemblies 2 and 3

The results of plate removal experiments in ZPR-VI assemblies 2 and 3 are shown in Table VII, where they are compared with calculation. The tables are diagrammatic representations of one quadrant of the core elevations. The regions are fully defined in references [6] and [7]. The calculated values were obtained using

TABLE VI

The leakage term as a function of radial position, comparing diffusion theory and the S_4 approximation (δk)

Radius (cm)	Diffusion theory	S_4	Ratio
2.5	2.96×10^{-8}	4.88×10^{-9}	6.07
4.9	5.00×10^{-7}	3.06×10^{-7}	1.64
7.4	2.82×10^{-6}	2.28×10^{-6}	1.24
9.9	9.64	8.57	1.13
12.1	2.20×10^{-5}	2.05×10^{-5}	1.07
14.4	4.48	4.25	1.05
16.7	8.11	7.79	1.04
19.8	1.98×10^{-4}	1.89×10^{-4}	1.05
22.8	3.46	3.33	1.04
25.4	4.49	4.37	1.03
28.0	6.33	6.18	1.03
30.6	8.56	8.36	1.02
33.2	1.11×10^{-3}	1.09×10^{-3}	1.02
35.7	1.40	1.37	1.02
38.3	1.71	1.67	1.02
40.9	2.03	1.99	1.02
43.5	2.35	2.30	1.02
46.1	2.66	2.59	1.03
48.7	2.93	2.85	1.03
51.2	3.16	3.05	1.04

a homogeneous model, first order perturbation theory and diffusion theory. Calculation gives good agreement with experiment at the centre of assembly 2, which had an L/D of unity, whereas the agreement at the centre of assembly 3, which had the same composition and the same plate structure but an L/D of $\frac{1}{3}$, is poor. A similar trend is apparent from the calculations of Helm and Travelli [8]. It is a discrepancy which shows itself in all the

TABLE VII

Comparison of calculation and experiment (ZPR VI)
Results expressed as 10^{-7} $\delta k/g$ of sodium

Assembly 2

- 1.72 - 1.52	- 1.26 - 1.35	- 1.19 - 1.10	- 0.77 - 0.82
- 0.92 - 0.96	- 0.98 - 1.14	- 1.27 - 1.29	- 1.21 - 1.29
- 0.43 - 0.45	- 1.02 - 0.89	- 1.37 - 1.34	- 1.65 - 1.57

Assembly 3

- 1.29 - 1.70				
- 1.11 - 1.30				
- 0.52 - 0.75				
- 0.04 - 0.28	- 0.24 - 0.48	- 0.48 - 0.55	- 0.50 - 0.55	- 0.47 - 0.39

The figures in each block are:-

Experiment
FD2 calculation

measurements near the centre and cannot be regarded as being the result of one wayward measurement. The calculated central term is too negative by about 0.25×10^{-7} δk/g, a larger error than any identified elsewhere in this paper.

There is clearly something which is not being accounted for in the theoretical models, i.e., in homogeneous, two-dimensional diffusion theory. No explanation of this discrepancy has so far been found. It must remain to throw some doubt on the interpretation of sodium coefficient measurements.

4.2 Heterogeneity Effects in Zero Power Reactors

Measurements in ZPR-VI assembly 3 where sodium plates were removed from cells with various plate arrangements provide information about heterogeneity effects. The plate distributions are shown in Table VIII which also compares experimental results with calculation. The two effects in the table are the result of:-

(a) the change in the fine structure in the broad group fluxes, calculated using the program CELPERT;

(b) the change in the self-shielding term, calculated using an approximate equivalence theorem.

These cells have also been studied by Meneghetti [9]. The values quoted represent the change in sodium coefficient from the standard cell (cell A). The calculations indicate that the self-shielding effect predominates and the comparison with experiment is consistent

TABLE VIII

Comparison of calculated heterogeneity effects with experiment
Results expressed as 10^{-7} δk/g

Cell			Calculation			Experiment
			CELPERT	RESONANCE	TOTAL	
A (30 cm high)	From	D N C E D N C D N E C D N	-	-	-	-
	to	D V C E D V C D V E C D V				
G (30 cm high)	From	D C E D N N C D E C D N N	+ 0.021	- 0.031	- 0.010	- 0.047 ± 0.022
	to	D C E D V V C D E C D V V				
H (30 cm high)	From	N N N N D C E D C D E C D	+ 0.028	- 0.072	- 0.044	- 0.144 ± 0.022
	to	V V V V D C E D C D E C D				
A (50.8 cm high)	From	D N C E D N C D N E C D N	-	-	-	-
	to	D V C E D V C D V E C D V				
D (50.8 cm high)	From	D N C E C N C D N D E D N	+ 0.011	+ 0.051	+ 0.062	+ 0.084 ± 0.019
	to	D N C E C N C D V D E D V				
E (50.8 cm high)	From	D N C E C N C D N D E D N	- 0.027	- 0.060	- 0.087	- 0.129 ± 0.019
	to	D V C E C V C D N D E D N				
F (50.8 cm high)	From	D N C E C N C D N D E D N	- 0.010	- 0.004	- 0.014	- 0.024 ± 0.019
	to	D V C E C V C D V D E D V				

Notes: 1. Values quoted represent difference between Na coeff. in lattice and that in A.

2. D = depleted uranium 3 mm thick
E = enriched uranium 1.6 mm thick
C = graphite 3 mm thick
N = sodium 6 mm thick
V = empty sodium can 6 mm thick

TABLE IX

Comparison of Zebra 7 experimental results with calculation (10^{-7} δk/g of sodium)

Zone (cm)	0–15.2	15.2–25.4	25.4–45.7	30.5–45.7	15.2–45.7
Calculation					
Leakage	- 0.05	- 0.26	- 0.63	- 0.70	- 0.51
Moderation	0.60	0.50	0.34	0.31	0.39
Absorption	0.12	0.10	0.06	0.05	0.08
Self-shielding	0.09	0.08	0.05	0.04	0.06
Total	0.76	0.42	- 0.17	- 0.30	+ 0.02
Experiment					
Cell 3 (Horiz.)	0.66 ± 0.03	0.29 ± 0.05	- 0.30 ± 0.05		- 0.11 ± 0.02
Cell 2 (Vert.)	0.65 ± 0.07				- 0.22 ± 0.03
Cell 1 (Horiz. and Vert.)	0.68 ± 0.07			- 0.49 ± 0.04	- 0.11 ± 0.04
Small Sample	0.45 ± 0.06	0.04 ± 0.06	- 0.42 ± 0.06	- 0.50 ± 0.06	- 0.25 ± 0.06

with this being underestimated by 50%. It is assumed that the most likely source of error lies in the heterogeneity correction, and an adjustment of 50 ± 50% should be applied to this correction in Zebra 7.

Since the effect calculated by CELPERT is small for these and other experiments (it is of the same order as the experimental errors), there is no evidence that it is, or is not, being correctly calculated. The effect, though small, is, like the sodium coefficient itself, a combination of positive and negative terms. Thus, although it is calculated as 0.02 x 10^{-7} δk/g at the centre of Zebra 7, this is probably uncertain by ± 0.04 x 10^{-7} δk/g.

Of the results quoted in Table VIII only that for cell H, containing a zone of four sodium plates (i.e., one inch) thick, cannot be explained in terms of a 50% error in the resonance self-shielding effect. In this case there is some evidence of a streaming effect, corresponding to an addition of about 20% in the leakage term.

5. THE ZEBRA 7 AND P.F.R. SODIUM COEFFICIENTS

5.1 The Zebra Core 7 Measurements

The Zebra 7 results provide experimental data closest to that for a plutonium-fuelled power reactor and so provide the best test of the reliability of the theoretical techniques applied to the Prototype Fast Reactor. Plate removal measurements at the core centre give experimental values of the combined absorption, moderation and self-shielding effects and similar measurements at the edge give experimental values of effects which are primarily due to leakage. Activation measurements with a sodium plate give a measure of the absorption term. Measurements at the edge of the core with different plate orientations indicate that the leakage effect can be increased by neutron streaming in some geometries.

Three series of plate removal measurements were made at the centre of the inner region of Core 7. In each series the measurements were similar but the orientation of the plates was changed. In the first series, the plates were partly horizontal and partly vertical. In the second series, to minimise the difficulties associated with calculating fine structure and resonance shielding effects, all the plates were horizontal. In the third and final series, all the plates were vertical to enhance streaming effects. The cell arrangements in these measurements are shown in Fig. 1. All the plate removal measurements were confined to the central 9 elements which were part of a zone of 25 identical elements (45 in the case of the first series of measurements). The remaining elements in the inner region of the core had similar compositions but a different plate structure. The major uncertainty in the experimental results lies in the correction applied to allow for changes in temperature in the core during the experiments. The results for the horizontal plates include a correction to allow for the reduction in core height when the stainless-steel clad sodium plates were replaced with stainless steel rings with the same weight as the cladding. This correction was small, being about 5% of the total effect, and introduced a negligible error.

In addition to the plate removal measurements, perturbation scans were made in the central element with a sodium sample, with a mean chord length approximately the same as that of a sodium plate, which sampled the average flux over $1\frac{1}{2}$ cells. The results of these and the plate removal measurements are summarised in Table IX.

An additional error which is not included in the experimental results is due to the uncertainty in the absolute reactivity. Two methods were used to establish the absolute reactivity scale in assembly 7. The first used period measurements and a calculated delayed neutron fraction. The second consisted of normalising the measured worth of a ^{239}Pu sample at the centre of the core to the value calculated using perturbation theory. The result obtained by the second method was 10% higher than the first. Although part of this discrepancy can be explained by errors in the ^{239}Pu data, the remainder must be attributed to some other uncertainty in the absolute reactivity scale. The measured sodium coefficients were obtained assuming the first method and should be increased by 5%, with an uncertainty of $\pm$ 5%.

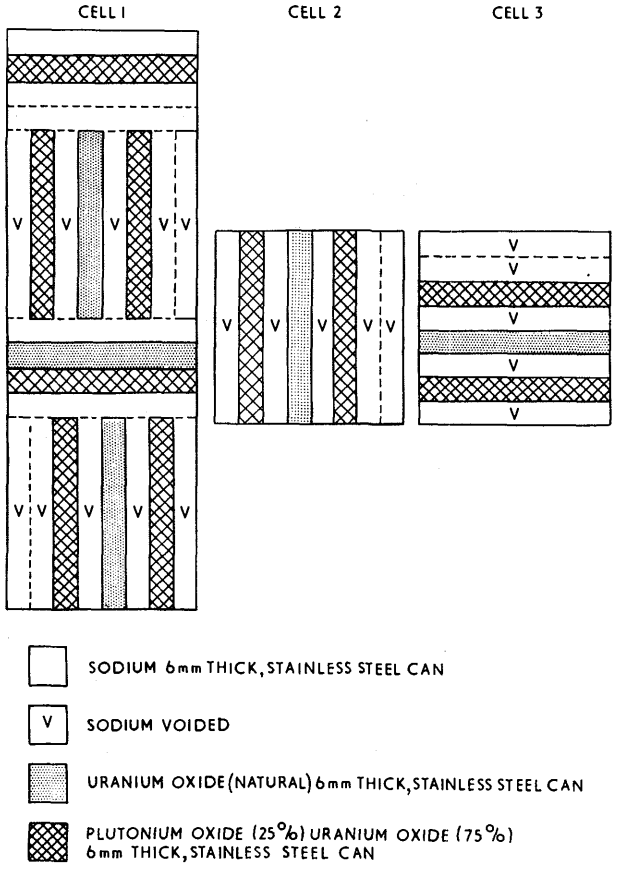

FIG.1. ZEBRA 7 central cells.

Comparison of the experimental results in Table IX for three different cell arrangements shows that all agree at the core centre. The difference between the plate results and that for a small cylindrical sample is thought to be due to a change in the self-shielding term. The differences between the measurements at the core edge are attributed to a modification of the leakage term by streaming. The main leakage direction is vertical and when the streaming paths in this direction are cut off by turning the plates through 90°, the change in the coefficient is 0.11×10^{-7} $\delta k/g$, which is 17% of the leakage term. When the plates are horizontal, there will be streaming in the radial direction but since the radial leakage is very small, the streaming effect should be negligible.

5.2 Comparison of Calculation with Experiment

The calculated results for Zebra 7 are also shown in Table IX. The calculations use a first order perturbation theory with the leakage term proportional to $\delta\Sigma_{tr}$.

TABLE X

Summary of adjustments to Zebra 7 sodium coefficient

	Central term	Leakage term
Theory		
Perturbation theory	+ 2 ± 2%	+ 7 ± 3%
Diffusion theory	+ 6 ± 2%	- 3 ± 1%
Self-shielding	+ 6 ± 6%	
CELPERT	- 2 ± 4%	
Total	+ 12 ± 8%	+ 4 ± 3%
Experiment		
Reactivity scale	+ 5 ± 5%	

The adjustments that need to be made to the experimental and calculated sodium coefficients in Zebra 7 because of the approximations used in the theoretical model are collected together in Table X together with their uncertainties. The adjustments to be made to the central term are expressed here in terms of percentages. Although these are adjustments which were derived for the sodium coefficient at the centre of the system they apply to other positions in the core, since, as can be seen from Table IX, the components of the central term vary proportionately away from the core centre. It must be emphasised that these percentage adjustments only apply to Zebra 7. For example, the absolute adjustment assigned to diffusion theory in Section 3.3 is + 0.05 x 10^{-7} $\delta k/g$. This corresponds to a percentage adjustment of 6% at the centre of Zebra 7 but clearly could result in a totally different percentage adjustment in another core.

Adjusted coefficients are compared in Table XI. The experimental coefficients are derived from the measurements made with cell 3, (all horizontal plates), in which the effect of streaming should be negligible. The remaining discrepancy will be the result of errors in the data in the FD2 set. The least squares estimates for the discrepancies due to data for the terms separately are - 19 ± 7% for the central term and + 10 ± 13% for the leakage term. The theoretical coefficients with these further adjustments applied are also compared in the table.

The most likely source of the 19% error in the central term, equivalent to 0.18 x 10^{-7} $\delta k/g$ at the centre, is the moderation term. The self-shielding term would have to be in error by a further factor of 2 beyond the adjustment already made to explain an error of this size. Also, activation measurements with a

TABLE XI

Comparison between adjusted coefficients (10^{-7} δk/g)

Adjusted according to Table X

Zone (cm)	Experiment	Theory	Central	Leakage
0 - 15.2	0.69 ± 0.04	0.86 ± 0.06	0.91 ± 0.06	- 0.05 ± 0.01
15.2 - 25.4	0.30 ± 0.05	0.49 ± 0.05	0.76 ± 0.05	- 0.27 ± 0.01
25.4 - 45.7	- 0.31 ± 0.05	- 0.15 ± 0.05	0.50 ± 0.04	- 0.65 ± 0.03

With further adjustment for data errors

Zone (cm)	Experiment	Theory
0 - 15.2	0.69 ± 0.04	0.68 ± 0.08
15.2 - 25.4	0.30 ± 0.05	0.32 ± 0.09
25.4 - 45.7	- 0.31 ± 0.05	- 0.32 ± 0.10

sodium plate at the centre of the core show that calculation underestimates the absorption term by only 10%, equivalent to 0.01 x 10^{-7} δk/g.

5.3 The Effect of ^{240}Pu Content

Zebra 7 contained plutonium with 5% ^{240}Pu content; the P.F.R. in its initial loading will contain 16% ^{240}Pu. Measurements in Zebra 6 [10] showed that calculation underestimated the effect of ^{240}Pu on the central sodium coefficient by 0.015 x 10^{-7} δk/g per % ^{240}Pu. Since the P.F.R. has a critical mass about three times that of Zebra 6, the corresponding error will be 0.005 x 10^{-7} δk/g per % ^{240}Pu. This is an adjustment of 0.06 x 10^{-7} δk/g in extrapolating from 5% to 16% ^{240}Pu, or 8% of the central term. An uncertainty equal to the size of the adjustment has been assumed.

5.4 The Sodium Temperature Coefficient of the P.F.R.

Table XII shows the sodium temperature coefficient for the core of a model of the P.F.R., together with the leakage and

TABLE XII

The PFR coefficient (core only)

Adjustments to be made	Central term	Leakage term
Data errors	- 19 ± 7%	+ 10 ± 13%
Diffusion theory	+ 6 ± 2%	- 3 ± 1%
^{240}Pu content	+ 8 ± 8%	
	- 5 ± 11%	+ 7 ± 13%
Adjusted coefficient 10^{-6} δk/°C		
	As calculated	Adjusted
Central term	+ 8.3	+ 7.9 ± 0.9
Leakage term	- 6.8	- 7.3 ± 0.9
Total	+ 1.5	+ 0.6 ± 1.3

central terms. This coefficient can be adjusted on the basis of the Zebra 7 measurements by making the following assumptions.

(a) The P.F.R. on start-up has the same composition as Zebra 7, except for ^{240}Pu content. Thus the discrepancies which were found in Section 5.2 between calculation and experiment for Zebra 7, and which were attributed to errors in nuclear data, can be applied as an adjustment to the P.F.R. An adjustment as detailed in Section 5.3 must also be made for the effect of the different ^{240}Pu content.

(b) In the P.F.R., heterogeneity effects are small. No adjustments need therefore be applied.

(c) First order perturbation theory is accurate for temperature coefficients. No adjustment need therefore be applied.

(d) The error in diffusion theory is independent of the size of the perturbation. An adjustment must be applied of the same size as that applied to the Zebra 7 calculations.

These adjustments and the adjusted coefficients are also in Table XII. The uncertainty quoted in the table is a standard deviation. Thus with 95% confidence, the sodium coefficient for the P.F.R. core is + 0.6 ± 2.6 x 10^{-6} δk/°C. This confidence level applies to the clean core, since no account has been taken of the effects of burn-up of the fuel.

That this level of uncertainty is reasonable can be seen more simply in the following way. A coefficient of 0.1 x 10^{-7} $\delta k/g$ of sodium is equivalent to 1.7 x 10^{-6} $\delta k/^{\circ}C$. An uncertainty of about 0.1 x 10^{-7} $\delta k/g$ in the central worth of sodium would be equivalent to about 1 x 10^{-6} $\delta k/^{\circ}C$ when averaged over the whole core. Thus the uncertainty of 0.9 x 10^{-6} $\delta k/^{\circ}C$ assigned to the central term is equivalent to an uncertainty of about 0.1 x 10^{-7} $\delta k/g$ in the central worth. The experimental uncertainty was 0.04 x 10^{-7} $\delta k/g$. The additional uncertainty has arisen in the interpretation of the measurement and in the extrapolation from Zebra 7 to the P.F.R. A "perfectly interpretable" experiment of the kind at present performed would not decrease the uncertainty by much more than a factor of two.

The confidence level of $\pm$ 2.6 x 10^{-6} $\delta k/^{\circ}C$ should be compared with the estimated P.F.R. temperature coefficient (all effects) of 25 x 10^{-6} $\delta k/^{\circ}C$, i.e., the uncertainty is $\pm$ 10% in the overall temperature coefficient. The uncertainty is also equivalent to $\pm$ 3% in the power coefficient, and to an uncertainty of $\pm$ 3 cents in the reactivity change on voiding a central subassembly. The uncertainty is, therefore, small from the point of view of reactor performance.

6. CONCLUSIONS

The methods used at present in the U.K.A.E.A. to calculate sodium coefficients are expected to predict the overall sodium temperature coefficient for the P.F.R. core correctly to within $\pm$ 2.6 x 10^{-6} $\delta k/^{\circ}C$ (confidence limit). This uncertainty is small from the point of view of reactor performance. It is not claimed that the methods would predict the sodium coefficient correctly within this uncertainty for fast reactors other than the P.F.R. This claim rests heavily on the prediction of the coefficient in a mock-up of the P.F.R., and the level of uncertainty has been assigned as a combination of calculation and experimental errors, and uncertainties introduced in extrapolating from the P.F.R. mock-up to the P.F.R.

The main problem in the interpretation of the measurements in Zebra 7 is the heterogeneity of Zebra 7. Resonance effects have been calculated using a simple approach and there is some evidence that this is not altogether satisfactory. The plate arrangement used in Zebra was sufficiently simple to allow an S.D.R. calculation [11], which should improve the estimate of these effects. The experiments indicate that streaming effects do exist in sodium coefficient measurements, but they are probably not important in favourable geometries. However, some theoretical means of checking this hypothesis is desirable.

It has been pointed out in Section 4.1 that the measurements made in ZPR-VI assembly 3 are anomalous when compared with those made in assembly 2. The anomaly is of the order of 0.25 x 10^{-7} $\delta k/g$ in the central term in assembly 3. The corresponding error in the P.F.R. temperature coefficient would be about 3 x 10^{-6} $\delta k/^{\circ}C$. No account of this anomaly was taken in assessing the confidence limit of $\pm$ 2.6 x 10^{-6} $\delta k/^{\circ}C$, since there is no evidence of an equivalent effect in Zebra 7. But since no explanation of the anomaly is available, there must remain a significant doubt.

7. REFERENCES

[1] SMITH, R. W., ROWLANDS, J. L., WARDLEWORTH, D., "The FD2 group averaged cross section set for fast reactor calculations," UKAEA Rep., AEEW-R 491.

[2] RAGO, A. L., HUMMEL, H. H., "Elmoe; an IBM-704 program treating elastic scattering resonances in fast reactors", USAEC Rep., ANL 6805.

[3] JAMES, M. F., MATTHEWS, J. D. "A perturbation method for multigroup transport calculations in plane lattices", UKAEA Rep., AEEW-R 219.

[4] WADE, R. D. et al., "Solution of the one dimensional multi-group stationary neutron transport equation on the IBM 7030 computer", UKAEA Rep., AWRE O-12/63.

[5] COLLINS, P. J., Private communication.

[6] GRIFONI, S., NOZAWA, M., KATO, W. Y., "Sodium void coefficient measurements in a large carbide fast assembly", Trans. Am. Nucl. Soc. 7 2 (1964) 250.

[7] HELM, F. H. et al., "Critical facility measurements of the sodium void coefficient in a large disc-shaped fast reactor core", Trans. Am. Nucl. Soc. 8 1 (1965) 245.

[8] HELM, F. H., TRAVELLI, A., "Calculation of the sodium void effect in a large carbide core", Proceedings of international conference on fast critical experiments and their analysis, Argonne (1966), USAEC Rep., ANL 7320.

[9] MENEGHETTI, D., "Calculational studies of sodium-void reactivity variations due to thin slab heterogeneities in fast critical assemblies", Proceedings of international conference on fast critical experiments and their analysis, Argonne (1966), USAEC Rep., ANL 7320.

[10] ADAMSON, J. et al., "Zebra 6: A dilute plutonium-fuelled assembly", Proceedings of international conference on fast critical experiments and their analysis, Argonne (1966), USAEC Rep., ANL 7320.

[11] BRISSENDEN, R. J., DURSTON, C., "Calculation on neutron spectra in the doppler region", Proceedings of the conference on the application of computing methods to reactor problems, May 1965, p.51, ANL-7050.

[12] BELL, G. I., "Theory of effective cross sections", USAEC Rep., LA-2322.

APPENDIX

A SIMPLE EQUIVALENCE THEOREM FOR A COMPLEX SLAB LATTICE CELL

Consider the slab cell

$$A\ M_1\ \underline{A}\ M_2\ A\ M_3$$

of three absorber plates, A, of the same kind and three different moderator plates, M. The flux in an absorber plate is given by

$$\phi = \frac{1}{E}\left\{\frac{\Sigma_s}{\Sigma} + P\left(1 - \frac{\Sigma_s}{\Sigma}\right)\right\}$$

where E is energy

Σ_s is the scattering cross section in the absorber

Σ is the total cross section in the absorber

P is the probability that a neutron which made its last collision in the absorber makes its next collision in any moderator region (see, for example, ref. [12]).

P is clearly the sum of two quite independent probabilities, for neutrons going to the right and for those going to the left. The flux is therefore the sum of two independent fluxes, that of neutrons impinging from the right, and that from the left. The average cross section for the plate,

$$[\sigma] = \frac{\int \sigma \phi \, d\,E}{\int \phi \, d\,E} \approx \tfrac{1}{2}\,(\sigma_R + \sigma_L)$$

is approximately the average of two independent cross sections, again from the right and from the left. The cross section from the right for the underlined plate will to a first approximation be that for a lattice whose basic cell is the binary, AM_2; that from the left the binary AM_1. The cross sections for the other plates can be similarly defined. These are then:-

$\tfrac{1}{2}\,(\sigma_1 + \sigma_2)$, for the underlined plate

$\left.\begin{array}{l}\tfrac{1}{2}\,(\sigma_1 + \sigma_3)\\ \tfrac{1}{2}\,(\sigma_2 + \sigma_3)\end{array}\right\}$ for the other two plates

where σ_1 corresponds to the binary lattice AM_1, etc.

The cross section for the cell, assuming a flat average flux through the cell, will be just the average of these, which is

$\tfrac{1}{3}\,(\sigma_1 + \sigma_2 + \sigma_3)$.

Thus a simple first approximation to the cross section for a cell is the average of the cross sections for the binary 'subcells' of which this cell is composed.

DISCUSSION

M.F. TROYANOV: Are your calculations two-dimensional?

J.L. ROWLANDS: Yes, they are.

M.F. TROYANOV: How, in your opinion, could the problem of the sodium coefficient be solved in the case of one-dimensional calculations?

J.L. ROWLANDS: We have not studied methods of obtaining sodium coefficients by one-dimensional methods, but I think that synthesis methods, such as those which you are developing, may provide a satisfactory solution.

H.W. KÜSTERS: How do you explain the widely observed discrepancies between the results of small-perturbation experiments and theory?

J.L. ROWLANDS: It has been suggested that the main difference between the measurements made by inserting a small sodium sample into a hole in the reactor and those made by inserting sodium plates into the reactor cell is due to a difference in the change of resonance shielding in the nearby uranium and plutonium (resulting from the change in background scattering). I think that, until we have a Monte Carlo calculation method capable of treating a sample placed in a hole in a heterogeneous reactor, small-sample experiments with scattering materials will not be very fruitful. Strongly absorbing samples are not so sensitive to these effects, and useful measurements might therefore be made for these, particularly when high accuracy is not required.

REDUCING THE VOID EFFECT IN A LARGE FAST POWER REACTOR

H. SPENKE
ABTEILUNG REAKTORENTWICKLUNG,
SIEMENS AG,
ERLANGEN, FEDERAL REPUBLIC OF GERMANY

Abstract

REDUCING THE VOID EFFECT IN A LARGE FAST POWER REACTOR. The coolant void effect has been recognized as one of the most serious safety problems of large, liquid-metal-cooled fast power reactors. Several proposals have been made to reduce the positive void reactivity effect. However, in all cases appreciable penalties with respect to internal breeding ratio, fissile inventory and, finally, economics have to be paid. All these proposals, like the pan-cake core reactor and the annular core reactor, have in common that neutron leakage out of all core zones is artificially increased. Some more detailed calculations of voiding characteristics of large sodium-cooled fast reactors with cylindrical cores indicate that the most important positive contribution to the void reactivity effect arises in the central core zone. Consequently it appears promising to reduce the void effect considerably by increasing deliberately neutron leakage only out of the central core region and not necessarily out of all core regions. Compared with other geometries discussed this suggestion should result in better breeding and economical performance concurrent with a satisfactory void effect.

To support this proposal an investigation was conducted on some significant reactor data (breeding ratios, fissile enrichment, power distribution, etc.) for three geometrically different sodium-cooled fast breeder reactors with a power of 1000 MW(e) each. In the first case a normal cylindrical core geometry (2 core zones, 1 axial and 1 radial blanket) with an H: D ratio of roughly 0.33 was considered. The second reactor was similar to the first, except that the height of the inner core zone was reduced by approximately 50% to enhance neutron leakage in the core centre, the lost core volume being balanced by increasing the outer radius of the second core zone. The third reactor had an annular core with dimensions consistent with those of the first reactor.

Results show a remarkable improvement in the void effect of the variable-core-height reactor compared with the first reactor, but obviously at the cost of a somewhat higher enrichment in fissile plutonium. To achieve a comparably good voiding behaviour in an annular core reactor a higher plutonium enrichment than in the second reactor would be necessary, with the consequence of lower internal breeding ratio and higher fissile inventory.

1. INTRODUCTION

The void effect has been recognized as the central safety problem of large, ceramic-fuelled, sodium-cooled fast power reactors, and much effort has been given to designing fast-breeder cores where this effect is reduced to a tolerable size. The most well-known solutions for this problem are the annular [1], the pancake [2] and the modular [3] core. Basically all these proposals use the same principle to decrease the void-reactivity gain. The sodium loss effect consists mainly of two parts, the positive spectral effect and the negative neutron leakage effect. The spectral effect is practically equal throughout the fissile region whereas the leakage effect increases considerably towards the core boundaries. To produce a low over-all void effect, it is merely necessary to enlarge deliberately the neutron leakage effect. This is exactly what has been done in all the proposals mentioned above. In the annular core as well as

in the pancake core the selected geometries do indeed strongly increase neutron leakage out of all fissile regions, and in the modular core the same effect is achieved in every single module because of its small volume. As a consequence these designs have much lower internal conversion ratios, plutonium specific rating, higher fuel doubling times and fuel-cycle costs than would be attained with a cylindrical core of a reasonably high length-to-diameter ratio.

Updated and refined calculations of these suggestions [4-6], apart from other variations have resulted in some changes of core data: the annular core was reduced in volume by decrease of the inner diameter, the pancake was made thinner so that the L/D ratio decreased from 0.172 to 0.116 and the modular core obtained a higher power density. All these variations, however, did not influence the over-all image of a considerably compromised core and cost characteristics.

2. PROPOSAL FOR AN IMPROVED DESIGN

Because of the economic incentive it appeared worthwhile to investigate further possibilities that reduce the void effect and simultaneously show better breeding and economical performance than the examples of design discussed.

A more careful look at the detailed voiding characteristics seems to indicate a possible method. If the void reactivity gain is plotted versus the radius of the voided zone, a curve with a maximum will usually be found. This maximum value arises approximately in the neighbourhood of the border between the two enrichment zones. It can be concluded from this that in such a reactor the central core regions do contribute positively and the outer core regions negatively to the sodium void effect. Consequently it appears possible to reduce the void effect considerably just by increasing deliberately the neutron leakage from the central fissile region only and not necessarily from the total fissile region, as has been done in the annular, pancake and modular cores.

This local leakage increase can be realized by a continuous or stepwise reduction of the fissile zone length or height from the core boundary to the core centre. Several different stepwise arrangements appear practicable. One extreme would consist of two steps, so that the length of the inner enrichment zone is constant and much lower than that of the outer enrichment zone; the other extreme has a different height of fissile material for each fuel element ring. The continuous reduction of the fissile core length may be of academic interest, but perhaps might be useful in order to compensate the radial power distribution, even within a fuel element, and thus ease the requirements for throttling the sodium flow in each cooling-channel.

It is expected that such a variable-core-length reactor would have satisfactory sodium voiding properties, and at the same time, because of better neutron efficiency, would achieve lower fissile inventories, higher breeding ratios and better economics than the suggestions mentioned previously.

3. PARAMETER SELECTION FOR A REACTOR COMPARISON

To support the variable-core-length concept a study on the main characteristics of three geometrically different, sodium-cooled, oxide-fuelled fast breeder reactors was performed. A power of 1000 MW(e) for each reactor was determined as being representative for future large nuclear power plants. The void effect will usually increase with reactor power, so that 1000 MW(e) appeared to be a good size for comparing the ability of the three selected reactor concepts to reduce the sodium loss reactivity gain.

The first fast breeder taken into consideration consisted of a cylindrical core with two enrichment zones of equal volume, an upper, a lower axial and a radial blanket, and a L/D ratio of approx. 0.33 was assumed. Subsequently this design will be called the normal breeder. Such a reactor will have a void effect of considerable positive size [7] but will be economically attractive.

The second breeder investigated comprises an annular fissile zone, a central, a radial and axial blankets. This core geometry causes a high neutron leakage out of the total fissile region. The annular-core reactor represents the safe but economically unfavourable fast breeder.

The third selected design, the fast breeder with variable core height, is similar to the fast reactor, except that the fissile material height of the first enrichment zone has been reduced by roughly 50%, the lost core volume being balanced by increasing the outer radius of the second enrichment zone. With this geometrical arrangement, the neutron leakage from the central fissile region only is enhanced, so that this reactor should achieve good voiding characteristics similar to the annular-core reactor, but should resemble the normal breeder as far as the other reactor performance data are concerned.

To enable a reasonable comparison to be made of the breeder concepts discussed, the following conditions were observed:

(1) The average core power density was equal for all reactors, i.e. the core volumes were equal. The peak core power density might have been a better standard, as the three reactors certainly will not have the same power peaking factors. To begin the calculations, however, it was considered reasonable to use the above assumption.

(2) The total volume of the axial and of the radial blankets is the same for all reactors.

(3) The length or height of the fissile region was the same for all reactors (except for the first zone of the variable-height breeder).

(4) The radius of the first enrichment zone was equal for all reactors.

Using these assumptions, together with those shown in Table I, the geometrical layout of all three reactors can be determined. Figure 1 shows the three designs in a reduced scale.

4. CALCULATIONS PERFORMED

The intention of the whole study was to obtain data for a relative comparison of the normal, the annular and the variable-height reactor. Therefore no elaborate burn-up calculations were done; only the fresh core and blankets with no fission products and no plutonium build-up were

TABLE I. INPUT DATA FOR ALL REACTOR DESIGNS

1. Reactor power: 2500 MW(th)

   Fissile core: 2400 MW(th), blankets: 100 MW(th)

2. Average core power density: 408 kW/l

3. Plant efficiency : 40%

4. Total volume of fissile regions: 5885 litres

5. Radii (cm):

	Normal breeder	Variable-core-height breeder	Annular-core breeder
Zone 1	99.8	99.8	99.8
Zone 2	141.1	157.9	172.8
Zone 3	181.1	202.7	221.8

6. Heights (cm):

Zone 1	94.1	46.5	116.0
Zone 2	94.1	94.1	94.1
Zone 3	174.1	138.9	116.0

7. Thicknesses of axial blankets (cm):

above and below			
Zone 1	40.0	92.4	0
Zone 2	40.0	44.8	21.9
Zone 3	0	0	0

8. Volume ratios:

	Fissile core and axial blanket	Radial blanket
Fuel (Oxide)	0.3	0.5
Structure	0.2	0.2
Coolant (Na)	0.5	0.3

9. Isotopic compositions (wt%):

   Plutonium: ^{239}Pu: 75; ^{240}Pu: 22; ^{241}Pu: 2.5; ^{242}Pu: 0.5

   Uranium depleted: ^{238}U: 99.75; ^{235}U: 0.25

   Steel: Fe: 68.9; Cr: 16.0; Ni: 13.8; Mo: 1.3

10. Smeared densities:

    Fissile core: 80% of theoretical density

    Blankets: 93% of theoretical density

taken into consideration, because differences between the main reactor properties should be obvious already in the unpoisoned core state.

The most important parameter was the sodium loss effect, which was determined by the method of successive k-calculations. According

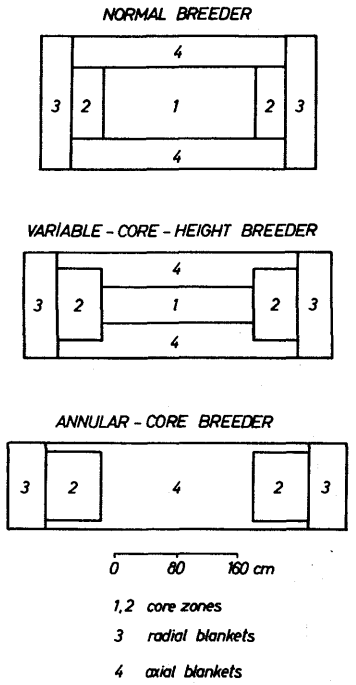

FIG.1. Geometrical core layouts.

to our experience it is advisable to use two-dimensional instead of one-dimensional diffusion theory, because in the latter case one can never be sure whether axial neutron leakage has been taken into account correctly in the different void cases. Consequently we used the following procedure to obtain the void effect:

For each breeder reactor one-dimensional calculations with the Soviet ABBN set gave roughly the critical enrichment. In a second step, macroscopic 26-group constants were condensed to 4-group constants, which were fed into a version of the two-dimensional TWENTY GRAND code. This step was repeated for every single, different void case.

For each reactor design the void reactivity gain was calculated as a function of increasing radius of the voided zone. It is also important to consider the influence of partial or complete axial sodium loss on the reactivity gain. Investigations have found [5] that maximum void reactivity gain will be achieved in a fast reactor when axial sodium loss amounts to approximately two-thirds of the fissile region height. At complete axial sodium loss, i.e. void over the whole reactor length, the reactivity gain will be substantially lower.

As this study was concerned only with relative voiding behaviour, only the case of complete axial sodium loss was calculated. Additionally one partial axial sodium loss case for the normal and the variable-height breeder reactor was considered.

Apart from the coolant void effect, which is not decisive for a breeder concept exclusively, the following significant reactor data for all designs were computed: fissile inventory, internal and total breeding ratios, power density distributions and power peaking factors. Finally these

parameters were used for a fuel-cycle cost calculation. The following assumptions were made: Private fuel ownership; radial blanket is separately exchanged every second core-loading; maximum burn-up 80 000 MWd/ton (U + Pu); fabrication and refabrication costs for core, axial and radial blanket were 1000, 240 and 200 DM/kg; reprocessing costs for core, axial and radial blanket were 330, 330 and 200 DM/kg; interest rate 7%; insurance rate 2.7%; and plant life 17 years.

5. RESULTS AND DISCUSSION

The results of this study are presented in Table II and Figs 2-5.

Figure 2 shows the void reactivity effect as a function of the radial void zone for the normal, the annular and the variable-height breeder reactor. Axially the coolant loss included core and blanket.

As indicated by earlier investigations [7], the reactivity change upon sodium loss of the normal breeder reactor is positive all over the fissile core. A maximum value of 2.5 $ is attained at the border of the two enrichment zones. Consequently the local void effect in this design is positive in the first and negative in the second core zone.

For the variable-height breeder core a remarkable improvement in the void reactivity behaviour was found compared with the normal breeder. Starting from the core centre towards the outer core regions the void effect steadily decreases to more and more negative values, which means that the local void effect, too, is negative throughout the fissile zones.

The annular breeder reactor also shows good voiding properties. The integral as well as the local void effect both assume only negative values in all reactor zones. However, at the end of the first zone and at the beginning of the second zone the void reactivity loss is not as high as in the variable-length breeder reactor. This situation can, of course, be changed by varying the annular core geometry, but this will probably result in even higher penalties with respect to fissile enrichment, breeding ratios, etc. One might also argue about the assumption of complete void in the central, fertile zone before sodium loss is propagated into the fissile annulus. If, however, sodium does fill the first zone and the coolant loss starts at the inner interface of the fissile zone, one has to expect a less negative or even positive reactivity change, because of the much better neutron reflection back into the fissile region.

It has already been mentioned that a maximum void reactivity effect will be found upon partial and not upon complete axial coolant loss. To find out whether this situation changes the favourable voiding behaviour of the variable-height breeder compared with the other designs, two more void calculations were performed. The first referred to a void case of the normal breeder, where radially sodium was lost up to the end of the first zone and axially up to 15 cm above and below the reactor midplane. The second case considered the same partial void in the variable-height breeder reactor. The first computation resulted in a $\Delta k/k$ of + 1.03% and the second in a $\Delta k/k$ of + 0.51%, i.e. under the same circumstances a positive reactivity is produced in the normal breeder twice as high as that in the variable-length breeder. The same calculation for the annular core breeder was not done, but in this case one would expect this reactor to have a void effect somewhat better or equal to that of the variable-height breeder.

TABLE II. RESULTS

	Normal breeder	Variable-core-height breeder	Annular-core breeder
1. Enrichments $\left(\text{at.}\% \frac{\text{Pu}^{\text{fissile}}}{\text{Pu + U}}\right)$			
Zone 1	12.47	16.85	0
Zone 2	16.57	16.85	19.24
Average	14.52	16.85	19.24
Average ($k_{eff} = 1$)	14.54	16.75	19.07
2. Breeding ratios			
Zone 1	0.511	0.216	0.189
Zone 2	0.306	0.446	0.550
Axial blanket	0.282	0.325	0.035
Radial blanket	0.246	0.237	0.268
Internal breeding ratio	0.817	0.662	0.550
Total breeding ratio	1.345	1.224	1.042
3. Fissile inventory for $k_{eff} = 1$ ($kg\ ^{239}Pu + ^{241}Pu$)	1944	2231	2541
4. Core fuel mass (kg Pu + U)	13325	13325	13325
5. Radial blanket fuel mass (kg U)	30650	30650	30650
6. Axial blanket fuel mass (kg U)	13054	13054	19637
7. Specific power of fissile material ($MW(th)/kg\ Pu^{fissile}$)			
$k_{eff} = 1$	1.235	1.076	0.945
8. $\frac{\text{Maximum power density}}{\text{Average power density}}$	1.452	1.456	1.536

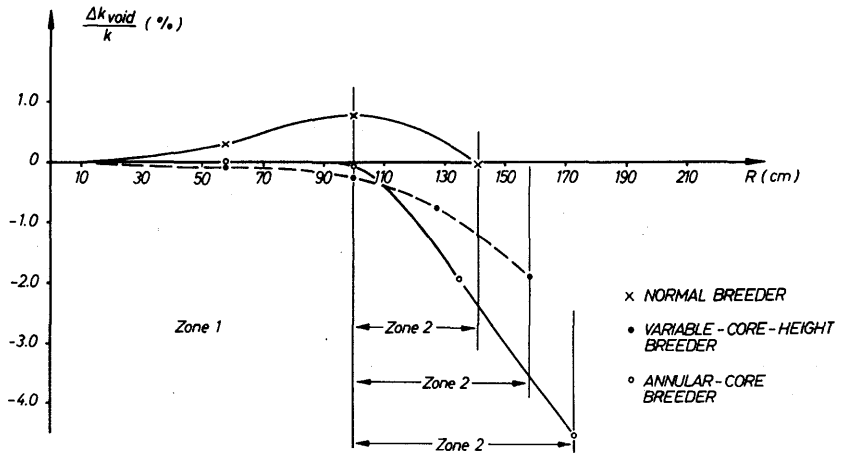

FIG.2. Void reactivity as function of voided radius.

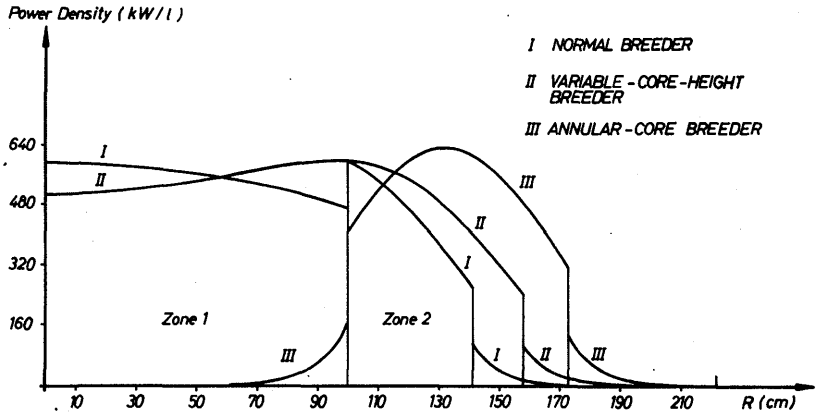

FIG.3. Radial power density distributions in the reactor midplanes.

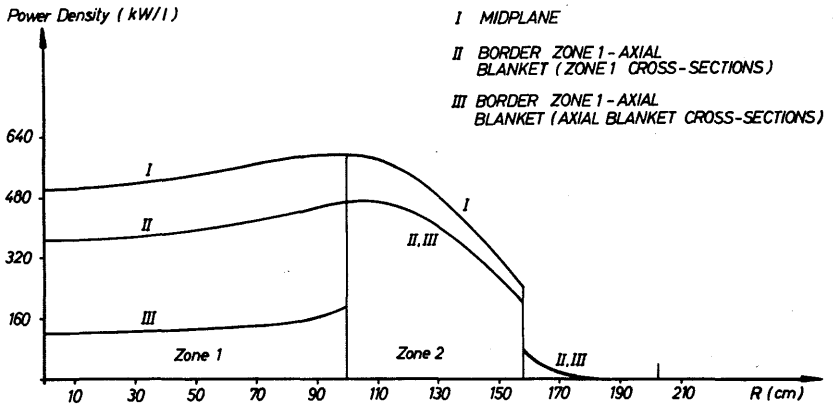

FIG.4. Radial power distributions in different planes for the variable-core-height breeder.

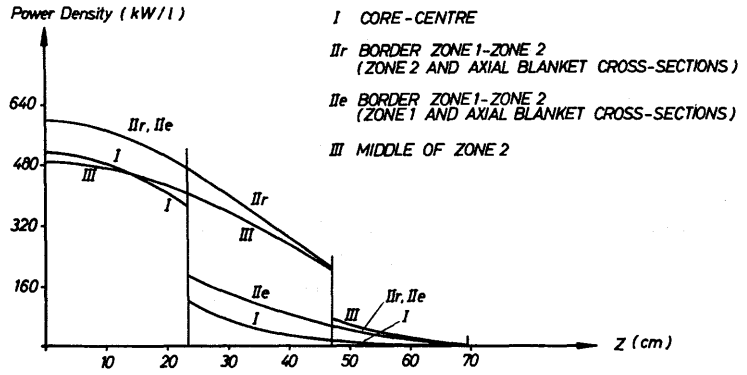

FIG.5. Axial power distributions at different radii for the variable-core-height breeder.

The maximum sodium loss effect for the three designs under investigation has not yet been determined. Qualitative reasoning will lead to the following conclusions:

(1) The normal breeder maximum void effect will be attained at an axial sodium loss up to two-thirds of the core height [5]. Therefore it will be higher than the value ($\Delta k/k = 1.03\%$) found in the above partial loss calculation.

(2) For the variable-height breeder the maximum void effect might already have been found by the above partial axial loss computation, although a definite answer can only be given after additional different radial and axial coolant loss cases have been investigated.

(3) A complete sodium loss out of the fissile annulus will result in a positive reactivity gain in excess of 1 $ [4]. As this value will not be the maximum, a more detailed study of partial axial coolant loss consequences will probably give values similar to those of the variable-height breeder.

Combining all results and reasoning it seems justified to conclude that the variable-height reactor will show a voiding behaviour that is much better than that of the normal breeder and as satisfactory as that of the annular breeder.

The calculations performed resulted in a number of other design data, listed in Table II. Different axial and radial power distributions are shown in Figs 3-5, where those of the variable core-height breeder in particular were considered in more detail.

Some of the data in Table II were corrected for k_{eff} values deviating slightly from exact criticality.

Considering the average fissile enrichments and inventories, the annular breeder (19.07 at.% and 2541 kg) ranks before the variable-height breeder (16.75 at.% and 2231 kg) and the normal breeder (14.54 at.% and 1944 kg). Because of low internal breeding ratios and fission product poisoning, much higher enrichments and fissile inventories have to be used for a realistic design. It should be noticed, however, that the necessary increase in enrichment would be highest for the annular breeder reactor and lowest for the normal breeder.

The internal and total breeding ratios of the three designs differ strongly. The best values are achieved by the normal breeder (0.817 and

1.345), followed by the variable-height breeder (0.662 and 1.224) and finally the annular breeder (0.550 and 1.042).

As far as the power distribution and the power peaking factors are concerned, the remarkable result was found that the selected variable-height breeder showed an optimum power peaking factor when the enrichments in both core zones were equal. The ratio of the maximum and the average power density is equally good for the normal and variable-height breeders (~ 1.45) and somewhat higher for the annular breeder (1.54). Consequently the start from equal average power densities for all three concepts now appears justified, at least for the normal and the variable-height breeder design. However, the annular breeder design data will have to be modified towards somewhat more unfavourable values than have been assumed in Table I.

The fuel cycle cost calculations gave the following results:

Normal breeder	0.361 Dpfg/kWh	(= 0.90 mills/kWh)
Variable-height breeder	0.437 "	(= 1.09 mills/kWh)
Annular breeder	0.493 "	(= 1.23 mills/kWh)

If the different power peaking factors and the different excess reactivities for the same burn-up were taken into account for all three breeder concepts, the fuel-cycle costs for the variable-core-height breeder would be closer, relatively speaking, to those of the normal breeder than to those of the annular breeder.

6. CONCLUSIONS AND OUTLOOK

From this preliminary study of a variable-core-height breeder design, which has been by no means optimized yet, a number of conclusions can be drawn:

(1) The increase of central neutron leakage by a reduction of the inner enrichment zone height will result in satisfactory negative over-all sodium loss effect. The maximum void effect for this concept will probably be similar to that of an annular-core breeder.

(2) With respect to fissile inventory, breeding ratios, power peaking and economics the variable-core-height breeder is definitely superior to the annular-core breeder. The same conclusion would be more or less valid for the pancake core and modular core breeders, because their main performance data have been shown to be very similar to those of the annular core reactor [4].

(3) Also the variable-core-height breeder has to pay for its satisfactory safety behaviour. Compared with the normal breeder, the reactor and cost data are less attractive.

In the future several properties of the variable-height breeder have to be investigated in more detail: the maximum void effect, influence of burn-up, etc. Optimization of the design and a quantitative comparison with the pancake and modular core breeders would have to follow.

Although some more detailed material appears desirable before coming to a definite conclusion on the merits of the variable-core-height breeder design, the results of this preliminary investigation have already indicated such interesting and favourable features with respect to the safety and economics of large fast breeder reactors that a continued study of this concept seems justified.

ACKNOWLEDGEMENT

The author is grateful to W. Böhm for many helpful discussions.

REFERENCES

[1] Large Fast Reactor Design Study, Rep. ACNP-64503 (1964).
[2] Liquid Metal Fast Breeder Reactor Design Study, Rep. GEAP-4418 (1964).
[3] STECK, R.B., Liquid Metal Fast Breeder Reactor Design Study, Rep. WCAP-3251-1 (1964).
[4] FARMER, W.S., STRAWSON, D.G., Rep. ANL-7120 (1965) 124.
[5] COHEN, K.P., O'NEILL, G.L., Rep. ANL-7120 (1965) 185.
[6] WRIGHT, J.W., GUNSON, W.E., HECK, F.M., DALEAS, R.S., Rep. ANL-7120 (1965) 205.
[7] SMIDT, D., MÜLLER, A., Referenzstudie für den 1000 MWe natriumgekühlten schnellen Brutreaktor (Na 1), Rep. KFK-299 (1964).

DISCUSSION

D.A. SMIDT: All high-leakage designs involve low Doppler coefficients. What are the Doppler coefficients for the design proposed by you?

H. SPENKE: Doppler coefficients have not yet been calculated for a breeder with variable core height. Qualitatively, I would expect the Doppler coefficient of this reactor to be better than those of breeders with annular and pancake cores, provided no additional moderation materials such as BeO are included in the latter cores.

F. STORRER: I should like to comment on the suggestion contained in this paper and on other similar suggestions for eliminating the positive sodium coefficient. One may succeed in solving that particular problem, but I am afraid one may thereby introduce many new ones. These problems, which are usually discovered only at the stage of detailed design, may relate to safety or more fundamental considerations. We are at present working on the detailed design of a prototype and are inclined to think that the simplest design is also the best design.

H. SPENKE: I completely agree with your point of view regarding simplicity of design. In our opinion, however, a variable-height core is, at least at first sight, no more complex than a normal cylindrical core. Moreover, the variable-height core offers certain advantages, such as equal enrichments in both core zones or – in a different arrangement – the reduction or elimination of coolant flow throttling, which make for even greater simplicity.

K.M. JIRLOW: What do you gain by reducing the core height only at the centre as opposed to flattening the core as a whole?

H. SPENKE: As I have explained in the paper, the positive contributions to the void effect arise in the central core region only. Accordingly, if a completely flattened pancake core and a variable-height core have an equal maximum reactivity gain through coolant loss, many neutrons are wasted in the pancake core because neutron leakage is also artificially high in the outer core region, where the void effect is negative even in a design with a high length-to-diameter ratio. As a result, a reduction in the height of the central core region gives better neutron economy than complete core flattening – and hence improvements with

respect to the internal conversion ratio, the fissile inventory and the fuel cycle cost.

K. M. JIRLOW: Did you use the same average rod rating when you compared the specific powers of different designs?

H. SPENKE: Yes, I assumed equal maximum and average linear rod ratings for the three designs investigated. As outlined in the paper, the results justified the assumption of equal average ratings for the normal core with high length-to-diameter ratio and for the variable-height core, whereas the average rating of the annular core would have to be reduced somewhat. This would lead to a slight deterioration in the performance data (enrichment, fissile inventory, breeding ratios) for reactors with this type of core (see Table II).

METHODES DE CALCUL UTILISEES DANS LA CONCEPTION DES GRANDS REACTEURS DE PUISSANCE A NEUTRONS RAPIDES

P. DE MYTTENAERE, M. EGLEME, P. GOLDSCHMIDT, S. PILATE, J. QUENON, A. RENARD ET M. STIEVENART
BELGONUCLEAIRE,
BRUXELLES, BELGIQUE

Abstract — Résumé

METHODS OF CALCULATION USED IN DESIGNING LARGE FAST-NEUTRON POWER REACTORS. Numerous codes have been devised in Belgium for calculations on fast-neutron power reactors. These codes are divided into three categories: neutron calculations, safety calculations, and economic calculations.

The methods developed and programmed for studying the neutron properties of fast reactors form a large complex of interconnected codes. The basic data for these codes are contained in a collection of 26-group sections, which are combined either with the PANOPLIE code, to solve diffusion equations, or the DTF-4 code, to solve transport equations. It is thus possible to determine the neutron distributions and importance values needed to establish the reactor parameters, power distributions and reactivity effects. Fuller information on the effects of geometry, power distribution and coolant voids is obtained with the two-way PANDA code, for which the PANOPLIE code provides the sections with a few groups and which makes possible the use of a triangular matrix. The effects of growth in reactor power and the appearance of fission products are studied with the PENDULE code, which follows the reactor's operation and permits the study of partial reloadings.

Three safety codes are in use or under development. The PROFUSION code was written to study the evolution of an oxide-fuelled fast reactor in cases of over-pressure and flow losses. It permits the calculation of the transitory melting phenomenon and possible fuel displacement. The code is suitable for investigating the beginning of accidents of the meltdown type. The PANIC code was developed to assess energy release in a fast reactor in which reactivity is inserted rapidly. It is suitable for studying the standard meltdown accident but can also be used to study the onset of sodium expulsion accidents. The CARMEN code, which is under development, will have wider applications; it will be suitable for calculating accidents liable to occur in a fast reactor. These include accidents of the reactivity-insertion, coolant-loss and assembly-blockage types. This code can be used to calculate the kinetics of a fast reactor, taking sodium expulsion into account.

The CORCYRE code was devised for parametric studies on fast reactors. It consists of two parts: with the first the reactor characteristics are determined, and with the second the fuel cycle characteristics and the fuel cycle cost characteristics are calculated.

Examples are given to illustrate the use of these codes and indicate the stages in the complete study of a fast power reactor.

METHODES DE CALCUL UTILISEES DANS LA CONCEPTION DES GRANDS REACTEURS DE PUISSANCE A NEUTRONS RAPIDES. De nombreux codes ont été mis au point en Belgique pour le calcul des réacteurs de puissance à neutrons rapides. Ces codes se subdivisent en trois catégories: calculs neutroniques, calculs de sécurité, calculs économiques.

Les méthodes développées et programmées en vue d'étudier les propriétés neutroniques des réacteurs rapides forment un large système de codes interconnectés, qui utilisent comme données de base une bibliothèque de sections à 26 groupes. Ces sections sont fournies soit au code PANOPLIE, qui résout les équations de diffusion, soit au code DTF-4, qui résout les équations de transport. On peut ainsi déterminer les distributions et importances neutroniques qui conduisent aux paramètres du réacteur, aux distributions de puissance et aux effets de réactivité. Pour être mieux renseignés sur les effets de géométrie, de distribution de puissance, de vide de réfrigérant, il faut utiliser le code à deux dimensions PANDA, auquel le code PANOPLIE fournit les sections à nombre réduit de groupes et qui permet l'utilisation d'un pas triangulaire. Les effets de l'évolution du réacteur en puissance et de l'apparition des produits de fission sont étudiés par le code PENDULE, qui suit le fonctionnement du réacteur et permet d'étudier les rechargements fractionnés.

Trois codes sont utilisés ou en cours de développement dans le domaine de la sécurité. Le code PROFUSION a été écrit pour étudier l'évolution d'un réacteur rapide à oxyde en cas de surpuissance et de perte de débit. Il permet le calcul transitoire du phénomène de fusion et de déplacement éventuel du combustible. Ce code convient, entre autres, pour l'investigation de l'origine d'accidents du type « meltdown accident » . Le code PANIC a été écrit pour évaluer la libération d'énergie dans un réacteur rapide soumis à une insertion rapide de réactivité. Ce code convient pour l'étude du classique « meltdown accident », mais il peut être utilisé également pour étudier l'initiation du «sodium expulsion accident ». Le code CARMEN, en cours de développement, sera d'application plus générale; il permettra de calculer les accidents pouvant survenir à un réacteur rapide. Il s'agit d'accidents du type insertion de réactivité, perte de réfrigérant et blocage d'assemblage. Ce code calculera la cinétique d'un réacteur rapide en tenant compte de l'expulsion du sodium.

Le code CORCYRE a été mis au point pour effectuer des études paramétriques de réacteurs rapides. Il comprend deux parties : dans la première, les caractéristiques du réacteur sont déterminées et dans la seconde, les caractéristiques du cycle et le coût du cycle du combustible sont calculés.

Des exemples d'application de ces divers codes indiquant la progression de l'étude complète d'un réacteur rapide de puissance seront présentés.

1. INTRODUCTION

L'intérêt économique du cycle du plutonium dans les réacteurs rapides a été démontré très tôt dans l'histoire de l'énergie nucléaire. Par ses propriétés remarquables de surgénération le réacteur rapide permet d'atteindre des taux d'épuisement beaucoup plus élevés que les réacteurs à eau actuels, réduisant ainsi la charge du combustible; de plus, il permet d'entrevoir une production d'énergie indépendante des approvisionnements extérieurs.

En entreprenant aujourd'hui la mise au point de projets et la construction de centrales prototypes, de nombreux pays mettent à profit les recherches qui, depuis vingt ans, ont permis d'accroître très appréciablement leurs connaissances des problèmes technologiques et physiques, en vue de rendre économiques et sûrs les réacteurs de puissance à neutrons rapides. La puissance spécifique que l'on espère atteindre au départ dans les réacteurs rapides est de l'ordre de 800 kW/kg de matière fissile, ce qui est comparable aux réacteurs à eau du type actuel; d'autre part, les densités de puissance sont de l'ordre de 400 à 500 kW/l de cœur comparées à 70 à 90 kW/l pour les réacteurs PWR.

En s'intéressant aux cœurs de gros volume utilisant les combustibles céramiques et refroidis au sodium, on s'est trouvé face à des spectres neutroniques mous s'étendant jusqu'aux régions de résonance des éléments lourds, et aussi face à des cœurs à peu de fuites et moins aisément contrôlables.

Parmi les causes essentielles qui ont retardé la progression des centrales rapides, il faut citer la nécessité de réaliser des cœurs de grande taille, qui posent des problèmes de sécurité, la technologie nouvelle, due à un cycle de refroidissement au sodium, la réalisation d'un combustible supportant une irradiation prolongée, un spectre neutronique sensible aux variations de température pouvant induire des effets de réactivité importants.

C'est ainsi que les études physiques, à la fois théoriques et expérimentales, ont été principalement orientées vers la détermination du coefficient de température du combustible et du réfrigérant. Ce sont les coefficients « Doppler » et de « vide sodium».

Quoique les incertitudes dans les évaluations de ces coefficients soient encore relativement larges, les méthodes et moyens d'estimer ces effets sont déjà bien développés et attendent surtout des données de base permettant des évaluations plus correctes, ce qui peut encore prendre un certain temps.

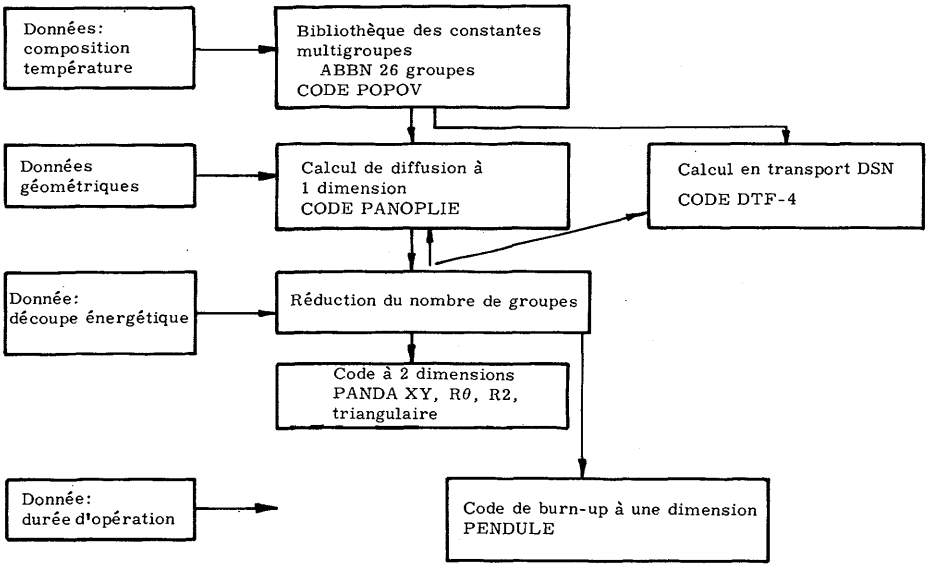

FIG.1. Exemple d'une chaîne de codes mise au point pour un ordinateur IBM 360/40.

Les méthodes qui sont actuellement les plus urgentes à développer sont celles qui doivent être utilisées en liaison directe avec les travaux d'avancement du projet tout en permettant de tenir compte de façon synthétique des effets cités plus haut, de manière à permettre les optimisations sur la structure.

Enfin, il importe de pouvoir calculer la protection nécessaire contre l'accident maximal prévisible, c'est-à-dire l'énergie libérée par cet accident ainsi que les barrières de sécurité pour contenir l'accident.

Les groupes industriels intéressés à la réalisation des réacteurs rapides et chargés de leur optimisation économique et d'assurer leur sécurité doivent mettre au point une série de codes dont on peut dire qu'ils se composent essentiellement de codes neutroniques d'analyses d'accidents et d'évaluations économiques. Pour cela il faut pouvoir disposer de moyens de calcul relativement larges car, jusqu'ici, il n'existe que peu de modèles synthétiques pour traiter la neutronique des réacteurs rapides.

A titre d'exemple on a représenté sur la figure 1 une chaîne de codes neutroniques qui a été programmée pour une machine de taille moyenne IBM 360/40 128 K et deux unités de disque. Les données de base sont fournies sous la forme proposée par les systèmes de constantes russe ABBN et allemand GfK. Ces systèmes multigroupes présentent l'avantage de fournir, pour chaque élément présentant des résonances à l'intérieur

d'un groupe, la valeur moyenne de la section efficace en prenant deux hypothèses simplificatrices mais réalistes.

$$\Phi(u) = \frac{1}{\Sigma_t(u)}$$

$$\Sigma_t(u) = [\sigma_{res}(u) + \sigma_0(\text{constant})] \cdot N$$

Les codes repris sur cette figure sont classiques; le chemin normal est constitué par un code de diffusion à une dimension qui comporte les principales sous-routines permettant l'étude des perturbations, la réduction du nombre de groupes, le calcul des paramètres importants : le temps de vie ($\bar{l}$), la fraction effective des neutrons retardés (β_{eff}), le gain de surgénération, les constantes réduites, qui sont fournies à un code d'évolution à une dimension ou à un code de diffusion à deux dimensions. Le code de transport 1D doit permettre d'étudier les phénomènes locaux aux endroits où d'importantes modifications neutroniques se produisent du fait de l'hétérogénéité matérielle et de modification spectrale.

Nous avons pris quelques exemples pratiques qui ont été adoptés pour le calcul des réacteurs rapides.

2. ANALYSE DE L'EFFET DE VIDE SODIUM

L'évaluation de l'effet réactif lié à une perte partielle ou totale du réfrigérant est un problème de première importance en vue des études de sécurité. La complexité de l'évaluation précise de cet effet est due à son double aspect : spectral (durcissement du spectre lors de la perte de réfrigérant) et spatial (influence de la localisation du vide sur l'importance des fuites).

On n'envisagera pas ici la sensibilité des valeurs réactives aux imprécisions des données nucléaires, ce problème étant du ressort des spécialistes des bibliothèques de sections efficaces.

L'effet spectral est mis en évidence par la figure 2, qui indique comment un durcissement du spectre peut influencer la réaction neutronique dans le réacteur.

Si l'on exclut les méthodes de synthèse ou les modèles de calcul à $1\frac{1}{2}$ dimension, qui sont difficilement utilisables lorsque le vide prend une extension spatiale importante (plus particulièrement s'il s'étend sur deux régions), on est réduit à résoudre un grand nombre de problèmes à deux dimensions, coûteux en temps machine.

Il convient donc de trouver un compromis entre une bonne représentation spatiale et une bonne représentation énergétique : une représentation spatiale valable est obtenue par un calcul à deux dimensions, une représentation énergétique efficiente nécessite un nombre de groupes adéquat.

Il convient de minimiser le temps machine, qui est sensiblement proportionnel au produit du nombre de points du réseau par le nombre de groupes. Un nombre optimal de points s'obtient en choisissant un rapport adéquat du pas moyen du réseau au coefficient de diffusion.

La recherche du nombre de groupes est un problème plus délicat. Partant d'une bibliothèque à 26 ou à 16 groupes, inutilisable en calcul

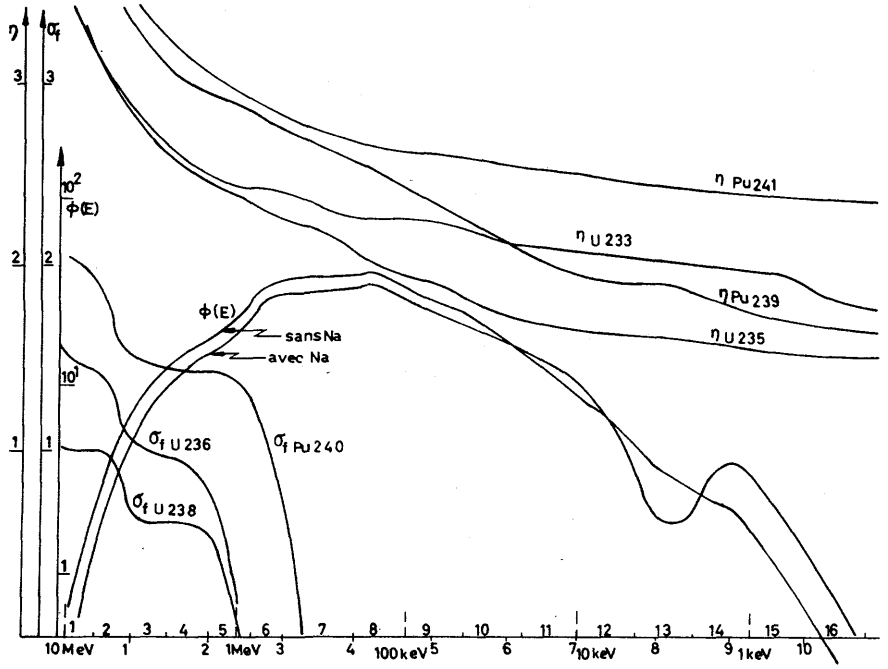

FIG.2. Effet spectral lié au vide sodium.

2D, on condense les sections à i groupes. Il convient de rechercher le meilleur choix des frontières de groupes pour conduire au système condensé à i groupes. Cette détermination peut se déduire de l'application des principes d'optimalité.

Introduisons, pour comprendre ce principe, le vecteur des variables de décision $[D_i]$ qui représente toutes les décisions à prendre pour définir une découpe à i groupes ((i - 1) limites de groupes), et la variable d'état K_i représentant l'état du système lors des décisions $[D_i]$. Formellement, on a

$$K_i = f[D_i]$$

où K_i représente l'écart E_i entre la variable d'état résultant du calcul à i groupes et la variable d'état initiale (système à condenser).

Il est possible de déduire une relation remarquable entre les découpes optimales moyennant deux hypothèses.

- Hypothèse de transitivité. Une condensation de i groupes en K groupes (i > K) suivie d'une condensation de K groupes en f groupes (K > f) conduit au point de vue de la variable d'état au même résultat qu'une condensation directe de i groupes à f groupes.
- Hypothèse de monotonicité. Si on appelle E_i l'écart optimal (minimal) lors d'une condensation de 26 en i groupes, cette hypothèse revient à supposer

$$E_{i+1} \leq E_i \leq E_{i-1}$$

TABLEAU I. RECHERCHE D'UNE DECOUPE OPTIMALE – NOMBRE MAXIMAL DE CALCULS NECESSAIRE

Découpe optimale à i groupes	1	2	3	4	5
Calculs systématiques	1	25	275	2300	12 650
Calculs par la méthode exposée	1	25	49	72	94

TABLEAU II. CALCUL D'UN EFFET DE VIDE SODIUM – COMPARAISON DES RESULTATS APRES CONDENSATION DE 26 EN 5 GROUPES ($\Delta k \times 10^{-5}$)

	Réacteur Pu		Réacteur ^{235}U	
	26 groupes	5 groupes	26 groupes	5 groupes
50% vide	2180	2230	288	340
100% vide	2510	2610	-43	-34

car en accroissant l'indice i on augmente le nombre d'informations pouvant être utiles.

Ces deux hypothèses permettent d'énoncer le principe suivant:

Si $[D_i^*]$ est le vecteur de décision optimal pour le modèle à i groupes, le vecteur de décision optimal pour un modèle à i - 1 groupes $[D_{i-1}^*]$ contient (i - 1) décisions communes avec le vecteur de décision optimal $[D_i^*]$. Il est donc possible de déterminer des découpes optimales à i groupes partant de découpes à i - 1 groupes, le nombre de calculs à effectuer étant minimal (tableau I). Ce procédé a permis de gagner un temps précieux pour l'application des codes à deux dimensions dans l'étude de phénomènes tels que le vide sodium.

Le tableau II montre une comparaison des résultats après condensation sur une découpe optimisée à cinq groupes, dans le cas d'un vide sodium au centre du réacteur.

On observe que les différences sont peu importantes (< 100 pcm), et ceci justifie une étude du coefficient de vide sodium à l'aide d'un code à deux dimensions avec un nombre très réduit de groupes.

3. POLITIQUE DE RECHARGEMENT DU CŒUR D'UN REACTEUR RAPIDE

L'optimisation de la politique de rechargement du cœur d'un réacteur devrait permettre une réduction sensible du prix de revient du kWh. C'est donc un problème important, mais complexe, pour lequel il faut trouver des méthodes de résolution simplifiées.

Pour augmenter le rendement d'un réacteur, on cherche à aplatir la distribution radiale de puissance. La solution généralement préconisée est de diviser le cœur en plusieurs zones concentriques d'enrichissement croissant vers la périphérie. Même ainsi, on ne peut empêcher la chute rapide du flux et de la densité de puissance à la périphérie du cœur. Or, pour diminuer le prix du cycle du combustible, on a intérêt à ce que tous les assemblages déchargés du cœur aient atteint un burn-up aussi proche que possible du burn-up maximal autorisé. Ainsi, pour augmenter le burn-up des assemblages situés dans la région périphérique, soumis à un flux plus faible, il a déjà été proposé de réaliser un cycle de déchargement plus lent de cette région.

Une méthode extrêmement simple a été mise au point, qui permet l'évaluation de l'accroissement du burn-up moyen de l'ensemble des assemblages déchargés lorsqu'on crée une sous-zone périphérique à rythme de déchargement plus lent.

On a constaté que la distribution radiale de puissance pouvait être correctement représentée dans chaque zone k d'un cœur multizone par une parabole :

$$p_k(r, t) = v_k(t) \left[1 - a_k(t)\ r^2 \right] \tag{1}$$

$$R_{k-1} \leqq r \leqq R_k$$

où R_k est le rayon extérieur de la kième région.

Le burn-up est donné par

$$\beta_k(r, t) = \int_0^t p_k(r, t)\ dt = u_k(t) \left[1 - \alpha_k(t)\ r^2 \right] \tag{2}$$

Le cœur de référence est divisé en lots de μ assemblages. La politique de rechargement consiste à ne retirer lors de chaque déchargement (tous les temps T) que l'assemblage le plus brûlé de chaque lot; chaque assemblage séjourne donc pendant μT dans le cœur.

Si l'on subdivise les régions en deux sous-zones de telle sorte qu'initialement on ait

$$\frac{\mu+1}{\mu}\ \beta_k(\rho) = \beta_{k\,max} = \beta_k(R_{k-1})$$

ρ étant le rayon de séparation des deux sous-zones, et si l'on forme dans la région (ρ, R_k) des lots de (μ + 1) assemblages, il est aisé de montrer que l'accroissement correspondant du burn-up moyen à un instant donné vaut

$$\frac{\Delta < \beta >_{cœur}}{< \beta >_{cœur}} = \frac{\sum_{k=1}^{n} \frac{1}{\mu} \int_{\rho}^{R_k} \beta_k(r)\ r\ dr}{\sum_{k=1}^{n} \int_{R_{k-1}}^{R_k} \beta_k(r)\ r\ dr} \tag{3}$$

La comparaison des équations (1) et (3) permet d'écrire le résultat sous une forme particulièrement simple.

Cette méthode a été appliquée au calcul du cœur d'un réacteur de 1000 MW(e) refroidi au sodium, à deux zones d'enrichissement, proposé par le Centre de Karslruhe (réacteur Na1).

La politique de rechargement de base considère des lots de μ assemblages. Lorsqu'on divise la zone extérieure en deux et que, dans la sous-zone périphérique, on forme des lots de $\mu + 1$ assemblages, l'accroissement du burn-up moyen vaut 7% si $\mu = 3$ et 6,4% si $\mu = 4$. Ces résultats sont en excellent accord avec des calculs de burn-up effectués à Karlsruhe [1].

Une politique de rechargement étant fixée a priori, il est toutefois indispensable de posséder un code de burn-up pouvant tenir compte des rechargements successifs, si l'on désire connaître, d'une part, l'évolution (discontinue) des caractéristiques générales (puissance, flux, k_{eff}, ...) du réacteur et, d'autre part, la composition isotopique et le taux de burn-up des assemblages déchargés. A nouveau, une solution approchée simple de ce problème a été recherchée, qui évite une représentation individuelle de chaque assemblage combustible.

Ne pouvant pas, par manque de temps et de place, donner ici les équations générales utilisées, nous traiterons le cas particulier du réacteur décrit plus haut à titre d'exemple.

Désignons par

T la période entre rechargements (supposée constante),

N^0 (kT) la densité moyenne d'un isotope quelconque d'un assemblage ayant séjourné pendant kT dans le réacteur,

N^k(kT) la densité moyenne d'un isotope quelconque du lot à l'instant kT c'est-à-dire après k rechargements.

Le tableau III schématise l'évolution des densités atomiques moyennes d'un lot de $\mu = 3$ assemblages et les densités atomiques de l'assemblage le plus brûlé de ce lot. Nous prendrons T = 6 mois.

La principale hypothèse simplificatrice est de supposer que les densités isotopiques d'un assemblage évoluent au cours du temps indépendamment de la composition des assemblages qui l'entourent (brûlés ou non).

Le burn-up se calcule par un procédé analogue. Ce calcul se fait en chaque point du cœur. Il est introduit actuellement comme sous-routine d'un code de burn-up à une dimension. Cette sous-routine permettra une première étude du démarrage d'un réacteur frais et de son évolution vers l'état de régime, en attendant de pouvoir faire des calculs plus précis par un code de burn-up à deux dimensions.

4. ETUDE DE LA SECURITE DES REACTEURS RAPIDES

Les études de sécurité des réacteurs rapides dépendent beaucoup des moyens de calcul dont on dispose, principalement des « codes d'accidents » et des codes de calcul des données décrits ci-avant qui servent à alimenter les premiers.

Certains des « codes d'accidents » pour réacteurs rapides qui ont été et continuent à être développés à la BelgoNucléaire sont énumérés ci-dessous, ainsi que les principaux problèmes dont ils permettent l'étude:

TABLEAU III. SCHEMA D'EVOLUTION DES DENSITES ATOMIQUES (μ = 3)

Numéro d'ordre du rechargement k	Composition moyenne du lot en début de période	Composition moyenne du lot en fin de période	Composition de l'assemblage le plus brûlé en fin de période
0	$N^0(0)$	$N^0(6)$	$N^0(6)$
1	$N^1(6) = \frac{2}{3} N^0(6) + \frac{1}{3} N^0(0)$	$N^1(12) = \frac{2}{3} N^0(12) + \frac{1}{3} N^0(6)$	$N^0(12) = \frac{3}{2}[N^1(12) - \frac{1}{3} N^0(6)]$
2	$N^2(12) = \frac{1}{3} N^0(0) + \frac{1}{3} N^0(6) + \frac{1}{3} N^0(12)$	$N^2(18) = \frac{1}{3}[N^0(6) + N^0(12) + N^0(18)]$	$N^0(18) = 3N^2(18) - N^0(12) - N^0(6)$
3	$N^3(18) \approx N^2(12)$ ⟷ état de régime		

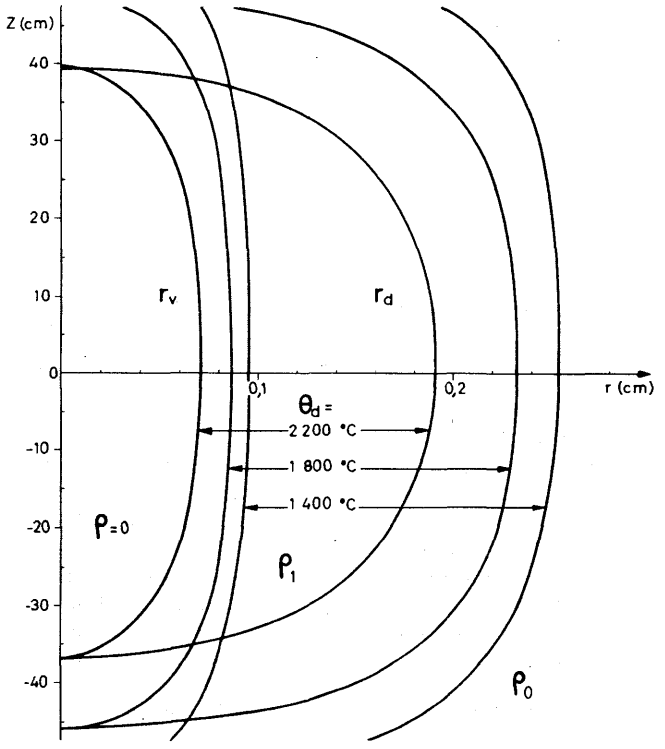

FIG.3. Configuration interne du crayon combustible central pour quelques valeurs de la température de densification.

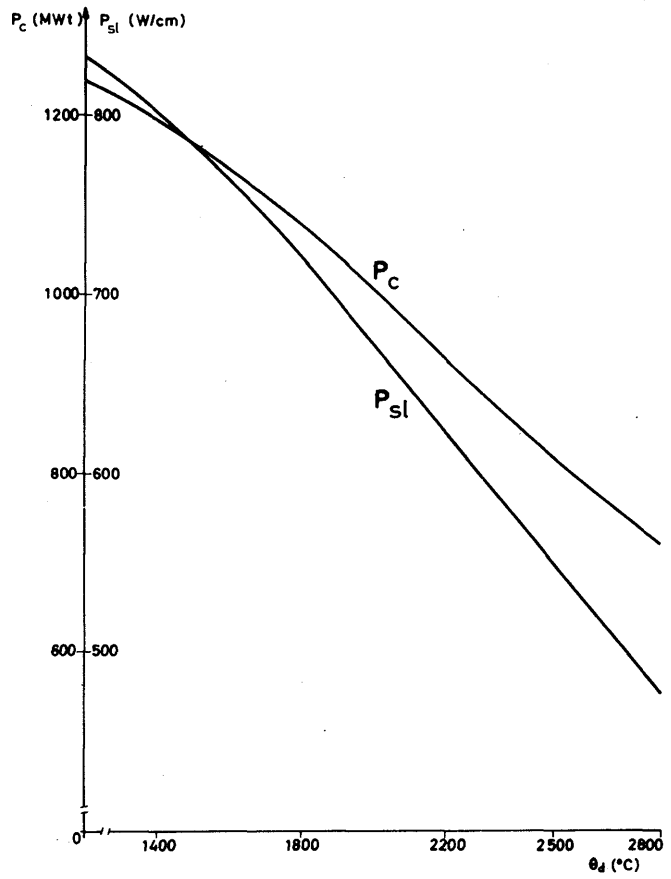

FIG.4. Variation de la puissance linéique maximale et de la puissance thermique d'un cœur multizone en fonction de la température de densification.

- PROFUSION est un code permettant le calcul de la fusion transitoire du combustible dans un réacteur rapide et d'effets réactifs qui peuvent être associés à l'effondrement éventuel du combustible fondu;
- PANIC est un code qui permet le calcul de l'évolution d'un réacteur rapide lorsque celui-ci est soumis à une insertion de réactivité suffisamment importante et qui engendre le « désassemblage » du cœur, tel qu'il est défini dans le modèle de Bethe-Tait;
- CARMEN est un code en cours de développement qui devrait permettre le calcul des transitoires de réacteurs rapides refroidis au sodium, pouvant impliquer tant la fusion et la vaporisation du combustible que l'échauffement exagéré du sodium provoquant l'ébullition explosive de ce dernier.

D'autres codes traitant d'aspects particuliers de la sécurité des réacteurs rapides existent également mais nous nous limiterons dans ce mémoire à ces trois codes car ils traitent les problèmes principaux que l'on doit étudier dans le domaine des accidents pouvant survenir à un réacteur rapide refroidi au sodium.

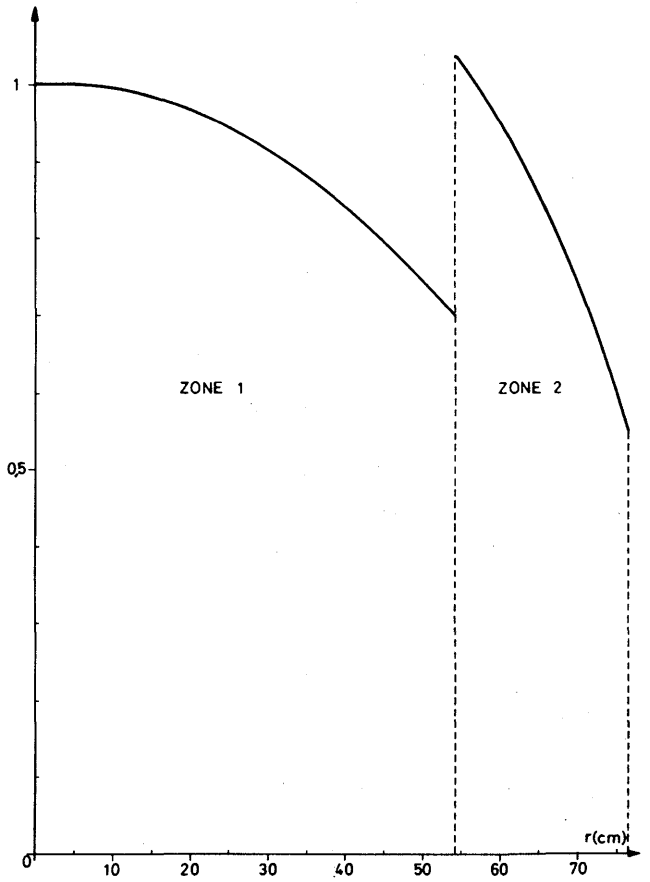

FIG.5. Distribution radiale de puissance dans le réacteur multizone.

4.1. Fusion du combustible – Effondrement du cœur

Le code PROFUSION a été écrit pour étudier la propagation de la fusion du combustible dans les aiguilles d'un réacteur rapide cylindrique pouvant comporter plusieurs zones. Ce code a déjà été décrit dans la littérature [2]. Rappelons-en brièvement les principales caractéristiques. La géométrie utilisée (2D) est cylindrique de révolution, pour les phénomènes tant microscopiques que macroscopiques. Les transferts de chaleur stationnaire sont calculés pour l'unité de longueur des crayons combustibles en chaque point du maillage (2D), de même que la structure de l'aiguille de combustible résultant du phénomène de migration des porosités dans le combustible chaud. Les distributions microscopiques et macroscopiques de température sont calculées pour les transitoires résultant de conditions de surpuissance ou de sous-débit arbitraire, les effets de contre-réaction n'étant pas pris en compte. De même, la propagation subséquente des phénomènes de fusion dans les aiguilles

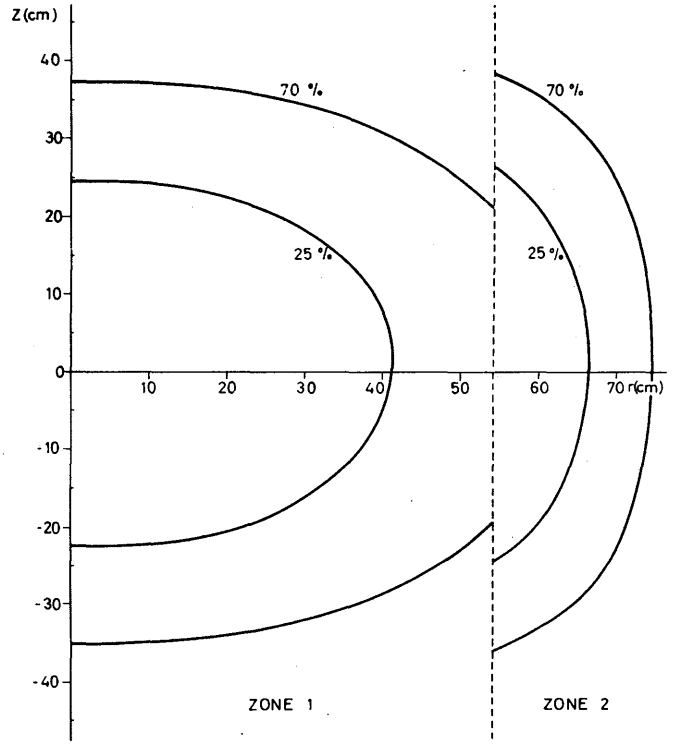

FIG.6. Limites de la fraction du cœur à l'intérieur de laquelle du combustible liquide est créé pour deux valeurs de la surpuissance.

combustibles est calculée en chaque point du maillage également. Pour un état donné du réacteur, transitoire ou asymptotique, des déplacements de combustible fondu sont effectués à l'intérieur des vides axiaux existant dans les aiguilles à l'état non rupturé et l'effet réactif associé est évalué par une formule de perturbation.

Ce modèle a été utilisé par exemple pour évaluer l'effet réactif qui peut résulter de l'effondrement de combustible fondu en raison de la surpuissance dans le projet de réacteur multizone Na2 décrit en [3] et [4].

Les figures 3 et 4 montrent pour ce réacteur l'influence de la température de densification θ_d respectivement sur les structures de l'aiguille combustible centrale et sur la densité linéique maximale de puissance correspondante, c'est-à-dire celle pour laquelle la fusion du combustible au bord du vide axial est atteinte dans l'aiguille la plus chargée, laquelle se trouve à l'entrée de la seconde zone radiale du cœur (voir ci-dessous). L'ordre de grandeur de la température de densification étant 1800°C, on voit que le phénomène de densification devrait permettre une augmentation du niveau maximal de puissance de fonctionnement de 50% environ par rapport à l'aiguille combustible initiale, si l'on n'était pas limité par la température du gainage.

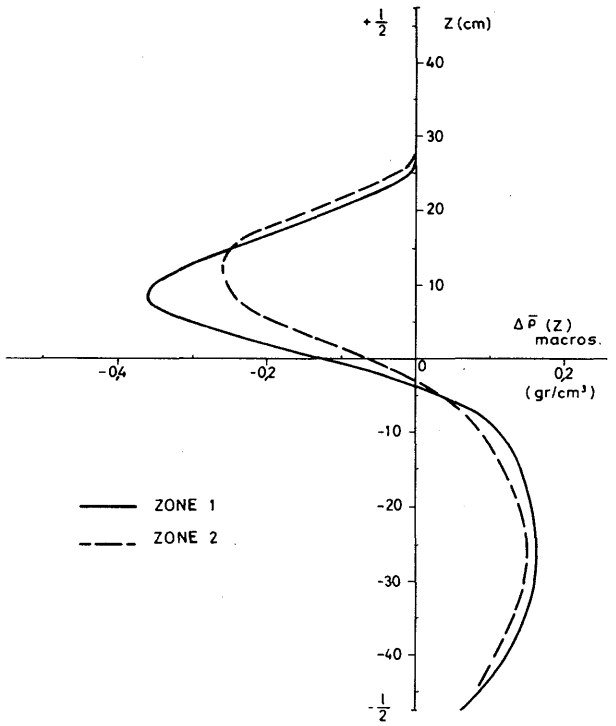

FIG.7. Distribution axiale de la densité macroscopique moyennée radialement dans chaque zone après effondrement du combustible liquide dans le bas des vides axiaux pour une surpuissance de 25% (θ_d = 1400°C).

La figure 5 montre la distribution radiale de la densité de puissance tandis que la figure 6 montre les limites de la fraction du cœur dans laquelle le combustible fondu est obtenu pour des surpuissances de 25% et 70%. Ces limites sont relatives à l'état asymptotique, c'est-à-dire pour $t = \infty$ si l'on admet que le combustible fondu ne se déplace pas. La production de combustible fondu ayant été calculée en chaque point du maillage (2D), on a calculé l'effet réactif de deux déplacements de combustible fondu, respectivement vers le bas des vides axiaux (cas A) et vers le plan médian du cœur dans les vides axiaux (cas B). Les figures 7 et 8 illustrent la distribution axiale de la variation radiale moyenne de la densité macroscopique $\Delta\bar{\rho}(Z)$ du combustible dans chacune des zones après effondrement (A). L'effet réactif lié au déplacement de combustible fondu est fortement dépendant de la surpuissance. La figure 9 montre cette dépendance ; on y voit, dans le cas A, que l'effet réactif est d'abord négatif et que l'effet le plus négatif est atteint pour 20% de surpuissance environ (θ_d = 1400 et 1800°C); au-delà, l'effet réactif a tendance à devenir positif sans pour cela dépasser une valeur maximale positive ayant lieu pour 70% environ (θ_d = 1400 et 1800°C). Pour le cas A (effondrement du combustible), la différence crête à crête est respectivement de l'ordre de 900 et 460 • 10^{-5} $\Delta k/k$, ou environ 3 et 1,5 dollars (1 \$ ~ 300 • 10^{-5}), pour θ_d = 1400 et 1800°C.

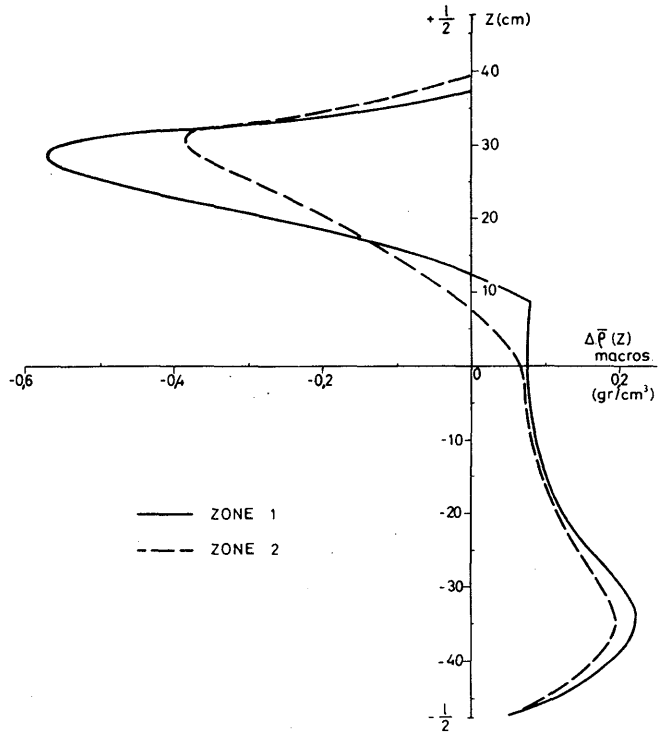

FIG.8. Distribution axiale de la densité macroscopique moyennée radialement dans chaque zone après effondrement du combustible liquide dans le bas des vides axiaux pour une surpuissance de 70% (θ_d = 1400°C).

La figure 9 montre aussi que, dans le cas du rassemblement de combustible fondu autour du plan médian (cas B), l'effet réactif est évidemment toujours positif et limité respectivement à 500 et 280 · 10^{-5} $\Delta k/k$, soit environ 1,6 et 1 dollar, pour θ_d = 1400 et 1800°C.

Ces résultats ont été établis à l'aide d'une formule de perturbation; on a montré [2] que l'évaluation de cet effet réactif par des calculs de diffusion neutronique adéquats (1D et 2D) est sous-estimée d'un facteur 2 environ pour un cœur à une zone d'enrichissement. On n'a pas encore évalué quantitativement ce que peut être cette sous-estimation pour un réacteur multizone, mais on pense qu'elle est du même ordre de grandeur que pour les cœurs à une zone.

L'ensemble des résultats que nous venons de discuter brièvement est un exemple d'application du code PROFUSION, qui est en soi un code d'étude des conditions pouvant engendrer un accident. Ce code subit actuellement des modifications en vue de permettre l'étude détaillée de l'origine de « meltdown accidents »; l'aspect transitoire des phénomènes y est particulièrement développé.

4.2. Etude de l'accident de base pour un réacteur rapide

Une partie importante de l'étude de sécurité d'un réacteur rapide est l'étude de l'accident de base [5]. L'accident de base doit d'abord être

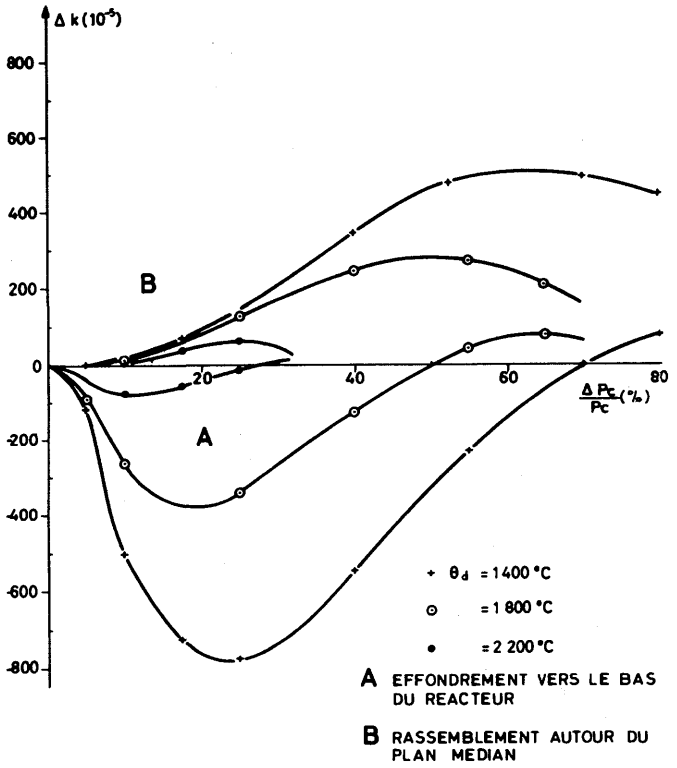

FIG.9. Variation de l'effet réactif dû au déplacement de combustible fondu dans un réacteur multizone ($W_m = 3,33 \cdot 10^{-7}$ Δk/k/gr).

défini, c'est-à-dire les conditions dans lesquelles il est engendré; ensuite, un modèle de calcul doit être établi, qui décrit l'évolution des phénomènes physiques impliqués dans son déroulement. Lorsque le calcul du déroulement de l'accident de base a été fait, on peut alors évaluer ses conséquences.

Le code PANIC a été décrit pour permettre le calcul du déroulement de l'accident de base selon un modèle développé par Nicholson [6] qui est une amélioration importante du modèle de Bethe et Tait. Ce code a déjà été décrit [7]. Il permet le calcul de l'évolution des principales grandeurs physiques du cœur d'un réacteur rapide lorsque celui-ci est soumis à une insertion rapide de réactivité. A titre d'exemple, nous commenterons brièvement ci-dessous quelques résultats obtenus [7] pour un cœur multizone similaire à celui décrit en [3], soumis à une insertion de réactivité de 59 $/s. Les principaux résultats de calcul relatifs à l'énergie destructive sont exposés à la figure 10, en fonction du coefficient Doppler (CD); les calculs ont été effectués selon quatre modèles ou groupes d'hypothèses. On voit que, lorsque l'on passe du modèle le plus simple au modèle le plus compliqué du point de vue de la géométrie et du désassemblage, c'est-à-dire : 1°) sphérique DA (DA = désassemblage axial), 2°) cylindrique à une zone DA, 3°) cylindrique à deux zones DA, 4°)

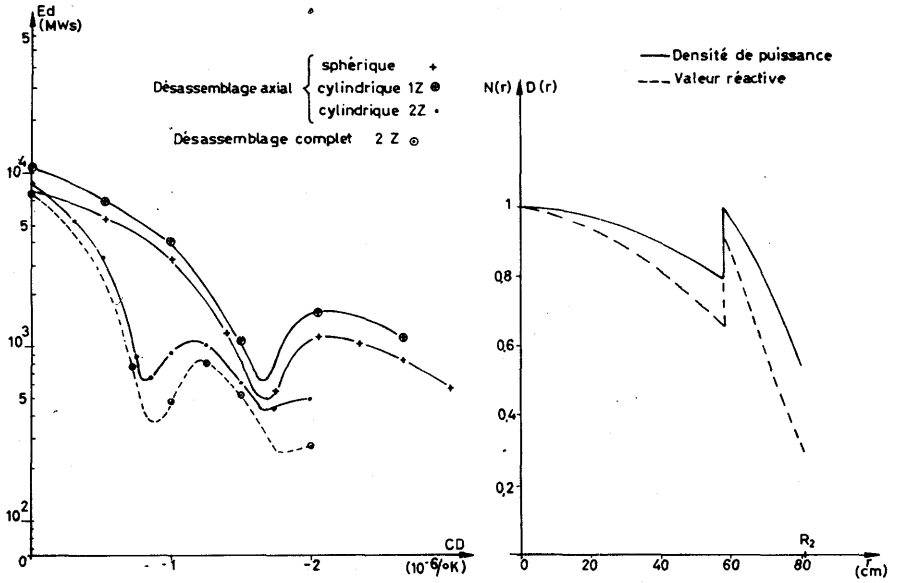

FIG.10. Modèle cylindrique à deux zones radiales (300 MW(e)).

cylindrique à deux zones avec désassemblage complet, la valeur de l'énergie destructive recherchée diminue dans l'ensemble, et que la diminution est fortement influencée par le coefficient Doppler. On peut donc dire qu'il est intéressant dans une certaine mesure de disposer d'un modèle de calcul suffisamment élaboré. On a également représenté sur la figure 11, en fonction du CD, la variation du temps de relâchement de l'énergie destructive, compté entre des limites inférieure et supérieure variables. On voit que l'effet Doppler a un effet temporisateur très prononcé.

Comme on peut le voir également sur cette figure, le temps de relâchement de l'énergie destructive est de l'ordre de la milliseconde ; cette valeur élevée tient essentiellement à la valeur relativement faible de l'insertion de réactivité définissant l'accident de base et du coefficient Doppler, dont la valeur pour le cœur envisagé est certainement supérieure à $1 \cdot 10^{-6}$ $\Delta k/degC$. Le code PANIC fournit de nombreux résultats autres que l'énergie destructive, mais nous renvoyons le lecteur à la référence [7] qui en contient une description plus détaillée.

Ces résultats sont généralement utilisés pour l'étude des dommages que l'accident cause au réacteur, par exemple l'écrasement des couches de matériaux entourant le cœur qui a explosé.

4.3. Etude de l'accident entraînant l'expulsion de sodium

Un des problèmes particulier aux réacteurs rapides refroidis au sodium est l'ébullition transitoire du sodium pendant un accident, car on a vu au paragraphe 2 que l'effet réactif qui y est associé peut être positif, d'autant plus que l'ébullition a généralement un caractère explosif surtout si la surchauffe du sodium est importante [8]. Un code dénommé CARMEN

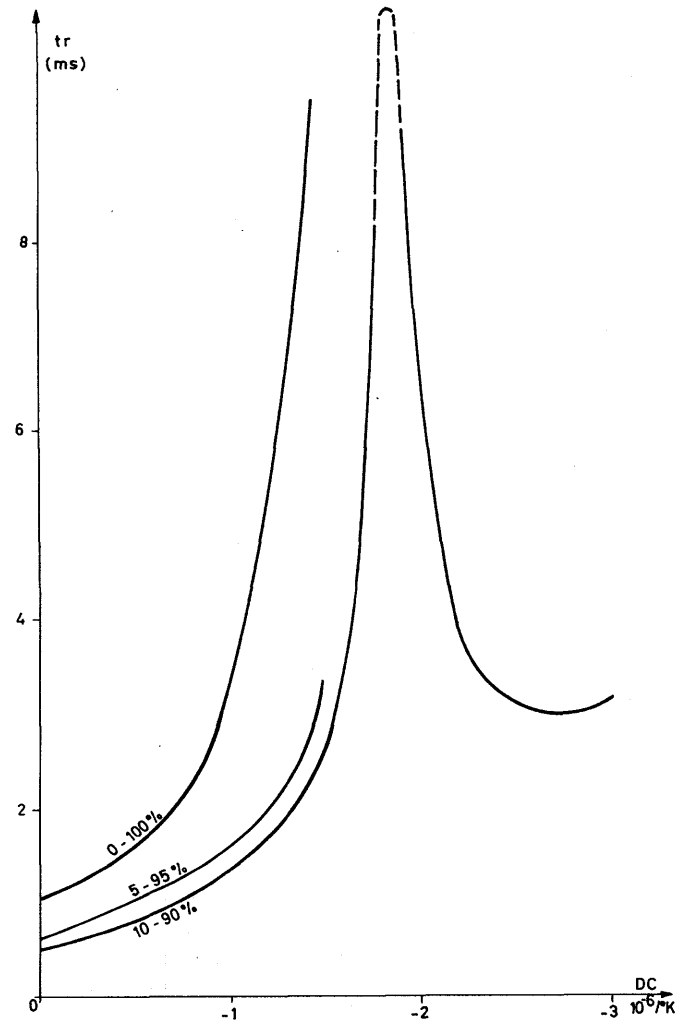

FIG.11. Variation en fonction du CD du temps de relâchement de l'énergie destructive pour Na-2, 59$/s en modèle sphérique.

(Calcul d'Accident Rapide avec Modèle d'Expulsion de Na) est en cours de développement, qui permettra l'étude détaillée des phénomènes suivants:

- Evolution des caractéristiques nucléaires du réacteur en fonction des actions extérieures (débit du réfrigérant, réactivité de contrôle) et des rétroactions (effet Doppler, effet de vide Na, désassemblage);
- Transfert thermique dans le combustible et gainage pour des éléments combustibles comportant des vides axiaux;
- Pressurisation des aiguilles combustibles et sollicitation des gainages en cas de transitoires sévères;
- Expulsion du sodium et effet réactif associé.

Ce code complétera à souhait la chaîne de codes d'accidents qui vient d'être brièvement décrite.

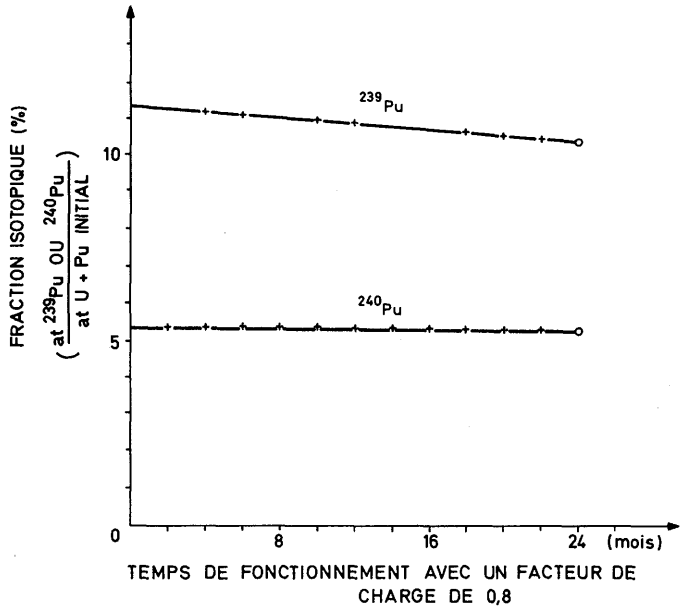

FIG.12. Comparaison entre les résultats CORCYRE et PENDULE - Evolution de ^{239}Pu et ^{240}Pu dans la zone interne du cœur.

—— PENDULE (meilleurs calculs)

O CORCYRE

\+ PENDULE (sans réévaluation des sections efficaces).

5. LE CODE CORCYRE (Coût Réel du Cycle de Combustible dans les Réacteurs)

Le code CORCYRE a été mis au point pour effectuer des études paramétriques de réacteurs rapides. Il a servi jusqu'à présent aux études d'optimisation de la couverture d'un réacteur rapide et de démarrage d'un réacteur rapide au moyen d'uranium enrichi. Ce code a été décrit dans un mémoire présenté au Colloque sur l'emploi du plutonium comme combustible dans les réacteurs [9]. Il comprend essentiellement deux parties. Dans la première, les caractéristiques du réacteur nécessaires pour le calcul économique sont déterminées. Dans la seconde, les caractéristiques du cycle du combustible sont d'abord calculées (temps de doublement, inventaires et consommations) ; les calculs d'actualisation sont alors effectués pour chaque zone du réacteur et les coûts sont exprimés en mills/kWh.

Aucun calcul de diffusion neutronique n'est effectué dans la première partie du code. Les compositions du combustible requises pour rendre le réacteur critique au moment du déchargement sont établies sur la base des coefficients d'équivalence définis par Baker et Ross [10] et d'une étude préalable, au moyen de la théorie de la diffusion, d'un réacteur de référence. Les calculs d'évolution (burn-up) sont entrepris dans chaque zone par résolution des équations différentielles bien connues donnant l'équilibre entre la production et la disparition des divers nucléides.

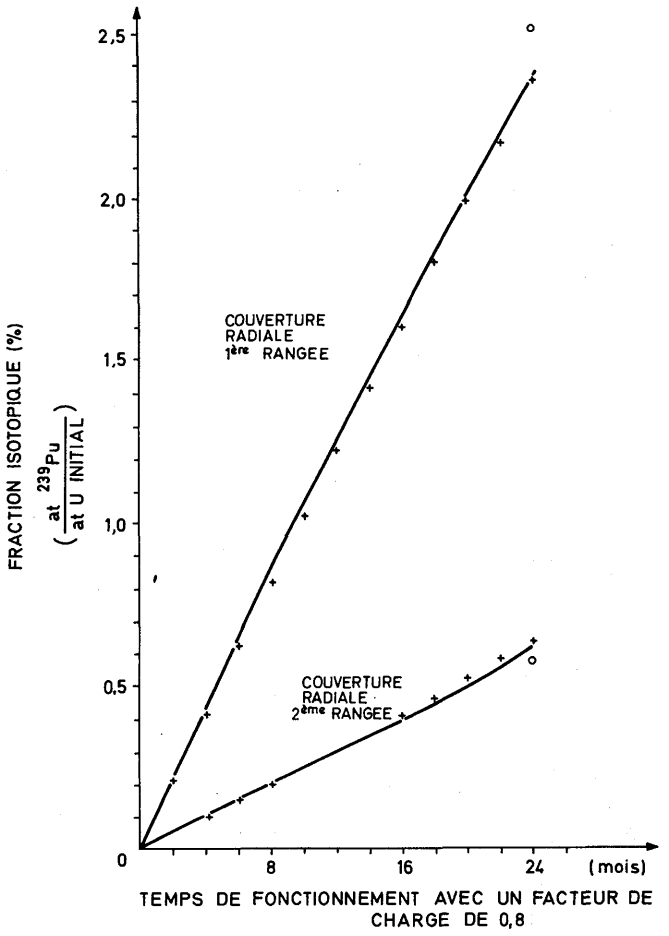

FIG.13. Comparaison entre les résultats CORCYRE et PENDULE - Evolution de ^{239}Pu dans la couverture radiale.

—— PENDULE (meilleurs calculs)
O CORCYRE
\+ PENDULE (sans réévaluation des sections efficaces).

La relation entre les flux moyens des diverses zones, qui normalement pourrait être établie par un calcul de diffusion neutronique, est déterminée grâce à un artifice de calcul (facteurs d'inventaire ou «balance factors»). Grâce à cette simplification, un calcul peut être effectué en moins d'une minute au lieu de 15 minutes pour un calcul de diffusion à une dimension (calcul du k_{eff} sans recherche de la composition critique). On peut ainsi se permettre d'entreprendre des études paramétriques intéressantes.

Une vérification de la validité de cette simplification a été effectuée. Dans une première étape, l'influence d'une erreur dans la détermination du coefficient ξ utilisé dans la définition du facteur d'inventaire a été

TABLEAU IV. INVENTAIRE EN MATIERE FISSILE

Masse en équivalent ^{239}Pu dans les zones	Différence entre déchargement et chargement			
	Cas ^{235}U		Cas plutonium	
	CORCYRE	PENDULE	CORCYRE	PENDULE
Cœur 1	- 269,30	- 268,65	- 70,51	- 73,85
Cœur 2	- 292,76	- 289,24	- 161,49	- 166,81
Couverture axiale 3	+ 152,10	pas	+ 199,37	pas
Couverture axiale 4	+ 90,98	calculé	+ 120,40	calculé
Couverture radiale 5	+ 184,68	+ 191,94	+ 249,12	+ 237,98
Couverture radiale 6	+ 84,64	+ 107,50	+ 120,76	+ 130,39

évaluée. Une erreur de 20% dans les zones de cœur et de couverture axiale et de 25% dans les zones de couverture radiale donne une erreur statistique de 0,7% sur le prix du kWh et de 1,5% sur le temps de duplication. Or il apparaît à la lumière des calculs de diffusion que cette erreur constitue une limite maximale.

Une autre vérification a été faite. Deux cas de réacteurs, chargés respectivement au plutonium (63 - 30 - 5 - 2) et à l'uranium enrichi, ont été calculés par le code CORCYRE d'une part, et par les codes de diffusion à une dimension PANOPLIE et de burn-up à une dimension PENDULE d'autre part. Les caractéristiques de criticalité et de variation de réactivité, d'évolution des combustibles et de breeding ont été comparées.

Les k_{eff} obtenus avec du combustible ayant les compositions déterminées par le code CORCYRE au moment supposé de la criticalité valent respectivement

0,9939 pour le réacteur au plutonium,

1,0160 pour le réacteur à l'uranium enrichi.

La variation de réactivité entre deux déchargements s'établit comme suit:

	Réacteur chargé au plutonium	Réacteur chargé à l'uranium enrichi
1) Sur la base des compositions déterminées par le code PENDULE	2,47%	3,65%
2) Sur la base des compositions déterminées par le code CORCYRE	2,33%	4,56%

Les variations de compositions isotopiques sont en excellent accord dans les zones de cœur, comme le montrent les figures 12 et 13. L'accord est un peu moins bon dans les zones de couverture. Le tableau IV montre l'inventaire en matières fissiles.

En conclusion on peut considérer que le code CORCYRE constitue un excellent outil pour les études paramétriques et d'optimisation.

REFERENCES

[1] SMIDT, D., MULLER, A., Referenzstudie für den 1000 MWe Natriumgekühlten schnellen Brutreaktor (Na 1), KFK-299 (1964).

[2] STIEVENART, M., RENARD, A., "Propagation of fuel melting in a fast reactor using a ceramic fuel", Symposium on the Safety of fast reactors, Aix-en-Provence, France, 19- 22 September 1967, CEA.

[3] SCHLECHTENDALL, E.G. et al., Safety Features of a 300 MWe Sodium Cooled Fast Breeder Reactor (Na-2), KFK-611 (1967).

[4] SCHLECHTENDALL, E.G., Communication personnelle..

[5] SCHIKARSKI, W., Überlegungen der schweren Reaktorunfällen, KFK-530 (1967).

[6] NICHOLSON, R.B., Methods for Determining the Energy Release in Hypothetical Fast Reactor Meltdown Accidents, APDA-150 (1962).

[7] STIEVENART, M., RENARD, A., « Estimation de l'énergie libérée en cas d'insertion accidentelle rapide de réactivité dans un réacteur à neutrons rapides en présence de rétroactions importantes», Symposium sur la sécurité des réacteurs à neutrons rapides, Aix-en-Provence, France, 19- 22 septembre 1967, CEA.

[8] MICHEL, A. et al., « Analyse du comportement thermique et hydraulique du sodium lors d'une insertion brutale de puissance dans un assemblage de combustible», Symposium sur la sécurité des réacteurs rapides, Aix-en-Provence, France, 19- 22 septembre 1967, CEA.

[9] EGLEME, M., DEBAY, W., HERMANS, L., « Coût de production de l'énergie dans un réacteur rapide par la méthode d'actualisation», Plutonium as a Reactor Fuel (C.r. Colloque Bruxelles, 1967) AIEA, Vienne (1967) 667.

[10] BAKER, A.R., ROSS, R.V., Comparison of the Value of Plutonium and Uranium Isotopes in Fast Reactors, ANL-6792 (1963).

REACTIVITY DEPENDENCE OF COOLANT DENSITY IN STEAM-COOLED FAST REACTORS

K. JIRLOW
AB ATOMENERGI,
STOCKHOLM, SWEDEN

Abstract

REACTIVITY DEPENDENCE OF COOLANT DENSITY IN STEAM-COOLED FAST REACTORS. The variation of reactivity with steam density has been studied for some typical steam-cooled designs for both H_2O and D_2O steam. The Speng code (spectrum programme in the B_1-approximation), the one-dimensional diffusion code Monday and the one-dimensional S_n-programme DTF IV have been used for the calculations. A general result is that for practical Pu compositions in the fuel all 'normal' designs of large oxide reactors will show increase in reactivity with decreasing steam density, or in other words, the steam (density) coefficient $dk/d\rho$ is negative (or the 'void' coefficient is positive). The reactivity dependence is very sensitive, in particular for H_2O steam, to the relative amount of ^{240}Pu as well as of the amount of fission products in the core, i.e. the average burn-up. In general the size of the steam coefficient decreases with increasing core buckling (neutron leakage) and operating steam density, whereas it gets larger with increasing ^{240}Pu content and burn-up. In comparing H_2O and D_2O we find that, for typical values of ^{240}Pu content, the D_2O steam coefficient is less negative than that for H_2O. This difference in steam coefficient between H_2O and D_2O increases with burn-up. Flooding with H_2O or D_2O of a typical steam-cooled core with equilibrium fuel will introduce a reactivity decrease of the order of 10%.

1. INTRODUCTION

It is intuitively clear that the insertion or removal of moderating materials like H_2O and D_2O in a fast reactor core may change the neutron spectrum and therefore the balance between different processes (as leakage, fission, capture in fissile material, capture in fertile material etc.) will change considerably. The leakage will, for instance, decrease rapidly with increasing amount of moderating material. In typical large fast steam-cooled cores with 'equilibrium' Pu fuel the positive reactivity contribution due to the change in leakage is usually more than counter-balanced by the negative contributions due to: (1) the decrease in the average η value for ^{239}Pu; and (2) the rapid increase in the relative capture rate in ^{240}Pu and fission products.

The influence of the coolant density on the reactivity in steam-cooled reactors is of great importance for the safety and operational stability of the entire reactor system. The variation of reactivity with steam density in the core up to flooded conditions has been studied for both H_2O and D_2O steam-cooled designs. The stability at normal operating conditions depends on the slope of the reactivity 'curve' at the actual steam density, i.e. the steam coefficient $dk/d\rho$ at the operating point. Studies of the dynamics of the entire reactor plant [1] have shown that the stability is mainly determined by the steam coefficient, the Doppler coefficient and the system pressure, and that other system parameters have much less influence.

2. PHYSICS ASPECTS OF THE SPENG PROGRAMME

The results referred to in the following sections, except section 6, are all produced by the spectrum programme Speng [2]. Speng starts from a basic microscopic cross-section library. In this all cross-sections are tabulated point by point from 10 MeV down to thermal energies (the energy mesh is chosen to represent the experimental information properly) except in the resonance region (for ^{238}U chosen as the interval 25 keV - 4 eV) where effective group cross-sections for the fissile and fertile isotopes are tabulated as function of 'background cross-section' and temperature. Effective cross-sections for the resonance absorbers (at present, ^{238}U, ^{235}U and ^{239}Pu) in the actual mixture at the actual temperature are produced by the programme with special interpolation formulas. The resonance heterogeneity effect is accounted for by calculating the 'background cross-section' according to the equivalence relations based on Wigner's rational approximation in which a 'Bell' factor is included. The Dancoff factor is estimated with the Bell approximation for rod lattices and with the usual exponential formula in the slab case.

Speng solves the transport equation in the B_1 approximation for a finite homogeneous medium, the geometry of which is represented by a buckling B^2. The source is a fission spectrum of the Maxwellian form. The widths and the number of the lethargy steps (groups) could be varied over wide ranges – up to 2000 steps are possible. To save computing time, the number of groups is, of course, minimized with respect to an adequate representation of the fine structure in the cross-sections involved. In these particular calculations 150 to 250 lethargy groups were used depending how far down in energy a non-negligible fraction of the neutrons reached. When the programme calculates the flux for a certain group, it uses $1/\Sigma_T$ -weighted cross-section averages for that group. A Speng calculation may well be described as a zero-dimensional calculation, almost equivalent to the fundamental mode method with a very large number of groups.

3. REACTIVITY-STEAM DENSITY INTERACTION FOR A TYPICAL H_2O STEAM-COOLED CORE

Consider a core design with the following parameters:

Volume fractions: fuel 0.45, steam 0.325, structure 0.225
Structure material: Incoloy 800, density 8 g/cm^3,
45 wt% Fe/35 wt% Ni/20 wt% Cr
Fuel density (mixed oxide) 9.361 g/cm^3
Fuel pin diameter: 6.5 mm
Fissile isotopes in fuel: ^{239}Pu
Fertile isotopes in fuel: ^{238}U and ^{240}Pu
Buckling of the core (including the reflector savings): $B^2 = 9$ m^{-2}.

The variation of the multiplication factor k_{eff} with steam density is plotted in Fig. 1 for three compositions of the fuel.

Upper curve (dashed line): no ^{240}Pu, and no fission products, enrichment 11.8%

Middle curve (dotted line): no ^{240}Pu but fission products, enrichment 12.7%.
Lower curve (full line): ^{240}Pu and fission products, enrichment 16.3%

Here we define the enrichment as the mass ratio of Pu isotopes and heavy isotopes. The amount of fission products included in the two latter fuel compositions is the same and corresponds to an average burn-up of 40 MWd/kg. The first two fuel compositions are, of course, purely hypothetical and they are included just to show the influence of ^{240}Pu and fission products. We note that for a core containing only fresh fuel with very clean plutonium the steam coefficient may be positive. In the third case with ^{240}Pu the Pu composition is 78 wt% ^{239}Pu and 22 wt% ^{240}Pu, which is considered as representative from reactivity aspects for equilibrium plutonium with combined core and blanket reprocessing. Thus the lower curve shows a typical reactivity behaviour for an H_2O steam-cooled core at equilibrium fuel cycle conditions. If we flood such a core (which is necessary at refuelling operations) the reactor will be approximately 10% sub-critical.

It is apparent from Fig. 1 that the slope of the reactivity curve is very sensitive to the relative amount of ^{240}Pu and/or fission products. The addition of either of these components will always decrease $dk/d\rho$ (i.e. make it more negative).

4. ANALYSIS OF THE REACTIVITY 'CURVE' IN TERMS OF IMPORTANT COMPONENTS IN THE NEUTRON BALANCE

The reactivity distributions in Fig. 1 have been analysed in terms of η_{239}, fast fission ratio, leakage per source neutron and other factors which are thought to be of importance for the reactivity variation. From Figs 2-4, where all these factors as function of steam density are displayed for the three fuel compositions, we find that the factors giving 'monotonic' negative contributions to reactivity change with increasing coolant density are:

(a) The decrease in η_{239} (Fig. 2)
(b) The decrease in fast fission ratio (Fig. 2)
(c) The increase in ^{240}Pu capture relative to ^{239}Pu absorption (Fig. 3)
(d) The increase in fission product capture per source neutron (Fig. 4);

of which (a) is mot important.

The factors which make 'monotonic' positive reactivity contributions are:

(e) The decrease in ^{238}U capture relative to ^{239}Pu absorption (Fig. 3)
(d) The decrease in leakage probability (Fig. 4).

We note that for the equilibrium fuel case the negative effect (c) almost compensates the positive contribution (e) (Fig. 3) for this particular equilibrium Pu composition and that the main negative effect (a) overrides the positive leakage effect (d). Regarding the influence on the reactivity curve of changes in the cross-sections involved, it is clear that the reactivity curves will be very sensitive to changes in capture cross-sections of ^{240}Pu or of ^{238}U and to changes in α-values of ^{239}Pu.

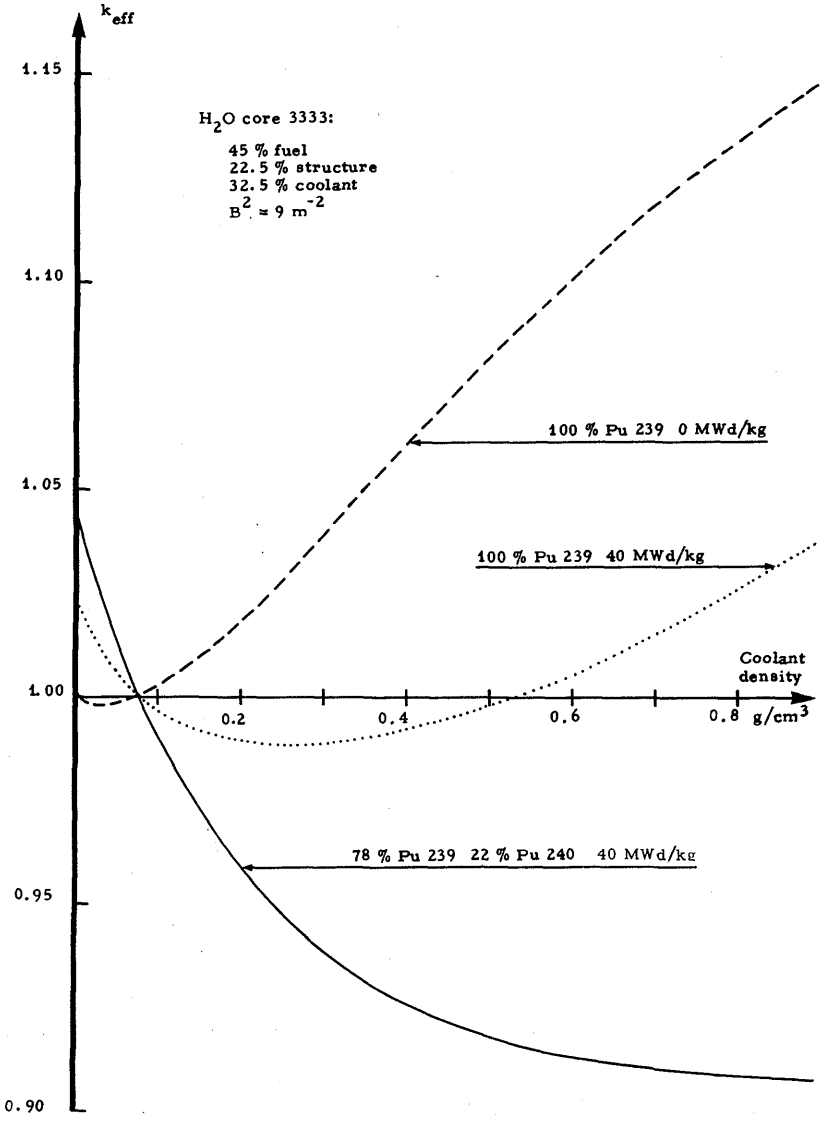

FIG. 1. k_{eff} plotted against coolant density.

5. THE DEPENDENCE OF THE STEAM COEFFICIENT ON CORE DESIGN

In a parametric survey study of breeding properties of steam-cooled fast power reactors [3] reported elsewhere, the dependence of the nuclear quantities, critical enrichment, breeding ratio etc. on core composition and geometry was calculated. The core composition was described by

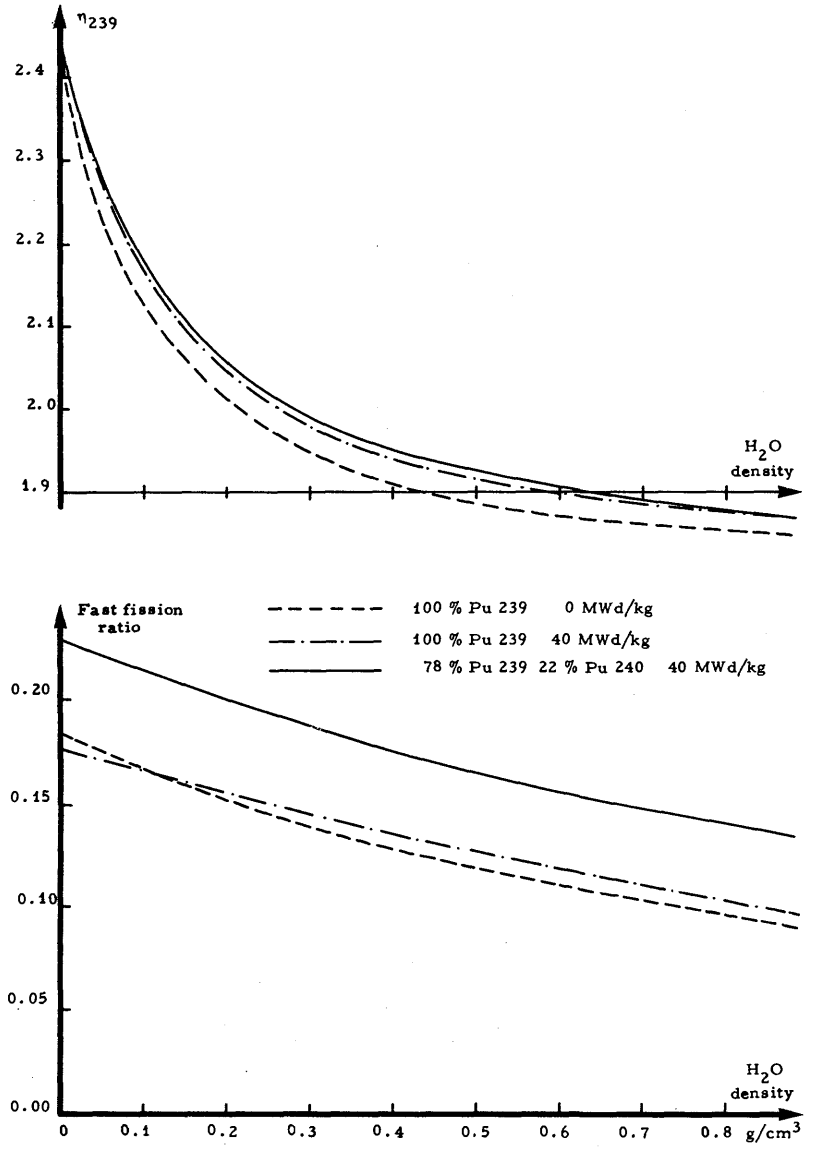

FIG.2. H_2O steam-cooled core: η_{239} and fast fission ratio plotted against coolant density.

three quantities, the steam to fuel mass ratio (x), the fuel volume fraction (y) and the structure to fuel volume ratio (z), and the core geometry was represented by the buckling (B^2). Second-order polynomials describing the nuclear quantities as functions of x, y, z and B^2 were derived by a least-squares fitting procedure.

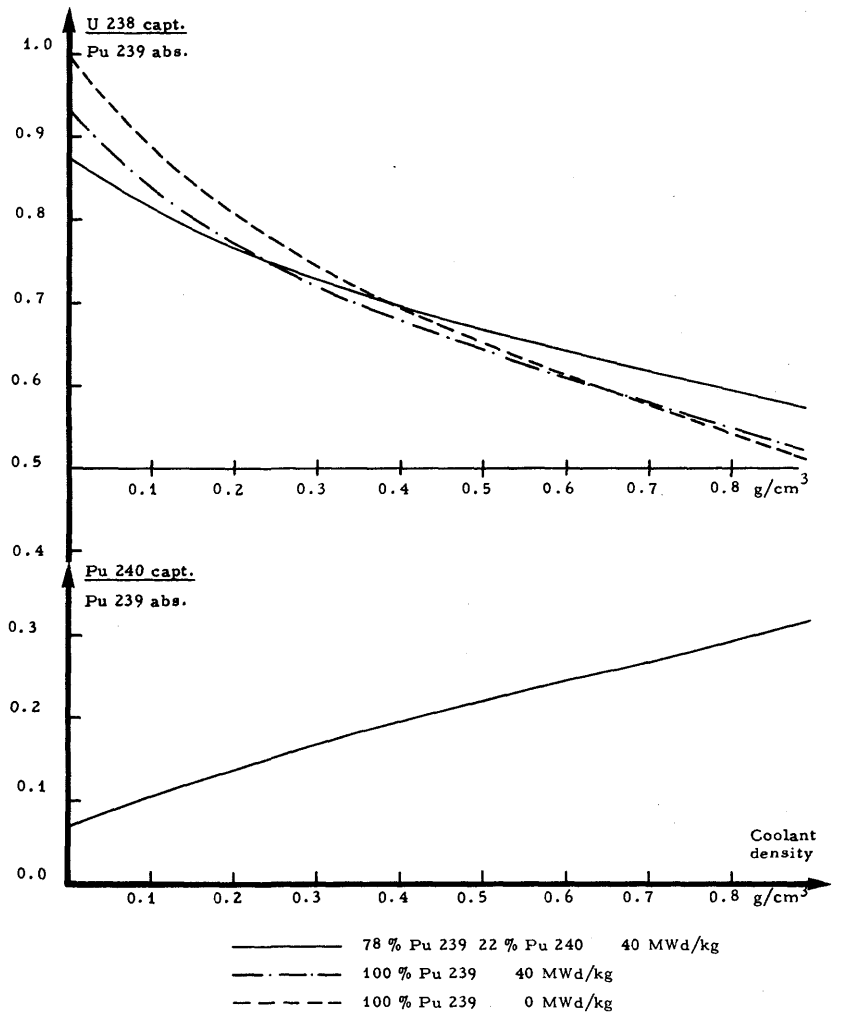

FIG.3. H_2O steam-cooled core: ratios of ^{238}U capture to ^{239}Pu absorption and of ^{240}Pu to ^{239}Pu absorption plotted against coolant density.

Here we have used the fitted function $E = f(x, y, z, B^2)$ and calculated the steam coefficient according to

$$\frac{\delta k}{\delta \rho} = -\frac{\delta k}{\delta E}\left(\frac{\delta E}{\delta \rho}\right)_{k=1}$$

$\delta k/\delta E$ was obtained from consecutive criticality iterations in Speng calculations. It is clear that this procedure involves crude approximations and thus the results in Figs 5 and 6 should only be considered as a description of trends. Two important monotonic trends in the steam

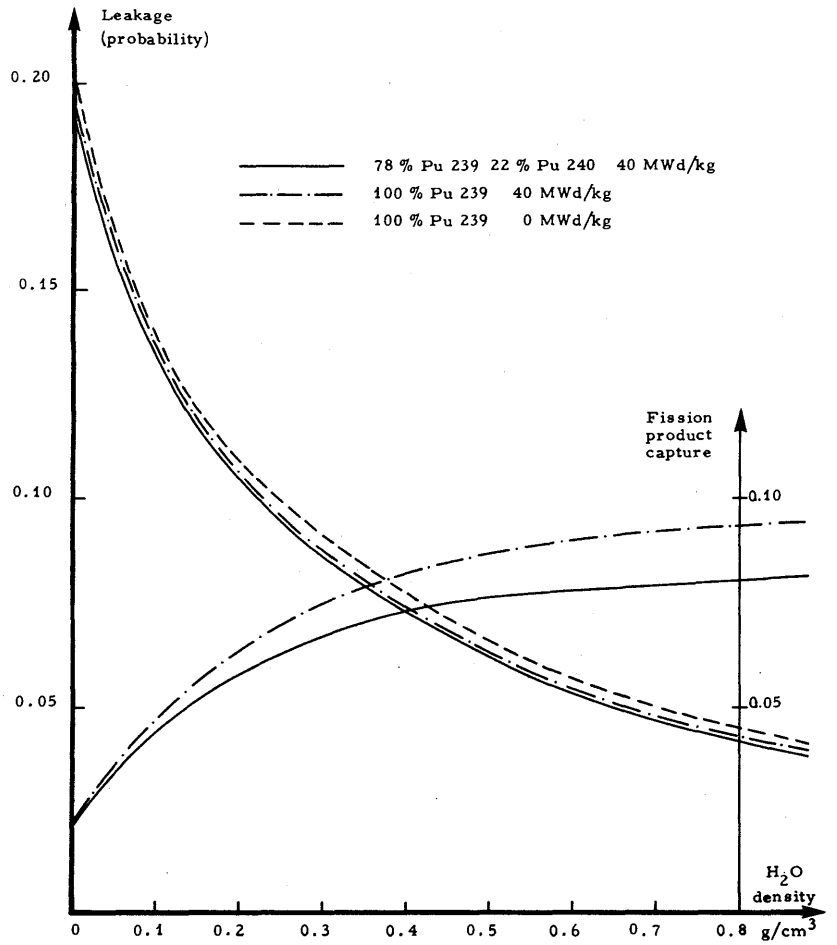

FIG.4. H_2O steam-cooled core: leakage and fission product capture per source neutron plotted against coolant density.

coefficient are apparent: firstly, $|dk/d\rho|$ decreases rapidly with increasing buckling and, secondly, it also goes to less negative values when the operating steam density increases. Calculations indicate that the variation with buckling is approximately linear in the B^2 range typical for large power reactors. We also note that for this typical Pu composition and burn-up the steam coefficient for D_2O are in general appreciably smaller than for H_2O.

6. STEAM COEFFICIENT FOR AN OPTIMIZED STEAM-COOLED CORE

In Fig. 7 the reactivity variation with steam density is shown for a core composition and core buckling which are characteristic for a 1000-MW(e) power reactor core optimized with respect to fuel costs

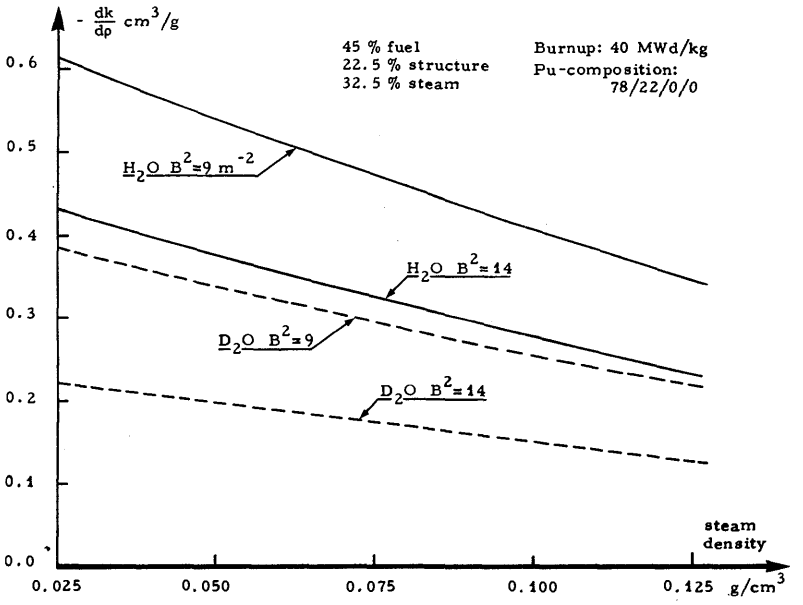

FIG.5. dk/dρ plotted against operating steam density ρ.

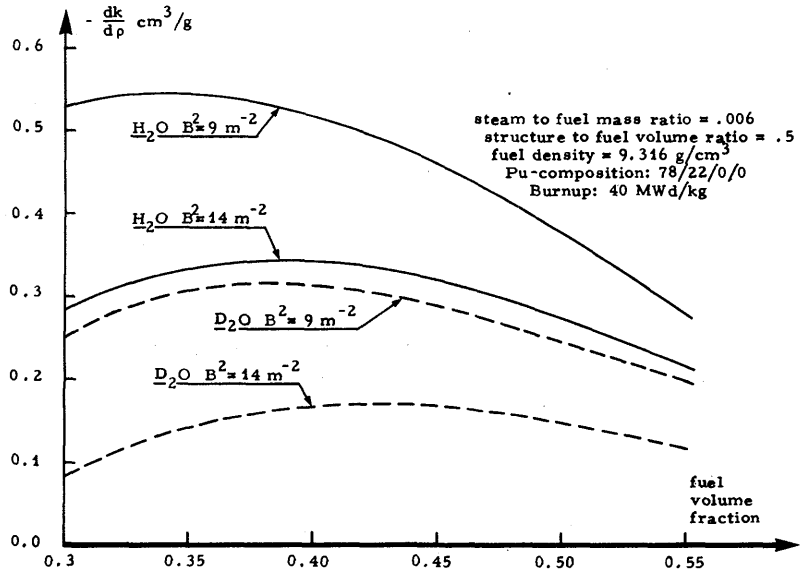

FIG.6. dk/dρ plotted against volume fraction.

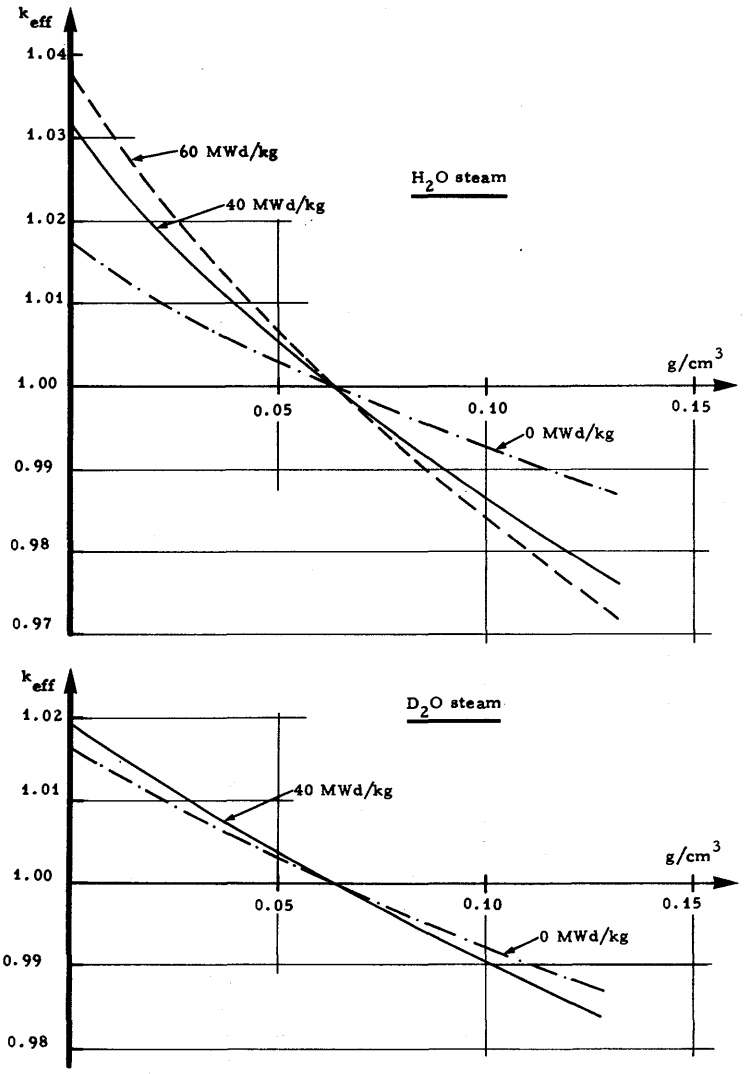

FIG.7. k_{eff} plotted against steam density for different burn-ups. Steam-cooled reference core: 48.5% fuel, 30.1% coolant, Pu composition 78/22/0/0, $B^2 = 11\ m^{-2}$.

within the frame of present technological knowledge [4]. From these curves we obtain the relevant quantities presented in Table I. Δk_L is the reactivity change at complete coolant loss and Δk_f is the change when the whole core is flooded with water (H_2O or D_2O).

We recognize again the strong influence of the average burn-up on Δk_L and $dk/d\rho$ for H_2O steam; for D_2O the effect is much smaller. An increase in ^{240}Pu content from 22 to 30% increases the steam coefficient by 10% in the H_2O case and by about half that value for D_2O steam. For burn-ups of 40 to 60 MWd/kg $dk/d\rho$ for D_2O are roughly 65% of $dk/d\rho$

TABLE I. COOLANT-REACTIVITY INTERACTION IN STEAM-COOLED REFERENCE REACTOR

Core volume fractions: 48.5% fuel 30.1% steam Operational density = 0.063 g/cm³ Buckling = 11 m⁻²		Δk_L	Δk_f	$-\frac{dk}{d\rho}$ (cm³/g)	$-\frac{dk/k}{d\rho/\rho}$	Doppler constant α
H_2O steam	0 MWd/kg 22% ^{240}Pu	+ 0.018	-0.070	0.22	0.0135	
	40 MWd/kg 22% ^{240}Pu	+ 0.032	-0.134	0.40	0.025	-0.0135
	60 MWd/kg 22% ^{240}Pu	+ 0.038	-0.158	0.47	0.030	
	40 MWd/kg 30% ^{240}Pu	+ 0.036	-0.157	0.44	0.028	
D_2O steam	0 MWd/kg 22% ^{240}Pu	+ 0.016	-0.077	0.23	0.014	
	40 MWd/kg 22% ^{240}Pu	+ 0.020	-0.106	0.27	0.017	-0.0008
	40 MWd/kg 30% ^{240}Pu	+ 0.021	-0.117	0.29	0.018	

for H_2O steam. This significant advantage with D_2O cooling from the stability aspect is, however, to a large extent counterbalanced by the disadvantage of the much smaller size of the Doppler constant (α). α_{D_2O} for this core is approximately - 0.008 (Table I) which is about 60% of the Doppler constant for H_2O steam. Assuming these values for the reactivity coefficients the dynamic studies [1] on similar core designs using a linear model indicate that the advantage with D_2O steam in this reference core with respect to the operational stability is rather marginal. However, the smaller size of Δk_L and Δk_F in the D_2O case is, of course, an important safety advantage for D_2O steam.

7. THE INFLUENCE OF THE BLANKET ON THE REACTIVITY DEPENDENCE ON COOLANT DENSITY

In the preceding sections all results referred to were produced by the zero-dimensional calculation with the Speng programme. This means

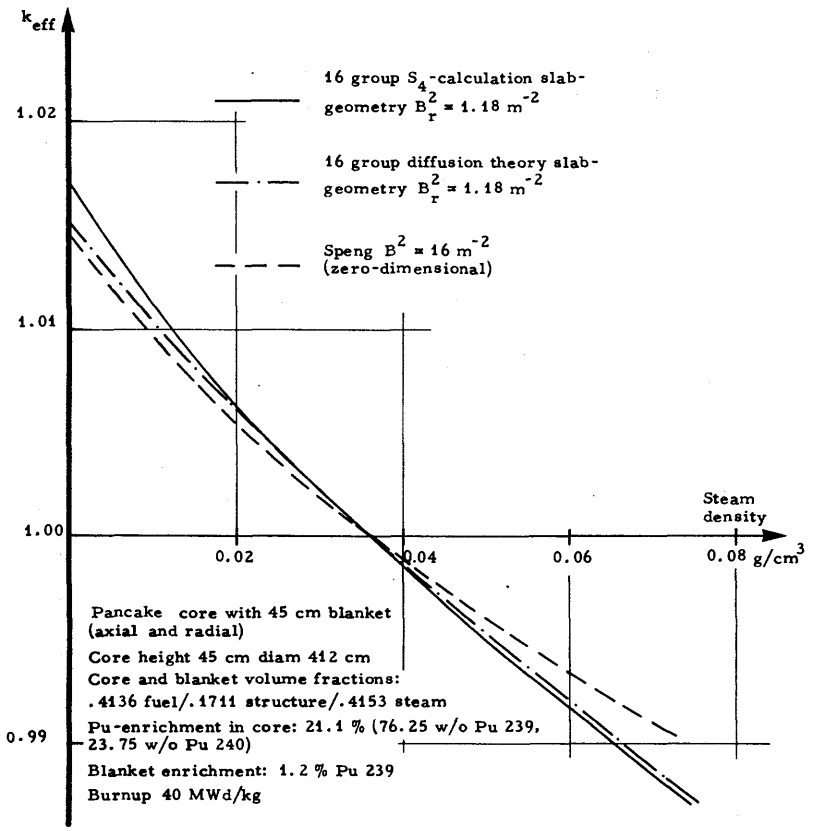

FIG. 8. H_2O steam-cooled 'pancake' design, k_{eff} plotted against steam density.

that the blanket was in effect replaced by an appropriate reflector saving. As shown in Ref. [5] the reflector saving varies slightly with steam density. However, as the cores considered here were large or, more precisely, had relatively small bucklings, we assumed tentatively that the influence of the blanket (due to varying reflector savings between different energy groups and different steam densities) could be neglected in the first approximation.

Comparison of multigroup diffusion calculations and the results with the Speng code for a few cases has shown that the zero-dimensional calculations underestimate the steam coefficients slightly. This deviation will be most significant when the reflector saving is an appreciable fraction of either the core height or core diameter. This would be the case for a very flat cylindrical core.

In Fig. 8 the reactivity distributions for a 'pancake' core, similar to the 1000-MW(e) steam-cooled design by General Electric, are presented. The S_4- and diffusion-calculations were one-dimensional in the axial direction (slab geometry) and were done with the programmes DTF IV and Monday respectively. The steam coefficients according to these

methods are quite similar – the S_4-coefficient being a few per cent larger than that of diffusion theory. As one might expect, the zero-dimensional coefficient is appreciably smaller, almost 20% lower than the one-dimensional values. However, even for such extreme geometries the difference is not so large that zero-dimensional calculations lose their meaning in giving estimates for survey studies.

ACKNOWLEDGEMENTS

The author would like to thank Mr. M. Lindberg for valuable help in the evaluation work, Mrs. P. Eriksson for skilful assistance with the machine calculations and Drs. H. Häggblom and P. Behrenz for stimulating discussions.

REFERENCES

[1] JOSEFSSON, R., VOLLMER, H., Results from Stability and Transient Studies of a Steam-cooled Fast Power Reactor, AE-RTR-265 (1967).

[2] NYMAN, K., Speng, a Computer Programme for Calculation of Neutron Spectrum and Group Cross Sections in a Finite Homogeneous Medium, AE-RFN-279 (1967).

[3] JIRLOW, K., LINDBERG, M., Survey of Breeding Properties of Fast Steam-cooled Power Reactors, AE-RFR-630 (1967).

[4] Swedish Evaluation Studies Concerning Full Scale Fast Reactors, Vol. 3. Fast H_2O Steam-cooled Breeder Reactor Study, to be published (1967).

[5] KIEFHABER, E., OTT, K., "Survey parameter study of large steam-cooled fast power reactors," Proc. Argonne Conf., Oct. 1965, ANL-7120.

DISCUSSION

E. KIEFHABER: What are typical calculation times with the Speng code for, say, 150 and 2000 lethargy groups?

K. JIRLOW: The calculation time for 150 lethargy groups is about two minutes on an IBM 7044, depending on how many isotopes are involved. For 2000 groups some 10 - 15 minutes are necessary.

E. KIEFHABER: Your more refined calculations appear to relate to H_2O. Does this mean that you are more interested in H_2O than in D_2O, in spite of the fact that – according to your findings – D_2O has somewhat better safety features and a considerably larger breeding ratio?

K. JIRLOW: We have used the same methods for H_2O and D_2O steam. We consider that D_2O steam offers a promising long-range solution provided the capital cost of a D_2O-cooled fast reactor system can be reduced to approximately that of an H_2O-cooled plant.

G. L. J. MINSART: How do you determine what figure to use for reflector savings – on the basis of a power distribution or from the form of the flux distribution, calculating in the transverse direction? The differences in reflector savings may well be large, depending on the groups considered, particularly if the water (steam) density is high.

K. JIRLOW: We use a reflector savings value (the same for all groups) which preserves $k_{eff} = 1$ when zero-dimensional and one-dimensional calculations are being compared.

G. L. J. MINSART: This means that you use an average weighted by the sizes of the different groups. Should not, however, the effect of the different extrapolation distances be taken into account in estimating the leakages at different energies, especially when one is considering a differential effect (variations as a function of H_2O density)?

K. JIRLOW: As I showed in the latter part of my paper, this assumption does introduce errors. However, for core dimensions typical of large power reactors the errors are small.

REACTIVITY COEFFICIENTS OF STEAM-COOLED FAST BREEDERS*

E. KIEFHABER
INSTITUT FÜR NEUTRONENPHYSIK UND REAKTORTECHNIK,
KERNFORSCHUNGSZENTRUM KARLSRUHE,
KARLSRUHE, FEDERAL REPUBLIC OF GERMANY

Abstract

REACTIVITY COEFFICIENTS OF STEAM-COOLED FAST BREEDERS. The influence of several design parameters on some nuclear quantities which are related to the safety and stability of a steam-cooled fast breeder is discussed. Almost all results refer to a 1000-MW(e) plant.

Two of the most important quantities for the stability behaviour of such a reactor, which are derived from the nuclear calculations, are the Doppler coefficient and the steam-density coefficient of reactivity. In addition there are several other nuclear quantities related to the safety of a steam-cooled fast reactor: the criticality changes upon loss of coolant, or flooding in the axial or radial direction. Two design parameters of great influence are the composition of the plutonium isotopes and the burn-up or the fission products: going from pure ^{239}Pu to "dirty plutonium" with a ^{240}Pu content of 30% decreases the criticality in the flooded state by an amount of 20-25%. Taking into account the fission products corresponding to an average burn-up of 50 000 MWd/t results in a criticality change of about 5% in the same state. The influence of both design parameters on the criticality change belonging to the loss-of-coolant accident, although smaller in magnitude, is of equivalent importance. The combined effect of both parameters causes a change of sign for the steam-density coefficient which in most cases has unfavourable effects on stability. In this connection one has also to take into account the type of material used for structure and cladding. The type of coolant (H_2O or D_2O) is the design parameter with the greatest influence on the Doppler coefficient.

The geometrical configuration of the reactor and the coolant pressure are further parameters which are considered with respect to safety.

1. INTRODUCTION

In the first generation of fast power reactors the fuel expansion coefficient of the metallic fuel was the most important quantity correlating the neutron physics with the safety behaviour of the reactor. For the second generation of fast reactors fuelled with ceramic fuel, the Doppler reactivity feedback, characterized by the Doppler coefficient (DC) of criticality, is the dominant nuclear quantity with regard to the safety and stability behaviour of the reactor. For steam-cooled fast breeders the steam-density coefficient (SDC) of criticality turns out to possess also a great influence on the stability behaviour, and there are other quantities to be considered in a reactor design which are equally related to changes in criticality resulting from changes in the coolant density. These quantities are shown in Fig. 1.

As reported elsewhere [1], the Karlsruhe design of a steam-cooled 1000 MW(e) breeder [2], the so-called D1-reactor, is near the boundary between the stable region and the unstable region. Taking into account

---

* Work performed within the association in the field of fast reactors between the European Atomic Energy Community and Gesellschaft für Kernforschung m. b. H., Karlsruhe.

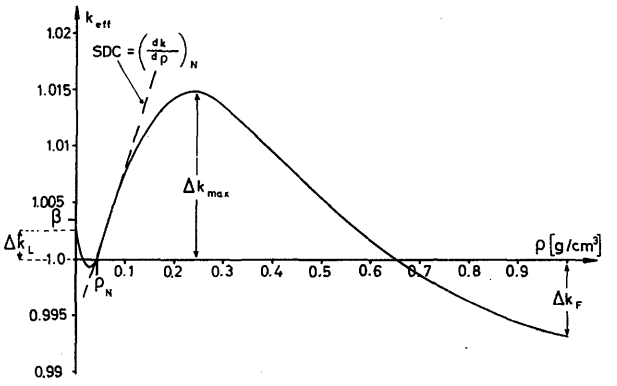

FIG. 1. Influence of coolant density on criticality.

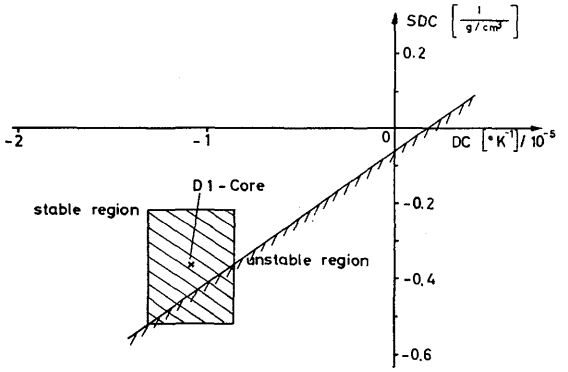

FIG. 2. Region of core stability.

the uncertainties of the DC and the SDC it would be possible for the D1-reactor to move into the unstable region (Fig. 2). This fact underlines the necessity of measuring both coefficients precisely, a task that will be fulfilled by the SNEAK facility. Furthermore, the influence of the design parameters on both coefficients and the other quantities shown in Fig. 1 should be examined to obtain an idea of the importance of various design parameters with regard to the nuclear quantities and to find out the possibilities of influencing these quantities in the desired direction by suitable changes in the design parameters. This is the purpose of the present paper.

2. THE DESIGN PARAMETERS AND THEIR VARIATIONS

Starting from a reference point corresponding to the D1-reactor a very large number of design parameters have been varied and these are listed in Table I.

The values of the design parameters corresponding to the D1-reactor which are listed in Table II together with the resulting atom densities have been used as a reference point.

2.1. Reasons explaining the variation of the parameters

2.1.1. Large variations

Besides the variation during burn-up the isotopic composition of plutonium depends on the origin of the plutonium and on the fuel management in fast reactors: reprocessing the fuel elements of the core together with those of the blankets of a steam-cooled breeder results in the composition (β) of Table I; separate reprocessing and selling the excess plutonium of the blankets leads to composition (γ) which shows a higher content of ^{240}Pu and is often called "dirty plutonium". To obtain the other extreme, i.e. "clean plutonium", composition (α) has been introduced.

For metallurgical reasons there is only one cladding material available at present which could probably meet the requirements on strength and creep behaviour at the high pressures and cladding temperatures for which the D1-reactor is designed. Nevertheless, it is interesting to take a look at the advantages shown by a cladding material which has been used in steam cycles, and which is more favourable from the neutron physics point of view because of its lower neutron absorption probability.

D_2O instead of the normal H_2O is an interesting alternative coolant because of its smaller moderation effect which leads to an increase of the mean neutron energy and to a strong decrease of the low energy part of the neutron spectrum. Several ratios of D_2O/H_2O have been used in the study to see whether the interesting quantities show a linear dependence on the D_2O content. The compensation of long-term changes in criticality by a variation of the D_2O content, as in the spectral shift reactors [3], is another reason for studying this coolant alternative.

The advantages of the fuel nitrides (UN, PuN) are a higher density and a lower moderation effect, compared with the fuel oxides (UO_2, PuO_2), the disadvantage being, however, the greater neutron absorption in one nitrogen atom, compared even with that in two oxygen atoms. The fuel carbides which apparently offer remarkable advantages in sodium-cooled reactors [4] have not been studied because they cannot be used together with steam as a coolant.

It is well known that the geometric arrangement of the core has an important influence on the breeding and safety behaviour of the reactor; see, e.g. the pancake-shaped cylindrical core of GE [5, 6]. Therefore, the effect of a drastic increase in geometric buckling has been studied.

Nearly all calculations have been made using the well-known Soviet group cross-section set of Abagjan et al., called the ABBN set [7]. To get an insight into the influence of the group cross-sections used, two additional calculations have been made for the reference point with the two sets prepared at Karlsruhe, i.e. the KFK set and the SNEAK set described in Refs [8, 9] respectively.

2.1.2. Small variations

These variations will be studied since we are not quite sure with regard to some of the design parameters that the desired values are obtainable with the present or future technology (e.g. the fuel density at a high burn-up), or because we intend or are forced to change the parameters by a small amount to match other requirements or to obtain a more

TABLE I. LIST OF VARIED PARAMETERS

(A) Large variations (step changes)

(1) Plutonium isotopic composition

	^{239}Pu	^{240}Pu	^{241}Pu	^{242}Pu
(α)	100	0	0	0
(β)	74	22.7	2.3	1.0
(γ)	63.7	30.5	3.4	2.4

(2) Cladding and structure material

	Material	Density (g/cm^3)	Weight-per cent of				
			Cr	Fe	Mo	Nb	Ni
(α)	Inconel 625	8.44	22	3	9	4	62
(β)	Incoloy 800	8.01	20	48	0	0	32

(3) D_2O-content in the normal H_2O steam coolant

	(α)	(β)	(γ)	(δ)	(ε)
H_2O	1.0	0.9	0.5	0.1	0.0
D_2O	0.0	0.1	0.5	0.9	1.0

(4) Type of ceramic fuel
- (α) Oxide
- (β) Nitride

(5) Magnitude of geometric buckling
- (α) $B_2 = 5.69 \times 10^{-4}$ cm^{-2}
- (β) $B_2 = 11.38 \times 10^{-4}$ cm^{-2}

(6) Set of group cross-sections used
- (α) ABBN !set
- (β) KFK set
- (γ) SNEAK set

(B) Small variations (quasi-continuous changes)

(7) Burn-up	increased by 10%
(8) Fuel density	decreased by 10%
(9) Steam density	decreased by 10%
(10) Coolant volume fraction	increased by 10%
(11) Buckling	increased by 10%

TABLE II. DESIGN PARAMETERS FOR THE REFERENCE POINT

	Type of material	Volume fraction
Fuel	UO_2 - PuO_2	0.454
Cladding + structure	Inconel 625	0.206
Coolant	H_2O - steam	0.32
Follower	Al_2O_3	0.02

Maximum core-averaged burn-up before reloading 1/3 of the core elements	3.0653 at.%
Fuel density	87% of theoretical
Plutonium isotopic composition	74:22.7:2.3:1.0
Normal mean steam density	0.0706 g/cm^3 at 170 atm abs. ≈ 2600 lb/in^2
Core height 150 cm Core diameter 260 cm	$B^2 = 5.69 \times 10^{-4}$ cm^{-2}
Thickness of axial and radial blankets	35 cm

Atom densities × 10^{-24} per cm^3 of core volume (AD) for each isotope or element (I or E)

I or E	Al	Cr	Fe	H	Mo	Nb
AD	7.34×10^{-4}	4.43×10^{-3}	5.62×10^{-4}	1.498×10^{-3}	9.82×10^{-4}	4.51×10^{-4}

I or E	Ni	O	^{239}Pu	^{240}Pu	^{241}Pu	^{242}Pu
AD	1.106×10^{-2}	2.127×10^{-2}	9.7044×10^{-4}	2.977×10^{-4}	3.016×10^{-5}	1.31×10^{-5}

I or E	^{238}U	Pairs of fission products
AD	8.10235×10^{-3}	2.977×10^{-4}

TABLE III. THE INFLUENCE OF CHANGES IN THE DESIGN PARAMETERS ON DK = -Tdk/dT, RSDC = $(dk/k)/(d\rho/\rho)_N$, $\Delta k_L = k_{eff}(\rho = 0) - k_{eff}(\rho_N)$, $\Delta k_F = k_{eff}(\rho = 1 g/cm^3) - k_{eff}(\rho_N)$, AR = $(N_{Pu-239} + N_{Pu-241})/(N_{U-238} + N_{Pu-240})$: CR = internal conversion ratio, M^2 = diffusion area, ℓ = neutron generation time

Change No.	Parameter changed	DK $\times 10^2$	RSDC $\times 10^2$	Δk_L $\times 10^2$	Δk_F $\times 10^2$	AR	CR	M^2 (cm^2) $\times 10^{-2}$	ℓ (μs)
0	Reference	1.69022	-1.84098	+3.7349	-4.6463	0.119118	0.980565	1.47213	0.444721
1	Pu 100	1.88161	-0.2155	+2.2217	+14.474	0.121568	0.883024	1.52407	0.551552
2	Pu 63.7	1.68410	-2.1615	+4.0693	-7.7078	0.116542	1.026592	1.45140	0.422241
3	Incoloy 800	2.10583	-0.74849	+2.0399	-3.3267	0.107520	1.054990	1.59404	0.525653
4	D_2O	0.97267	-2.606	+3.0419	-10.734	0.117581	1.087751	1.68866	0.335977
5	Nitride	1.53406	-2.602975	+4.4489	-6.4918	0.103127	1.081165	1.26323	0.304060
6	B^2 doubled	1.39856	-1.072005	+2.5202	-2.751	0.140696	0.844599	1.44561	0.383044
7	KFK set	1.67540	-3.085	+5.0207	-10.8771	0.129911	0.98097	1.33421	0.439911
8	SNEAK set	1.64679	-2.3965	+4.0027	-7.3327	0.139273	1.00264	1.32505	0.444475
9	H_2O:D_2O = 0.9:0.1	1.64730	-1.9245	+3.7162	-5.0968	0.119073	0.98895	1.48951	0.435428
10	H_2O:D_2O = 0.5:0.5	1.42217	-2.293	+3.5669	-6.8223	0.118743	1.02711	1.56702	0.395119
11	H_2O:D_2O = 0.1:0.9	1.08168	-2.5885	+3.1950	-9.2064	0.117919	1.07431	1.66146	0.348715
12	Burn-up increased	1.66165	-1.9525	+3.8762	-4.9746	0.120087	0.974824	1.46918	0.440294
13	Fuel dens. decreased	1.64696	-1.8185	+3.8215	-4.4266	0.127015	0.926155	1.67446	0.482096
14	Steam dens. decreased	1.63217	-1.8180	+3.5156	-4.7432	0.118629	0.991698	1.50485	0.433141
15	Cool. vol. fract. incr.	1.72816	-1.7960	+3.9236	-4.1685	0.123016	0.943757	1.57010	0.479779
16	Buckling increased	1.65895	-1.7575	+3.6025	-4.4566	0.121163	0.965875	1.46959	0.438058

economical reactor. In the event of an increase in the coolant volume fraction the volume fractions of the cladding and the fuel would change in a consistent manner keeping the ratio of cladding-to-fuel volume constant.

When changing the design parameters criticality at normal steam density ρ_N was maintained by an appropriate variation of the enrichment ($k_{eff}(\rho_N) = 1.0 \pm 10^{-5}$).

3. RESULTS

All results of this study have been obtained from fundamental-mode diffusion calculations for the homogeneous reactor. During the design of the D1-reactor many one- and two-dimensional diffusion calculations have been carried out [10], dealing partially with similar questions. However, because of the various design steps these calculations do not refer to the same reference point. It can be concluded from these calculations that with respect to safety and stability behaviour the fundamental-mode calculations are sufficiently accurate for a large reactor of the type chosen in the D1-design; even Δk_L is not influenced very much by the change in the buckling or the corresponding savings which occur when the steam density is reduced. The relative tendencies observed on the variation of some parameters, in particular, are reproduced pretty well by the fundamental-mode results, with the possible exception of strongly changing the geometric form of the core. It goes without saying that for determining the power distribution or the total breeding ratio two-dimensional calculations are necessary.

A number of interesting quantities have been determined from the nuclear calculations: as mentioned before, the Doppler coefficient (DC) = dk/dT and the Doppler constant (DK) = -Tdk/dT, as well as the steam-density coefficient (SDC) = $(dk/d\rho)_N$ and the reduced steam-density coefficient (RSDC) = $(dk/k)/(d\rho/\rho)_N$, are the most important nuclear quantities related to the stability behaviour of the reactor. Apart from these, the other quantities shown in Fig. 1, Δk_L and Δk_F, are reported which may influence to some degree the safety of the reactor; the quantity Δk_{max} has no special meaning for the cases studied in this paper, because in all cases except one it is identical with Δk_L, the only exception occurring for "clean plutonium" for which Δk_{max} coincides with Δk_F. For the sake of completeness some other quantities have also been included in the study: (a) the atom ratio (AR) of fissile-to-fertile material = $(N_{Pu-239} + N_{Pu-241})/(N_{U-238} + N_{Pu-240})$ which is correlated in a simple manner to the enrichment E = AR/(1+AR) and, therefore, provides a hint regarding changes in fuel cycle cost, fuel rating and related quantities, e.g. the doubling time; (b) the conversion ratio (CR) as a measure of internal breeding; (c) the diffusion area M^2 which characterizes the diffusion process, and together with the geometric buckling B^2, to some degree the external breeding; and (d) the prompt neutron generation time ℓ which is important to strong short-term perturbations of reactor criticality. Regarding the accuracy of the methods of calculation used to determine the quantities studied, some remarks may be found in Ref. [10].

For all the changes in the design parameters the results for the interesting quantities DK, RSDC, Δk_L, Δk_F, AR, CR, M^2, ℓ are given numerically in Table III and graphically in Figs 3-6.

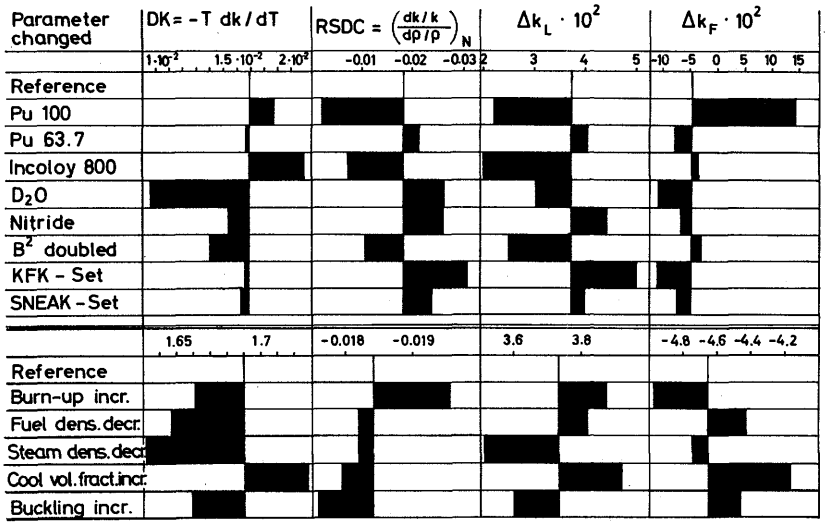

FIG. 3. Influence of various design parameters on reactivity coefficients.

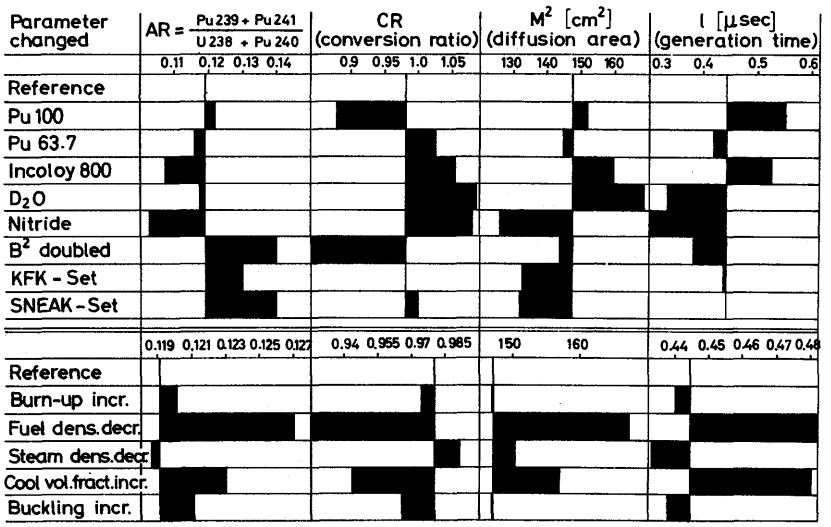

FIG. 4. Influence of various design parameters on several nuclear quantities.

We shall now discuss the influences which the changes in the design parameters exert on the quantities studied.

3.1. Plutonium-composition 100:0:0:0

It is known that the multiplication factor of ^{241}Pu is superior to that of ^{239}Pu, whereas the multiplication factor of ^{240}Pu is superior to that of

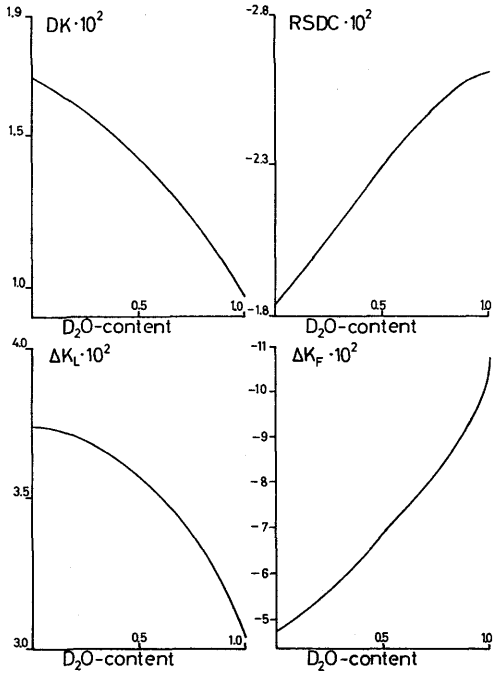

FIG. 5. Influence of D_2O content on reactivity coefficients.

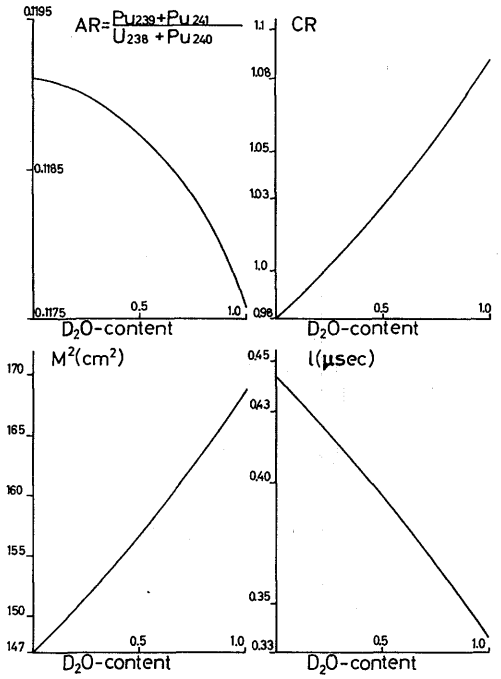

FIG. 6. Influence of D_2O content on several nuclear quantities.

^{238}U, the latter being due to the lower fast-fission threshold in ^{240}Pu. Therefore, with the use of "clean plutonium", AR has to be increased. The same effect of a reduction in fast-fission processes causes a considerable decrease in $|RSDC|$ and Δk_L which favourably influences the stability behaviour. Because of the absence of ^{240}Pu with its low-energy resonance at about 1 eV, Δk_F shows a tremendous increase, an effect which has already been described in Ref. [11]. The influence of the resonance self-shielding causes (a) a reduction in the effective cross-section of the fuel, especially of the fertile material, and (b) an increase in the low-energy part of the neutron spectrum (softer spectrum) giving rise to a decrease in CR and an increase in DK, M^2 and ℓ, the increase of DK also influencing the stability behaviour in a favourable direction.

3.2. Plutonium-composition 63.7:30.5:3.4:2.4

In all cases the influence of "dirty plutonium" is the opposite to that discussed in Section 3.1 for "clean plutonium", and can be explained by similar arguments.

3.3. Incoloy 800

Because of the smaller parasitic absorption of Incoloy 800 compared with Inconel 625 (with its high nickel content and the "neutron poisons" molybdenum and niobium), AR is decreased by a considerable amount causing an increase in CR. A reduction of the total absorption and transport cross-section, and a softening of the neutron spectrum, are further consequences of the change in the structure and cladding material which cause the changes in DK, M^2 and ℓ. The changes in RSDC and Δk_L, which are quite remarkable, and the slight change in Δk_F are due to the energy dependence of the absorption cross-section of the structure and cladding materials considered.

3.4. D_2O

The criticality difference resulting from the use of D_2O instead of H_2O in a reactor, the other conditions of which remain unchanged, is small. Therefore, the change in AR or in enrichment which is necessary to preserve criticality is also small. The influences on most quantities (DK, Δk_F, CR, M^2, ℓ) are caused by the smaller cross-section and the smaller moderation of D_2O compared with H_2O leading to a harder neutron spectrum and an increased leakage rate. The change in the leakage rate following a reduction in the steam density is always smaller than with H_2O, but for Δk_L the effect of the expected and considerably smaller difference in k_∞ – the multiplication factor of an infinitely large reactor of the same composition – is dominating, thus producing a lower value of Δk_L. As to RSDC, the corresponding difference in k_∞ is a little larger for the reasons explained below, so that together with the smaller difference in the leakage rate RSDC adopts a more negative value. For small steam densities the criticality depends almost linearly on the steam density when the coolant is D_2O; however, when it is H_2O, the slope of the curve $k_{eff}(\rho)$ becomes flatter (less negative) with increasing steam density. This is due to the fact that for the same density and with H_2O

as a coolant many more neutrons have a chance to be slowed down into the low energy (thermal and epithermal) region of high neutron importance than with D_2O. This effect causes the larger difference in k_∞ for D_2O which is responsible for the more negative RSDC mentioned above.

3.5. Nitride

Due to the higher density of the fuel nitrides (UN, PuN), compared with the oxides (UO_2, PuO_2), the diffusion area M^2 is considerably smaller and the same applies to the neutron-leakage out of the core. Consequently, AR is reduced which results in an increase of CR. The larger macroscopic capture and fission cross-sections of the fuel, giving rise to a hardening of the neutron spectrum and, therefore, to a reduction of DK, also causes a reduction of ℓ and a slight decrease of Δk_F. The variation of RSDC and Δk_L may be explained easily, when we take into account that both quantities depend on changes in the leakage rate and changes in k_∞, which are produced by a variation of the steam density. Both the leakage rate and k_∞ become larger when the steam density is reduced; thus they have opposite influences on k_{eff}. With the use of nitride the differences in the leakage rate following a reduction of the steam density are smaller than with oxides. The reason is mentioned above; on the other hand the differences in k_∞ following a reduction of the steam density show a small increase, so that $|RSDC|$ and Δk_L become larger than with oxides.

3.6. B^2 doubled

A doubling of the geometric buckling B^2 requires an increased value of AR and therefore reduces CR. Because of the higher enrichment and the hardened neutron spectrum, DK decreases (ℓ too), but RSDC increases by a larger amount so that the stability behaviour is more favourable. The effect on Δk_L and Δk_F is the expected one, since an increase in B^2 decreases criticality, the more so, the smaller the coolant density will be (keeping the enrichment at a constant level in this case).

3.7. KFK set and SNEAK set

The group cross-section set can, of course, not be regarded as a real design parameter. It is changed in our study in order to see how the uncertainties in the nuclear data finally give rise to uncertainties in the interesting quantities. The results show that besides the enrichment (characterized by AR) RSDC and Δk_L are changed by a considerable amount in the unfavourable direction. It is the same for DK, though by a much smaller amount. The stability behaviour would be much worse than with the ABBN set, especially with the use of the KFK set, which is, of course, not very suitable for the calculation of steam-cooled reactors. But even with the probably more suitable SNEAK set the changes in RSDC, Δk_L and Δk_F are quite large. Although the enrichment has to be drastically increased, CR shows a small increase, indicating a better internal breeding; however, M^2 is reduced to a very low value. Thus, the leakage rate and probably the external breeding is reduced. ℓ decreases because of the increase in AR.

3.8. Varying D_2O content

As may be seen from Figs 5 and 6 all quantities show a good linear dependence on the D_2O content of steam as long as the content is small. For contents of 50% or more the loss of moderation comes into operation more strongly causing deviations from the linear behaviour. This is especially true for the quantities depending on the variations of the steam density. The reasons are the same as those given in Section 3.4 for the change from H_2O to D_2O. For the normal steam density chosen the absolute value of the change in k_∞ corresponding to a small variation of the steam density (i.e. RSDC for $B^2 = 0$) would even show a maximum for a D_2O content of 70-80%. Thus, the partial compensation of changes in k_∞ and in the leakage rate are responsible for the special dependence of RSDC shown in Fig. 5.

3.9. Increase of a burn-up

A higher burn-up requires a higher value of AR to compensate for the higher parasitic absorption of the fission products. Consequently, CR and M^2 slightly decrease. The decrease of DK and ℓ is caused chiefly by the harder neutron spectrum. Due to the fact that the absorption cross-section of the fission products increases rapidly with decreasing neutron energy, $|RSDC|$, Δk_L and $|\Delta k_F|$ become larger. Increasing the average burn-up from 2.75 to 5 at.% gives rise to the following changes, as reported in Ref. [10], which may be verified qualitatively by the present results: δDK: -12.4%, $\delta|RSDC|$: +42%, $\delta\Delta k_L$: +0.013, $\delta\Delta k_F$: -0.024, δAR: +3.3%, δCR: -0.034, δM^2: 2.1 (cm^2), $\delta\ell$: -0.03 (μs). Going from 5 to 0 at.%, i.e. completely disregarding the fission products, would change criticality in the flooded stage by about 5% the value of Δk_L by 0.03 and cause a change of sign for SDC (see Ref. [10]).

3.10. Decrease of fuel density

At a lower fuel density a higher value for the enrichment has to be chosen (larger AR) which causes a reduction of CR and DK and a slight increase of Δk_L and Δk_F. A natural consequence of the lower fuel density (lower macroscopic capture and fission cross-sections) is the increase of ℓ and the considerable increase of M^2, the higher leakage rate being the reason for the small increase of RSDC.

3.11. Decrease of steam density

A reduction of the mean steam density reduces the moderation effect of the coolant and results in a harder neutron spectrum, which is the reason for the reduction of AR, DK, Δk_L and ℓ and for the increase of $|\Delta k_F|$ and CR. The harder spectrum together with the lower coolant density gives rise to an increase of M^2. The small increase in RSDC is not caused by this increase of M^2, but simply by the smaller steam density itself; the SDC becomes more negative; this means a steeper slope of the curve $k_{eff}(\rho)$, as mentioned before in Section 3.4.

3.12. Increase of coolant volume fraction

A first consequence of this change is a softer neutron spectrum. This is the reason for the increase in DK and ℓ which are not so much influenced by the higher enrichment (larger AR) required by the softer spectrum and the lower fuel volume fraction. The two effects, which have just been mentioned, are responsible for the reduction of CR. The reduction of the fuel volume fraction has a stronger influence on M^2 than the softer spectrum and, therefore, M^2 increases causing a small increase in RSDC.

3.13. Increase of buckling

This change has been included for completeness only, to demonstrate the influence of a small change in the geometric configuration together with the influences of other small changes in the design parameters. The variations of the determined quantities and the reasons for these variations are analogous to those described in Section 3.6.

4. CONCLUSIONS

4.1. Large variations

It can easily be seen from Fig. 3 that all changes in the design parameters, except for the cases where "clean plutonium" and Incoloy 800 are used, result in a decrease of the Doppler constant DK = -Tdk/dT. Since the two exceptions show also a more favourable value of the reduced steam-density coefficient RSDC = $(dk/k)/(d\rho/\rho)_N$, the stability behaviour would be much better. Doubling the geometric buckling B^2 has also a favourable influence on the stability behaviour because of the considerable reduction of RSDC, whereas nitride and D_2O, in particular, would make it much worse. The most important parameters influencing Δk_L, the change in criticality following a loss of coolant, are Incoloy and, as has been expected, "clean plutonium" as well as the doubling of B^2. Δk_F, the criticality change upon flooding the reactor, is very sensitive to the ^{240}Pu-content of the fuel and to the coolant used. Besides the expected changes in AR (the atom ratio of fissile (^{239}Pu + ^{241}Pu) to fertile (^{238}U + ^{240}Pu) material) which come about if we use nitride or double B^2, the use of Incoloy 800 instead of Inconel 625 gives rise to the largest reduction in AR. Cooling with D_2O-steam and the use of nitrides as a fuel or Incoloy 800 as a structure and cladding material would produce a considerable increase in internal breeding, characterized by the conversion ratio CR whereas the doubling of B^2 and the use of "clean plutonium" would have the opposite effect. The most important changes in the diffusion area M^2 are caused by D_2O and nitride and, to a smaller extent, by Incoloy 800. Together with "clean plutonium" the same design parameters lead to the largest variations in the prompt neutron generation time ℓ.

4.2. Small variations

All changes, except for an increase in the coolant volume fraction, cause a reduction of DK, the decrease in the steam density being the most

important one. An increase in burn-up decreases RSDC, whereas an increase of the buckling increases RSDC, bringing about a better stability behaviour in spite of the accompanying reduction of DK. The most pronounced improvement in stability behaviour is caused by an increase of the coolant volume fraction, since both important quantities, DK and RSDC, change in the desired direction. Increasing the burn-up or the coolant volume fraction causes an increase of Δk_L, whereas the decrease of the mean steam density shows the opposite tendency, as was expected. An increase in burn-up naturally leads to a lower value of Δk_F; an increase in the coolant volume fraction or a decrease in the fuel density has an influence which goes in the opposite direction. Among all these variations the decrease of the fuel density requires that the enrichment (characterized by AR) has to be raised to the largest extent; to a smaller extent an increase of the coolant volume fraction will yield the same effect. The corresponding tendencies are shown by CR, M^2 and ℓ. This underlines the fact that with regard to stability behaviour the determination of burn-up is the most important factor, whereas from the point of view of economics the determination of the fuel density is of the greatest importance.

The influence of the different cross-section sets illustrates the uncertainties that exist in determining the interesting quantities and that are caused by uncertainties in the nuclear data; consequently it demonstrates the necessity to check the theoretical results by appropriate experiments, as will be done, e.g. in the SNEAK facility.

ACKNOWLEDGEMENT

I would like to thank Mr. K. Wagner for his assistance in evaluating the results.

REFERENCES

[1] FRISCH, W., HELLER, F., HÜBSCHMANN, W., MALANG, S., MÜLLER, A., SCHIKARSKI, W., SMIDT, D., WOITE, G., "Safety aspects of steam cooled fast breeder reactors", Paper presented at the Int. Conf. on the Safety of Fast Reactors, Aix-en-Provence, Sep. 1967; see also Rep. KFK-613 (1967).

[2] MÜLLER, A.et al., Referenzstudie für den 1000 MW(e) dampfgekühlten schnellen Brutreaktor (D1), Rep. KFK-392 (1966).

[3] EDLUND, M. C., "Developments in spectral-shift reactors", Int. Conf. peaceful Uses atom. Energy (Proc. Conf. Geneva, 1964) 6, UN, Geneva (1964) 314.

[4] SMIDT, D. et al., Safety and cost analysis of a 1000 MW(e) sodium-cooled fast power reactor, Rep. ANL-7120 (1965) 33.

[5] McNELLY, M.J., Liquid metal fast breeder reactor design study (1000 MW(e) UO_2-PuO_2 fueled plant), Rep. GEAP-4418 (1964).

[6] COHEN, K.P., O'NEILL, G.L., Safety and economic characteristics of a 1000 MW(e) fast sodium-cooled reactor design, Rep. ANL-7120 (1965) 185.

[7] ABAGJAN, L.P., BAZAZJANC, N.O., BONDARENKO, I.I., NIKOLAEV, M.N., Gruppenkonstanten schneller und intermediärer Neutronen für die Berechnung von Kernreaktoren, Rep. KFK-tr-144.

[8] KÜSTERS, H., METZENROTH, M., The influence of some important group constants on integral fast reactor quantities, Rep. ANL-7120 (1965) 423.

[9] KÜSTERS, H. et al., "The group cross-section set KFK-SNEAK: preparation and results", these Proceedings, SM-101/12.

[10] KIEFHABER, E., Konfiguration und nukleare Kenngrößen eines Dampfgekühlten Schnellen Brutreaktors, Kernforschungszentrum Karlsruhe, Externer Bericht INR-4/67-13.

[11] REYNOLDS, A. B., WOLFE, B., Physics analysis of the mixed spectrum superheater, Trans. Am. nucl. Soc. 5 1 (1962) 123.

DISCUSSION

K. M. JIRLOW: I feel that there is an intrinsic difficulty in calculating the steam-voiding effect with a fixed 26-group set, due to the change in spectrum when you go from normal steam density to the voided core (which may change the microscopic removal cross-sections). Have you made any corrections for this effect?

E. KIEFHABER: Not in the calculations presented in the paper. However, such corrections are possible: we can take into account the change in the slope of the spectrum by calculating the macroscopic removal cross-section not in the usual way, but with the actual spectrum at the steam density considered. This procedure is referred to as "method B" in paper SM-101/12.

C. P. GRATTON: Have you considered the effect of control rods on the steam density coefficient?

E. KIEFHABER: Yes, we have performed first-approximation calculations for high burn-up in a reactor that is just critical and then repeated the calculations at a lower burn-up, compensating for the increase in criticality by the addition of absorber material. We have found that the steam density coefficient does not change very much. We therefore conclude that it remains nearly unchanged during the core lifetime.

L. I. TIRÉN: I believe that the slope of the curve of reactivity versus steam density is strongly affected by processes at energies below, say, 5 eV. In this energy region heterogeneity effects are strong, and results obtained with a homogeneous model should therefore be treated with caution. I think these low-energy processes are appreciable even at a steam density corresponding to the operating point. Would you please comment on this?

E. KIEFHABER: I agree that, when dealing with the low-energy resonances of, for example, ^{239}Pu and ^{240}Pu, it is difficult to take into account heterogeneity effects and up-scattering in the thermal region. I also agree that the steam density coefficient may be influenced to some extent by the treatment of the low-energy part of the spectrum.

H. VOLLMER: Your calculation of the density coefficient of reactivity assumes a homogenized core. In a power reactor, density varies strongly along the channel. What impact does this spatial effect have on the use of the average coefficient? How do local and average density coefficients compare?

E. KIEFHABER: In determining the real steam density coefficient, of, say, the D1 reactor, we have performed reactor calculations in the axial direction, taking into account the spatial variation in the steam density, and have found good agreement with the fundamental-mode results for the homogenized core at an average density. The one-dimensional results have been obtained by perturbation theory and by changing the density in each axial zone, superposition of the zones corresponding simply to adding the coefficients of the different zones.

K. E. J. WIRTZ: Apparently we are faced with fairly unfavourable coolant density effects. Would you care to comment on the consequences for steam-cooled fast power reactors?

E. KIEFHABER: Of course, the loss of coolant leads to a considerable increase in criticality. However, the absolute increase in reactivity introduced may be less important than the rate of increase. If that is the case, the situation is not so serious since the coolant is not lost at a very fast rate.

K. M. JIRLOW: Did you use a heterogeneity correction of the type described by Mr. Wintzer in paper SM-101/13, or were your calculations strictly homogeneous?

E. KIEFHABER: We used the heterogeneity correction described by Mr. Wintzer.

K. M. JIRLOW: I should like to comment on your comparison between steam coefficients calculated with the ABBN, KFK and SNEAK sets. We have found that the ABBN and KFK sets give smaller steam coefficients than we obtain with our microscopic cross-section library (paper SM-101/52).

With regard to the influence of control rods, I would mention that we have had the same experience as Mr. Kiefhaber.

VARIATION OF k-inf WITH COOLANT DENSITY FOR A PLUTONIUM-FUELLED STEAM-COOLED FAST REACTOR LATTICE
Comparison of experiment with prediction

M.J. ARNOLD, W.N. FOX, C.F. GEORGE AND R. RICHMOND*
UNITED KINGDOM ATOMIC ENERGY AUTHORITY,
ATOMIC ENERGY ESTABLISHMENT,
WINFRITH, DORCHESTER, DORSET,
UNITED KINGDOM

Presented by C.G. Campbell

Abstract

VARIATION OF k-inf WITH COOLANT DENSITY FOR A PLUTONIUM-FUELLED STEAM-COOLED FAST REACTOR LATTICE: COMPARISON OF EXPERIMENT WITH PREDICTION. The design of a steam-cooled fast reactor with satisfactory safety and control characteristics and an acceptable breeding performance requires an accurate knowledge of the neutron balance and its variation with coolant density. When an assessment of such a system was undertaken the basic nuclear data available for use in the lattice calculation was of insufficient accuracy and little integral information on lattices of the required composition was available. A programme of experimental measurements of the neutron balance and its variation with coolant density in lattices of this type was therefore undertaken.

Measurements of important neutron reaction rates and of k-infinity were carried out in the reactor DIMPLE at A.E.E., Winfrith, in a small central fast reactor zone driven critical by a surrounding thermal reactor zone. This system produced at its centre the correct fast spectrum while requiring only 50 kg of plutonium in the central fast test zone. Three lattices were studied in which appropriate polypropylene plates were inserted in a regular array to simulate the flooded condition, and the operating condition (0.1 g/cm^3 equivalent steam density); the voided condition was studied by removing the plates.

In all three lattices studied, the most important reaction rates influencing the coolant coefficient of k-infinity were fission in ^{239}Pu, capture in ^{238}U and to a lesser extent capture in ^{239}Pu. Particular attention was therefore paid to the direct measurement of these quantities which, together with other relatively unimportant fission rates, accounted for 80-90% of the total lattice absorptions. In one lattice these measurements were supplemented by a direct measurement of k-infinity to provide a check on the calculation of unmeasured reaction rates.

1. INTRODUCTION

As part of a general assessment of fast reactors using different coolants, the performance of a steam cooled fast reactor has been assessed at A.E.E. Winfrith. Of particular interest in the case of steam coolant was the change in reactivity on varying the coolant density from the operating value, because of the implications on the safety and control aspects of the reactor. The extent of the loss in breeding performance associated with steam coolant compared with sodium was also of significance. At the time the assessment study was initiated, uncertainties in nuclear data were such that these performance parameters could not be predicted with confidence. No relevent

---

* Now at E.I.R., Würenlingen, Switzerland

integral data was available against which performance estimates based on existing data sets could be checked. A limited programme of integral experiments was therefore undertaken to provide tests of these features of the predicted performance for a steam cooled system.

The experiments were limited to providing a check of the important fission and absorption events in a system of typical steam-cooled fast reactor composition, but made no attempt to study neutron transport and leakage effects. They were undertaken in a zone of typical steam-cooled fast reactor composition in which the neutron spectrum was characteristic of that of a critical system. The experiment was designed as a mixed critical assembly, with a central fast reactor test region, containing about 50 kg of plutonium, which was driven critical by an outer thermal reactor zone. The annulus between the fast and thermal regions contained a buffer zone to filter the neutron spectrum leaking into the fast central region.

2. THE EXPERIMENTAL PROGRAMME

The composition of a typical steam-cooled fast reactor lattice is given in Table I which presents the volume occupied by the various materials together with the constituent isotopic number densities. In practice the steam density may vary over a wide range but the current experiments were restricted to a simulation of the three coolant conditions:

(a) normal operating density of 0.1 g/ml;

(b) the voided situation, corresponding to a complete loss of coolant;

(c) the fully flooded situation which may arise due to accident or normal start-up conditions.

These three lattice conditions have widely different neutron spectra and consequently different neutron balances. Fig. 1 shows the relevant calculated spectra (using the methods discussed in Section 5.2) and Table II lists the calculated balance of neutron events. In every case ^{239}Pu fissions and ^{238}U captures are the most important reaction rates. Particular attention was given therefore to the measurement of the ratio ^{238}U captures to ^{239}Pu fissions. ^{238}U and ^{235}U fission rates relative to the ^{239}Pu fission rate were also planned since although they are not of great importance in the neutron balance they provide useful spectral information. These measurements of reaction rate ratios cover some 80-90% of total lattice absorption rates and provide an important check on the variations of k-infinity with coolant density, but in order to provide additional confidence in the results, a more direct measurement of k-infinity was made in one situation (Section 4.5).

3. THE MIXED CRITICAL REACTOR

Survey calculations indicated that a neutron spectrum typical of a steam cooled fast reactor lattice could be achieved to the required accuracy at the centre of a small section of the lattice surrounded by a driver lattice of thermal composition, so achieving a considerable saving in fissile material inventory. Although similar experimental assemblies had been used previously [1] no data were available which

TABLE I

Composition of a typical steam cooled fast reactor core

Material	Volume Fraction (%)
Fuel	39
Steel	27
Coolant	22
Void	12
Nuclide	**Average Number Density (atoms $cm^{-3} \times 10^{-22}$)**
^{239}Pu	0.0981
^{240}Pu	0.0110
^{241}Pu	0.0014
^{235}U	0.0057
^{238}U	0.775
O	1.783
Fe	2.153
Cr	0.114
Ni	0.043
C	0.005 (Voided) 0.084 (Operating) 0.771 (Flooded)
H	0.000 (Voided) 0.159 (Operating) 1.543 (Flooded)

would provide a basis for the design for such a system, and it was necessary to base the design on the calculated performance of the mixed critical system (Section 5.2).

The reactor configuration adopted is illustrated in Figs. 2 and 3. Fuel elements of square cross section (5 cm x 5 cm) containing the fuel and coolant arrangement simulating the fast reactor composition were surrounded by a zone of similarly shaped natural uranium oxide elements and by a 5 cm thick steel filter which together served as spectrum matching and filtering regions and hence reduced the ^{239}Pu fuel requirements. The annular light water moderated driver regions, fuelled with 3% ^{235}U enriched UO_2 was constructed in two zones to economise in fuel while ensuring a negative moderator temperature coefficient for safety reasons.

The dimensions of the assembly were chosen to provide a neutron balance at the centre of the reactor close to that which would be

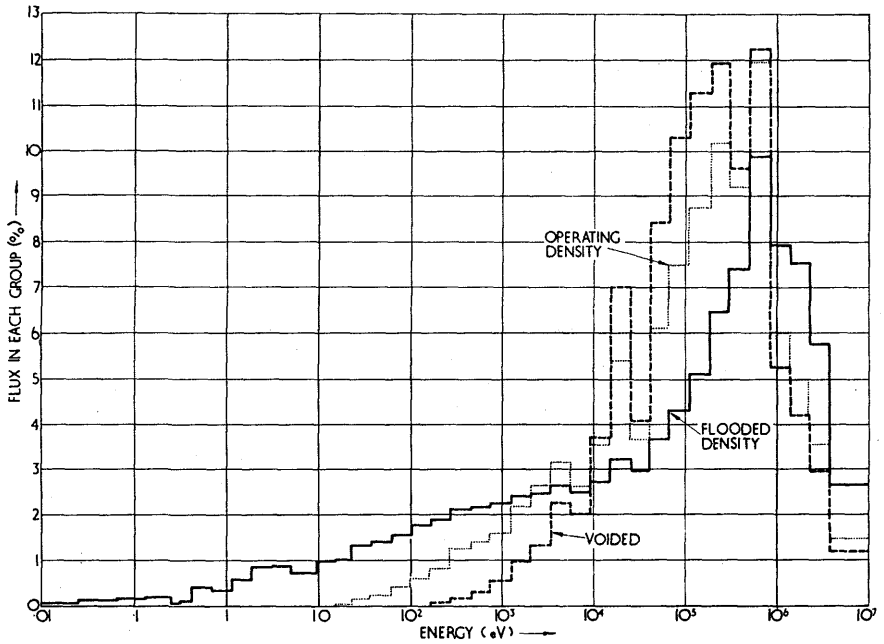

FIG.1. Neutron energy spectrum in critical fast reactor.

obtained in a bare critical assembly of the fast reactor fuel. It was not necessary for the two situations to be identical since the final calculations using the data to be tested were made directly for the experimental situation; it was sufficient that the two situations were close enough to enable conclusions on data adequacy to be applicable to both. With the size of assembly chosen, the survey calculations showed that the k-infinity appropriate to the core centre varied by less than $\pm$ 0.5% when:

(a) the radius of the fast reactor zone was changed from 12 in. to 16 in. and the height from 33 in. to 40 in.;

(b) the driver fuel was changed from 3% ^{235}U enriched UO_2 to ^{235}U aluminium alloy;

(c) the data set used was changed from FD1 [2] to FD2 [3].

These results gave confidence that the actual neutron balance at the core centre was typical of the composition of the centre zone and insensitive to the properties of the outer zones.

Table III shows the close similarity between reaction rates in the mixed critical and actual fast reactor situations as calculated using the FD2 data (see Section 5.1).

TABLE II

Neutron Balance in the Steam-Cooled Fast Reactor

Lattice Condition	Nuclide	Fission	Non-fissile capture	Neutron Production
Voided	U235	0.0222	0.0067	0.0548
	U238	0.0646	0.405	0.180
	Pu239	0.358	0.0729	1.060
	Pu240	0.0079	0.0131	0.0243
	Pu241	0.0086	0.0013	0.0256
	Steel		0.0356	
	Oxygen		0.0030	
	Total	0.462	0.538	1.345
Operating	U235	0.0242	0.0102	0.0595
	U238	0.0551	0.3771	0.152
	Pu239	0.3350	0.1141	0.985
	Pu240	0.0061	0.0251	0.0188
	Pu241	0.0097	0.0025	0.0288
	Steel		0.0379	
	Oxygen		0.0026	
	Total	0.430	0.570	1.244
Flooded	U235	0.0232	0.0122	0.0567
	U238	0.0325	0.2448	0.0900
	Pu239	0.3325	0.1701	0.970
	Pu240	0.0029	0.1009	0.0090
	Pu241	0.0106	0.0039	0.0313
	Steel		0.0602	
	Oxygen		0.0017	
	Hydrogen		0.0034	
	Total	0.402	0.598	1.158

4. THE EXPERIMENTAL MEASUREMENTS

4.1 The Lattice Cell

The fuels available for this work were in the form of plates of approximate dimensions about 2 in. x 2 in. x 0.25 in. canned in 0.010 in. thick stainless steel, and of compositions:

(a) 25% PuO_2/75% natural UO_2 by weight;

and (b) natural UO_2.

Calculations using a mean chord length equivalence showed that plates of this thickness could be used to simulate a power reactor situation with 0.2 in. radius fuel pins, that is, one of practical importance. In voided and operating density situations the k-infinity differences between the experimental and power reactor

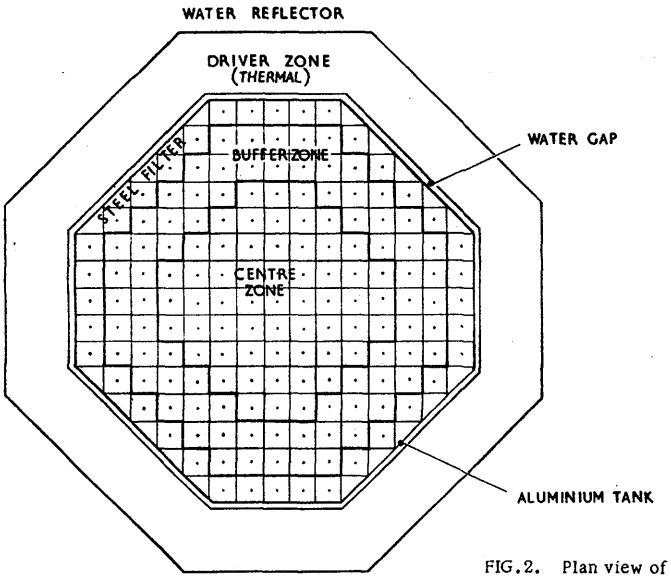

FIG.2. Plan view of basic mixed critical lattice.

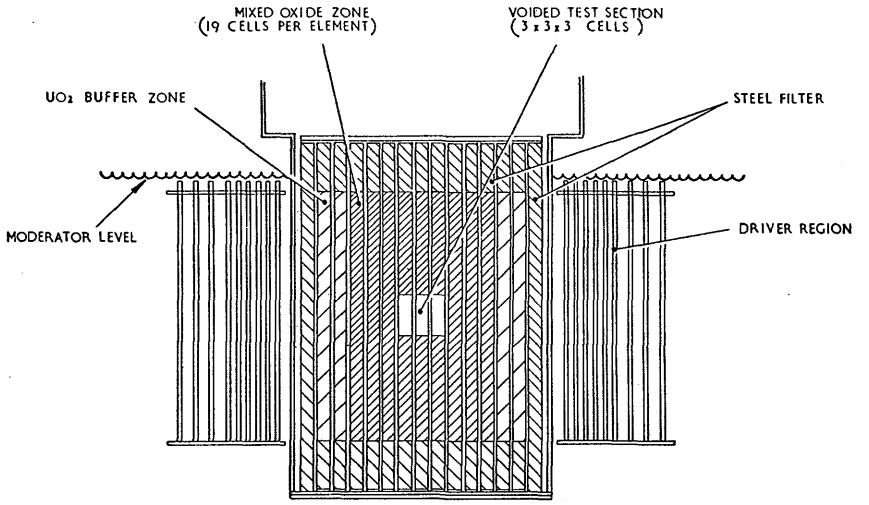

FIG.3. Elevation section of mixed critical core.

situations having the same mean material composition were less than 2%. The flooded situation was less well simulated, the difference in k-infinity rising to 6%, but since uncertainty in the reactivity of the flooded lattice was unlikely to cause practical difficulties in power reactor design, this was acceptable.

The actual lattice cell was constructed from alternate plates of the two fuels separated by 0.2 in. thick U-sections of steel the operating density coolant was simulated by 0.018 in. thick

TABLE III

Comparison of lattice parameters in the mixed critical system and in the fast reactor

Lattice Condition	Lattice Parameter	Critical Fast Reactor	Mixed Critical (Centre Zone)	Mixed Critical / Fast Reactor
Voided	σ_{f5}/σ_{f9}	1.0691	1.0655	0.997
	σ_{f8}/σ_{f9}	0.0226	0.0230	1.018
	σ_{f0}/σ_{f9}	0.1962	0.1995	1.017
	σ_{c8}/σ_{f9}	0.1449	0.1424	0.983
	σ_{c9}/σ_{f9}	0.2016	0.2020	1.002
	k-inf	1.3345	1.3453	1.008
Operating	σ_{f5}/σ_{f9}	1.2422	1.2460	1.003
	σ_{f8}/σ_{f9}	0.0211	0.0208	0.986
	σ_{f0}/σ_{f9}	0.1653	0.1633	0.988
	σ_{c8}/σ_{f9}	0.1423	0.1424	1.001
	σ_{c9}/σ_{f9}	0.3376	0.3406	1.009
	k-inf	1.2483	1.2444	0.997
Flooded	σ_{f5}/σ_{f9}	1.2034	1.2033	1.000
	σ_{f8}/σ_{f9}	0.0124	0.0124	1.000
	σ_{f0}/σ_{f9}	0.0779	0.0779	1.000
	σ_{c8}/σ_{f9}	0.0931	0.0931	1.000
	σ_{c9}/σ_{f9}	0.5115	0.5116	1.000
	k-inf	1.1576	1.1576	1.000

by 1.5 in. square plates of polypropylene inserted inside the steel sections, while the flooded situation was produced by placing 2 in. square plates of steel together with 2 in. square plates of polythene between the fuel plates. This latter arrangement was designed to reduce errors due to the more severe variations in reaction rates at the flooded cell edge. Fig. 4 shows the cell arrangements.

4.2 The Scope of the Measurements

The neutron balance is determined by the reaction rates actually occurring within the materials of the lattice cell, and consequently the primary aim of the measurements was the determination of the reaction rates of the fuel materials averaged through the fuel plates themselves. No attempt was made to measure reaction rates of other materials or fuel materials in the gaps between plates since although these would have provided spectral information they were not of primary interest. Reaction rates were measured using foil activation techniques, the foils being

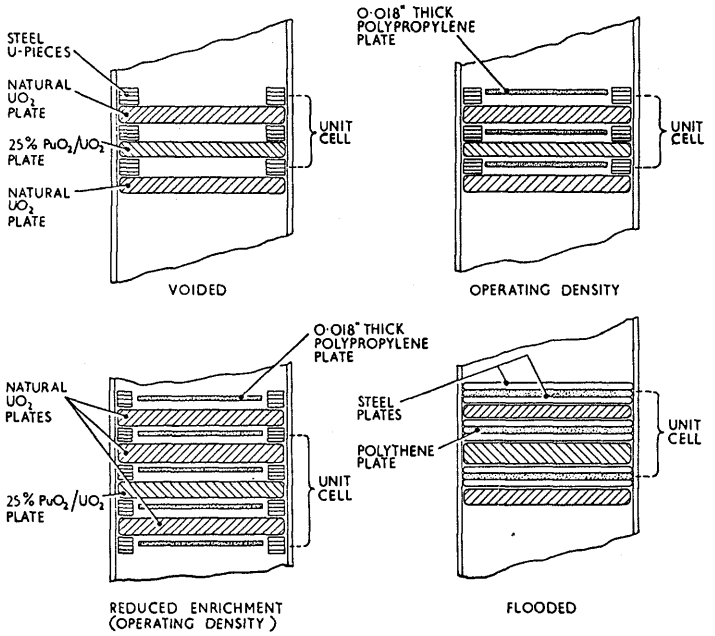

FIG.4. Lattice cell of mixed oxide region.

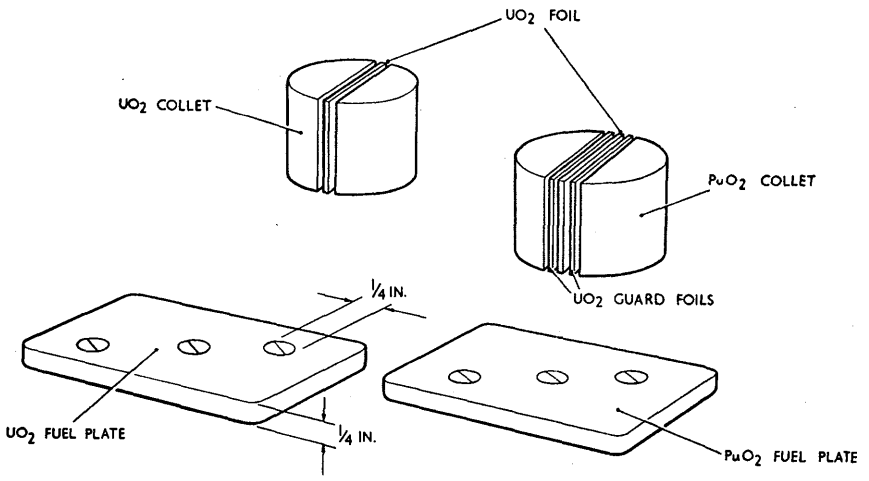

FIG.5. Location of oxide foils in fuel plates.

arranged between split collets of fuel plate material, and their edges accurately located to align with the plate surfaces (Fig. 5). In both the voided and operating density conditions, radial heterogeneity effects were negligible and the measurements provided the correctly averaged fuel plate reaction rates. To measure the effects of the more severe reaction rate variations which occur

near the edge of the flooded cell, additional reaction rate measurements were made at edge locations.

The following sections summarise the experimental techniques used.

4.3 Fission Rate Ratios

All the foils were of nominal dimensions 0.25 in. x 0.25 in. x 0.010 in. The difference foil sets contained in turn each of the isotopes of interest, viz. ^{238}U, ^{235}U and ^{239}Pu. All the foils were coated in 0.0005 in. nickel to retain fission products and they were protected by 0.001 in. thick foils of aluminium when located within the fuel plates. After a standard irradiation period of two hours their induced fission product γ activities were measured by the use of γ scintillation counters set to accept activity of energy above 1.3 MeV. Separate calibration measurements were made to determine the relations between fission rates in a foil during irradiation and the subsequent emission of fission product γ-rays.

The calibration experiments were made using fission chambers of the type used in ZEBRA and which had been calibrated to measure absolute fission rates [4]. The chambers were in turn positioned in a back-to-back arrangement with a dummy chamber of identical geometrical construction and located within the fast reactor zone (Fig. 6). Foils of the compositions appropriate to the actual chamber deposits were fixed to the dummy chamber radiator and were irradiated for the standard period while the fission chambers were used to measure fission rates. A subsequent measurement of the induced fission product γ-activities of the foils then determined the required calibration relationships. Possible variations in these calibration factors with neutron energy were checked by repeating the calibration measurements in all three coolant simulations, and found to lie within the statistical errors of measurement of $\pm 3\%$. As an additional check, foils of ^{235}U and ^{239}Pu were irradiated in a thermal spectrum in which the cross sections were known. Subsequent fission product γ-counting gave a calibration factor which was within 2% of the mean fast value.

Detailed results of the fission rate measurements are given in Tables VII and VIII. It is worth noting that the mean ^{238}U fission rate as measured in the fuel plates differs by 9% from that measured within the calibration fission chamber. This indicates the magnitude of possible errors involved in directly measuring fission rates with chambers in soft spectrum fast reactor lattices.

4.4 The Ratio of ^{238}U Captures to ^{239}Pu Fissions

The ^{238}U capture and ^{239}Pu fission rates are the most important contributions to the neutron balance and most of the experimental effort was directed to the determination of their reaction rate ratio. The method adopted for the ^{238}U capture rate determination was based on that used in thermal studies at A.E.E., Winfrith and relies on the measurement of the coincident emission of γ-ray and X-ray quanta with energies in the vicinity of 100 keV in the decay of ^{239}Np. The ^{239}Pu fission rate was determined as described in the previous section.

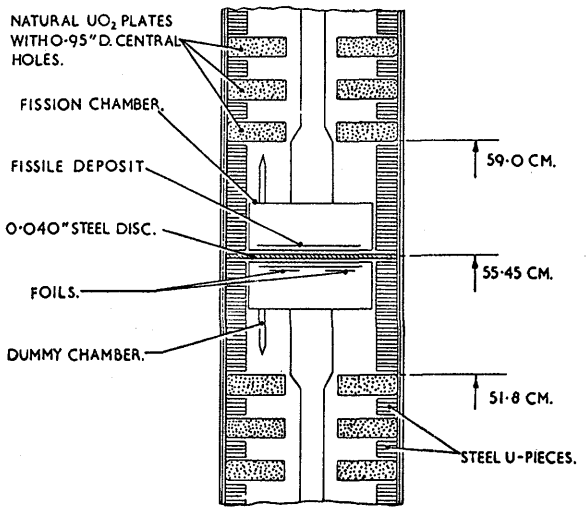

FIG.6. Mounting of ZEBRA fission chambers in the operating and flooded cores.

In principle the measurement is carried out by irradiating in each lattice plate, a foil of the same material as the plate. The emission rate of 100 keV γ-X-ray coincidences from each foil is then proportional to the ^{238}U capture rate, while the fission product γ-ray emission rate from the PuO_2/UO_2 foil (after correction for the contributions from other fissile nuclides) is proportional to the ^{239}Pu fission rate. The relative efficiency of detection of the two activities is determined by a simultaneous irradiation in which foils containing ^{238}U and ^{239}Pu are irradiated in a thermal neutron spectrum in which the relevant cross sections are known.

In practice it was found that the PuO_2/UO_2 foil in its unirradiated state produced a very large background of 100 keV coincidences which obscured the ^{239}Np activity. For this reason the ^{238}U capture rate in the PuO_2/UO_2 plate was measured by means of a UO_2 foil. This could lead to errors because the screening of the ^{238}U resonances in the foil might differ from the screening in the fuel plate. Measurements of the ^{238}U capture rate using foils of various thicknesses indicated however that such errors were less than 1.5%.

The results are given in Table VII.

Development work is continuing on the possible use of a high resolution Li-drifted germanium detector which enables the 75 keV γ-ray occurring in the decay of ^{239}U to be well resolved from interfering activities, and hence used to monitor the ^{238}U capture rate. This method would allow the use of actual fuel plate material and the consequent elimination of errors referred to previously.

4.5 The Measurement of k-infinity

A number of workers have used the principle of the null-reactivity change technique for the measurement of lattice k-infinity [5] [6] but their methods have differed in detailed application.

The method used in the current experiments has been described in detail elsewhere [7] and will only be summarised here. The operating density lattice cell was modified to lower its mean enrichment by inserting an extra natural UO_2 fuel plate in each lattice cell; the same coolant volume fraction was however retained. The reactivity change on voiding a 3 x 3 x 3-cell high cell array at the core centre was measured using a doubling time technique, and repeated with small plates of boron steel inserted adjacent to the fuel plates. After correction for the residual steel cladding of the element sheaths local to the 3 x 3 x 3 array which were not removed during the voiding measurement, it was found that the null reactivity change condition (corresponding to a k-infinity of unity) was produced by the insertion of only 0.02 ± 0.05 g of boron per cell. A calculation using FD2 data for the boron loaded cell geometry indicated that the boron adsorption was equivalent to $(0.2 \pm 0.5)\%$ in k-infinity. The k-infinity of the lattice without boron is therefore 1.002 ± 0.005. In applications of the technique where both the sample and its surroundings are poisoned to give a null reactivity change condition, systematic errors are small [7].

The reaction rate measurements discussed previously were repeated in the reduced enrichment lattice cell. This data when combined with the measured value of k-infinity yields the magnitude of the unmeasured reaction rates which are dominated by capture in ^{239}Pu. This deduction arises from the definition of k-infinity which is the ratio of neutron production to absorption rates. A value is calculated for ν, the spectrum average number of neutrons per fission, and having measured the important capture rates and fission rates relative to fission in ^{239}Pu, the unmeasured reaction rates are deduced. The small absorption and fission contributions from higher Pu isotopes and from steel absorption are calculated to adequate accuracy to yield the mean ^{239}Pu capture rate relative to the mean ^{239}Pu fission rate ($\bar{\alpha}_9$).

The systematic errors and assumptions involved are discussed in detail elsewhere [7] and the value of $\bar{\alpha}_9$ deduced was

$$0.57 \pm 0.13.$$

4.6 Summary of Results

The detailed results of the capture and fission rate ratios are given in Tables VII and VIII, and are compared with calculated quantities in Section 6.

5. THEORETICAL METHODS AND NUCLEAR DATA SETS

5.1 Nuclear Data Set

The results of the measurements described provide a test of the performance of the standard fast reactor data set in use at A.E.E., Winfrith in a steam cooled fast reactor application.

The data set currently in use is known as FD2 [3]. It is a 33-group set derived from the U.K.A.E.A. Nuclear Data Library [8]. In the present application it was extended to 40 groups to include thermal data.

5.2 The Method of Calculation

A common method of calculation using the FD2 data set was used for both the lattice cell and whole reactor predictions. This calculation is coded as GMS II [9] and is a 40-group method using transport theory in slab, spherical and cylindrical geometry. The limitations of the one-dimensional method are reduced by the method of representing leakage in the unrepresented directions by a pseudo absorption $\frac{\lambda_T B_G^2}{3}$ which can differ from group to group or region to region (B_G^2 is the geometric buckling in the unrepresented direction and λ_T is the transport mean free path).

Resonance self screening in the code is represented by a tabulation of cross sections as a function of the potential scattering cross section per absorber atom (σ_p) for all fissile and fertile isotopes. An approximate expression for σ_p for the lattice cell materials was used to allow for the difficulty in representing the two dissimilar types of fuel plate in each cell (Appendix 1). The effects of this approximation are discussed later.

The whole reactor calculations were made in 25 rather than 40 groups to economise in computer usage by first producing cell calculations appropriate to each radial region, applying the resulting 40 group disadvantage factors and after condensation to 25 groups, using the mean cell data in a cylindricalised representation of the reactor. The axial bucklings used in each region were appropriate to the measured values and were shown by calculation to be constant to the desired accuracy in every energy group; the value in the driver was however varied to achieve criticality.

5.3 Possible Limitations in Calculation or Data

The limits of validity of the data and calculation method have been tested in a number of subsidiary calculations.

The 40 groups in FD2 have been produced by condensing the detailed basic nuclear data over typical sodium cooled fast neutron spectra and might therefore be expected to give a good representation for systems of broadly similar spectra. However the flooded reactor has a very significantly different spectrum, and the inappropriate condensing spectrum might give rise to significant errors. Subsidiary calculations indicated that the operating density and voided situations were well represented but that errors of up to 6% in k-infinity could be expected in the flooded lattice predictions. Table IV shows the magnitude of the possible errors.

The approximate representation of the resonance screening effects has recently been checked by a method by Fayers [10] which allows the treatment of two types of fuel plate per cell. Such errors are small as shown in Table V, and have not been taken into account.

TABLE IV

Effect of Condensing Spectrum on

one-group effective cross sections

Change in effective one-group cross sections when SSCFR condensing spectrum is used instead of FD2					
^{238}U Capture		^{239}Pu Fission		$\frac{^{239}U \text{ Capture}}{^{239}Pu \text{ Fission}}$	
Operating	Flooded	Operating	Flooded	Operating	Flooded
+ 0.7%	- 3.0%	+ 0.3%	+ 2.8%	+ 0.4%	- 5.8%

TABLE V

Effect of a more rigorous treatment

of resonance self screening

Change in predicted cross section when method of Fayers is used to derive σ_p			
	σ_{c8}	σ_{f9}	σ_{c8}/σ_{f9}
Voided	- 1.0%	- 0.1%	- 0.9%
Operating	- 1.9%	+ 0.3%	- 2.2%
Flooded	+ 1.5%	+ 0.3%	+ 1.2%

TABLE VI

Total change in prediction after

corrections for condensing spectrum and self screening

	σ_{c8}/σ_{f9}
Voided	- 0.9%
Operating	- 1.8%
Flooded	- 4.6%

The combined effect of the condensing spectrum and resonance screening inaccuracies on the predicted value of the ^{238}U capture to ^{239}Pu fission rate ratio is shown in Table VI.

A number of small effects were considered, including the exact way of homogenising the steel of the plate cladding and element sheaths, and the effect of the S_N approximation. With the S20 approximation in operating density and voided lattice predictions errors were negligible. The flooded lattice was affected slightly by the radial inhomogeneity (σ_{f5}/σ_{f9} by 2%, σ_{c8}/σ_{f9} by ± 1%).

The calculated parameters are compared with measured quantities in Table VII.

TABLE VII

Comparison of Measured and Calculated Cross Section Ratios

Lattice Condition	Reaction Rate Ratio (per atom)	Measured Value	Calculated Value (FD2)	Measured/FD2
Voided	σ_{f8}/σ_{f9}	0.0250 ± 0.0008	0.0230	1.087 ± 0.036
	σ_{f5}/σ_{f9}	1.008 ± 0.025	1.066	0.946 ± 0.024
	σ_{c8}/σ_{f9}	0.1405 ± 0.0039	0.1424	0.987 ± 0.027
	σ_{c9}/σ_{f9}	-	0.2020	-
Operating	σ_{f8}/σ_{f9}	0.0225 ± 0.0007	0.0208	1.082 ± 0.033
	σ_{f5}/σ_{f9}	1.177 ± 0.024	1.2460	0.945 ± 0.023
	σ_{c8}/σ_{f9}	0.1372 ± 0.0039	0.1424	0.963 ± 0.027
	σ_{c9}/σ_{f9}	-	0.3406	-
Operating (Reduced Enrichment)	σ_{f8}/σ_{f9}	0.0170 ± 0.0005	0.0159	1.069 ± 0.031
	σ_{f5}/σ_{f9}	1.161 ± 0.0037	1.287	0.902 ± 0.029
	σ_{c8}/σ_{f9}	0.1310 ± 0.0037	0.1436	0.912 ± 0.026
	σ_{c9}/σ_{f9}	0.57 ± 0.13	0.3873	1.47 ± 0.34
Flooded	σ_{f8}/σ_{f9}	0.0106 ± 0.0003	0.0124	0.855 ± 0.024
	σ_{f5}/σ_{f9}	1.039 ± 0.019	1.2033	0.863 ± 0.016
	σ_{c8}/σ_{f9}	0.0868 ± 0.0014	0.0931	0.932 ± 0.015
	σ_{c9}/σ_{f9}	-	0.5115	-

6. COMPARISON OF EXPERIMENTAL RESULTS WITH PREDICTIONS

6.1 Flux and Spectrum Variation in the Measurement Region

Detailed measurements of neutron balance were confined to the centre lattice cell of the fast zone although a few measurements were made to check two possible sources of systematic error:

(a) the plate structure of the lattice could allow radial streaming of thermal neutrons from the buffer region to the core centre where their effect would be serious.

Elements were staggered axially to reduce the streaming and any residual effect monitored by measuring the ^{239}Pu cadmium ratio at different radii. Results showed that the low energy contribution to the total ^{239}Pu reaction rate was negligible over a central region 16 cm in diameter in excellent agreement with calculation;

(b) the gross features of the spectrum variation over the centre region were investigated by measuring the variation of the $^{238}U/^{235}U$ fission rate ratio. It was found that over the centre 16 elements the ratio was constant to within $\pm 1\%$ supporting the evidence of the survey calculation that the central neutron balance corresponds closely to that in a critical reactor with the composition of the centre zone.

6.2 Reaction Rates within the Centre Lattice Cell

Appendix 2 gives the dimensions and isotopic number densities for the lattice cells studied.

The comparison of measured and calculated reaction rates is given in Table VII.

The FD2 predictions of ^{238}U fission rates are generally underestimated, an observation which has been noted in comparisons made elsewhere between thermal reactor lattice results and calculations using data from a similar source [11]. The ^{235}U fission rate relative to that of ^{239}Pu is overpredicted in all cases.

Good agreement for the ^{238}U capture to ^{239}Pu fission rate ratio is obtained for the voided lattice but the agreement becomes increasingly worse in operating and flooded lattices. When allowance is made however for the effect of the inappropriate condensing spectra and the smaller effect introduced by the σ_p treatment (Section 5), the disagreements are removed to within the errors of measurement, except for the reduced enrichment lattice where a residual disagreement remains.

The measured capture to fission ratio of ^{239}Pu is significantly greater than the calculated value, implying an error in the ^{239}Pu cross section data in the FD2 data set. This conclusion is consistent with evidence obtained from measurements on typical sodium cooled lattices in ZEBRA and with recent reassessments of basic nuclear data [12].

In addition to giving information on the overall neutron balance, the foil activation measurements show the variation of the reaction rates in the different plates of the lattice cell. Table VIII gives the comparison between the measured fuel plate average reaction rates and those calculated using the FD2 data set with GMS II in the S20 approximation. The increase in the ^{238}U fission rate in the PuO_2/UO_2 plate is about 6% greater than the calculated value in all cells. This is not caused by errors in the S_N approximation. The poor agreement for ^{239}Pu fission is expected because of the poor representation of resonance self screening in a ^{239}Pu foil placed in the natural UO_2 plate (estimates of the true effect using Fayers' method are given in

TABLE VIII

Cell Fine Structure

Cross Section	PuO_2/UO_2 Plate / UO_2 Plate					
	Voided Cell		Operating Density Cell		Flooded Density Cell	
	Measured	Calculated	Measured	Calculated	Measured	Calculated
σ_{f8}	1.089 ± 0.016	1.021	1.113 ± 0.011	1.051	1.183 ± 0.010	1.118
σ_{f5}	1.030 ± 0.015	0.997	1.003 ± 0.006	0.979	0.685 ± 0.002	0.679
σ_{f9}	0.964 ± 0.027	0.999	0.910 ± 0.021	0.828 (0.90*)	0.423 ± 0.003	0.365 (0.39*)
σ_{c8}	0.99 ± 0.02	0.997	1.015 ± 0.011	1.042	1.040 ± 0.020	1.043

*Estimates of the values that would be obtained using values of σ_p for ^{239}Pu derived by the method of Fayers

TABLE IX

The changes in k-infinity corresponding to the differences between calculated and experimental reaction rate ratios

Lattice Condition	Reaction Rate Ratio	Amount by which Experiment Differs from FD2 prediction (%)	Change in predicted k-infinity (%)	
			From + 1% change in reaction rate ratio	From use of experimentally determined ratios
Voided	σ_{f8}/σ_{f9}	+ 8.7 ± 3.3	+ 0.068	+ 0.59 ± 0.22
	σ_{f5}/σ_{f9}	- 5.4 ± 2.5	+ 0.019	- 0.10 ± 0.05
	σ_{c8}/σ_{f9}	- 1.3 ± 2.7	- 0.41	+ 0.53 ± 1.11
	σ_{c9}/σ_{f9}	-	- 0.07	-
Operating	σ_{f8}/σ_{f9}	+ 8.2 ± 3.1	+ 0.067	+ 0.55 ± 0.21
	σ_{f5}/σ_{f9}	- 5.5 ± 2.4	+ 0.021	- 0.12 ± 0.05
	σ_{c8}/σ_{f9}	- 3.7 ± 2.8	- 0.38	+ 1.41 ± 1.06
	σ_{c9}/σ_{f9}	-	- 0.11	-
Operating (Reduced Enrichment)	σ_{f8}/σ_{f9}	+ 7.2 ± 2.9	+ 0.093	+ 0.67 ± 0.26
	σ_{f5}/σ_{f9}	- 9.8 ± 3.2	+ 0.044	- 0.43 ± 0.14
	σ_{c8}/σ_{f9}	- 8.7 ± 2.9	- 0.48	+ 4.20 ± 1.30
	σ_{c9}/σ_{f9}	+ 47 ± 23	- 0.105	- 4.96 ± 2.3
Flooded	σ_{f8}/σ_{f9}	- 14.5 ± 2.8	+ 0.044	- 0.64 ± 0.12
	σ_{f5}/σ_{f9}	- 13.7 ± 1.9	+ 0.025	- 0.34 ± 0.05
	σ_{c8}/σ_{f9}	- 7 ± 2	- 0.20	+ 1.40 ± 0.40
	σ_{c9}/σ_{f9}	-	- 0.14	-

selected cases, and indicate much better agreement). The remaining ratios show reasonable agreement between theory and experiment.

6.3 k-infinity

The change in k-infinity arising from a change in a given reaction rate ratio may be calculated approximately by assuming that the values of the other reaction rate ratios are unchanged. The increments in k-infinity corresponding to differences between measured and calculated reaction rate ratios have been estimated using this method and are shown in Table IX. Errors in the FD2 predictions of ^{235}U fission rates lead to negligible errors in k-infinity while ^{238}U fission rate discrepancies give rise to errors which are just significant at about 0.5%. The ratio of ^{238}U capture to ^{239}Pu fission has the most important effect on k-infinity, the discrepancy between calculation and experiment contributing between 0.5 and 4% to k_∞. Although the ^{239}Pu capture rate is less than the ^{238}U capture rate, the large error in the FD2 prediction of $\bar{\alpha}_9$ produces the largest single contribution to the error in the k-infinity of the reduced enrichment lattice.

Additional information on k_∞ is available for the operating density lattices. In the reduced enrichment lattice the k-infinity was measured directly with an error of only $\pm 0.5\%$. If the $\bar{\alpha}_9$ appropriate to the normal operating density lattice is assumed to be in error by the same amount as that deduced for the reduced enrichment case, the error in k-infinity becomes $3.2 \pm 2.7\%$.

7. SUMMARY AND CONCLUSIONS

The present series of measurements has confirmed the value of the mixed critical type of experiment in fast reactor experiments. Measurements have been made of neutron capture and fission rates and k-infinity in a wide range of steam cooled fast reactor lattices containing only 50 kg of plutonium.

Foil activation techniques developed in thermal reactor studies have been modified to the fast reactor application and shown to be of particular value where lattice heterogeneity significantly affects the neutron balance.

A null reactivity change technique for the direct measurement of k-infinity has been applied to a fast reactor lattice and in combination with reaction rate measurements has allowed the capture to fission ratio of ^{239}Pu to be deduced.

The FD2 data set [3] which is in current use for fast reactor calculations at A.E.E., Winfrith has been used to provide predictions of the neutron balance in the four simulated steam cooled fast reactor lattices studied using the multigroup transport code GMS II. The following conclusions were obtained:

(a) the ^{238}U fission rate relative to that of ^{239}Pu is significantly underpredicted in both operating density and voided lattices, although due to the small contribution of the ^{238}U fission rate to the neutron balance, k-infinity is not significantly affected;

(b) the ^{235}U fission to ^{239}Pu ratio is overestimated in all lattices, but again this does not significantly affect the k-infinity predictions;

(c) in the reduced enrichment operating density lattice, the calculated ^{239}Pu capture to fission ratio is significantly lower than given by experiment. This is in agreement with preliminary work on other fast reactor cores and with a re-assessment of available basic nuclear data at A.E.E., Winfrith;

(d) ^{238}U captures relative to ^{239}Pu fissions are not well predicted in the lattices with significant resonance self-shielding (i.e., the reduced enrichment and flooded cases). This has been shown to lie in the method of compiling the FD2 group data. A spectrum typical of a sodium cooled fast reactor was used to condense the basic data from the U.K.A.E.A. data library into the FD2 group data, and this weighting is not appropriate to these softer spectrum lattices.

This work has shown the general validity of the FD2 data set for the design of steam cooled fast reactors and indicated its limits of applicability.

APPENDIX 1

THE THEORETICAL TREATMENT OF RESONANCE SELF-SCREENING

The GMS libraries have cross sections listed as a function of the potential scattering cross section per absorber atom, σ_p, for the fissile and fertile elements. The value of σ_p for each of these isotopes is fed in as input data to GMS, different values being permitted in different materials.

The values of σ_p appropriate to the present work are derived [13] in the following way

$$\sum_p = \sum_{\substack{\text{Fuel} \\ \text{Mixture}}} N_i \lambda_i \sigma_{si} + \frac{\nu}{\bar{l}_f} \qquad (1)$$

where $$\nu^{-1} = 1 + \frac{V_f}{\bar{l}_f \sum_{\substack{\text{Non-} \\ \text{fuel}}} N_j' \sigma_j'}$$

and N_i is the actual number of atoms/c.c. of isotope in the fuel plate,

λ_i is a function of the probability that a neutron scattered in a resonance of material i suffers its next collision outside the resonance, and is here assumed to be unity,

σ_{si} is the microscopic potential scattering cross section of isotope i,

ν is the Dancoff factor, i.e. a factor which takes into account the mutual shielding of fuel plates in close packed lattices,

V_f is the volume fraction of the fuel in the cell,

$\bar{l}_f$ is the mean chord length of the fuel,

N'_j is the number density of atoms of isotope j if the cell were homogenised,

σ'_j is the total microscopic cross section of isotope j.

The value of σ_p for an isotope k present in the fuel plate in a quantity N_k atoms/c.c. is then given by $\sigma_p = \frac{\Sigma_p}{N_k}$.

In the test zone cells, two fuel plates are present. One of these contains the heavy atoms ^{239}Pu, ^{240}Pu, ^{235}U and ^{238}U, whereas the other contains only ^{235}U and ^{238}U. In the initial derivation of the Σ_p values for the plutonium isotopes, V_f was taken as the volume fraction of the plutonium bearing plate relative to the whole cell composed of one mixed oxide plate, one natural oxide plate, steel and polypropylene. In the calculation of Σ_p for the uranium isotopes, which appear in both plates but in different quantities, the cell was first treated as though it consisted of only one fuel plate whose composition was an average of the two actual fuel plates, plus a proportionate amount of moderator and steel. To derive the σ_p value for each plate, the actual number of atoms/c.c. (N_k) was used, this being different for the two plates.

APPENDIX 2

THE DIMENSIONS AND COMPOSITIONS OF THE LATTICE CELLS

(1) The fuel plates

	Mixed oxide plate	Natural uranium oxide plate
Mass of PuO_2	32.94 g	0
Mass of UO_2	97.34 g	133.8 g
Mass of stainless steel can	17.68 g	19.4 g
Thickness of cladding	0.038 cm	0.038 cm
Plate thickness and dimensions (excluding S.S. can)	0.552 cm x 4.953 cm x 4.953 cm	0.552 cm x 4.862 cm x 4.862 cm

(2) The steel spacers and element sheaths

Weight of the 0.488 cm thick U-spacer, 31.0 g

Weight of the 0.124 cm thick flat spacer, 23.53 g (flooded)

Weight of the sheath per unit length, 18.92 g/cm

(3) The coolant simulants

Polypropylene plate: 0.0483 cm thick; weight 0.611 g (operating density)

Polythene plate: 0.254 cm thick; weight 5.990 g (flooded)

(4) The cross sectional area of a cell

For all densities: 5.441 x 5.441 cm.

The homogenised isotopic number densities used in the calculations for each of the four lattice cells are given below in units of 10^{24} atoms/cm^3.

	Voided	Normal Operating	Flooded	Operating (Reduced Enrichment)
^{239}Pu	9.809×10^{-4}	As for Voided	9.677×10^{-4}	6.539×10^{-4}
^{240}Pu	1.097×10^{-4}		1.082×10^{-4}	7.311×10^{-5}
^{241}Pu	1.439×10^{-5}		1.420×10^{-5}	9.594×10^{-6}
^{242}Pu	9.780×10^{-7}		9.649×10^{-7}	6.520×10^{-7}
^{235}U	5.683×10^{-5}		5.606×10^{-5}	5.978×10^{-5}
^{238}U	7.753×10^{-3}		7.649×10^{-3}	8.154×10^{-3}
O	1.783×10^{-2}		1.759×10^{-2}	1.783×10^{-2}
G	1.136×10^{-3}		1.121×10^{-3}	6.014×10^{-4}
Ni	4.313×10^{-4}		4.254×10^{-4}	1.889×10^{-4}
Fe	2.153×10^{-2}		2.650×10^{-2}	2.160×10^{-2}
H	-	1.586×10^{-3}	1.534×10^{-2}	1.585×10^{-3}
C	4.472×10^{-5}	8.379×10^{-4}	7.715×10^{-3}	8.304×10^{-4}

8. REFERENCES

[1] MOUNTFORD, L. A., MOREWITZ, M. A., "The advanced epithermal thorium reactor (AETR) critical experiments", Nuclear Science and Engineering, No. 4, April 1965, 21.

[2] ROWLANDS, J. L., WARDLEWORTH, D., "A 19-group extension to the YOM cross section set", AEEW M 172.

[3] SMITH, R. W., ROWLANDS, J. L., WARDLEWORTH, D., "The FD2 group averaged cross section set for fast reactor calculations", AEEW R 491.

[4] BROOMFIELD, A. M., STEVENSON, J. M., "Measurement and calculation of ratios of effective fission cross sections in the zero power fast reactor ZEBRA", AEEW R 526.

[5] DONAHUE, D. J. et al., "Determination of k_∞ from critical experiments with the PCTR", Nuclear Science and Engineering 4 (1958) 297.

[6] ENGELDER, P. C. et al., "Spectral shift control reactor basic physics programme. Measurements of k_∞ and other lattice parameters by the small lattice experiment technique", BAW-1283.

[7] FOX, W. N. et al., "The measurement of ^{239}Pu capture to fission ratios in fast reactor lattices", Journal of BNES, No. 1, 6.

[8] MILLER, P. C., PARKER, K., List of data files available in the UKAEA Nuclear Data Library as at 15th April, 1966, AWRE Report No. O-55/65.

[9] GRATTON, C. P., SMITH, P., "GMS I. A generalised multigroup system of calculations using the IBM 7030 (stretch) computer", AEEW-M 458.

[10] FAYERS, F. J., TERRY, M. J., "Determination of resonance integrals for an infinite lattice of plates containing two different types of fuel plates on a repeated basis", AEEW-M 729 (not for publication).

[11] FAYERS, F. J., KINCHIN, G. H., "Uranium and plutonium fuelled lattices with graphite and water moderation - A comparison of experiment and theory", Joint international conference on the physics problems in thermal reactor design, BNES, June 1967.

[12] SOWERBY, M. J., Private Communication.

[13] HICKS, D., "Nuclear calculation methods for light water moderated reactors", AEEW-R 64.

DISCUSSION

H.W. KÜSTERS: Did you conclude from your measurements that the high α values for ^{239}Pu reported by Dr. Schomberg (paper SM-101/41) were justified? Our theoretical value of $\sigma_f(^{238}U)/\sigma_f(^{239}Pu)$ was also larger (by 7%, compared with your 8%), as were our overestimates of $\sigma_c(^{238}U)/\sigma_c(^{239}Pu)$. Our calculations were performed with the SNEAK set and relate to the ZPR III/48.

C.G. CAMPBELL: In answering this question I should perhaps give the historical background. The DIMPLE measurements using the PCTR technique indicated a substantial increase in the α value for ^{239}Pu. Perturba-

tion studies in ZEBRA also indicated the need for a large ^{239}Pu α value, but did not suggest that it was necessary to increase the α value for ^{235}U by anything like the large amount indicated by Dr. Hellstrand's results (paper SM-101/2). The differential data were re-evaluated and gave α values, based on total and fission cross-section measurements with allowance for scattering, which are consistent with the integral measurements carried out in the United Kingdom. The measurements being carried out at Harwell tend to confirm the high α values. Thus, all the evidence points to increased α values for ^{239}Pu, and I do not know of any evidence to substantiate the FD2 values.

M. DALLE DONNE: What effect does the very large increase in the α value for plutonium have on the breeding ratio of large steam-cooled fast reactors at high pressure?

C.G. CAMPBELL: Our studies of steam-cooled fast reactors were abandoned (partly because of the evidence presented in the paper), since such reactors are likely to have a low breeding gain - possibly approaching zero.

N. V. KRASNOYAROV: It has been shown by calculation in other papers on this subject that k_{eff} decreases with increasing steam density. This has also been demonstrated experimentally in your paper. This means that the power effect of reactivity has a positive component. Is this swamped by the Doppler effect?

E. KIEFHABER: Perhaps I can answer this question. As you can see from Fig. 2 of paper SM-101/15, we carried out a stability analysis for our D1 reactor design and found that its kinetic behaviour lay just at the boundary of the region of stability, corresponding to a negative power coefficient. I have shown that, taking into account all uncertainties in the power density and Doppler coefficients, it is quite possible for our reactor to move into the unstable region.

H. VOLLMER: I should like to add that the problem of designing a stable steam-cooled fast reactor plant is an economic one. A stable system can always be designed if economy is sacrificed.

R. VIDAL: On the basis of your experience with DIMPLE, do you intend to continue your investigations using the PCTR method?

C.G. CAMPBELL: Yes, we have now built into ZEBRA the first of a series of integral assemblies with a clean geometry, and we have found the composition for which k-infinity is unity, as tested by the removal of a central section with a zero reactivity effect. The assembly is approximately spherical. Integral quantities such as ^{238}U capture and the various fission rate ratios will be measured with a view to adjusting the nuclear data. Differential values for ν and α will be checked in the knowledge that k-infinity is unity.

PARAMETRIC STUDY OF THE DYNAMIC BEHAVIOUR AND STABILITY OF A STEAM-COOLED FAST REACTOR WITH AN INTEGRATED COOLING CYCLE*

W. HÜBSCHMANN, F. ERBACHER,
W. FRISCH+, S. MALANG, L. RITZ
AND G. WOITE
INSTITUT FÜR REAKTORBAUELEMENTE,
KERNFORSCHUNGSZENTRUM KARLSRUHE,
KARLSRUHE, FEDERAL REPUBLIC OF GERMANY

Abstract

PARAMETRIC STUDY OF THE DYNAMIC BEHAVIOUR AND STABILITY OF A STEAM-COOLED FAST REACTOR WITH AN INTEGRATED COOLING CYCLE. The paper shows that in a steam-cooled fast breeder reactor it is possible, in principle, to produce inherent stability and safety from accidents by the feedback of the cooling cycle on the core. The effects of various parameters on stability and safety are determined for the following disturbances: reactivity disturbance, blower failure, load changes, various pipe ruptures, and inadvertent fast unflooding. Trends and limits are put forward that should be observed in the design of the components and the arrangement of the cooling cycle. In particular, it is shown that a cooling cycle integrated in a common pressure vessel produces easily inherent stability and safety of a steam-cooled fast reactor.

1. INTRODUCTION

In a steam-cooled fast reactor the coolant density coefficient is generally negative. If the average steam density in the core decreases, this implies a reactivity increase. The rate at which this reactivity increase occurs determines the extent of a possible damage caused by a failure of the safety system.

It has been shown in Ref.[1] that a compact cycle integrated in a pressure vessel is able to inherently fulfil the conditions of stability and safety from accidents to such an extent that these do not depend exclusively on the functioning of the control and safety systems. If this characteristic of inherent stability and safety from accidents is made a primary requirement it will influence the design of the cycle and of its components.

As shown in Fig. 1, such a cycle consists of the core C, the plenum volumes for superheated and saturated steam V_h and V_s, the evaporators E, the steam blowers B, the water storage V_w, and the pipe lines connecting them. The blowers are driven by turbines T_b which are connected in series with the main power turbine T_p. The broken line indicates that the whole cooling cycle is surrounded by a common pressure vessel.

---

* Work performed within the association in the field of fast reactors between the European Atomic Energy Community and Gesellschaft für Kernforschung mbH, Karlsruhe.

+ Institut für Reaktorentwicklung, Kernforschungszentrum Karlsruhe.

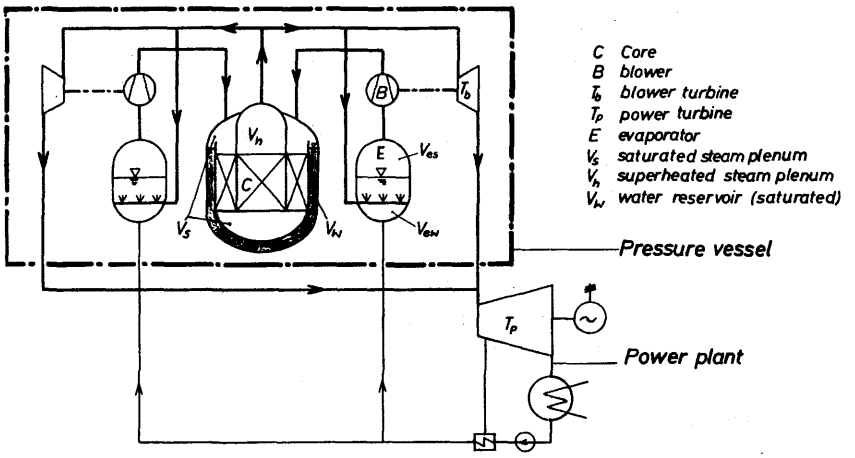

FIG.1. Scheme of the cooling cycle.

The purpose of this parametric study was to investigate the influence of the design and arrangement of the listed components on the stability of the cycle and its accident safety. The calculations are based on the core dimensions and the reactivity curve of the D-1 design [2].

The reported results were obtained by means of various digital codes for special problems and an analogue model of the complete reactor cooling cycle [3].

2. INHERENT STABILITY AND INHERENT SAFETY FROM ACCIDENTS

If a reactivity increment Δk_d is introduced into the core, the power Q of the reactor after a short overshooting rises asymptotically to a value $Q+\Delta Q$. The quotient $(\Delta Q/Q)/\Delta k_d$ is called the reactivity gain K_k. This is

$$K_k = \frac{\Delta Q/Q}{\Delta k_d} \tag{1}$$

where Q = reactor power
K_k = reactivity gain
Δk_d = reactivity disturbance.

If the power increment ΔQ is not consumed by the main turbine, the increased steam generation in the evaporator will cause the pressure in the cooling cycle to rise at a rate which is inversely proportional to the energy storage capacity C(MWs/atm).

The rise of the pressure p and the rise of the average density ρ of the steam reduce the power increment in the case of a negative steam density coefficient $\alpha\rho$ so that the ultimate value will be precisely the power that is taken from the main turbine. This mechanism may be utilized for the self-stabilization of reactor power in case of minor

disturbances as well as for the self-control in case of changes in the power consumption.

Figure 2a shows the time behaviour of the reactor power after a step-like reactivity increase $\Delta k_d = 0.2$ \$ without cycle feedback. The beginning of all curves, which hold for various reactivity gains, is identical because of the prompt critical power step.

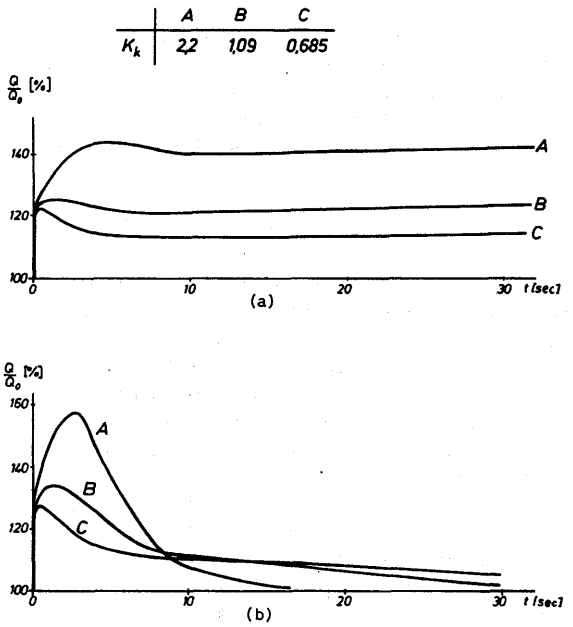

FIG.2. Power transient following a 0.2 $ reactivity step.
(a) Reactor power without feedback of the cooling cycle.
(b) Reactor power with feedback of the cooling cycle.

The higher the reactivity gain the more the reactor power rises in the case of a reactivity increase. For reasons of safety and stability the reactivity gain should be as small as possible, as is evident from Fig. 2a. The favourable influence of a low reactivity gain is obvious also from Fig. 2b, in which the feedback of the cycle has been taken into account.

The pressure increase in the cycle will start with a delay because of the various delay and dead times of the energy transport from the reactor to the water in the evaporators. These periods are combined in the delay time T_u. In case of an excessive delay time T_u the reactor power may be excited into oscillations. A buildup of these oscillations is prevented, if

$$K_k \times \alpha\rho \times \frac{d\rho}{dp} \times \frac{y \times Q}{C} \times T_u < A_{crit.}$$

Here, y is the ratio of the quantity of superheated steam flowing to the evaporators to the total quantity of steam flowing through the core.

The term $K_k \times \alpha\rho \times d\rho/dp$ is called pressure gain K_p below. It is negative with a negative steam density coefficient. Hence, the stability condition is

$$- K_p \times \frac{y \times Q}{C} \times T_u < A_{crit.} \tag{2}$$

The value of $A_{crit.}$ depends on the composition of the delay time T_u and is a minimum of $\pi/2$ under the assumption of a pure dead time and is 4 under the assumption of two delay times of equal length.

Since there are several time constants of the same order of magnitude in this system, $A_{crit.}$ is between these limits as shown in Ref. [4].

$$\frac{\pi}{2} < A_{crit.} < 4$$

For the stability of the system a short delay time T_u is of primary importance. Because a reheater of the usual design heated with live steam results in a relatively long delay time and, moreover, long pipe lines have a particularly unfavourable influence upon stability owing to the pure dead time they cause, a cooling cycle without reheater and of a compact design was selected as the starting point of this study.

These and similar measures result in a reduction in the energy storage capacity C. The lower limit is determined by the steam and water quantities in the evaporators. A suitable evaporator is being developed [5]. A low-energy storage capacity has the consequence that the cycle feedback starts not only as early as possible but also sufficiently strongly, so that the power rise and thus the increase in can temperature are controlled sufficiently fast. However, the energy storage capacity must not fall below a lower limit for reasons of stability.

Finally, the absolute value of the pressure gain K_p is kept small for safety reasons in order to cause the reactor power to increase as little as possible during a pressure decrease. In addition, K_p should be negative in order to have the cycle feedback occur in the right sense.

This results in these three requirements with respect to inherent stability:

(1) The dead time T_u should be as short as possible.
(2) The pressure gain K_p should be small in absolute terms, but negative.
(3) The energy storage capacity C should assume an optimum value dependent on T_u and K_p.

In addition to the requirement of inherent stability there is the one of inherent safety from accidents. Special accident risks of the steam-cooled breeder reactor are provided by the possible reverse flow of superheated steam into the core, the density reduction due to a leak in the cycle, and the unflooding accident. These accident risks are influenced by the design and arrangement of the cycle components and the water and steam volumes.

The influence of the following parameters on stability and safety is investigated in this paper:

Water and steam volumes in the evaporators
Volume of steam inlet- and outlet-plenum at the core
Volume of water reservoir at core inlet
Power density of fuel rods
Number and characteristics of blowers
Arrangement and design of blower turbines
Arrangement of cooling cycle inside or outside the reactor pressure vessel.

The effect of these parameters is investigated on the following disturbances:

Reactivity disturbance
Blower failure
Load changes
Rupture of superheated-steam pipe
Rupture of saturated-steam pipe
Unflooding accident.

3. DISTURBANCES

3.1. Reactivity disturbance

The effects of a reactivity disturbance have been described qualitatively in Ref.[6]. Below it is shown on what quantities the disturbance behaviour depends and what the influence of an increase in rod power is quantitatively.

The reactivity gain K_k can be calculated from the relations for the reactivity feedback, because in the transient state the sum of disturbance reactivity Δk_d and reactivity feedback Δk_f must become zero:

$$\Delta k_d + \Delta k_f = 0 \tag{3}$$

For an approximative treatment it is sufficient to consider only the Doppler coefficient α_D and the steam density coefficient $\alpha\rho$. Then it holds that

$$\Delta k_f = \alpha_D \times (\vartheta_F - \vartheta_{Fo}) + \alpha\rho \times (\rho - \rho_0) \tag{4}$$

Here and below the symbols have these meanings:

ϑ_F fuel temperature
ϑ_{Fo} fuel temperature before disturbance
ϑ_{st} steam temperature
ρ steam density
ρ_0 steam density before disturbance
c_p specific heat of the steam
$\dot{m}$ steam throughput per fuel rod
q power per fuel rod
R heat transfer resistance fuel/steam

All values are averaged over the core. From the heat transfer equations and the energy balance sheets we derive

$$\vartheta_F - \vartheta_{Fo} = \left(\frac{1}{2 \times c_p \times \dot{m}} + R \right) \times \Delta q \tag{5}$$

$$(\rho - \rho_0) = \frac{1}{2 \times c_p \times \dot{m}} \times \left(\frac{d\rho}{d\vartheta_{st}} \right) \times \Delta q \tag{6}$$

From Eqs (1) and (3) to (6) results finally the reactivity gain

$$K_k = \frac{\Delta q/q}{\Delta k_d} = -\left[\frac{1}{q \times \alpha_D \times R + \frac{q \times \alpha_D}{\dot{m} \times 2 \times c_p} + q \times \alpha\rho \times \frac{1}{2 \times c_p \times \dot{m}} \times \left(\frac{d\rho}{d\vartheta_{st}} \right)} \right] \tag{7}$$

On the basis of this equation the main influencing quantities will be discussed.

The first two terms and the last one in the denominator have a reversed sign. K_k is positive and the core is stable if the first two terms which characterize the Doppler feedback are absolutely larger than the last term which gives the feedback of steam density. By reducing K_k, i.e. by increasing the first two terms or reducing the last term, it is possible to improve the stability. A possibility which is accompanied with economic advantages is the increase in rod power with a simultaneous increase in the steam throughput per channel so that inlet and outlet temperatures remain unchanged [7].

Because of the simultaneous increase in q and $\dot{m}$ the last two terms in the denominator of Eq. (7) remain unchanged, while the first term becomes larger.

Figure 3 shows how the reactivity gain K_k becomes smaller with increasing rod power. Besides K_k, the Doppler coefficient α_D has been plotted which becomes smaller because of the higher average fuel temperature with increasing rod power. Yet, the Doppler feedback is increased because in the case of disturbance the absolute changes in fuel temperature are higher.

Therefore, the high rod power required in the interest of low fuel cycle costs contributes at the same time to the stability of the reactor. However, the increase of rod power must not result in exceeding the permissible temperature and stress of the canning. So, a precondition of an increase in power density is the intensification of heat transfer and the reduction of the hot channel factor, which can be achieved by cross mixing. These requirements are met by the fuel element schematically shown in Fig. 4, which was developed specially for the steam-cooled fast breeder reactor. It is characterized by canning tubes with six integral helical fins which serve simultaneously the purpose of spacing and cross mixing. Experiments proved that in this way and by application of surface roughening, even with steam cooling, rod powers of 600 W/cm at maximum can temperatures between 600 and 650°C can be achieved [8].

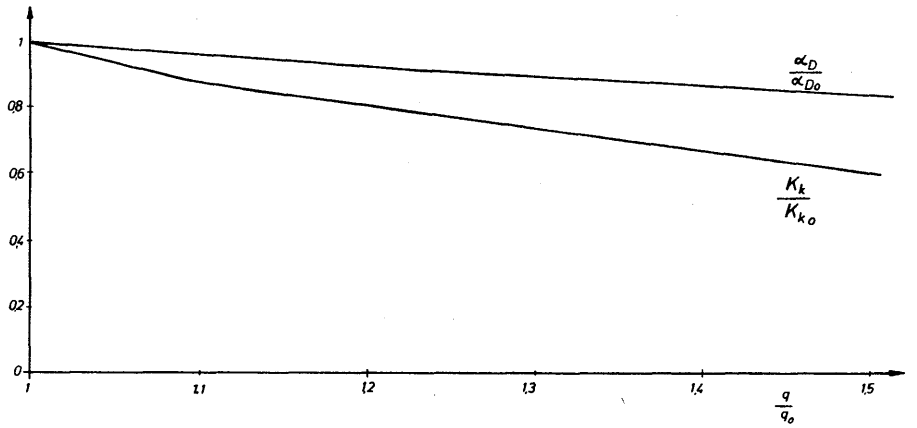

FIG.3. Relative changes of Doppler coefficient and reactivity gain versus rod power.

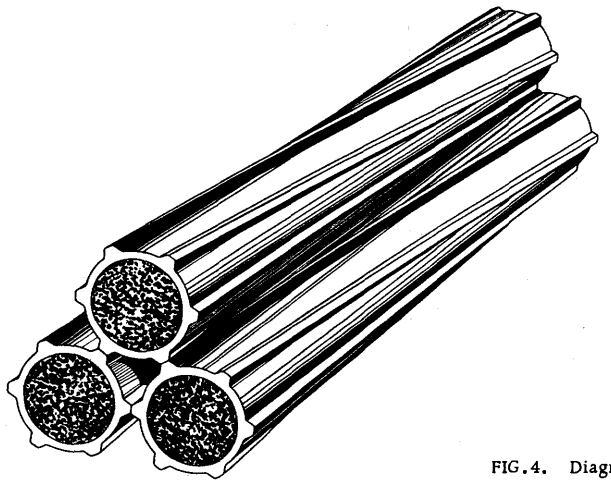

FIG.4. Diagrammatic view of the fuel element.

3.2. Blower failure

As the blowers are movable parts they must be regarded as being potentially susceptible to failure. Hence, special attention should be paid to the effects of the failure of a blower.

After the failure of a blower the pressure in the inlet plenum of the reactor decreases because less steam is supplied. In the outlet plenum the pressure rises because of the reduced steam removal.

The reduced pressure head then results in a reduced steam throughput through the core. The consequence is an increased heating of the steam so that the average density of the steam decreases while the reactivity increases. This causes the power of the reactor to rise. This power rise is limited to a value which is the lower:

(1) the smaller the power gain of the core due to a density reduction,
(2) the more blowers are used, i.e. the less the missing quantity of supply matters in terms of percentage,
(3) the flatter the blower characteristics, since with decreasing supply pressure the blowers still operating will supply more than in the case of steep characteristics,
(4) the larger the water reservoir kept at boiling temperature and connected with the inlet plenum, because it will slow down by evaporation the pressure decrease,
(5) the faster the system pressure rises after the power increase of the reactor, i.e. the shorter the delay time and the smaller the capacity of the cycle.

Figure 5 shows the time behaviour of the steam quantity delivered, of the reactor power and of the can temperature after failure of one blower. The number and characteristics of the blowers are varied.

The upper diagram shows the reduction in the steam flow through the core, which is much more pronounced with four blowers than it is with six. Moreover, it shows how much the delivery of the still operating blowers increases. Because of its flatter characteristics the radial blower proves to be superior to the axial blower.

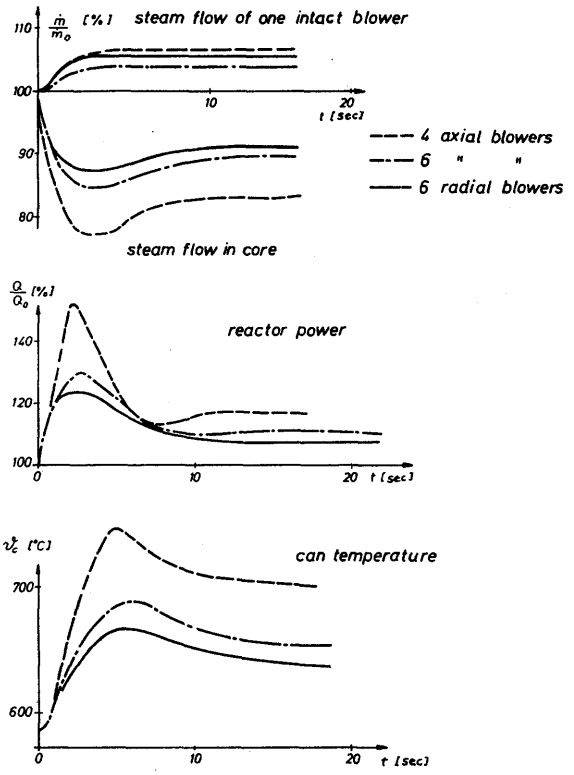

FIG. 5. Influence of number and type of blowers on cycle dynamics after blower failure.

The middle diagram shows that the reactor power increases more the larger the reduction in the steam mass flow.

The lower diagram shows that the can temperature rises in the case of four axial blowers within some 5 s from 585°C by 160°C to 745°C, not taking into account the hot channel factor. When the number of blowers is increased from four to six, it only rises by 105°C to 690°C. When six radial blowers are used instead of six axial ones, the maximum of the can temperature is additionally reduced by 25°C.

A further decrease in the rise of reactor power and can temperature can be achieved by a reduction in the energy storage capacity C of the cycle. Figure 6 shows that a reduction of this capacity from 750 to 325 MWs/atm results in an overshooting of the pressure at the reactor outlet by 1 atm, but that it also reduces the maximum of the canning temperature by another 25°C.

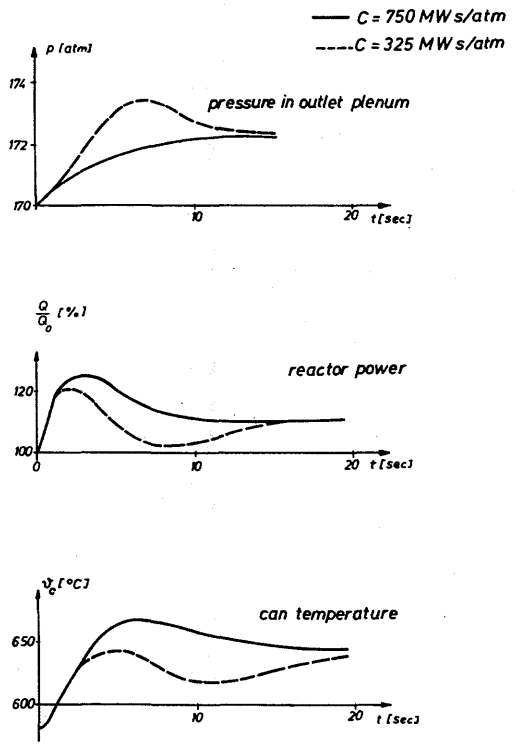

FIG.6. Influence of the capacity of the cycle on cycle dynamics after blower failure.

In the case of a failure of one of four radial blowers a realistic energy storage capacity of the cycle will result in a short-time rise of the can temperature by about 100°C. The increase in stress caused by this temperature rise is most dangerous on the inside wall of the fuel element can. Under the adverse assumption that the steam temperature does not change, the short-time stresses produced on the inner wall of the can were determined. In the case of a temperature step of 100°C, at the beginning as well as at the end of the life of the can,

they remain some 15 kp/mm^2 below the yield strength if Inconel 625 is used, taking into account the hot channel factor. Hence, the temperature step produced by the restriction to four blowers does not entail an undue load on the canning.

Nevertheless, the aim of development was to achieve high operational safety of these blowers. Figure 7 shows how this was safeguarded by an overhung arrangement of a centripetal turbine and a centrifugal blower on a shaft equipped with condensate-lubricated bearings. Such an enclosed design reduced the problem of leakage to insignificant proportions and avoided contamination of the cycle by a lubricating agent other than the working medium. Two prototype blowers of this type have proved their reliability on the test bed [9].

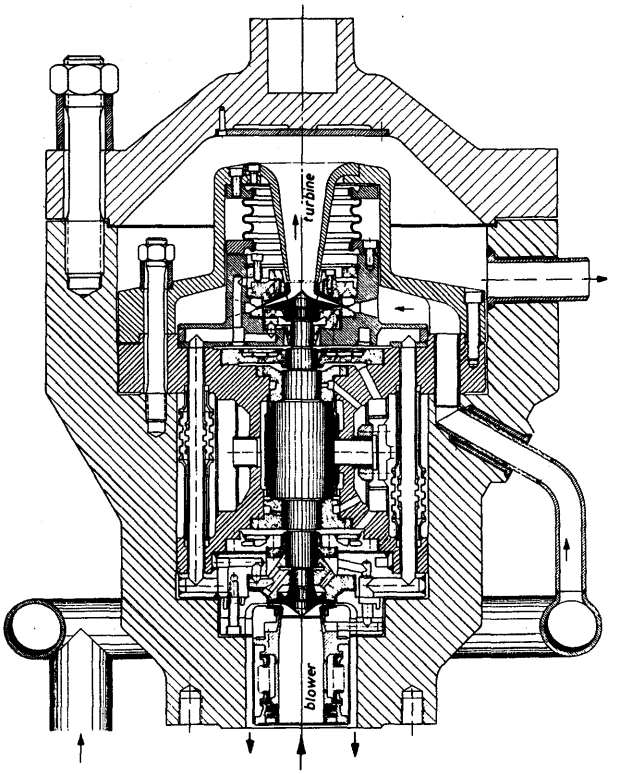

FIG.7. Turbine driven steam blower.

3.3. Load changes

If the power consumption and the steam requirement of the main turbine change, the reactor power has to follow this change as rapidly as possible. If the aim is an inherently good load following behaviour, this requirement must be harmonized with inherent safety from a superheated-steam pipe rupture, as will be explained later.

	A	B	C	D
energy storage capacity C [MWs/atm]	750	750	750	325
water reservoir V_W [m^3]	400	400	0	50
arrangement of blower turbine	parallel	series	series	series

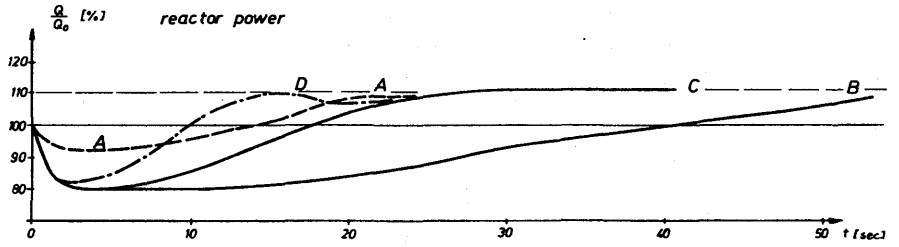

FIG. 8. Rate of power change following a 10% load increase.

Figure 8 shows the time behaviour of the reactor power after a 10% increase in the steam consumption of the main turbine. First, the reactor power will decrease because, owing to the higher throughput through the core, the steam will not be heated to such an extent and its density will increase. Later on, the reactor power will increase again, since with a decrease in system pressure also the steam density will decrease. The power increases until finally 110% of the initial value has been reached, i.e. exactly the value which is taken from the main turbine.

The initial reduction in power is more pronounced if series turbines are used as blower drive (curves B, C, D) than in the case of parallel turbines (curve A). This is due to the fact that the whole steam quantity flowing to the main turbine, which is increased when the load is higher, flows through the series turbines. The power of the turbines and thus the quantity supplied by the blowers into the core increase. This results in an additional increase in steam density and hence in a reduction of reactivity and reactor power. In an otherwise identical cooling cycle it will take more time therefore for series turbines to reach the desired power increment than for parallel turbines, as is shown by curves A and B. The load following behaviour, however, can be much improved by reducing the water reservoir (curve C) and the capacity of the cycle (curve D).

3.4. Rupture of a superheated-steam pipe

The behaviour of the reactor in the case of a rupture of a superheated-steam pipe qualitatively equals the behaviour in load increase of the main turbine, because in both cases a major steam quantity is taken from the outlet plenum and because it is the same to the reactor whether this flows to the main turbine or through a leak. A qualitatively different behaviour would be desirable, since in increasing the turbine load the power of the reactor should follow the increased demand as rapidly as possible, whereas the power should drop as soon as there is a rupture of a

superheated-steam pipe. These conflicting requirements to inherent safety from the consequences of the rupture of a superheated-steam pipe, on the one hand, and inherently good load following behaviour, on the other hand, result in contrary design tendencies which will be explained below.

Figure 9 shows the time plot of the reactor power following a rupture of a superheated-steam pipe. As in an increase in the steam quantity on the main turbine, the reactor power first drops. The blower drives considered here are parallel turbines. When using series turbines the initial power drop would be more pronounced (cf. Fig. 8). Afterwards, the power will increase the more rapidly the bigger the quantity leaking out (curves A, B, C) and the lower the energy storage capacity of the cycle (curve D). This shows the significance of an effective limitation of the leakage quantity.

	A	B	C	D
energy storage capacity C [MWs/atm]	750	750	750	325
water reservoir V_w [m³]	400	400	400	50
leaking steam flow [$\frac{kg}{s}$]	112	225	450	450

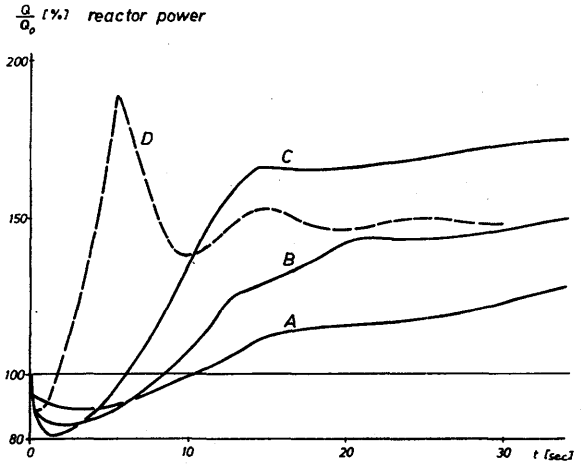

FIG. 9. Rate of power change due to rupture of superheated-steam pipe.

In a disintegrated design or if the blowers are driven by parallel turbines, the quantity leaking out must be limited by Venturi nozzles. Such Venturi nozzles are used for the KRB boiling water reactor at Gundremmingen. In a steam-cooled fast reactor a more economic and effective limitation of the leakage quantity can be realized by an integrated design coupled with the use of series turbines as the blower drive. As long as the pressure vessel is intact, leaks are then possible only behind the series turbine whose nozzle ring is always designed to operate with high steam velocities.

Since this velocity cannot rise to more than the velocity of sound, this is an automatic and effective limitation of the steam flow. Moreover, contrary to the use of Venturi nozzles, no additional pressure loss has to be taken into account, the steam flow can be limited to 1.3 times the design value by a suitable design of the series turbines, which reduces the effects of the rupture of a superheated-steam pipe to insignificant proportions.

Another advantage of the series turbine is its ability to supply a fast shutdown signal for the reactor by the strong increase in blower speed already at a time at which the reactor power has not yet risen above the design value.

3.5. Rupture of a saturated-steam pipe

This section investigates the following pipe ruptures with respect to their effect:

(1) Saturated-steam pipe between blower and inlet plenum
(2) Simultaneous rupture of saturated and superheated-steam pipe in concentric pipe design.

In a reactor with disintegrated layout in which all cycle components are arranged independent of each other outside the reactor pressure vessel and interconnected by pipes, all steam pipes are loaded by the full pressure. In this case the average steam density in the core will decrease faster following a rupture in the saturated-steam line than due to the rupture of a superheated-steam line, because in the first case the pressure as well as the coolant flow through the core decrease, whereas in the second case the pressure decreases, but the coolant flow increases and consequently the average steam temperature decreases.

With the rupture of only the saturated-steam pipe the pressure on the inlet side may become smaller than that on the outlet side, so that the direction of flow reverses. The inflow of superheated steam will cause the rate of density change to rise very steeply. This reversal of flow occurs earlier the larger the evaporator volumes, because with a pressure decrease the evaporation in the evaporators delays the pressure decrease on the outlet side of the reactor. Since the water volume V_{ew} and the steam volume V_{es} reduce the reduction of pressure in the evaporators in qualitatively the same way, these two volumes were combined in the volume V_e.

$$V_e = V_{ew} + V_{es} / R$$

The constant R is determined so that R m^3 steam in a pressure decrease have the same volume increment as 1 m^3 of water.

Figure 10 shows the influence on the rate of density reduction of the steam and water storage volumes at the core inlet V_i and outlet V_h. Water and steam volumes at core inlet were combined to V_i in a corresponding way as in the case of V_e. With large V_i the size of V_h has only a slight influence upon $d\rho/dt$. This influence increases strongly with decreasing V_i. The larger V_h, the more slowly the pressure will decrease at the core outlet and the faster the pressure difference between

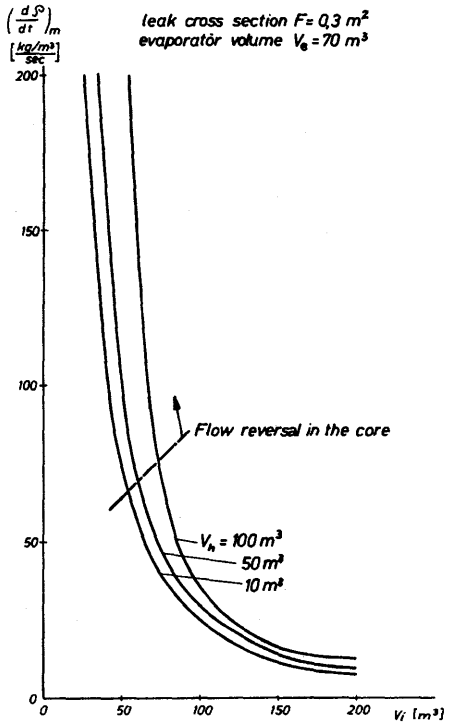

FIG. 10. Density reduction rate as caused by rupture of saturated-steam pipe and influenced by the volumes.

core inlet and outlet will be reduced. This results in a reduction in steam flow through the core and thus in a higher steam temperature.

If V_h exceeds or V_i falls below a certain value, the pressure at the outlet exceeds that at the inlet and the direction of flow will be reversed. If a certain maximum rate of density change is postulated, Fig. 10 will indicate pairs of values of V_i and V_h which permit these limits to be kept by design measures. This limit can be shifted in the direction of smaller volumes by reducing the evaporator volumes V_e. Such a limit for $V_e = 70$ m^3 is shown in Fig. 11 for a $d\rho/dt = 90$ kg/m^3 s, which corresponds to a ramp slope of 10$/s.

Even if there is no flow reversal at full power, there may well be under partial load. Figure 12 shows the dependence of the rate of density reduction on the steam mass flow at 50% partial load for three different evaporator volumes. In each case the rate of density reduction increases with decreasing mass flow. This decrease of mass flow is required to maintain a constant steam temperature at partial load. For the evaporator volume $V_e = 200$ m^3 the curve of the rate of density reduction shows, in principle, a different behaviour to that at $V_e = 50$ m^3, which is due to the flow reversal brought about with the large evaporator volume. If a maximum ramp slope of 10$/s is permitted (which roughly corresponds to a rate of density reduction of $d\rho/dt = 90$ kg/m^3 s), the volume of the evaporators must be kept very small in the disintegrated design, and

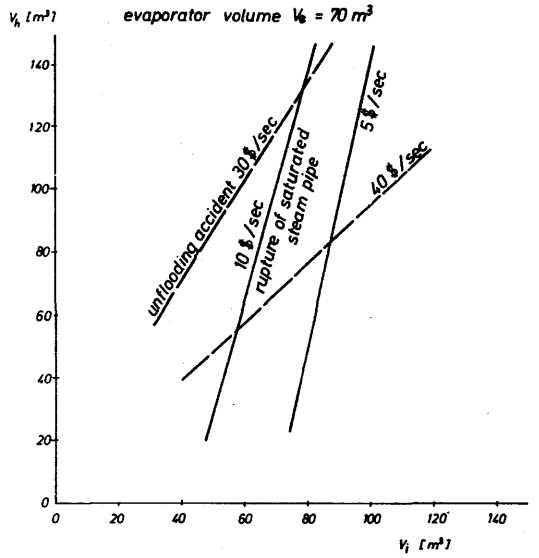

FIG.11. Design range of volumes as limited by acceptable reactivity ramps.

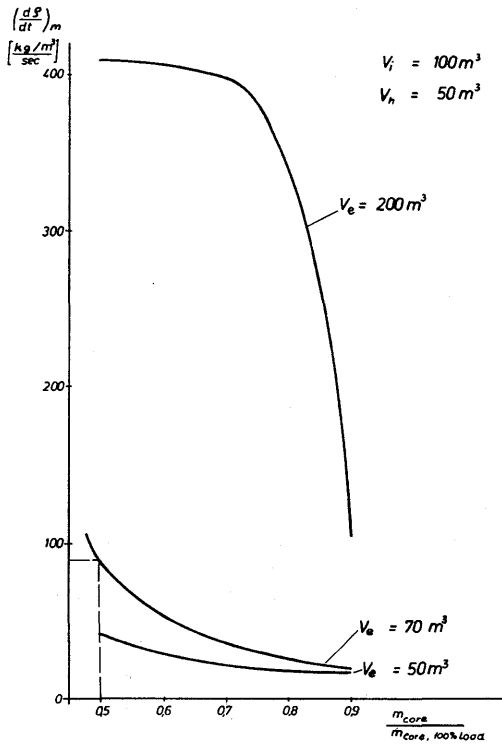

FIG.12. Density reduction rate as caused by rupture of saturated-steam pipe at 50% load.

in the case of the realistic values for the inlet- and outlet-volumes adopted as the basis of the diagram it must not exceed 70 m^3.

In a partially integrated design in which the components of every partial cooling cycle are combined in one unit each and connected with the reactor by concentrically arranged superheated- and saturated-steam pipes, only the outer saturated-steam pipes have to withstand the load by the operating pressure. The superheated-steam pipes on the inner side are designed only for the differential pressure and will consequently also rupture if the outer saturated-steam pipes should rupture. The outlet volume V_h and the evaporator volume V_e in that case have a very small influence on the rate of density change. If these volumes are very small, the pressure at the core outlet will decrease more quickly, but this results in a larger steam flow through the core and thus in a smaller average steam temperature. As the calculations have shown, the influences of pressure and temperature about balance each other. However, the inlet volume V_i is of decisive importance, as shown in Fig. 13. If the rate of density reduction brought about is not to exceed 90 kg/m^3 s, the inlet volume must be $V_i > 40$ m^3.

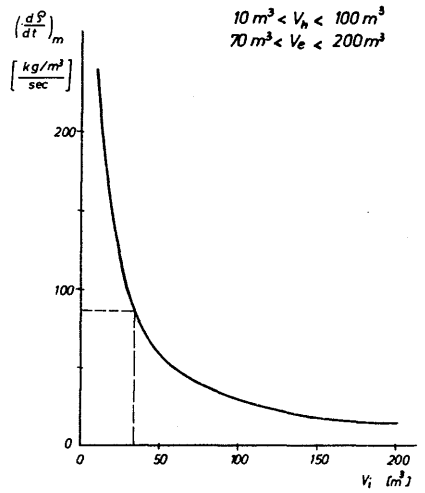

FIG. 13. Density reduction rate as caused by simultaneous rupture of the superheated- and saturated-steam pipes and influenced by the inlet volume.

Figure 14 is a plot of the rate of density change as a function of the number of blowers. It is seen that this influence is very much stronger in a partially integrated and especially in disintegrated designs and, moreover, that the resulting rate of density change is larger by several orders of magnitude than in a fully integrated design coupled with the use of series turbines as the blower drive.

The fact that the integrated design can avoid the rupture of a saturated-steam pipe and that the rupture of a superheated-steam pipe results in a very low rate of density reduction demonstrates the importance of the integrated design, especially for steam-cooled fast breeder reactors.

The requirement of integration and adequate accessibility to the individual components results in a pressure vessel of prestressed concrete,

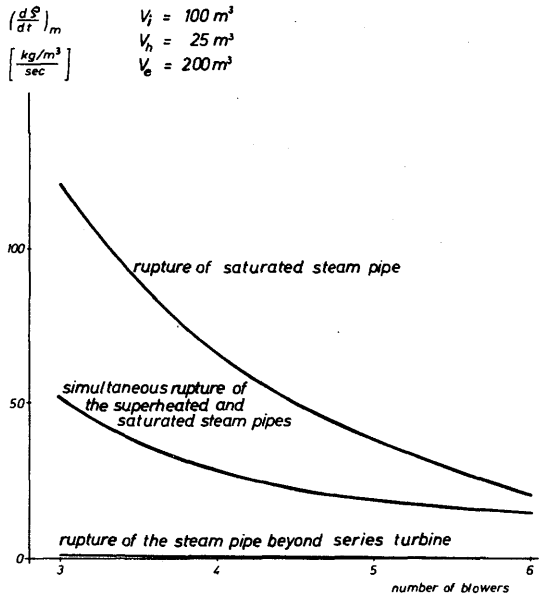

FIG.14. Density reduction rate as caused by various pipe ruptures and influenced by the number of blowers.

owing to the high pressure of about 150 atm and the status of the present technology. The layout of such a plant is shown in Figs 15 and 16. The centrally arranged core is freely accessible from the top and the bottom, so that the refuelling can be carried out without any injury by the control-rod system below the core. The conventional control system, shown in the figure, can be replaced by a fully hydraulic-operated system which requires only a few pipe penetrations of small diameter through the pressure vessel. Such a hydraulic-control system is being developed and is described in Ref.[10]. The evaporators and the steam blowers are arranged around the core and connected with it by short pipes. An integral layout like this therefore permits small volumes and thus the desired short delay and dead times.

Table I gives a comparison of the volumes required to ensure inherent stability with those obtained by the arrangement selected. This shows that the realized volumes satisfy the requirements of inherent stability. If these are met and an integrated design is adopted, the preconditions for inherent accident safety are provided as well.

3.6. Unflooding accident

The integrated layout of the cooling cycle shown also permits good accessibility to the individual components, especially to the core. Loading and unloading of the core is performed at full sight in the flooded state. The transition from this state to power operation may be the cause of another accident because the reactor may become prompt-critical by unflooding under certain circumstances. As is shown in Ref.[1], this

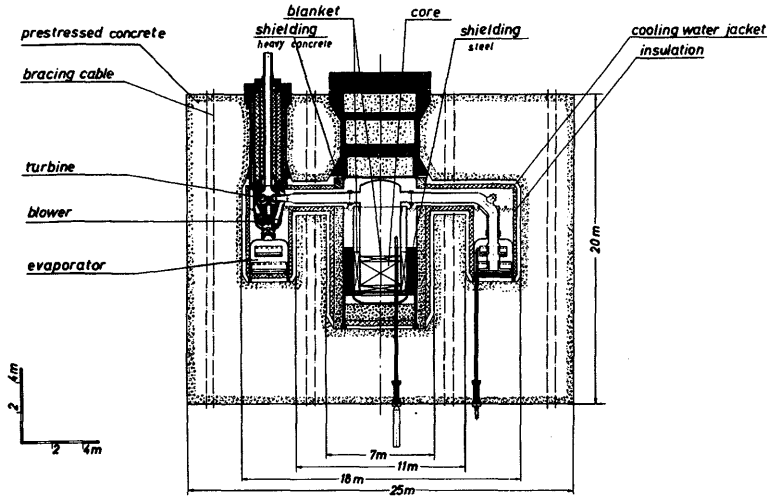

FIG.15. Arrangement of an integrated cooling cycle for a 1000-MW(e) steam-cooled fast breeder reactor (longitudinal cross-section).

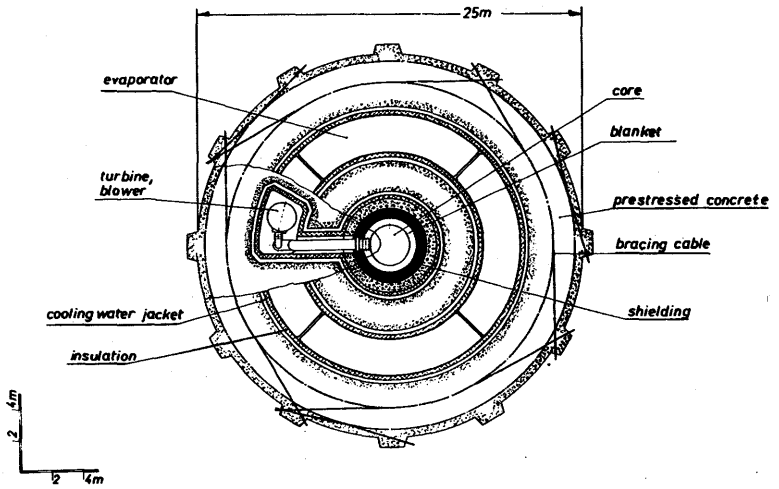

FIG.16. Arrangement of an integrated cooling cycle for a 1000-MW(e) steam-cooled fast breeder reactor (horizontal cross-section).

unflooding accident, which will be treated below, can result in unlimited reactivity ramps. By 'unlimited' we mean that these reactivity ramps, unless controlled by the scram system, will lead to a Bethe Tait excursion which is finished by the disassembly of the core. It will be shown below how it is possible to limit inherently the maximum possible reactivity ramps of these accidents by suitable arrangement and dimensioning of the cooling cycle.

Figure 17 shows the dependence of reactivity on the coolant density. Curve A was taken from the D-1 study [2] and holds for a coolant

TABLE I. VOLUMES AS REALIZED BY AN INTEGRATED COOLING CYCLE FOR A 1000-MW(e) STEAM-COOLED FAST BREEDER REACTOR

Location of volumes	Realized volumes (m^3)	Required volumes for inherent stability (m^3)	
		Favourable value	Upper limit
Water reservoir around the core (V_w)	60	50	200
Water in the evaporators (V_{ew})	60	50	100
Steam in the evaporators (V_{es})	200	100	300
Saturated-steam header (V_s)	60	50	200
Superheated-steam header (V_h)	40	30	120

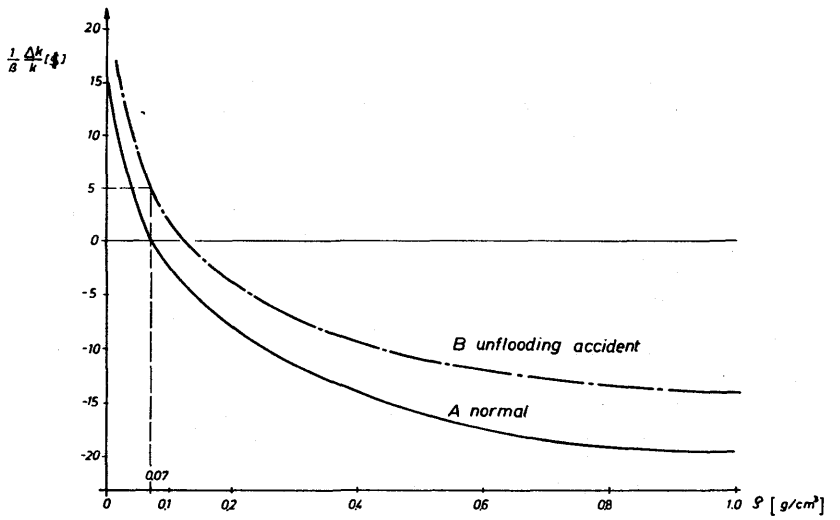

FIG. 17. Reactivity versus steam density.

homogeneously distributed throughout the core. One of the preconditions of the unflooding accident is that the reactivity of the flooded core, which is below -15 to -20 $ normally (curve A, Fig. 17), has been increased by mistake to such a level as to make the core go critical during unflooding (curve B). Such increase in the reactivity of the flooded core is possible by overloading the core during refuelling or by erroneous withdrawal of control rods.

If the cooling cycle, which is pressurized and at boiling temperature, is opened, e.g. by maloperation of a valve, a water-steam mixture of a critical mass flow will flow out. This critical mass flow of a two-phase flow corresponds to the flowing out of a single-phase flow at sonic velocity. This maximum possible mass flow was calculated by the theory of Moody [11]. If the outlet opening is below the water level, there will be very rapid unflooding of the core. In the case of the reactivity curve B (Fig. 17) this results in very steep reactivity ramps. To preclude these from arising, it must be safeguarded by the design that no steam lines penetrate the pressure vessel below the water level in the flooded condition.

Unless this requirement is met, the conditions shown in the model on Fig. 18 may come about. The leakage causes the pressure in the system to drop. This produces steam bubbles in the water so that the average specific volume increases. This has a positive effect on the outlet plenum V_h, because in this way the reduction of the water level is slowed down. However, it has an adverse effect on the water reservoir V_w, because its evaporation slows down the further pressure reduction and thus the continued evaporation in V_h. Thus, it appears that V_h and V_w will have contrary effects in an unflooding accident. V_h should be large while V_w should be small in order to prolong the unflooding time.

In the calculatory treatment it is assumed by way of approximation that in unflooding the average coolant density in the core changes with a constant average speed. This shall be defined as follows:

$$\left(\frac{d\rho}{dt}\right)_m = \frac{\rho_w - \rho_{st}}{\Delta t}\left[\frac{kg}{m^3\ s}\right]$$

where ρ_w = Density of the water with the reactor flooded (m^3/kg)
ρ_{st} = Density of the steam with the reactor unflooded (m^3/kg)
Δt = Flow time for unflooding the core (s)

If the rate of density change is calculated by the above equation, it turns out that the effect of the smaller mass flow at lower pressure is compensated in part by the greater difference in density between water and steam. This explains the flat peak of the curves in Fig. 18 in which $(d\rho/dt)_m$ was plotted as a function of pressure and of the storage volume at the core inlet V_i. Here, V_i is a combination of V_s and V_w in correspondence with Section 3.5.

To obtain the reactivity ramp from the rate of density change, $(d\rho/dt)_m$ must be multiplied by the coolant density coefficient $(dk/d\rho)_m$. This is shown by Fig. 17 to depend on the steam density. From this figure it is evident that the slope of the reactivity curve increases with decreasing density. The reactivity ramp dk/dt therefore will be particularly large in an unflooding accident if the reactor becomes critical only at small density.

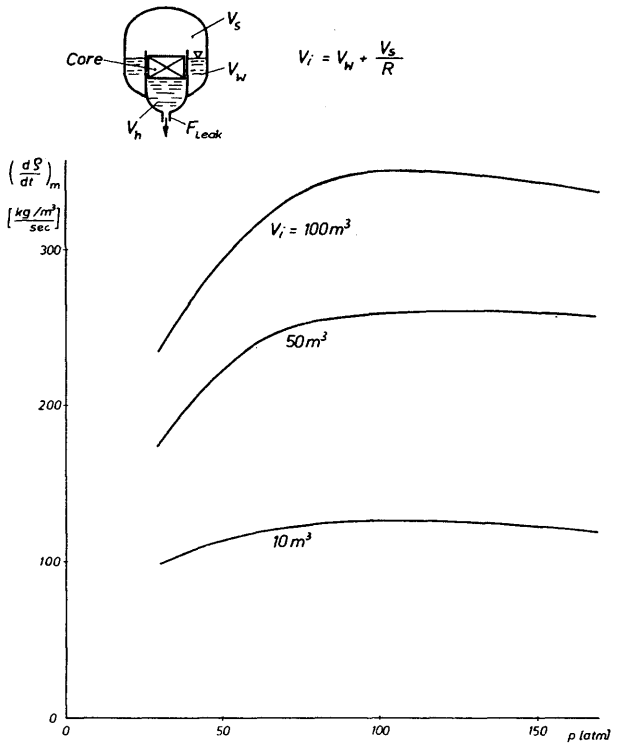

FIG. 18. Density reduction rate of unflooding accident as influenced by the pressure.

However, it should be considered in the determination of the coolant density coefficient that about 5 to 10 $ reactivity, depending upon the initial temperature, must be introduced into the core to heat the fuel up to evaporation [12]. The average cooling density coefficient during the introduction of this reactivity therefore is the highest if the reactivity curve is displaced upward just so much as to make the unflooded reactor some 5 $ supercritical (reactivity curve B in Fig. 17).

For these reasons, a $(dk/d\rho)_m$ was determined for the different pressures which is defined as follows:

$$\left(\frac{dk}{d\rho}\right)_m = \frac{\Delta k}{\Delta \rho} = \frac{5\ \$}{\rho_{st} - \rho_{crit.}}$$

Here, $\rho_{crit.}$ was chosen so that the reactivity at this density is smaller by 5 $ than at ρ_{st}. Figure 19 shows the calculated reactivity ramp as a function of pressure. It reaches a maximum around 50 atm which is less than twice as high as the value at 150 atm. Therefore, a pressure of 50 atm will be used as the most unfavourable case in the calculations below.

Figure 20 shows the rate of density change $(d\rho/dt)_m$ as a function of volumes V_h and V_i under the assumption of a leak of 400 cm^2. The restriction of the leakage cross-section to such a small value is only

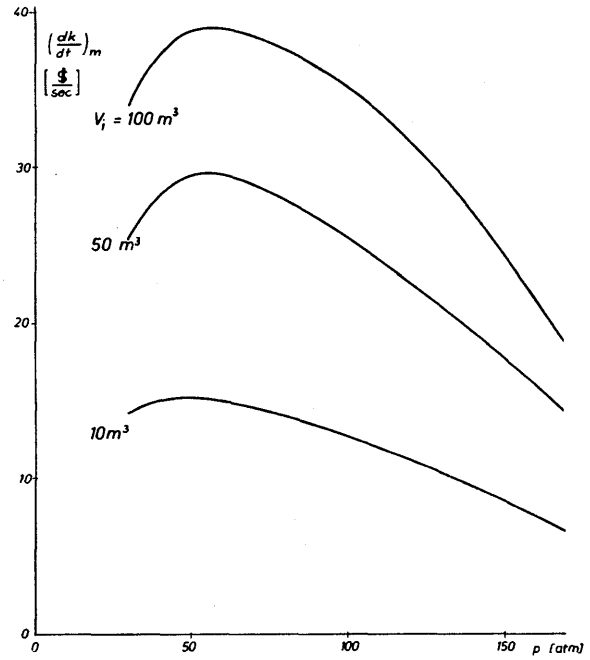

FIG. 19 Reactivity rate of unflooding accident as influenced by the pressure.

possible by using series turbines as blower drive. With rising V_i, $d\rho/dt$ also rises so that V_i may not be any arbitrary size because of the unflooding accident. For the size of V_h there is a theoretical optimum size as a function of V_i, but this is so high at practicable values of V_i as to make the delay time too long.

If an upper limit is fixed for the reactivity ramp and thus for the rate of density reduction in an unflooding accident, it is possible to read pairs of values of V_h and V_i from Fig. 20 which permit this limitation by design measures. Figure 11 shows two limits for unflooding ramps of 30 and 40 \$/s. A reactivity ramp of 30 \$/s should not be exceeded essentially in order to avoid a can burst. This limitation requires a very large superheated-steam plenum V_h. This results in a delay time of the heat transport from the core to the evaporators which is undesirably long with respect to stability. This conflict between the requirements of stability and safety does not occur, however, if all steam lines penetrate the pressure vessel above the water level in the flooded condition. If there is an additional sufficiently large steam volume between the water level and the discharge opening, the unflooding rate and thus the highest possible reactivity ramp are decisively reduced without impairing the stability.

4. CONCLUSION

It has been shown that with a negative steam density coefficient the feedback of the cooling cycle can be utilized to achieve inherent stability

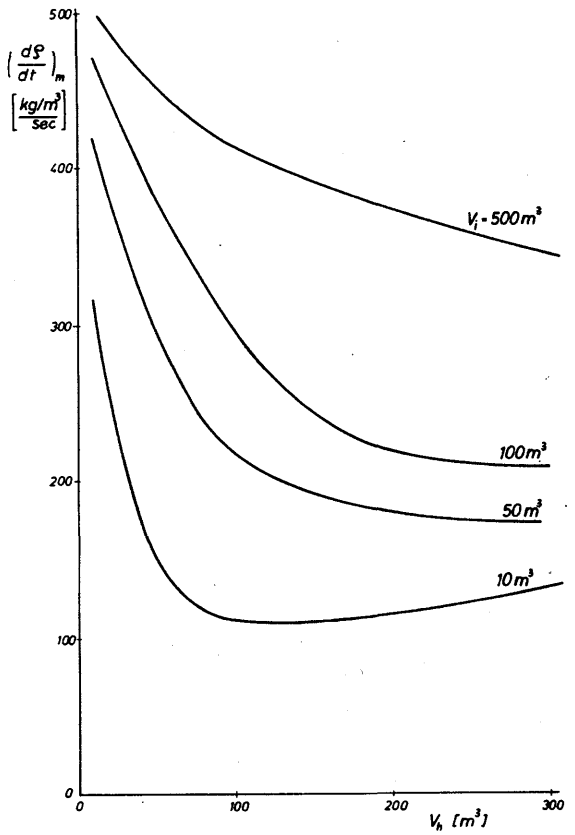

FIG.20. Density reduction rate of unflooding accident as influenced by the volumes.

and safety from accidents. The limits to be observed in the design of the cycle were determined and were found to be implementable on the basis of a design example.

The corresponding development of the components disclosed no fundamental difficulties. Their joint operation in a closed cycle is the subject of a comprehensive experimental programme. A loop specially built for this purpose is in operation.

If these experiments confirm the analytical considerations described in this report, the requirements for engineered safeguards would be reduced and the selection of potential sites of steam-cooled breeder reactors would be made much easier.

REFERENCES

[1] ERBACHER, F., FRISCH, W., HÜBSCHMANN, W., RITZ, L., WOITE, G., "The safety of steam-cooled fast reactors as influenced by the design and arrangement of their components", Proc. Int. Conf. on Fast Reactor Safety, Aix-en-Provence, 19-22 Sept. 1967, KFK 655 (Oct. 1967).

[2] MÜLLER, A., Referenzstudie für den dampfgekühlten schnellen Reaktor (D-1), KFK 392 (Aug. 1966).

[3] FRISCH, W., WOITE, G., Analogrechenmodell für dampfgekühlte schnelle Reaktoren mit Direktkreislauf, KFK 657 (to be published).

[4] KREBS, L., Die Stabilität von starr zurückgeführten Regelstrecken ohne Ausgleich am Beispiel eines dampfgekühlten Reaktors, KFK 656 (Sept. 1967) EUR 3691d.
[5] ERBACHER, F., SCHMIDT, H., WIEHR, K., Die Entwicklung von Verdampfern für dampfgekühlte Reaktoren, EUR 3695d, KFK 659, Oct. 1967 (in press).
[6] FRISCH, W., HELLER, F., HÜBSCHMANN, W., MALANG, S., MÜLLER, A., SCHIKARSKI, W., SMIDT, D., WOITE, G., Safety aspects of steam-cooled fast breeder reactors, KFK 613 (Jun. 1967).
[7] SMIDT, D. et al., "Systems analysis of a fast steam-cooled reactor of 1000 MW(e)", KFK 636, these Proceedings, SM-101/10.
[8] BAUMANN, W., CASAL, V., MÖLLER, R., RITZ, L., RUST, K., Brennelement-Hüllrohre mit integralen Wendelrippen für dampfgekühlte Brutreaktoren, KFK 658, EUR 3694d (Nov. 1967) (in press).
[9] ERBACHER, F., RADTKE, F., Die Entwicklung von Dampfgebläsen für dampfgekühlte Reaktoren, KFK 545 (Feb. 1967).
[10] MÜHLHÄUSER, O., Zur Entwicklung eines vollhydraulisch betriebenen und gesteuerten Regel- und Abschaltsystems für wasser- bzw. dampfgekühlte Kernreaktoren, KFK 665, EUR 3699 (Aug. 1967).
[11] MOODY, F.J., Maximum flow rate of a single component, two phase mixture, J. Heat Transfer, Trans. ASME, Series C. Vol. 87 (1965).
[12] HÜBSCHMANN, W., Grenzreaktivitätsrampen im dampfgekühlten schnellen Reaktor, KFK 664, EUR 3682d (Nov. 1967) (in press).

DISCUSSION

W. H. HANNUM: Could you elaborate on the significance of a high lineal power rating; in particular, do problems occur at less than full power or is the object to keep the core volume small?

W. HÜBSCHMANN: The main result of the growth in linear rod power is the increase in temperature gradient in the fuel. This increases the Doppler feedback and decreases the reactivity gain K_k, as follows from Eq. (7). This equation is based on constant core size, so that the possible decrease in core size at constant reactor power is not taken into account. At a low power level, in fact, the reactor becomes unstable, which is yet another reason for operating at a high linear rod power, so as to confine the unstable regime to as low a power level as possible.

H. VOLLMER: Do the requirements imposed by stability and by accident behaviour call for the same reactor design or may they be contradictory?

W. HÜBSCHMANN: Some of the requirements for good dynamic behaviour run contrary to those for accident safety, and even the requirements for different accidents can be contradictory. This is readily seen in the case of capacity requirements. The capacity, in particular the superheated and saturated steam plenums, and the water reservoir should be small on the one hand, in order to achieve a fast cycle response at load changes or blower failure (see Figs 6 and 8), but safety requires that these same quantities should also be large as a protection against steam pipe ruptures (see Figs 9, 10 and 13). The unflooding accident, on the other hand, calls for a small saturated steam plenum and small water reservoir, together with a large superheated steam plenum.

A compromise, depending on the cycle design, must be found for each of these parameters. In the unintegrated design the suitable range of parameters is narrow, whereas it is broader in the integrated design due to the fact that saturated steam pipe rupture is not likely (see Fig. 11). We are confident that in the integrated design the requirements for inherent safety as well as for inherent stability can be met satisfactorily.

SYSTEMS ANALYSIS OF A FAST STEAM-COOLED REACTOR OF 1000 MW(e)*

D. SMIDT, W. FRISCH, F. HOFMANN, E. KIEFHABER**,
H. MOERS+, K. SCHRAMM AND H. SPILKER
INSTITUT FÜR REAKTORENTWICKLUNG,
KERNFORSCHUNGSZENTRUM, KARLSRUHE,
KARLSRUHE, FEDERAL REPUBLIC OF GERMANY

Abstract — Résumé

SYSTEMS ANALYSIS OF A FAST STEAM-COOLED REACTOR OF 1000 MW(e). The Karlsruhe design of a steam-cooled fast reactor (D1) has been the subject of a systems analysis. Here the dependence of fuel inventory, breeding ratio, rating, core geometry and plant efficiency on coolant pressure, and coolant temperature has been studied for two different rod powers. The effect of artificial surface roughness has been investigated. For some configurations the resulting fuel-cycle and capital costs have been determined and discussed.

The main influence results from pressure. The lower pressure allows for higher breeding ratios, but lower efficiencies and vice versa. From this the fuel-cycle costs show an optimum at around 150 atm abs. The capital costs on the other side decrease with pressure. The over-all optimum of the power generating costs for the presently studied parameter range is at about 170 atm abs., a coolant outlet temperature of 540 °C and a rod power of 420 W/cm. Artificial roughness (boundary layer type) leads for a required system pressure and outlet temperature to a larger coolant volume fraction and, therefore, to reduced breeding ratios but higher efficiencies.

As another part of the work some stability characteristics of the cores were studied. The dependence of the core stability on the varied parameters is shown.

1. INTRODUCTION

The design of a steam-cooled fast breeder reactor (D1) [1] was the subject of a systems analysis. It comprises a systematic variation of various design parameters of the core and its influence on the power generating costs. One of the problems of this investigation was the lack of reference points from other designs, another one the great number of independent parameters, which had become evident already during the work on the D1 study. The wide scope of possible variations had to be narrowed down to permit the target to be reached within a reasonable time. Thus, to mention just one important possibility of variation, the design concept, i.e. the external structure and the flowsheet of the plant, were incorporated from D1 without any change. On this basis the dynamic, safety and thermodynamic nuclear considerations are developed.

A major objective of the thermohydraulic, nuclear and cost investigations communicated in this report was the possibility of making qualitative statements about the economical potential of a steam-cooled breeder reactor and, in addition, to establish quantitative design criteria for a

* Work performed within the association in the field of fast reactors between the European Atomic Energy Community and Gesellschaft für Kernforschung mbH., Karlsruhe.

** Institut für Neutronenphysik und Reaktortechnik.

† Delegated from Gutehoffnungshütte Sterkrade AG., Oberhausen.

prototype. Here, the preference of low power generating costs or a high breeding ratio played a special part. Therefore, in particular the coolant pressure was varied between 120 and 170 atm. abs. to show clearly to what extent the higher breeding ratio at lower pressures must be paid for in terms of reduced economy.

The dynamic and safety investigations for the D1 plant carried out at the same time are reported elsewhere [2]. Only the influence of the varied parameters on some interesting dynamic characteristics are dealt with.

2. CHARACTERISTIC DATA OF THE 1000-MW(e) REFERENCE REACTOR (D1 STUDY)

The nuclear reactor facility used as the basis for these studies is a steam-cooled fast breeder reactor with two steam turbines of 500 MW(e) each in a direct cycle. One of the main features is the external generation of the saturated steam which is superheated in the reactor and taken to the consumers, i.e. secondary steam generator, re-heater, injection evaporator, and the turbines (Fig. 1).

The reactor steel vessel houses the cylindrical core which is surrounded by the blanket and the internal shield. The core itself consists of two zones of different fuel enrichment. It consists of 163 hexagonal fuel elements with 469 fuel rods each. Integral parts of the core elements are the upper and the lower axial blankets which, therefore, have to be exchanged together with the core elements, while the exchange cycle of the radial blanket elements can be determined independently upon economic viewpoints.

To reduce the moderating effect of the coolant to a minimum, the coolant fraction must be small; 32 vol.% was chosen as a practical minimum.

The coolant enters the reactor at the bottom, flows first upwards through the radial blanket and then downwards through the core and the axial blankets into the inner one of two concentric tubes at the bottom of the reactor vessel. The steam conditions at the reactor outlet are 170 atm abs. and 540°C. The net efficiency of the power plant was calculated to be 39.7%.

Under the conditions outlined an over-all breeding ratio of 1.15 was determined with a smeared fuel density of 87% of the theoretical density. With an average burn-up of 55 000 MWd/t of the fuel as discharged and a plutonium price of $10/g and a load factor of 0.7, a value of mills 1.3/kWh was calculated for the fuel-cycle costs and mills 5.25/kWh for the power-generating costs.

A detailed description of the reactor plant is given in the reference design study of the steam-cooled fast breeder reactor [1].

3. PARAMETERS

3.1. Independent parameters

The main objective of the analysis consisted in investigating the influence of the most significant design parameters upon the costs of

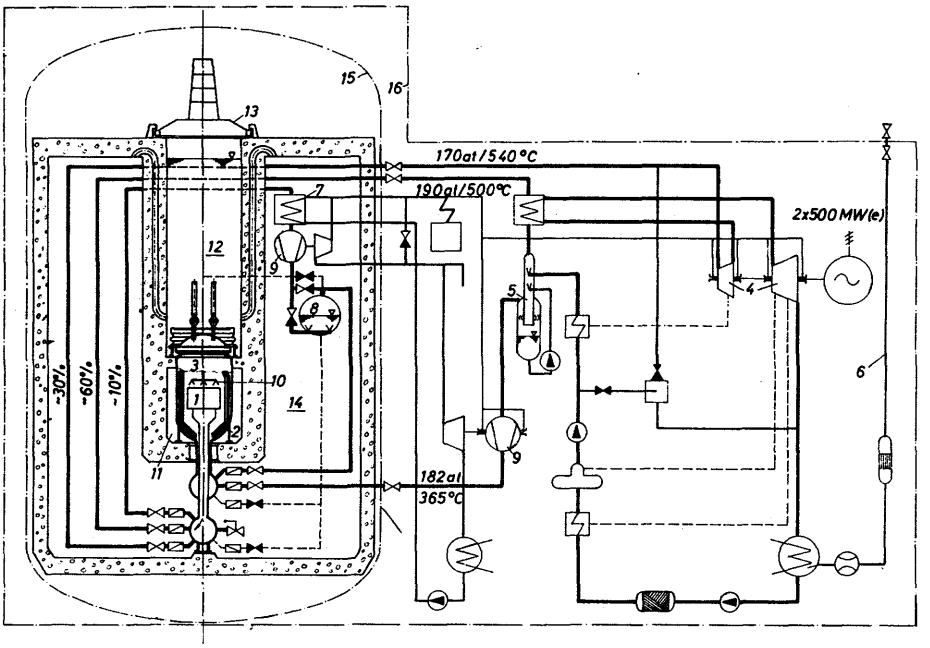

FIG.1. Simplified flow diagram of the D1 plant.

1. Reactor core	9. Blower
2. Inner shielding	10. Spray system
3. Reactor pressure vessel	11. Reactor cell
4. Main turbine	12. Refuelling pool
5. Steam generator	13. Heavy cover bridge
6. Off-gas system	14. Dry well
7. Heat exchanger	15. Inner containment
8. Ruths-accumulator	16. Gas-tight envelope

power production. These main parameters were varied within reasonable limits, corresponding to the special requirements of steam cooling:

(a) The system pressure p_2 was varied from 120 to 170 atm abs. at reactor outlet. The lower limit is due to the fact that, similar to D1, re-heating is planned. At pressures above 170 atm abs. the breeding gain will decrease drastically.

(b) The coolant temperature ϑ_2 at the reactor outlet was another parameter which was varied between 480 and 560°C. The lower limit is dictated by the required steam quality at the end of expansion, the upper one by the properties of the materials chosen for the turbine.

(c) The maximum nominal linear rod power X was varied within the limits of 370 - 420 W/cm.

Compared with the D1 study it was possible to increase the rod power in general on the basis of an improved analysis of the hot channel factors. The values of X apply to the maximum linear rod power without hot channel factors. Considering these factors and burn-up the values are increased by some 15%. In another investigation the influence of turbulence promoters was analysed.

As a result of the variations mentioned above, the following properties were varied: Core geometry, net efficiency, critical mass, breeding ratio of the individual zones, specific power and hence, necessarily, capital and fuel cycle costs.

3.2. Parameters kept constant

The following parameters are taken directly from the D1 study (Q_{el} = 1000 MW(e)) without variation:

(a) The maximum can temperature T_{max} in the hot channel (hot channel factor included) is not to exceed 700°C because of creep collapse. This value will be encountered at the hot spot on the inside of the fuel can, assuming cross mixing of the coolant as is possible with the helical spacers. Because of the poorer heat transfer properties with steam as compared with sodium (a factor of about 10) the temperature of the can, in addition to the temperature in the centre of the fuel, became a special criterion of core design.

(b) The diameter of a fuel rod with can is 7 mm; the thickness of the wall of the can is 0.37 mm.

(c) Apart from the investigations with turbulence promoters the volume fraction of the coolant α in the core and in the axial blanket was restricted to the minimum of 32 vol.% in the interest of a good breeding ratio; this value is the minimum permissible from the engineering standpoint.

(d) For the other core materials the volume fractions are as follows:

Structural material in the core and the axial blanket	20.6 vol.%
Fuel (oxide fuel) in the core	45.4 vol.%
in the radial blanket	55.6 vol.%
Control rod follower (Al_2O_3)	2.0 vol.%

(e) The canning and structural materials are:

In the core and the axial blanket	Inconel 625
In the radial blanket	Incoloy 800

(f) The nuclear calculations are carried out with the ABN 26 group constants set.

(g) The smeared density of the fuel is 87% of the theoretical density; the isotopic Pu composition is 74/22.7/2.3/1.0.

(h) The average burn-up over time is 27 500 MWd/t.

(i) The volumes of the two core areas of different enrichments always are of equal size.

(k) The enrichment in the two core areas is selected such as to make the maximum power densities in the two zones equal and cause the reactor to reach the desired criticality.

(l) For the reactors investigated an axial and radial blanket thickness of 35 cm is assumed.

(m) The evaluation of the fuel-cycle costs is based on a plant lifetime of 25 yr at 70% load factor. In the calculations fuel transport costs of $5/kg and delays of 0.5 yr in fabrication and 0.6 yr in reprocessing were taken into account.

(n) For the capital investment an interest rate of 7% and a tax rate of 2.7% as well as a 1% insurance rate are assumed.
(o) The price of the plutonium and the depleted uranium is included in the calculations with rates of \$10/g and \$3/kg, respectively.

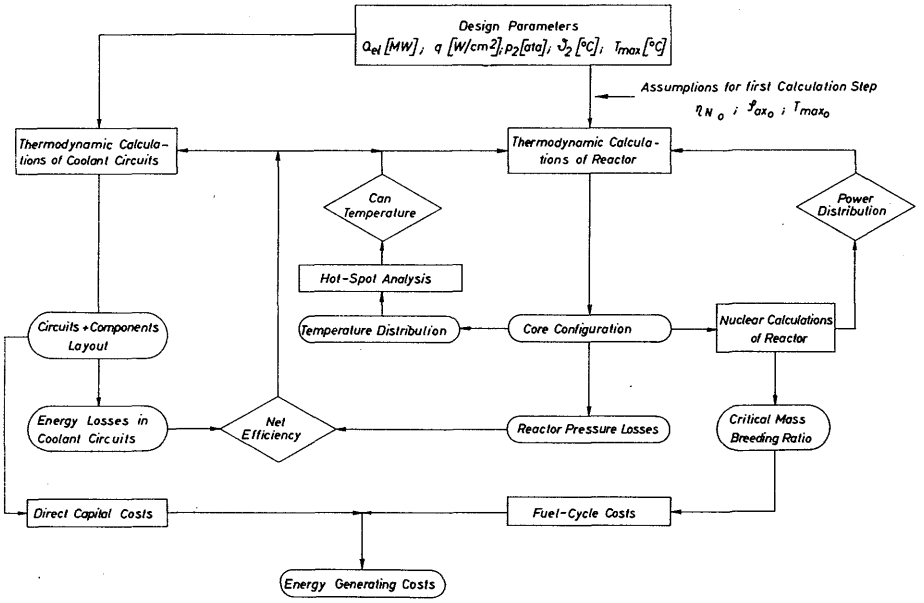

FIG.2. Flow sheet of calculation method.

4. METHODS OF CALCULATION

4.1. Flowsheet

The flowsheet is shown in Fig. 2. On the basis of estimated values of net efficiency, rod power, power distribution and can temperature the thermodynamic calculation first determines the core configuration, pressure losses in the reactor and the temperature distribution in the core in the first approximation. The following calculations of reactor physics and hot channel factors together with the results of the calculations for the coolant circuits result in new values of net efficiency, rod power, axial power peak factor and maximum can temperature. In this way the required design quantities net electrical power, maximum linear nominal rod power and maximum can temperature were determined by iteration. Finally the power generating costs are evaluated.

4.2. Thermodynamic cycle calculation

The thermodynamic calculation of the circuits is performed by means of a digital programme [3]. On the basis of the input data, such as net electrical power, steam pressure and temperature at reactor outlet, and

pressure drop in the reactor, this programme calculates mass flows, steam conditions, and net efficiency for the whole cooling circuits including all energy losses. The design analysis of the components of the circuits (steam generator, re-heater, blower) is then carried out, also by digital programmes [4, 5], on the basis of the determined mass flows and steam conditions.

4.3. Thermodynamic reactor model

The model of the thermal calculation of the reactor starts with the assumption of a cosine shaped power distribution in the axial direction in the core. It accounts for the better heat transfer in the bundle compared with the circular tube. The calculation of the core is performed in several axial zones in each case with and without turbulence promoters. The corresponding changes in the state variables and properties of the steam are included in the calculation as functions of pressure and temperature.

4.4. Nuclear calculations

For the core configuration given by thermodynamics the interesting nuclear quantities, i.e. critical mass, breeding ratio of the individual zones and the power peak factors, are calculated with the Karlsruhe nuclear programme system NUSYS. Suitable use of results of zero and one-dimensional calculations permit a considerable reduction in computing time required for the two-dimensional calculations.

4.5. Cost calculations

As was mentioned above, the D1 study supplied the plant concept and the flowsheet of the circuit for the systems analysis. The varied reactor parameters by necessity also resulted in changes or rather adaptations of the rest of the cycle. A digital programme was used to evaluate the necessary design changes. The influence of these design modifications upon direct plant costs were taken into account. Also the influence of changes in core geometry upon the costs of pressure vessel, containment and reactor building are included in the analysis. Plant components and reactor systems, which do not specifically depend on steam conditions, were included under the prices corresponding to the D1 data.

The fuel-cycle costs are calculated by using the digital programme BAKO [6]. The input data required are taken from two-dimensional nuclear calculations. These are the geometry of the zones, their fuel and fertile material compositions, and the corresponding breeding ratios. Moreover, other input data are the thermal power, net efficiency and burn-up. The programme then calculates, for various thicknesses of the axial and radial blankets and different lifetimes of the radial blanket, in addition to the detailed costs, the specific fuel cycle costs. In case the direct and indirect capital costs are fed in, the specific capital and energy generating costs are also computed.

The most important cost terms of fuel-cycle cost are the costs of fuel-element fabrication, reprocessing, and of fissile material. For a given fuel fabrication plant throughput the fabricating costs are calculated for

the core elements by the formula

$$K_{FC} = 86.1 + 4100 \left(\frac{1}{DPIN} + \frac{0.62}{DPIN^2}\right)\left(1 - \frac{HC}{278}\right) \quad (DM/kg) \qquad (1)$$

In this formula DPIN = diameter of the pellets (mm) and HC = height of core (cm). At constant pin diameter this results in core fabricating costs which are dependent only on the core height.

5. RESULTS

5.1. Thermodynamic and nuclear results

The most important results of the thermodynamic and nuclear investigations will be discussed on the basis of Figs 3-6. The figures show the influence of system pressure, coolant outlet temperature, and rod power on the net efficiency of the plant η_N and on core geometry (core volume V_c, ratio of core height/core diameter H_c/D_c) and on the breeding ratio BR, critical mass M_{crit}, and rating RA.

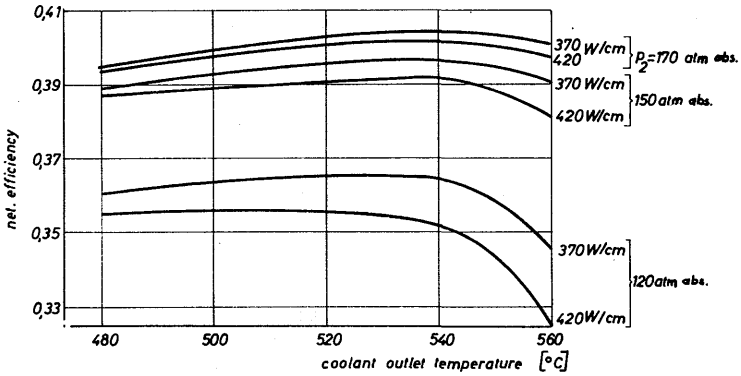

FIG.3. Influence of system pressure and maximum rod power.

5.1.1. Influence on net efficiency

The net efficiency (Fig. 3) rises with increasing system pressure, mainly due to the increasing density and specific heat capacity (less pumping power) of the steam. The step from 120 to 150 atm abs. contributes about twice as much gain (about 3% absolute) as the transition from 150 to 170 atm abs.

An increase in the coolant outlet temperature, on one hand, results in an increase in the thermodynamic efficiency; however, on the other hand, under the boundary conditions postulated (T_{max} = const., α = const.), it also requires an increase in pumping power for the reactor. The resulting net efficiency, therefore, increases as a function of coolant outlet temperature only as long as the gain in thermal efficiency exceeds the corresponding losses due to increased pumping power. Figure 3 illustrates

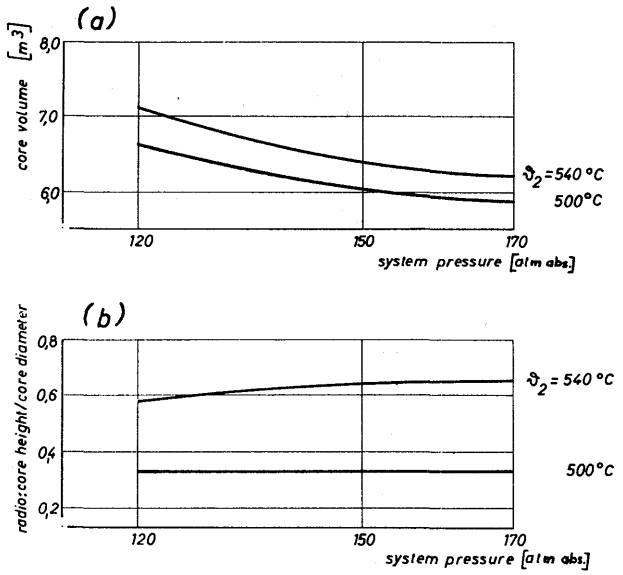

FIG. 4. Influence of coolant outlet temperature.

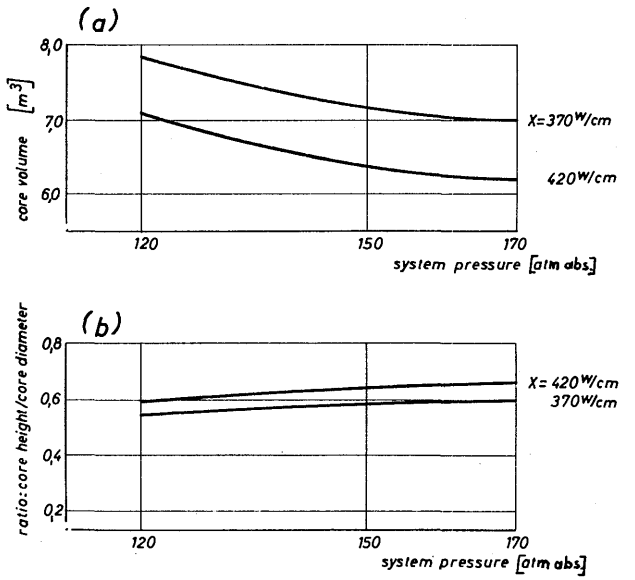

FIG. 5. Influence of maximum rod power.

that the net efficiency will gradually rise with temperature to the peak and then drop very rapidly. The peaks move towards higher coolant outlet temperatures with increasing system pressure, namely from 120 atm abs. to 170 atm abs. while going from $\vartheta_2 \approx 500°C$ to $\approx 540°C$.

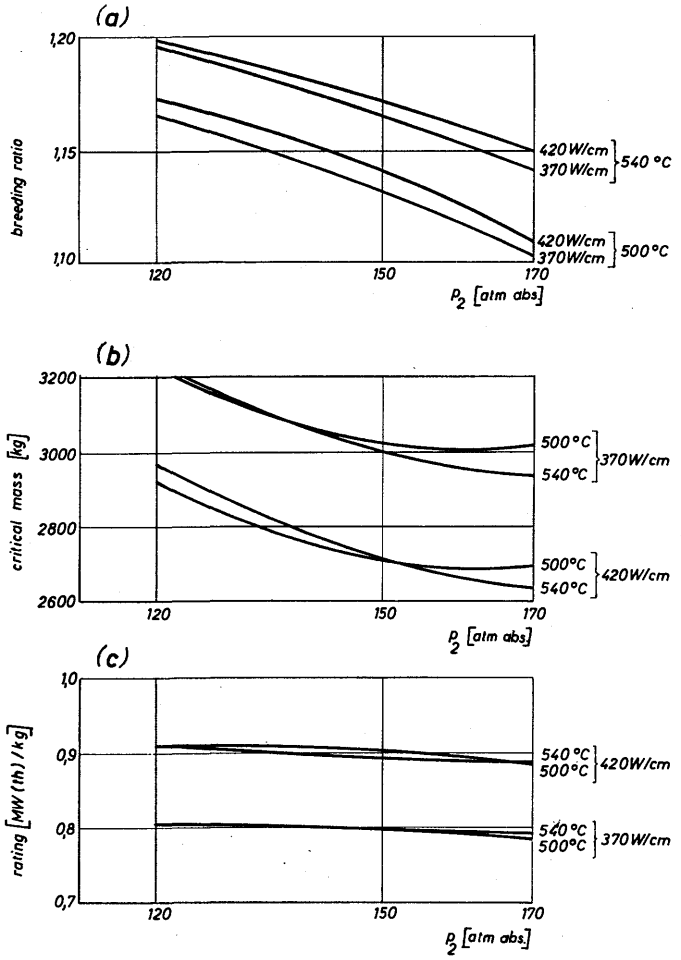

FIG.6. Influence of coolant outlet temperature and maximum rod power.

Because of the higher pumping power in the core (larger coolant mass flow and core height (see section 5.1.2)) an increase in rod power is at the expense of the net efficiency.

5.1.2. Influence on core geometry

As has been said earlier, the net efficiency of the plant increases with rising system pressure. This means that the gross power to be generated in the core and hence also the core volume will become smaller with increasing system pressure (Fig. 4a). Under the boundary conditions listed in section 3.2, particularly the fact that the can temperature should not exceed 700°C, the investigations also show the core height to change only very slightly with rising system pressure. (In a change from 120 to 170 atm abs. there is some 3-4% change in core height.) This has only a

minor feedback upon the axial power peak factor. The volume change as a function of system pressure, therefore, is caused essentially by the change in the core diameter ($V_c \sim D_c^2$). The core-height/core-diam. ratio changes only slightly in the process (Figs 4b, 5b).

However, under the existing boundary conditions (T_{max} = const., α = const.) an increase in the coolant outlet temperature requires a considerably stronger increase in the core height. In a transition from 500°C to 540°C the core height increases by about 50%. This results in higher pressure loss and also a worse axial power peak factor. On the whole, a higher outlet temperature causes a greater core volume and at the same time a considerable increase in the core-height/core-diam.ratio (Figs 4a, 4b).

Because of the higher power density an increase in rod power will result in a roughly proportional reduction of the core volume and a roughly proportional increase in the coolant velocity (Fig. 5a). To be able to keep again within the required can temperature, the core height is bound to increase slightly at a given core outlet temperature so that the H_c/D_c ratio also becomes larger in this case (Fig. 5b).

5.1.3. Influence on the breeding ratio and the critical mass of fissile material in the core

The dependence of the breeding ratio and the critical fuel mass in the core on pressure (Figs 6a, 6b) can be understood more easily if one considers that with rising pressure the neutron spectrum will become softer because of the higher coolant density. This decreases the average η-value of the fuel (worse η-value of plutonium and less fast fission; $\eta = \nu\Sigma_f/\Sigma_a$) so that the enrichment must be increased, which results in a reduction of the breeding ratio. An additional reduction of the breeding ratio is caused by the fact that the capture cross-section of the fertile material below an average neutron energy of 100-200 keV increases less markedly towards lower energies than the absorption cross-section of the fissile material. On the other hand, there is a reduction in the critical mass with rising pressure (up to 10%), because the increase in enrichment with rising pressure is more than compensated by the simultaneous reduction in the core volume.

The changes in geometry required in the case of an increase in the coolant outlet temperature result in a reduction in the geometrical buckling B^2. This leads to somewhat less external breeding, which has a negative influence upon the total breeding ratio. The changes in geometry mentioned above, are of such a kind, however, to make the height increase sharply and the diameter decrease markedly. This shifts the external breeding process from the axial into the radial blanket, which has a favourable influence upon the breeding ratio in the D1 reactor (caused by the higher fuel volume fraction in the radial blanket and the use of Incoloy 800 instead of Inconel 625). This effect is much more marked than the effects of a reduction of B^2 so that, on the whole, there is a definite increase in the over-all breeding ratio (about 0.03 - 0.04) with rising outlet temperature. An increase in the coolant outlet temperature has two opposite effects upon the critical mass of fuel.

(a) The core volume increases, as explained under 5.1.2; and
(b) The enrichment decreases because of the smaller leakage losses (reduction of B^2).

These two effects almost compensate, except for slight differences which depend on the pressure and the rod power.

With the increase in rod power the change in core diameter is considerably smaller than with the previously discussed increase in coolant outlet temperature. The breeding process, which is more favourable in the radial blanket, can thus have only a weak effect so that the increase in the breeding ratio is also much smaller than in the case where the outlet temperature is increased. The volume reduction connected with the increase in rod power almost completely results in a reduction of the critical mass of fissile material in the core owing to the nearly unchanged enrichment.

5.1.4. Influence upon rating

In accordance with the usual definition the rating was calculated as

$$RA = \frac{Q_{th}}{M_{crit}} = \frac{Q_{el}}{\eta_N \cdot M_{crit}}$$

It changes only very slightly at constant electric power as a function of the system pressure and the coolant outlet temperature because of the controversal behaviour of net efficiency η_N and critical mass M_{crit} (a maximum change of 1.5% (Fig. 6c)). As a function of rod power, however, the change is very marked ($\approx$ 12%), especially so because of the big change in critical mass.

5.2. Results of cost calculations

Figure 7 represents the capital cost trends of four important groups of components of the plant. The "reactor" group (Fig. 7a) comprises the core support components, e.g. core support plate, upper core guide plate, core clamping and other reactor internals and the pressure vessel itself with top shield, superheated steam and saturated steam headers with studs. The entries under "reactor building" (Fig. 7b) include the costs of foundation of the reactor building, all the concrete installations, the steel containment and the outer concrete shell. Figure 7c summarizes the costs of the plant components under the heading of "cooling circuits" as there are various circulation blowers, injection steam generators, secondary steam generators, steam accumulator, feed pumps and the corresponding piping. The "turbine system" shown in Fig. 7d includes the two turbo machines with condensers, re-heaters and the interconnecting pipes.

The more marked variations of the costs shown in these figures for the various groups of components appear less pronounced when the costs of these components are added which do not specifically depend on changes in the steam parameters.

The over-all direct capital cost trend of the investigated plants is shown in Fig. 8. This figure shows that the direct plant costs for the same reactor outlet temperature and rod power change only 3.3% in the transition from 120 to 170 atm abs. at the maximum.

The indirect capital costs are taken generally as 30% of the direct costs. They include contingencies, engineering expenses of the customer and start-up costs.

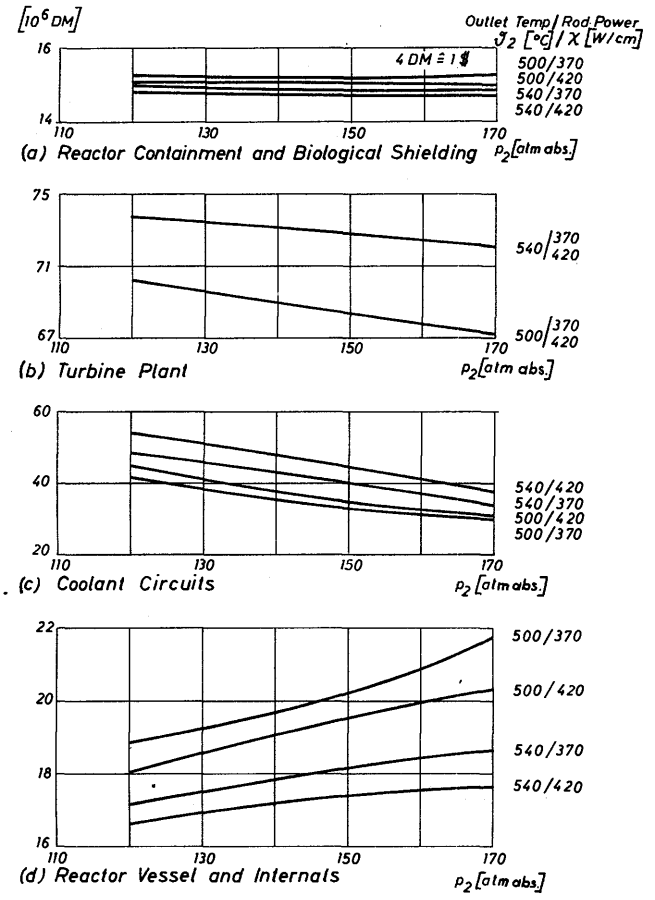

FIG.7. Different components of direct plant costs vs. system pressure.

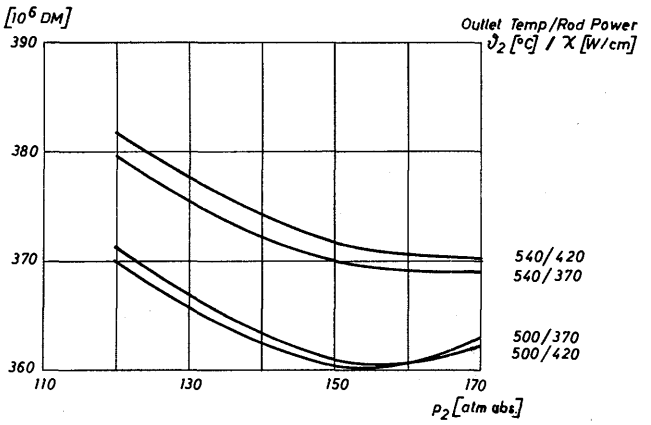

FIG.8. Direct plant costs vs. system pressure with ϑ_2 and χ as parameters.

The fabrication costs of the core fuel elements depend, as already mentioned in our cases, only on the core height. According to Eq.(1) in section 4.5 this results in decreasing fabricating costs per kilogram with rising outlet temperature. The weighting of these costs, including the costs of the axial and radial blankets with the corresponding amounts of fuel, results in less expenditure for the high rod power. After distribution over the generated power the curves shown in Fig. 9a then exhibit a plot proportional to $1/\eta$.

The decreasing trend of the reprocessing costs with rising pressure in Fig. 9b is due to the change in fuel masses. The cost differences at constant pressure but varied outlet temperature and rod power are due to the differences in efficiency.

In the costs of fissile material plotted in Fig. 9c the influences of various parameters superimpose. Rising pressure, on one hand, increases net efficiency, i.e. decreasing costs and, on the other hand, a lower

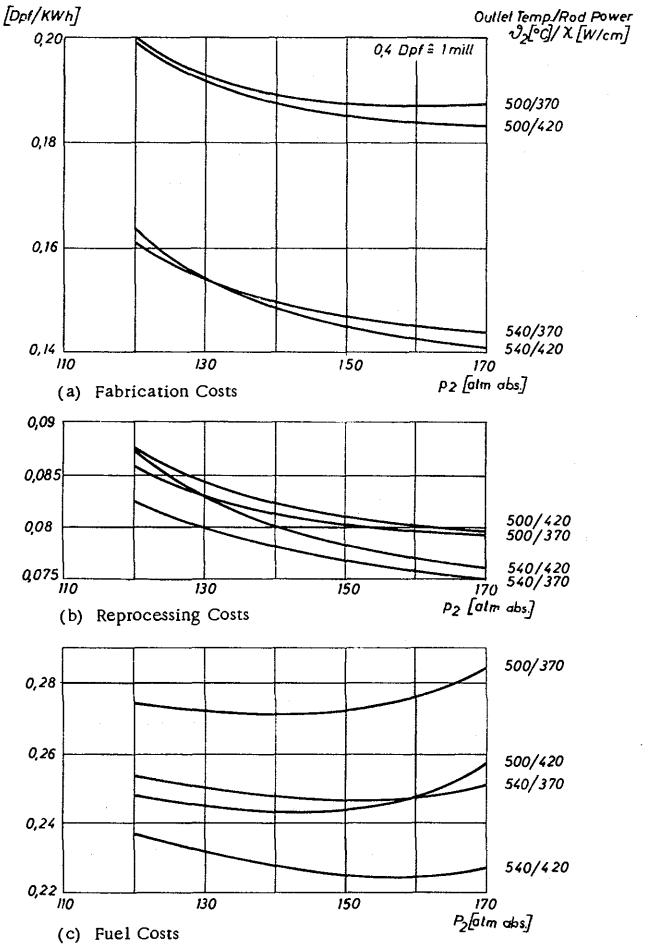

FIG. 9. Different parts of fuel-cycle cost vs. system pressure with ϑ_2 and χ as parameters.

breeding ratio, that implies rising costs, which explains the occurrence of a minimum in the curves. Higher rod power at constant temperature results in an improved breeding ratio and a lower net efficiency; both have an influence on costs in a way that the minimum hardly shifts with pressure. At constant rod power and rising outlet temperature the increasing net efficiency and the improved breeding ratio also have a cost decreasing effect, but the minimum shifts toward higher pressures with higher temperature owing to the more marked change in the breeding ratio.

The costs of the fissile material also include interest rates and the reimbursement for the bred plutonium. While the first factor results in cost savings with rising pressure because of the smaller amounts of fuel, the plutonium reimbursement term results in increasing costs with higher pressure because of the proportionality with $(BR-1)/\eta$, since both BR and η are influenced unfavourably.

The total fuel-cycle costs are shown in Fig. 10, which also includes the costs of fuel transport. The total fuel-cycle costs dealt with in the figure and Table I are calculated for a lifetime of the radial blanket at about two core times.

Summing up the specific fuel-cycle and capital costs results in the total cost of power generating plus a constant amount for plant operating cost (mills 0.3/kWh) (Fig. 11). The plot shows that the cost minimum shifts towards higher pressures with rising temperatures. The maximum cost gain arising out of a transition from 120 to 170 atm abs. appears with

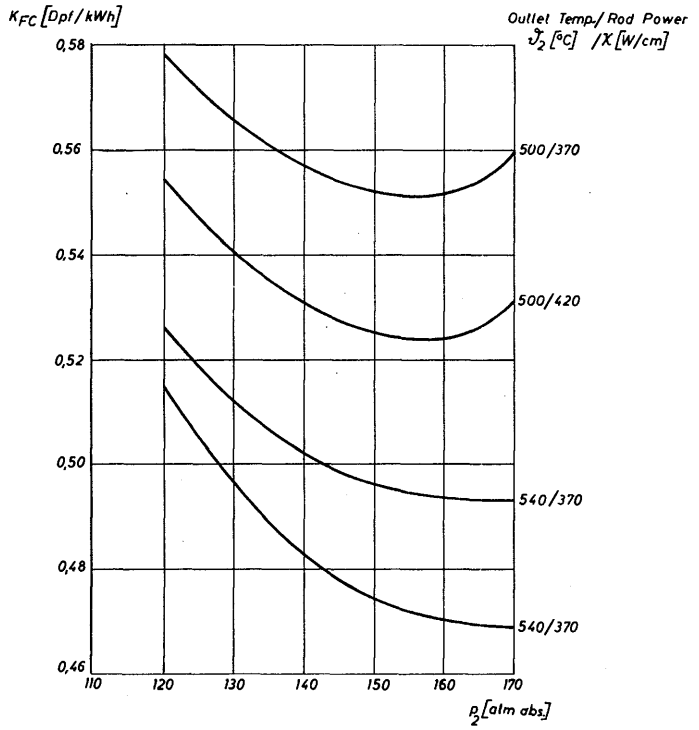

FIG. 10. Fuel-cycle costs vs. system pressure with ϑ_2 and X as parameters.

the highest rod power and coolant temperature. In this case the cost decreases from mills 4.2/kWh to mills 4.05/kWh.

The cost programme also allows the determination of the doubling times for the different reactors. They are shown in Fig. 12. The analysis has made it evident that the most favourable reactors from the viewpoint of doubling time are the reactors with the highest power generating costs.

5.3. Influence of turbulence promoters

For a system pressure of 120 atm abs. at core outlet the influence of an artificial roughening [7] was investigated and compared with a case of a smooth surface with respect to possible improvement of heat transfer. This roughening consists of circumferential transverse fins with rectangular cross-section over only 75% of the core height so as to keep the necessary increase in compressor power as a consequence of the roughening effect as low as possible. With respect to the producibility and the arising corrosion phenomena the values of the following ratios were fixed:

$$\frac{\text{fin pitch}}{\text{fin height}} = 10$$

$$\frac{\text{fin height}}{\text{equiv. diam.}} = 0.015$$

This type of surface roughening increases the local heat-transfer coefficient by about a factor of three and the friction factor by about a factor of nine.

The results shown in Fig. 13 are the net efficiency and the ratio H_c/D_c as functions of the coolant outlet temperature for smooth fuel elements and for elements equipped with turbulence promoters. The coolant fraction α is 32 vol.%, the rod power χ = 420 W/cm, the maximum can temperature T_{max} = 700°C in both cases.

It is shown that roughening will generally improve the efficiency, with the relative maximum shifting towards higher outlet temperatures. With respect to the core geometry this requires a marked flattening of the cores. For the case represented here the maximum efficiency increases from ≈ 36% at 500°C (smooth case) to ≈ 37% at 540°C (rough case). The H_c/D_c ratio drops by about 50% (from 0.3 to 0.15).

However, if the same core geometry as in the smooth case is to be maintained, it is necessary, by means of constant coolant volume fraction (Fig. 13), to increase the outlet temperature considerably. For H_c/D_c ratios larger than 0.3 the outlet temperature assumes values already exceeding 580°C. At outlet temperature as high as this, there will no longer be any gain in terms of efficiency, let alone the problems of turbine materials.

Figure 14 shows the influence of the coolant fraction α on the roughening described above. The same conditions apply as in Fig. 13. It is seen that an increase in the coolant fraction results in an additional increase in efficiency. The relative peaks shift towards an even higher outlet temperature (see Fig. 13). In the transition from α = 32 vol.% to 50 vol.% the peak changes from ≈ 540°C to ≈ 580°C, the efficiency rising by 1-2% absolute.

With respect to the core geometry an increase in α at constant outlet temperature results in an increase in the H_c/D_c ratio. However, to obtain

TABLE I. NUMERICAL DATA OF SYSTEMS ANALYSIS (SMOOTH HEAT TRANSFER SURFACES)

Varied parameters													
System pressure	(atm abs.)	120	120	120	120	150	150	150	150	170	170	170	170
Max. nom. rod power	(W/cm)	370	420	370	420	370	420	370	420	370	420	370	420
Core outlet temp.	(°C)	540	540	500	500	540	540	500	500	540	540	500	500
Thermodyn. + nuclear results													
Core diameter	(cm)	263	249	318	296	248	232	306	286	245	228	309	286
Core height	(cm)	144	146	92	96	148	152	92	94	148	152	88	92
Net efficiency	(%)	36.5	35.2	36.4	35.6	39.7	39.2	39.3	38.9	40.6	40.3	39.9	39.8
Core pressure drop	(atm)	10.5	14.4	4.5	6.7	8.4	11.6	3.4	4.6	7.2	9.8	2.5	3.5
Coolant mass flow	(t/s)	4.01	4.17	4.68	4.81	3.54	3.61	4.23	4.28	3.38	3.44	4.06	4.09
Total breeding ratio		1.194	1.198	1.166	1.173	1.166	1.173	1.131	1.141	1.142	1.15	1.103	1.11
Mass of fissile mat.	(kg)	3236	2964	3226	2921	2996	2711	3029	2705	2945	2640	3030	2701
Mass of fertile mat.	(t)	25.7	23.4	23.8	21.6	23.5	21.1	22.0	19.7	23.1	20.5	21.6	19.4
Rating	(MW(th)/kg)	0.80	0.91	0.81	0.91	0.80	0.89	0.80	0.90	0.79	0.89	0.79	0.88
Costs results													
Direct plant costs	(10^6 DM)	379.2	383.4	370.1	372.5	369.9	373.3	360.8	361.7	369.2	370.4	363.1	362.3
Fuel-cycle costs	(Dpf/kWh)	0.526	0.515	0.578	0.554	0.496	0.474	0.552	0.525	0.493	0.469	0.56	0.531
Energy gen. costs	(Dpf/kWh)	1.7	1.7	1.72	1.71	1.64	1.63	1.67	1.65	1.63	1.61	1.68	1.65
Doubling time	(a)	42.5	37	52	43.5	51	43.5	71	57	60.5	51	103	81.5
Stability													
Power coefficient	($)	-1.59	-1.71	-161	-170	-1.56	-1.77	-1.75	-1.87	-1.64	-1.81	-1.98	-2.08
Distance from stability boundary		0.414	0.385	0.371	0.354	0.461	0.404	0.366	0.345	0.461	0.418	0.314	0.307

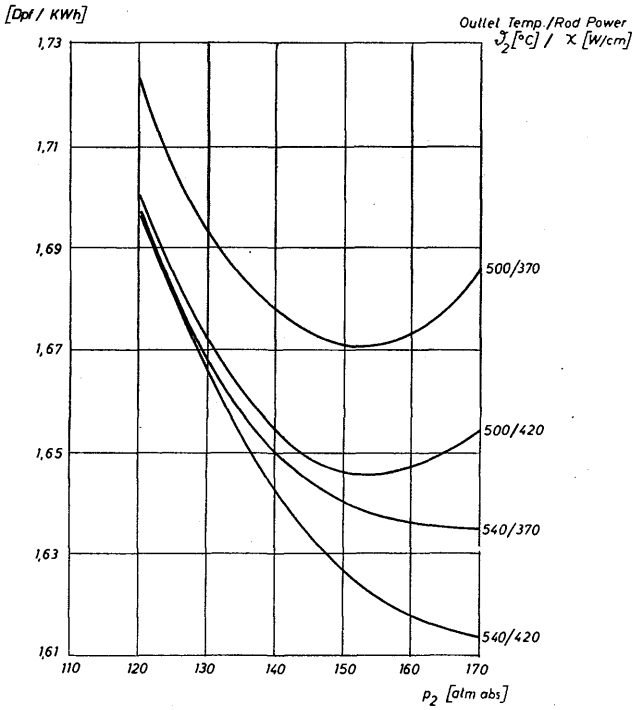

FIG. 11. Power-generating costs vs. system pressure with ϑ_2 and χ as parameters.

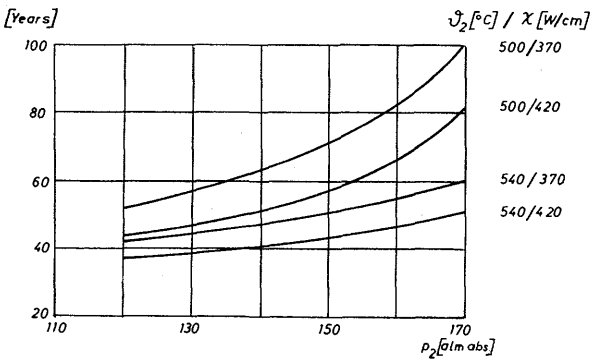

FIG. 12. Doubling time vs. system pressure with ϑ_2 and χ as parameters.

values for H_c/D_c of $\approx$ 0.3 to 0.6 in a reasonable temperature range $\vartheta_2 \lesssim 560°C$ it is necessary to increase the coolant fraction to more than 45 vol.%. This has a very negative effect on the total breeding ratio. Moreover, the gain in terms of efficiency will be less.

Another possibility of increasing the H_c/D_c ratio is reducing the maximum can temperature at constant outlet temperature (Fig. 15: rough case; α = 37 vol.%; χ = 420 W/cm). However, this always entails a loss

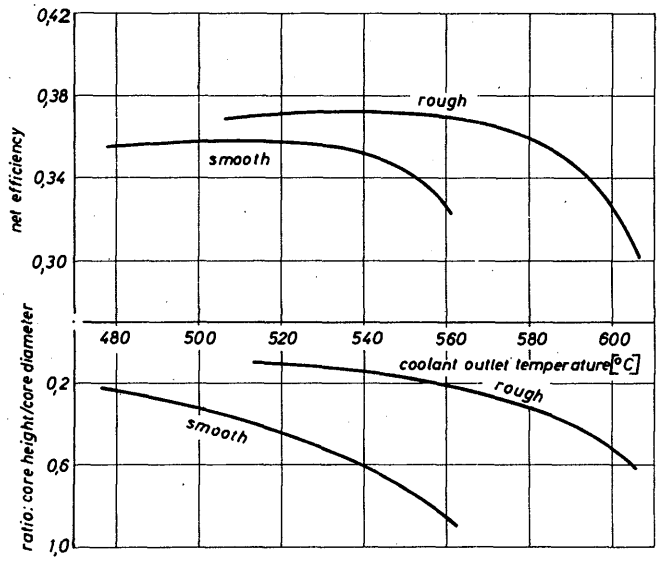

FIG. 13. Influence of artificial surface roughening.

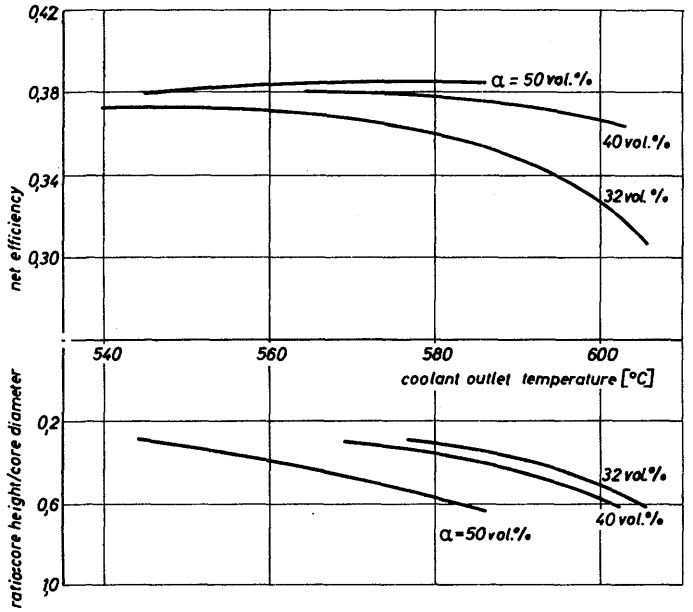

FIG. 14. Influence of coolant volume fraction.

in efficiency which very strongly increases with rising outlet temperature. Also at constant H_c/D_c the transition to a lower can temperature results in a reduction in efficiency. The desirable tendencies, lower can temperature

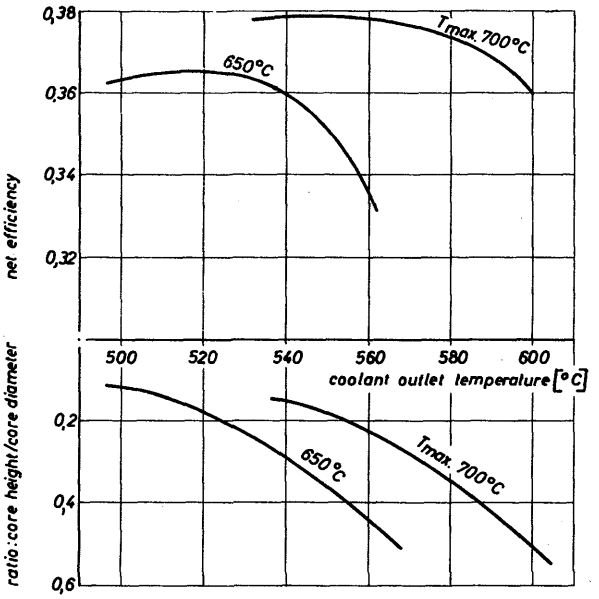

FIG.15. Influence of can temperature.

(T_{max}< 700°C), lower outlet temperature (ϑ_2 < 560°C) and larger H_c/D_c (H_c/D_c > 0.3) thus have to be paid for by a smaller efficiency in any case.

Finally it should be pointed out here that the results of artificial roughening discussed in this section apply to a power of 1000 MW(e). For smaller reactors it is still possible that artificial roughening would improve the core performance more significantly.

5.4. Core stability

The main investigations of the dynamics and the safety of the D1-plant are represented in a special report [2]. The influence of varied parameters on the power coefficient and the distance from the stability boundary are represented here. Both quantities are a characteristic for stability and safety.

The power coefficient $\Delta k/(\Delta P/P)$ is a measure for the feedback reactivity induced by a power change. The stability condition for the core is $\Delta k/(\Delta P/P) < 0$.

The relative distance from the stability boundary $\alpha_\rho/\alpha_{\rho gr}$ is a stability characteristic related to the important coolant density coefficient α_ρ. $\alpha_{\rho gr}$ is the coolant density coefficient at the stability boundary, α_ρ the value achieved from the nuclear calculations. The stability condition is $\alpha_\rho/\alpha_{\rho gr} < 1$.

Figure 16 shows $-\Delta k/(\Delta P/P)$ and $\alpha_\rho/\alpha_{\rho gr}$ as functions of p_2, χ and ϑ_2 for an average burn-up. Increase of the rod power χ and decrease of the outlet temperature ϑ_2 lead to an improvement in stability. With increasing system pressure stability improves, especially at ϑ_2 = 500°C.

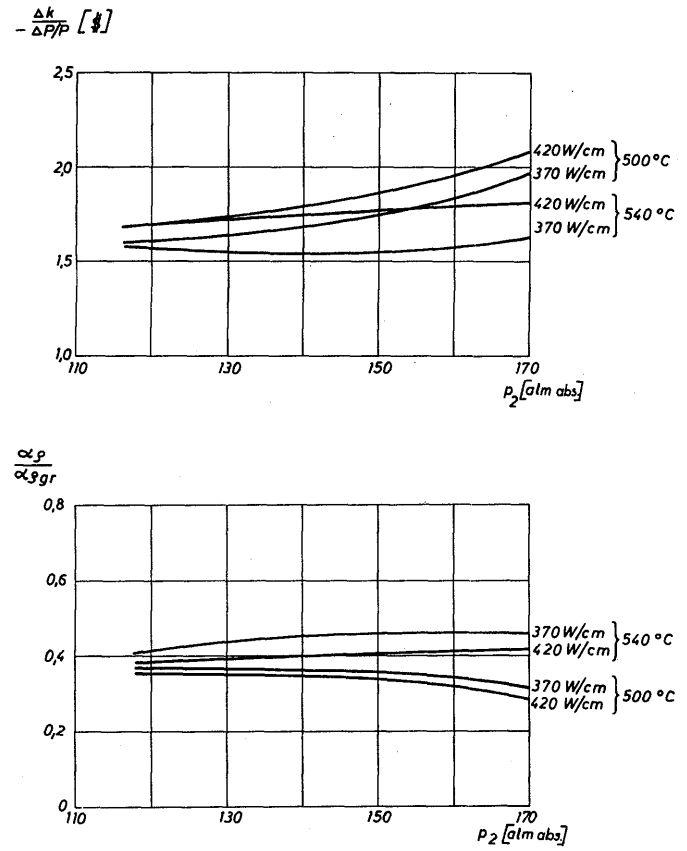

FIG. 16. Power coefficient $\Delta k/(\Delta P/P)$ and relative distance from the stability boundary $\alpha_\rho/\alpha_{\rho_{gr}}$

6. CONCLUSIONS

(a) The maximum of the net efficiency depends considerably on system pressure and coolant outlet temperature. Increasing rod power leads to a lower efficiency.

(b) Increasing pressure allows for a smaller core volume at nearly unchanged core height. Higher rod power allows for lower core volumes.

(c) The breeding ratio decreases with increasing pressure and decreasing coolant temperature. Higher rod powers lead to higher breeding ratios. The critical mass decreases with increasing pressure and is decreased with increasing rod power.

(d) The rating is nearly unchanged with system pressure and coolant outlet temperature.

(e) The fuel cycle costs show an optimum which mainly depends on pressure and temperature. At 500°C reactor outlet temperature it is in the range of 150 to 160 atm abs. It shifts to higher pressures with increasing temperature at lower costs. An increase in rod power decreases costs but does not change the mentioned tendency.

(f) The direct capital costs decrease with increasing pressure. The rod power has a negligible influence on capital costs.

(g) The power generating costs sharply depend on system pressure in the range of 120 to 150 atm abs. At higher pressures the main influence is given by temperature and rod power. The lowest power generating costs appear at high pressure, high temperature and high rod power.

(h) Artificial roughness means an increase in net efficiency, and for 1000 MW(e) a strong flattening of the cores. It can be compensated by
   (1) An increase of the coolant volume fraction, i.e. lower total breeding ratio,
   (2) An increase of the coolant outlet temperature, i.e. problems with turbine materials,
   (3) A decrease of the maximum can temperature, i.e. a lower net efficiency.

At a net electrical power less than 1000 MW(e) the same artificial roughening causes a lower flattening of the core. This leads to a smaller coolant volume fraction or a lower coolant outlet temperature for a constant H_c/D_c ratio.

(i) Higher rod power, higher system pressure and lower coolant outlet temperature lead to an improvement in stability.

NOMENCLATURE

B^2 (cm^{-2})	Geometrical buckling
BR	Total breeding ratio
H_c/D_c	Ratio: core height/core diameter
K_{FC} (Dpf/kWh)	Fuel-cycle costs
M_{crit} (kg)	Critical mass of fissile material
P_2 (atm abs.)	System pressure at core outlet
Q_{el} (MW)	Net electrical output
RA (MW(th)/kg)	Rating
T_{max} (°C)	Maximum can temperature
V_c (m^3)	Core volume
α	Coolant volume fraction
α_ρ $\left(\frac{1}{g/cm^3}\right)$	Coolant density coefficient
$\Delta k/(\Delta P/P)$ ($)	Power coefficient
η	Average number of neutrons produced per neutron absorbed.
η_N	Net efficiency
ϑ_2 (°C)	Coolant temperature at core outlet
ν	Average number of neutrons per fission
Σ_a (cm^{-1})	Macroscopic absorption cross-section
Σ_f (cm^{-1})	Macroscopic fission cross-section
χ (W/cm)	Maximum linear rod power

REFERENCES

[1] MÜLLER, A. et al., Referenzstudie für den 1000 MW(e) dampfgekühlten Schnellen Brutreaktor (D1), KFK 392 (1966).

[2] FRISCH, W. et al., Safety Aspects of Steam Cooled Fast Breeder Reactors, KFK 613 (1967).

[3] SPILKER, H., Ein Programm zur elektronischen Berechnung des thermodynamischen Kreisprozesses und des Kühlkreislaufes dampfgekühlter Kernreaktoren, KFK, Externer Bericht No.8/66-2 (1966).

[4] SCHNAUDER, H., Rechenprogramm zur Auslegung von dampfbeheizten Zwischenüberhitzern, KFK, Externer Bericht No.8/66-3 (1966).

[5] SCHNAUDER, H., Rechenprogramm zur Auslegung von dampfbeheizten Dampferzeugern, KFK, Externer Bericht No.8/66-4 (1966).

[6] JANSEN, D., BAKO – Ein Programm zur Kosten- und Strategienberechnung von Brüterkraftwerken mit der Barwertmethode, KFK 644 (1967).

[7] WILKIE, D., Forced Convection Heat Transfer from Surfaces Roughened by Transverse Ribs, EAES-Heat Transfer Symp. Superheated Steam or Gas (1966).

DISCUSSION

K. JIRLOW: When comparing different designs, did you not have to assume some basic criteria about the pressure drop in order to conserve, albeit approximately, the same mechanical complexity?

D. SMIDT: We made no assumptions on pressure drop. Since the coolant fraction was a constant 32% the pressure drop was completely re-calculated each time for the total circuit.

H. VOLLMER: I notice that Fig. 16 of your paper shows a weak dependence of stability on system pressure. Our studies of entire plant stability show a marked increase in the stable range (plotted as density versus Doppler coefficient) with decreasing pressure i.e. roughly a factor of 2 when going from 160 bar to 100 bar. The working point may shift towards the stability limit with decreasing pressure, thereby explaining your Fig. 16.

D. SMIDT: In the case of our variations, especially at ϑ_2 = 500°C, it is certainly true that with decreasing pressure the working point in the plane of the Doppler coefficient and the coolant density coefficient moves more than the stability boundary itself, so that the distance between working point and stability boundary decreases with decreasing pressure, though the stability area in the above-mentioned plane increases.

N. KRASNOYAROV: Have you studied the stability of the apparatus for small deviations or taking non-linearity into account, since in the feed-back activity the stability for small and for large deviations may differ for positive and negative coefficients?

D. SMIDT: Yes, we took non-linearities into account and found that fast reactors with a negative Doppler coefficient and a negative coolant density coefficient are far enough from the additional stability boundary induced by the non-linearity of the neutron kinetics. However, these reactors are close to the stability boundary based on the condition that the feedback reactivity must be negative, which means that the power coefficient must be negative. This stability boundary is naturally independent of the non-linearity of the neutron kinetics and since it is the most important one for steam-cooled reactors, it was the one mentioned in our paper. The curves shown in Fig. 16 are for small power deviations. Taking into account the non-linearities of the feedback (steam density etc.) the power coefficient improves, i.e. becomes more negative, with increasing positive power deviations.

FAST PULSED REACTORS

(Session IX, Part 2)

Chairman: M. F. TROYANOV

THEORETICAL ANALYSIS OF HYPOTHETICAL DESTRUCTIVE ACCIDENTS IN A PULSED FAST REACTOR

J. RANDLES
EURATOM,
JOINT RESEARCH CENTRE,
ISPRA (VARESE), ITALY

Abstract

THEORETICAL ANALYSIS OF HYPOTHETICAL DESTRUCTIVE ACCIDENTS IN A PULSED FAST REACTOR. The novel feature of a pulsed fast reactor is the existance of a relatively heavy rotating pulsation device carrying part of the reflector. The worst hypothetical accident in such a system takes the form of a fracture in the device during operation and the creation of a high speed fragment which strikes and compresses the core into a dangerously prompt critical assembly. The kinematics and dynamics of this collision process are described on the basis of a series of models which make possible an estimate of the reactivity input accompanying the accident. The effect of this input is described by means of a modified Bethe-Tait model of the neutronics and hydrodynamics of fuel vaporization and core destruction. The equation of state required to calculate the pressures generated during this process and the subsequent conversion of the energy release into mechanical work are discussed and calculations which evaluate the required parameters on the basis of the principle of corresponding states (using a computer programme EQUSTA) are described. The presentation of the above models is accompanied by a detailed mathematical exposition. A numerical method of solving the equations is described briefly and the results of applying this method to a SORA-type system, using a computer programme SOREX 1, are presented. These results give an upper limit to the available mechanical work in a large range of hypothetical accidents. The necessity for further information on the equation of state of fuel materials at high pressures and temperatures is demonstrated.

INTRODUCTION

This paper presents the mathematical models set up to estimate the outcome of a worst hypothetical accident in a pulsed fast reactor. The type of system visualized in the theory is exemplified by the reactor SORA proposed by Euratom (Fig. 1). The essential feature of such a device is a rapidly rotating arm carrying on its end a neutron reflecting block which, with each passage in front of an appropriately designed area of the core (window), generates an intense pulse of fission power. To simplify construction and improve safety the whole of this rotor, including the block, will generally be divided into a number of independent laminar pieces. In SORA, there will probably be four such pieces as shown in Fig. 1.

The hypothetical accident discussed in the text consists of a sudden fracture in one of these laminar pieces of the rotor (for example, lamina 3 in Fig. 1) followed by the collision of the broken fragment with the reactor near the centre of the sensitive window region (see Fig. 2). To strike the window in this region, the broken fragment must of necessity possess a large tangential momentum which, despite the large frictional force, carries it across the window almost simultaneously with the part of the block which remains attached to the unbroken part of the rotor. Thus, were it not for the collision, the reactivity input would be almost the same as usual. However, the effect of the collision is to compress the core

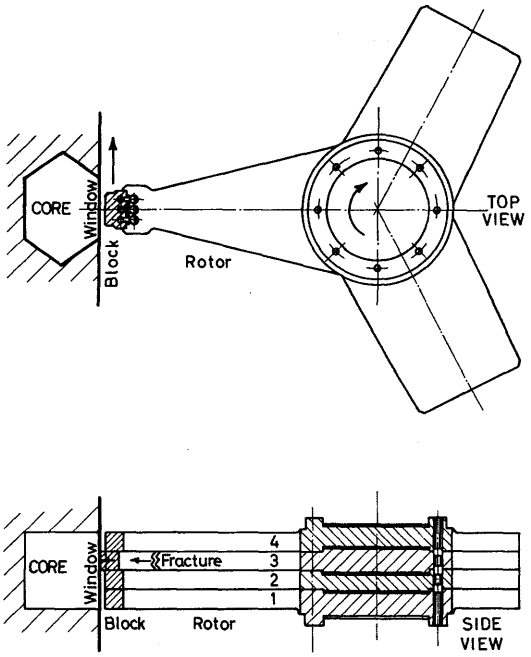

FIG.1. Schematic diagram of core and pulsation device of a pulsed fast reactor; side view shows typical breakage accident.

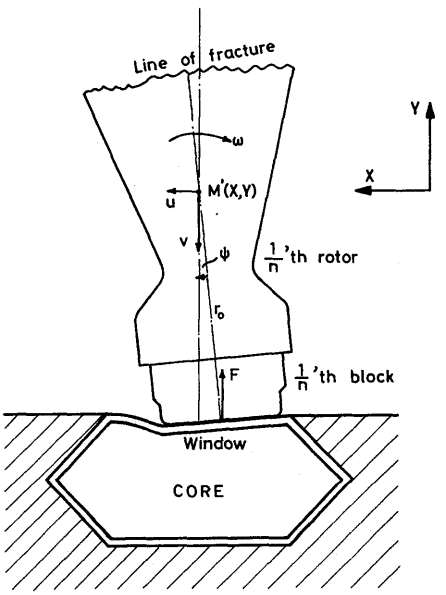

FIG.2. Diagram showing the manner in which the broken rotor fragment strikes the core window.

transiently into a more critical assembly and generate a reactivity pulse in addition to that arising from the passage of the reflector block (now in two parts). If these two pulses occur sufficiently near in time, the resultant reactivity input will, in many cases, be capable of producing an excursion which vaporizes the fuel and destroys the core explosively. It is the purpose of the theory given in this paper to provide a means of calculating the heat and mechanical energy released in such an excursion.

The problem falls naturally into two parts: that of evaluating the reactivity input; and that of evaluating the total fission energy resulting from this input.

The evaluation of the reactivity input necessitates above all a careful analysis of the collision process. The other processes occurring are relatively easy to deal with. The situation which has to be considered is that of a spinning body striking a complex structure – the reactor core. The response of such a structure to a large impact is very complicated since it consists of a tight cluster of cylindrical fuel elements immersed in a liquid metal coolant. This liquid is not rigidly contained in the core but can be expelled (if the duration of the collision is long enough) into the outer coolant circuit. Thus, the forces generated by the colliding fragment in the coolant are by no means a simple function of the core deformation. Furthermore, if this deformation reaches a magnitude where the fuel slugs themselves become deformed, the additional forces thus generated are not the usual linear elastic forces but something more complicated. These matters are all studied in the text where a model for the numerical evaluation of the core volume change (as a function of time) and the accompanying reactivity input is presented. The total reactivity input is obtained by adding the component due to the quasi-normal passage of the divided reflector block.

The evaluation of the energy release relies on a modified form of the well-known Bethe-Tait model [1-3]. In this model, the excursion is terminated by the flow of core material into regions of lower importance along the pressure gradient generated by the vaporized fuel. To derive this pressure gradient, an equation of state with two linear regions is used [4]. This has been found capable of fitting the available data quite well for practical purposes. The parameters of the two-region equation of state are obtained by the common practice [5-7] of assuming the validity of the principle of corresponding states for fuel materials and calculating the pressure-energy-specific volume relationship from some well-known thermodynamic tables [8]. A very similar procedure is used to evaluate the possible mechanical energy made available by a destructive excursion.

The model representing the collision process and that describing the neutronics and destruction of the system are combined within the framework of a Fortran computer programme (SOREX-1) which evaluates the whole course of a hypothetical accident from the instant of fracture in the rotor to the time when the resulting nuclear excursion has terminated itself in core disassembly. The output of the programme contains both the total energy release and the maximum available work. At the end of the paper are presented some typical excursion studies performed by the use of SOREX-1.

1. REACTIVITY INPUT GENERATED BY A HYPOTHETICAL ROTOR BREAKAGE ACCIDENT

1.1. Qualitative discussion

In formulating the picture on which the mathematical models of a rotor breakage accident are based, it is necessary to bear in mind that the rotor and reflector block are fabricated in a number of equal independent laminar pieces. Although Fig. 1 shows four such pieces, we shall treat the problem as if there were an arbitrary number, n.

It is supposed that a fracture occurs suddenly in one of the laminar pieces of the rotor at an instant when it is moving towards the window. The probability of a simultaneous fracture in one of the other laminar pieces is assumed negligible. From this hypothesis of a sudden fracture, it follows that the broken rotor piece moves out of its normal circular trajectory, strikes and compresses the core with its $(1/n)^{th}$ part of the important neutron reflecting block foremost and subsequently, under the influence of a large momentum tangential to the core, slides across the window very close behind the unbroken part of the rotor (see Figs 1 and 2). Because of its laminated structure, the latter is practically unaffected by the fracture and continues in its usual circular path.

From this picture, we can already deduce the general type of (time dependent) reactivity input resulting from a rotor breakage accident. It will be a superposition, on top of negative prompt background reactivity $-\epsilon_{00}$, of essentially three different reactivity pulses separated in time, namely:

(1) The pulse due to the neutron reflecting properties of the $((n-1)/n)^{th}$ part of the block carried by the unbroken part of the rotor as it passes in front of the window. This will be referred to as reflectivity pulse 1, $\epsilon_{ref\,1}(t)$.

(2) The similar pulse due to the (delayed) passage of the $(1/n)^{th}$ part of the block carried by the broken part of the rotor. This pulse, which includes a part coming from the closing of the gap between block and core, will be referred to as reflectivity pulse 2, $\epsilon_{ref\,2}(t)$.

(3) The pulse due to the compression and decompression of the core following the impact of the broken fragment. This pulse, which includes a component coming from the enhanced neutron reflecting properties of the $(1/n)^{th}$ part of the block on the broken fragment due to its entry into the core during collision, will be referred to as the compression pulse, $\epsilon_{com}(t)$.

The total prompt reactivity as a function of time during a rotor breakage accident will be given by

$$\epsilon_0(t) = \epsilon_{ref\,1}(t) + \epsilon_{ref\,2}(t) + \epsilon_{com}(t) - \epsilon_{00} \qquad (1)$$

Let us suppose that, at the instant of fracture, the angular displacement of the pulsation rotor from its central position in front of the window is θ. Let us also assume for purposes of discussion that the mass M of the broken fragment is always the same. By considering the time delays between the above three reactivity pulses, it is possible, if M is constant, to infer the manner in which the nuclear energy release will vary with θ. When θ is small, the velocity of the broken fragment has only a small component towards the window but a large component directed tangentially. Thus,

the broken fragment will fly past the window and strike the core only after reflectivity pulses 1 and 2 have died away. In this case, the compression pulse is too delayed to have an effect on the resultant reactivity pulse maximum and the induced nuclear excursion is innocuous. As θ increases, however, the collision point moves backwards onto the window region and the collision pulse begins to arrive early enough to add to reflectivity pulses 1 and 2. Thus, as the breakage angle increases from small values, the nuclear energy release also increases. When the point of collision lies somewhere near the centre of the window, there arises a combination of the three pulses which gives the maximum possible resultant. For the angle $\theta = \theta_c$ at which this occurs, the induced nuclear energy release has its highest value. For $\theta > \theta_c$, the condition of optimum mutual support between the pulses is disturbed by the further backward movement of the collision point towards the edge of the window. In this case, instead of arriving too late to boost the reflectivity pulses, the collision pulse arrives too early. For sufficiently large θ, the collision will no longer contribute appreciably to the resultant reactivity pulse and the nuclear excursion will again be innocuous.

From this description it will be readily seen that the destructive nuclear energy release is only non-zero when the breakage angle lies within a relatively narrow range $\theta_0 < \theta < \theta_1$ and that it has a maximum W_{max} at some value θ_c. The exact values of the parameters θ_0, θ_1, θ_c and W_{max} will depend only on the mass M of the broken fragment (typically $\theta_0 \sim 8°$, $\theta_c \sim 11°$ and $\theta_1 \sim 14°$). This type of dependence of the energy release on θ is illustrated in a later section dealing with numerical results (see Fig. 6).

1.2. Kinematic model of the collision process and time relations between the reactivity pulse components

It will be noted from Eq. (1) that the problem of evaluating the total reactivity $\epsilon_0(t)$ accompanying a rotor breakage accident reduces to that of deriving formulae for the pulse components $\epsilon_{ref\,1}(t)$, $\epsilon_{ref\,2}(t)$ and $\epsilon_{com}(t)$. The first step in this direction is to take note of the time relations between them. Unless otherwise stated, the time variable t will be measured relative to the instant when the unbroken part of the rotor occupies a central position in front of the window, i.e. relative to the maximum of reflectivity pulse 1.

With this system of reference, three important time points can be distinguished:

- t_1, the instant of fracture
- t_2, the instant of impact when the broken fragment begins to compress the core
- t_3, the instant when the $(1/n)^{th}$ reflector block on the broken fragment passes the central position in front of the window.

If V is the normal speed of the outer tip of the reflector block and R_0 its radius of motion, then clearly

$$t_1 = -\frac{R_0\theta}{V} \qquad (2)$$

The quantities t_2 and t_3, however, cannot be evaluated without a kinematic model.

To provide such a model, we assume:

(1) After fracture, the centre of the outer tip of the broken fragment flies in a straight line (determined by its velocity at the instant of fracture) towards the collision point in the window region

(2) During flight, the fragment turns under its own momentum so that it lands 'squarely' on the window, i.e. the impact is distributed uniformly over the area of the $(1/n)^{th}$ block (which lies for foremost)

(3) The motion of the fragment parallel to the window is conserved, i.e. the momentum of the fragment is much too large to be affected by the force of friction with the window.

These assumptions are pessimistic with respect to the reactivities later derived from them. They leave out of account the effects which might arise from the detailed structure of the system in the window region. Inclusion of these effects would reduce the pessimism of the model but greatly complicate the analysis.

From the above assumptions, it is now easy to derive the expressions

$$t_2 = \frac{h}{V\sin\theta} - \frac{R_0}{V}\left(\theta - \tan\frac{\theta}{2}\right) \tag{3}$$

and

$$t_3 = \frac{R_0}{V}\left(\tan\theta - \theta\right) \tag{4}$$

where h is the normal minimum effective gap width between the core and block. It will be noted that the moment t_3 when reflectivity pulse 2 reaches its maximum is much less sensitive to θ than the impact moment t_2.

1.3. The reflectivity pulses

The reactivity pulse $\epsilon_p(t)$ caused by the normal passage of the reflector block in front of the window can be represented quite well [9, 10] by the expression

$$\epsilon_p(t) = \max(0, \epsilon_{p0}(t)) \tag{5}$$

where

$$\epsilon_{p0}(t) = \begin{cases} rt + \dfrac{r^2}{4B} + \epsilon_m + \epsilon_{00} & \text{if } t \le -t_0 \\ \epsilon_m + \epsilon_{00} - Bt^2 & \text{if } -t_0 \le t \le t_0 \\ -rt + \dfrac{r^2}{4B} + \epsilon_m + \epsilon_{00} & \text{if } t \ge t_0 \end{cases} \tag{6}$$

and

$$t_0 = \frac{r}{2B} \tag{7}$$

r being the initial (final) ramp rate of rise (fall) of the pulse, $\epsilon_m + \epsilon_{00}$ its total amplitude and B a parameter defining the 'sharpness' of the

maximum. It is obvious that $r \propto V$ and $B \propto V^2$. This pulse is superimposed on a background with a reactivity of $-\epsilon_{00}$ relative to prompt criticality. Thus, the quantity ϵ_m is the prompt reactivity of the system at the peak of a normal operational pulse when the reflector block is in a central position in front of the window.

Under the conditions of a rotor breakage accident, the block becomes separated into two parts, the broken part being delayed in its arrival at the centre-window position by a time t_3. Furthermore, the speed with which the tip of the broken fragment crosses the window is reduced from V to $V\cos\theta$. Thus, the pulse $\epsilon_p(t)$ becomes split into two parts, ϵ_{p1} and ϵ_{p2}, corresponding to the transit of the unbroken and broken parts of the rotor respectively:

$$\epsilon_p(t) = \max(0, \epsilon_{p1}(t)) + \max(0, \epsilon_{p2}(t - t_3)) \tag{8}$$

where

$$\left.\begin{aligned} \epsilon_{p1}(t) &= a_n \epsilon_{p0}(t) \\ \epsilon_{p2}(t) &= b_n \epsilon'_{p0}(t') \end{aligned}\right\} \tag{9}$$

and

$$\epsilon'_{p0}(t') = \begin{cases} r\cos\theta\, t' + \dfrac{r^2}{4B} + \epsilon_m + \epsilon_{00} & \text{if } t' \le -t'_0 \\ \epsilon_m + \epsilon_{00} - B\cos^2\theta\, t'^2 & \text{if } -t'_0 \le t' \le t'_0 \\ -r\cos\theta\, t' + \dfrac{r^2}{4B} + \epsilon_m + \epsilon_{00} & \text{if } t' \ge t'_0 \end{cases} \tag{10}$$

with $t'_0 = t_0/\cos\theta$. The numbers a_n and b_n are the reactivity worths of the blocks on the unbroken and broken parts of the rotor respectively relative to the worth of the whole block. If all laminar pieces are assumed to have the same reactivity worth, then

and

$$\left.\begin{aligned} a_n &= \frac{n-1}{n} \\ b_n &= \frac{1}{n} \end{aligned}\right\} \tag{11}$$

Equation (8) is not the whole reactivity generated by the neutron reflecting properties of the two pieces of the block since the broken part crosses the gap which normally separates the block from the core (this gap including also the gaps which may lie inside the window structure) and its efficiency as a reflector is thereby raised. To write down the additional reactivity introduced by this effect, we make use of the 'wobble coefficient' of the block, ϵ', which is defined as the change in the maximum reactivity of a normal pulse (ϵ_m) when the whole block is advanced a unit distance towards the core. The 'wobble coefficient' of one of the laminar pieces will (on the same basis as equations (9)) be equal to $b_n\epsilon'$. Using the kinematic model described in section 1.2, the broken piece arrives at the normal gap separation distance at a time

$$t_g = \frac{R_0}{V}\left(\theta - \tan\frac{\theta}{2}\right) \tag{12}$$

It will be assumed that until this time, the reactivity $b_n \epsilon_{gap}$ generated by the crossing of the gap is zero but that between t_g and the moment of impact t_2, ϵ_{gap} increases at a rate proportional to the speed of the fragment towards the window:

$$\epsilon_{gap}(t) = \begin{cases} 0 & \text{if } t \leq t_g \\ \epsilon' V \sin\theta\,(t - t_g) & \text{if } t_g \leq t \leq t_2 \\ \epsilon' h & \text{if } t \geq t_2 \end{cases} \qquad (13)$$

The reactivity introduced by the still further advance of the broken fragment into the core during collision will be included in the compression pulse. It now follows that reflectivity pulse 1 is given by

$$\epsilon_{ref\,1}(t) = a_n \max(0,\ \epsilon_{p0}(t)) \qquad (14)$$

and reflectivity pulse 2 by

$$\epsilon_{ref\,2}(t) = b_n \left\{ \max(0,\ \epsilon'_{p0}\ (t - t_3)) + \epsilon_{gap}(t) \right\} \qquad (15)$$

1.4. Dynamical models to describe the collision process

1.4.1. The rotor fragment

The first model necessary to describe the collision process is one dealing with the dynamics of the broken rotor fragment. Such a model is presented in Appendix A where the essential point in the problem is shown to be the fact that not only does the translational energy of the fragment contribute to the compression of the core, but also a part of its rotational energy. The amount of rotational energy converted into elastic strain in the core is derived as a function of the translational energy E_{trans} of the fragment on the pessimistic assumption that the fragment remains perfectly rigid during the collision. In this way it is shown (pessimistically) that the rotational motion of the fragment can be ignored in the evaluation of the core strain energy provided that the translational energy E_{trans} is replaced by a larger quantity E_{tot}. The relationship between E_{tot} and E_{trans} is derived in Appendix A.

On the basis of E_{tot} and for purposes of simplifying the further description of the collision process, the rotor fragment is then replaced in the theory by a hypothetical mass m of the same dimensions as the $(1/n)^{th}$ block on the broken fragment but with a speed V (the normal operational speed of the outer tip of the block), an angle of incidence on the core of θ (the breakage angle) and no rotation (see Fig. 3). The value of the mass m is chosen so that $\frac{1}{2} m V^2 = E_{tot}$.

In any particular system, the distribution of mass along the rotor, the number of laminar pieces n and the rotor speed will be known. In this case it is possible to evaluate the hypothetical mass m explicitly as a function of the position of the fracture on the rotor. In Appendix A this calculation is performed for the four-piece rotor system proposed for the SORA reactor (see Table I).

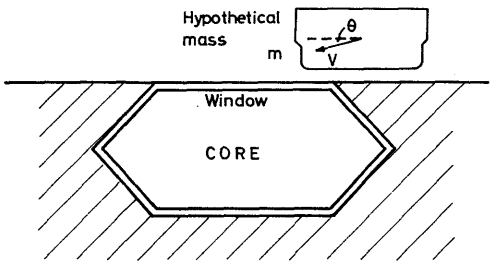

FIG.3. Diagram showing the hypothetical mass used in the simulation of the collision.

TABLE I. PARAMETERS OF A QUARTER-ROTOR BROKEN FRAGMENT AND THE MAGNITUDE OF AN EQUIVALENT HYPOTHETICAL MASS AS A FUNCTION OF THE FRACTIONAL POSITION OF THE BREAKAGE ALONG THE ROTOR (SORA)

ρ	0.7	0.8	0.88	Block with keys	Block without keys
M(kg)	9.6	5.8	3.2	1.7	0.8
X_M	0.811	0.864	0.919	0.958	0.967
V_M (m/sec)	230	245	260	271	274
m(kg)	7.9	5.1	2.9	1.6	0.8

1.4.2. Core compression

The second model required in the study of the collision dynamics is one which describes the slowing down of the fragment and compression and decompression of the core subsequent to the moment of impact t_2. Here, we make the pessimistic assumption that all of the energy lost by the fragment goes into straining the core. The required information can then be obtained by solving the equations of motion of the fragment under the influence of the elastic forces evoked by the change in volume of the core.

To accomplish this, we exploit further the 'hypothetical mass' picture described in section 1.4.1. Since the energy available for core compression is (on the basis of the rigid rotor hypothesis) the same for the hypothetical mass as for the real fragment, the effect on the core structure will be practically the same in each case.

In the spirit of the kinematic assumptions made in section 1.2, we suppose that the hypothetical mass m (assumed identical in shape to the $(1/n)^{th}$ block on the broken part) strikes the core 'squarely' at time point t_2 and applies a uniform thrust over the whole area A presented to the core. If A_0 is the surface area of the outer tip of the whole reflector block, then obviously $A = A_0/n$. As a result of the applied thrust, the core volume will decrease by an amount ΔV.

The processes underlying this volume change are sufficiently complicated to give difficulty in the prediction of the elastic forces generated. The core is not a homogeneous medium with rigid walls but a parallel assembly of long fuel slugs, each held within a thin metallic clad. In cores using a metallic fuel, there may also be a coolant-filled annular gap between slug and cladding (bonded elements). Along the channels formed between these elements, liquid metal coolant flows at a velocity of the order of 5 m/sec while the coolant in the bond region of the elements is free to flow out axially in response, for example, to thermal expansion. Thus, although the lateral boundary of the core (pressed close to the fuel bundle and backed by heavy reflector material) may behave approximately like a rigid wall, the end boundaries (where the coolant leaves and enters the core) is open. The effect of compression on such a structure is qualitatively as follows. As the colliding area A pushes upon the window, the fuel slugs will at first suffer no deformation owing to the inherent 'looseness' of the fuel bundle. For example, in a system with bonded fuel elements, the slugs will not be subjected to any stress until the bond gap has been closed at the points where the local forces act. Thus, the only significant force opposing the motion of the fragment at the beginning of the collision is that due to the compression of the coolant, F_c. If the energy E_{tot} (hypothetical mass m) is small, this force F_c alone will be sufficient to stop and repel the fragment. If E_{tot} is large, however, the core volume decrease $\Delta\mathscr{V}$ will go beyond the value $\Delta\mathscr{V}_1$ for which slug deformation commences and a further force, F_s, will arise. The total repulsive force acting on the fragment is then $F_c + F_s$.

The main complication in the derivation of an expression for F_c is the fact that, on compression, the coolant tends to be ejected out of the core through its entrance and exit. This ejection is not instantaneous but delayed by the time required by compression waves in the coolant to propagate axially along the compressed part of the core. Thus, although the ejection process weakens the ability of the coolant to resist the fragment, F_c remains quite large if the time-scale of the collision is less than the acoustic transit time along the compressed length of core. This problem is treated in some detail in Ref. [11] and Appendix B where it is shown that the effect of coolant ejection can be taken into account approximately by scaling down the bulk modulus of elasticity of the coolant. The scaling factor is derived as a function of the hypothetical mass m and evaluated numerically for the particular case of the SORA system (see Table II). Assuming that the pressures are not so high as to require a non-linear stress-strain relation, it follows that

$$F_c = A\,\kappa'\,\frac{\Delta\mathscr{V}}{\mathscr{V}}$$

where κ' is the scaled-down bulk modulus of elasticity and $\mathscr{V}$ the volume of coolant in the compressed zone of the core. If f_0 is the volume fraction of coolant in the core as a whole and $\mathscr{V}_c$ the volume of the core, then $\mathscr{V} = f_0\,\mathscr{V}_c/n$, which gives, on substituting $A = A_0/n$:

$$F_c = \frac{A_0\kappa'}{f_0}\,\frac{\Delta\mathscr{V}}{\mathscr{V}_c} \qquad (16)$$

TABLE II. PARAMETERS MEASURING THE EFFECT OF COOLANT EJECTION DURING THE COLLISION OF A QUARTER-ROTOR BROKEN FRAGMENT (SORA)

ρ	0.7	0.8	0.88	Block with keys	Block without keys
ω_0(sec^{-1})	14110	17560	23280	31350	44330
$\omega_0\tau_0$	0.282	0.351	0.466	0.627	0.887
κ'/k	0.0199	0.0308	0.0542	0.0983	0.1965

The force F_s due to the compression of the fuel slugs depends on the particular type of lattice geometry and the (unknown) manner in which this might become reshuffled under deformation. The uncertainties in this respect are so considerable that very elaborate models describing fuel compression are probably superfluous. Thus, we have made use of a model in which the fuel slugs are assumed to lie in a square array and undergo no reshuffling. The model is analysed in detail in Appendix C where it is shown that the force F_s can be represented approximately by the formula

$$F_s = \begin{cases} 0 & \text{if } \dfrac{\Delta\mathscr{V}}{\mathscr{V}_c} \leq \alpha \\ \dfrac{\beta\left(\dfrac{\Delta\mathscr{V}}{\mathscr{V}_c} - \alpha\right)}{2 - \ln n - \ln\left(\dfrac{\Delta\mathscr{V}}{\mathscr{V}_c} - \alpha\right)} & \text{if } \dfrac{\Delta\mathscr{V}}{\mathscr{V}_c} \geq \alpha \end{cases} \qquad (17)$$

where $\alpha = \Delta\mathscr{V}_1/\mathscr{V}_c$ and

$$\beta = \frac{\pi ERLN}{1 - \nu^2} \qquad (18)$$

E being the Young's modulus of the fuel slug, R its radius, L its length, ν its Poisson ratio and N the average number of fuel elements in the rows parallel to the window. The volume change $\Delta\mathscr{V}_1$ required before the $(1/n)^{th}$ fragment begins to compress the fuel slugs is inversely proportional to the number of laminar pieces: $\Delta\mathscr{V}_1 = \Delta\mathscr{V}_0/n$, where $\Delta\mathscr{V}_0$ is the volume change required if the whole block with its area A_0 compresses the core. Thus

$$\alpha = \frac{\Delta\mathscr{V}_0}{n\mathscr{V}_c} \qquad (19)$$

With formulae (16) and (17) it is now possible to write down the equations of motion of the hypothetical mass m. In the direction vertical to the window (Y-axis) we have:

$$m\ddot{Y} = -F_c - F_s$$

In the X-direction parallel to the window, we have (according to point (3) in the kinematics model in section 1.2) $\ddot{X} = 0$. Since we have assumed that the block lands 'squarely' on the window, we can write $\dot{Y} = \Delta\mathscr{V}/A$ and if we define

$$y = \frac{\Delta\mathscr{V}}{\mathscr{V}_c} \tag{20}$$

the equation of motion leads to the following equation in y:

$$\frac{d^2y}{dt^2} = -G_c(y) - G_s(y) \tag{21}$$

where

$$G_c(y) = \frac{A_0^2 \kappa'}{nmf_0 \mathscr{V}_c} y \tag{22}$$

and

$$G_s(y) = \begin{cases} 0 & \text{if } y \leq \alpha \\ \dfrac{\dfrac{\beta A_0}{nm\mathscr{V}_c}(y-\alpha)}{2 - \ln n - \ln(y-\alpha)} & \text{if } y \geq \alpha \end{cases} \tag{23}$$

The boundary conditions to Eq. (21) are clearly

$$\begin{aligned} y &= 0 && \text{for } t \leq t_2 \\ \dot{y} &= \frac{A_0 V}{n\mathscr{V}_c} \sin\theta && \text{for } t = t_2 \end{aligned} \tag{24}$$

Equation (21) is the mathematical model for the evaluation of the reactivity input accompanying the compression of the core.

1.5. The compression pulse of reactivity

For any particular reactor, the 'volume coefficient of reactivity', η, is defined as the ratio of the increase in reactivity to the fractional core volume decrease producing it, the mass of the core being assumed constant and all structures but the core being assumed stationary. In the present case, if we know the η corresponding to a volume decrease imposed from the window side, then the reactivity generated by the core compression will be ηy. This reactivity, however, is not the only component of the compression pulse, since, in addition to a change of volume, the $(1/n)^{th}$ reflector block enters the core, in effect, a distance $\Delta\mathscr{V}/A$. The reactivity accompanying this advance is assumed to be $b_n \epsilon' \Delta\mathscr{V}/A$ on the same basis as the gap reactivity, ϵ_{gap}, derived in section 1.3. Expressing $\Delta\mathscr{V}$ in terms of y and substituting $A = A_0/n$, we thus obtain for the compression pulse of reactivity:

$$\epsilon_{com}(t) = \left(\eta + \frac{n b_n \epsilon' \mathscr{V}_c}{A_0}\right) y(t) \tag{25}$$

2. NUCLEAR EXCURSION GENERATED BY A HYPOTHETICAL ROTOR BREAKAGE ACCIDENT

2.1. Neutronic-hydrodynamic model

On the basis of the well-known theory of Bethe and Tait [1], an extensive literature dealing with models for the study of destructive nuclear excursions has been built up. References [2-4] represent but a small sample of this literature. In the present work, the version of the Bethe-Tait method adopted for application is essentially that of Nicholson [3].

The causal event in a destructive nuclear excursion is the insertion of a reactivity $\epsilon_0(t)$ which makes the system super prompt critical. In our case, $\epsilon_0(t)$ arises from the combination of the three basic pulse components $\epsilon_{ref\,1}(t)$, $\epsilon_{ref\,2}(t)$ and $\epsilon_{com}(t)$. From Eqs (1), (14), (15) and (25) we have

$$\epsilon_0(t) = a_n \max(0, \epsilon_{p0}(t)) + b_n \left\{ \max(0, \epsilon'_{p0}(t - t_3)) + \epsilon_{gap}(t) \right\} + \left(\eta + \frac{n b_n \epsilon' \%_c}{A_0} \right) y(t) - \epsilon_{00} \qquad (26)$$

where ϵ_{p0}, ϵ'_{p0}, ϵ_{gap} and $y(t)$ are given respectively by Eqs (6), (10), (13) and (21). Since the fuel temperature rise during an excursion will inevitably be very large, the Doppler effect may also be important and we include it by means of the formula

$$\epsilon_{Dopp} = 2\gamma T_0 \left\{ 1 - \left(1 + \frac{T}{T_0} \right)^{-\frac{1}{2}} \right\} \qquad (27)$$

where T_0 is the mean absolute fuel temperature before the excursion, T the average temperature rise during the excursion and γ the Doppler coefficient of reactivity at temperature T_0. Equation (27) is based on the Nicholson - 3/2 power law connecting the Doppler effect and temperature [13] in highly enriched systems with very hard spectra. (The SORA reactor is such a system.)

With the onset of destruction, yet a further component of reactivity, $\tilde{\epsilon}(t)$, will appear. This arises from the movement of material inside the core due to the very large pressures generated by the vaporized fuel. The total reactivity is thus given by

$$\epsilon = \epsilon_0 + \epsilon_{Dopp} + \tilde{\epsilon} \qquad (28)$$

The evaluation of $\tilde{\epsilon}$, which is responsible for terminating the excursion, is the main objective of the neutronic-hydrodynamic model.

Owing to the large amount of existing literature on the subject, this model will be dealt with rather briefly. It begins by making three simplifications, the first being that of sphericalization: the core is transformed into a uniform sphere of such a radius R_c that its volume and mass is conserved. The second simplification is the assumption that the energy release per unit mass of fuel, $Q(r,t)$, and the reactivity worth per unit core volume, $D(r)$, can both be represented by means of parabolic

spatial distribution functions which retain the same profile throughout the excursion, i.e.

$$Q(r,t) = Q_0(t)\left(1 - q\,\frac{r^2}{R_c^2}\right) \tag{29}$$

and

$$D(r) = g_0 - \frac{1}{2}\,g\,\frac{r^2}{R_c^2} \tag{30}$$

where r is any radial position inside the sphericalized core, $Q_0(t)$ the energy per unit mass of fuel at the core centre, D(r) the decrease in reactivity caused by the removal of a unit volume of core material from a spherical shell at r and the constants q, g and g_0 are determined by fitting the formulae (29) and (30) with the results of neutron transport theory.

The third sumplification made in the model concerns the relationship of the vapour pressure p and temperature rise T of the hot fuel to the energy content Q. Although there are other components present in the core in addition to the fuel slugs, it is assumed that the excursion occurs too rapidly for a significant amount of heat transfer to occur and that, consequently, only the fuel generates pressure. The physical background to this pressure generation is discussed in detail in Appendix D. Extensive calculations [14] have proved the validity of the approximation of Wolfe et al. [4] within the limitations of the principle of corresponding states and existing data [8]. In this approximation, the p-Q relation falls into two linear regions, the low pressure regime:

$$p(r,t) = \begin{cases} 0 & \text{if } Q(r,t) \le Q_2^* \\ \gamma_2 \rho_f\,(Q(r,t) - Q_2^*) & \text{if } Q_2^* \le Q(r,t) \le Q_0^* \end{cases} \tag{31}$$

and high pressure regime:

$$p(r,t) = \gamma_1 \rho_f\,(Q(r,t) - Q_1^*) \qquad \text{if } Q(r,t) \ge Q_0^* \tag{32}$$

where ρ_f is the density of the fuel after expansion into all available voids in the core and γ_1, Q_1^*, γ_2 and Q_2^* are constants chosen to give a fit with the known data (see Appendix D). Q_0^* is given by

$$Q_0^* = \frac{\gamma_1 Q_1^* - \gamma_2 Q_2^*}{\gamma_1 - \gamma_2}$$

The calculations [14] show that the average temperature rise T can also be related to the energy by means of a series of linear regions. The solid phase at low temperatures would be the first region, for example, and the solid/liquid, liquid/vapour and above-critical phases would constitute an additional three regions at most. It has been established, however, that the effect

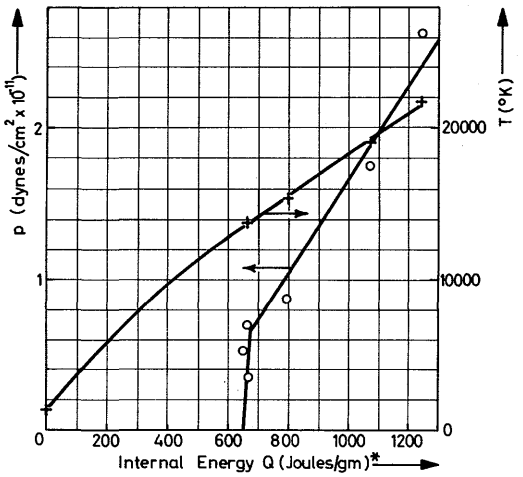

* Q measured relative to liquid Uranium at melting temperature (1400°K)

FIG.4. Pressure and temperature of uranium metal with density 14 g/cm² as a function of internal energy.

of ϵ_{Dopp} on the excursion is extremely insensitive to the detailed dependence of T on Q and it is sufficient to take

$$T = \frac{Q}{H} \tag{33}$$

where H is some average specific heat in the range between the starting and critical temperature. Figure 4 shows curves of pressure and temperature against Q for uranium metal with $\rho_f = 14$ g/cm^3, the circles and crosses being the calculated points.

Formulae (31) and (32) relate the pressure and internal energy of the fuel at constant density ρ_f. Therefore, two effects are neglected when these formulae are used to describe the pressure distribution: (a) the fall in density due to the bulk expansion of the core, (b) the propagation of a relaxation wave from the core boundary inwards. Due to the very small material movements necessary to terminate an excursion, the former is nearly always unimportant while the latter can be disregarded if the duration of the excursion is small compared to the transit time of waves along R_c. This condition is satisfied in all but the most 'mild' (least interesting) rotor breakage accidents.

Following the well-known procedure based on hydrodynamics [3] the second time derivative of the shut-down reactivity is obtained in the form

$$\frac{d^2\tilde{\epsilon}}{dt^2} = -\frac{4\pi}{\rho_c}\int_0^{R_c} \frac{\partial p}{\partial r}\,\frac{dD}{dr}\,r^2 dr$$

where ρ_c is the mean density of the core as a whole (including cladding

and coolant materials). Substituting for D(r) from Eq. (30), p(r, t) from Eqs (31) and (32) and using Eq. (29) we get, after some manipulation:

$$\ddot{\tilde{\epsilon}} = -\frac{8\pi}{5}\frac{\rho_f}{\rho_c} gq R_c Q_0(t)\left\{\gamma_1\left(\frac{S_1}{R_c}\right)^5 + \gamma_2\frac{S_2^5 - S_1^5}{R_c^5}\right\} \tag{34}$$

where

$$S_2(t) = \begin{cases} 0 & \text{if } Q_0(t) \le Q_2^* \\ R_c\left(\dfrac{Q_0(t) - Q_2^*}{qQ_0(t)}\right)^{\frac{1}{2}} & \text{if } Q_2^* \le Q_0(t) \le \dfrac{Q_2^*}{1-q} \\ R_c & \text{if } Q_0(t) \ge \dfrac{Q_2^*}{1-q} \end{cases} \tag{35}$$

and

$$S_1(t) = \begin{cases} 0 & \text{if } Q_0(t) \le Q_0^* \\ R_c\left(\dfrac{Q_0(t) - Q_0^*}{qQ_0(t)}\right)^{\frac{1}{2}} & \text{if } Q_0^* \le Q_0(t) \le \dfrac{Q_0^*}{1-q} \\ R_c & \text{if } Q_0(t) \ge \dfrac{Q_0^*}{1-q} \end{cases} \tag{36}$$

are the outer boundaries of the (spherical) core regions subjected to the low and high pressure regimes respectively.

The whole system of equations can now be completed by introducing the equation of neutron kinetics:

$$\tau\ddot{Q}_0 = \epsilon\dot{Q}_0 + \epsilon_{00} S \tag{37}$$

where τ is the neutron generation time, $-\epsilon_{00}$ the background reactivity and S the prompt source power per unit mass of fuel at the core centre (due to delayed neutrons) just prior to the onset of the accident pulse $\epsilon_0(t)$. Since the excursion is extremely rapid in comparison with the decay time of the delayed neutron emitters, the source is essentially constant during the times of interest. The boundary conditions to equation (37) are $\dot{Q}_0 = S$ and $Q_0 = 0$ at $t = -t_b$, where $-t_b$ is the moment (obtained from Eq. (26)) when $\epsilon_0(t)$ begins to rise above $-\epsilon_{00}$, i.e. Q is measured relative to the initial energy content of the fuel.

During the course of an excursion, Q_0 at first rises slowly at a rate depending directly on S but accelerates very sharply when $\epsilon_0(t) > 0$. After arrival at the threshold Q_2^* of the low pressure regime, the shut-down reactivity $\tilde{\epsilon}(t)$ becomes dominant very quickly and $Q_0(t)$ converges to its final value $Q_0(\infty)$. $Q_0(\infty)$ is very insensitive to the value of S. If M_f is the total mass of fuel in the core, it is easy to see from Eq. (29) that the total energy released by the excursion after $t = -t_b$ is

$$Q_{tot} = \left(1 - \frac{3}{5}q\right) M_f Q_0(\infty) \tag{38}$$

2.2. Available work

Clearly, only a part of the above energy becomes transformed into mechanical work. The remainder exists as residual heat after the blast has been dissipated. The determination of the potential amount of mechanical energy made available by an excursion is obviously of great importance since it is this which constitutes the first major threat to the containment. (The further dangers which follow the blast, such as the residual static pressure, or are secondary to it, such as the flash boiling of coolant, are different problems.)

The maximum explosive work, W, which the vaporized fuel is able to perform on the environment is that corresponding to an isentropic expansion down to atmospheric pressure. In common with previous authors, we have used W as a measure of the available work released by an excursion. To calculate W from the evaluated energy distribution $Q(r,\infty)$ at the end of the excursion, it is necessary to know the work W_s done by a unit mass of fuel in expanding isentropically from a high pressure state with internal energy Q (relative to that before the excursion) down to a state at atmospheric pressure. (For further discussion see Appendix D.) Our calculations [14], which follow the standard procedure (for example [5, 7]), indicate that the available data is well fitted by the formula

$$W_s = \begin{cases} 0 & \text{if } Q \le \bar{W}_2^* \\ k(Q - W_2^*) & \text{if } W_2^* \le Q \le W_0^* \\ \ell\,(Q - W_1^*) & \text{if } Q \ge W_0^* \end{cases} \qquad (39)$$

for all fuel densities ρ_f. The constants ℓ, k, W_1^* and W_2^* are fitting parameters and

$$W_0^* = \frac{\ell W_1^* - k W_2^*}{\ell - k}$$

Figure 5 shows W_s as a function of Q for uranium metal.

From the above definitions we have

$$W = \frac{4\pi M_f}{\gamma_c} \int_0^{R_c} W_s r^2 dr$$

which, using Eqs (29) and (39), gives

$$W = M_f \left\{ k \left[(Q_0 - W_2^*) \frac{r_2^3 - r_1^3}{R_c^3} - \frac{3}{5} q Q_0 \frac{r_2^5 - r_1^5}{R_c^5} \right] + \ell \left[(Q_0 - W_1^*) \frac{r_1^3}{R_c^3} - \frac{3}{5} q Q_0 \frac{r_1^5}{R_c} \right] \right\} \qquad (40)$$

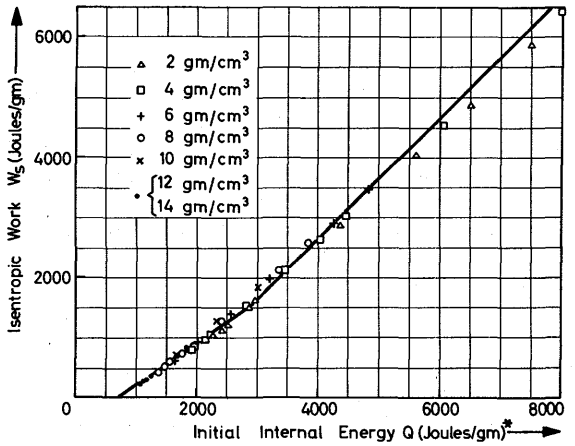

FIG.5. Work done by U-metal in expanding isentropically to one atmosphere.

where $Q_0 = Q_0(\infty)$, the final converged value of Q_0, and

$$r_2 = \begin{cases} 0 & \text{if } Q_0 \le W_2^* \\ R_c\left(\dfrac{Q_0 - W_2^*}{qQ_0}\right)^{\frac{1}{2}} & \text{if } W_2^* \le Q_0 \le \dfrac{W_2^*}{1-q} \\ R_c & \text{if } Q_0 \ge \dfrac{W_2^*}{1-q} \end{cases} \tag{41}$$

$$r_1 = \begin{cases} 0 & \text{if } Q_0 \le W_0^* \\ R_c\left(\dfrac{Q_0 - W_0^*}{qQ_0}\right)^{\frac{1}{2}} & \text{if } W_0^* \le Q_0 \le \dfrac{W_0^*}{1-q} \\ R_c & \text{if } Q_0 \ge \dfrac{W_0^*}{1-q} \end{cases} \tag{42}$$

3. SOLUTION OF THE EQUATIONS

3.1. Numerical method

The problem is essentially that of simultaneously solving the three differential equations (21), (34) and (37) describing respectively the relative core volume decrease $y(t)$ due to the collision of the broken fragment, the feedback of reactivity $\tilde{\epsilon}(t)$ due to the disassembly of the core and the deposition of fission energy $Q(r,t)$ during the excursion. All other equations can be regarded as supplementary to these three.

The numerical method adpoted is the conventional one of expressing Eqs (21), (34) and (37) in finite difference form over a chain of time points and evaluating the solution step by step. The step length is systematically

reduced when the excursion accelerates and the accuracy is thereby kept roughly constant during the whole calculation. The type of finite difference representation used has been found successful in a related problem of pulsed fast reactor dynamics [15].

The arithmetic necessary in the above scheme is executed by a computer programme SOREX 1 written in Fortran 4 for the IBM 7090 and 360 series machines. SOREX 1 provides a numerical description of a whole accident starting from the moment when the input reactivity starts to rise, passing through the stage where the rotor fragment (hypothetical mass m) compresses the core and ending at the point where the shut-down due to disassembly becomes effective and the energy release converges to its final value Q_{tot}. A detailed account of the numerical method and SOREX 1 programme will be issued separately at a later date.

3.2. Application to the study of rotor breakage accidents in a SORA-type reactor

Typical values of the input parameters to SOREX 1 for a reactor of the SORA type, fuelled with uranium metal and cooled with liquid sodium, are given in Table III. The initial fuel temperature of $T_0 = 473°K$ represents the start-up condition (for which an accident is slightly more dangerous than for normal operation) and the values of S, γ, Q_1^*, Q_2^*, W_1^* and W_2^* correspond to this condition. Some of the key equations in which the parameters appear are listed in parentheses.

The two independent variables of an accident are the breakage angle θ and the fractional distance ρ of the line of breakage along the rotor. The value of the hypothetical mass m and the scaling factor κ'/κ (for the evaluation of the effective coolant elasticity κ') are given as functions of ρ in Tables I and II respectively. Insertion of this data into the SOREX 1 programme yield the results of Fig. 6 which shows the available work W released in an excursion as a function of θ and ρ. The case 'block with keys' refers to the accident in which the $(1/n)^{th}$ reflector block alone breaks away from the rotor but carries its fixation keys with it. The accident in which the keys are left in the rotor does not lead to a destructive excursion. Because of the conservatism of the models used, these curves of W are pessimistic.

The structure of the results of Fig. 6 is precisely as expected from the discussion in section 1.1. For any value of ρ the energy release is destructive only within a range $\theta_0 < \theta < \theta_1$ and the available work has a maximum W_{max} at some angle θ_c within this range. It will be noted that the size of the range (θ_0, θ_1) is very narrow, making the probability of a destructive excursion small even in the event of a rotor breakage. For example, the fracture at $\rho = 0.88$ gives destructive excursions only within the range $7.8° < \theta < 13.6°$, which means that the probability of a destructive excursion in the event of an accident is only 5.8/360; less than 2%. The very rapid decrease in W_{max} as ρ increases is due to the increasing importance of the coolant in slowing down the fragment as the hypothetical mass m decreases.

The results for a fracture at $\rho = 0.88$ have been used to illustrate the manner in which a rotor breakage accident develops in time. Figure 7 shows the history of the accident occurring at the peak ($\theta = 10.8°$) of the $\rho = 0.88$ curve. In the upper graph the reactivity input $\epsilon_0(t)$ and

TABLE III. PARAMETERS USED IN THE SOREX 1 STUDIES OF ROTOR BREAKAGE ACCIDENTS IN A SORA-TYPE REACTOR

No. rotor laminar pieces, $n = 4$	Effective fuel density, $\rho_f = 14$ g/cm^3
Neutron generation time, $\tau = 2 \times 10^{-8}$ sec	Core volume, $\mathcal{V}_c = 5.9$ litres
Vol. coef. react., $\eta = 0.37$ (Eq. (25))	'Wobble' coef., $\epsilon' = 0.01 \Delta k/cm$ (Eqs (13), (25))
Doppler coef., $\gamma = 2 \times 10^{-6} \Delta K/^\circ K$ (Eq. (27))	Initial fuel temp., $T_0 = 473^\circ K$ (Eq. (27))
Pulse onset rate, $r = 93 \Delta k/sec$ (Eqs (6), (10))	Source power, $S = 2.2 \times 10^{-8}$ W/g (Eq. (37))
Pulse max., $\epsilon_m = 0.00092$ (Eqs(6), (10))	$Q_1^* = 7.3 \times 10^9$ erg/g $Q_2^* = 9.3 \times 10^9$ erg/g $\gamma_1 = 2.3$ $\gamma_2 = 36.0$ (Eqs (31), (32))
Sharpness, $B = 4.805 \times 10^5 \Delta k/sec^2$ (Eqs(6), (10))	
Background react., $-\epsilon_{00} = -0.038$ (Eqs(6), (10))	
Power distr. factor, $q = 0.59$ (Eq. (29))	
React. distr. factor, $g = 6.8 \times 10^{-4} \Delta k/cm^3$ (Eq. (30))	$W_1^* = 15.3 \times 10^9$ erg/g $W_2^* = 9.3 \times 10^9$ erg/g $k = 0.676$ $\ell = 1$ (Eq. (39))
Mean core density, $\rho_c \approx \rho_f$	
Slug elast. factor, $\beta = 8 \times 10^{14}$ dyn (Eq. (18))	
Coolant elast., $\kappa = 7.4 \times 10^{10}$ dyn/cm^2	$H = 5.7 \times 10^5$ erg/g °K (Eq. (33))
Core 'loooseness', $\Delta \mathcal{V}_0 / \mathcal{V}_c = 0.03$ (Eq. (19))	Area block, $A_0 = 264$ cm^2 (Eqs (16), (22), (23), (25))
Window gap, $h = 0.45$ cm (Eqs (3), (13))	Radius rotor, $R_0 = 90$ cm Speed tip, $V = 238$ m/sec (Eqs(2), (3), (4), (12))
Mass fuel, $M_f = 70$ kg (Eqs(38), (40))	

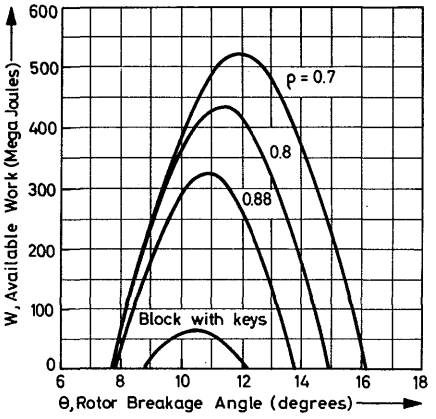

FIG.6. Available work released by a nuclear excursion following a rotor breakage accident as a function of the angle θ and fractional distance ρ of the breakage along the rotor.

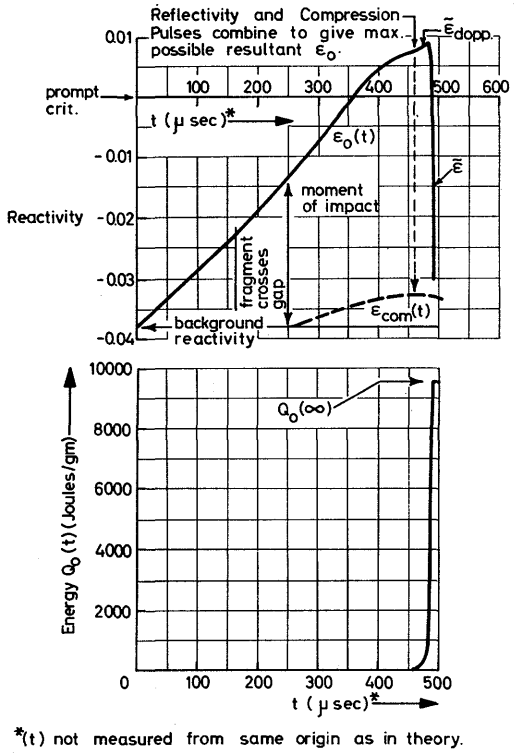

FIG.7. Development with time of the accident caused by a fracture at θ = 10.8° and ρ = 0.88.

Doppler feedback $\epsilon_{Dopp}(t)$ are plotted and it will be noted how rapidly these are overpowered by the shut-down reactivity $\tilde{\epsilon}$ when disassembly begins. The time required by $\tilde{\epsilon}$ to terminate the excursion is only ~8 μsec. The

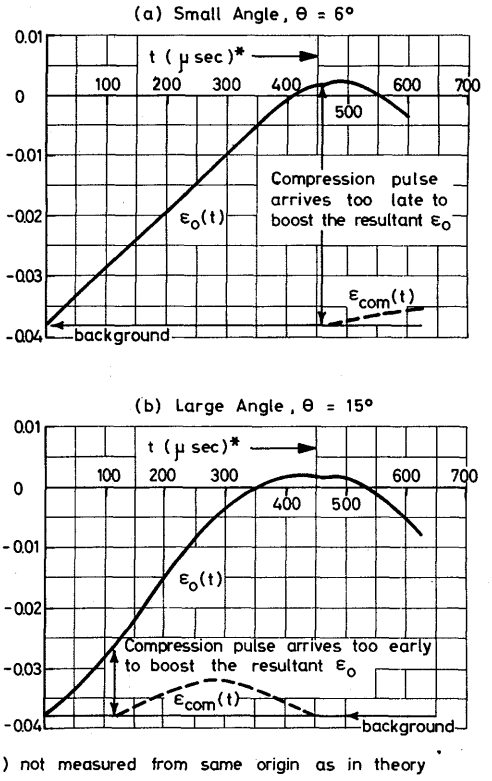

FIG. 8. Influence of breakage angle on reactivity input for the $\rho = 0.88$ accidents.

lower graph shows the behaviour of $Q_0(t)$, the energy release per unit mass of fuel at the core centre. The time variable t appearing in these graphs is measured from the moment when $\epsilon_0(t)$ begins to rise above the background reactivity $-\epsilon_{00}$ and not from the maximum of reflectivity pulse 1 as the theory.

To illustrate the discussion in section 1.1, Fig. 7 includes a plot of the compression pulse $\epsilon_{com}(t)$ accompanying the $\rho = 0.88$, $\theta = 10.8°$ accident. The peak of $\epsilon_{com}(t)$ falls exactly on that of the reflectivity pulses, giving the maximum possible resultant $\epsilon_0(t)$ as expected. The effect of changing the breakage angle θ is shown in Fig. 8 where the time evolution of two other accidents at $\rho = 0.88$ is given. These depict $\epsilon_0(t)$ and $\epsilon_{com}(t)$ for $\theta = 6°$ (Fig. 8a) and $\theta = 15°$ (Fig. 8b), both of which lie outside the region where the $\rho = 0.88$ accidents give destructive nuclear excursions. For the small angle $\theta = 6°$ it will be noted that the compression pulse does not arrive until the reflectivity pulses have already reached their maximum and is therefore too late to have an amplifying effect on $\epsilon_0(t)$. In the case of the large angle accident at $\theta = 15°$, the compression pulse arrives too early. For both accidents, the tendency of $\epsilon_0(t)$ to spread into two maxima is clearly shown. The separation of the two reflectivity pulses (to make three maxima) is not sufficiently large to show up in the graphs.

This is due to the fact, mentioned in section 1.2, that the delay t_2 in the compression pulse is much more sensitive to θ than the delay t_3 between the reflectivity pulses.

3.3. Assessment of results

The physical and mathematical models presented in this paper are able to predict the course and outcome of extreme hypothetical accidents and the illustrative numerical results are fully consistent with 'common sense' expectations. These results naturally contain the uncertainties implicit in the models, but the approximations and assumptions involved have all been made on the conservative side and the theory is therefore expected to be pessimistic. At the moment, the degree of this pessimism is unknown.

The numerical results bring out an extremely important problem with regard to the equation of state (Fig. 4). In addition to the errors incurred by assuming the validity of the principle of corresponding states and using data under the somewhat extreme conditions of high fuel density, there is also the fact that the programme SOREX 1 is free to extrapolate the assumed linear equation (32) to as high a pressure as is necessary to terminate an excursion. Thus, for example, the maximum pressure reached by SOREX 1 in the accident shown in Fig. 7 (ρ = 0.88, θ = 10.8°) is about 3×10^6 atm while the calculated equation of state (Fig. 4) reaches only to about 3×10^5 atm. In this case the data are therefore being extrapolated 10 times beyond the calculated range.

It is almost certain that such linear extrapolation is conservative since the behaviour of the real fluid at very high pressures deviates more and more from that of an ideal gas. As a consequence the real pressure must be considerably above that obtained by linear extrapolation and give a higher shut-down reactivity $\bar{\epsilon}$ than that calculated in SOREX 1. Such errors can only be rectified by further research into the properties of fuel materials at high pressures and temperatures.

APPENDIX A

MODEL FOR DESCRIBING THE COLLISION OF THE BROKEN ROTOR FRAGMENT WITH THE WINDOW

The purpose of this appendix is to evaluate the energy available for compressing the core. The main problem here is that of finding the proportion of rotational energy which might also contribute. Fig. 2 shows a diagram of the rotor fragment and core at some point during the collision. M' is the centre of mass of the fragment a distance r_0 from the tip of the $(1/n)^{th}$ reflector block and ω the normal angular speed of rotor. The position of M' is measured by the rectangular co-ordinates (X, Y), which are respectively parallel and perpendicular to the (undisturbed) window. The orientation of the fragment in the XY plane is denoted by the angle ψ and the total force acting between the core and fragment by F.

The behaviour of the fragment during collision will obviously be very complex since it may undergo deformation and fracture and is subjected

to frictional as well as elastic forces. To avoid all the difficulties associated with these complications, we make the following very conservative assumptions:

(1) The rotor behaves as an ideal rigid body
(2) The force due to friction (in the X-direction) is negligible and F acts in the Y-direction through the central point of the colliding face of the block.

As a result of these assumptions, the equations of motion take on the form

$$\left.\begin{aligned} \ddot{X} &= 0 \\ M\ddot{Y} &= F \\ I\ddot{\psi} &= r_0 F \sin\psi \end{aligned}\right\} \qquad \text{(A1)}$$

where M is the mass of the fragment and I its moment of intertia about M'. The force F arises from the deformation of the core and is therefore a complicated function of X, Y and ψ. However, we shall overlook this fact by treating F as if it were a constant $\bar{F}$ (equal to some average value) on the ground that only the overall and not the detailed behaviour of the fragment is significant in the present context. In addition, since we are interested only in small values of the orientation ψ (glancing collisions), we can take $\sin\psi = \psi$. Hence, equations (A1) reduce to

$$\left.\begin{aligned} \ddot{X} &= 0 \\ M\ddot{Y} &= \bar{F} \\ I\ddot{\psi} &= r_0 \bar{F} \psi \end{aligned}\right\} \qquad \text{(A2)}$$

with the initial conditions (applying at the moment of impact t_2)

$$\left.\begin{aligned} \dot{X} &= u \\ \dot{Y} &= -v \\ \dot{\psi} &= -\omega \\ \psi &= \psi_0 \end{aligned}\right\} \quad \text{at } t = t_2 \qquad \text{(A3)}$$

where, owing to our exclusive interest in glancing collisions (terms in θ^2 negligible):

$$\left.\begin{aligned} \psi_0 &\approx \frac{\theta}{2} \\ u &\approx \omega(R_0 - r_0) \\ v &\approx \omega(R_0 - r_0)\,\theta \end{aligned}\right\} \qquad \text{(A4)}$$

R_0 being the total radius of the rotor.

Putting $t' = t - t_2$, the solution of Eqs (A2) and (A3) is

$$\left.\begin{aligned} \dot{X} &= u \\ \dot{Y} &= \frac{\bar{F}}{M} t' - v \\ \psi &= \psi_0 \cosh \xi t' - \frac{\omega}{\xi} \sinh \xi t' \end{aligned}\right\} \qquad \text{(A5)}$$

where

$$\xi = \sqrt{\frac{\bar{F} r_0}{I}} \qquad \text{(A6)}$$

For glancing collisions, the angular velocity $\dot{\psi}$ of the fragment will never fall far below ω and ψ should therefore be given approximately by

$$\psi \approx \psi_0 - \omega t'$$

Noting that the maximum loss of rotational energy occurs before $\psi = 0$, we see that the times of interest are less than ψ_0/ω which is small enough to justify expanding the hyperbolic functions in (A5) in a power series in $\xi t'$. The result is

$$\dot{\psi} = -\omega + \xi^2 t' \left(\psi_0 - \tfrac{1}{2}\omega t'\right) \qquad \text{(A7)}$$

Denoting by E_{trans} the energy of the centre-of-mass motion of the fragment and by E_{rot}, the rotational energy, i.e.

$$E_{trans} = \tfrac{1}{2} M(\dot{Y}^2 + u^2)$$

and

$$E_{rot} = \tfrac{1}{2} I \dot{\psi}^2$$

We see from Eqs (A5) and (A7) that the change in these quantities during the collision is

$$\Delta E_{trans} = \bar{F}t' \left(v - \frac{\bar{F}}{2M} t' \right)$$

$$\Delta E_{rot} = \omega I \xi^2 t' (\psi_0 - \tfrac{1}{2} \omega t') \tag{A8}$$

where terms of second order in $(\psi_0 - \frac{1}{2}\omega t')$ have been ignored. Thus, the total energy converted into core deformation is (substituting for ξ from Eq.(A6)).

$$\Delta E_{tot} = \bar{F} \left[(v + \omega r_0 \psi_0) t' - \tfrac{1}{2} \left(\frac{\bar{F}}{M} + \omega^2 r_0 \right) t'^2 \right] \tag{A9}$$

From Eq.(A8) it follows that the maximum energy converted into core deformation in the absence of rotation is

$$\Delta E_{trans}^{max} = \tfrac{1}{2} M v^2 \tag{A10}$$

while the maximum energy converted when rotation is included is

$$\Delta E_{tot}^{max} = \tfrac{1}{2} M v^2 \frac{\left(1 + \frac{\omega r_0 \psi_0}{v} \right)^2}{1 + \frac{M\omega^2 r_0}{\bar{F}}} \tag{A11}$$

In general (provided the collision angle θ is not extremely small) the mean force of impact $\bar{F}$ between a rigid body and a very heavy structure can be expected to be much larger than centripetal-like forces such as $M\omega^2 r_0$. Thus it will often be reasonable to assume that $\bar{F} \gg M\omega^2 r_0$. If this assumption is not valid, however, the effect of using it will only be to give pessimistic results, since it leads to an overestimate in ΔE_{tot}^{max}. Neglecting the second term in the denominator of the above equation, we get (very conservatively)

$$\Delta E_{tot}^{max} = \left(1 + \frac{\omega r_0 \psi_0}{v} \right)^2 \Delta E_{trans}^{max} \tag{A12}$$

By introducing the variable

$$X_M = \frac{R_0 - r_0}{R_0}$$

which signifies the fractional distance along the rotor of the centre of mass M' (at the instant of fracture t_1) and using formula (A4), Eq.(A12) reduces to

$$\Delta E_{tot}^{max} = \tfrac{1}{4} \left(1 + \frac{1}{X_M} \right)^2 \Delta E_{trans}^{max} \tag{A13}$$

On the basis of this result, a very simple model of the collision has been developed (see Fig. 3). In this the real fragment is replaced by a hypothetical rotation-free body of mass m incident on the window with a speed V (normal speed of the outer tip of the block) and angle θ. The kinetic energy of the hypothetical mass is taken to be

$$\tfrac{1}{2} m V^2 = \mathscr{E} \frac{M V_M^2}{2} \qquad \text{(A14)}$$

where $V_M (= \sqrt{v^2 + u^2})$ is the velocity (before collision) of the centre of mass M' of the real fragment and

$$\mathscr{E} = \tfrac{1}{4} \left(1 + \frac{1}{X_M}\right)^2 \qquad \text{(A15)}$$

is the factor (taken from Eq. (A13)) responsible for scaling up the energy to include an appropriate rotational component. For purposes of satisfying all dynamical and neutronic requirements, the hypothetical mass is imagined to have dimensions and neutron reflecting properties identical to those of the $(1/n)^{th}$ block on the broken part of the rotor. Only its mass, calculated from Eq. (A14), is supposed different.

To provide an illustration of the use of the above theory, we apply it to a system close to the pulsation device proposed for the SORA reactor (see Fig. 1). In this, the rotor consists of four laminar pieces (n = 4) of 90 cm radius (inclusive of the beryllium reflector block) rotating at 50 rev/sec (V = 283 m/sec). If we denote by ρ the fractional position along the rotor of the line of fracture (see Fig. 2), then the quantities M, X_M and V_M can be computed as functions of ρ from the design data. From Eqs (A14) and (A15) we then obtain the hypothetical mass m. The results of this calculation are all assembled in Table I. The last two columns of this table refer to accidents in which the 1/4 block alone breaks away from the rotor; in one case it is assumed that the block carries its fixation keys with it and in the other that the keys remain with the rotor.

APPENDIX B

MODEL FOR DESCRIBING THE EJECTION OF LIQUID METAL COOLANT DURING THE COLLISION

One of the main complications in the analysis of the collision process is the fact that, on compression, the coolant is able to escape from the core through the open entrance and exit of the system. The direction of flow is therefore axial, which is at 90° to the direction of compression. For this reason, the relaxation of the coolant is not instantaneous, but delayed by the time required for acoustic waves to traverse the compressed length $(1/n)^{th}$ of core.

In analysing this phenomenon, we do not include the effect of wave propagation across the core but assume (conservatively) that, in this direction, the whole fuel bundle is compressed uniformly. It is assumed, in other words, that although the effect of the impact is transmitted

instantaneously across the fuel bundle, the speed of propagation in the axial direction is finite and equal to the velocity c of acoustic waves in the coolant.

On the basis of this picture, we now consider the impact of the hypothetical mass m incident with a collision area $A (= A_0/n)$ and velocity $v (= V\sin\theta)$ normal to the window. By neglecting the transfer of kinetic energy to the core and reflector and ignoring the fact that the core volume change will nearly always reach the point where the fuel slugs are deformed, it is shown in Ref.[11] that the motion of the fragment is governed by the equation

$$\frac{d^3y(t)}{dt^3} + \omega_0^2 \frac{dy(t)}{dt} = \begin{cases} \dfrac{\omega_0^2}{\tau_0}\, y(t) & \text{if } t \le \tau_0 \\ \dfrac{\omega_0^2}{\tau_0}\,(y(t) - y(t-\tau_0)) & \text{if } t \ge \tau_0 \end{cases} \tag{B1}$$

where

$$y = \frac{\Delta\mathscr{V}}{\mathscr{V}_c}$$

is the fractional core volume change,

$$\omega_0 = \sqrt{\frac{\kappa A_0^2}{nmf_0\mathscr{V}_c}} \tag{B2}$$

is the natural frequency of the collision process in the absence of coolant ejection and the quantities τ_0 and κ are respectively the transit time of acoustic waves along the compressed length of core and bulk modulus of elasticity of the coolant. The boundary conditions to Eq.(B1) are

$$\left.\begin{aligned} y &= 0 \\ \text{and} \quad \frac{dy}{dt} &= \Omega \end{aligned}\right\} \text{ at } t = 0 \tag{B3}$$

where $\Omega = A_0 V \sin\theta / n\mathscr{V}_c$. Since there is no need in the present context to relate the time variable to the moment of impact t_2, t is measured from zero.

From Eq.(B1) it is clear that the importance of the ejection process depends on the magnitude of $\omega_0\tau_0$. If $\omega_0\tau_0 \gg 1$ (i.e. the natural period of the compression process small compared with the wave transit time), then the effect of ejection is negligible and Eqs (B1) and (B3) have the solution

$$y = \frac{\Omega}{\omega_0} \sin\omega_0 t \tag{B4}$$

If, however, $\omega_0\tau_0$ is not large, coolant ejection becomes significant and the terms on the right-hand side of Eq.(B1) must be taken into account. In Ref.[11], Eq.(B1) is integrated numerically and the enhancement in the amplitude and duration of the volume change caused by the ejection process are both clearly revealed. It is shown that for $\omega_0\tau_0 \lesssim 1.75$ (which covers most practical situations), the enhancement factor F is given by $F = 2/\omega_0\tau_0$.

For purposes of application in the accident studies it is sufficient to describe the coolant ejection process by writing the relative volume change in the approximate form

$$y = \frac{\Omega}{\omega_0'} \sin \omega_0' t \tag{B5}$$

where ω_0' is the reduced frequency of the collision process. The approximation (B5) fits the numerical results quite well up to the maximum of y but is poor afterwards. This error has been tolerated because the manner in which the core decompresses involves mechanisms other than the coolant and Eq.(B1) breaks down anyway. The reduction in the frequency from ω_0 to ω_0' can be regarded as due to a reduction in the bulk modulus of elasticity from κ to κ'. Using the known enhancement factor $F = 2/\omega_0\tau_0$, we can compute the reduced elasticity κ' from the fact (comparing Eqs (B4) and (B5) and using Eq.(B2)) that $\kappa/\kappa' = (\omega_0/\omega_0')^2 = F^2$. We get

$$\frac{\kappa'}{\kappa} = \tfrac{1}{4}(\omega_0\tau_0)^2 \tag{B6}$$

Applying the above theory to the particular case of a SORA-type system (for which we assume a Na coolant with $\kappa = 7.4 \times 10^{10}$ dyn/cm^2 and n = 4, $A_0 = 264$ cm^2, $f_0 = 0.139$, $\mathscr{V}_c = 5.9$ litres, $\tau_0 = 20\,\mu$sec) and using the values of m given in Table I, we get the results shown in Table II. The independent variable is again taken as ρ, the fractional distance along the rotor of the line of breakage, and the tabulated quantities are ω_0, $\omega_0\tau_0$ and the scaling ratio κ'/κ.

APPENDIX C

MODEL FOR DESCRIBING THE COMPRESSION OF THE FUEL SLUGS

In formulating the mechanics of fuel slug compression, a square lattice representation of the fuel bundle was chosen: (a) because of its amenability to analysis, (b) because more elaborate models are not more capable of eliminating the uncertainties, and (c) because it allows a larger core volume change than other lattice geometries and is therefore relatively conservative.

During compression, it is assumed that the rows of the hypothetical square array parallel to the window are all pushed together uniformly, but that the columns (perpendicular to the window) do not come in contact.

From this assumption, it follows that all the fuel slugs are deformed in the same way. They are 'squashed', effectively, by two rigid flat surfaces at opposite ends of the same diameter, the direction of this diameter being perpendicular to the window. If we let R be the radius of the undisturbed fuel slugs, E the Young's modulus, ν the Poisson's ratio and F the force per unit length of fuel slug, then the width b of the two flattened areas of the circumference where the force is applied and the depressed diameter $2(R - \delta)$ in the direction of the force are given by the well-known theory of Hertz [12]:

$$b = \left(\frac{4F(1-\nu^2)R}{\pi E}\right)^{\frac{1}{2}}$$

and

$$\delta = \frac{2F}{\pi E}(1-\nu^2)\left[\ln\frac{4R}{b} - \tfrac{1}{2}\right]$$

Writing $z(= \delta/R)$ for the relative deformation of a slug and defining

$$x = \frac{(1-\nu^2)F}{4\pi ER}$$

these equations give

$$z = -4x(\ln x + 1) \qquad (C1)$$

Equation (C1) is not in a convenient form since it expresses the deformation as a function of the force whereas we require the force as an explicit function of the deformation. Such a function can be obtained at the cost of a little accuracy by taking the logarithm of Eq. (C1):

$$\ln z = \ln x + \ln[-4(1 + \ln x)]$$

and noting that the value of the second term on the right-hand side of this expression is practically a constant equal to 3 in the whole range of interest ($0.02 \lesssim z \lesssim 0.1$). Thus we can write approximately $\ln x = \ln z - 3$, which, on substitution into Eq. (C1) gives

$$x = \frac{z}{4(2 - \ln z)} \qquad (C2)$$

This formula can be rewritten in terms of the core compression variables. Remembering that slug deformation does not begin until

$\Delta\mathscr{V} = \Delta\mathscr{V}_1$, it is obvious that

$$z = \begin{cases} 0 & \text{if } \dfrac{\Delta\mathscr{V}}{\mathscr{V}_c} \leq \alpha \\ n\left(\dfrac{\Delta\mathscr{V}}{\mathscr{V}_c} - \alpha\right) & \text{if } \dfrac{\Delta\mathscr{V}}{\mathscr{V}_c} \geq \alpha \end{cases} \qquad \text{(C3)}$$

where $\alpha = \Delta\mathscr{V}_1/\mathscr{V}_c$. In addition, if N is the mean number of fuel elements in the rows parallel to the window, L the length of the core and F_s the total force applied to the slugs by the $(1/n)^{th}$ rotor fragment, then the mean force per unit length on one slug is given by

$$F = \frac{n}{NL} F_s$$

i.e.

$$x = \frac{(1-\nu^2)n}{4\pi ERLN} F_s \qquad \text{(C4)}$$

Combination of Eqs (C2), (C3) and (C4) leads immediately to Eq.(17).

APPENDIX D

BEHAVIOUR OF THE FUEL MATERIAL AT THE HIGH TEMPERATURES AND PRESSURES GENERATED DURING A DESTRUCTIVE EXCURSION

There are two problems to consider: the generation of pressure prior to the termination of the nuclear excursion and the expansion of the fuel subsequent to termination.

(a) Pressure generation

The relationship between the pressure p and energy input per unit mass Q (section 2.1) must be derived within the proper context. Before the commencement of the excursion, the fuel is in the solid state at a temperature T_0 and the coolant is present in the core. This starting condition is different from that assumed for an extreme hypothetical accident in a fast power reactor. In a power reactor, the initiating event is usually taken to be a stoppage in the flow of the coolant followed by its evaporation out of the core and the melting of the fuel and cladding material. The collapse of this molten assembly under gravity is then supposed responsible for the insertion of a destructive reactivity ramp, the effective fuel density during the excursion being reduced from the theoretical value by the fact that the fuel can expand internally to fill the voids vacated by the coolant.

In the case of a pulsed fast reactor, the nuclear excursion is not preceded by a core melt-down and consequently the coolant still occupies the coolant channels when the fuel temperature begins to rise. The melting and thermal expansion caused in the fuel by this rise leads immediately to the swelling and breaking of the cladding and the compression of the coolant in the channels between the fuel elements. The lateral dimensions of these channels are very small in the compact core of a pulsed fast reactor so that the effect of the pressure rise in the fuel propagates into the coolant channels within a fraction of a microsecond. The effective fuel density in this case is much closer to its normal density than for the usual power reactor since the only internal expansion which occurs is that performed in compressing the coolant.

It is for this reason (i.e. the relative absence of internal void) that the threshold for pressure generation, Q_2^*, is significantly lower for a pulsed fast reactor than a power reactor. The calculation of Q_2^* and the other parameters γ_2, Q_1^* and γ_1 of the p-Q relation assumed in Eqs (31) and (32) is somewhat complicated by the unknown extra volume made available to the fuel by the compression of the coolant. However, since the total volume of coolant is small anyway, not much error is incurred by assuming that the fuel expands to fill the whole volume occupied by coolant. This assumption is definitely conservative since it has the effect of lowering the calculated pressures and thereby the predicted shut-down reactivity.

The problem which now presents itself in the light of the above discussion is that of evaluating the p-Q relation in the same way as has been done for power reactors, i.e. on the assumption of an initial voidage equal to the volume of coolant in the core. The only difference is that, because of the close-packed character of the fuel bundle, this voidage is much smaller in the present case than for a normal power reactor.

During disassembly, the overall core volume change necessary to terminate an excursion is so small that the generation of pressure can be assumed to occur at essentially constant fuel density. Thus, it is a good approximation to evaluate the pressure p and temperature T on the assumption that the specific volume of the fuel v remains constant and that the heat input Q is equal to the specific internal energy E.

To do this, it is necessary to know the p-v-T relation (equation of state) and T-E relation (with v = const.) for fuel materials over a wide range, including the two phase liquid/vapour region. Information for these materials, however, is almost totally lacking and workers in the field have been forced to deduce the above relations from the properties of other materials, using the principle of corresponding states (e.g. Refs [5-7]).

Despite the uncertainties in this approach (particularly for a metallic fuel) it appears to be the best available at present. Our calculations [14] therefore follow the same pattern. For purposes of speed and flexibility, a two-part computer programme (EQUSTA) has been designed [14] to perform (in its first part) all the necessary arithmetic. EQUSTA contains a library of all the relevant data tabulated by Hougen et al. [8] and processes this automatically for any conditions and materials of interest.

In Fig. 4 is shown the calculated pressure and temperature of uranium metal with a constant density of 14 g/cm^3, Q being measured relative to

liquid uranium at the melting temperature of 1400°K. 14 g/cm^3 is the density of the fuel in SORA after expansion into the coolant channels in accordance with the above assumption. (In the studies of section 3.2 the fuel was initially at 473°K and it was necessary to imagine the p-curve shifted by 280 J/g.) The molten fuel fills all the coolant channels before the normal boiling temperature is reached, which accounts for the rather sudden initial rise in the pressure. It must be stated, however, that the errors in the basic data [8] are appreciable for such a large density as 14 g/cm^3 and the results in Fig. 4 would be somewhat inaccurate (as can be seen from the scattering in the calculated points) even if the principle of corresponding states were valid.

(b) Isentropic expansion

After the completion of the nuclear excursion the hot fuel expands rapidly and the work performed in this process serves to accelerate and/or compress all objects in the environment of the core, including the material of the core itself. The kinetic and/or strain energy thus generated is equal to the work done and the hazard to the containment can therefore be assessed in terms of the work.

The process of expansion occurs so rapidly that heat transfer effects can probably be neglected. For this reason it is usual (e.g. Ref. [5,7]) to evaluate the work done by assuming that the expansion of the fuel is isentropic. If this assumption is not good, the only consequence will be that the calculated work is conservative. Given Q (i.e. $Q(r,\infty)$), the internal energy of a unit mass of fuel, the problem is therefore to determine the isentropic work W_s done as this unit mass expands to atmospheric pressure.

Because of the lack of information on fuel materials it is again necessary to appeal to the principle of corresponding states. On this basis, the second part of the programme EQUSTA evaluates the W_s - Q relation using the tables of Hougen et al., a calculation which can be performed for any conditions or materials.

The results of applying EQUSTA to metallic uranium are shown in Fig. 5. Calculations were performed for several initial fuel densities and, within fluctuations in the data, the W_s - Q relation seems to be independent of ρ_f. Q is again measured relative to just-molten uranium.

REFERENCES

[1] BETHE, H.A., TAIT, J.H., UKAEA Rep. RHM (56)/113 (1956).

[2] JANKUS, V.Z., Physics of Fast and Intermediate Reactors (Proc. Semin. Vienna, 1961) 3, IAEA, Vienna, (1962) 209.

[3] NICHOLSON, R.B., Nuc. Sci. Engng. 18 2 (1964) 207.

[4] WOLFE, B., FRIEDMAN, N., RILEY, D., ANL-6792 (1963) 171.

[5] BROUT, R.H., APDA-118 (1957).

[6] MEYER, R.A., WOLFE, B.E., Trans. Am. Nuc. Soc. (June 1964).

[7] MENZIES, D.C., UKAEA TRG Rep. 1119 (D) (1966).

[8] HOUGEN, O.A., WATSON, K.M., RAGATZ, R.A., Chemical Process Principles, Part II: Thermodynamics, Chap. 14, Wiley, New York, 2nd ed. (1959).

[9] RIEF, H., KSCHWENDT, H., JAARSMA, R., Proc. Int. Conf. Research Reactor Utilization and Reactor Mathematics, Mexico City (May 1967) and private communication.

[10] BONDARENKO, I.L., STAVISSKII, YU.YA., J. nucl. Energy A/B 14 (1961) 55.
[11] RANDLES, J., JAARSMA, R., to be published in a Euratom report (1967).
[12] FLÜGGE, W. (Ed), Handbook of Engineering Mechanics, McGraw-Hill (1962) 42-4.
[13] NICHOLSON, R.B., APDA 139 (1960).
[14] RANDLES, J., to be published.
[15] RANDLES, J., J. nucl. Energy A/B 20 (1966) 713.

DISCUSSION

P. VANDEPLAS: In order to avoid the type of accident you mentioned, could you not align the moving parts in a plane parallel to the reactor window, rather than in a plane perpendicular to it?

J. RANDLES: I'm afraid the answer to this question is rather outside the scope of my paper. Parallel alignment is not feasible from the engineering viewpoint since the bearing of the pulsation device would tend to obstruct the coolant circuit. In the early design stage of SORA a semi-parallel solution was contemplated but this involved so many complications that it was abandoned. Though the present (final) solution involves a velocity component towards the window, it embodies a much higher mechanical safety factor than the previous designs and therefore has greater overall safety. In particular, rotation can be realized in a horizontal plane without distorting the rest of the system and the irradiation of the bearings and rotor is minimized.

A NEW FAST PULSED REACTOR, VIPER

J.W. WEALE, H. GOODFELLOW, M.H. McTAGGART AND E.G. WARNKE
UNITED KINGDOM ATOMIC ENERGY AUTHORITY,
ALDERMASTON, BERKS, UNITED KINGDOM

Abstract

A NEW FAST PULSED REACTOR, VIPER. The design of a new, versatile fast pulsed reactor is described. The reactor is fuelled with uranium of medium enrichment in the form of metal rods set in a matrix block. The composition of the matrix block and the disposition of the fuel elements can be varied. The reactor is pulsed into the prompt critical condition by rapid insertion of a fuel rod and the subsequent nuclear transient is terminated by the inherent negative temperature coefficient of reactivity. The important new features of this reactor are that the Doppler effect in ^{238}U provides a large part of the temperature coefficient and that the core composition can be changed so as to vary both the neutron lifetime and the Doppler effect.

INTRODUCTION

A new pulsed fast reactor named VIPER has recently been commissioned at the United Kingdom Atomic Energy Authority Establishment, Aldermaston. It is designed as a research reactor producing very intense pulses of neutron and γ radiation at a frequency of one or two pulses per day. VIPER is similar to earlier fast pulsed reactors in being driven prompt critical by the rapid insertion of a central fuel rod and in terminating the pulse by an inherent temperature coefficient of reactivity, but it has several important new features. In particular it utilises the Doppler effect in ^{238}U to provide a large part of the inherent temperature coefficient, and the core is designed so that its composition can be changed, thus varying both the neutron lifetime and the Doppler effect. The design and performance of VIPER are therefore of some interest in the general field of fast reactor physics studies. In the present paper a general description of the design and construction of the reactor are given and in a companion paper [1] the physics characteristics established in the commissioning programme are described.

DESIGN PRINCIPLES

The basic design specification was to provide a source of neutrons and γ-rays corresponding to a burst of about 2.10^{17} fissions in a period of the order of 1 msec. It was considered desirable to be able to change the pulse width when necessary without changing the total dose, and provision was required for the accommodation of experimental samples.

It was decided that sufficient flexibility to meet the likely requirements for variation of pulse width or of irradiation space would best be provided by using fuel in the form of rod-shaped fuel elements. These could then be re-arranged as necessary to vary the composition, the size or the shape of the core. However, since the provision of a large irradiation cavity inside a fast reactor core requires a rather large inventory of fissile material, it was decided that a cavity for large irradiation samples would be provided by incorporating it in a thick non-moderating reflector. The provision of a reflector has the additional advantages that it reduces the critical mass of the system and de-couples the core from its surroundings. The latter is a desirable feature in a pulsed reactor because the increment of reactivity above prompt critical must be carefully controlled.

The relationships between the basic quantities determining the characteristics of a fast pulsed reactor are as follows [2]:-

$$F = \frac{2\rho}{\mu} \qquad \ldots\ldots\ldots(1)$$

$$W = \frac{3.5}{\alpha} = \frac{7\tau}{F\mu} \qquad \ldots\ldots\ldots(2)$$

$$K_o - K_f = 2K_o\rho \qquad \ldots\ldots\ldots(3)$$

$$\left(\frac{dF}{dt}\right)_{max} = \frac{\alpha F}{4} \qquad \ldots\ldots\ldots(4)$$

In these equations

F = total number of fissions produced in the pulse

ρ = reactivity increment above prompt critical

μ = prompt temperature coefficient of reactivity

W = width of pulse at half maximum

τ = mean neutron lifetime

$\alpha = \frac{\rho}{\tau}$ = reciprocal of prompt period

$K_o = 1 + \rho$ = prompt multiplication factor immediately after the reactivity insertion

K_f = prompt multiplication factor when the pulse is complete.

The number of fissions that can safely be produced per pulse is determined by the heat capacity of the fuel and by the maximum temperature to which the fuel can be raised without deterioration of its physical properties. The design was based on uranium metal fuel able to withstand repeated pulsing to a maximum of 400°C, and this then determined the required mass of fuel for a 2.10^{17} fission pulse as about 200 kg.

If the fuel is packed to a reasonably high density the ^{235}U critical mass of a reflected system is very much less than 200 kg and the design therefore allows the use of uranium at an intermediate enrichment. It is then possible to take advantage of the Doppler effect as a major component of the inherent shut-down mechanism and this is a desirable step because without a Doppler contribution the inherent shut-down would be provided only by longitudinal expansion of the fuel rods and would be inconveniently low. It can be seen from equation (1) that if the shut-down coefficient μ is small the required yield F is produced by a small reactivity increment, and the accurate control of F can then be achieved only by very precise control of reactivity. Also, from equation (2), if F and τ are fixed, a small value for μ leads to a large pulse width which is an undesirable limitation. It turns out that by using uranium at 37% enrichment and incorporating a small proportion of hydrogenous material to increase the low energy neutron population the Doppler temperature coefficient can be made large enough to compensate fully for the loss of effective fuel expansion in two dimensions. Thus the flexibility of a fuel pin core construction can be obtained without sacrificing the required characteristics of the reactor pulse. Typical reactor characteristics for a 400°C pulse can be obtained by substituting

$F = 2 \times 10^{17}$ fissions, $\mu = -1.5 \times 10^{-5}$ per °C and $\tau = 10^{-7}$ sec into equations (1), (2), (3), and (4). We obtain, $\rho = 20$ cents, $W = 400$ μsec, $\left(\frac{dF}{dt}\right)_{max} = 20\ 000$ MW.

The calculated neutron dose, peak neutron flux and γ-ray dose at the core centre for a system with these parameters are 10^{15} n/cm^2, 3×10^{18} n/cm^2 sec and 3×10^4 rad respectively.

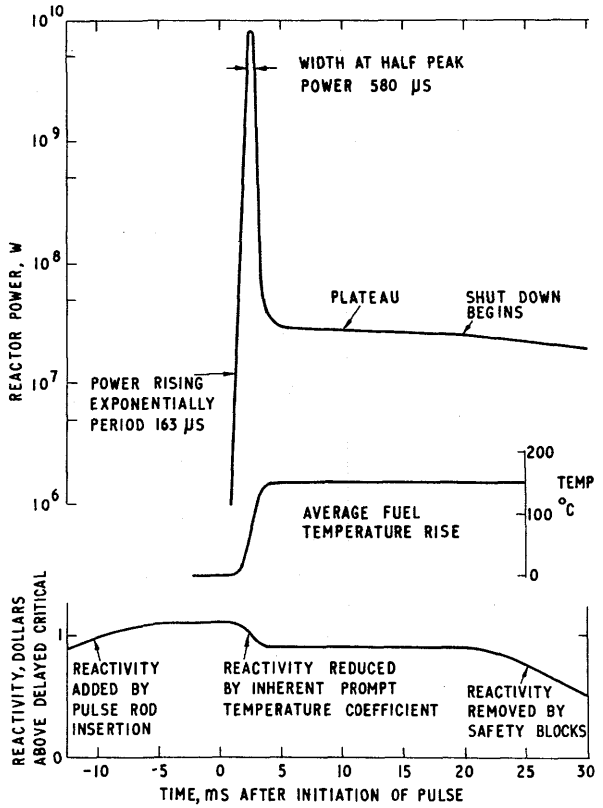

FIG.1. Time variation of reactor power, temperature and reactivity in a prompt critical pulse.

The general characteristics of a reactor pulse are illustrated in Figure 1 (for convenience a half-size pulse is shown). The insertion of the pulse rod causes a step increase of reactivity to 10 cents above prompt critical; the power transient then begins and rises with a 163 μsec period until significant heating starts. As heating continues the reactivity is reduced by the temperature coefficient until it falls below prompt critical at which point the power starts to fall again. Heating however continues until the power falls to a relatively low value and the reactivity is then as far below prompt critical as it was initially above prompt critical (equation (3)). The power then flattens off at a value of about 20 MW, maintained at this level by the multiplication of delayed neutrons. The transient is then terminated by the movement of shut-off blocks.

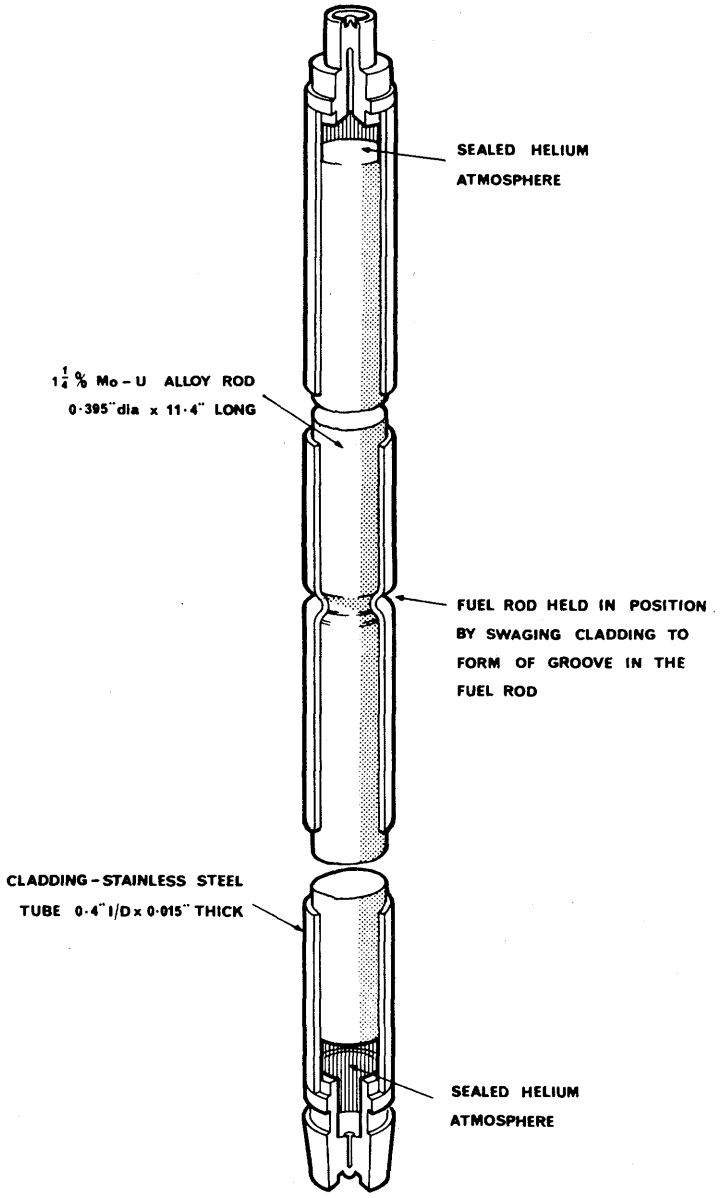

FIG.2. Fuel can assembly.

CORE CONSTRUCTION

The uranium fuel, at 37.5% enrichment, is in the form of cylindrical rods, each 11.4 in. long and 0.400 in. in diameter, clad in stainless steel. The cladding is designed to prevent corrosion if the core is exposed to air when hot, and also to provide a means of holding each fuel rod at its mid-

point so that the forces developed during the pulsed heating are balanced and do not load the reactor structure. The cladding is secured to the fuel rod by forming it into a circumferential notch which is cut into the fuel rod around its centre. An illustration of the fuel element design is shown in Figure 2. Each element is cast and machined to size and contains 418 g of uranium, thus 155 g of ^{235}U.

The fuel rods are loaded into the core as a triangular lattice of pitch 0.51 in. as shown in the core plan in Figure 3. There is a fixed central block, 8 in. by 15 in., which contains spaces for 478 elements and two side blocks each containing spaces for 133 elements. Each block is enclosed in a stainless steel box. The side blocks are attached to hydraulic rams and can be slowly raised into position to assemble the critical core, or rapidly driven down to shut down. There is a central hole into which the pulse rod is driven to initiate the prompt critical transient. A section view of the

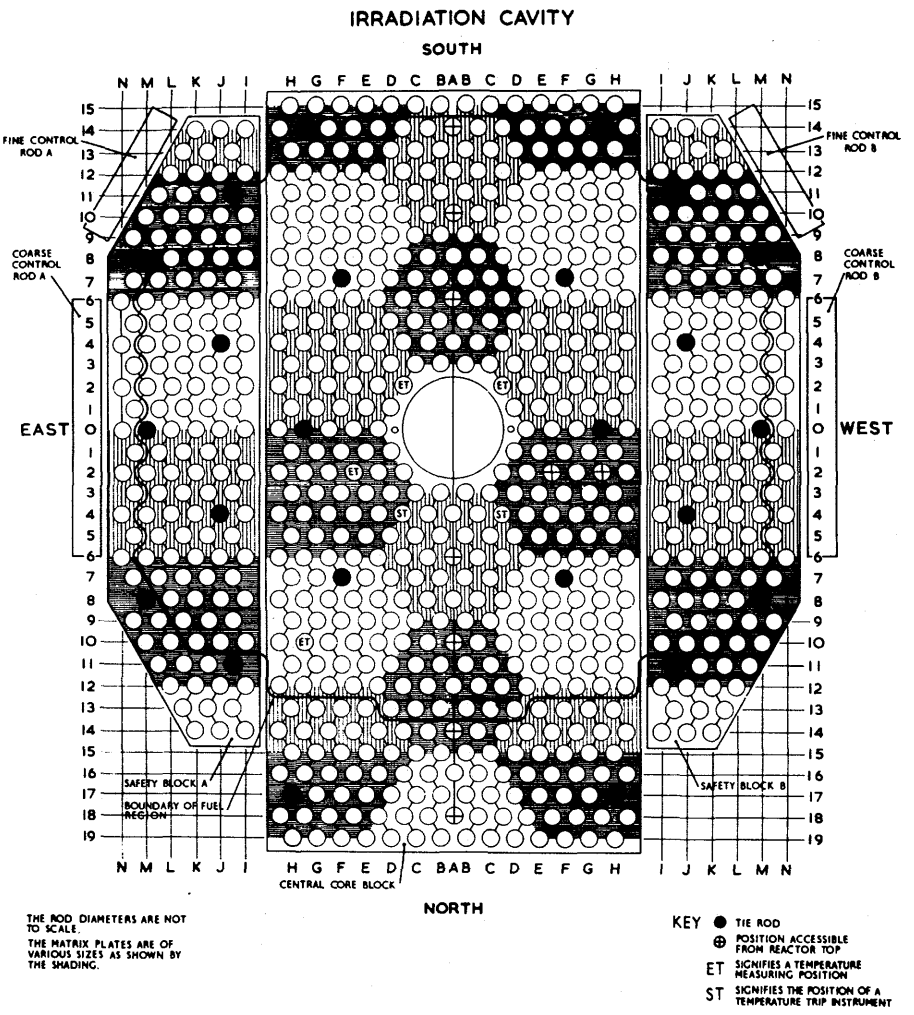

FIG.3. VIPER pulsed reactor core plan.

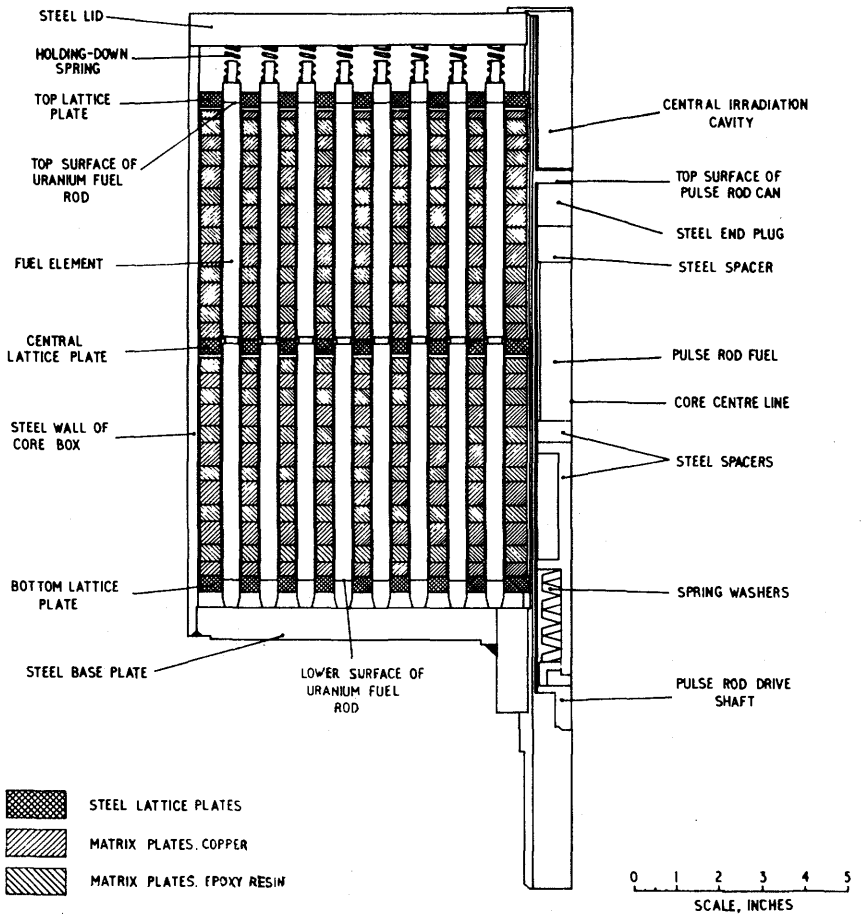

FIG.4. Vertical section of the pulsed reactor core from the centre line to the north side.

core is shown in Figure 4. The fuel elements are located by three low-expansion-steel lattice plates which accurately define the triangular matrix. The holes in the central plate are displaced radially outwards by 0.010 in. with respect to the holes in the top and bottom plates so that the fuel elements are prevented from bowing inwards when heated. The elements rest on a steel base plate and are held down by springs bearing on the core box lid. The springs are strong enough to ensure that each element remains seated on the base plate after the pulse expansion and contraction cycle is complete. The space between the fuel elements and the lattice plates is filled with matrix plates which can be of copper or of an aluminium-loaded epoxy-resin. The matrix plates are available in thicknesses of 0.375 in. or 0.187 in. and in various shapes designed to fit together as shown in Figure 3 to form layers which fill the core boxes. The matrix area is divided in this way to provide room for the expansion of the materials when the reactor is heated. The amount of hydrogen in the core can be varied by varying the number of epoxy-resin pieces loaded into the core matrix. Generally the matrix material is the same in any one horizontal layer, as shown in Figure 4,

which represents the loading used for the first assembly, VIPER 1. The core is loaded to critical and any spare lattice positions are then filled with copper rods of approximately the same dimensions as the fuel elements. The outline of the core loading used for VIPER 1 is indicated by a black line in Figure 3. Provision is made for access through holes in the core and reflector lids to certain fuel element positions for reaction rate measurements required during reactor commissioning. Holes can be made as required in any other position but access is then obtained only by raising the lid. Certain positions, indicated by the black circles in Figure 3, are occupied by tie rods which secure the core box lids to the base plates.

An illustrative isometric view of the reactor core is shown in Figure 5.

The maximum volume fraction of uranium alloy in the core is 45% and the minimum voidage amounts to 12.6%. The actual volume fractions in VIPER 1 are as follows:-

Fuel	Steel	Copper	Epoxy Resin	Void
45.0	14.0	14.0	9.5	17.5

The atomic ratio $H/^{235}U$ is 0.46.

Although the core construction allows a large number of different systems to be built, it is likely that, for reasons of simplicity and safety, only two other variants will be constructed. One, designed to produce a wider pulse, will contain approximately twice as much moderator and one, designed to produce a narrow pulse, will contain no moderator.

REACTOR LAY-OUT

A plan of the reactor core and reflector is shown in Figure 6 and a section view is shown in Figure 7. The core is surrounded by a solid copper reflector at least 8 in. thick on all sides, the top reflector being in the form of a single slab which can be raised to give access to the top of the core. Two fine and two coarse control rods loaded with boron enriched in ^{10}B are provided at the outer edge of the core for reactivity adjustment. They are driven up or down by motors mounted on the reflector lid. When fully down the boron-loaded region extends over the full core height and when fully raised the space is filled by brass followers. Part of the side reflector is in the form of removable blocks and the base plate is extended on that side so that a large irradiation cavity about 13 in. square and 11 in. long can be provided when necessary by re-arranging the reflector blocks. This cavity can be directly adjacent to the reactor core and provision is therefore made to insert a "Boral" plate to decouple the core from any slow neutrons produced in an irradiation experiment. A space for smaller irradiation experiments is provided by the top portion of the central hole in which the pulse rod moves, access being provided by a removable plug in the top reflector. This central irradiation cavity is 1.75 in. diameter and 3.5 in. long and is 3 in. from the core centre at its nearest point. Two other experimental holes are provided in the corners of the reflector. On the north side of the reactor there is a 4 in. plug which can be removed to allow access for a pulsed neutron source used for neutron lifetime measurements and for time of flight spectrometry. For the latter experiments provision

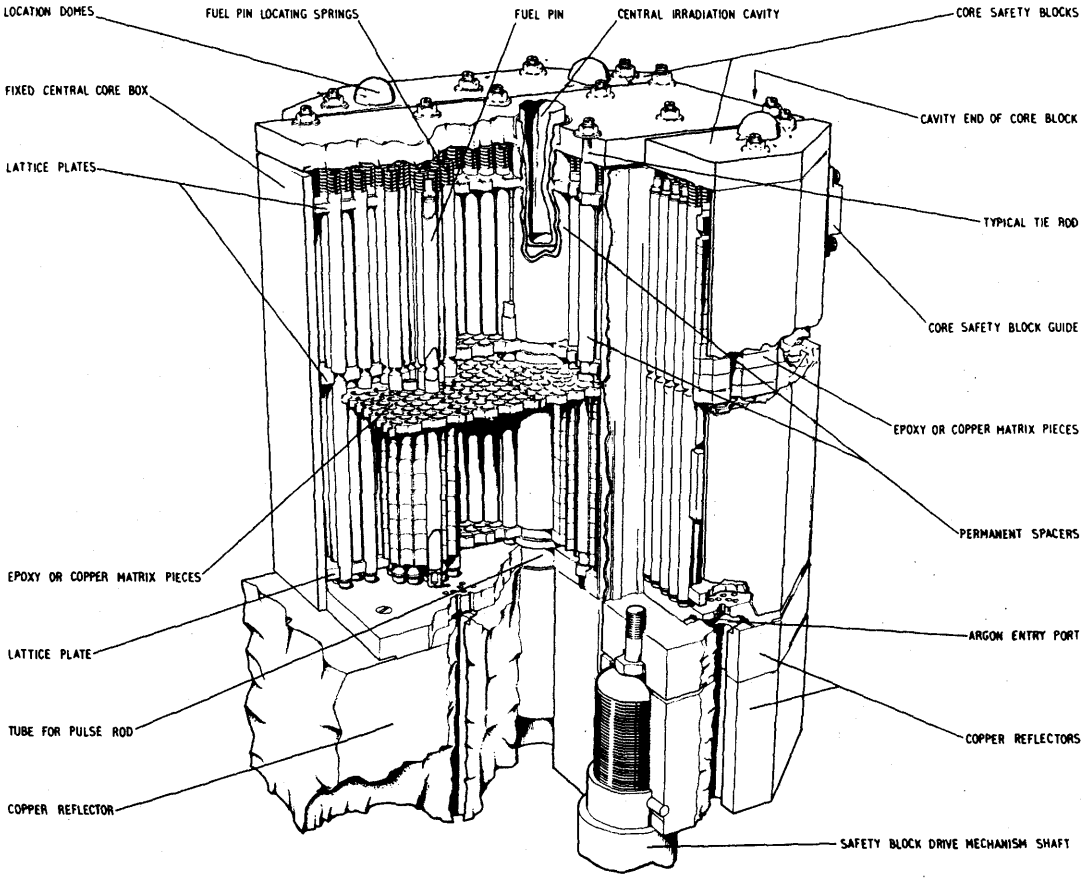

FIG.5. Pulsed reactor core.

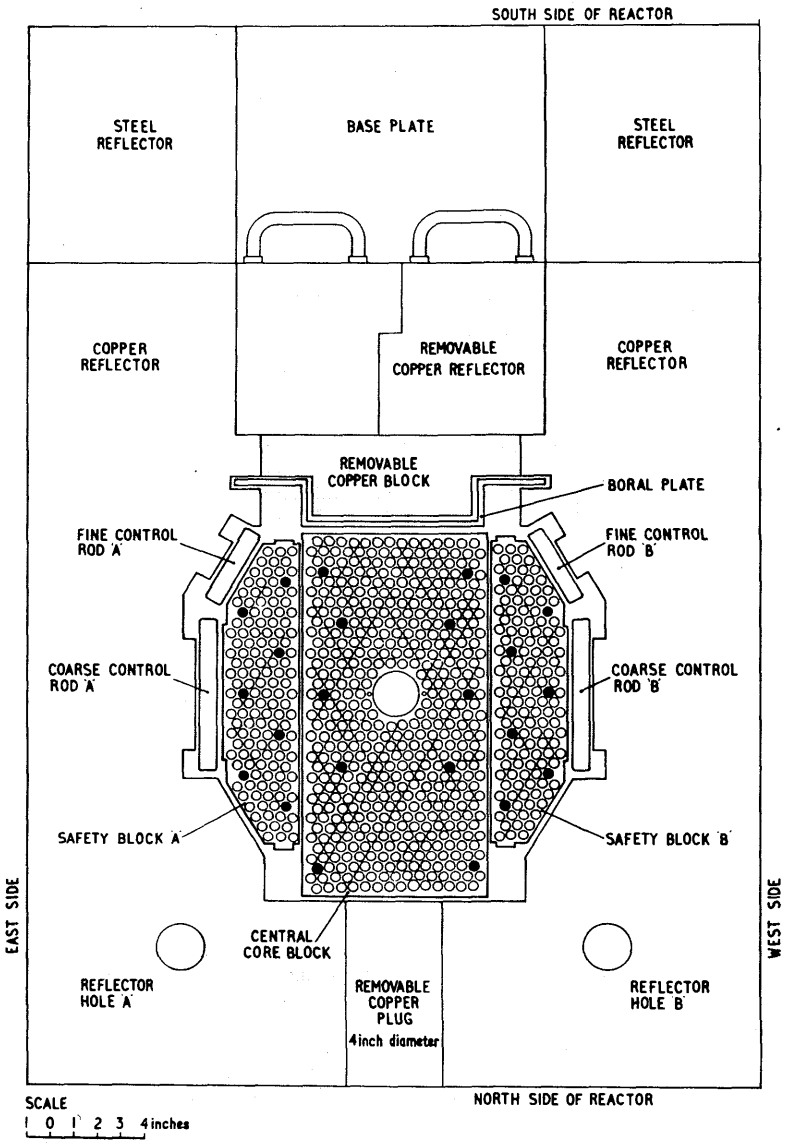

FIG.6. Plan of the core and reflector of the VIPER pulsed reactor.

is made to extract a neutron beam through the region of removable blocks on the south side. The reflector region below the core is extended in the form of a skirt to act as a radiation shield around the safety blocks when they are lowered.

A general view of the reactor is shown in Figure 8. It has a base measuring 9 ft × 9 ft, is 13 ft high and weighs 12 tons. The main feature of the operating mechanism is the hydraulic system for fast withdrawal of the safety blocks immediately after the reactor pulse. Energy for this purpose

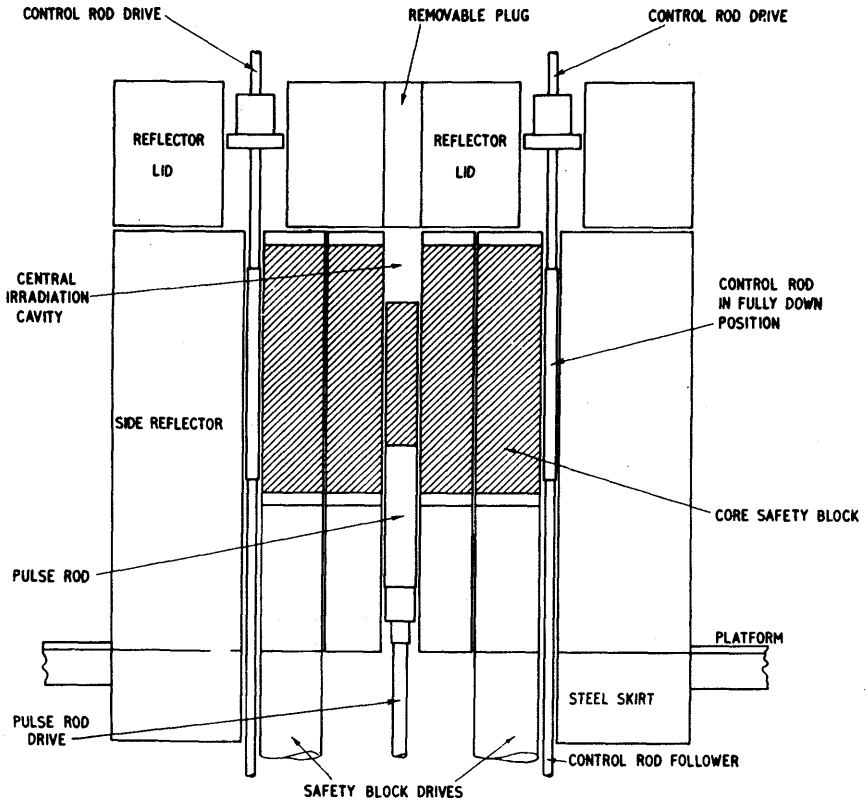

FIG.7. Vertical section of the core and reflector of the VIPER pulsed reactor.

is stored in compressed nitrogen in a series of hydraulic accumulators, three for each safety block. Other ancillary items are a neutron source to provide an adequate neutron flux during start-up, a pneumatic drive system for the pulse rod and a hoist for the reflector lid. There is also a pulsed neutron source to initiate the reactor pulse when required. Provision is made to supply argon gas to the reactor core continuously so that the core components are always surrounded by an inert atmosphere when hot. The reactor has no forced cooling system and it requires about 6 hours to cool after a full size pulse.

The reactor is mounted on a substantial frame which can be moved along rails. It is housed in a large concrete-walled containment cell which also houses the low power experimental fast reactor VERA [3]. VIPER and VERA are operated as alternative facilities and the VIPER reactor is mounted on rails so that it can use the accelerator-driven pulsed neutron source and the neutron flight tube when necessary during commissioning experiments. The lay-out of the reactors and other facilities is shown in Figure 9.

MODES OF OPERATION

For pulsed operation the reactor is first brought to delayed critical by the normal reactor assembly procedures, with the pulse rod fully down. An accurate balance point is obtained and one of the control rods is then adjusted

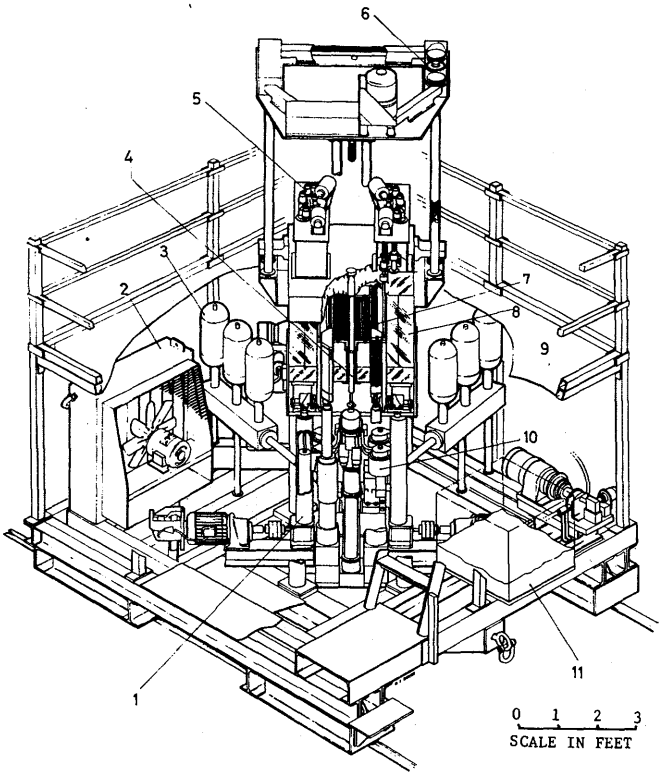

1 Core safety block drive mechanism
2 Hydraulic oil cooler
3 Safety block drive hydraulic accumulators
4 Pulsing rod
5 Control rod drive mechanism
6 Top reflector lifting mechanism
7 Core
8 Reflector
9 Working platform
10 Packaged hydraulic unit for core safety block mechanism
11 Neutron source storage block

FIG.8. General view of the VIPER pulsed reactor.

to reduce the reactivity of the system by the necessary amount. The adjustment is chosen so that when the pulse rod is fully raised the required increment of reactivity above delayed critical is obtained. Thus the pulse rod worth and its stroke remain constant (for any particular reactor system) but the starting point on the reactivity scale is varied. As a check on this starting point the necessary control rod adjustment is made and the reactor is re-balanced by raising the pulse rod. The control rod positions are then locked, the pulse rod is driven fully down and one of the safety blocks is lowered so that the neutron population decreases to a low level. After 15 min, when the neutron population is sufficiently low so that a persistent chain reaction is unlikely to start during the reactivity increment, the safety block is raised to its fully up position and the pulse rod is driven fully up. As soon as the pulse rod is fully up the pulsed neutron source is operated to start the reactor transient. By operating in this way the time of occurrence of the transient is fixed and the plateau following the pulse can be terminated very rapidly by a pre-set shut-down signal from a sequence control unit. This procedure ensures that the full fission yield is concentrated in the pulse region of the transient.

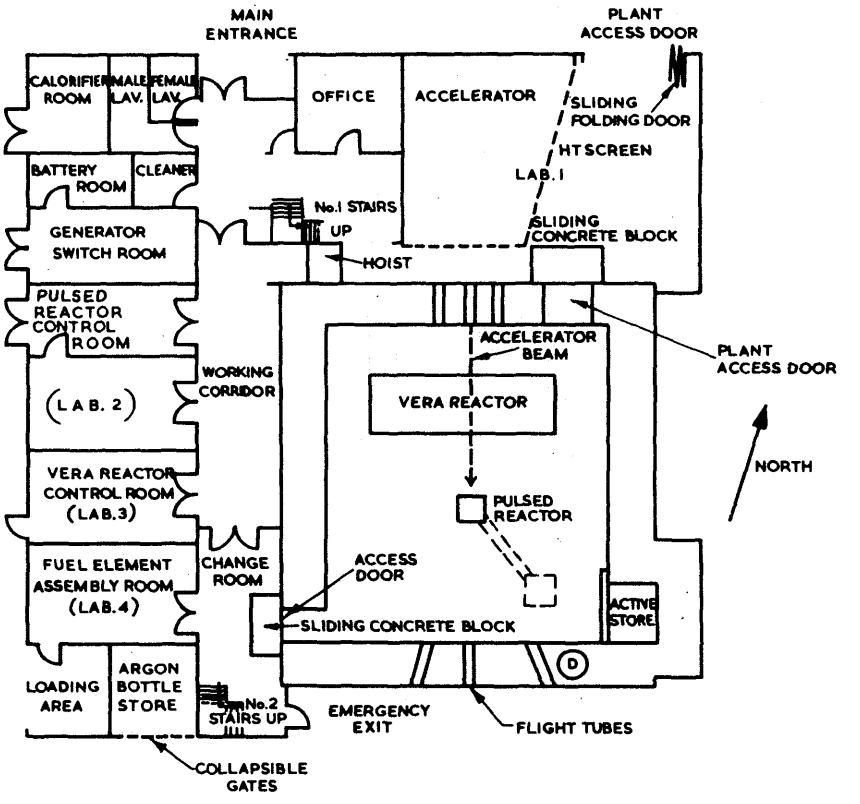

FIG.9. Ground floor plan of the reactor building.

During the commissioning of the reactor, in order to establish safely the size of the temperature coefficient, it is necessary to operate transients which do not reach the prompt critical region. For these the sequence timer is not used. The transient is then terminated by high power or high temperature signals or by the manual control of the operator.

CONTROL AND INSTRUMENTATION

The reactor is controlled by movement of safety blocks or control rods. The safety blocks, which are portions of the fuel region of the core, are each worth at least 5% in reactivity. They are lowered to provide the necessary margin of safety when the reactor is being loaded with fuel or with irradiation samples and they are subsequently raised as the first step in the approach to critical. Upward movement over the 12 in. stroke is complete in 3 min. The blocks are driven rapidly down, with an acceleration of about 5 g, to terminate the plateau heating following a prompt critical reactor pulse. Each block is supported on a 3 in. diameter rod driven by a double-acting 4 in. diameter hydraulic piston. The pressures on either side of this piston are adjusted so that the net upward force is sufficient to raise the block but its movement is accurately controlled by a lead-screw and nut. When rapid shut-down is required the trip signal opens vent valves in the lower cylinder and the pressure in the upper cylinder then drives

the block down, using stored energy from a hydraulic accumulator. The block begins to move 18 msec after the current supply to the vent valves is broken by the trip signal and the block moves 7.5 in. in 100 msec.

The control rods are brass boxes loaded with enriched boron. Each coarse rod contains about 440 g of ^{10}B and is worth about 1.2 dollars; each fine rod contains about 70 g of ^{10}B with a reactivity worth of about 0.3 dollars. The control rods provide sufficient reactivity to balance the effect of irradiation samples and to provide an alternative means of reactor shut-down and they are also used to balance the reactor accurately at the critical condition. The drive speeds are 6 in. min^{-1} for the coarse rods and 3 in. min^{-1} for the fine rods and the stroke is 12 in. The control rods cannot be driven unless both safety blocks are fully raised. If the safety lines are broken all four control rods drop under gravity to their fully down positions.

The pulse rod, which is illustrated in Figure 4, consists of a steel tube containing a 1.55 in. diameter, 5 in. long cylinder of uranium metal which is of the same type and enrichment as used for the fuel elements. The mass of fuel, approximately 1 kg of ^{235}U, is adjusted to provide the necessary increment above prompt critical when the pulse rod is driven from its fully out to its fully in position. A pneumatic drive insertion system is provided and this drives the rod through its 14 in. stroke in about 200 msec at a maximum speed of 16 ft sec^{-1}. The pulse rod may also be driven slowly by a nut and lead-screw system.

During start up and steady state operation three low power pulse channels and three medium power current channels are used. The pulse detectors are fission chambers, located in polythene cylinders at the outside of the reflector. Each detector is connected to a type 4065B amplifier with low, high and period trip circuits and the output pulse rates can be recorded on a scaler, or displayed on a linear or logarithmic recorder. The RC6 type ion chambers for medium power are contained in similar polythene cylinders. Each is connected to a type 4061B amplifier with low, high and period trip circuits and all the outputs can be displayed, as the logarithm of the power, on a pen recorder.

The pulse channels cover the power range 0.2 mW to 100 mW and the current channels cover the range 20 mW to 2 kW.

An additional current channel which has no trip circuits, provides a linear output covering the power range from 20 mW to 2 kW. Its output is used for period measurements and reactivity calibration.

During all transient and pulsed operations two channels using NaI scintillators and photodiodes are used to shut the reactor down at a preset power level between 20 W and 3 MW. These trips operate the safety block release mechanism directly, thus providing a rapid shut-down. The safety blocks start to move 45 msec after the trip level is exceeded. Each detector has a pulsed light source built into the scintillator assembly to provide a calibrating and test current corresponding to 3 MW reactor power. The detectors are mounted on the north side of the reflector.

A plastic scintillator photomultiplier channel is provided for measuring reactor power during transients in the power range up to 10 MW. The output is recorded on an ultra-violet chart recorder or on an on-line computer which is used for rapid analysis of reactor period as a function of time. For higher power transients a plastic scintillator photodiode channel is used and the output is recorded on an oscilloscope. Both of the transient measuring units are mounted on the top frame of the lid hoist.

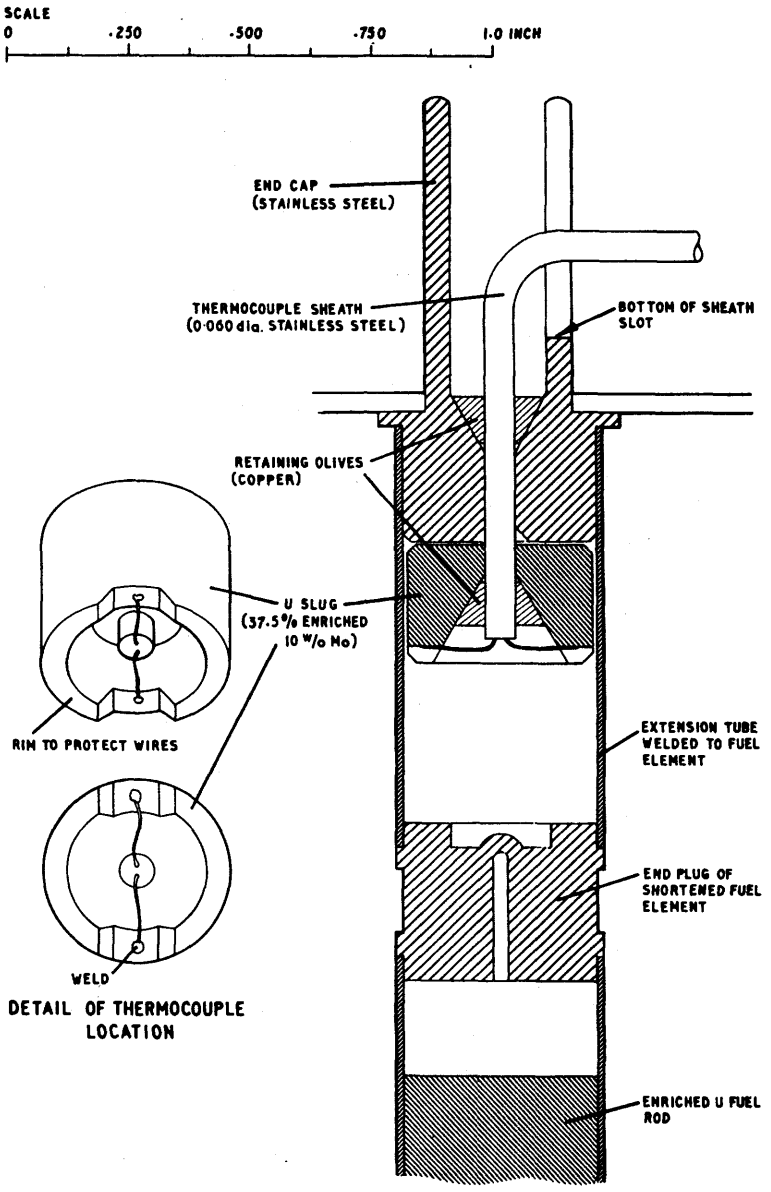

FIG.10. VIPER thermocouple assembly for fast response temperature trip (channels ST1 and ST2).

Two thermocouples are used to shut the reactor down if a pre-set temperature of the fuel is exceeded. These thermocouples are welded to cylindrical fuel pieces mounted in shortened fuel elements as shown in Figure 10. The materials used are chromel-alumel and the wires are separately welded to the uranium. The trip increment setting is variable from 10°C to a temperature corresponding to a central fuel temperature of 200°C. (The

setting depends on the stage reached during commissioning and the position of the fuel rod containing the thermocouple.) The amplifier (type AEI FNC61) contains test and interlock features which are designed to make it trip if the thermocouple continuity is broken or the unit fails to function correctly. The trip relays are connected directly to the safety block release mechanism and the response is sufficiently rapid to start the safety blocks moving 70 msec after the pre-set temperature is reached.

Because the output from the trip thermocouples is not suitable for recording, the signals from two similar thermocouples with a range from 50°C to the equivalent of 800°C central fuel temperature are used for this purpose. They are displayed on charts visible to the reactor operator and can also be recorded on the ultra-violet chart recorder.

To ensure that the reactor pulse does not start from too high a temperature and that the reactivity balancing is not significantly affected by temperature drift the temperature of the centre part of the central lattice plate is monitored by a thermocouple feeding a trip amplifier. If this temperature exceeds 20°C above ambient the reactor cannot be started. During steady state operation at high power, if the core temperature exceeds 40°C this thermocouple will trip the reactor. A similar thermocouple is used to monitor the temperature of the epoxy resin in this region.

The most accurately controlled system of shutting down the reactor after a transient is by means of the sequence timers. Two of these are provided, both fulfilling the same function. Normally these are the effective shut-down signals and the γ-sensitive trip units and temperature-sensitive trip units have only a safety back-up function. The main advantage of the timer is that it can be set to terminate the transient immediately after the prompt pulse is complete thus eliminating most of the heating from the plateau region (Figure 1). The timer is set to initiate the prompt transient by firing the pulsed neutron source as soon as the pulse rod is fully in, and to initiate the shut-down action shortly before this. Thus the reactor pulse takes place during the interval after the shut-down signal has been initiated but before the safety blocks have started to move.

LIMITATIONS OF MATERIALS

The maximum pulse yield is determined by the permissible growth of the uranium under thermal cycling, the possibility of deformation or fracture of the uranium as a result of the stresses caused by rapid heating, and the deterioration of the epoxy resin due to chemical changes at high temperature.

It was considered that uranium alloyed with 3% (by atoms) of molybdenum would be more resistant to thermal cycling growth than unalloyed uranium. Tests were done at various temperatures up to 600°C against the specification that the growth produced by 1000 cycles up to at least 400°C should not exceed 1%. The results showed that both materials would meet the specification but that the 3% Mo alloy was preferable. It appears that 500°C is a reasonable limit for routine pulses but that an occasional pulse to 600°C would not be damaging.

The uranium-molybdenum alloy was tested to determine its ultimate tensile strength and its ductility at various temperatures. It was demonstrated that the room temperature properties were adequate to prevent damage in machining and handling; that the yield stress at the temperature corresponding to the maximum design pulse was five times the calculated peak stress at the notch of the fuel element; and that the fracture load at the temperature corresponding to the maximum design pulse was ten times the calculated peak

dynamic load. Fuel element failure is predicted to occur at a pulse yield of 4×10^{17} fissions with a pulse width of 200 μsec, that is for a pulse of twice the planned size. For assemblies containing appreciable amounts of moderator the pulse widths would be larger and the stresses would therefore be reduced. In these systems the maximum fuel temperature is more likely to be determined by the onset of uranium-steel reactions which start at 600°C (about 5×10^{17} fissions).

The hydrogenous moderator has to be fabricated into rather complicated shapes yet be undamaged when heated to 250°C or, locally, to 280°C. It must not distort in such a way as to obstruct the fuel channels and it must not suffer appreciable loss of hydrogen. An epoxide resin containing 15% of aluminium (for ease of machining) was selected. Its chemical composition by w/o, is:-

Aluminium	28.2
Carbon	50.8
Hydrogen	4.30
Oxygen	16.70

Its density is 1.44 g cm^{-3} and it contains 0.062 g of hydrogen per cm^3.

The weight loss is practically zero below 200°C but increases rapidly above 300°C. Allowing for the total time spent above 200°C during a life of 1000 pulses at 10% more than normal full yield, the expected loss of weight is 1%. Changes in linear dimensions of pieces held at 200°C for 16 hours were exceedingly small compared with the clearances provided. At temperatures exceeding 350°C the epoxy resin gives off a mixture of volatile decomposition products and at 400°C it is extensively damaged. The maximum working temperature for the bulk epoxy resin is taken to be 280°C.

SAFETY PRINCIPLES

When designing a reactor to operate in the prompt critical region questions of safety need particularly thorough consideration. The general principles of safety used in the design and operation of VIPER are as follows:-

(1) The reactor has the normal safety circuits and shut-down mechanisms appropriate to a low-power fast reactor system.

(2) There are additional fast-acting safety mechanisms and fast-response instruments of diverse characteristics to ensure rapid termination of the plateau heating following a pulse.

(3) Fuel element bowing which provides a possible positive reactivity temperature coefficient is eliminated by the core design, as described above. The expansion effect is tested by perturbation measurements in the steady-state phase of reactor commissioning.

(4) The reproducibility of the safety block, control rod and pulse rod drives is sufficiently accurate to ensure that the necessary accuracy of 0.5 cents is achieved in the starting point and in the reactivity increment for a reactor pulse.

(5) Thorough staff training and comprehensive operating instructions ensure that the proper procedures are used to

determine the reactivity increment required for a given prompt critical transient.

(6) Before prompt transients are undertaken, the adequacy of the fuel expansion and the Doppler coefficient as inherent shut-down mechanisms are first tested by a series of special fast-transient experiments in the sub-prompt critical region where manual control is still effective. The reactor transient, at for example a period of 0.5 sec, is allowed to develop until sufficient heating has taken place to change the reactor period appreciably. From measurements of the temperature rise and the change in period the prompt temperature coefficient can be determined to 20% accuracy.

(7) The reactor is contained in a strong concrete cell which would prevent any appreciable release of radioactive material if a reactor accident occurred.

FEATURES OF PARTICULAR RELEVANCE TO THE PHYSICS AND SAFETY PROBLEMS OF FAST REACTORS

Apart from its role in materials testing, the main interest of the VIPER reactor in the field of fast reactor physics is the use of the Doppler effect as a principal shut-down mechanism. The reactor provides a direct demonstration of the efficiency of this mechanism and, by subtracting the expansion effect, a quantitative check on Doppler effect calculations for ^{238}U systems. Additionally, since the composition and construction of the core are fairly uniform, the reactor can be used as a source of integral data for checking the nuclear cross section sets and the calculation methods used in general fast reactor calculations.

ACKNOWLEDGMENTS

Acknowledgment is due to Mr. E. Cann, Mr. L.J. Dalby, Mr. J. Howden, Dr. R.L. Long, Mr. J. Sullivan and Mr. G.V. Stupart for their contributions to the design and construction of the reactor.

REFERENCES

[1] MCTAGGART, M.H., GOODFELLOW, H., LONG, R.L., WEALE, J.W., Measurements of the physics characteristics of the fast pulsed reactor, VIPER, Symposium on Fast Reactor Physics and Related Safety Problems, these Proceedings, SM-101/44.

[2] WIMETT, T.F., et al., Godiva II. An unmoderated pulsed irradiation reactor, Nuclear Sci and Eng. 8 (1960) 691.

[3] WEALE, J.W., McTAGGART, M.H., GOODFELLOW, H., PATERSON, W.J., "Exponential and Critical Experiments", Vol. 1, IAEA, Vienna (1964) 159.

MEASUREMENTS OF THE PHYSICS CHARACTERISTICS OF THE FAST PULSED REACTOR, VIPER

M.H. McTAGGART, H. GOODFELLOW, R.L. LONG* AND J.W. WEALE
UNITED KINGDOM ATOMIC ENERGY AUTHORITY,
ALDERMASTON, BERKS, UNITED KINGDOM

Abstract

MEASUREMENTS OF THE PHYSICS CHARACTERISTICS OF THE FAST PULSED REACTOR, VIPER. The VIPER pulsed reactor was first made critical on 26 May 1967. The physics measurements carried out during its subsequent commissioning to prompt critical are described. These experiments include the measurement of reaction rate distributions, perturbation effects, neutron spectrum, neutron lifetime, and prompt temperature coefficients of reactivity. The measured characteristics of prompt critical transients are compared with predictions based on calculated expansion and Doppler effects.

INTRODUCTION

The VIPER pulsed reactor, first made critical on 26th May 1967 produced its first full size pulse on 17th August 1967. The reactor is described fully in an earlier paper to this symposium [1]. This paper describes the measurements made of the physics properties of the reactor during the commissioning process. The pulse is terminated by an inherent temperature coefficient of reactivity and the main purpose of the commissioning is to establish the existence and magnitude of this coefficient before driving the reactor prompt critical. Other measurements include control rod calibrations to ensure that an adequate margin for control is provided, reaction rate distributions, measurements of the reactor spectrum, pulsed and Rossi-alpha determinations and estimates of the steady state temperature coefficient of reactivity.

CRITICAL SIZE AND REACTIVITY CALIBRATIONS

The core (shown in Figure 3 of reference [1]) contains 547 fuel elements, 90 in each safety block and 367 in the centre box. All the stacks of matrix materials which contain fuel have the same composition, namely 12 × 0.95 cm layers of epoxy and 12 × 0.95 cm, 9 × 0.48 cm layers of copper (Figure 4 of reference [1] shows the precise stacking pattern). The surrounding stacks, ie, the end ones in each safety block and the five stacks at the north end of the central block, are made entirely from copper matrix pieces.

The reactor was loaded initially with 180 fuel elements in the central block and 90 in each safety block. Fuel elements were added 30 at a time after each initial approach, which consisted in raising both safety blocks and all four control rods, until criticality was achieved with a loading of 534 fuel elements, both coarse control rods raised and both fine rods partly raised.

The calculated critical mass, including a margin for reactivity control and adjustments for the central cavity, was 73 kg of ^{235}U with an estimated uncertainty of 5%. The first critical loading contained 82.6 kg of ^{235}U. The core plan shown in Figure 3 of reference [1] which, with 2 elements removed to provide access holes, is the core used for all pulsed operation contains 84.2 kg of ^{235}U (228 kg U-Mo alloy).

---

* Temporary Research Associate July 1966 to August 1967 at Aldermaston, on leave of absence from Nuclear Engineering Department, University of New Mexico, Albuquerque, New Mexico, United States of America.

TABLE I

Control Rod Worths and Gradients

	Coarse Control Rods		Fine Control Rods	
	CRA	CRB	FRA	FRB
Total worth (cents)	113	116	20	21
Boron content (g)	430	460	69	71
Maximum gradient (cents/in.)	12.35	12.8	2	2
Maximum reactivity insertion rate (cents/sec)	1.2	1.2	0.1	0.1

The control rods were calibrated by positive period measurements making movements of about one inch at a time. The period was obtained either from a fission counter feeding pulses directly to the Argus 400 on-line computer, programmed to process the data directly, or from a current integrating device fed by a large current fission chamber [2]. The total worths of the control rods and their maximum gradients are given in Table I. Differences in the mass of enriched boron in the coarse rods are responsible for the observed difference in their worths. Significant interaction was observed between each fine rod and its adjacent coarse one.

The delayed neutron data used to relate the observed period to reactivity were from Keepin [3], with allowance made for the delayed neutron spectrum and the calculated proportion of ^{238}U fissions.

An estimate of the reactivity removed by each safety block was made by observing the sub-critical multiplication of the reactor chemical source as the block was moved. Each removes 6.7 dollars, of which 3.7 dollars is removed in less than 80 msec after a trip signal. Thus, together they provide a shut-down margin of 13.4 dollars and even if one were to fail the other gives a shut-down margin of nearly 5%. Reflector lid movement is worth approximately 1 dollar per inch.

The pulse rod as first loaded contained a 2 in. length of 1.55 in. diameter fuel alloy and was worth 72 cents. At its fast drive speed the maximum rate of reactivity insertion was 14 dollars per second. A full size pulse rod for this core inserts reactivity at 25 dollars per second when driven in at full speed.

The reproducibility of safety blocks, control rods, pulse rod and reactor lid in terms of reactivity change is better than 0.1 cent or 10^{-5}. Deviations in the critical setting vary from day to day by up to 0.2 cents, mainly due to changes in the reactor or cell temperature.

REACTOR MEASUREMENTS AT OR BELOW DELAYED CRITICAL

^{235}U and ^{238}U fission rate distributions were measured throughout the reactor core to establish (a) the expected temperature distribution during pulsed operation, and (b) the power calibration of the reactor instrumentation. 1/4 in. fission chambers and ^{235}U foils were used, the chambers located in the access holes provided in the central block and the foils in less accessible positions such as inside the safety blocks. Foils were also placed at the important thermocouple positions and on the pulse rod so as to relate the measured temperature to the peak temperature which occurs inside the pulse rod. The fission product γ activity of the foils was measured and normalised

to the fission rate in the known mass of ^{235}U in the 1/4 in. chamber at a suitable position.

The observed distribution was not cylindrically symmetric because of (a) the perturbing effect of the steel membranes forming the edges of the central block and each safety block, (b) the presence of partly withdrawn boron control rods adjacent to the safety blocks, and (c) the extra steel at the centre in the lattice plate.

Some fission chamber results are shown in Figure 1. All fission rates were measured with the pulse rod in the core.

Small cylindrical samples were driven into the core using the central block access holes as for fission counter scans. By compensating for the insertion by adjusting a fine control rod, the reactivity changes which they produced were measured. 93% ^{235}U, depleted uranium and U-Mo fuel alloy samples were included. Figure 2 shows the worth per gram of ^{235}U as a function of the distance of the sample from the core centre. Extrapolating from the measured positions to the core centre gives 0.17 ± 0.02 cents/g of ^{235}U which agrees with the calculated value of 0.19 ± 0.01 and with the value of 0.17 ± 0.05 cents/g deduced from the pulse rod. The worth of ^{238}U is 1.2 ± 0.4% of ^{235}U. Similarly, integrating the worth per unit mass along the length of a fuel pin gives the total reactivity effect of removing a fuel pin at any position. Except at the core edges integrals calculated in this way agreed with the reactivity changes observed when fuel elements were removed.

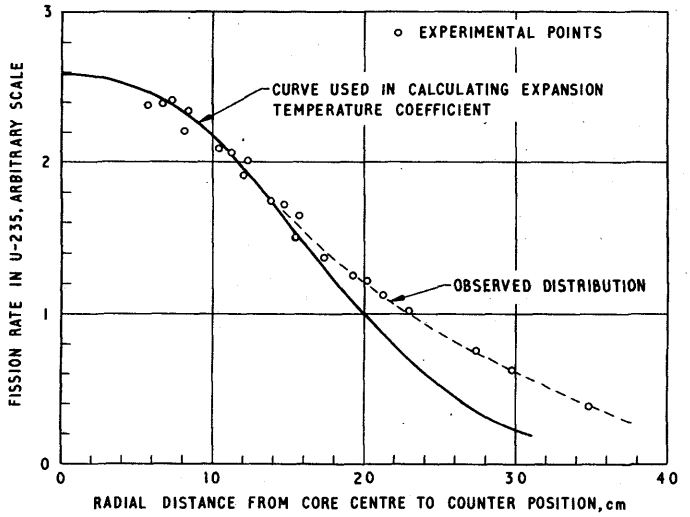

FIG.1. ^{235}U fission reaction rate distribution.

Confirmation of the magnitude of the expansion temperature coefficient

In the design stage a model of the temperature distribution and the worth distribution was used to estimate the expected expansion and bowing coefficients of reactivity. Both distributions were assumed to be spherically symmetric and products were formed of the fuel movement and the gradient of the worth in the direction of movement. The fuel movement terms included (a) expansion of the fuel rods, and (b) bowing, with and without the restraint of the three lattice plates. The products were integrated over the reactor core cylinder. The curves used in these calculations are shown in Figures 1 and 2 to compare them with the observed distributions. The calculations

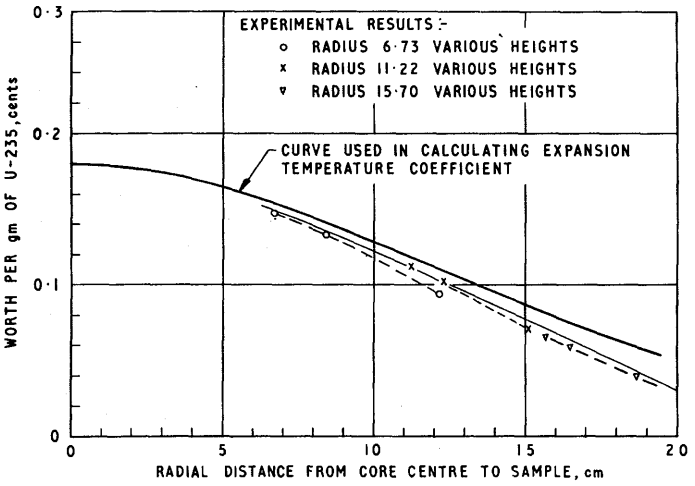

FIG.2. Reactivity worth of ^{235}U as a function of position.

gave an expansion coefficient of -3×10^{-6} °C^{-1}. The experiments indicate that the worth gradients are somewhat steeper and that the expansion coefficient is therefore larger than calculated, probably at least -5×10^{-6} °C^{-1}. The lattice plates ensure that the bowing coefficient is negative and probably nearly zero. The calculations show that it is less than 1/3 of the expansion coefficient.

Spectrum measurement and the Doppler effect

The spectrum in the core region was measured from 140 eV to 100 keV by time of flight and the result is shown in Figure 7 of reference [4]. It is this region which contributes to the Doppler effect. The observed flux is higher than the calculated flux. The calculations of Doppler effect used artificially generated resonance data [5] and the SWAN code [6] for the criticality calculations. The core temperature was assumed to be uniform and, for a temperature change from 0 - 300°C, the coefficient calculated was -5.8×10^{-6} °C^{-1}. The measured spectrum indicates that the expected Doppler coefficient could be as much as a factor of two greater, ie, about -10^{-5} °C^{-1}.

Prompt neutron decay experiments

The prompt decay in VIPER was measured in the range from 2 dollars subcritical to delayed critical; the subcritical measurements were by a pulsed 14 MeV neutron source and the one at delayed critical was by Rossi-alpha [7]. Generally the decay was followed for 50 - 100 μsec before background effects obscured it. The results can be expressed as N(t) counts per unit time at time t. For each experiment $\alpha = \frac{1}{N}\frac{dN}{dt}$ was calculated as a function of time after the pulse (or in the case of Rossi-alpha after the initiating event). Figure 3 shows α at 20 μsec as a function of reactivity.

Alpha at delayed critical varied from $(4.0 \pm 0.15) \times 10^4$ sec^{-1} at 20 μsec to $(3.0 \pm 0.2) \times 10^4$ sec^{-1} at 80 μsec. The range of α is greater at ∿ 3.2 dollars subcritical where it decreases from $(12.8 \pm 0.15) \times 10^4$ sec^{-1} at 20 μsec to $(10.2 \pm 0.15) \times 10^4$ sec^{-1} at 35 μsec. These results are typical of reflected systems and give a smaller value of α at delayed critical than the calculated one of 6.7×10^4 (derived from the calculated β = 0.73% and $l = 1.09 \times 10^{-7}$ sec).

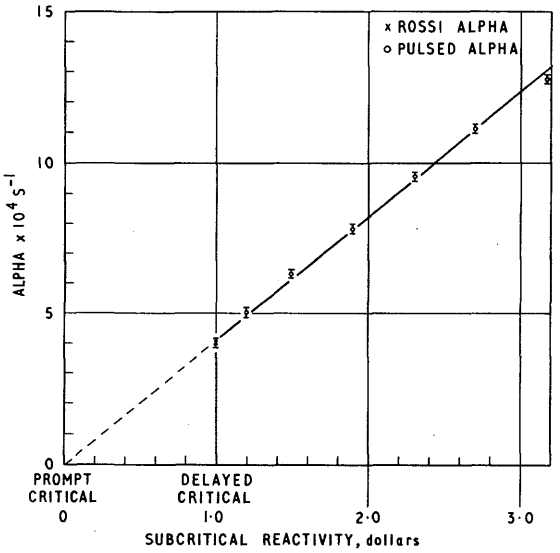

FIG.3. Pulsed and Rossi-alpha measurements.

High steady power operation

Operation at approximately 1.5 kW for 10 - 15 min was undertaken to establish (a) the power calibration of the high power instrumentation which does not give a measurable signal at the normal power of 1 - 10 W for steady state experiments, and (b) the steady state reactivity temperature coefficient. Both objectives were met in a 13 min run in which the core was heated by approximately 25°C. During the cooling afterwards the reactor was kept delayed critical at a power of 1 W and the reactivity change with temperature was measured. A coefficient of (0.10 ± 0.02) cents $°C^{-1}$ was measured while the core cooled from 40 to 30°C. The main error in the measurement is associated with the unusual temperature distribution which occurs during the cooling period.

An aluminium disc, attached to the copper plug in reflector hole B during this experiment was irradiated and the reactivity from the Al(n,α)Na reaction which has a 15 hour half-life was measured. This system then constitutes a calibrated total power integrating device. A disc was irradiated during most subsequent transients.

REACTOR OPERATION BETWEEN DELAYED AND PROMPT CRITICAL

Having established the basic reactor control parameters and properties, operation was extended to successively shorter asymptotic periods up to and beyond prompt critical. The phase of operation up to prompt critical has two main objectives: (a) to establish a value for the prompt negative temperature coefficient before prompt pulsed operation, and (b) to extrapolate the measured period versus reactivity relationship to prompt critical. The latter objective is achieved by varying the pulse rod reactivity insertion up to the limit set by its size and measuring the reactor period. A new larger pulse rod is then substituted and the same process extended to the new limit. The period versus reactivity relationship can be measured in this way up to prompt critical without operating at power levels which produce a significant temperature rise. Objective (a) is achieved by operating at power levels where heating occurs so that the prompt temperature coefficient causes the

reactivity to change and so alters the reactor period. Although the time-scale of the heating is longer than during a prompt pulse, the reactor power and temperature measurements enable an accurate estimate to be made of the temperature coefficient before the reactor is made prompt critical. This was shown by operating a number of successively faster transients.

Reactor period up to prompt critical

Figure 4 shows the measured period as a function of reactivity insertion up to near prompt critical. To avoid confusion the reactivity scale is in standard inches of coarse control rod A. The inhour relation based on the calculated delayed neutron fractions is included. The deviations are consistent with there being too small an abundance for both the two shortest lived delayed neutron groups. The periods were measured from the current output of a scintillator plus photomultiplier; the signal was converted to digital form and stored as a function of time in the on-line computer which was then used to calculate the period.

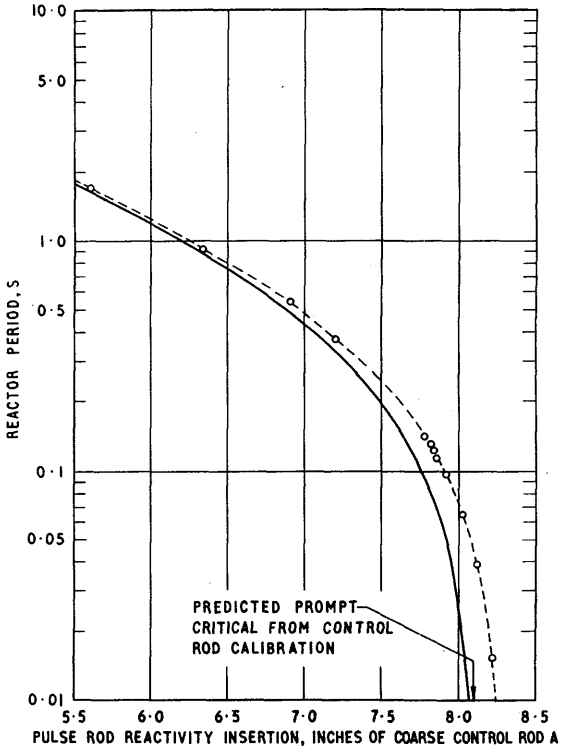

FIG.4. Reactor period as a function of pulse rod reactivity insertion.

Sub-prompt critical heating transients

The shape of the power versus time function in a heating transient depends on the temperature coefficient and the inhour relationship. A series of calculations of a one-point model of the VIPER core was made using the RKSF kinetics code [8] for a range of temperature coefficients from $+0.5 \times 10^{-5}$ to 1.8×10^{-5}. Figure 5 shows a typical set. Because it is difficult to normalise the

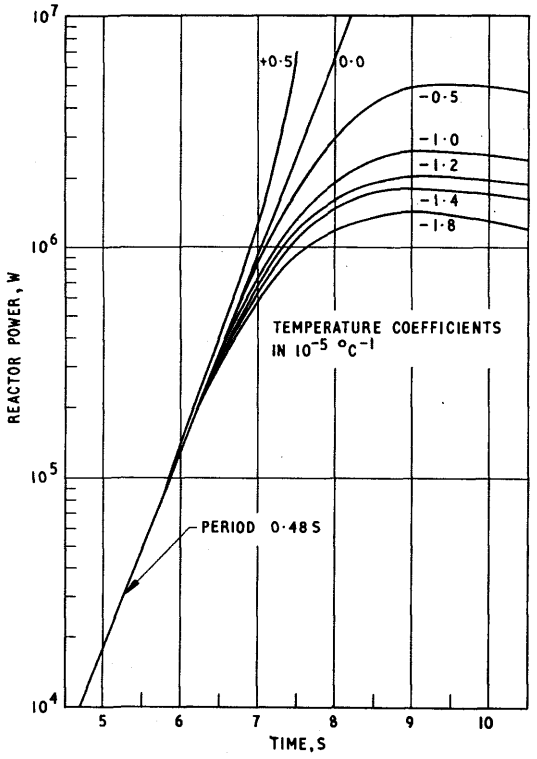

FIG.5. Power plotted against time during sub-prompt critical heating transient.

observed power versus time curve to these calculations the calculations were re-plotted as shown in Figure 6 which gives the ratio of the power for a zero temperature coefficient (P_z) to the power calculated for a range of values of the temperature coefficient (P_{T_C}) as a function of the average temperature rise of the fuel.

Three heating transients were performed and Table II summarises their characteristics. The average fuel temperature was observed by recording thermocouples at the tops of central fuel pins. The core average temperature rise computed from the measured fission distribution was 1.23 ± 0.08 times the observed temperature rise of these thermocouples.

TABLE II

Characteristics of Sub-prompt-critical Heating Transients

Nominal Reactivity Insertion (cents)	Asymptotic Period (sec)	Observed Rise (°C)	Approximate Duration of Heating (sec)
70	1.70	7	3
85	0.54	34	2
95	0.122	10.5	0.3

The observed and average temperature rise are included in Figure 6, which shows that the reactor behaviour is consistent with a temperature coefficient of between -1.4 and -1.6 × 10^{-5} °C^{-1}. The shape of the observed curve differs from the shape of the calculated ones. A possible explanation is that the thermocouples are losing heat to their surroundings during the transients. This tends to shift the observed curve towards the right and would imply that the temperature coefficient was smaller than the "best" value of -1.6 × 10^{-5} °C^{-1} though still within the estimated uncertainty of about 20%. In the transient shown in Figure 6 preliminary estimates of the temperature loss suggest it might be 5 to 10°C.

As a precaution against operating errors, the first two heating transients were done with a pulse rod worth less than one dollar. The third was done with a rod worth 121.5 cents, making a control rod adjustment of 26 cents to obtain the 95 cent transient. This confirmed that the temperature coefficient was large and negative, and the commissioning was then allowed to proceed beyond prompt critical.

SUPER-PROMPT CRITICAL HEATING PULSES

Having reached the limiting period of 15 msec shown in Figure 4 the next transient, estimated to have a period of 3 msec, showed the spike followed by a plateau typical of a super-prompt critical transient. At this stage a different method of extrapolating to find the prompt period and the yield was employed. The inhour equation gives

$$\rho = \frac{\ell}{\beta T} + \sum_i \left(\frac{a_i}{1+\lambda_i T}\right),$$

where ρ = reactivity (in dollars) above delayed critical
ℓ = prompt neutron lifetime
β = delayed fraction
a_i = relative abundance of the i^{th} group of delayed neutrons
λ_i = decay constant of the i^{th} group of delayed neutrons
T = reactor period

If prompt critical is defined as the point where $\Sigma\left(\frac{a_i}{1+\lambda_i T}\right)$ is effectively equal to unity, and ρ-1 is the prompt reactivity then (ρ-1) versus T^{-1} is a straight line with slope β/ℓ. The quantity β/ℓ is equal to the Rossi-alpha value at delayed critical. At first a slope of 4 × 10^4 sec^{-1} was used to extrapolate from one pulse to the next, but as the measurements proceeded an experimental curve was constructed. Figure 7 shows the reciprocal of the observed prompt period as a function of reactivity insertion. The slope is 4.6 × 10^4 sec^{-1} compared with the Rossi-alpha value of between 3 and 4 × 10^4 sec^{-1}.

The yield (or temperature rise) in a super-prompt pulse is also expected to be proportional to the prompt reactivity (see equation (1) of reference [1]). Figure 8 shows the pulse temperature rise, ie, the total rise less the plateau heating, as a function of reactivity insertion.

Since the maximum insertion with the 3.75 in. (121.5 cent) pulse rod was only capable of producing a pulse 80% of the design limits, set at 280°C bulk epoxy temperature and 400°C maximum fuel temperature, a larger pulse rod was installed. It was 4.125 in. long (131.5 cents ≡ 10.654 in. of coarse control rod A) and the full yield was reached by inserting its full worth reduced by 0.454 in. of coarse control rod A, ie, a nominal insertion of 126 cents. This resulted in an estimated average fuel temperature rise of 250°C a peak fuel temperature rise of 390°C, ie, a peak fuel temperature of 420°C, and a peak epoxy temperature of 290°C. The number of fissions produced was about 3 × 10^{17}.

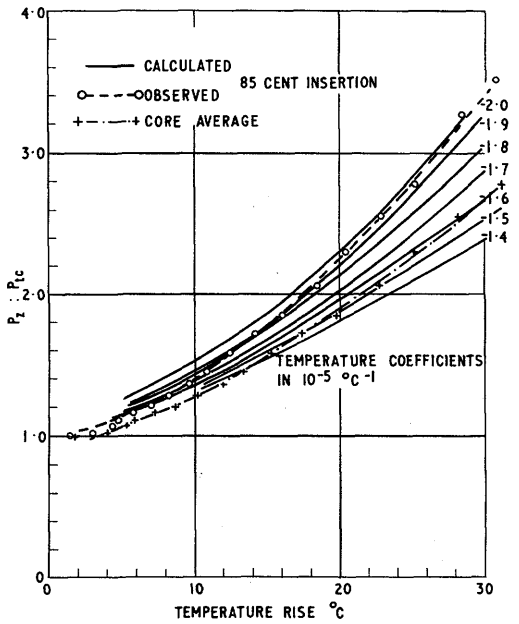

FIG.6. $P_Z : P_{tc}$ as a function of temperature rise during a sub-prompt critical heating transient.

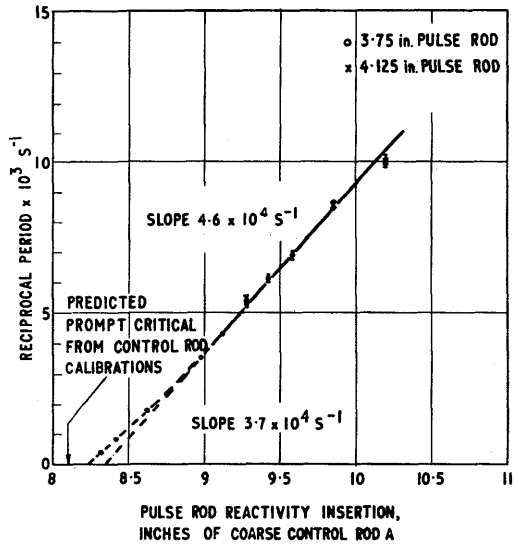

FIG.7. Reciprocal prompt reactor period plotted against reactivity insertion.

CHARACTERISTICS OF THE SUPER-PROMPT CRITICAL PULSE

The shape of the recorded pulse of mixed γ radiation and neutron flux is shown in Figure 9. The fast sequence timer was set to allow the plateau to be measured. For a full size pulse the timer is normally

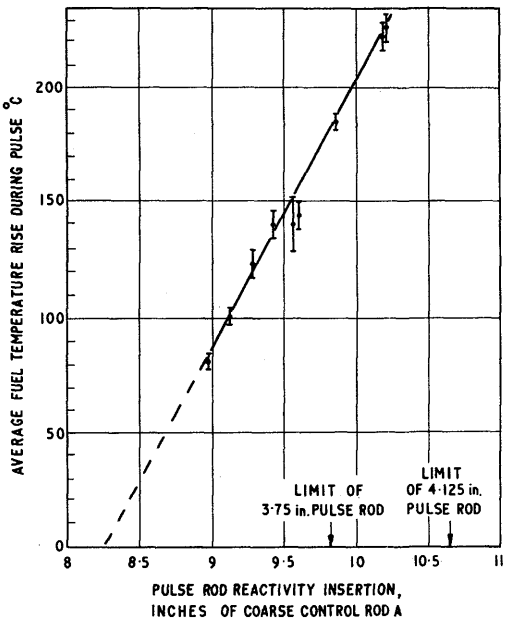

FIG. 8. Pulse temperature rise plotted against reactivity insertion.

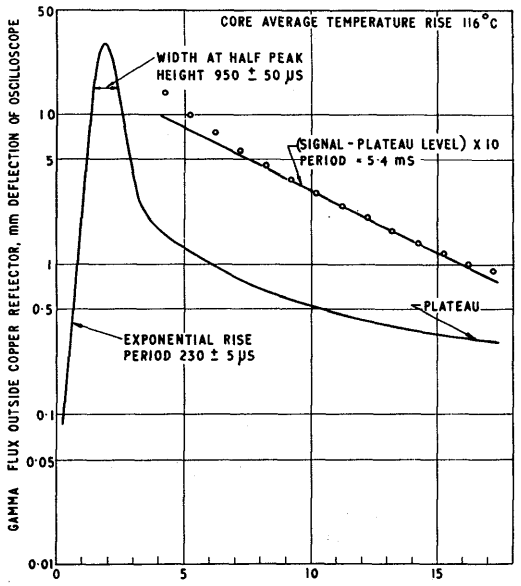

FIG. 9. Observed pulse shape.

set to start safety block movement within 5 ms of the pulse. The detector was a plastic scintillator viewed by a photodiode and produced a peak current of about a milliampere.

The pulse width is 4.5 - 4.8 times the prompt positive period of the power rise compared with the value 3.5 expected (equation (2) of reference

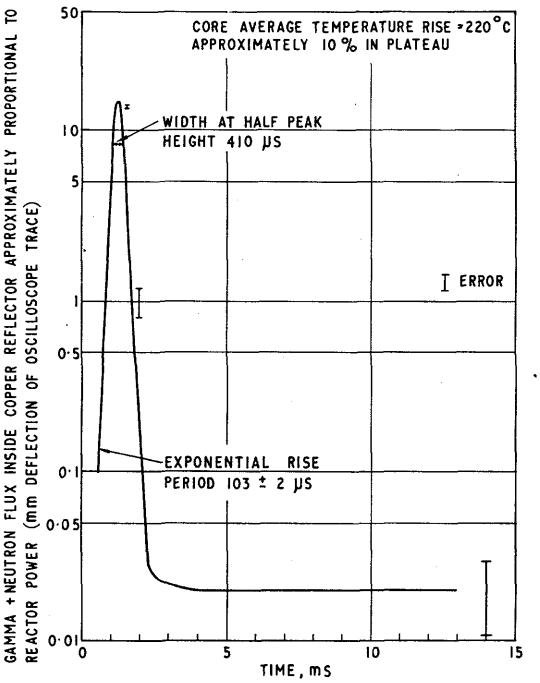

FIG.10. Typical pulse shape, full size pulse.

[1]). It is also asymmetric and if the nearly level plateau between t = 24 msec and 27 msec is subtracted from the trailing edge of the pulse a 5 msec decay is observed. The same decay is observed in all pulses. One suggestion for this broadening of the pulse and of the 5 msec delay was that an extra group of delayed neutrons with a 200 sec^{-1} time constant existed. The curvature of the line shown in Figure 7 suggested such a short lived group might be affecting the prompt kinetics; adding a group of 2% abundance and 200 sec^{-1} time constant produces this curvature.

The contribution of this group to the plateau was however much larger than the effect of adding a delayed neutron group with a 200 sec^{-1} time constant and a 2% abundance to the inhour equation. Tests were also done to see whether "room return" neutrons were responsible. The cell is approximately a 10 m cube and the flight time of a neutron to cross the cell is 5 msec. When most of the outer reflector surface of VIPER was covered with cadmium the observed pulse shape was entirely unaffected. The copper reflector itself is in any event a very effective shield for thermal neutrons. The possibility that VERA, which occupies the same cell and contains a large quantity of natural uranium, might be acting as a thermal fast convertor was also eliminated by covering it too with cadmium sheet. The VIPER pulse shape was unaffected.

More recently two pulse shape detectors were installed within the reflector. One of them was the same design as the scintillator and photodiode used outside the reflector which gave the pulse shape shown in Figure 9. However, it was exposed directly to the neutron and γ flux from the core and shielded by lead blocks from γ radiation from the cell walls and the outer surface of the reflector. The other was an evacuated fission chamber installed in the pulse rod cavity. It contained an electrode coated with ^{238}U. The pulse shapes produced by

both these detectors are virtually identical and it is shown in Figure 10. The pulse is narrower than the corresponding pulse given by the detector outside the reactor, its width at half peak is about 4 times the prompt positive period. The plateau is considerably reduced and is much closer to the expected pulse shape.

There is also evidence from dynamic thermocouple measurements and from dynamic measurements of the expansion of a fuel element during and immediately after a pulse that the pulse shape of Figure 10 is correct and the 5 msec period plateau is due to the positioning of the detector. Thermocouple and fuel expansion indicate that nearly 90% of the heating in a full size pulse occurs during the pulse and about 10% during the plateau, which lasts about 30 msec. The integral of Figure 9 would indicate that only 60 - 70% of the heating occurred during the pulse.

PROMPT TEMPERATURE COEFFICIENT

From the shape and yield in the prompt pulse it is possible to derive a better value of the temperature coefficient than that obtained in the sub-prompt heating transients. The yield versus reactivity relation (equation (1) of reference [1]) shows that the pulse yield is proportional to the excess prompt reactivity and inversely proportional to the temperature coefficient. However the plateau yield is not negligible and has to be subtracted from the total yield to obtain the pulse yield. The broadening effect of the pseudo-group of 5 msec delayed neutrons has also to be taken into account. Though variations in the plateau heating could introduce errors, the pulse yield has been arbitrarily defined as the heat produced up to a time 15 msec after the pulse. This is the temperature shown in Figure 8 as a function of reactivity insertion. Figures 7 and 8, according to equations (1) and (2) of reference [1], should both be straight lines and should intercept the reactivity axis at the same point, namely at prompt critical. A straight line fit to Figure 8 passing through the axis at the same point as the curve in Figure 7 gives a temperature coefficient of -0.0174 ± 0.0007 in. of coarse control rod A per °C temperature rise. This, converted to reactivity on the basis of the original control rod calibration, is (-0.215 ± 0.008) cents $°C^{-1}$ or (-1.57 ± 0.06) × 10^{-5} $°C^{-1}$. However, if prompt critical is redefined as the intercept of the reciprocal period curve with the axis, rather than the point predicted from the control rod calibrations (Figure 7), ie, 8.24 in. of coarse control rod A, the conversion gives a coefficient of (-0.211 ± 0.008) cents $°C^{-1}$ and (-1.54 ± 0.06) × 10^{-5} $°C^{-1}$. This is somewhat larger than the calculated coefficient which is the sum of -5 × 10^{-6} $°C^{-1}$ for expansion and -6 × 10^{-6} $°C^{-1}$ Doppler giving a total of -1.1 × 10^{-5} $°C^{-1}$. The time of flight spectrum indicates that the Doppler effect is probably larger than the calculated value. A detailed calculation of the expansion coefficient is being made and by subtracting this from the total coefficient it should be possible to obtain a more accurate estimate of the Doppler coefficient.

ACKNOWLEDGMENTS

The authors gratefully acknowledge the assistance given by Mr. Paterson (spectrometry and pulsed alpha), by Mr. Stupart (high power instrumentation), by Mr. Benjamin (the Argus computer), by Mr. McCormick (the RKSF kinetics calculations) and by the supervisory and operating staff of the reactor.

REFERENCES

[1] WEALE, J.W., GOODFELLOW, H, McTAGGART, M.H., WARNKE, E.G., A new fast pulsed reactor, VIPER, Symposium on Fast Reactor Physics and Related Safety Problems, these Proceedings, SM-101/39.

[2] VINCENT, C.H., SAPSFORD, G., A precision current integrator, Nucl. Instr. and Methods 14 2 (1962) 160.

[3] KEEPIN, G.R., "Physics of Nuclear Kinetics", Tables 4-7, Addison-Wesley (1965).

[4] PATERSON, W.J., BENJAMIN, P.W., HATTON, D., McCORMICK, W.B., WEALE, J.W., Neutron spectrum measurements in the fast reactor assembly VERA 19A and tests of the time of flight spectrometry method in VERA 5A and VIPER 1, Symposium on Fast Reactor Physics and Related Safety Problems, these Proceedings, SM-101/40.

[5] BRISSENDEN, R.J., DURSTON, C., Proceedings of the conference on the application of computing methods to reactor problems, ANL-7050 (1965) p.51.

[6] BRICKSTOCK, A., DAVIES, A.R., SWAN, a multi-group one-dimensional diffusion code for the IBM 7030, AWRE Report No. 0-99/65 (1965).

[7] WEALE, J.W., PATERSON, W.J., GOODFELLOW, H., McTAGGART, M.H., Pulsed neutron research, IAEA Symposium (May 1965) Vol II p.759.

[8] BRICKSTOCK, A., DAVIES, A.R., RKSF. A reactor kinetics code for the IBM 7030, AWRE Report No. 0-4/66 (1966).

DISCUSSION

G.S. BRUNSON: What type of detector did you use to follow the reactor pulse?

M.H. McTAGGART: The detectors were plastic scintillators sensitive to both neutron and gamma radiations, and were not loaded.

J. RANDLES: Were the fuel elements used metallic, and if so were there any elastic oscillations caused by the thermal shock and what was the decay time of the oscillations?

M.H. McTAGGART: Yes, the elements were metallic. We have not observed elastic oscillations of amplitude greater than 5% of the total expansion, though our measuring instrument is not at present capable of resolving to better than about 3%.

W.H. KÖHLER: Could you give an idea of how long you would have to wait for the excursion to start after insertion of the pulse rod, if you did not use a pulsed source to initiate the transient?

M.H. McTAGGART: Although this phenomenon has been observed in reactors like GODIVA where the intrinsic source strength is low, our experience has been that a pulse is more likely to pre-initiate, that is, initiate from a naturally occurring source neutron rather than from our pulsed source. We have always used the pulsed source so would not have observed any delays and about one pulse in four has been pre-initiated.

PANEL DISCUSSION

Moderator: R.D. SMITH (United Kingdom)

Panel members:

K.H. BECKURTS (Federal Republic of Germany)
N.V. KRASNOYAROV (Union of Soviet Socialist Republics)
W.B. LOEWENSTEIN (United States of America)
R. RICHMOND (Switzerland)
F. STORRER (France)

R.D. SMITH (Moderator): A factor which may have a very great influence on the design of power reactors, and may even play a part in the choice of coolant, is the capture cross-section for plutonium. It is remarkable that, after so many years of fast reactor work, we still do not know the capture cross-section of perhaps the most important material, ^{239}Pu. Several papers (for example, SM-101/2, SM-101/41 and SM-101/43) have been presented on this topic, and I think it is fair to say that all of them strongly favour the idea that the so-called high values of α are more likely to be right than the values which have hitherto been in general use.

However, these nuclear data measurements still entail some uncertainty, especially in the 1-10 keV region, where the changes in α particularly affect sodium-cooled reactors and where it is very difficult to carry out nuclear physics measurements. Integral measurements are also subject to quite large errors and, as we have seen, have suggested that there are some additional unexplained discrepancies in the α value for ^{235}U.

It seems that the higher values of α may well be correct, but that values even lower than those we are using or considerably higher than those suggested are nevertheless possible.

This would merely be an interesting scientific problem were it not for the fact that the value of α has a particularly large effect on the breeding gain and hence on the economics of power reactors. The loss of a neutron by capture in plutonium has a double effect: you lose the neutron which could have given rise to another atom of ^{239}Pu, and you destroy an atom of ^{239}Pu in the capture process. How serious are the effects of a change in the value of α? A simple spherical calculation shows that, if you replace the older data for ^{239}Pu by the newer data, based on the higher capture values and on the slightly lower fission values of White, and then adjust the enrichment so that the system remains critical, the breeding gain declines by about 0.1, depending on the particular system under consideration. However, this may not be the whole story; if your previous criticality calculations have been shown by zero-power

experiments to be correct, then there must be an error in some other cross-section, and this must be altered in such a way as to maintain constant criticality. From this point the situation becomes increasingly complicated.

The trouble is that one does not know which other cross-sections may be wrong. It could be the ^{238}U cross-section (of course, a change in the ^{238}U cross-section gives rise to different effects in the core and in the blanket), but it could equally well be the steel cross-sections. In either case the change in breeding gain would be different. It does seem, however, that the α values we are using are too low and that breeding gains will be reduced to some extent. If that is so, it will affect the design of fast reactors, and I think we must therefore look more carefully at those designs in which the breeding gain is higher. With the sodium-cooled fast reactor, for example, this would mean added interest in the use of carbide fuel or metal blankets, although knowledge of α does not of course in itself give us a better breeding ratio.

Nevertheless, I think we do need to know as soon as possible what the values are, so that we can choose the right course for future development (for example, with regard to the emphasis to be placed on carbide fuel). My personal view, however, is that while we should obviously continue with nuclear physics and integral measurements, we shall not obtain sufficiently accurate values of α until we have carefully irradiated in power reactors known pure isotopes or isotopic mixtures and analysed the resulting material.

I should now like to ask the members of the panel for their views on three main points: the best α values; the effect these values will have on the design of power reactors; and the measurements that should be made in order to resolve this controversy.

I believe Mr. Beckurts has some graphs illustrating the data under discussion, so I shall ask him to speak first.

K.H. BECKURTS: To show how difficult it is to measure α for plutonium, I have prepared a short table summarizing the various available methods:

Methods of measuring α

A. Differential methods ($\rightarrow \alpha(E)$)

1. from $\eta = \nu \cdot \frac{\sigma_f}{\sigma_f + \sigma_c}$
2. from σ_t, σ_{nn}, σ_f, $\sigma_c = \sigma_t - (\sigma_f + \sigma_{nn})$
3. liquid scintillation tank; delayed identification of fission events
4. simultaneous fission and γ recording

B. Integral methods ($\rightarrow \overline{\alpha(E)}$)

1. reactivity perturbation
2. post-irradiation analysis

Method A1 works well with thermal neutrons. Its usefulness for fast neutrons, however, is limited by the fact that it is impossible to get "black" samples; nevertheless, it was used in early work in this field.

Method A2 is inherently inaccurate since σ_c is obtained as a difference of large numbers, which normally have substantial uncertainties.

Method A3 works very well with monoenergetic neutron beams, but it cannot normally be used in conjunction with time-of-flight methods since several microseconds are required for fission event identification.

Methods of the type A4 have not been used very much in the past and should be developed; a very promising example of such a method was described in paper SM-101/41. One slight drawback of such methods may be the fact that they entail additional normalization measurements.

The integral methods B1 and B2 are fairly accurate in determining the $\bar{\alpha}$ value. However, it is normally difficult to decide over which neutron spectrum averaging is performed.

Let us now turn to some actual results of α measurements. Fig. 1 shows values between 3 keV and 1 MeV. In addition to some early Soviet data obtained by method A1, there are two sets of more recent results obtained by method A3 and in good agreement. The Schmidt compilation is based on the more recent data, and I believe they are quite reliable. Nevertheless, since both sets of data were obtained by the same method, it would be useful to confirm them by means of an independent experiment. Additional points would be needed, especially between 80 keV and 200 keV.

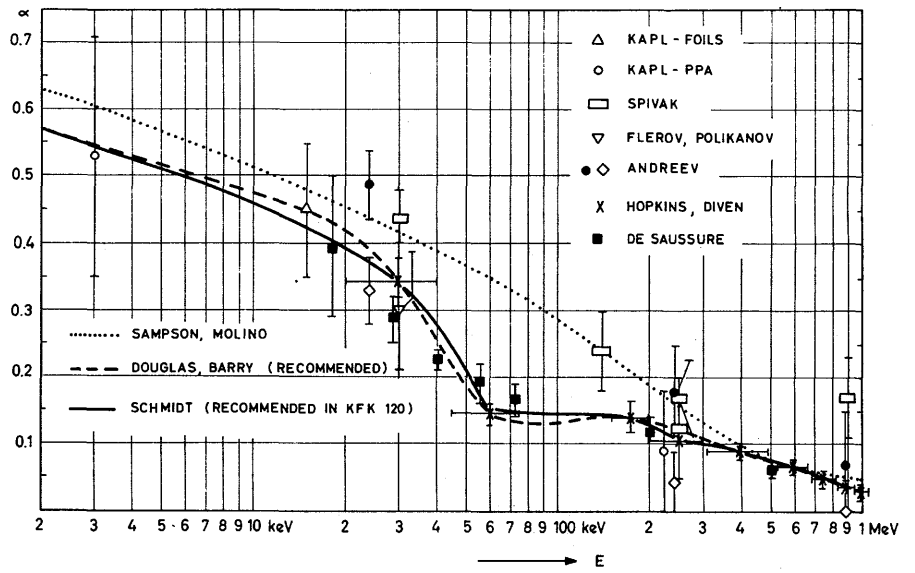

FIG. 1. Values for α in the range 3 keV to 1 MeV for ^{239}Pu.

Fig. 2 shows data in the range 100 eV-10 keV. The Schmidt curve is a smooth extrapolation of the high-energy data; it passes through the results of some early integral measurements and runs smoothly into

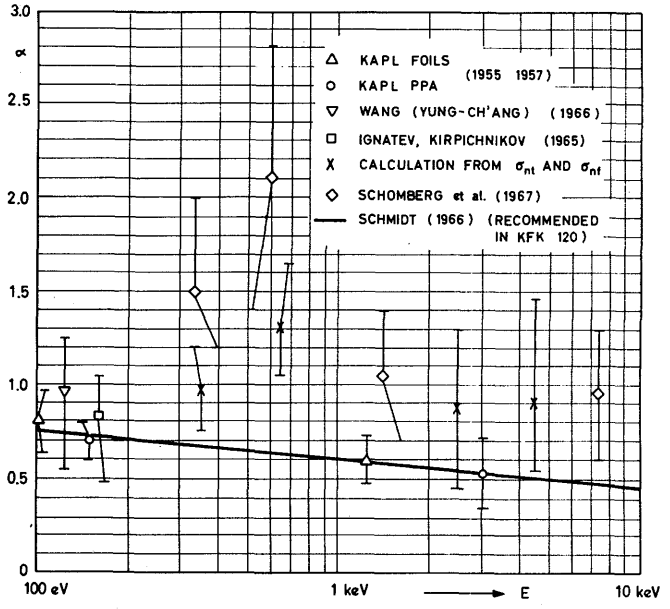

FIG.2. Values for α in the range 100 eV to 10 keV for ^{239}Pu.

low-energy data obtained by Ignatev et al. with method A4 and by Wang (Yung-ch'ang) with method A3. Although these data have so far seemed consistent, we have heard at this symposium reports concerning several new integral experiments and also Mr. Schomberg's new results, from which some points are plotted in Fig. 2. All these new data suggest that the Schmidt data should be taken as a lower limit, the probable α value being considerably higher. In view of the large error limits of the experimental data, it seems premature to recommend a new "best value".

In my opinion, more experiments in this energy range should be carried out and further methods of the type A4 developed (in this connection, the final results of the recent Harwell experiment should prove interesting). Moreover, use should be made of techniques such as that based on the slowing-down time spectrometer and of the nuclear explosion/time-of-flight method. It will also be necessary to perform more integral experiments.

W.B. LOEWENSTEIN: Regarding the question as to the best values of α, the error limits of the differential data are very large, and I therefore feel that, if one wished to design a reactor today, one would probably use material replacement data or some other integral data. In other words, one would take data that are consistent with measurements of the type ν-1-α rather than utilize differential data with large error limits. My reason for saying this is that, when there has in the past been a large discrepancy between ν as obtained from differential data and ν as implied by integral data, the integral data have later been substantiated. I think the same applies in the case of ^{240}Pu, for which the earlier integral

data now seem to be more or less consistent with the later differential measurements.

With regard to the possible effect of high α values for ^{239}Pu on the design of reactors, I suppose one could conceivably build a steam-cooled reactor in a modular array. In this way, one would certainly alleviate the α problem to some extent, though if one must use steam-cooled systems, one should perhaps go over to the ^{233}U-thorium cycle.

With regard to the measurements which still need to be made, Mr. Smith has already referred to a useful class of measurements which does not belong to the differential category and does not require the knowledge of a large number of parameters, namely irradiations of small samples of fairly pure materials, such as those which have been carried out in the EBR-1 and EBR-2 reactors. Admittedly these were carried out in very hard spectra, and the results are very difficult to interpret. However, I can imagine a series of such experiments, in which small samples are placed in various parts of high-flux reactors (e.g. SEFOR, Dounreay, EBR-2, BR-5) and surrounded with varying amounts of moderator to adjust the spectrum incident on the samples. While it is certainly very difficult to analyse such experiments, if one did enough of them one might perhaps get a feeling for the parameter that seems so elusive.

N.V. KRASNOYAROV: I should like to start by considering the measurements that need to be carried out in the future. With all due respect to the differential methods, which give the most detailed information, we must in the final analysis translate the energy-dependence of α into an effective α which will determine the actual breeding gain. This requires knowledge of the spectrum in which the calculations are being performed. However, there are many resonances which may interfere with one another, so that the question again arises of verifying differential measurements by integral methods.

It is, of course, necessary to make differential measurements, but what is most needed are high-precision integral measurements in realistic spectra that can be determined theoretically and experimentally. In my opinion, the long-term irradiation of pure samples (as suggested by Mr. Smith and Mr. Loewenstein) represents the best approach. I would mention that, for this purpose, one should distribute the samples not in random fashion, but in such a way that each sample is surrounded by materials that produce a definite spectrum.

A second approach that seems promising to me is the measurement of integral values such as α in actual spectra by relating capture gammas to the fission count. If we did this in a pulsed reactor using the time-of-flight method, we might obtain differential and integral values in a real spectrum.

I should now like to say a few words about the consequences of an increase in the value of α for plutonium.

Clearly, all reactors with a breeding coefficient near unity would become less efficient breeders, since their doubling time would have increased. Steam-cooled reactors would be affected most of all.

Although sodium-cooled reactors with oxide fuel would be affected more seriously than reactors with carbide and metallic fuels, we should

not stop the development of oxide fuels since we can expect sodium-cooled reactors with oxide fuels to give valuable sodium technology and reactor operation experience. Moreover, it is easy to convert from oxide to carbide or metallic fuels. Finally, I think it would be well worth considering oxide or carbide cores into which a number of metallic fuel sub-assemblies might be inserted, thereby forming local breeding zones and increasing the overall breeding rate.

R. RICHMOND: Measurements of the α value for ^{239}Pu reported during the past year have all given results indicating that the previously assumed values of α are significantly low in the energy region around 1 keV. The new results are consistent and all have relatively large error values. I therefore feel that we should take, as our current best value of α, a mean of the values indicated by these recent experiments, so as to reduce the effects of systematic errors in the individual measurements. In a typical power reactor spectrum this would lead to an α value 25-30% higher than the value given by the earlier data.

One important result of this higher α value will be to cause power reactor designers to move towards systems with harder neutron spectra in order to retain breeding performance. It will also be necessary to minimize the parasitic loss of neutrons by capture in structural materials in order to compensate, as far as possible, for the additional loss of neutrons by capture in ^{239}Pu.

As other speakers have already remarked, one of the most important ways of improving our knowledge of the α value for ^{239}Pu consists in irradiating plutonium samples in a fast power reactor and then performing an isotopic analysis. It is important, however, that such irradiations take place in a neutron spectrum characteristic of a civil power reactor. Fast power reactors currently in operation have much harder spectra and do not give a significant fraction of neutrons in the important 1-keV region, in which recent measurements have indicated the higher α values. It is worth noting in this connection that, until about a year ago, zero-energy experiments on plutonium-fuelled cores were restricted almost entirely to hard-spectrum systems. Because of the lack of neutrons in the 1-keV region, comparisons of measured and calculated values of k_{eff} for these systems are not relevant to the recently observed increases in α.

From the point of view of zero-energy measurements of α, I feel that, because of the importance of obtaining an accurate value, we should aim to improve both differential and integral measurements in order to avoid dependence on the systematic errors of one particular type of measurement. I understand, in this connection, that the differential measurements reported in paper SM-101/41 are expected ultimately to give errors of the order of 5-10%. This will significantly improve our knowledge of α. Similarly, the zero-reactivity measurements currently being carried out in ZEBRA on "clean" lattices will give significantly smaller errors than the experiments on more complicated lattices carried out in DIMPLE (paper SM-101/43), and the results should also substantially improve our knowledge of α.

F. STORRER: Mr. Beckurts has indicated two methods of measuring α in integral experiments. I would add a third method which, while less direct, should also shed some light on the value of α. I am referring to the adjustment of cross-sections which, as we heard in Session III, is becoming widely used. With this method one uses all available experimental information (e.g. critical masses, spectral indices, etc.), and not just information derived from experiments aimed specifically at the determination of α.

We have employed this method, and Table A, which is based on paper SM-101/58, shows the relative increase in α.

TABLE A. RELATIVE VARIATIONS IN α(E) FOR ^{239}Pu (BARRAKA METHOD)

Energy	$d\alpha/\alpha$
100 - 800 keV	+ 35%
10 - 100 keV	+ 15%
0.3 - 10 keV	+ 40%

Our reference α values (Table B) are essentially those of Lottin and de Saussure (Paris, Oct. 1966) above 20 keV and those of F.D.2 below 20 keV.

We do not claim that the figures in Table A are very accurate, especially since there are so few plutonium criticals. It is interesting to note, however, that they also show a general trend towards an increase in α. Everybody will probably agree that we need more plutonium criticals.

I think that most people attending this symposium are interested mainly in integral quantities; differential data and methods of calculation are secondary considerations.

Table C gives a partial answer to Mr. Smith's second question. It shows the effect of a 30% increase in α on certain asymptotic parameters of the central zone of Phenix. TRI stands for the internal conversion ratio and CNA for the spectral component of the sodium coefficient.

It should be noted that below 20 keV the new α values presented by Mr. Schomberg (paper SM-101/41) are 100% higher than our reference values.

The consequences of an increase in α are particularly detrimental to steam-cooled reactors, and the reports we have heard at this Symposium have therefore reassured us that our choice of sodium as a coolant was a good one.

As Mr. Vendryès said in his presentation of paper SM-101/66, we are preparing a careful isotopic analysis of the fuel coming out of Rapsodie. The views expressed during this panel discussion provide us with a new and powerful incentive for doing this very carefully, even though the spectrum of Rapsodie is harder than we would like.

TABLE B. ALPHA VALUES FOR ^{239}Pu (CADARACHE CROSS-SECTION SET)

E	α	E	α
14.5 - 3.68 MeV	0.002	3.36 - 2.04 keV	0.555
3.68 - 2.23 "	0.005	2.04 - 1.23 "	0.583
2.23 - 1.35 "	0.011	1.23 - 0.748 "	0.612
1.35 - 0.821 "	0.026	748 - 454 eV	0.647
821 - 498 keV	0.054	454 - 275 eV	0.700
498 - 302 keV	0.085	275 - 101 eV	0.803
302 - 183 "	0.110	101 - 22.6 eV	0.876
183 - 111 "	0.140	22.6 - 3.06 eV	0.674
111 - 67.4 "	0.170	3.06 - 0.414 eV	0.242
67.4 - 40.9 "	0.210	Th.	0.370
40.9 - 24.8 keV	0.301		
24.8 - 15.0 "	0.410		
15.0 - 9.12 "	0.500		
9.12 - 5.53 "	0.518		
5.53 - 3.36 "	0.547		

TABLE C. INFLUENCE OF HIGHER ^{239}Pu α VALUES ON CERTAIN PARAMETERS OF THE PHENIX CENTRAL ZONE

Energy	$d\alpha/\alpha$	dk/k	d TRI/TRI	d CNA/CNA	$d\ell/\ell$
50 keV - 1.4 MeV	+ 30%	- 0.5%	- 2.9%	- 2%	- 1%
0.2 keV - 50 keV	+ 30%	- 0.9%	- 5%	+ 20%	- 6%

I should like to make one final remark. An increase in α at low energies would tend to make the Doppler coefficient of plutonium less positive, or even negative. One should not discuss α values for plutonium without bearing in mind the unexpected results of Doppler experiments with plutonium samples.

D. STEGEMANN: I should like to ask Mr. Campbell what he thinks needs to be done to increase the accuracy of k-infinity measurements

of the type he mentioned in the paper by Arnold et al. (SM-101/43), which he presented.

C.G. CAMPBELL: I should first like to say that, in my opinion, k-infinity, which can at present be measured to within 0.5%, is not the limiting quantity in the determination of α (a detailed analysis of the contributions to the uncertainty in determination of α is given in Ref. [7] of SM-101/43). Clearly capture in ^{238}U relative to fission in ^{239}Pu is also an important quantity, and any systematic error in it is reflected directly in an uncertainty in the α value. Moreover, while fission values are less important, the uncertainty in the assumed value of ν for plutonium is of considerable significance.

In my opinion, we should be concentrating our efforts on improving our knowledge of ν as a function of energy and on differential measurements of α using integral measurements as a check. We must also learn more about ^{238}U capture and about plutonium fission relative to other fission rates. Finally, the information must be assembled in such a way as to be consistent with the uncertainties involved.

H.W. KÜSTERS: There is some disagreement on the influence of a higher α value on breeding; Mr. Storrer has predicted a 5% decrease in breeding gain for the Phenix reactor, while Mr. Smith has mentioned a figure of 0.1. Perhaps they would care to comment on this discrepancy.

R.D. SMITH: I think my opening remarks contained a hint of the explanation. One has to be very careful to define exactly what one means when one speaks about the effect of α on the breeding gain because, if one simply changes α, the reactor becomes sub-critical and one has to re-establish criticality. Perhaps Mr. Storrer would care to say how he maintained criticality.

F. STORRER: We did so by changing the enrichment.

Returning to the original question raised by Mr. Küsters, I would mention that the breeding ratio cited in my earlier statement was the internal breeding ratio (TRI) in the asymptotic mode. We predicted a 5% decrease in breeding gain as a result of a 30% increase in α. As indicated by Mr. Schomberg (paper SM-101/41), a 100% increase in breeding gain results in a 15% decrease in the internal breeding ratio and a decrease of 0.09 in the total breeding ratio. This is in agreement with the value quoted by Mr. Smith.

R.D. SMITH: I am afraid the time has come to close the discussion. In doing so, I should like to mention briefly those aspects of the Symposium that have appeared most interesting to me.

I have been struck by the increase in work on heterogeneity problems and by the number of interesting new methods of calculation discussed. There has been a noteworthy suggestion for setting up a standard spectrum assembly, and several proposals concerning the use of thermal reactors for fast reactor experiments. Finally, there is an increased interest in the study of steam-cooled fast reactors, which, whatever else one may think about them, certainly pose some interesting physics problems.

G. BRUNSON (Scientific Secretary): Before the Symposium closes I should like to make a few technical comments.

First, speakers have mentioned in passing the apparent discrepancy between measured and calculated lifetimes. The people who collect and analyse such data generally attribute this discrepancy to incorrect cross-section sets. As an experimentalist with some background in this particular field, I should like to warn against this assumption: there are four different experimental groups represented at this Symposium which have found significant discrepancies between the dollar as measured by the asymptotic positive period method and as measured by kinetic experiments such as Rossi-α or pulsed neutron die-away. The discrepancy has generally been found to be about 30%, although in one case, in the Rapsodie mock-up in the ZPR-3 reactor, the discrepancy was about 80%. Before these lifetime measurements are considered in the evaluation of cross-section sets, let us therefore try to understand them better.

Second, although a considerable number of papers have dealt with steam-cooled reactors, and particularly the coolant void effect in such reactors, I should like to know why more people are not working on reactors cooled by heavy steam. This approach might offer a way out of the coolant void problem.

Third, the reactors which we have been discussing may not be built for 5, 10 or 20 years, and in that time the physical and economic boundary conditions governing reactor design can change significantly. I should therefore like to leave you with the following question: what would be the effect on fast-reactor physics and design if an important break-through in thermonuclear research were to create a substantial market for tritium?

SYMPOSIUM ON FAST REACTOR PHYSICS AND RELATED SAFETY PROBLEMS

HELD AT KARLSRUHE, 30 OCTOBER - 3 NOVEMBER 1967

CHAIRMEN OF SESSIONS

Session I	B.I. SPINRAD	IAEA
Session II	S. YIFTAH	Israel
Session III	K.E.J. WIRTZ	Federal Republic of Germany
Session IV	M. BOGAARDT	Netherlands
Session V	F. STORRER	France
Session VI	E. HELLSTRAND	Sweden
Session VII	W.B. LOEWENSTEIN	United States of America
Session VIII	R.D. SMITH	United Kingdom
Session IX	M.F. TROYANOV	Union of Soviet Socialist Republics

SECRETARIAT OF THE SYMPOSIUM

Scientific Secretaries:	G.S. BRUNSON D.A. YASHIN	Division of Nuclear Power and Reactors, IAEA
Editor:	L.A. SELF	Division of Scientific and Technical Information, IAEA
Records Officer:	E.M. PEMBRIDGE	Division of Languages, IAEA
Administrative Secretary:	A. GREBENSTCHIKOV	Department of Technical Operations, IAEA

LIST OF PARTICIPANTS

AUSTRALIA

Gemmell, W.	Australian Atomic Energy Commission Research Establishment, Lucas Heights, Private Mail Bag, Sutherland, N.S.W.

AUSTRIA

Pucker, N.	Institute for Theoretical Physics, University of Graz, Universitätsplatz 5, 8010 Graz

BELGIUM

Debrue, J.G.C.G.	C.E.N., 200 Boerentang, Mol-Donk
De Coster, M.	C.E.N., 200 Boerentang, Mol-Donk
De Leeuw, Ghislaine	C.E.N., 200 Boerentang, Mol-Donk
De Leeuw, S.	C.E.N., 200 Boerentang, Mol-Donk
De Myttenaere, P.	BelgoNucléaire, S.A., 35, rue des Colonies, Bruxelles 1
De Raedt, C.M.J.	C.E.N., 200 Boerentang, Mol-Donk
Eglème, M.	BelgoNucléaire, S.A., 35, rue des Colonies, Bruxelles 1
Fabry, A.	C.E.N., 200 Boerentang, Mol-Donk
Minsart, G.L.J.	C.E.N., 200 Boerentang, Mol-Donk
Motte, F.	C.E.N., 200 Boerentang, Mol-Donk
Penelle, G.M.J.	Service "Etudes de Sécurité", C.E.N., 200 Boerentang, Mol-Donk
Rotter, W.	C.E.N., 200 Boerentang, Mol-Donk
Vandeplas, P.	C.E.N., 200 Boerentang, Mol-Donk
Van Dievoet, J-P.	BelgoNucléaire, S.A., 35, rue des Colonies, Bruxelles 1
Vanhaelewyn, R.A.L.	C.E.N., 200 Boerentang, Mol-Donk

BRAZIL

Ferreira, H.A.	Comissão Nacional de Energia Nuclear, Avenida Almirante Barroso, 81, 2°andar, Rio de Janeiro, E.G.

CANADA

Millar, C.H.	Atomic Energy of Canada Ltd, Chalk River, Ont.

CHINA

Chou, J-C.	Chung-shang Institute of Science and Technology, P.O. Box No.1-1, Lung-Tan, Taiwan

CZECHOSLOVAK SOCIALIST REPUBLIC

Čermák, J.	Institute of Nuclear Research of the Czechoslovak Academy of Sciences, Řež near Prague
Jirák, Z.	Ministry of Power, Jungmannova 29, Prague 1

FRANCE

Acket, C.	Groupement Atomique Alsacienne Atlantique, 20 Ave Edouard Herriot, 92-Le Plessis-Robinson
Barberger, M.	Electricité de France, Direction des Etudes et Recherches, 12 place des Etats-Unis, Paris 16e
Barré, J.	DRP/SETR, C.E.N., de Cadarache, B.P. No.1, 13-St.Paul-lez-Durance
Bouchard, J.	C.E.N., B.P. No.6, 92-Fontenay-aux-Roses
Bussac, J.	C.E.N. de Saclay, DEP/SPM, B.P. No.2, 91-Gif-sur-Yvette
Chapuis, J.	Alcatel, Société Alsacienne de Constructions Atomiques, 1, Ave Berthelot, 93-Sevran
Durand-Smet, R.	Société SOCIA, 48, rue la Boétie, Paris 8e
Ebersoldt, F.	Association Euratom-CEA, C.E.N. de Cadarache, DRP/SETR, B.P. No.1, 13-St.Paul-lez-Durance
Ferrari, A.	C.E.N. de Cadarache, B.P. No.1, 13-St.Paul-lez-Durance
Govaerts, P.	Association Euratom-CEA, C.E.N. de Cadarache, B.P. No.1, 13-St.Paul-lez-Durance
Jégu, J.	Groupement Atomique Alsacienne Atlantique, 20, Ave Edouard Herriot, 92-Le Plessis-Robinson
Khairallah, A.	C.E.N. de Cadarache, DRP/SETR, B.P. No.1, 13-St.Paul-lez-Durance
Kremser, J.	C.E N. de Cadarache, DRP/SECNR, B.P. No.1, 13-St.Paul-lez-Durance

Morawek, T.	Service d'Etudes de Sûreté Radiologique, Commissariat à l'Energie Atomique, 29-33 rue de la Fédération, Paris 15e
Mougniot, J-C.	C.E.N. de Cadarache, DRP/SECNR, B.P. No.1, 13-St.Paul-lez-Durance
Provost, L.E.L.	Commissariat à l'Energie Atomique, 29-33 rue de la Fédération, Paris 15e
Pujol, Martine	C.E.N. de Saclay, DEP/SPM, B.P. No.2, 91-Gif-sur-Yvette
Storrer, F.	C.E.N. de Cadarache, DRP/SETR, B.P. No.1, 13-St.Paul-lez-Durance
Tretiakoff, O.	C.E.N. de Cadarache, DRP/SECNR, B.P. No, 1, 13-St.Paul-les-Durance
Vendryès, G.	C.E.N. de Saclay, B.P. No.2, 91-Gif-sur-Yvette
Vidal, R.	C.E.N., B.P. No.6, 92-Fontenay-aux-Roses

GERMANY, FEDERAL REPUBLIC OF

Beckurts, K.	Kernforschungszentrum Karlsruhe, Postfach 947, 75 Karlsruhe
Böhm, W.G.	Abteilung Reaktorentwicklung, Siemens AG, 852 Erlangen
Böhme, R.	Kernforschungszentrum Karlsruhe, Postfach 947, 75 Karlsruhe
Comper, W.	Kernforschungszentrum Karlsruhe, Postfach 947, 75 Karlsruhe
Ehret, A.	Gutehoffnungshütte Sterkrade AG, 42 Oberhausen-Sterkrade
Eitz, A.W.	Rheinisch-Westfälisches Elektrizitätswerk AG, Kruppstr.5, 43 Essen
Engelmann, P.A.	Kernforschungszentrum Karlsruhe, Postfach 947, 75 Karlsruhe
Finke, G.	Kernkraftwerk-Betriebsgesellschaft mbH., 7501 Leopoldshafen
Gebhardt, W.	Interatom, Friedrich-Ebert-Str., 506 Bensberg
Günther, J.	Arbeits- und Sozialministerium Baden-Württemberg, Rotebühlplatz 30, 7 Stuttgart 1
Habermann, F.W.A.	Kernforschungszentrum Karlsruhe, Postfach 947, 75 Karlsruhe

Häfele, W.	Kernforschungszentrum Karlsruhe, Postfach 947, 75 Karlsruhe
Henzel, N.	Battelle-Institut e.V., Wiesbadener Str., 6 Frankfurt
Huschke, H.	Kernforschungszentrum Karlsruhe, Postfach 947, 75 Karlsruhe
Jager, W.K.L.	NUKEM, Nuklear Chemie und Metallurgie, Wolfgang bei Hanau
Jahns, A.	Institut für Reaktorsicherheit der Technischen Überwachungs-Vereine e.V., Lukasstr. 90, 5 Köln-Ehrenfeld
Jansen, A.	Kernforschungszentrum Karlsruhe, Postfach 947, 75 Karlsruhe
Joest, K-H.	Interatom, Friedrich-Ebert-Str., 506 Bensberg
Kiefhaber, E.	Kernforschungszentrum Karlsruhe, Postfach 947, 75 Karlsruhe
Kleinmann, A.	Wirtschaftsministerium Baden-Württemberg, Theodor-Heuss-Str.4, 7 Stuttgart
Kliefoth, W.	Ministerium für Wirtschaft und Verkehr des Landes Schleswig-Holstein, Düsternbrooker Weg 94, 23 Kiel
Koop, W.	Rheinisch-Westfälisches Elektrizitätswerk AG, Kruppstr.5, 43 Essen
Krug, H.H.	Forschungsstelle für Reaktorsicherheit, Tengstr.38, München
Küsters, H.	Kernforschungszentrum Karlsruhe, Postfach 947, 75 Karlsruhe
Lill, G.W.	Allgemeine Elektrizitäts-Gesellschaft, AEG-Hochhaus, Frankfurt/M.
Linhardt, J.	Bayerisches Staatsministerium für Wirtschaft und Verkehr, Prinzregentenstr.28, München 22
Maier, W.	Bayernwerk AG, Blutenburgstr.6, 8 München 2
Metzenroth, M.	Kernforschungszentrum Karlsruhe, Postfach 947, 75 Karlsruhe
Müller, A.	Abteilung für Reaktorentwicklung, Siemens AG, Postfach 325, 8520 Erlangen
Münster, H.K.	Interatom, Friedrich-Ebert-Str., 506 Bensberg
Olivier, H.	Ministerium für Wirtschaft, Mittelstand und Verkehr des Landes Nordrhein-Westfalen, Haroldstr.4, 4 Düsseldorf

Ording, B.	Deutsches Atomforum, Adenauerallee 240, Bonn
Pahlke, G.	Nordwestdeutsche Kraftwerke AG, Schöne Aussicht 14, 2 Hamburg 22
Pohl, W.K.	Oberste Baubehörde im Bayerischen Staatsministerium des Innern, München
Regnet, K.M.	Maschinenfabrik Augsburg-Nürnberg AG, Katzwangerstr.101, 85 Nürnberg
Ritz, L.	Kernforschungszentrum Karlsruhe, Postfach 947, 75 Karlsruhe
Ritz, H.	Kernkraftwerk-Betriebsgesellschaft mbH, 7501 Leopoldshafen
Schaffer, O.J.E.	Kernforschungsanlage Jülich des Landes Nordrhein-Westfalen e.V., Postfach 365, 517 Jülich
Schulze, E.	Gutehoffnungshütte Sterkrade AG, 42 Oberhausen-Sterkrade
Schuster, G.	Bundesministerium für wissenschaftliche Forschung, Heussallee, Bonn
Seufert, H.	Kernforschungszentrum Karlsruhe, Postfach 947, 75 Karlsruhe
Smidt, D.A.	Kernforschungszentrum Karlsruhe, Postfach 947, 75 Karlsruhe
Spenke, H.	Abteilung für Reaktorentwicklung, Siemens AG, Postfach 325, 8520 Erlangen
Spielvogel, F.J.	Maschinenfabrik Augsburg-Nürnberg AG, Katzwangerstr.101, 85 Nürnberg
Stegemann, D.	Kernforschungszentrum Karlsruhe, Postfach 947, 75 Karlsruhe
Teuchert, E.	Kernforschungsanlage Jülich des Landes Nordrhein-Westfalen e.V., Postfach 365, 517 Jülich
Wintzer, D.	Kernforschungszentrum Karlsruhe, Postfach 947, 75 Karlsruhe
Wirtz, K.E.J.	Kernforschungszentrum Karlsruhe, Postfach 947, 75 Karlsruhe
Wolf, L.	Kernforschungsanlage Jülich des Landes Nordrhein-Westfalen e.V., Postfach 365, 517 Jülich
Ziegler, A.	Abteilung für Reaktorentwicklung, Siemens AG, Postfach 325, 8520 Erlangen

INDIA

Rastogi, B.P.	Reactor Engineering Division, Eng. Hall No.1, Bhabha Atomic Research Centre, Trombay, Bombay-74

ISRAEL

Rothenstein, W.	Department of Nuclear Science, Technion - Israel Institute of Technology, Haifa
Segev, M.	Israel Atomic Energy Commission, Soreq Nuclear Research Centre, Yavne
Yeivin, Y.	Department of Theoretical Physics, Hebrew University of Jerusalem, Jerusalem
Yiftah, S.	Israel Atomic Energy Commission, Soreq Nuclear Research Centre, Yavne

ITALY

Azzoni, P.	Centro di Calcolo, C.N.E.N., Programma Reattori Veloci, Via Mazzini 2, Bologna
Calori, A.	C.N.E.N., Via Belisario 15, Rome
Campos Venuti Barca, Gloria	Istituto Superiore di Sanità, Laboratori di Fisica, Viale Regina Elena 299, Rome
Cecchi, P.	Centro di Calcolo, C.N.E.N., Programma Reattori Veloci, Via Mazzini 2, Bologna
Cecchini, G.	C.N.E.N., Centro di Studi Nucleari della Casaccia, Strada Provinciale Anguillarese, Rome
Cuoco, A.	C.N.E.N., Via Belisario 15, Rome
Galvagni, R.	C.N.E.N., Via Belisario 15, Rome
Melandri, Annamaria	Centro di Calcolo, C.N.E.N., Programma Reattori Veloci, Via Mazzini 2, Bologna
Salvatores, M.	C.N.E.N., Centro di Studi Nucleari della Casaccia, Strada Provinciale Anguillarese, Rome
Tavoni, R.	Centro di Calcolo, C.N.E.N., Programma Reattori Veloci, Via Mazzini 2, Bologna

JAPAN

Ishikawa, H.	Japan Atomic Energy Research Institute, Tokai-Mura, Naka-gun, Ibaraki-ken
Kuroi, H.	Japan Atomic Energy Research Institute, Tokai-Mura, Naka-gun, Ibaraki-ken

MEXICO

Prieto, F.E.	Comisión Nacional de Energía Nuclear, Avenida Insurgentes, Mexico, D.F.

NETHERLANDS

Bogaardt, M.	Technological University, Insulindelaan 2, Eindhoven
Bustraan, M.	Reactor Centrum Nederland, Petten (N.H.)
Coehoorn, J.	Reactor Centrum Nederland, Petten (N.H.)
Dragt, J.B.	Reactor Centrum Nederland, Petten (N.H.)
Kleijn, H.R.	Reactor Instituut, Berlageweg 15, Delft
Mos, A.P.J.	Reactor Centrum Nederland, Petten (N.H.)
Türkcan, E.	Reactor Centrum Nederland, Petten (N.H.)

POLAND

Arkuszewski, J.	Institute of Nuclear Research, Z-XXI, Otwock-Swierk
Dabek, W.	Institute of Nuclear Research, Z-XXI, Otwock-Swierk
Dabrowski, C.A.	Institute of Nuclear Research, Z-XXI, Otwock-Swierk

SPAIN

Alonso, A.	Junta de Energia Nuclear, Ciudad Universitaria, Madrid-3
Rodriguez-Mayquez, E.	Junta de Energia Nuclear, Ciudad Universitaria, Madrid-3
Verdaguer, F.	Junta de Energia Nuclear, Ciudad Universitaria, Madrid-3

SWEDEN

Behrenz, P.G.	Allmänna Svenska Elektriska AB, Fack, Västerås 1
Hellstrand, E.	AB Atomenergi, Studsvik, Nyköping
Jirlow, K.M.	AB Atomenergi, Liljeholmsvägen 32, Stockholm 43
Kockum, J.	Research Institute of Swedish Defence, Stockholm 80
Lindberg, M.O.J.	AB Atomenergi, Box 43041, Stockholm 43
Nilsson, E.T.R.	Reactor Safety Committee, Swedish Atomic Energy Board, Fack, Stockholm 2
Tirén, L.I.	AB Atomenergi, Studsvik, Nyköping
Vollmer, H.	AB Atomenergi, Studsvik, Nyköping

SWITZERLAND

Hager, H.G.	Eidgenössisches Institut für Reaktorforschung, 5303 Würenlingen
Hälg, W.	Dept. of Nuclear Engineering, Swiss Federal Institute of Technology, Universitätsstr. 20, 8006 Zürich
Junker, K.	Eidgenössisches Institut für Reaktorforschung, 5303 Würenlingen
Killias, H.R.	General Electric Co., Research & Development Center, Pelikanstr.37, 8001 Zürich
Moser, H.P.	Eidgenössisches Institut für Reaktorforschung, 5303 Würenlingen
Richmond, R.	Eidgenössisches Institut für Reaktorforschung, 5303 Würenlingen
Rutgers, E.	Laboratoire de Génie Atomique, Ecole Polytechnique de l'Université de Lausanne (EPUL), Avenue de Cour 33, 1000 Lausanne
Sarlos, G.	Institut Fédéral de Recherches en Matière de Réacteurs, 5303 Würenlingen
Telleschi, P.	Eidgenössisches Institut für Reaktorforschung, 5303 Würenlingen
Utzinger, E.A.	Eidgenössisches Institut für Reaktorforschung, 5303 Würenlingen
Wälti, P.	Institut für Reaktortechnik der Eidgenössischen Technischen Hochschule, Universitätsstr.20, 8006 Zürich

UNION OF SOVIET SOCIALIST REPUBLICS

Krasnoyarov, N.V.	Atomic Reactor Research Institute, Melekess
Troyanov, M.F.	Physics and Engineering Institute, Obninsk

UNITED KINGDOM

Beynon, T.D.	Department of Physics, University of Birmingham, P.O. Box 363, Birmingham 15
Campbell, C.G.	Fast Reactor Physics Division, Room 334, Bldg. A 32, UKAEA, AEE Winfrith, Dorchester, Dorset
Cave, L.	Atomic Power Constructions Ltd., Vigilant House, Sutton, Surrey
Constantine, G.	UKAEA, AERE, Harwell, Didcot, Berks.

Gibbs, D.C.C.	Department of Nuclear Science and Technology, Royal Naval College, Greenwich, London, S.E.10
Gratton, C.P.	Room 233, Bldg. A 32, UKAEA, AEE Winfrith, Dorchester, Dorset
Hart, W.	UKAEA, Risley, Warrington, Lancs.
McTaggart, M.H.	UKAEA, AWRE, Aldermaston, Berks.
Mann, J.E.	UKAEA, Risley, Warrington, Lancs.
Pendlebury, E.D.	Bldg. E1, UKAEA, AWRE, Aldermaston, Berks.
Pickering, W.J.	Atomic Power Constructions Ltd., Sutton Court Road, Sutton, Surrey
Rowlands, J.L.	UKAEA, AEE Winfrith, Dorchester, Dorset
Schomberg, M.G.	UKAEA, AERE, Harwell, Didcot, Berks.
Scott, J.A.	Nuclear Design and Construction Ltd, Cambridge Road, Whetstone, Leics.
Smith, R.D.	UKAEA, Risley, Warrington, Lancs.
Tait, D.	UKAEA, DERE, Dounreay, Caithness
Vaughan, R.I.	Nuclear Plant Design Branch, Central Electricity Generating Board, Walden House, Cathedral Place, London, E.C.4
Weale, J.W.	UKAEA, AWRE, Aldermaston, Reading, Berks.
Wright, H.A.	Inspectorate of Nuclear Installations, Ministry of Power, Millbank, London, S.W.1

UNITED STATES OF AMERICA

Albrecht, R.W.	Department of Nuclear Engineering, University of Washington, Seattle, Wash.
Foell, W.K.	Nuclear Engineering Department, University of Wisconsin, Madison, Wisc.
Gurewitsch, A.M.	General Electric Co., Schenectady, N.Y.
Hannum, W.H.	Fast Reactor Physics Division, UKAEA, AEE Winfrith, Dorchester, Dorset, United Kingdom.
Köhler, W.H.	Department of Nuclear Engineering, Texas A&M University, College Station, Texas
Livolsi, A.Z.	Babcock & Wilcox Co., Lynchburg, Va.

Loewenstein, W.B.	Argonne National Laboratory, 9700 S. Cass Ave., Argonne, Ill. 60439
Pitterle, T.A.	Atomic Power Development Associates, 1911 First St., Detroit, Mich.
Shon, F.J.	Division of Operational Safety, US Atomic Energy Commission, Washington, D.C. 20545

YUGOSLAVIA

Sušnik, I.	Nuclear Institute "Josef Stefan", Jamova 39, Ljubljana

INTERNATIONAL ORGANIZATIONS

E.N.E.A.

Solanes, Marie	38 Boulevard Suchet, Paris 16e, France.

EURATOM

Ancarani, A.	Euratom, 51, Rue Belliard, Bruxelles 4, Belgium
Calamida, I.	Euratom C.C.R., BR 2, Mol, Belgium
Dalle Donne, M.	Kernforschungszentrum Karlsruhe, Postfach 947, 75 Karlsruhe, Fed. Rep. of Germany.
Lenders, H.K.J.	Euratom C.C.R., BR 2, Mol, Belgium
Patzelt, H.	Euratom, 51, Rue Belliard, Bruxelles 4, Belgium
Randles, J.	Euratom, C.C.R., Ispra, Varese, Italy
Rief, H.	Euratom C.C.R., Ispra, Varese, Italy

IAEA

Sultan, M.	Department of Safeguards and Inspection, IAEA, 11 Kärntner Ring, 1010 Vienna, Austria

AUTHOR INDEX

Roman numerals are volume numbers. Arabic numerals underlined refer to the first page of a paper. Other Arabic numerals refer to a contribution to the discussions.

TRANSLITERATION INDEX

Абагян, Л.П.	Abagyan, L.P.
Бондаренко, В.В.	Bondarenko, V.V.
Воропаев, А.И.	Voropaev, A.I.
Голубев, В.И.	Golubev, V.I.
Голяев, Н.Д.	Golyaev, N.D.
Звонарев, А.В.	Zvonarev, A.V.
Зиновьев, В.П.	Zinoviev, V.P.
Колеганов, Ю.Ф.	Koleganov, Yu.F.
Колосков, Б.В.	Koloskov, B.V.
Краснояров, Н.В.	Krasnoyarov, N.V.
Николаев, М.Н.	Nikolaev, M.N.
Орлов, М.Ю.	Orlov, M.Yu.
Поливанский, В.П.	Polivansky, V.P.
Сироткин, А.М.	Sirotkin, A.M.
Слесарев, И.С.	Slesarev, I.S.
Троянов, М.Ф.	Troyanov, M.F.
Халов, Е.М.	Khalov, E.M.
Хромов, В.В.	Khromov, V.V.
Шагалин, Н.М.	Shagalin, N.M.
Юрова, Л.Н.	Yurova, L.N.

IAEA SALES AGENTS

Orders for Agency publications can be placed with your bookseller or any of our sales agents listed below:

ARGENTINA
Comisión Nacional de
Energía Atómica
Avenida del Libertador
General San Martin 8250
Buenos Aires - Suc. 29

AUSTRALIA
Hunter Publications,
23 McKillop Street
Melbourne, C.1

AUSTRIA
Georg Fromme & Co.
Spengergasse 39
A-1050, Vienna V

BELGIUM
Office international de librairie
30, avenue Marnix
Brussels 5

BRAZIL
Livraria Kosmos Editora
Rua do Rosario, 135-137
Rio de Janeiro

Agencia Expoente Oscar M. Silva
Rua Xavier de Toledo, 140-1° Andar
(Caixa Postal No. 5.614)
São Paulo

BYELORUSSIAN SOVIET SOCIALIST REPUBLIC
See under USSR

CANADA
The Queen's Printer
Ottawa, Ontario

CHINA (Taiwan)
Books and Scientific Supplies
Service, Ltd.,
P.O. Box 83
Taipei

CZECHOSLOVAK SOCIALIST REPUBLIC
S.N.T.L.
Spolena 51
Nové Mĕsto
Prague 1

DENMARK
Ejnar Munksgaard Ltd.
6 Nörregade
Copenhagen K

FINLAND
Akateeminen Kirjakauppa
Keskuskatu 2
Helsinki

FRANCE
Office international de
documentation et librairie
48, rue Gay-Lussac
F-75, Paris 5e

GERMANY, Federal Republic of
R. Oldenbourg
Rosenheimer Strasse 145
8 Munich 8

HUNGARY
Kultura
Hungarian Trading Co. for Books
and Newspapers
P.O.B. 149
Budapest 62

ISRAEL
Heiliger and Co.
3 Nathan Strauss Street
Jerusalem

ITALY
Agenzia Editoriale Internazionale
Organizzazioni Universali (A.E.I.O.U.)
Via Meravigli 16
Milan

JAPAN
Maruzen Company Ltd.
6, Tori Nichome
Nihonbashi
(P.O. Box 605)
Tokyo Central

MEXICO
Librería Internacional
Av. Sonora 206
Mexico 11, D.F.

NETHERLANDS
N.V. Martinus Nijhoff
Lange Voorhout 9
The Hague

NEW ZEALAND
Whitcombe & Tombs, Ltd.
G.P.O. Box 1894
Wellington, C.1

NORWAY
Johan Grundt Tanum
Karl Johans gate 43
Oslo

PAKISTAN
Karachi Education Society
Haroon Chambers
South Napier Road
(P.O. Box No. 4866)
Karachi 2

POLAND
Ośrodek Rozpowszechniana
Wydawnictw Naukowych
Polska Akademia Nauk
Pałac Kultury i Nauki
Warsaw

ROMANIA
Cartimex
Rue A. Briand 14-18
Bucarest

SOUTH AFRICA
Van Schaik's Bookstore (Pty) Ltd.
Libri Building
Church Street
(P.O. Box 724)
Pretoria

SPAIN
Librería Bosch
Ronda de la Universidad 11
Barcelona

SWEDEN
C.E. Fritzes Kungl. Hovbokhandel
Fredsgatan 2
Stockholm 16

SWITZERLAND
Librairie Payot
Rue Grenus 6
1211 Geneva 11

TURKEY
Librairie Hachette
469, Istiklâl Caddesi
Beyoğlu, Istanbul

UKRAINIAN SOVIET SOCIALIST REPUBLIC
See under USSR

UNION OF SOVIET SOCIALIST REPUBLICS
Mezhdunarodnaya Kniga
Smolenskaya-Sennaya 32-34
Moscow G-200

UNITED KINGDOM OF GREAT BRITAIN AND NORTHERN IRELAND
Her Majesty's Stationery Office
P.O. Box 569
London, S.E.1

UNITED STATES OF AMERICA
National Agency for
International Publications, Inc.
317 East 34th Street
New York, N.Y. 10016

VENEZUELA
Sr. Braulio Gabriel Chacares
Gobernador a Candilito 37
Santa Rosalía
(Apartado Postal 8092)
Caracas D.F.

YUGOSLAVIA
Jugoslovenska Knjiga
Terazije 27
Belgrade

IAEA publications can also be purchased retail at the United Nations Bookshop at United Nations Headquarters, New York, at the news-stand at the Agency's Headquarters, Vienna, and at most conferences, symposia and seminars organized by the Agency.

In order to facilitate the distribution of its publications, the Agency is prepared to accept payment in UNESCO coupons or in local currencies.

Orders and inquiries from countries where sales agents have not yet been appointed may be sent to:

Distribution and Sales Group, International Atomic Energy Agency,
Kärntner Ring 11, A-1010, Vienna I, Austria

INTERNATIONAL
ATOMIC ENERGY AGENCY
VIENNA, 1968

PRICE: US $12.00
Austrian Schillings 310,-
(£5.0.0; F.Fr. 58,80; DM 48,-)